INFORMATION TO USERS

This manuscript has been reproduced from the microfilm master. UMI films the text directly from the original or copy submitted. Thus, some thesis and dissertation copies are in typewriter face, while others may be from any type of computer printer.

The quality of this reproduction is dependent upon the quality of the copy submitted. Broken or indistinct print, colored or poor quality illustrations and photographs, print bleedthrough, substandard margins, and improper alignment can adversely affect reproduction.

In the unlikely event that the author did not send UMI a complete manuscript and there are missing pages, these will be noted. Also, if unauthorized copyright material had to be removed, a note will indicate the deletion.

Oversize materials (e.g., maps, drawings, charts) are reproduced by sectioning the original, beginning at the upper left-hand corner and continuing from left to right in equal sections with small overlaps.

Photographs included in the original manuscript have been reproduced xerographically in this copy. Higher quality 6" x 9" black and white photographic prints are available for any photographs or illustrations appearing in this copy for an additional charge. Contact UMI directly to order.

Bell & Howell Information and Learning
300 North Zeeb Road, Ann Arbor, MI 48106-1346 USA
800-521-0600

UMI®

Université d'Ottawa · University of Ottawa

Université d'Ottawa · University of Ottawa

FACULTÉ DES ÉTUDES SUPÉRIEURES ET POSTDOCTORALES

FACULTY OF GRADUATE AND POSTDOCTORAL STUDIES

BURKE, Stephen J.

AUTEUR DE LA THÈSE - AUTHOR OF THESIS

M.A.Sc. (Civil Engineering)

GRADE - DEGREE

Department of Civil Engineering

FACULTÉ, ÉCOLE, DÉPARTEMENT - FACULTY, SCHOOL, DEPARTMENT

TITRE DE LA THÈSE - TITLE OF THE THESIS

An Experimental Study on the Non-Destructive Evaluation of Corroded Bridge Steel

Michel Bruneau

DIRECTEUR DE LA THÈSE - THESIS SUPERVISOR

EXAMINATEURS DE LA THÈSE - THESIS EXAMINERS

J. Gardner

M. Saatcioglu

N. Holtz

J.-M. De Koninck, Ph.D.

LE DOYEN DE LA FACULTÉ DES ÉTUDES SUPÉRIEURES ET POSTDOCTORALES

SIGNATURE

DEAN OF THE FACULTY OF GRADUATE AND POSTDOCTORAL STUDIES

An Experimental Study on the Non-Destructive Evaluation of Corroded Bridge Steel

(Chapter 1 to Chapter 8)

by

Stephen J. Burke

Thesis submitted to the School of Graduate Studies
in partial fulfilment of the requirements for the
Master of Applied Science Degree in Civil Engineering
under the auspices of the
Ottawa-Carleton Institute for Civil Engineering

September 2000

Department of Civil Engineering, University of Ottawa
Ottawa, Canada, 2000

To my family

Abstract

Many older steel bridges have been affected by the deteriorating effects of corrosion. As bridges age and the material loss caused by both pitting and uniform corrosion becomes more severe, the structural capacity of the various members becomes questionable. An experimental investigation was undertaken to non-destructively quantify the effects that the uniform and pitting corrosion have upon the steel's load carrying and hysteretic energy dissipating capabilities. Various non-destructive evaluation technologies were reviewed in an attempt to determine which methods would be best suited for the purpose of creating accurate thickness and roughness maps of the corroded steel. Existing corroded bridge steel was non-destructively evaluated using the various technologies and tensile and cyclic tests were then performed to determine the accuracy of the various methods' thickness and roughness mapping methods.

Acknowledgments

My sincere thanks go to my supervisor, Dr. Michel Bruneau, for all his help, insight and patience throughout this work. I would also like to thank the technicians at the University of Ottawa machine shop and structures laboratory, Mr. Frank Clyburn, C.G.S.B. Level III and Mr. Mike Partridge, C.G.S.B. Level II of Steel Inspection Services, Mr. Bill Cole, P.Eng. Of Baycar Steel, Mr. Ted Chapman, C.E.T. of the National Research Council, Mr. Bob Stachnick of the Testex Corporation, the Veeco Corporation, the Zygo Corporation, Dr. Bryan Kaye of Laurentian University, Dr. David Schindel, P.Eng. Of Micro Acoustics, Mr. Bill Woodson, C.E.T. of the Canadian General Standards Board, and Mr. Bryan Parkinson, P.Eng. of J.L. Richards and Associates for their guidance and advice throughout this work and their donations of time and materials. Finally, I would like to acknowledge my family for their endless support throughout my life and studies.

Table of Contents

List of Tables

List of Figures

Notations

B,	Overall length of a structural section, mm
E_{TOT},	Total energy dissipation, KN-mm
E_{NORM},	Normalized energy dissipation,
E_E,	Elastic energy dissipation, KN-mm
E_P,	Plastic energy dissipation, KN-mm
E_X,	Modulus of elasticity, MPa
E_{SH},	Modulus of strain hardening, MPa
F_Y,	Yield stress, MPa
G_{XY},	Shear Modulus, MPa
I,	Moment of inertia, mm^2
L,	Distance between the applied load and the under side of the cyclic specimens, mm
M_P,	Plastic moment, KN-m
P,	Applied force, KN
PR_{XY}, PR_{XZ},	Poisson's Ratio
PV,	Maximum peak to valley height, μm
R_A,	Arithmetic mean roughness, μm
R_{TM},	Mean peak to valley roughness, μm
R_Z,	Ten point height of irregularity roughness, μm
RMS,	Root mean square roughness, μm
t,	Thickness of a material, mm
Z,	Plastic modulus, mm^3
Δt,	Percentile difference in mean thickness between two cyclic test specimens, %
ΔR_T,	Percentile difference in ten point height of irregularity roughness between two cyclic test specimens, %
ΔED_{EST},	Estimated difference in total energy dissipation between two tests, %
ΔED_{EXP},	Experimental difference in total energy dissipation between two tests, %
ΔED%,	Difference between the estimated and experimental difference in total energy dissipation between two tests, %

Δ_Y,	Yield displacement, mm
σ^2,	Variance of a sample
σ,	Standard deviation of a sample
σ_X,	Standard error of the mean
σ_Y,	Yield stress of a steel, MPa
σ_U,	Ultimate stress of a steel, MPa
σ_{SH},	Strain hardening stress of a steel, MPa
δ,	Fractional dimension
ϵ_Y,	Yield strain of a steel, mm/mm
ϵ_U,	Ultimate strain of a steel, mm/mm
ϵ_{SH},	Strain hardening strain of a steel, mm/mm
$\bar{x}$,	arithmetic mean of a sample

CHAPTER 1
INTRODUCTION

1.1 Statement of the Problem

Bridge rehabilitation is one of the more challenging and expanding fields in structural engineering today. With ever tightening government budgets, less money is being made available to care for the ageing infrastructure. As a result, owners are often not able to provide funding for complete demolition and replacement of all but the most deteriorated structures. Designers are therefore being asked to provide safe, economically sound design solutions for rehabilitation, rather than replacement of structures. Arriving at this solution requires the structural evaluation of the existing structure which can become quite complicated when the bridge is significantly corroded and situated in a seismically active area.

In new construction, the size, strength and capacity of all of the building materials used in the project are specified by the designer. This information can then be used to perform an accurate engineering evaluation to fully understand how the structure will react to the anticipated earthquake loading. In structural rehabilitation, a large portion of the structure to be analyzed has been in existence for some time and its member's capacities have been deteriorated by corrosion. The designer must therefore first make an attempt to quantify what capacity remains in the existing structure before he/she can proceed with producing a retrofit design that will accomplish the desired goals of the project.

Uniform and pitting corrosion are two of the more common types of corrosion. Uniform corrosion accounts for a large percentage of the total material loss from a bridge. It acts over large areas of steel and causes a decrease in cross sectional area of structural members. From a

designer's point of view, any loss of cross sectional areas corresponds to a decrease in the capacity of the member. Pitting corrosion is much more localized than uniform corrosion. It occurs in small areas on the steel surface such as where there is a break in the member's protective paint coating. Material loss from pitting corrosion is not as much of a concern to engineers as the potential for the pits to act as stress raisers during cycling. In those steel members that are expected to yield and dissipate energy during an earthquake, this may result in unstable cyclic behavior occurring before the full energy of the earthquake has been dissipated. Conceptually, if a single defect or notch is present on the surface of the material, the notch will act as a stress raiser causing a plastic zone and crack nucleation to initiate at the defect's tip. The crack will then propagate through the cross section until the load cannot be carried any longer. In terms of the fatigue of corroded materials, the surface is covered with potential stress raising pits and defects caused by the chemical attack of corrosion. If crack nucleation occurs at many of these defects the many different plastic zones will only have to propagate through the material until they reach the adjacent area of cracking, rather than through the entire cross section, to cause failure.

In terms of assessment of corrosion damage, the methods currently available to the designer are mostly qualitative and overly conservative. Periodic inspections of a bridge are an excellent method of monitoring the overall, relative degradation of a structure and determining what members have deteriorated to a point that they require complete replacement. However, it is not possible to perform an accurate engineering analysis of the structure, such as may be required for an earthquake retrofit project, from an inspectors qualitative field notes and photographs. Current practice is to analyze the structure using conservative factors of safety to account for the corrosion damage that has occurred. In terms of the relative cost of a project, this procedure may be acceptable for small scale projects aimed more towards structural maintenance where only a few members of the structure will need to be replaced. However, for larger scale retrofit projects, where the costs are high, any step towards a more conservative analysis results in large increases in the total project cost.

Currently, when an engineer must evaluate an existing corroded steel bridge to bring it up to current earthquake resistant design codes he/she can not simply analyze the structure using the original sections that were used in construction; instead he/she must make conservative judgements as to what capacity remains in the members from an inspectors qualitative field notes and photographs. For example, he/she may make an assumption that a certain member has been corroded to 40% of it's original cross sectional area. Two problems with this approach are apparent. First, the corrosion attack was probably not uniform over the entire cross section, for the full length of the member. The electrochemical reaction that causes corrosion is likely to be more aggressive in areas where water can pool. This could be at a connection or perhaps at the flange to web intersection. The possibility therefore exists that certain portions of the member are 60% corroded and others are only 20% deteriorated which may matter in certain instances. Secondly, the designer has assumed that corroded material will exhibit stable hysteretic behavior. A limited number of corrosion fatigue tests (Bruneau and Zahrai, 1998) have shown that good hysteretic energy dissipation is possible, but only up to a certain point and in a way that could not be related to an analytical model. The result of such an assumption is that the project cost may be increased beyond what is actually required.

For these reasons, this research will focus on reviewing and comparing non-destructive techniques to produce continuous quantitative mapping of thickness and roughness of a corroded steel and investigating how these methods can be applied for estimating the low-cycle fatigue life of yielding corroded steel members, using some simple tests for this purpose. It is hoped that a better knowledge of the performance of cyclically loaded corroded steel will result from the analysis of the collected data. The thickness mapping will be used to produce finite element models of corroded bridge steel members and compare the analytical force displacement curves to actual monotonic experimental testing results. The roughness mapping will attempt to mathematically quantify the roughness of a corroded surface and determine if the numerical results have any relation to the energy dissipating capabilities of the material. More precisely, if an increase in surface roughness results in a decrease in the material's energy dissipation capabilities.

1.2 Objectives

The objectives of this thesis are as follows:

(i) To review various non-destructive testing technologies that are currently available and determine which methods would be best suited to producing continuous mapping of the thickness and roughness of corroded steel.

(ii) Using the available techniques, perform a non-destructive evaluation of thickness of corroded specimens and create finite element models from the thickness data. The finite element models are being produced in an attempt to accurately quantify the variation in stresses across the specimen caused by the changing thicknesses and model what effect it has on the material's force-displacement curves. The resulting analytical force-displacement curves from the finite element modeling will be compared to those from the actual tensile testing to determine which method of testing produces the most accurate results and what effect the grid spacing of the discrete thickness measurements has upon the finite element model's performance.

(iii) Using the results from the monotonic testing, evaluate which method of thickness mapping shows the most potential and apply this method, along with those determined to be the most promising for roughness mapping to specimens to be tested cyclically.

(iv) Perform cyclic testing on corroded bridge girders.

(v) Analyze the results from the cyclic testing to determine if there is a correlation between the materials surface roughness or thickness and it's energy dissipation capabilities.

1.3 Outline of Thesis

This thesis has been written in eight major sections as are outlined below:

(i) In Chapter 2, the existing non-destructive testing technologies that are available to

perform the required tasks are reviewed.

(ii) In Chapter 3, the results of the non-destructive evaluation of the corroded tensile test specimens is reviewed.

(iii) In Chapter 4, an assessment of the results of the monotonic testing is performed using finite element modeling. This will determine the scope and method of testing to be performed on the cyclic test specimens.

(iv) In Chapter 5, the experimental approach is outlined.

(v) In Chapter 6, the experimental results are presented

(vi) In Chapter 7, the experimental results are compared and discussed.

(vii) In Chapter 8, conclusions and requirements for future research are discussed.

CHAPTER 2
REVIEW OF NON-DESTRUCTIVE TESTING TECHNIQUES

2.1 Introduction

Non-destructive testing is a term used to describe a broad range of physical methods used to evaluate the integrity of a material without impairing it's future use. The material's chemical and physical properties should not be altered in any way during the testing. In comparison, visual inspections result in more qualitative results based upon the inspector's experience. There is an extensive list of available techniques and a few are useful in creating accurate maps of surface roughness and thickness of corroded specimens. These methods are reviewed in this thesis to assess their limitations and applicability to the problems being studied. This review particularly addresses accuracy, portability for in-field testing, range of applications, level of operator training required, and cost.

It should be noted that although one review criteria is applicability to in-field testing, failure to meet this criteria is not a cause to reject the method. The situation may arise that methods are found that produce excellent thickness or roughness maps of the tensile specimens but have little or no value in terms of actual in-field evaluation of bridges. The possibility exists however, that useful insight may be gained into the performance of a corroded material using a technique that currently can only be used in a controlled environment. Also, the potential exists that future research may make the method more suited to in-field testing of corroded bridges.

2.2 Thickness Measurement

2.2.1 General

Thickness measurements are performed in industry to provide an estimate of what capacity remains in a material. These measurements must often be performed under in-service condition and their accuracy can affect the reliability of the subsequent engineering analysis. The objective here is to determine what methods are best suited to produce thickness maps of corroded steel tensile specimens. The methods to be reviewed in this section include: Dial calipers, screw micrometers. ultrasonic testing technologies and industrial radiography.

2.2.2 Precision Dial Calipers

Dial calipers are one of the most common tools used for determining the thickness of a material. They operate by simply pushing closed the calipers at the area of interest on the specimen and reading the resulting thickness from the dial. Dial calipers can be purchased for a broad range of thickness values at a relatively low cost. A common size of dial caliper that was considered for use in this thesis is shown in Figure 2.1 (Ultra test). It has a measurement range of 0 to 150 mm with increments of 0.0254 mm. The resulting accuracy of the measurements will be half of the increment, or 0.0127 mm.

Advantages of using the dial caliper are it's portability, simple operation and low cost. The main disadvantage of this method is that the dial caliper does not measure irregular surfaces well. For example, a thin area surrounded by thicker areas would not be properly measured by dial calipers. The head of the caliper would still be resting on the adjacent thick portion of the surface resulting

in the thinner measurement not being taken into account in the analysis. For this reason, precision dial calipers are not used for the experiments in this thesis.

2.2.3 Screw Micrometers

Another common method used to measure thickness is the screw micrometer, as can be seen in Figure 2.2. It is obvious from the construction of this instrument that it is better suited to creating an X-Y grid of thickness measurements across a corroded surface than the dial calipers because the C-shaped frame allows the user to position the anvil directly over the area of interest on the specimen. This allows for thinner sections to be properly measured without having adjacent areas interfere with the measurement. The interference limitation of this method now becomes the diameter of the anvil and spindle head. When a thickness reading is taken at a specific location on the surface, the measurement is not necessarily that of the thinnest section under the anvil. The thicker material surrounding the thinner area at the contact point is measured. Although this problem was the main reason for not using dial calipers, the magnitude of the error here has been significantly reduced. To further reduce the errors involved in properly measuring thinner areas on the surface, a variety of anvil attachments are available to further decrease the area of the measuring surface.

Advantages of this method are similar to those of the dial calipers. The method is simple to use, portable and inexpensive. The screw micrometers have an additional advantage of possessing a C-shaped frame that allows a more accurate mapping of a material's thickness. For this reason, screw micrometers, with a variety of anvil attachments are one of the methods retained for thickness mapping in the experiments. The screw micrometer purchased has a measurement range of 0 to 25.4 mm with 0.00254 mm increments and an anvil diameter of 6.35 mm. The resulting accuracy is again half of the increment, or 0.00127 mm. Additional anvil attachments to be used in this experiment were a 5.08 mm diameter ball, a 0.9906 mm diameter comparator tip and a 1.981 mm diameter spline type attachment, as are shown in Figure 2.3, 2.4 and 2.5 respectively (Mitutoyo).

2.2.4 Ultrasonic Technologies

Ultrasonic testing uses high frequency sound waves (20KHz to 25MHz) to detect internal discontinuities and measure the thickness of a material. The technology is based upon the concept of acoustic impedance differences between most materials and air. When an ultrasonic wave traveling in a material encounters an interface with air it will be reflected almost completely back to its point of origin. Therefore, if the velocity of the sound wave passing through the material and the time for the wave to travel the distance from the point of origin to the reflective face and back to the point of origin are known, then the depth to the reflective interface, or the thickness of the material, can be determined.

As is the case with audible sound waves, three conditions must be present for an ultrasonic wave to exist. There must be a vibrating sound source, a medium for the wave to travel through and some method of receiving the sound. In hearing, the sound source may a car horn with the sound waves traveling through air and hitting the human eardrum as a receiver. In ultrasonic testing the source is a piezoelectric crystal introducing sound waves into a medium, such as steel, and the receiver is again the same piezoelectric crystal.

The term piezoelectric is used to describe a material that has the ability to transform electrical energy into mechanical energy and mechanical energy back to electrical energy. To accomplish this task the crystal is subjected to an alternating current. As an electric current is applied, removed and reversed, the crystal will shrink, return to it's original thickness and expand. As a result, if a 1000 cycle per second electrical current is applied to the crystal, a 1000 cycles per second mechanical wave will be introduced into the test piece. The piezoelectric crystal must be protected from the environment and for this reason it is contained within the ultrasonic transducer as shown in Figure 2.6 (NDE Institute of Canada, 1995). The transducer consists of the following parts: The coaxial connector to supply the alternating current, the front and back

electrical connectors to apply the current to the crystal, the crystal, the case to hold the unit's parts together and for protection from the environment, the wear face to protect the crystal from damage and the backing material which serves the purpose of damping out unwanted sound waves. Only the waves generated from the bottom of the crystal are required in testing so all other waves must be eliminated.

Once the sound wave has returned to the crystal and has been transformed back to an electrical current, it must be converted into a display that is readable by the engineer or technician using the equipment. The most common method of displaying the results is through an oscilloscope. In ultrasonic testing, this method of display is called an A-scan display. It is the standard method used to interpret information attained from ultrasonic flaw detectors. Figure 2.7 (Panamatrics) is a photograph of a Panametrics Epoch III flaw detector and it's A-scan display. To review the theory of how a flaw detector's display is interpreted, Figure 2.8 shows a test specimen of thickness "t" with a flaw at one end of the sample at a depth of "t/2". As can be seen from this figure, the transducer is located at two separate locations on the surface of the material during the inspection. The A-scan results from Position 1 are shown in Figure 2.9 and the results from Position 2 are shown in Figure 2.10. For both screens, the X-axis has a unit of distance and the Y-axis has a unit of amplitude. Both the X and Y-axis scale units can be set by the operator. The first thing noticeable in Figure 2.9 is the peak that indicates the transmission pulse that the crystal created, or the initial pulse. This point marks the time when the ultrasonic wave left the crystal. Following this, a second peak of equal magnitude is shown at a distance of "t" from the beginning of the transmission pulse indicating the thickness of the test piece. This second pulse occurs on the A-scan display only when the sound wave returns to the piezoelectric crystal. Alternatively, in Figure 2.10, when the transducer is in Position 2 three pulses are visible on the A-scan display. The first pulse is again from the initial transmission pulse, the second is the echo from the flaw located at "t/2" and the third is the echo from the back wall, indicating a thickness of "t".

The above review of idealized ultrasonic theory does not account for energy losses that may occur as the sound wave travels through the test material. Ultrasonic transducers must be properly

coupled to the test piece to ensure that a large enough portion of the wave can be transmitted into the material to achieve the goals of the testing. Also, once the wave has been sent into the material they can be scattered, absorbed and diffracted which all decrease the energy of the returning wave.

One of the main problems with ultrasonic testing is achieving a good coupling of the transducer to the specimen to ensure that no air is present at the interface. This problem is addressed by spreading a couplant on the surface of the material to be tested. Couplants range in viscosity from light oil to extremely thick industrial greases, depending of the level of roughness of the surface to be tested. In industry, when corrosion surveys are done, it is standard practice to use a grinder to clean all of the corrosion product from a small area of the surface in order to obtain a smooth area to spread the couplant and apply the transducer. Here, since grinding the entire surface of the specimen smooth would defeat the purpose of the experiment, an extremely thick industrial grease is used in an attempt to achieve a good coupling between the specimen and the transducer.

Once the sound wave has entered the material, several factors may cause energy losses from the wave before it returns to the transducer. In the case of testing corroded materials the main source of loss of wave energy is scattering. Scattering occurs to some extent in all materials. In the case of a corroded material, much of the scattering occurs at the irregularly shaped back wall of the specimen. As the wave reaches the back wall it encounters a reflection surface that is not perpendicular to the waves. These non-perpendicular surfaces cause the wave to be reflected in all different directions, decreasing the amount of energy that returns to the transducer. In this situation it may not be possible to attain a proper reading since no distinct peak appears on the A-scan screen, if the waves have sufficiently scattered. When scattering results in ultrasonic waves traveling in all different directions after they hit the back wall, and therefore returning to the transducer at all different times, if at all, results in only low amplitude "noise" showing up on the oscilloscope. In such a situation, it is difficult, if not impossible, to make an accurate statement about the thickness of the material.

Diffraction and absorption are two more causes for a decrease in the energy of the returning ultrasonic wave. Diffraction is a concern in thick materials where the time of flight is relatively long. As the wave travels through the material it will spread, and the cross sectional area that it is traveling through will therefore increase. As this occurs the energy per unit area of the wave will decrease and result in less energy being returned to the transducer. Absorption is also a concern in thick materials. It is caused by the friction of the particles in the material. As the sound wave excites them, they vibrate back and forth causing energy loss in the form of heat. In this research, diffraction and absorption are not a major concern due to the small thicknesses of the test pieces.

There are several advantages in performing testing using an ultrasonic flaw detectors. First, the units are very portable, with overall dimensions of approximately 300 mm wide by 450 mm long by 150 mm high. Secondly, tests are accurate with a skilled technician being able to obtain accuracies within 1% of the thickness of the material being tested. Other advantages include the fact that testing requires access to only one side on the material and that extremely thick specimens can be tested. The main disadvantage of using flaw detectors for thickness mapping is the amount of training required to properly obtain and interpret the results. Natural Resources Canada is the government agency that controls the certification of technicians working in industry. As with the engineer-in-training program, the certification of technicians is an apprenticeship. Attainment of level I and II certifications in ultrasonic testing respectively requires 480 and 1440 hours of on-the-job training directly related to ultrasonic testing, supervised by a level II or III technician. Both level I and II certifications also require 80 hours of in class training and the successful completion of practical and written exams. Another disadvantage of using flaw detectors is that the cost is somewhat prohibitive. The price of ultrasonic flaw detectors range from $15000 to $30000 depending on the quality of the unit. Finally, as described earlier, ultrasonic inspection technologies work best in the presence of smooth test surfaces and back walls, which is not the case with this research.

Another method of performing ultrasonic testing exists that is much simpler to interpret and therefore removes many of the potential problems that may be caused by an unskilled operator. The depth meter, or D-meter, shown in Figure 2.11 (Panametrics), works on the same principle as the flaw detector but it can only be used for thickness measurements with no abilities to interpret internal flaws. Advantages are that once the signal has returned to the piezoelectric crystal the result is displayed on a screen in a numeric format. They are approximately half the size of full scale flaw detectors, basic units can be purchased for as little as $2000, and very little training is required for accurate and efficient use. The main disadvantage is that faulty thickness reading may be attained if an internal flaw, such as a lamination, exists in the test piece. If a large portion of the sound waves are echoed from a flaw at half the thickness, the numeric reading shows the distance to the flaw, rather than the full thickness of the material. In comparison, if this situation is encountered using a flaw detector, a pulse representing the small portion of the wave that traveled the full distance to the back wall is also visible on the A-scan output screen. It is therefore not possible for the operator to investigate suspect readings while using a D-meter.

A final ultrasonic technique investigated in the course of this work is the air-coupled transducer. This technique may seem contrary to the previous discussion of coupling and acoustic impedance, in which air was considered to be detrimental to the ultrasonic process, but special transducers have recently been designed to allow coupling to air. The main advantages of air-coupled transducers is that they can provide much more rapid scanning capabilities than standard transducers. This may be an extremely positive aspect of this technique considering the size of the areas that must be inspected on steel bridges.

Several methods have been devised to allow coupling of ultrasonic transducers to the surrounding air. The main problem with coupling to air is the large difference in the acoustic impedance between ceramic piezoelectric crystal and the surrounding air. The first technique uses a modified version of the standard piezoelectric crystal to couple the transducer to the surrounding air. The modification involves changing the mechanical and electrical properties of the transducer material using a ceramic polymer composite. This process increases the transmission capabilities of the

transducer in air but the resulting transducer has an extremely narrow bandwidth of applications. The result of changing the chemical make-up of the transducer therefore produces crystals that are acceptable for use in only one or two specific applications. Therefore, this type of air-coupled transducer cannot be used in this research.

The second method, that is still the subject of research and further development involves changing all of the materials used in the construction of the device and using a slightly different approach to developing the required ultrasonic waves. The micro-machined capacitance transducer is shown schematically in Figures 2.12 and 2.13 (Schindel et al., 1995). In this design, a solid silicon backing plate is machined to a set topography. A dielectric film is then stretched over the backing plate leaving pockets of air in the machined indentations in the backing plate. The ultrasonic waves are created by applying an alternating current between the backing plate and the metallized layer of the dielectric film. This process induces vibration in the layer of insulation that is placed between the two electrodes causing an alternating compression and expansion of the underlying air pockets. In this set-up, the pockets of air almost act as springs, driving the ultrasonic waves away from the transducer through the air. The reverse occurs when the transducer is acting as a receiver. This type of air coupling has been found to produce a transducer that can be used over a wider bandwidth, for a much broader range of applications than the ceramic polymer mix transducer. It should be noted at this point that the air-coupled transducer is not yet commonly used in industry and access to a unit is difficult to obtain. This technique currently still under development might be used in the future to produce accurate thickness and roughness maps of corroded steel structures.

2.2.5 Industrial Radiography

Industrial radiography uses radiation waves to penetrate an object and create a permanent record on an underlying film. For use in thickness mapping, the film will show thicker sections of the test specimens lighter than the thinner areas. This is due to the waves being absorbed more

completely when passing through the thicker sections and less radiation reaching, and developing, the film which the test piece is placed upon. The ability of a wave to penetrate any given material is a function of the radiation sources wavelength and the thickness and density of the test piece. There are two sources of radiation used in industrial radiography: Gamma-rays and X-rays.

The first source uses actual radioactive materials to produce Gamma-rays. A material is considered to be radioactive if it is unstable with it's current arrangement of neutrons, protons and electrons. In an attempt to reach a more stable configuration the material will either rearrange it's atomic configuration or emit particles. As the atom stabilizes the total energy in the atom is reduced resulting in Gamma-rays being emitted from the radioactive source. This process occurs naturally due to the decay of the radiation source, which is usually Cobalt 60 or Iridium 192. Gamma-rays have frequencies between approximately 10^{19} to 10^{24} Hz which correspond to wavelengths of between 10^{-11} and 10^{-16} m and posses energies in the megaelectronvolt (MeV) range. Gamma-ray sources typically include a 2.5 mm to 10 mm diameter by 1 mm thick radioactive wafers surrounded by shielding materials to protect the operator from radiation and focus the Gamma-rays.

The second form of radiation used in industrial radiography uses high-speed electron bombardment to create instability in a suitable target. The result of the instability is electrons being knocked out of their quantum orbits, the energy in the atom changing and X-rays being emitted. X-rays have frequencies of between 10^{16} to 10^{19} Hz which correspond to wavelengths of 10^{-8} and 10^{-11} m and possess energies in the kiloelectonvolt (KeV) range. A typical X-ray source is shown in Figure 2.14 (CGSB, 1981). The source consists of a highly evacuated vacuum glass tube, two electrodes, a filament, a focusing cup and a target. The glass tube is evacuated to ensure that the only source of electrons is from the electrodes. The electrons are released from the cathode by heating the filament using low level current. The number of electrons released from the filament is directly controlled by the temperature, and therefore the current, passing through the filament. The electron stream is then focused at the target by the focusing cup and propelled by a high voltage potential between the electrodes. The target is made of material with

an extremely high melting point, usually tungsten. When the electrons hit the target the required X-rays are emitted and focused through a window at the base of the tube. The force at which the electrons are propelled at the target is directly proportional to the voltage that runs through the electrodes. An increased current in the electrodes increases the force at which they hit the target, thereby decreasing their wavelengths and increasing their ability to penetrate materials. Voltages in industrial X-ray tubes range from 100KV to 2000KV.

To record the results of work done using radiography techniques the test piece is placed between the source of X-rays or Gamma-rays and a radiographic film. The film consists of an outer protective layer on each side of the film and an inner layer of chemicals that have been designed to have their physical structure change when exposed to radiation. Many different types of film are manufactured and are suited to different types of inspection depending upon the type of radiation, wavelength of the radiation, level of accuracy required and the type of material to be inspected. Once the image has been captured on the radiographic film it must be exposed to a developing chemical to create the final readable image.

The advantages of radiographic testing are as follows. The method is accurate to within 2% of the thickness of the material being tested while producing a permanent, film record of the test. Also, most sizes of structural steel can be examined since the method has the ability to penetrate up to 300mm of steel. Finally, the beam direction is not affected by irregular shaped surfaces as is the case with our corroded specimens. Disadvantages with this method are, as with ultrasonic testing, the cost and level of operator training required for the proper execution of the work. New radiation sources, including a lab, dark room and license can cost over $50,000 with every hour of a trained technician's time costing around $100. Training required to obtain level I and II certification respectively are again 480 hours and 1440 hours of radiography specific on-the-job training and a two week practical course and successful completion of exams. Another disadvantage is that access is required to both sides of the material. This may not be possible for the upper flanges of girders that support the deck slab in a bridge. Finally, a major problem with radiography is that is usually used as a qualitative tool to search for internal volumetric flaws.

When the method is used for this purpose an internal flaw or void will be registered as a lighter portion on the film since the waves have passed through less material. The technician performing the inspection will only be able to state that there is a flaw present at a certain location, without quantitative statements about it's size or location along the axis parallel to the radiation.

To make an attempt to numerically quantify the thickness of a corroded specimen, a smooth, calibration, sloped wedge can be machined from the tested material and placed beside the corroded specimen during testing. This provides a known thickness of a similar material tested for comparison to the actual corroded specimen. To ensure that all thicknesses are accounted for, the thick end of the slope wedge must have a greater thickness than the maximum found on the corroded test pieces and the thin end must be thinner than the minimum thickness found on the test pieces. In using this procedure, it is possible to digitize the radiography image, open the scanned image in a photo editor and compare the grey scale image of the slope wedge to that of the test specimen. Assigning the known thickness from the slope wedge to values along the grey scale allows the thickness of the material at various locations on the test piece to be determined.

2.3 Roughness Measurement

2.3.1 General

Fatigue of a material is a result of the cumulative damage that occurs when a member is subjected to varying cyclic stresses. During the cycling of a member in bending the maximum stress levels occur at the extreme tension and compression fibers, or at the member's outer surfaces. It is for this reason that fatigue is considered to be a surface sensitive process. One factor that may have an effect upon a materials ability to withstand cyclic loading is the roughness of the member's surface. The pitting that occurs during corrosion may act as stress raising notches and increase the surface stress levels beyond what would be expected at a given level of loading for a smooth material. Figure 2.15 (Bill, 1982) shows the relationship between the depth of corrosion pits and

the threshold surface stress range of 12% Cr and 2.0% NiCrMoV steels. It can be seen from this graph that as the pit depth increases the allowable stress range decreases. Figure 2.16 (McAdam, 1980) illustrates that the number of cycles to fatigue failure decreases as a function of corrosion time for steels subjected to various corrosive environments. Both of these graphs level out asymptotically as corrosion exposure time or pit depth increase. This indicates a significant loss of fatigue life rapidly occurs as pitting corrosion develops. However, both figures address high-cycle fatigue, for applied stress ranges below the yield stress.

In earthquake engineering applications, stable cyclic hysteretic behavior is required from structural members to dissipate the seismic energy, and low cycle fatigue is therefore more relevant. Bruneau and Zahrai (1998) have subjected several corroded members to inelastic cyclic loading. Typical results, shown in Figures 2.17 and 2.18, demonstrate that a limit is reached at which point the hysteretic energy dissipating abilities of the specimen are sharply affected. Before this point the corroded lacing bars and girders exhibit stable hysteretic behavior; beyond the limit, the member's ability to dissipate energy decreases rapidly. These two distinct stages are related to crack nucleation and crack propagation to failure. Once the flaw has appeared on the surface of the material and begun to propagate, it is possible to quantitatively relate the crack's size to some measure of damage or remaining life using fracture mechanics. During the stage prior to the appearance of the crack however, it might be possible to relate the potential for cracking or remaining fatigue life to a mathematical quantification of the topography of a corroded surface. Here, the possibility of such a quantification is sought in terms of standard measures of roughness. Existing roughness measurement methods are reviewed to identify which method can be applied to highly stressed areas of specimens that will be cycled to failure help establish if there is any relationship between the measured roughness and the specimen's ability to dissipate energy expressed in terms of cumulative hysteretic energy dissipated prior to fracture.

This section is thus divided into two separate sub-sections. The first sub-section reviews definitions of parameters used to quantify the degree of pitting on the surface of corroded specimens. These include the mean line, the average roughness, the maximum peak-to-valley

height, the root-mean-square roughness, the average peak-to-valley roughness and the ten-point-height of irregularities. It should be noted that the roughness parameters will be described in terms of roughness along a line (i.e. in two dimensions) for simplicity. The formulas can be modified to express roughness over a surface (i.e. in three dimensions) by inserting the elevation reading Z at point (X,Y) in place of the elevation reading Y at point X. The second sub-section provides some theoretical background on the instruments and technologies used to measure the aforementioned parameters.

2.3.2 Roughness Parameters

2.3.2.1 Mean Line

The mean line, or center line, is a reference line running parallel to the X-axis that is used in the calculation of the roughness parameters. It's position is calculated such that the areas above and below it are equal. As such, it may be considered to be the zero elevation reference line of the roughness profile. The location of the mean line can be calculated using the least square method of curve fitting. Figures 2.19 to 2.23 (Zygo Catalogue, 1999) show the location of the mean line along with roughness parameters discussed below.

2.3.2.2 Arithmetic Mean Roughness (R_a)

The arithmetic mean roughness, R_a, is defined as the average deviation of the absolute value of the distances between the mean line and all data points in the profile. The equation for the arithmetic mean roughness is given in Equation 2.1 and shown schematically in Figure 2.19 (Zygo Catalogue, 1999).

$$R_a = \left(\frac{1}{N}\right)\sum_{i=0}^{N} |Y_i| \qquad (2.1)$$

where N is the number of data points in the profile, and Y_i is the distance between data point "i" and the mean line.

2.3.2.3 The Maximum Peak to Valley Height (R_t or PV)

The maximum peak to valley height of a sample, R_t or PV, is the vertical distance between the top of the highest peak to the bottom of the lowest valley within an entire sample's profile. It is defined algebraically in Equation 2.2 and shown schematically in Figure 2.20 (Zygo Catalogue, 1999).

$$R_t = Y_P + Y_V \tag{2.2}$$

where Y_P is the distance between the highest peak in the profile and the mean line, and Y_V is the distance between the lowest valley in the profile and the mean line.

2.3.2.4 The Mean Peak-to-Valley Roughness (R_{tm})

The mean peak-to-valley roughness of a specimen, R_{tm}, is described algebraically in Equation 2.3 and schematically in Figure 2.21 (Zygo Catalogue, 1999).

$$R_{tm} = \frac{PV_1 + PV_2 + PV_3 + PV_4 + PV_5}{5} \tag{2.3}$$

where PV_1, PV_1, PV_1, PV_1 and PV_1 are the five largest peak-to-valley deviations within a profile. In two dimensions, it can be described as the average peak-to-valley roughness value of five separate values obtained by dividing the full profile length into five equally spaced sample lengths and finding the maximum peak-to-valley value within each of these separate sampling lengths. In the three dimensional space, it may be described in the same way but the three dimensional surface is divided into nine sample areas.

2.3.2.5 The Root-Mean-Square Roughness (R_q or RMS)

The root-mean-square roughness, R_q or RMS, is the root-mean-square deviation of all data points within an entire sample's profile. It is defined algebraically in Equation 2.4 and shown schematically in Figure 2.22 (Zygo Catalogue, 1999).

$$R_q = \left[\left(\frac{1}{N}\right)\sum_{i=1}^{N}(Y_i)^2\right]^{1/2} \tag{2.4}$$

2.3.2.6 The Ten-Point Height of Irregularities (R_z)

The ten-point height of irregularities, R_z, is defined as the distance between the mean of the five highest peaks and the five lowest valleys within a profile length. The ten-point height of irregularities is defined algebraically in equation 2.5 and shown schematically in Figure 2.23 (Zygo Catalogue, 1999).

$$R_z = \frac{(Y_{P1} + Y_{P2} + Y_{P3} + Y_{P4} + Y_{P5}) - (Y_{V1} + Y_{V2} + Y_{V3} + Y_{V4} + Y_{V5})}{5} \tag{2.5}$$

where Y_{Pi} are the five highest peaks in the profile and Y_{Vi} are the five lowest valleys in the profile.

2.3.2.7 Fractional Dimensions

The fractional dimension is a relatively recent development in the problem of describing rough or irregular lines, areas and volumes. Some of the original work on the subject was done by Mandlebrot in his book Fractals: Form, Chance and Dimensions (Mandlebrot, 1977). As compared to the roughness parameters described in sections 2.3.2.2 to 2.3.2.5, the fractional

dimension does not use classic Euclidian geometry to describe irregular boundaries. Instead, the line, area or surface is quantified in terms of its space filling ability with a greater space filling ability being described with a larger fractional dimensions. The entire concept of fractional dimensions are based upon the idea that classic Euclidian definitions of one, two and three dimensional objects are purely a matter of convenience and do not fully describe certain lines, areas and volumes. In the case of this research, a cross section of sample will be studied to determine if the outline of the corroded cross sectional surface has a fractional dimension between the first and second dimension.

As a first step in understanding the concept of fractional dimension, the topological and fractional dimensions of a set of lines, shown in Figure 2.24 (Kaye, 1989), will be compared. As can be seen from the left hand column, the topologist would consider all of the lines to have a topological dimension of one. This is because in the study topology, if a set of lines can be stretched and squeezed so that they can be laid directly over one another, the topological dimension is considered to be unity. This concept can be extended to the second dimension by considering a set of poorly drawn circles and to the third dimension by considering a group of sponges with different void ratios. In comparison, the fractional dimensions of the set of lines increases in magnitude as their ruggedness or space filling ability increases as can be seen in the right hand column of Figure 2.24.

In order to describe how a fractional dimension is calculated, one of the basic fractal questions will be reviewed. The question asked by Mandlebrot (Mandlebrot, 1977) was "How long is the coastline of Britain?" This question has no definitive answer without referencing what resolution or step size was used to measure the perimeter of the island. For example, if the coastline is measured with 1 m step as compared to 1 mm step sizes, two different perimeter values will be obtained. The perimeter value for the 1 mm step size will be larger because much more detail of the coastline will be measured. The coastline of Britain is shown in Figure 2.25 (Kaye, 1989) with various step sizes or resolutions, with λ_1 being the longest and λ_3 being the shortest. Also shown in this figure is the measurement of the largest dimension of the coast which will be used to

normalize the perimeter values. In order to calculate the fractional dimension of the coastline. a log-log plot of the normalized perimeter values versus the step size if constructed. The fractional dimension is then calculated as being:

$$\delta = 1 + |m| \tag{2.6}$$

where δ is the fractional dimension and $|m|$ is the absolute value of the slope of the constructed curve. As can be seen from Figure 2.26 (Kaye,1989), the fractional dimension of the coastline of Britain is 1.24. For this research, the image of the irregular surface will be captured using an optical microscope, traced onto an electronic graphics pad and the length of the line will be calculated at various step sizes. This will result in a log-log plot that will show the approximate fractional dimension of the surface being studied.

2.3.3 Technologies Used in the Quantification of Roughness

2.3.3.1 Replication Tape

The first problem encountered in quantifying the roughness of corroded bridge steel is finding a reliable, in-situ roughness measurement technology that has the ability to measure surface roughness and obtain repeatable and accurate measurements from a bridge site. A replication tape, manufactured by Testex of Newark, Delaware, was found to effectively address this problem. This replication tape is currently being used in the inspection of steel structures when a surface is being prepared for the application of a coating system for which there is an optimum range of roughness that allows for the strongest bond between the steel and paint. Along with relative humidity and temperature, surface roughness is a key parameter of interest to engineers involved in the coating of structural steels that will be exposed to corrosive environments.

The replication tape consists of a layer of crushable micro-foam coated onto 50 μm of an uncrushable plastic backing film. The tape can be purchased with foam thicknesses ranging from 0 to 163 μm with the range of thicknesses of the various grades and cost per sample of tape

shown in Table 2.1. All of the grades of tape can also be purchased with a metallized surface to facilitate measurement using optical profiling devices or scanning electron microscopes. A photograph of an unused piece of the replication tape and it's burnishing tool has been included as Figure 2.27 (Testex, 1999).

To use the tape the white adhesive release paper that holds the pressure sensitive tape in place during sampling must first be removed from the black cardboard tape holder. Next, the replication tape is placed, metalized surface down, over the area to be sampled, and rubbed with a finger to ensure good contact over the entire area of the replication tape and adhesive paper. This process serves to set the adhesive and ensure that no motion of the replication surface occurs during testing. Following this, firm pressure is applied uniformly over the back of the replication area by the burnishing tool until the back of the tape becomes a uniform grey. The backing has been designed such that as the foam is being crushed the plastic backing above it changes colors from white to grey. The tape can then be removed from the surface and the resulting reverse replica can be measured using a variety of methods. Several measurement methods are described in the following sections.

2.3.3.2 Dial Calipers

The quickest and simplest method for measuring the roughness of the replication tape is by using the dial thickness gauge produced by Mitutoyo. Currently used to measure replica tape roughness during surface preparation for protective coating application, the gauge allows for on-site measurement of the ten-point height of irregularities roughness of the replication tape in order to determine if the roughness of the sand blasted steel is within the required tolerances of the coating product. The gauge has an accuracy of ± 5 μm and a range of measurement of 25 to 1250 μm. The measurement is attained by closing a 6.35 mm diameter anvil onto the surface of the Testex tape with a set closing force of 1.5 N. For uniformly roughened surfaces, the closing force of the anvil elastically crushes the peaks on the tape until the anvils come into contact with the maximum

amount of micro-foam that can be crushed with a force of 1.5 N. Once the anvil has come to rest it is assumed that it will lie on a horizontal plane at the approximate mean line of the sample. The measurement attained is the distance between this assumed mean line and bottom of the incompressible plastic backing. Advantages of using the Mitutoyo gage include it's portability, speed of operation, low level of operator training required and it's relatively low cost of around $300. Also, the dial calipers have been experimentally proven to be accurate within ± 5 μm for the measurement of the ten-point-height of irregularities of sand blasted surfaces.

2.3.3.3 Stylus Instruments

Stylus instruments provide a continuous roughness profile by pulling a detector head over a surface to record the vertical variation along a straight line. Stylus instruments are available from full size laboratory units that include a testing table and personal computer with analysis software, or as simple hand held units with LCD numeric printout screens. A photographs of a typical hand held unit is shown in Figures 2.28 (Mitutoyo). Due to the nature of this research only the portable, hand held units are investigated.

The portable unit investigated is the Surftest SJ 201, that can be purchased from Mitutoyo for approximately $2500. It has a maximum peak-to-valley profile range of 1 to 300μm and can measure R_a, R_q, R_y and R_z over profile lengths up to 2.5 mm with an accuracy of 0.5 μm. The instrument works by pulling a 90° diamond cone with a 5 μm radius tip over the rough surface at a speed of 0.5mm/s. As the tip is pulled over the surface, the unit records all of the two dimensional information required to obtain the required roughness parameters. Advantages of this type of unit are that it is very portable, there is virtually no operator training required and many measurements can be made in a very little time. The disadvantages are the limited profile length that can be sampled and maintaining contact between the stylus and corroded surface at extremely corroded locations where large peak-to-valley values exist.

2.3.3.4 Optical Microscopes

Optical microscopes are one of the oldest and most useful tools used to study fine details on the surface of a material. Although optical microscopes are available over a huge range of prices and capabilities for an even larger field of applications their basic components are all very similar. A standard optical microscope includes an illumination source, a condenser, light filters, the objective lens, the eyepiece and the stage and stand.

The illumination source provides light for inspection of the test piece. A wide variety of methods are available for illumination with the most common being the low-voltage tungsten filament lamp. The intensity of the light is controlled by altering the level of current running through the filament. The condenser lense focuses the light at the desired point along the optical path. Two diaphragms are placed in front of the condenser to control internal glare and reflections within the microscope and to control image sharpness, contrast and depth of field of the image. Light filters are used to modify the light source before it arrives at the test piece. These filters serve a wide variety of purposes from decreasing the amount of light that is allowed to pass through them to changing the color of the light to allow for a closer match to the test piece and an overall easier viewing of the test surface. The most important part of the optical microscope is the objective lens. It collects as much light as possible from the specimen and combines and magnifies it to produce an image. Most optical microscopes have several different objective lenses mounted on a turret just above the specimen to allow the operator to view the specimen at a variety of magnifications. The eyepiece controls the distance of the eye to the actual lense of the eye piece and further magnifies the image from the objective lense. Many eye pieces are equipped with a grid used to locate, measure and compare various features on the surface of the specimen. Finally, the stage is the horizontal surface located just below the objective lense that the specimen is mounted on and the stand is the solid frame used to house all of the components of the optical microscope.

Two examination modes, within the field of optical microscopy, are investigated during this research. The first method uses a standard optical microscope with magnifications of 5,10, 20 and 40X. This microscope uses a bright-field illumination mode to examine the specimen. In this examination mode, light passes through the objective and strikes the specimen's surface perpendicularly. Features on the surface that are normal to the incoming light are reflected back to the eye piece brightly and features that are not normal to the incoming light appear dark since less light is reflected directly back to the eyepiece. The larger the angle that the features have with the plane normal to the light the darker they will appear.

The second type of optical microscope investigated uses interference techniques to construct extremely accurate images of the three dimensional surface topology of a specimen. Optical interference microscopes work by splitting a single light source into two separate beams in the objective. One beam travels to the surface of the specimen and the other to a perfectly flat reference surface. When the two light beam are recombined, they undergo constructive and destructive interference due to the fact that the two beams have not traveled the same path, to the same surface. The result of the interference is a pattern of light and dark fringes appearing above the objective. This image is recorded by a camera and transformed into the required three dimensional image. The degree of interference that occurs is directly related to the degree of surface roughness on the specimen. For example, if the specimen were perfectly flat, interference would not occur and the resulting image that appeared above the objective would consist of equally spaced, parallel lines of equal thicknesses.

The main disadvantage of using optical microscopes is that it is very difficult, if not impossible, to obtain quantitative values for roughness without having access to customized computers and software built specifically for the field of metrology. Because of this, any use of these types of microscopes must be coordinated with a testing facility whose main field of interest is the imaging and inspection of the surface of materials.

2.3.3.6 Scanning Electron Microscopes

The scanning electron microscope is a powerful tool used to study the micro-features on the surface of a specimen. The technology was reviewed to extend the level of magnification that could be studied beyond what is possible from an optical microscope. Due to the complex nature of the equipment and the extremely high level training required to develop testing programs. its theory and potential will only be briefly discussed.

The scanning electron microscope works by focusing a beam of electrons, rather than light photons, onto the specimen. Using this technique allows for an increased resolution and higher depth of field than are possible with optical microscopes. Also, Scanning Electron Microscopes have magnification capabilities up to 30,000X. The scanning electron microscope can be subdivided into three main systems. The illumination system works in much the same way as an X-ray tube. A filament is heated using a low level current to release the electrons which are accelerated towards the specimen by increasing the potential between the filament and the anode. In this case the electron beam is further focused, using a series of lenses, before it hits the specimen. The next part of the microscope is the information system. The basis of the technology is that as the electrons hit the specimen various signals are released that contain information regarding the composition and structure of the specimen. Of interest here is the back scattered electrons that result from elastic collisions between electrons from the beam and those from the specimen. These particles contain important information about the specimens surface topology. To capture these particles a back scattered electron detector is located just above the specimen and the results are transmitted to a cathode ray tube for viewing. Lastly, the vacuum system removes any all unwanted particles from the testing chamber to ensure that they do not interfere with the testing. The same problem that was encountered with the optical microscopes also becomes a concern with the scanning electron microscopes. Although the technique provides extremely clear three dimensional images, no methods were found that can numerically quantify the level of surface roughness. For this reason, the scanning electron microscope is only used in this research project to obtain qualitative results from the image.

CHAPTER 3
PERFORMANCE OF NON-DESTRUCTIVE TESTING TECHNIQUES

3.1 Introduction

This chapter will evaluate the performance of the various non-destructive testing methods that were used to quantify the thickness and roughness of corroded steel. The methods will be assessed in terms of the time and cost involved in the testing, the limitations of the method, problems that arose during testing, advantages and disadvantages of the method, the overall quality of the results and the potential for further investigation of the technique's capabilities.

3.2 Thickness Mapping

3.2.1 General

All of the non-destructive testing discussed in this section was performed on corroded lacing bars from a corroded steel bridge that was constructed in the 1950's. The lacing bars were machined from their original dimensions down to standard ASTM long tension test specimens size, as is shown in Figure 3.1. The surface of the 203.2 mm by 38.1 mm test area was then divided into a 6.35 mm square grid for testing, resulting in a fine grid of 6 spaces wide by 32 spaces long. This grid size was chosen to match the anvil size of the screw micrometer and the smallest ultrasonic transducer that will be used. The specimens showed varying degrees of corrosion over their lengths with some portions of the lacing bars being only approximately half the thickness of sections on the same lacing bars that were located only a few inches away.

In this section all of the methods that were reviewed in Section 2.2 will first be qualitatively evaluated in terms of their performance during the thickness mapping of the test coupons. The methods that successfully completed the task of producing full thickness maps of the corroded test coupons will be further compared in Section 3.3.3 to gain a better understanding of the numerical quality of the results. The comparison of the numerical quality of the results will be in terms of descriptive statistical and graphical summaries of the data that was obtained during the thickness mapping.

3.2.2 Screw Micrometers

The first method used to evaluate thicknesses was the screw micrometer. Five ASTM long tension test specimens were machined from the available lacing bars, leaving the two corroded 38.1 mm wide sides of the specimens in their original corroded condition. These specimens were then vigorously cleaned with a wire brush to remove any loose scale and marked with the required 6x32 grid using a soft lead pencil. Each specimen was measured using the standard micrometer with no anvil attachments, the 5.08 mm diameter ball tip, the 0.991 mm diameter comparator tip and the 1.981 mm diameter spline attachment for a total of four grids of 192 readings per grid or 768 thickness measurements per specimen.

Once the use of the screw micrometers had begun it became apparent that it would be one of the methods used to perform thickness mapping. They provided a simple and accurate method for attaining thickness measurements in each 6.35 mm^2 grid partitions. The results were reviewed every 64 readings (two full rows of readings) and suspect results were easily double checked. The cost of using the screw micrometer for testing a specific width of specimen was the one time cost of purchase of the required screw micrometer. Wider specimens could be tested by purchasing micrometers with longer frames that are capable of taking measurements further in from the edge.

The main disadvantage of the micrometer is the time involved in testing. Using an estimate of 30 seconds for the operator to move, tighten and read the three scales on the calipers and then enter the results into a computer or note pad would result in just over 205 hours of work being required to cover 1 m^2 of steel with the same grid spacing as was used in this experiment. Also, the time involved in testing may result in operator fatigue. Fatigue, or a loss of concentration, would not be due to any form of physical exertion but instead the potential for errors would be created due to the extremely tedious and repetitive nature of the task.

One error that may result from an operator becoming fatigued and losing concentration is a tilting error. This error occurs when the anvil head is not parallel to the surface that is being measured. Although few portions of the test coupons are completely parallel to the surface that they were placed upon, every effort should be made to ensure the anvil and spindle were at the center of the same grid box in the thickness map on the top and bottom surfaces of the coupon. Figure 3.2 shows a magnified view of the face of an anvil not parallel to the surface of the coupon and the derivation of the resulting tilt error. Figure 3.3 graphically shows the results of tilt errors between 0 and 10°, which was considered to be the maximum possible tilt error.

3.2.3 Ultrasonic Testing

The first ultrasonic technique that was investigated was the flaw detector. Access to a Parametric Epoch III flaw detector and a 6.35 mm (0.25 in) diameter transducer were attained. The flaw detector was first calibrated to ensure that the instrument was using the correct value for the speed of sound in the material so that the correct thickness values would be obtained. Calibration is performed by coupling the transducer to calibration blocks that were machined from the same material as the corroded steel. Three blocks were used in this experiment. They were machined smooth from steel from the Grigg bridge and their thicknesses were 3.81 mm (0.15 in), 6.35 mm (0.25 in) and 8.89 mm (0.35 in). The calibration procedure involves coupling the transducer to the thickest test block and adjusting the instrument's velocity until the oscilloscope is reading 8.89

mm. If the thickness reading is too low then the instrument's velocity is too high and if the thickness readout is too high then the velocity is too low. Once the flaw detector is reading the proper value for the thickest test block the transducer is coupled to the thinnest test block to adjust the velocity at the other end of the thickness range. This procedure is continued, using all three test blocks, until all thickness readings are correct. Once the calibration is performed the flaw detector is ready to perform thickness testing on the test coupons.

Once the transducer was placed on the test coupon, it became immediately apparent that the ultrasonic wave was not performing in the same manner as it had while the flaw detector was being calibrated. During calibration the oscilloscope screen showed the initial pulse from the transducer followed by a small amount of low level noise and finally, an excellent indication of the echo of the wave returning from the back wall of the specimen, located at the proper thickness on the A-Scan display. In comparison, when the transducer was coupled to a corroded coupon the A-scan display included the initial pulse echo followed by an erratic array of multiple responses and moving peaks with no obvious back wall echo. Attempts were made to adjust the reject level of the instrument to remove some of the low level noise from the oscilloscope. Some success was attained from this procedure but the resulting response peak was still of only a slightly higher amplitude than the other indications on the screen and it was continually disappearing and reappearing at different locations on the screen with various amplitude levels, indicating a variety of thicknesses.

The cause of the limited results from the ultrasonic flaw detector can most likely be attributed to scattering caused by the fact that many portions of both surfaces of the test coupons were not perpendicular to the incident sound waves. As was discussed previously, rough and irregular surfaces, that result from corrosion, can render a specimen practically impossible to inspect by ultrasonic techniques. Scattering of the incident ultrasonic sound wave can occur at the front and back faces of the specimen. If the transducer was not completely coupled to the front interface, much of the ultrasonic energy would be immediately returned to the transducer and begin showing up on the A-scan display just after the end of the initial pulse signal. This would result in very

little ultrasonic energy traveling through the entire thickness of the coupon and questionable results. Scattering from the back wall results in the sound waves being reflected in all directions. As a result only a small portion of the energy would travel the path required to result in the proper thickness measurement being obtained. After reflection off the back wall the waves may randomly travel through the specimen until they come into contact with the transducer again by chance. Another source of error was that the wear face of the transducer was often not horizontally stable on the surface of the material. This error can be visualized in the same manner as the tilt error sensitivity error as is shown in Figure 3.2. If a transducer was resting at a peak on the test surface, any tipping of the transducer would result in the ultrasonic waves being introduced into the material at an angle causing them to travel a longer path before they return to the crystal. This error may be the cause of the response peak disappearing from the A-scan screen and reappearing, showing a different thickness than was originally obtained as the transducer tilts around it's central axis. As the face of the transducer is tilted slightly the resulting thickness that is recorded would increase as the angle of tilt increases. The potential also exists that if the angle of tilt is sufficient the ultrasonic wave will not return to the transducer before the next pulse occurs, resulting in extremely questionable thickness measurements.

After discussing the potential use of the ultrasonic flaw detector with several qualified technicians it was decided that the depth meter, or D-meter, would be better suited to this problem for an operator with a limited amount of training. The main advantage of the depth meter is that built in controls interpret the returning signal for the operator and display it numerically instead of the A-scan display having to be interpreted. The result is that a numeric value for thickness will almost always be obtained. Access to an older model of the Wylam Hill Portable D-meter was attained for this portion of the testing through Mr. M. Partridge CGSB Level II, and Steel Inspection Services of St. Catherines, Ontario.

To begin the D-meter testing the instrument was calibrated for the material from the lacing bars. After calibration had been completed, the first test specimen was coated with couplant and the testing program commenced. With respect to obtaining numeric results for the thickness mapping

of the specimens the D-meter performed quite well. The instrument was calibrated every 64 readings (every two rows) to ensure the accuracy of the results. Most of the readings were obtained in around 10 seconds, giving the operator a chance to stabilize the transducer over the grid location and record the reading. This resulted in just under 70 hours of work to test 1 m^2 of surface area with a 6.35 mm^2 grid size. It should be noted that many newer D-meters have data storage capabilities that can decrease the time required for testing.

Many of the problems that occurred during the use of the flaw detector most likely occurred to some degree when the D-meter was being used. Some of the readings that were obtained during testing were quite a bit lower than what was expected. When these suspect readings were compared to those recorded by the screw micrometer it was found they were incorrect. This may have been a result of the D-meter recording the low level noise that was seen with the A-scan display as the full returning energy of the echo from the back wall and interpreting it as a thickness. There may also have been an internal flaw such as a lamination at those locations that was reflecting the waves back to the transducer and causing the faulty readings. The readings that were considered to be questionable were double checked with the D-meter and if the measurements did not differ from the original they were recorded as displayed on the D-meter. Although the D-meter did record many readings that were considered questionable, thickness maps of the test coupons were obtained and the results will be analyzed along with those from the screw micrometer in section 3.3.3.

The final type of ultrasonic testing that was used during this investigation was the air-coupled micro-machined capacitance transducer . Access to this method was attained during a tour of the Non-Destructive Testing Group of the Aerospace Research Institute at the National Research Council. It should be noted at this point that only one tensile coupon was tested by this method. Dr. D. Schindel, the co-inventor of the transducer, took the time to run a test grid over the coupon to obtain a printout of the materials thickness to demonstrate the method's potential. Copies of these printout are included as Figures 3.4 and 3.5 for the two sides of the test specimen.

The main advantage of this type of testing was the speed at which testing was performed. It took only a few minutes to perform the testing of the specimen. Also, the wave can be focused onto a point on the surface as small as 200 μm and the accuracy of the through transmission thickness readings have recently been proven to be accurate within ± 5 μm of total thickness. These tolerances would allow for an extremely accurate thickness mapping of a bridge to be obtained. Also, with these tolerances, the potential for the method to be used to map the roughness of bridge steel exists. After discussing the potential usefulness of the technology with Dr. Schindel it was determined that applying the principles of the air-coupled capacitance transducer would be a very simple process that could lead to a large amount of data being generated in short time periods. Unfortunately, Dr. Schindel no longer has access to the testing table that would be needed to test the full sized bridge girders to assess the techniques abilities to produce roughness and thickness maps. Also, before this technology could be used for in field testing of bridges several issues would have to be addressed. The first problem would be in creating a method to carry the transducer along the various structural members of the bridge while maintaining a known position of the transducer in the X-Y-Z co-ordinate system of the bridge. Secondly, the readings would have to be adjusted to account for the effect of temperature and wind upon the speed of the wave in an outdoor environment. Although only a small amount of data was generated from this method it has the potential to become an extremely useful tool in the future inspection of corroded bridges.

3.2.4 Radiography

Industrial radiography was first used to measure the thickness of corroded steel at the National Research Council in Ottawa, Ontario. During a tour of the facilities, Mr. T. Chapman offered to take an X-ray of one of the steel coupons to demonstrate the capabilities of their equipment and the potential for its future use in the testing of full size bridge girders. Figure 3.6 is the digitized and colorized image of the X-ray that was captured on film. The image shows a test coupon and a slope wedge beside it. It should be noted that the slope wedge was not made from the same

material as the test coupons, it was placed in the image and X-rayed to demonstrate the potential of the method. The slope wedge was 216 mm long with a knife edge for the thin section and a maximum thickness of 14 mm. The thinnest sections of the wedge were burnt through by the X-rays. This means that the thickness of material up to the point where the image starts to become red did not absorb enough X-rays to be noticeable on the film. The result was that the film recorded this area as if there were no material above it. As the thickness of the step wedge increased the colors changed from red to orange to green to blue, with the areas on the test piece that correspond to these colors having approximately the same thicknesses as indicated on the slope wedge. Although no quantitative data can be obtained from the X-ray shown in Figure 3.6, since the coupon and slope wedge are made of different materials, it does show the potential of the technology, since each pixel on the screen has it's own color value that corresponds to a unique thickness on the slope wedge. The potential therefore exists for an extremely accurate map of the thickness of corroded materials to be constructed.

To gain a better understanding of what potential industrial radiography would have in the mapping of the thickness of corroded materials it was decided that the coupons would be X-rayed by a technician working in industry, rather than a researcher working at the National Research Council. This would allow for a better insight to be gained into what results can actually be obtained using the portable equipment used by technicians every day in industry. Although the results from the National Research Council showed good potential, the equipment that was used was more sensitive and expensive than any equipment available to testing companies working in industry. During a tour of the facilities it was seen that the X-ray equipment was used almost exclusively for research and development purposes in the aerospace industry.

The use of an X-ray tube, film and a technician's time was donated by Steel Inspection Services of St. Catherines, Ontario. The testing was performed by a Mr. M. Partridge, CGSB Level II. Before any testing could be performed, a slope wedge had to be machined from the same material as was used for the lacing bars to be X-rayed and placed beside the test specimens as a thickness reference during testing. Figure 3.7 and 3.8 show the elevation and plan dimensions of the

reference block respectively. Once the slope wedge had been machined it was sent to Mr. Partridge, along with the five corroded coupons. The standard X-ray report is included as Figure 3.9 and the digitized films are included as Figures 3.10 to 3.14 for Specimens one through five respectively. The first noticeable feature of these images is that large portions of Specimens one and three were to thin too register any resistance to the radiation and therefore the film recorded the thicknesses as zero. The thinner portions of the slope wedge were also "burnt through" by the radiation, removing indications from steel thicknesses below approximately 6 mm. Note that the test blocks that were used for ultrasonic testing were also placed in the image for comparison. The 8.89 mm thick test block is visible while the 6.35 mm block is practically non-existent on the film and the 3.81 mm cannot be seen at all.

Several factors could have been better controlled to avoid having areas of the specimens appear on film as having no thickness. The first aspect of the testing that could have been more closely monitored was the potential between anodes. As the potential increases, the force at which the electron beam hits the target increases, thereby decreasing the wavelength of the radiation and increasing their ability to penetrate the inspected material. The testing was performed at a potential of 160 KV. This was too high for Specimens one and three. This control should have been decreased below 160 KV to decrease the penetrating abilities of the radiation and the potential for burn through of the steel. Another option to allow for the full range of thicknesses to be measured would be through the use of lead screens to filter out the shorter, more penetrating wavelength. When the potential of testing is reported it is described in terms of the maximum voltage that was applied by the alternating current. This means that for a testing voltage of 160 KV, currents between 0 KV to 160 KV are being applied as the alternating current moves through a half cycle. In many cases lead filter screens are placed in front of the test piece to absorb the shorter wavelength and decrease the penetrating ability of the radiation. This may have resulted in all of the thicknesses being recorded on the radiographic film.

Once the films had been digitized the resulting files were opened in several commercial image viewers. Although methods were found to determine what grey level had been assigned to the

pixels in the digitized image by moving the mouse around the screen, no commercial packages were found that were capable of creating a printout of all values for all pixels in the digitized image. Although X-ray testing showed good potential for future use in this type of work, tighter control of the testing and a method of transferring the grey level data to an ASCII file must be found before the technique can be used to create accurate thickness maps.

3.3 Summary of Thickness Mapping Results

3.3.1 General

As a first step in the analysis of the thickness measurements attained from the screw micrometers and the depth meter, all of the results were first normalized by the results from the screw micrometers with no anvil attachments. Once the data had been normalized frequency distributions or histograms were created for each data set. Figures 3.15 to 3.18, 3.19 to 3.22, 3.23 to 3.26, 3.27 to 3.30 and 3.31 to 3.34 show the frequency histograms that were obtained after normalization for Specimens one through five respectively. The results were normalized to better understand if the differing values obtained from the other measurement methods were normally distributed around the central reference value of 1.0. This means that if a set of data recorded using the ball anvil attachment matched those taken with no anvil attachments exactly the frequency distribution would consist of a single bar of 32x6=192 observations located at the central reference value of 1.0. Since this will not be the case, various descriptive statistical parameters were calculated to evaluate the central tendencies and dispersion of the frequency distributions for each data set. For each of the normalized data sets the arithmetic mean, median, mode, skewness and kurtosis were calculated to better understand the central tendencies of the observations. To measure the dispersion of the data, the variation, standard deviation and standard error of the mean of the samples were calculated. Also, the range, and the minimum and maximum values that were obtained during sampling were calculated as a simple measure of the spread of the normalized values. A summary of the calculated descriptive statistical parameters

that were calculated are included as Tables 3.1 to 3.5 of this report. The statistical parameters that were calculated for the normalized data are defined in the following sub-section with the algebraic descriptions being included when necessary.

3.3.2 Statistical Parameters

The arithmetic mean or mean of a sample is the value such that the sum of the deviations of the observations from it are zero. The mean of a sample passes through the centroid of the area of a histogram and it is shown algebraically in Equation 3.1.

$$\bar{x} = \frac{1}{n}\sum_{i=1}^{n} x_i \tag{3.1}$$

where $\bar{x}$ is the arithmetic mean of a sample, n is the number of observations in the sample and x_i is a specific observation.

The median of a sample can be described as the middle observation of a sample, it divides the area of a frequency distribution in two. If there is an even number of observations in the sample, as is the case with this study, the median is taken as the mean of the two center values of the sample.

The mode is the value within a sample that occurs most frequently, it represents the highest peak on the frequency distribution. In most cases there is only one mode in a sample, however it is possible for there to be two distinct modes within one sample. When this occurs the sample is considered to be bi-modal.

The skewness is a measure of the degree of symmetry of the observations around it's mean. Lack of symmetry occurs in a sample when the mean, median and mode are not all equal. When the skewness of a sample is positive it is skewed to the right of the mean and when it is negative it is skewed to the left of the mean. The skew of a sample is defined algebraically in Equation 3.2.

$$SKEWNESS = \frac{n}{(n-1)(n-2)} \sum_{i=1}^{n} \left[\frac{x_i - \bar{x}}{\sigma} \right]^3 \qquad (3.2)$$

where σ is the sample standard deviation and the other variable have previously been defined.

The final measure of central tendency of the sample that was calculated for this research was the kurtosis of the sample. The kurtosis is a measure of a sample's closeness to normality in terms of it's peakedness or flatness. When the kurtosis of a sample is positive it is said to be leptokurtic or peaked and when it's value is negative it is said to be platykurtic, or flat. The formula that was used to calculate the kurtosis of the samples is shown algebraically in Equation 3.3.

$$KURTOSIS = \left[\frac{n(n+1)}{(n-1)(n-2)(n-3)} \sum_{i=1}^{n} \left(\frac{x_i - \bar{x}}{\sigma} \right)^4 \right] - \frac{3(n-1)^2}{(n-2)(n-3)} \qquad (3.3)$$

Although the parameters calculated for the central tendencies of a sample yield values that typify the entire group of observations, they do not give sufficient information with respect to the dispersion of the observations within a sample. For this reason the variation, standard deviation and standard error of the mean of the samples were calculated in an attempt to quantify the dispersion of the observations. The variance of the observations within any given sample is the mean square of all the deviations between the observations and the mean of the sample. It is shown algebraically in Equation 3.4.

$$\sigma^2 = \frac{\sum_{i=1}^{n} (x_i - \bar{x})^2}{n} \qquad (3.4)$$

Although the variance is a useful measure of the average deviations between the sample's mean and the various observations a more common parameter used to report this information is the standard deviation of the sample.

The standard deviation of a sample is simply the square root of the sample's variance, or the root-mean-square of the deviations, and is shown in Equation 3.5.

$$\sigma = \sqrt{\frac{\sum_{i=1}^{n} (x_i - \bar{x})^2}{n}} \tag{3.5}$$

The final measure of dispersion that was calculated during the course of this work was the standard error of the mean. It can be described as the average standard deviation of the observations and is shown in Equation 3.6.

$$\sigma_{\bar{x}} = \frac{\sigma}{\sqrt{n}} \tag{3.6}$$

The final three statistical parameters calculated for this work are the range, the minimum and maximum values that occurred in the normalized testing results. These parameters are straight forward and require no further explanation or algebraic clarification.

3.3.3 Discussion of Results

An initial review of the histograms that were created from the normalized data for Specimens one through five, as can be seen in Figures 3.15 to 3.34, show that the data possess generally bell shaped histograms, which is a characteristic of normally distributed data. The exception to this is the histogram for the data recorded using the D-meter for Specimen 1, as can be seen in Figure 3.18. It has a mode of 0.9670 which is in the same range as the other data sets but a second, smaller peak exists at approximately 0.5. Similar results occurred for Specimen 2 with the histogram shown in Figure 3.22. From this figure it can be seen that the second, smaller peak again occurred at approximately 0.5. This slightly bi-modal behavior may be due to internal laminations in the specimen causing the wave to be rebounded at approximately half the full

thickness of the specimen or the inherent difficulty of recording thickness measurements of a corroded surface using ultrasonic techniques.

The next step in reviewing the data was to compare the various statistical parameters that were calculated to measure the central tendencies of the normalized data. The arithmetic means for the data collected for the thickness mapping were all of a similar magnitude. The average of the twenty means was 0.9716 and the largest deviation from it for the screw micrometers was under 1.3% of the calculated average mean. The results obtained using the D-meter differed slightly from the sets of data recorded using the screw micrometers. The bi-modal behavior of the data for Specimen 1 resulted in an arithmetic mean of 0.8588, almost 11.6% lower than the average calculated average mean for all results. The calculated medians and modes were all of a similar order of magnitude with averages of 0.9795 and 0.9698 being calculated for the median and mode respectively for all five specimens. The maximum deviations from these averages for the mean and mode were 2.3 and 5.7% respectively. The calculated skewness of the samples ranged from 1.2768 to -2.9856 with an absolute average value mean of 0.5456 and a mean of -0.3795. This translates to the average of all values being skewed to the left of the central value of 1.0. The final measure of central tendency that was calculated was the kurtosis. The calculated values had a mean of 3.1856 and ranged from a positive, leptokurtic (peaked) value of 10.4526 to -0.5474 for the D-meter results for Specimen 1. It is interesting to note that this was the only negative or platykurtic (flat) value obtained for the kurtosis of all the samples.

To compare the dispersion of the observations within the data sets the variance, standard deviation and standard errors for the four measurement methods for all five specimens were calculated. Generally all of the results obtained from the screw micrometer were within the same order of magnitude and the results from the D-meter were more scattered. The average values obtained for the variance, standard deviation and standard errors for the screw micrometer data were 0.0005484, 0.02298 and 0.001660 respectively. These average values were only 4.3, 25.7 and 25.7% of the calculated values for the D-meter which were 0.01290, 0.08952 and 0.006446 for the data sets' variance, standard deviation and standard error respectively. It can therefore be

stated that the data obtained from the D-meter was more scattered that the results from the screw micrometer.

The final statistical parameters that were calculated were the range of values and the minimum and maximum values that occurred in the normalized data sets. As with the measures of central tendency, the results for these parameters were of a similar magnitude for the screw micrometer and varied slightly for the D-meter. The average range of values for the screw micrometer results was 0.1739 which was only 34% of the average range for the D-meter of 0.5122. The average minimum value calculated for the screw micrometer results was 0.8921 which was 27.7% larger than the average minimum for the D-meter of 0.6988 and the average maximum value for the screw micrometers was 1.0659 which was only 88% of the value of 1.2110 which was obtained when using the D-meter.

As a final review of the quality of the results that were obtained from the various thickness measurement methods, a summary of the statistical results will be performed. The summary will compare the various statistical results that were calculated for the normalized readings and examine the magnitude of the dispersion of the actual thickness readings as compared to the quantify able errors involved in the measurement methods. These errors include the reading and tilt sensitivity errors for the screw micrometers and the reading error for the D-meter.

As a first step, the statistical measures of central tendency for the normalized results will be compared. The results are summarized in Table 3.6. Generally all of the results are of a similar magnitude with the maximum deviation from the average mean, median and mode's of the five samples being only 2.7, 0.6 and 1.9% of the average values. This indicates that all four measurement methods have strong central tendencies and implies that there may not be large differences in the quality of the results for the various thickness measurement methods. To better understand the scatter of the discrete observations within the five data sets the variance, standard deviation and standard error were calculated. A review of these values in Tables 3.1 to 3.5 for the five samples indicates that the results from the D-meter are much more dispersed throughout

the data sets than those results from the screw micrometer. Table 3.7 summarizes this data in terms of what percentage of the D-meter results are the measures of dispersion are for the screw micrometer readings. As can be seen from Table 3.7 the results from the screw micrometer are much less dispersed around the central value of 1.0 with results ranging from 1.2 to 53.4% of the standard deviation and standard error values of the D-meter results and 1.4 to 28.9% of the variance values for the D-meter. These results indicate that the screw micrometer produces much less scattered results than the D-meter. Another statistic that indicates that the screw micrometers produce a better quality of results is the range of the normalized data. The average values obtained for the screw micrometer for the five samples are only 1.6, 26.7, 65.8, 52.6 and 68.0% of the range of normalized range values for the D-meter. As with the measures of dispersion, this indicates much more scattered results for the D-meter which can be considered to be a negative result for D-meter thickness mapping potential.

The final comparison that was made for this research was to compare the standard error, or average standard deviation, to the tilt sensitivity graph. This was done to understand at what point on the tilt sensitivity graph do the errors associated with this sort of problem increase in magnitude beyond the result of the standard error calculation. It should be noted that included in the tilt sensitivity calculations was the reading error for the screw micrometers of 0.00005 in. For the screw micrometer being used with no anvil attachments for the micrometer at tilts of only 1, 1, 2, 1 and 1° are required to produce errors larger than the calculated standard error for the actual thickness measurements for Specimens 1, 2, 3, 4 and 5 respectively. When the micrometer is being used with an anvil attachment the tilt sensitivity error is approximately half of those that occur with no anvil attachments. In this case the micrometer has to be tilted at only 2, 1, 3, 1 and 1° to produce errors larger than the standard error for Specimens 1, 2, 3, 4 and 5 respectively.

After reviewing the aforementioned results it has been concluded that the screw micrometer with no anvil attachments will be used to record thickness values for the eight cyclic tests. The screw micrometer was considered to be a more accurate method than the D-meter due to the minimal amount of scatter that occurred as compared to the D-meter results. With respect to the use of

the various anvil attachments, the results were considered to be of a similar magnitude with no attachment producing significantly superior results than the micrometer with no anvil attachments in light of the tilting errors that may occur during testing.

3.4 Roughness Mapping

3.4.1 General

In this section the various methods that were used to examine the corroded surface of the material and the replication tape will be discussed. The investigation began with the purchase of a standard package of Testex replication tape. Included in this package were ten *medium gold coated* samples, ten *coarse* and ten *extra coarse* samples that were not metalized. Because no information was available regarding the depth of pitting, a range of tape thicknesses were purchased to begin the study of surface roughness.

3.4.2 Bright Field Illumination Optical Microscope

The use of a bright field illumination optical microscope was obtained through The Fine Particle Research Lab in the Physics Department at Laurentian University in Sudbury, Ontario. The system was originally constructed for the purpose of quantification of fine particles from aerosol cans and dust in industrial environments in terms of fractional dimensions. Due to the nature of the equipment set up it would not allow for an accurate and direct quantification of roughness. However, the opportunity to view the replicated samples using a microscope was a good first step towards understanding what magnitude of roughness was present on the samples.

The system consisted of a viewing table and microscope mount, the microscope with objective lenses of 5X, 10X, 20X and 40X magnifications, a black and white camera and television to

capture the image, a MACINTOSH personal computer and photo editor, and an electronic pencil and graphics pad. The sample is fixed to a glass slide which is itself clamped to the viewing table to avoid any motion during the examination. Following this the desired objective is selected and the image of the sample appears on the black and white television. Table 3.8 is a summary of the microscope's image calibration which shows the width of the captured image, in units of pixels and micrometers, for the various objective lenses. These factors are required to properly convert all of the data from the graphics pad and electronic pencil from pixels into micrometers. To obtain optimum results, the image showing on the television is further focused using the fine and coarse adjustments on the main microscope and by controlling the amount of light that is being used in testing to obtain optimum results. Once an acceptable image is displayed on the television screen it is captured, sharpened and the brightness and contrast adjusted to their optimum values using the photo editor. The image can then be printed out and placed on the graphics pad for tracing which results in an X-Y plot of the pixels that were traced and from this a fractal plot of the results can be constructed.

The investigation using the bright field illumination optical microscope began with a training period on the use of the equipment, following this access to the laboratory and equipment was granted. To begin the investigation, the surface of the material was replicated using the Testex replication procedure outlined in Section 2.3.3.1. One end of the tape was then glued to a glass viewing slide with the length of the tape parallel to the line of sight of the microscope, or perpendicular to the viewing table and slide. This was done to allow inspection of the cross section of the tape along it's sides in an attempt to obtain a traceable image that would allow for the estimation of the maximum peak-to-valley distances. Using this testing procedure could not be guarantee that the tape was perfectly perpendicular to the glass slide and peaks of the tape behind the outer edge appeared in the image. However, this work was conducted to gain a rudimentary insight into the replicated surface and the use of optical microscopes. Several example images that were captured by this method are included in Figures 3.40, 3.41 and 3.42 and their respective fractal plots are included as Figures 3.43 to 3.45. Also, the values of the maximum peak-to-valley roughness results (R_t) obtained for the coarse and extra coarse replica

tapes at various magnifications are included in Table 3.9. These values were calculated as shown in Section 2.3.2.3. It can be seen in Table 3.9 that as the magnification increases, thereby decreasing the field of view, the Peak-to-Valley values obtained generally decreases. This seems reasonable since the slide and tape were not moved during the changes in magnification. As the magnification increases, smaller sections of the tape will be seen in the image which will result in less of the roughness of the material being recorded.

During this portion of the research it was apparent that very little accurate numeric data could be obtained using this system. It was however considered to be an effective tool to gain preliminary insight into the study of materials using optical microscopes. Even if no experimentally useful data was obtained, the results helped to identify the preferred grade of tape that should be used. The results attained from the lowest level of magnification (5X) and largest field of view, indicated that further investigation should concentrate on the thicker grades of tape. The reason being that at this magnification the microscope covers the largest field of view of 2 mm, which is quite small in the perspective of the hundreds of square meters of surface area typically present on corroded bridges.

3.4.3 Scanning Electron Microscope

Access to a Scanning Electron Microscope was obtained through the Geosciences Laboratory of the Geological Survey of Canada at the Willot Green Center in Sudbury, Ontario. The supervisor of the laboratory agreed to perform a limited survey of the replica tape using a scanning electron microscope. As with the work done with the bright field illumination optical microscope, the study to be conducted using the scanning electron microscope was performed in order to obtain further insight into the magnitude of roughness on the surface of the material, rather than for the purpose of numerical quantification of the roughness. A sample of *gold coated medium* grade tape was prepared to facilitate the examination by scanning electron microscopy and the resulting image is included as Figure 3.46. The image was recorded at 100X magnification with a field of

view of approximately 920 μm wide by 780 μm high. Although no numerical roughness values were obtained from this work it did allow for an extremely detailed reproduction of a small area of the replica tape. One aspect of the surface roughness that did become apparent during this testing resulted from the large areas of the tape that did not replicate the surface of the material in any way. These flat areas of the tape between areas with an obvious surface topology were most likely a result of too thin a grade of tape being used. The *medium* grade replica tape that was used in this work did not possess enough micro-foam to properly contour the deeper valleys on the surface of the original sample. This result confirmed observations made following the work done using the bright field illumination microscope at Laurentian University, that the thicker grades of tape would be better suited for the quantification of the roughness of corroded steel coupons.

3.4.4 Optical Interference Microscopes

3.4.4.1 General

After an exhaustive search, two companies were found that were willing to perform a limited amount of Optical Interference Microscope testing, free of charge, to determine if the technology showed any potential for further use in roughness quantification. The two companies were Zygo Corporation of Middlefield, Connecticut and Veeco Metrology of Tucson, Arizona. Both companies agreed to run tests on two replicated tape samples and an original steel sample. Although no usable numerical values for surface roughness were obtained while using the bright field illumination optical microscope and the scanning electron microscope, several useful qualitative results were obtained. These results proved to be valuable when work was being performed using optical interference microscopes. These tests had to be performed with extreme diligence since access to the equipment was difficult to obtain and extremely expensive, costing over $500 per hour with approximately five to ten replica tape specimens being tested in an hour. Following the results from the bright field illumination and scanning electron microscopes it was

decided that the *extra coarse plus* grade of tape would be used for this portion of the research. To obtain better results from the optical interference microscopes a special order was made from Testex in which they metalized their extra coarse plus grades of replica tape which is not usually done. This resulted in a maximum thickness of micro-foam of approximately 200 μm. Another aspect of the testing process that was observed during the initial work on roughness mapping was that a better cleaning procedure was required to ensure that all of the corrosion products had been effectively removed from the pits and crevices on the surface of the material. Small flakes of corrosion product could be seen on the surface of the replica tape during the testing with the Bright Field Illumination and Scanning Electron Microscope testing. In order to avoid including the corrosion product in the roughness measurements it was decided that an increased level of cleaning, beyond vigorous wire brushing and washing with pressurized water, would be required before replication of the sample could be performed.

3.4.4.2 Cleaning Procedure

To improve cleaning of corrosion product, for all subsequent roughness readings the American Standards for the Testing of Materials (ASTM) specification G1-90 "Standard Practice for Preparing, Cleaning, and Evaluating Corrosion Test Specimens" was followed. The specification was originally written for atmospheric corrosion tests, where determining the rate of corrosion, in grams per year, is of interest. As part of the testing for that specification, all of the resulting corrosion product must be removed to ensure that only the remaining base material is weighed when determining the corrosion rate. The cleaning procedure that was used here is found in Table A1 of the standard under Designation C.3.5, for the cleaning of iron and steel. It requires solution of 500 ml of hydrochloric acid, 3.5 g of hexamethylene tetramine and distilled water to make a total of 1000 ml of cleaning solution. The corroded specimen is left in the solution for ten minutes at 20 to 25°C. For the purpose of this work, a smaller volume (100 ml) of cleaning solution was sufficient, and the proportions were therefore scaled down accordingly since the actual size of the steel specimen to be cleaned and replicated was only 38.1 x 25.4 mm.

The first step in this cleaning procedure was to weigh the original sample before any of the corrosion product had been chemically removed. This was done to allow quantification of the amount of corrosion product that has been removed during each wash. Between washes the sample was thoroughly rinsed with distilled water to remove any solution and latent corrosion product and allowed to dry completely before it was re-weighed. With this information a cumulative weight loss graph, shown in Figure 3.47, was constructed. Cleaning was stopped when the weight loss rate graph became asymtopic. From this figure, it can be seen that approximately 63% of the total corrosion product was removed during the first wash, and 95% by the end of the second wash. It was decided that sufficient cleaning had been performed after the fourth wash and that the sample was ready for the Testex replication procedure to be performed.

3.2.4.3 Zygo Corporation Testing

Once the 38.1 x 25.4 mm steel sample had been properly cleaned a 9.5 x 9.5 mm square area of the surface was clearly identified to ensure that both Testex replication procedures and laboratory tests were performed on the same area on the surface of the 38.1 x 25.4 mm steel specimen. After the Testex replication procedure had been performed on the 9.5 x 9.5 mm area marked off on the steel sample, the steel sample and the two *extra coarse plus* metalized samples were sent to the Zygo corporation for inspection. Zygo's inspection routine consisted of studying five 1.45 x 1.08 mm square areas within the 9.5 x 9.5 mm marked of area on the surface of the steel sample and each of the two replica tape samples. Within each of the five testing areas for each of the three tests, a grid of 320 x 280 = 89,600 readings was used to construct the desired three dimensional profiles. This resulted in 5 x 89,600 = 4,480,000 readings being recorded from the steel sample and the two replication tape surfaces. All of the testing was performed using a 10X magnification objective. From each of the five sampled area's collected data, the maximum peak-to-valley height (R_t or RV), the mean peak-to-valley roughness (R_m), the root-mean-square roughness (RMS) and the arithmetic mean roughness (R_a) were calculated. Copies of the measurement set up and summaries have been included as Figures 3.48, 3.49 and 3.50 for the steel sample, Replica

2 and Replica 1 respectively. A summary of the mean calculated values has been included as Table 3.10.

From Figures 3.48 to 3.50 it can be seen that all of the calculated roughness parameters for the steel sample and the replica tape samples were of a similar level of magnitude. However, for all roughness parameters, the steel sample had the largest mean roughness values followed by Replica 2 (Figure 3.49) and Replica 1 (Figure 3.50) which had the lowest mean values. On average, Replica 1 and 2 mean values for all four roughness parameters were 26.1 and 15.4% lower than the steel sample results. These values can be further broken down to PV, R_m, RMS and R_a mean values being 15, 27.6, 31.1 and 30.8% lower than the steel sample for Replica 1, and 9.3, 12.3, 10.8 and 19.1% lower than the steel sample for Replica 2.

There are several possible causes for the lower roughness values obtained with the replica tape. It is possible that slightly thicker tape is required to fully record all of the peaks and valleys of the steel samples surface. If there are surface features on the original sample in the 250 to 300 μm range, a tape with a micro-foam thickness of 200 μm would not fully replicate all of the extreme surface features from the original sample. (Note that replica tape having larger foam thicknesses can be manufactured by special order). Another possible cause of lower readings was that not enough pressure was applied to the back of the tape during the replication process. This would result in the foam not being fully pushed into the extreme valleys on the steel sample's surface and the maximum peaks not fully depressing the foam of the replica tape. The result of this would be a smoother, more rounded replica surface than is actually present on the steel sample. Another possible cause of the lower roughness parameters for the replicas is the natural variation on the surface of the original sample. Since the five sampling areas within the 9.5 x9.5 mm surface areas were not necessarily at the exact same location on the two replica tape and steel sample surfaces, it is possible that less rugged areas of the surface were sampled on the replicas, resulting in lower roughness parameters.

3.2.4.4 Veeco Corporation Testing

Once the steel sample and the two pieces of replica tape were received back from the Zygo Corporation, they were immediately shipped to the Veeco Metrology Group for inspection. The testing performed involved using a stitching routine to join data sets from adjacent surface areas to combine them into one data file for the entire 9.5 x 9.5 mm surface of the replica tape and the steel samples. Using this methodology, a sampling area of approximately 9.5 x 9.5 mm = 90.25 mm^2 was studied (as compared to a 5 x 1.446 x 1.085 mm = 7.845 mm^2 sample areas for the Zygo testing program). For the steel and replica tape samples studied, there were 1816 x 1446 = 2,625,936, 1917 x 1758 = 3,370,086 and 2009 x 1724 = 3,463,516 readings taken for the steel sample, Replica 1 and Replica 2 respectively. All of the inspection done by the Veeco Corporation was performed using a 2.5X magnification objective.

It was found that the Veeco study resulted in much larger roughness parameters than those obtained by the Zygo Corporation. Table 3.10 provides a summary and comparison of all calculated statistics for the two series of tests. The main cause for the difference in results is the cutoff filters that were used by the Veeco Corporation. A cutoff filter can be defined as the wavelength at which the microscope differentiates between surface waviness and the actual surface roughness that is to be quantified. The two components of the surface texture, the roughness and waviness can best be understood by reviewing a simplified example of the cutoff filter shown in Figure 3.51 (Zygo Catalogue, 1999). If should also be noted that full outputs from Veeco have been included as Figures 3.52 to Figure 3.62. In Figure 3.51, a set of sample input profile, and the separated waviness and the final roughness profiles, including the mean line, are shown. The process of filtering out the waviness data removes all of the larger surface features that have a magnitude larger than the resolution of interest. In the case of the work by Veeco, the technician did not remove cylindrical and curvature effects, as can be seen from the bottom left hand corner of the surface data and 3D plot sheets from Veeco. The only term removed is the tilt of the sample. As a result, a 1 mm thickness change that occurs over the 10 mm width of the sampling area would be incorrectly considered to be part of the roughness of the surface. In

comparison, for the Zygo Corporation testing results, included as Figures 3.48 to 3.50, it can be seen that the cylinder effects have been removed, resulting in only the desired surface roughness to be measured.

3.2.4.5 Summary

In conclusion, for the purpose of this research, the testing program conducted by the Zygo Corporation produced more useable results than those from the Veeco Corporation. The main reason for this was that the Zygo Corporation used a filtering algorithm that removed the effects of cylindrical waviness features on the surface of the steel and replica tape samples, whereas the Veeco program did not. Also, the field of view and test area for the Zygo Corporation was smaller, further limiting the effect of surface waviness on the final statistical results. It is important to note that both firms are capable of producing similar results if comparable cut off filters, magnifications and stitching routines were used.

When reviewing the results from the Zygo and Veeco Corporations, the method of quantifying surface roughness using proper cleaning procedures, the Testex replication procedure and an optical interference microscope show excellent potential for future use. However, due to the limited amounts of test data available to quantify the accuracy of the results and the high cost of testing, the optical microscope method was not used to quantify the roughness of the cyclic test specimens presented in subsequent chapters. The roughness will instead be determined using standard Testex dial gauges after the replicas have been made from the cleaned surface of the specimens. This method will be used because of the lack of experimental data available outlining the accuracy of the optical interference microscope method. Also, the manufacturers of the replica tape have offered to perform testing on approximately 50 *extra course plus* samples, free of charge, to further increase the potential uses of their product.

CHAPTER 4
FINITE ELEMENT MODELING

4.1 Introduction

Following the nondestructive thickness evaluation of the specimens, the five corroded specimens and a smooth control specimen were sent to a material testing lab for tensile testing. The resulting force-displacement curves from the tensile tests were then compared to the force-displacement curves from various finite element models that were created. For this research, the finite element models were used to investigate if the analytical force-displacement results from the finite element analysis matched the force-displacement curves obtained from the tensile testing and to better understand what effect finer and coarser grid spacing of the thickness measurements had upon the analytical force-displacement curves. This chapter first reviews and comments upon the results from the tensile testing. Following this, a detailed review of the construction methodology for the various finite element models is presented. This includes a review of the model's geometry, elements, material properties and loading conditions. Finally, the force-displacement curves from the tensile tests and the various finite element models are compared.

4.2 Tensile Test Results

To better understand the quality of the results from the thickness mapping, the five corroded ASTM long tensile test specimen and the control specimen were sent to a material testing laboratory for tensile testing. The control specimen was a standard ASTM long test specimen with a 203.2 mm gauge length and a 38.1 mm gauge width, as can be seen in Figure 3.1. All

corrosion products were mechanically removed from the control specimen to obtain a uniform cross section and therefore accurate estimates for the yield and ultimate stress of the material being studied. With knowledge of the material's yield and ultimate stresses multi-linear models of the material's behavior can be constructed. The models include stress-strain points at yield, at the beginning of strain hardening, and at the ultimate stress of the material, all connected by linear segments.

To record the results from the tensile testing, a 203.2 mm (8 inch) long extensometer was connected to the specimens over their full gage lengths. The result of the testing was a data file that included all of the recorded information including the time, strain, stress, position of the testing apparatus and the applied loads. It should be noted that the recorded stress is only meaningful for the smooth control specimen (due to the varying cross section of the corroded specimens) and that the recorded position included all displacements that occurred during testing including the tightening of the instrument's grips. After each test had been completed, the final gage length was measured to obtain the elongation of the specimen at rupture. The data files were imported into a spread sheet to construct the required force displacement curves. The six tensile test reports are presented as Figures 4.1 to 4.6 and the force displacement graphs in Figures 4.7 to 4.11. It should be noted that the specimen dimensions of 1.5 x 0.375 inches and the yield and ultimate strengths, shown in units of p.s.i. have meaning only for the smooth control specimen. This is due to the fact that specimens one to five posses varying cross sections and could therefore not be related to specific sectional dimensions or stresses. Also note that Laboratory Number 233970-1999 shown on the upper right-hand corner of the tensile test report shown in Figure 4.1 is the report identification for Specimen 1. Laboratory Numbers 233971-1999, 233972-1999, 233973-1999 and 233974-1999 are for Specimens two through five respectively and Laboratory Number 233975-1999 is the report for the control specimen.

The first step performed in the analysis of the tensile test report results was to calculate the yield and ultimate forces that correspond to the given yield and ultimate stresses. This procedure involved multiplying the given stress value by the assumed member cross sectional dimensions of

38.1 x 9.525 mm (1.5 x 0.375 inches). Table 4.1 summarizes these yield and ultimate force results. Also shown in this table are the ratios of the yield to ultimate forces and the over all percentage of material loss for each specimen as compared to Specimen 5 which had the largest mean thickness. From this table it can be seen that the yield force values range from a low of 56.55 kN to a high of 84.57 kN and the ultimate forces range from a low of 79.82 kN to a high of 121.60 kN for the five corroded specimens. The control specimen had yield and ultimate forces of 114.35 and 162.64 kN respectively. Also of interest in this table is the fact that Specimen 3, which had the most material loss as compared to Specimen 5 had the lowest yield and ultimate forces and Specimen 1, which had the second most material loss had the second lowest yield and ultimate forces. It can also be seen in this table that although the range of ultimate and yield forces for the specimens was significant the ratios of their yield to ultimate forces were all within 3% of the mean value. This result is reasonable for testing being performed on steel from the same sample population with the range of yield and ultimate force values that were obtained being a result of the varying actual cross sectional areas of the samples.

The resulting force displacement curves for the five corroded specimens are shown in Figures 4.7 to 4.11 for Specimens one through five respectively. With reference to Figure 4.7, it can be seen that the force and displacement data was recorded through the yield point and strain hardening beyond the ultimate strength of the specimen to a point of necking and final rupture. Such complete stress-strain curves were needed to be able to compare the experimental force displacement curves with analytical results from the finite element models. However, after plotting the data from the files received from the commercial testing laboratory, it was found that the recorded data for Specimens two through five, were not of the same quality. The quality of the results for Specimen 2 was reasonably good up to the yield point for the linear elastic portion of the curve, but questionable beyond this point. After discussing this situation with the technician that performed the testing, it was discovered that the extensometer had popped off the specimen just after the yield point. This is the reason for the almost horizontal portion of the force displacement curve from an approximate displacement of 3 mm to 27 mm. When reviewing the data file for this section of the graph, it can be seen that the displacement value jumps from 3.76

mm to 10.17 mm in just more than one second and then up to 26.52 mm before another three seconds has elapsed. For this reason, the technician became nervous about the possibility of damage to his equipment and removed the extensometer from Specimens three to five just beyond the yield point and the required data from yield to final rupture was not obtained. As shown in Figures 4.9 to 4.11, the force displacement curves for Specimens three to five, displacements were only recorded up to approximately 2 mm. Also, the initial portion of the curve, to the yield point, is not linear. This causes concern with respect to the performance of the extensometer during the testing of Specimens three to five. The possibility exists that the instrument was damaged when it fell during the testing of Specimen 2. Although full data sets were not obtained for all of the specimens, the yield point was recorded for all five specimens and some useable information was obtained. In particular, it is important to note the absence of a sharp transition from the elastic to plastic range. This is consistent with what was observed by Bruneau and Zahrai (1998), and attributed to the variable cross-section due to the irregular material loss due to corrosion.

4.3 Finite Element Modeling

4.3.1 Finite Element Model Construction

To investigate the quality of the nondestructive thickness mapping, finite element modeling was performed for the five specimens. Each of the five specimens was mapped using five measurement methods, resulting in a total of twenty-five thickness maps. For each of the thickness maps two geometric and two material property model variations were investigated. The first geometric model used all of the thickness data collected to construct a fine mesh geometric model. The second geometric model was constructed to determine if there was a loss of finite element analysis accuracy if fewer thickness readings were recorded during the nondestructive testing. The material property variations consisted of performing the analysis using the yield and ultimate stress results that were obtained from the tensile testing of the control specimen for the

first model, and for the second model using the yield and ultimate stresses taken directly from The American Institute of Steel Construction Handbook for Iron and Steel Beams from 1873 to 1952 (AISC, 1953) for A7 bridge steel from the 1950s. The fine and coarse geometric models were both analyzed using each previously mentioned two material property models separately. This resulted in the fine mesh model being analyzed with two separate material property models and the coarse mesh model being analyzed with the same two material property models.

For the purpose of this work, an educational copy of ANSYS 5.5.2 was purchased. This version is a scaled down version of the full ANSYS package. The program provides graphical user interface with pull down menus to accomplish most modeling steps. The program limits for the ANSYS/ED professional version are: a maximum number of degrees of 2,000 degrees of freedom; a maximum of 1,000 nodes; and, a maximum of 500 elements. The largest model constructed here had 1,632 degrees of freedom, 544 nodes and 231 elements, all of which are within the allowable limits of the package.

The element type from the program library that was considered most applicable to this problem was the SOLID45 element, used for three dimensional modeling of solid structures. The element is defined by eight nodes. Each node has a degree of freedom in the global x, y and z directions. This element type is well suited for our model since rotational degrees of freedom are not required and would cause the fine mesh model to have too many degrees of freedom for the ANSYS/ED package. Also, this element type can model large deformations and large strains as required for the nonlinear analysis in this work.

In terms of general material properties, a constant isotropic property type was chosen with the following values being entered into the program:

E_X = 200,000 MPa = 29,000,000 psi (Modulus of Elasticity)

$PR_{XY} = PR_{XZ}$ = 0.3 (Poisson's Ratio)

G_{XY} = 77,000 MPa = 11,170,000 psi (Shear Modulus)

The data table's option of the preprocessor was used to input the stress-strain curves for the two

chosen material type. For this, a multi-linear isotropic model was chosen. This allowed the user to enter up to 20 stress-strain points to model the material's behavior. Here, two separate stress-strain curves were used to model the specimen's behavior. The first stress-strain curve is the one shown in Figure 4.12. The yield stress and ultimate stress were taken directly from the control specimen test results adapted for use in the finite element modeling with several standard assumptions being used to complete the stress-stain curve. The standard assumption consisted of locating the beginning of strain hardening at fifteen times the yield strain and the modulus of strain hardening being equal to the elastic modulus divided by thirty. The stress-strain data points used to define the first material type, which had a yield stress of 315.1 MPa (45,700 psi) and an ultimate stress of 448.2 MPa (65,000 psi) was determined in the following way:

$$\sigma_Y = 315.1\,MPa$$

$$\varepsilon_Y = \frac{\sigma_Y}{E} = \frac{315.1}{200000} = 0.001526$$

$$\sigma_{SH} = 315.1\,MPa$$

$$\varepsilon_{SH} = 15\varepsilon_Y = 15(0.001526) = 0.02288$$

$$\sigma_U = 448.2\,MPa$$

$$E_{SH} = \frac{E}{30} = \frac{200000}{30} = 6666\,MPa$$

$$\varepsilon_U = \varepsilon_{SH} + \frac{(\sigma_U - \sigma_{SH})}{E_{SH}} = 0.02363 + \frac{(448.2 - 315.1)}{6666} = 0.04359$$

The second stress-strain curve was constructed using yield and ultimate forces that would typically be used in design for ASTM-A7 bridge steel from the 1950s (AISC, 1953). The graph

construction methodology was similar than for the aforementioned curve, with the values calculated as below giving the resulting stress-strain curve shown in Figure 4.13.

$\sigma_Y = 248.2\,MPa$
$\varepsilon_Y = 0.001241$

$\sigma_{SH} = 248.2\,MPa$
$\varepsilon_{SH} = 0.01862$

$\sigma_U = 381.3\,MPa$
$\varepsilon_{SH} = 0.03858$

The finite element model was then constructed by translating the thickness mapping data into the required node and element systems. For this work, two geometric models were used. The first model used a fine mesh which consisted of 544 nodes and 231 elements. The second model with a coarse mesh, possessed 216 nodes and 85 elements. Both models were created from the 192 thickness readings that were recorded using various methods during the nondestructive evaluation portion of this work. Several assumptions were made to facilitate the construction of the fine and coarse meshes. First, the thickness readings were assumed to be located at the center point of each 6.35 mm x 6.35 mm squares on the measurement surface. This created a 6x32 system of 192 thickness measurements located at discreet points on the coupon's surface. As can be seen from the partial plan view of the 203.2 mm x 38.1 mm test surface shown in Figure 4.14, the x and y origin is located in the bottom left corner of the surface. Also shown on this figure are the assumed locations of the thickness readings and a portion of the original 6 x 32 mesh of thickness measurements. The zero point along the z axis was assumed to be located at the center point of all thickness values. This means that for each of the 192 thicknesses reading, half of the thickness of the material is located above the x-y plane and half is located below the x-y plane.

The 544 node, 231 element fine mesh model was created using the previously mentioned assumptions and thickness data. Figure 4.15 is included to assist in the description of the model construction. The first step to generate the fine mesh geometric model was to assign the 192

actual thickness values to nodes in the model. Since the model uses eight node, three-dimensional elements, these absolute thickness values were evenly divided between the upper and lower face of the coupons. For example, if a thickness reading of 8 mm was recorded at x= 3.175 mm, y= 34.925 mm (shown in Figure 4.15 as Node A), the two nodes at that point would have coordinates of x_1 (Node A) = 3.175 mm, y_1 (Node A) = 34.925 mm, z_1 (Node A) = -4 mm and x_2 (Node A) = 3.175 mm, y_2 (Node A) = 34.925 mm, z_2 (Node A) = +4 mm. Following this methodology, 2x192=384 nodes were created for the model. To model the rest of the specimens surface, a series of nodes was created using the thickness values from the closest of the 384 nodes that have already been created from the original 192 thickness values. With reference to Figure 4.15, it can be seen that the three nodes labeled NODE AA at the top left hand corner of the figure are nearest to NODE A, a location of one of the original thickness measurements. For this reason, all six nodes at these locations have been assigned the same coordinate values as the two nodes previously calculated for NODE A above and below the X-Y plane. The same process applies to NODE B and NODE C, with the secondary nodes, NODE BB and NODE CC taking on their respective coordinate values above and below the X-Y plane. Once the nodes on the periphery of the testing surface were defined, a mesh of 8x34x2=544 nodes had been created to allow the three-dimensional element formulation to be performed. The total of 7x33=231 8-node cubic elements including:

- 4 - 3.175 mm x 3.175 mm corner elements
- 62 - 6.35 mm x 3.175 mm edge elements
- 10 - 3.175 mm x 6.35 mm end elements
- 155 - 6.35 mm x 6.35 mm center elements

The 216 node, 85 element coarse mesh was created to determine the effect of taking fewer of the thickness readings upon the accuracy of the finite element models. It was produced using a procedure similar to those used to construct the fine geometric mesh model. Figure 4.16 is presented to illustrate the coarse mesh construction methodology. The locations of some of the original 192 thickness readings, the outline of their corresponding 6.35 mm x 6.35 mm measurement areas, as well as the locations of some of the 216 nodes are also shown in Figure 4.16. The first noticeable aspect of this model is that a uniform element size of 12.7 mm x 12.7

mm could not be used for the entire surface of the specimen to obtain an even node spacing. The first column of nodes is located at x= 0 mm, the second column is located at x= 9.525 mm. Thereafter, except for the last column, they are located at an even spacing of 12.7 mm, with a final spacing of 3.175 mm. The specimens were divided in this way so that the nodes for this second model would fall at the same points along the x-axis where actual thickness measurements were taken. In this way, each node could be assigned a thickness value corresponding to a 6.35 mm x 6.35 mm area of the original grid. With this construction method, the coarse mesh can model the effect of taking fewer thickness measurements. With reference to Figure 4.16, the assignment of thicknesses to the nodes was performed as follows:

- Node 1 was assigned the value of Thickness 1
- Node 2 was assigned the value of Thickness 2
- Node 3 was assigned the value of Thickness 4
- Node 5 was assigned the value of Thickness 8
- Node 19 was assigned the value of Thickness 33

A similar construction methodology was followed for the entire coarse mesh geometric model. The coarse mesh resulted in a 216 node, 85 element model that had:

- 2 - 9.525 mm x 9.525 mm left corner elements
- 2 - 3.175 mm x 9.525 mm right corner elements
- 3 - 9.525 mm x 6.35 mm left end elements
- 3 - 3.175 mm x 6.35 mm right end elements
- 30 - 12.7 mm x 9.525 mm top and bottom edge elements
- 45 - 12.7 mm x 6.35 mm center elements

Once the fine and coarse mesh's geometric construction had been completed, the number of finite element models was determined. For this research, a total of five corroded specimens were tested. For each specimen there are five measurement methods, which includes four micrometer thickness grids and a depth meter grid. Also, each of the five specimen is modeled using two sets of yield and ultimate stresses. The first set uses a yield stress of 315.1 MPa (45.7 ksi) and an ultimate of 448.2 MPa (65.0 ksi) taken from the tensile testing results for the control specimen. The second model uses yield and ultimate stresses of 248.2 MPa (36.0 ksi) and 381.3 MPa (55.3

ksi), representative of ASTM A7 bridge steel. This results in a total of two geometric meshes times five samples times five measurement methods/sample times two stress-strain curves, for a total of 100 finite element modeling scenarios.

It was decided that induced displacements, rather than induced forces would be used to load the various models. This was done because displacement-based loading produces a more stable analysis terms of solution convergence. For all models, the nodes at one end of the specimen were fixed with zero displacement in the x, y and z directions. At the other end of the specimen, between 5.08 mm and 10.16 mm of displacement was applied along the x-axis, depending on the specimen. For example, for the Specimen 1 coarse mesh, all ten models were able to converge at a total displacement of 10.16 mm. This displacement was applied in 300 sub-steps, or in displacement increments of 0.03387 mm. However, some of the models did not converge at total displacements greater than 5.08 mm. When attempts were made to decrease the size of the sub-steps, problems were encountered due to limitations in computer memory capacity. The program would run the model up to a point and then abort the run and exit the program. This lower total displacement was not of great concern since force displacement information for Specimens two through five are only available up to approximately 2 mm. To complete the analysis of all of the finite element models, between 300 and 600 incremental displacement sub-steps were required for the various modeling scenarios.

4.3.2 Comparison Finite of Element Results

As previously mentioned, four finite element models were created for each of the five measurement techniques used for the thickness mapping of the five specimens. This resulted in one hundred finite element models constructed and analyzed for this research. For each of the twenty-five measurement maps, several material and geometric alterations were investigated. Two geometric models were considered in this work. The first utilized the actual thickness measurements to almost directly construct a system of nodes that was then meshed into the fine mesh geometric model. A second set of nodes was created to gain insight into whether a loss of

accuracy resulted when only approximately half of the thickness readings were used in mesh generation. This second set of nodes was used to construct the coarse mesh geometric model. The final alterations to the finite element models that were investigated were the effect of altering the material property characteristics. The first model utilized the actual tensile and ultimate stresses that were obtained from the tensile testing of the control specimen and the second variation used nominal yield and ultimate stresses for A7 bridge steel. Both of the material property models were constructed using the methodology discussed in section 4.3.1.

For each of the five specimens, four graphs have been included. Figures 4.17 to 4.20 show the results for each of the four models for Specimen 1, graphed separately. All of the figures compare the force displacement curves for the five measurement techniques to those from the actual specimen. Figure 4.17 shows results for the coarse mesh geometric model with a yield stress of 248.2 MPa (36.0 ksi), Figure 4.18 for the coarse mesh model with a yield stress of 315.1 MPa (45.7 ksi), Figure 4.19 for the fine mesh with a yield stress of 248.2 MPa, and Figure 4.20 for the fine mesh and a yield stress of 315.1 MPa. A similar methodology was followed for Figures 4.21 to 4.36 for Specimens two through five respectively. Tables 4.2 to 4.6 are summaries of the approximate yield, ultimate and final forces for the five samples and the actual tensile testing, Tables 4.7 to 4.11 are summary comparisons of the material property variations for the coarse and fine mesh geometric models and Tables 4.12 to 4.16 are summary comparisons of the fine and coarse mesh geometric models for the two material property variations.

With reference to Figures 4.17 to 4.36, it can be seen that the finite element modeling results produce similar force displacement results for all five measurement techniques. In most cases the force displacement results are grouped within approximately 5% of their total values along the full length of the curves. The exception to this is the D-meter result for Specimen 1, as can be seen in Figures 4.17 to 4.20. In these graphs, the D-meter's force displacement results are approximately 15% lower at the yield, ultimate and final forces as compared to the micrometer results. This variation can be explained by the questionable thickness readings that were obtained when using the ultrasonic depth meter on this sample. In many cases the instrument indicated thicknesses that were substantially lower than those obtained from the screw micrometer. The most likely cause

for these lower D-meter thickness readings was the suspected presence of an internal lamination at some point through the thickness of the material for Specimen 1. This would have caused the finite element model to yield at an earlier stage in the loading because of the lower thickness and the resulting higher stresses that would be encountered at these points.

Another aspect of the finite element modeling results that can be seen in Figures 4.17 to 4.20 is the difference between the finite element and tensile testing results along the descending portion of the curves. The average decreases in applied force between the ultimate and final readings were only 11.95 kN for the micrometer and D-Meter curves as compared to 69.42 kN for the actual tensile test as can be obtained from Table 4.2. The main cause of this was that the finite element models did not account for the appearance and effects of cracking on the surface of the material and the resulting decrease in applied force. Although the program was able to model the effects of large stains and deformations, a fracture mechanics model of the cracking and necking that occurred during the actual tensile testing at approximately 8mm was not performed. As a result, the final section of the force displacement curve was not properly modeled for Specimen one.

With respect to the performance of the various finite element models, the comparison of the higher to the lower yield strength models is summarized in Tables 4.7 to 4.11 for Specimens one to five respectively. In these tables, the yield and ultimate (or final) force values for the lower yield models were compared with those from the higher yield models for the coarse and fine mesh geometric models separately. Once all of the relative differences had been calculated, from Tables 4.2 to 4.6, the mean difference between the yield and ultimate forces was divided by the mean of the yield and ultimate forces for the lower and higher yield models to determine what percentage of these values the difference represented. As an example, for the standard micrometer's yield force for the coarse mesh model for Specimen 1, the higher yield model had a yield point of 76.78 kN and the lower yield force model produced a yield point of 60.60 kN for a resulting difference of 16.18 kN, as shown Table 4.7. The resulting mean of the differences of 15.46 kN was calculated for all of the measurement techniques. Dividing the value by the mean of the yield point results for the lower and higher yield models, the mean difference value is found to

correspond to 26.7 % of the lower yield model results and 21.0% of the higher yield model results. Note that similar results are obtained when comparing the two material property models' actual yield point values of 248.2 MPa and 315.1 MPa. The difference between the two yield points is 66.9 MPa which represents 27.0% and 21.2% of the lower and higher yield point values respectively. When a similar calculation is performed for the ultimate strength of the two material property models, it is found that the resulting difference of 66.9 MPa represents 17.5 and 14.9% of the lower and higher yield strength model's ultimate strength values of 381.3 MPa and 448.3 MPa respectively. As can be seen in Tables 4.7 to 4.11, the results for the two material property variations to the finite element models were of a similar magnitude as compared to the two actual material property differences and typical for all five specimens. It should be noted at this point that the bold values in Table 4.11 were not considered to be relevant to this comparison since they were comparing models that converged at different final displacement values. For this reason, the final force values occurred at different points on the force displacement curves. However, other than the results shown in bold the differences in finite element modeling results were almost directly related to the choice of the material's yield and ultimate stresses. This direct relation between a material property's stress strain curve and the resulting finite element force displacement curves emphasizes the care that a designer must take when modeling the material properties of an existing steel structure.

When reviewing the data contained in Tables 4.12 to 4.16, it can be seen that the fine geometric model variation translated into no appreciable gains in the accuracy of the results. In most cases, the mean difference between the results obtained for the fine and coarse geometric models was less than 5%. As mentioned in the previous paragraph, in several cases the fine and coarse geometric models could not be compared since they did not converge at the same final displacement values. For example, for Specimen 2, the fine model would not converge beyond 5.08 mm where as the coarse model computed results up to 7.62mm. Comparing the fine model, which had a total displacement of 5.08mm, to this coarse model was not considered to be an accurate indication of the difference between the two geometric modeling results and as such the results have been shown in bold in Tables 4.12 to 4.16.

In terms of the finite element models accuracy in matching the actual tensile testing results, the lower yield models generally produced slightly conservative results. Although the control specimen had an actual yield stress of 315.1 MPa and ultimate stress of 448.2 MPa, when these values were used as material properties, the yield and ultimate forces of the corroded specimens were overestimated. One factor that may have influenced the performance of the corroded samples was the presence of corrosion pitting. The corrosion pits may have acted as stress raisers and crack initiation points during tensile testing of the corroded samples. This problem would obviously not have affected the performance of the machined smooth control specimen. One aspect of the tensile testing that points to the potentially damaging effect of corrosion pitting was the elongations at failure. When reviewing the test reports included as Figures 4.1 to 4.6, it can be seen that the control specimen fractured at an elongation of 27%. In comparison Specimens one through five fractured at elongations of 5, 16, 10, 18 and 15%, at average elongations less than half of that of the control specimen. With respect to a corroded material's energy dissipation characteristics, a common dividing line between brittle and ductile materials is 5% elongation at failure (Fitzgerald, 1967). This would result in Specimen 1 being considered a minimally ductile material even though the original non-corroded structural steel was most certainly ductile, as revealed by the 27% elongation for the control specimen. This raises concern regarding the corroded material's ability to carry monotonic loading in a ductile manner. The possibility therefore exists that as the corrosion pits are stressed to an increased level, crack initiation occurs and there is a redistribution of the applied forces to a cross section of a lower area causing a premature, less ductile failure of the corroded member.

When reviewing the specific force displacement curves from the finite element analysis, compared to the tensile test results it can be seen that the material property model using the actual yield and ultimate stresses obtained from the control specimen produced overly liberal estimates of the corroded sample's behavior.

- For Specimen 1 the coarse mesh, lower yield model, shown in Figure 4.17, produced the most accurate modeling of the actual force displacement results along the full length of the curve.

- At yield the average of the micrometer results was 1.4% lower than the actual curve, and at ultimate, the finite element model was 0.9% higher than the experimental curve.
- In comparison, the coarse mesh yield model produced results that were 24.9 and 18.1% higher than the actual force displacement curve at yield and ultimate.
- The results for the yield points of Specimens two and four were similar to those for Specimen 1 with the coarse mesh lower yield model producing the most accurate modeling of the actual force displacement curve.
- For Specimen 2 as shown in Table 4.3, the coarse mesh lower yield models' yield point was 4.1% lower than the actual yield and that the coarse mesh higher yield model resulted in a finite element yield point that was 18.3% higher than the actual.
- For Specimen 4 the results show a 9.5% lower yield point for the lower yield model and a 14.4% higher yield force for the higher yield model as compared to the actual tensile testing results.
- For Specimen 3 the fine mesh higher yield model resulted in the most accurate modeling of the yield point.
- This model resulted in an estimation of the yield point of 59.91 kN as compared to 56.02 kN for the actual testing, or a 6.9% over estimation.
- Although these results produced the closest modeling of yield point for Specimen 4, the results from the lower yield model would be more acceptable for design since they are conservative by 13.4%.
- For Specimen 5, the lower and higher yield point models produced curves that were approximately equal distances below and above the actual force displacement curves for both the coarse and fine mesh models.
- The lower yield point model results approximately 11.4% below the actual tensile test results and the higher model results approximately 11.3% above the actual force displacement curve.

While reviewing the various force displacement curves, it can be seen that in most instances the models using the 248.2 MPa (36 ksi) yield point produced results that were slightly conservative and more acceptable for design purposes than the higher yield model. However, when comparing

the actual force displacement curves from the tensile testing to the various results from the finite element modeling, concern arose about the potentially detrimental effect of the surface imperfections caused by corrosion. Tensile testing of the control specimen revealed that the steel had a yield point of approximately 315 MPa, well above the 248 MPa minimum design value for steel from this era (AISC, 1953). However, the corroded samples did not perform to the 315 MPa yield level. This suggests that a designer could potentially under-design a rehabilitation project based upon his/her belief that the steel would perform to a yield level obtained by performing tensile testing on ground smooth control specimens from the actual corroded structure.

CHAPTER 5
EXPERIMENTAL APPROACH

5.1 General Description of Specimens

For this research, two long segments of wide flange beams were flame-cut from a bridge that was demolished in the 1990s. The original structure was a six bay Warren truss constructed in Ontario in the 1950s. These beams were selected because they were representative of the various levels of corrosion present on that bridge. The first was an end cross-beam and the second was an interior cross-beam. They were originally specified on the drawings as 24"WF@80 and 27"WF@91 structural shapes.

To allow controlled testing in the laboratory, the specimens were prepared as smaller sections cut from the salvaged beams from the bridge. Approximately 1.0 to 1.5 m long sections were cut using a band saw. The ends of the four specimens were then ground smooth to remove any small defects or notches that may act as stress raisers during the cyclic testing of these samples. In total, four samples were prepared for the nondestructive tests and cyclic tests conducted during this stage of the research, namely two 267 mm long 27"WF@91, one 356 mm long 27"WF@91 and one 356 mm long 24"WF@80.

5.2 Experimental Set-up

The experimental set-up used for the cyclic testing of the floor beams was not intended to replicate the actual seismic effects that would occur on a bridge beam during an earthquake. Instead, a convenient set-up was designed to test the wide flange sections in cyclic weak axis

bending at their most corroded cross section, the flange-to-web intersection. Cyclic weak axis testing was chosen for this research over shear testing due to the fact that this type of cyclic loading has a more significant effect upon the surface damage caused by pitting corrosion. The setup consisted of a strong reaction column, a rigid base, and a small hydraulic actuator with a maximum loading capacity of 25 kN, connected as shown in Figure 5.1. Since the reaction arm and rigid base had already been fabricated for a previous experiment, the only additional preparation required was the drilling of holes in the web and flanges of the specimens to allow for their bolting to the actuator and rigid base respectively. Four holes were drilled at the mid-height of the web of the three 27"WF@91 specimens, but eight holes were required on the webs of the 24"WF@80, four centered at 267 mm and four centered at 343 mm from the underside of the flange, (required to keep the actuator at a constant height). This potentially allowed two tests per specimen. After the first flange-to-web intersection of a specimen was tested to failure, it was unbolted from the rigid base, flipped over and reconnected to the base allowing, for the second flange-to-web intersection to be tested. To minimize the potential for rotation of the flanges at each flange-to-web intersections, six 19 mm diameter holes (three on each side of the web) were drilled in the top and bottom flanges of each specimen. These holes were located as close to the vertical face of the web as possible in an attempt to minimize the moment arm between the center line of the web and the two lines of bolts.

5.3 Instrumentation

Instrumentation of the specimens included a load cell and LVDT internal to the actuator, and four external LVDTs. The internal load cell and LVDT were used to monitor the applied loading and displacement of the specimen. Two of the external LVDTs were used to monitor rotation of the web to flange intersection and the final two external LVDTs were used to determine if any slippage was occurring between the rigid base and the concrete floor, and between the specimen and the rigid base. Figure 5.2 shows the location of the four external LVDTs. A high resolution

data acquisition system was used to record all of the information generated during the cyclic testing of the corroded specimens.

Each of the eight tests began with a few test cycles that were used to determine the approximate yield displacement for each member. Following this, the specimens were subjected to a preprogramed hysteretic displacement history. The displacement history consisted of three cycles of $\pm 0.5\delta_Y$, $\pm 1.0\delta_Y$, $\pm 2.0\delta_Y$, $\pm 3.0\delta_Y$, followed by cycling to failure at $\pm 4.0\delta_Y$. The loading rate for all of the testing was 1.0 cycles/minute cyclic loading continued until the specimen's capacity decreased below approximately 20% of the maximum capacity.

5.4 Non-Destructive Evaluation of the Specimens

Before cyclic testing of the specimens could begin, thickness and roughness measurements were recorded. Based on the results of the finite element modeling (Chapter 4), a micrometer with no anvil attachment and a measurement grid spacing of 12.7 mm was selected for the thickness mapping. For the roughness measurements, three replica tape samples were taken at the top and bottom of each specimen on each side of the web, for a total of 48 *extra coarse plus* replica tape samples. These samples were then sent to Testex in Newark, Delaware for roughness quantification using a Mitutoyo replica tape thickness gage.

The thickness mapping was performed from the middle of the web-to-flange intersection up to a point between 38.1 and 50.8 mm along the web toward the other flange. The recorded data can be seen in Tables 5.1 to 5.4 for Specimens one to four respectively. Note that the extent of the initial cracking is shown in these tables by the thickness readings indicated in bold. From Table 5.1, it can be seen that six rows of thickness measurements were recorded for this specimen, as can be seen in Figure 5.3 three rows of measurements taken at the top of the specimen and three at the bottom. It should be noted that no readings were recorded at the center of Specimens one and two because the screw micrometer used had a maximum reach of 152 mm from the edge,

which is less than half of the width of these specimens. Also measurements were not taken elsewhere on the web since the moment at these locations was significantly less than at the actual flange-to-web intersection. Similar results were recorded for Specimens two to four, with between six and eight rows of measurements recorded. In terms of the original web thicknesses, Specimens one, three and four were 27WF@91 sections whose original web thickness was 12.3 mm and Specimen two was a 24WF@80 section with an original web thickness of 11.6 mm.

Data in Table 5.1 revealed that Specimen 1 has an average thickness of 11.04 mm, with minimum and maximum thicknesses of 9.53 mm and 13.69 mm respectively. The top section of the specimen was slightly thinner with the average thickness of 10.51 mm versus 11.56 mm for the bottom. The maximum value of 13.69 mm may be greater than the original web thickness for several reasons. Although each specimen was vigorously cleaned with a wire brush before the thickness measurements were taken, some corrosion product did remain around the web-to-flange intersection. Due to the fact that the objective of this research, to investigate the effect of surface roughness on the material's energy dissipation capability, removal of corrosion using a grinder or other mechanical means was not an acceptable option. Also, as discussed in Section 3.2.2 slight tilting of the screw micrometer is always possible and causes an overestimation of the thickness of a material. As can be seen in Figure 3.3 which shows that a tilt of 10° results in a reading error of approximately 1.1 mm.

Specimen 2 was significantly thinner than Specimen 1, with an average thickness of 6.94 mm ranging from a minimum value of 4.65 mm to a maximum value of 9.33 mm. For this specimen four rows of thickness measurement were taken at the top and bottom of the specimen, for a total of eight rows of measurements. The bottom of the specimen was minimally thinner than the top, with thickness averages of 7.47 mm for the top portion and 6.41 mm for the bottom section of this specimen. A total of seven rows of measurements were taken on Specimen 3, with three being taken from the top and four from the bottom. The bottom section of this specimen is significantly thinner than the top portion, with average thicknesses of 11.84 mm and 8.72 mm for the top and bottom sections respectively. The average thickness for this specimen was 10.06 mm,

with values ranging from a low of 5.87 mm to a high of 12.30 mm. The thickness mapping of Specimen 4 resulted in an average thickness of 10.32 mm, with values ranging from a low of 8.50 mm to a high of 12.10 mm. The top portion of this specimen had an average thickness of 11.20 mm as compared to the bottom section which had an average thickness of 9.44 mm.

Following the thickness mapping, the four specimens were taken to the Environmental Engineering Laboratory of the Civil Engineering Department at Ottawa University and placed in a fume hood for cleaning of the remaining corrosion product. The cleaning solution was mixed in the proportions described in Section 3.4.4.2. To avoid having to submerge the entire wide flange section into the solution, a 75 mm long 100 mm diameter section of PVC pipe was attached to the web using window putty. The putty served to hold the pipe in place and to seal the interface between the corroded web steel and the PVC pipe. Once the bottom of the pipe had been sealed, the cleaning solution was poured into the pipe. This allowed continuous washing time per cycle for the removal of corrosion product. The procedure resulted in a 100 mm diameter circular area where the corrosion product had been removed as can be seen in Figure 5.4. In most cases, the corrosion product was removed at areas of minimal thickness. Note that although new thicknesses could have been measured at the locations where enhanced removal of corrosion product was achieved chemically, this would have led to inconsistency in the thickness readings, with some values inside and outside of the chemically cleaned areas. Given that cleaning of the entire cross-section to be tested was prohibitive, it was deemed more appropriate to only use the thicknesses measured as reported prior to cleaning. It also consistent with the expected site conditions where chemical cleaning over large surfaces for the purpose of performing the Testex replication procedure is unlikely to be done.

The results of the roughness testing from Testex can be seen in Table 5.5. From this table it can be seen that only the mean ten point height of irregularities roughness values were measured for this work since this is the only roughness parameter that the Mitutoyo replica tape thickness gage is capable of recording. This parameter is however an accepted indicator of surface roughness. The Structural Steel Painting Council (SSPC), American Society for the Testing of Materials (ASTM), and the National Association of Corrosion Engineers (NACE) all use this parameter in

their respective work. From Table 5.5 it is seen that the average ten point height of irregularities roughness values range from a low of 99 μm to a high of 185 μm with an over all average value of 145 μm. It can also be calculated that Specimen 1 possesses the least amount of surface roughness with a mean value of 136 μm, followed by Specimens 3, 4 and 2 which have mean values of 138 μm, 148 μm, 159 μm. With respect to the eight tests to be performed the surface for Test 2 possesses the least amount of roughness followed by Tests 6, 7, 5, 1, 3, 8 and 4 which have mean values of 131 μm, 137 μm, 137 μm, 139 μm, 140 μm, 153 μm, 158 μm and 165 μm respectively. This results in a maximum deviation from the mean of all values of 20 μm or 13.8%.

CHAPTER 6
EXPERIMENTAL RESULTS

6.1 Introduction

An MTS Testar system was used to control the cyclic testing and record some of the results (deflection and applied loading using a load cell and LVDT internal to the actuator). The system also recorded the displacements measured by four external LVDTs installed to determine if sliding was occurring at the base of the specimen or the underside of the rigid base, or if plastic rotation at the flange to web intersection point was occurring. After reviewing the data from the four external LVDTs it was found that no significant sliding of the rigid base or specimen, or rotation at the web-to-flange intersection points occurred. The largest deflections that these four LVDTs recorded was less than 0.5% of the maximum deflections and were therefore not considered to be significant. The resulting data files ranged in size from a minimum of 4,864 data points for Test#8 to a maximum of 11,494 data points for Test#2. At each data point, the time, applied force, deflection and the displacements of the four external LVDTs were recorded.

Throughout each experiment, the hysteretic curves were closely monitored for decreases in applied forces. If any such drop in strength was noticed, the cyclic testing was stopped and the specimen was inspected for signs of cracking. If cracks were found during the inspection, they were photographed and cataloged as to location and size. Likewise, the propagation of any visible cracking was monitored by periodically stopping the cycling of the specimen and recording the crack's new size and direction of propagation.

A total of four specimens were prepared as described in Chapter 5. A total of eight tests were performed since both flange-to-web intersection areas on each member could be tested. The first

step in each test was to determine an approximate yield deflection for the specimen. Since the analytical calculation of the yield deflection was difficult to perform due to the varying cross-sectional areas, it was considered to be at the approximate intersection points of lines drawn asymptotically from the nonlinear and linear portions of the force displacement curve. To obtain the approximate yield point each specimen was subjected to applied loading that pushed the specimen into the nonlinear range. The specimen was then unloaded to determine if there had been any non-recoverable deflections, indicating that the yield point had been exceeded. After the yield deflection had been determined, its value was entered into a preprogrammed cyclic loading history. For this research it was decided that the specimen's would be loaded using induced deflections for three cycles at each of $\pm 0.5\delta_Y$, $\pm 1.0\delta_Y$, $\pm 2.0\delta_Y$ and $\pm 3.0\delta_Y$ followed by cycling to failure at $\pm 4.0\delta_Y$. A specimen was considered to have reached a point of failure when the level of applied forces had decreased to approximately 20 to 30% of the original required applied force at the $\pm 4.0\delta_Y$ level. After the first test on each specimen, the external LVDTs and actuator were removed, the specimen was flipped over and reconnected to the rigid base, and the next test was conducted. Note that throughout these tests, the center line axis of the actuator was considered to be acting in the North-South direction, with South being considered the direction of positive displacements.

A view of the experimental set up, looking North-East, is shown in Figure 6.1. The rigid base, actuator, reaction arm, specimen, and the location of three of the four external LVDTs can be seen in this figure. This experimental set up was typical for all eight tests. The cumulative energy dissipation per cycle for all eight tests can be seen in Figure 6.1(a).

6.2 Test 1 - Specimen 1 - First Web-to-Flange Intersection Point

The results of the nondestructive evaluation for this test have been included as columns one to three in Table 5.1 and in Table 5.5. Table 5.1 summarizes the thickness mapping for the top and bottom test areas of Specimen 1 and Table 5.5 shows information for the roughness testing for all

specimens. From Table 5.1 it can be calculated that the average thickness of the material for this test is 10.51 mm with a minimum value of 9.53 mm. The mean ten point height of irregularities roughness values obtained from the Testex replication procedure, were 148 and 132 μm for the south and north sides of the web respectively.

From the initial, exploratory loading of the member, it was judged that yield occurred at a displacement of 11.5 mm and a loading of 6.37 kN. The hysteretic force displacement curve for this test is shown in Figure 6.2. It should be noted that a wooden block that was placed under the actuator to support it before it was bolted to the specimen was accidentally left in place during initial cycling of the material, before cracking had occurred. This caused an increase in applied loads shown on the curve during the negative displacement portion of the loading as the block was compressed. This portion of the curve was not included in the energy dissipation calculations.

From Figure 6.2 it can be seen that the hysteretic behavior of the specimen is stable up to the 86th cycle. During the 87th cycle a slight decrease in the applied loading was noticed and the testing was stopped to allow for a detailed inspection of the specimen. Figure 6.3 shows the 30 mm long hairline crack that was found during the inspection. Note that the crack was initiated just below the area that was cleaned for roughness testing. This area was chosen for roughness testing because it was judged to one of the thinner areas on the top side of the web. This crack was located from approximately 80 to 110 mm from the east side of the specimen on the south face of the web along the row of thickness measurements closest to the top flange. The mean of the thickness measurements for this area of 10.02 mm is 4.7% below the mean thickness value of 10.51 mm. The thickness readings from this area are shown in bold in column one of Table 5.1 and the location of the initial crack can be seen in Figure 5.5. An inspection of the north face of the web at this point revealed no visible cracking. Between cycles 87 and 97 there was a relatively constant decrease in the applied loading of approximately 1.5% per cycle. During this period, the original crack propagated approximately 150 mm east and new cracking appeared to the west of the original crack location, as can be seen in Figure 6.4. From the 97th cycle to the

111th cycle, there was an almost uniform degradation in applied loading of approximately 5% per cycle, relative to the previous cycle. By the 111th cycle the cracking had propagated through the thickness of the material for almost the full length of the member. The extent of cracking on the specimen at this point can be seen in Figures 6.5 and 6.6 for the south and north sides of the web respectively. A photo showing the approximately 5 mm wide crack opening after the cycling was completed is shown in Figure 6.7.

Table 6.1 is a summary of the displacement, load, displacement ductility, hysteretic energy and cumulative hysteretic energy per cycle data and the resulting normalized energy dissipation for the test. The cumulative energy dissipation per cycle for all eight tests can be seen in Figure 6.1(a). From Table 6.1 and Figure 6.1(a) it can be seen that a total of 84,312 kN-mm of energy was dissipated during the cycling of this specimen. This resulted in a normalized cumulative energy dissipation of 1151. This quantity is defined for all eight tests as the total energy dissipated during a test, normalized by the yield force and displacement for the web-to-flange intersection of the specimen being tested. Almost 80% of the total energy that was dissipated during this test occurred between the 13th and 86th cycles, before visible crack initiation was noticed. This range of cycles represented 65% of the total number of cycles that were applied to the specimen during this test. Once the cracking appeared, the following decreases in the hysteretic energy dissipation capabilities occurred during each cycle until the failure point. From cycles 87 through to 92, the energy dissipated per cycle decreased by approximately 1% relative to the previous cycle. Following this point there was a decrease in energy dissipated per cycle of approximately 5% up to cycle 99. From cycle 100 to the point of failure, the dissipated energy per cycle decreased at a rate between 3 and 5% per cycle and during the final loading cycle, only 200 kN-mm of energy was dissipated. This value represents a 78% decrease in the energy dissipation per cycle capabilities of the specimen.

6.3 Test 2 - Specimen 1 - Second Web-to-Flange Intersection Point

The results of the nondestructive evaluation for this test have been included as columns four to six in Tables 5.1 and in Table 5.5. From Table 5.1 it can be calculated that the average thickness of the material for this test is 11.56 mm with a minimum value of 10.02 mm. The mean ten point height of irregularities roughness values obtained from the Testex replication procedure, were 111 and 150 μm for the south and north sides of the web respectively.

From the initial loading of the member, it was determined that yield occurred at a displacement of approximately 11.5 mm and a loading of 7.00 kN. The hysteretic force displacement curve for this test is shown in Figure 6.8. From this figure it can be seen that the hysteretic behavior of the specimen is relatively stable up to the 82nd cycle. Although there were slight decreases in the applied loading between the 43rd and 82nd cycles, visible cracking was not found until the 82nd cycle and the decrease in energy dissipation capabilities for this range of cycling was less than 1% in total relative to the maximum value of 1051 kN-mm. Figure 6.9 shows the location of three of the five hairline cracks that were found during the inspection of the south face of the web after the 82nd cycle. These cracks were located between 60 and 75 mm from the east side of the specimen along the line of measurements closest to the bottom flange of the specimen. As with Test 1 these initial hairline cracks were located in the area of the web that had been cleaned for roughness testing. The thickness measurements that correspond to the approximate location of the five hairline cracks that were found have been shown in bold in column number six in Table 5.1 and the location of the initial cracks can be seen in Figure 5.6. Figure 6.10 shows the two hairline cracks that were found closer to the center of the south face of the web. The mean of the thickness measurements for the area that the five cracks covered of 10.17 mm is 12.0% below the mean thickness value of 11.56 mm. Cracking on the north face of the web was not found until the specimen was inspected after cycle 87. At this point, a long hairline crack was found between approximately 90 and 215 mm from the west side of the specimen as can be seen in Figure 6.11. During the inspection of the specimen after cycle 88, it was also found that the two cracks located in the center of the south face of the specimen had increased in length from 10 to 25 mm and that

more cracking had appeared in this area as can be seen in Figure 6.12. Also, two of the three cracks that were found in the cleaned area of the south face joined and propagated to the east and west sides of the web. Once the inspection of the specimen had been completed, the cycling was restarted and continued up to the 92nd cycle. At this point, a larger decrease in required applied force, relative to the previous decreases, was noticed on the real-time hysteretic curve. Upon closer inspection of the specimen it was discovered that the cracking on the north and south faces of the web had opened to approximately 1 mm in width and had propagated over almost the full length of the specimen. However, the cracking had not yet passed through the full thickness of the material and the energy dissipating capabilities of the specimen had not yet been severely affected. A typical section of this cracking can be seen in Figure 6.13. Beyond the 92nd cycle the decrease in the load carrying ability of the member was relatively constant. During this period of cycling there was a decrease in applied force of approximately 3.5% per cycle, relative to the previous cycle. Through this period of cycling the cracking on the north and south faces of the specimen were penetrating deeper into the web and propagating to the east and west. Figure 6.14 shows the final condition of the north face of the specimen after the 112th cycle.

Table 6.2 is a summary of the displacement, load, displacement ductility, hysteretic energy and cumulative hysteretic energy per cycle data and the resulting normalized energy dissipation for the test. The cumulative energy dissipation per cycle for all eight tests can be seen in Figure 6.1(a). From Table 6.2 and Figure 6.1(a) it can be seen that a total of 98,844 kN-mm of energy was dissipated during the cycling of this specimen. This results in a normalized cumulative energy dissipation of 1228. Almost 74% of the total energy that was dissipated during this test occurred between the 13th and 82nd cycles, before visible crack initiation. This range of cycles represented 62% of the total number of cycles that were applied to the specimen during this test. Once the visible crack appeared, the following decreases in the hysteretic energy dissipation capabilities occurred until the failure point. From cycles 82 through to 92 the energy dissipated per cycle decreased a total of approximately 2.4% relative to the value at the 82nd cycle of 1034 kN-mm. Following this point there was a decrease in energy dissipated per cycle of approximately 3% up

to cycle 97. From cycle 98 to the point of failure the dissipated energy per cycle decreased at a rate of approximately 4.5% per cycle and during the final loading cycle, only 237 kN-mm of

energy was dissipated. This value represents a 78% decrease in the energy dissipation per cycle capabilities of the specimen.

6.4 Test 3 - Specimen 2 - First Web-to-Flange Intersection Point

The results of the nondestructive evaluation for this test have been included as columns five to eight in Tables 5.2 and in Table 5.5. From Table 5.2 it can be seen that the average thickness of the material for this test is 6.41 mm with a minimum value of 4.59 mm. The mean ten point height of irregularities roughness values obtained from the Testex replication procedure, were 162 and 143 μm for the south and north sides of the web respectively.

After a review of the hysteretic curves from Tests 1 and 2, it was decided that the yield point had been underestimated at 11.5 mm. The actual yielding of the specimens did not occur until between 13 and 14 mm of displacement. For Test 3 the yield was judged to occur at 13.5 mm and at a loading of 1.83 kN. The hysteretic force displacement curve for this test is shown in Figure 6.15. From this figure it can be seen that the hysteretic behavior of the specimen is relatively stable up to the 72nd cycle. Following this there were slight decreases in the applied loading between the 73rd and 92nd cycles. Visible cracking was not found until the 78th cycle. Figure 6.16 shows the location of three hairline cracks that were found during the inspection of the south face of the web after the 78th cycle. One of these cracks was located between 138 and 150 mm from the west side of the specimen along the line of measurements second closest to the bottom flange of the specimen and the other two were located at approximately 63 mm from the west side of the specimen along the same line of measurements. The thickness measurements that correspond to the approximate location of the three hairline cracks have been shown in bold in column number seven in Table 5.2 and the location of the initial crack can be seen in Figure 5.7.

The mean of the thickness measurements for the area that the three cracks covered of 5.42 mm is 15.5% below the mean thickness value of 6.41 mm. Cracking on the north face of the web was not found until the specimen was inspected after cycle 80. At this point, a small hairline crack was found between approximately 75 and 80 mm from the west side of the specimen as can be seen in Figure 6.17. During the inspection of the specimen after cycle 83, it was found that the two areas of cracking on the south face of the specimen opened and propagated, as can be seen in Figure 6.18. At this time the initial crack found on the north side of the web had doubled in size to 10 mm. Following the inspection after cycle the loading was continued to the 92nd cycle. Figures 6.19 and 6.20 show the extent of cracking on the south and north faces of the web after the 92nd cycle. Beyond the 92nd cycle the decrease in the load carrying ability of the member was relatively constant. During this period of cycling there was a decrease in applied force of approximately 1.6% per cycle, relative to the previous cycle. Through this period of cycling the cracking on the north and south faces of the specimen were penetrating deeper into the web and propagating to the east and west. Figure 6.21 shows the final condition of the south face of the specimen after the 139th cycle.

Table 6.3 is a summary of the displacement, load, displacement ductility, hysteretic energy and cumulative hysteretic energy per cycle data and the resulting normalized energy dissipation for the test. The cumulative energy dissipation per cycle for all eight tests can be seen in Figure 6.1(a). From Table 6.3 and Figure 6.1(a) it can be seen that a total of 36,701 kN-mm of energy was dissipated during the cycling of this specimen. This results in a normalized cumulative energy dissipation of 1486. More than 61% of the total energy that was dissipated during this test occurred between the 13th and 78th cycles, before visible crack initiation. This range of cycles represented 49% of the total number of cycles that were applied to the specimen during this test. Once the visible crack appeared, the following decreases in the hysteretic energy dissipation capabilities occurred until the failure point. From cycles 79 through to 92, the energy dissipated per cycle decreased a total of approximately 4.5% relative to the value at the 78th cycle of 326 kN-mm. Following this point there was a decrease in energy dissipated per cycle of between 1 and 3% to the point of failure. During the final loading cycle, only 63 kN-mm of energy was

dissipated. This value represents an 81% decrease in the energy dissipation per cycle capabilities of the specimen.

6.5 Test 4 - Specimen 2 - Second Web-to-Flange Intersection Point

The results of the nondestructive evaluation for this test have been included as columns one to four in Tables 5.2 and in Table 5.5. From Table 5.2 it can be seen that the average thickness of the material for this test is 7.47 mm with a minimum value of 4.65 mm. The mean ten point height of irregularities roughness values obtained from the Testex replication procedure, were 173 and 155 μm for the south and north sides of the web respectively.

From the initial, exploratory loading of the member, it was found that yield occurred at a displacement of 13.5 mm and at a loading of 2.58 kN. The hysteretic force displacement curve for this test is shown in Figure 6.22. From this figure it can be seen that the hysteretic behavior of the specimen is relatively stable up to the 52nd cycle. At this point, a slight decrease in the applied loading was noticed and several hairline cracks were found on the south face of the web. Figure 6.23 shows the location of the five hairline cracks that were found during the inspection of the south face of the web after the 52nd cycle. These cracks were located between zero and 50 mm in from the east side of the specimen along the line of measurements second closest to the bottom flange of the specimen. The thickness measurements that correspond to the approximate location of the five hairline cracks have been shown in bold in column number two in Table 5.2 and the location of the initial crack can be seen in Figure 5.8. The mean of the thickness measurements for the area that the five cracks covered of 6.48 mm is 13.3% below the mean thickness value of 7.47 mm. Cracking on the north face of the web was found when the loading was reversed during the 53rd cycle. Several hairline cracks were found between 20 and 50 mm from the east side of the specimen as can be seen in Figure 6.24. These cracks were located in approximately the same area as the cracking that had occurred on the south face of the web. During the inspection of the specimen after cycle 56, it was found that the more cracking had occurred at 80 mm from the

west of the specimen on the south face of the specimen. Also, the many hairline cracks on the south and north face of the web at the west end of the specimen had propagated into single, larger cracks and begun to grow to the west. By the 88th cycle the cracking at the east of the specimen had penetrated through the thickness of the material and propagated to the east to 100 mm as can be seen in Figures 6.25 and 6.26 for the north and south faces of the web. The crack that was located in the area that was cleaned for roughness testing on the south face of the web had also propagated extensively as can be seen in Figure 6.27, and passed through the thickness of the material. Figure 6.28 shows the final condition of the north face of the specimen after the 82nd cycle. Note that the two areas of cracking had joined to form one large crack from the east edge of the specimen and propagated through almost the entire width of the specimen.

Table 6.4 is a summary of the displacement, load, displacement ductility, hysteretic energy and cumulative hysteretic energy per cycle data and the resulting normalized energy dissipation for the test. The cumulative energy dissipation per cycle for all eight tests can be seen in Figure 6.1(a). From Table 6.4 and Figure 6.1(a) it can be seen that a total of 33,227 kN-mm of energy was dissipated during the cycling of this specimen. This results in a normalized cumulative energy dissipation of 954. Almost 60% of the total energy that was dissipated during this test occurred between the 13th and 52nd cycles, before visible crack initiation. This range of cycles represented 44% of the total number of cycles that were applied to the specimen during this test. Once the visible crack appeared, the following decreases in the hysteretic energy dissipation capabilities occurred until the failure point. From cycles 52 through to 59, the energy dissipated per cycle decreased by approximately 1.8% per cycle. Following this point up to cycle 66 the loss of energy dissipation ability slowed to 1% per cycle. From cycle 66 to 82, the dissipated energy per cycle decreased at a rate of approximately 1.6% per cycle and between the 52rd cycle and failure the decrease per cycle was approximately 3.9%. During the final loading cycle, only 89 kN-mm of energy was dissipated. This value represents an 82% decrease in the energy dissipation per cycle capabilities of the specimen.

6.6 Test 5 - Specimen 3 - First Web-to-Flange Intersection Point

The results of the nondestructive evaluation for this test have been included as columns four to seven in Table 5.3 and in Table 5.5. From Table 5.3 it can be calculated that the average thickness of the material for this test is 8.72 mm with a minimum value of 5.87 mm. The mean ten point height of irregularities roughness values obtained from the Testex replication procedure, were 151 and 126 μm for the south and north sides of the web respectively.

From the initial loading of the member, it was determined that yield occurred at a displacement of 13.0 mm and at a loading of 2.88 kN. The hysteretic force displacement curve for this test is shown in Figure 6.29. From this figure it can be seen that the hysteretic behavior of the specimen is relatively stable up to the 24th cycle. At this point, there was a loud "popping" sound and an unexpected decrease in the applied loading of approximately 9%. During the inspection of the specimen, a long tearing failure was found on the south face of the web. The tear was located from approximately 70 to 145 mm from the east side of the member on the first row of thickness measurements up from the flange, as can be seen in Figure 6.30. The opening was 1 mm in width and penetrated several millimeters into the web of the specimen. The thickness measurements that correspond to the approximate location of the tear have been shown in bold in column number two in Table 5.3 and the location of the initial crack can be seen in Figure 5.9. The mean of the thickness measurements for the area that the tear covered of 10.36 mm is 18.8% greater than the mean thickness value of 8.72 mm. A thorough inspection of the north face of the web at this point revealed no visible cracking. However, an internal lamination was found within the thickness of the web while inspecting the smooth west end section of the specimen. This lamination can be seen in Figure 6.31. It is thought that the lamination was created in the specimen during the steel rolling process. The testing of the specimen was restarted and continued until the 30th cycle. Figure 6.32 shows a close up view of a lamination found on the east end that had opened and Figure 6.33 shows the extent of the propagation of the south face tear after the 30th cycle. At this point, only small hairline cracking was visible on the north face of the web. With reference to the hysteretic curve shown in Figure 6.29 and to Table 6.5, it can be

seen that the negative load required at this point in testing was only 2.50 kN as compared to 3.70 kN for the positive loading. This type of negative and positive loading requirements were typical for the hysteretic curve to the point of failure. The cause for this trend may be as follows: As the actuator is retracted for the negative portion of the loading, the tear on the south face opens and the south face material offers no resistance to the induced displacements. In comparison, during the positive portion of the loading, the tear closes and resists the induced displacements through material compression. This compressive force would be countered by a tensile force in the north, uncracked portion of the web material. This process can be visualized when viewing Figure 6.34 and noting the separated south face and solid north face of the web. Figure 6.35 shows the solid, uncracked west end of the specimen at the 30th cycle. The first significant crack on the north face of the web did not occur until the 45th cycle. The view of the 25 mm long hairline crack on the north face of the web has been included as Figure 6.36 and Figure 6.37 shows the south face tear at this same point in the testing. By cycle 59 the north face crack had propagated across most of the width of the specimen as can be seen in Figure 6.38. At this point, the specimen was considered to have failed and the cycling was stopped. Figures 6.39 and 6.40 show the condition of the east and west ends of the specimen at failure respectively.

Table 6.5 is a summary of the displacement, load, displacement ductility, hysteretic energy and cumulative hysteretic energy per cycle data and the resulting normalized energy dissipation for the test. The cumulative energy dissipation per cycle for all eight tests can be seen in Figure 6.1(a). From Table 6.5 and Figure 6.1(a) it can be seen that a total of 16,804 kN-mm of energy was dissipated during the cycling of this specimen. This results in a normalized cumulative energy dissipation of 449. Almost 47% of the total energy that was dissipated during this test occurred between the 13th and 24nd cycles, before the tear in the south face occurred. This range of cycles represented 20% of the total number of cycles that were applied to the specimen during this test. Once the tear appeared in the south face of the web, the hysteretic energy dissipation capabilities decreased from 1% to 7.7% per cycle as compared to the previous cycle. Between cycles 24 and 31, the energy dissipated per cycle dropped by 40% as compared to 42% for the 29 cycles from

cycle 31 to failure. During the final cycle the member dissipated 92 kN-mm of energy which represents an 82% decrease in the energy dissipation per cycle capabilities of the specimen.

6.7 Test 6 - Specimen 3 - Second Web-to-Flange Intersection Point

The results of the nondestructive evaluation for this test have been included as columns one to three in Table 5.3 and in Table 5.5. From Table 5.3 it can be seen that the average thickness of the material for this test is 11.84 mm with a minimum value of 11.17 mm. The mean ten point height of irregularities roughness values obtained from the Testex replication procedure, were 131 and 142 μm for the south and north sides of the web respectively. A preliminary inspection of the east and west ends of this specimen revealed very slight indications of internal laminations near the intersection point. These hairline indications were visible upon extremely close visual inspection and attempts to photograph them were not successful.

From the initial loading of the member, it was found that yield occurred at a displacement of 15.0 mm and at a loading of 7.38 kN. The hysteretic force displacement curve for this test is shown in Figure 6.41. From this figure it can be seen that the hysteretic behavior of the specimen is relatively stable up to the 42nd cycle. At this point, a slight decrease in the applied loading was noticed and several hairline cracks were found on the south face of the web. Figure 6.42 shows the location of the five hairline cracks that were found during the inspection of the south face of the web after the 42nd cycle. These cracks were located between 130 and 155 mm from the west side of the specimen along the line of measurements closest to the bottom flange of the specimen. The thickness measurements that correspond to the approximate location of the hairline cracking has been shown in bold in column number one in Table 5.3 and the location of the initial crack can be seen in Figure 5.10. The mean of the thickness measurements for the area that the five cracks covered of 11.26 mm is 5.0% below the mean thickness value of 11.84 mm. Cracking on the north face of the web was found when the loading was reversed during the 42nd cycle. Several hairline cracks were found between 90 and 200 mm from the east side of the specimen as can be

seen in Figure 6.43. During the inspection of the specimen after cycle 49, it was found that the cracking on the south face of the specimen propagated to extend from 100 mm to 160 mm from the east face of the specimen as can be seen in Figure 6.44. Also, when the loading was reserved it was found that the north face crack had also extended as can be seen in Figure 6.45.

During the 52nd cycle a loud "popping" noise was heard and the cycling was stopped. Upon close inspection, it was found that the surface cracking on the south and north faces of the specimen had grown dramatically. They had increased in width to 2.0 and 1.0 mm for the south and north faces of the web respectively and extended over most of the width of the specimen. These cracks can be seen in Figures 6.46 and 6.47 for the south and north faces of the web respectively. The cycling of the specimen continued until more popping was head during the 58th cycle and the testing stopped. Upon closer inspection of the specimen it was found that the crack on the south face had grown to approximately 4 mm in width and propagated over 90% of the width of the specimen. The applied load at this point was only 50% of what was required during the 52nd load cycle. Also, note that the crack had not yet extended to the east or west ends of the specimen, as can be seen in Figure 6.48. Upon load reversal, a similar situation, in terms of crack width and location was found on the north face of the web. This crack can be seen in Figure 6.49. An examination of the ends of the specimen at this point revealed that the internal lamination indication found prior to testing had not opened up or propagated. By the end of the 61st cycle the specimen had reached the point of failure. The required applied load of 167 kN was only 14% of the load required for cycles 43 to 52. Figures showing the final conditions of the south and north faces are shown in Figures 6.50 and 6.51 respectively.

Table 6.6 is a summary of the displacement, load, displacement ductility, hysteretic energy and cumulative hysteretic energy per cycle data and the resulting normalized energy dissipation for the test. The cumulative energy dissipation per cycle for all eight tests can be seen in Figure 6.1(a). From Table 6.6 and Figure 6.1(a) it can be seen that a total of 74,342 kN-mm of energy was dissipated during the cycling of this specimen. This results in a normalized cumulative energy dissipation of 672. Almost 66% of the total energy that was dissipated during this test occurred

between the 13th and 42nd cycles, before visible crack initiation. This range of cycles represented 48% of the total number of cycles that were applied to the specimen during this test. Once the visible crack appeared, the following decreases in the hysteretic energy dissipation capabilities occurred until the failure point. From cycles 42 through to 52, the energy dissipated per cycle decreased by a total of only 1.7% for the cycle. Following the popping noise that was heard during the 53rd cycle to the next occurrence of popping the energy dissipation capabilities decreased at a rate of an average of 4% per cycle relative to the previous cycle. After the 57th cycle to failure the energy dissipation capabilities decreased a total of 81% in only 5 cycles and during the final 61st cycle only 273 kN-mm of energy was dissipated. This value represents an 84% decrease in the energy dissipation capabilities of the specimen in under twenty cycles.

6.8 Test 7- Specimen 4 - First Web-to-Flange Intersection Point

The results of the nondestructive evaluation for this test have been included as columns four to six in Table 5.4 and in Table 5.5. From Table 5.4 it can be calculated that the average thickness of the material for this test is 9.44 mm with a minimum value of 8.50 mm. The mean ten point height of irregularities roughness values obtained from the Testex replication procedure, were 148 and 126 μm for the south and north sides of the web respectively. From an inspection of the east and west ends of the specimen, several lamination indications were found. On the west end of the specimen a lamination was found between 25 to 100 mm from the underside of the flange. On the east end the lamination occurred from 170 to 185 mm from the underside of the flange. As with Test 6, attempts to photograph these indications was not successful.

From the initial loading of the member, it was found that yield occurred at a displacement of 12.0 mm and at a loading of 4.00 kN. The hysteretic force displacement curve for this test is shown in Figure 6.52. From this figure it can be seen that the hysteretic behavior of the specimen is relatively stable up to the 52nd cycle. However, when testing was stopped after the 54th cycle, very small hairline surface cracks were noticed on the north and south faces of the web. The crack

on the north face was located from between 100 and 120 mm from the east end of the specimen and can be seen in Figure 6.53. The south face crack was located between 95 and 105 mm from the west face and can be seen in Figure 6.54. Both cracks were located just above the measurement line closest to the bottom of the flange. The thickness measurements that correspond to the approximate location of the hairline cracks have been shown in bold in column number six in Table 5.4 and the location of the initial crack can be seen in Figure 5.11. The mean of the thickness measurements for the area that the two areas of cracking covered of 9.11 mm is 3.5% below the mean thickness value of 9.44 mm.

During the 58th cycle a slight decrease in applied force was noticed. The inspection of the specimen at this point revealed that the cracks on the north and south face had propagated to the east and west and increased in width. Figures 6.55 and 6.56 show the extent of cracking on the south and north faces respectively. By the 75th cycle the cracking on the north face had propagated from 20 to 200 mm from the east end of the specimen and the crack on the south face was now located between 15 and 175 mm from the west of the specimen. The extent of cracking at this point can be seen in Figure 6.57 and 6.58 from the north and south faces respectively. An inspection of the laminations after the 80th cycle revealed that the west end lamination had joined with the surface crack and opened significantly as can be seen in Figure 6.59. The lamination on the east end had remained internal and opened slightly, as can be seen in Figure 6.60. By the end of the 83rd cycle the cracking had extended for almost the full width of the specimen. Figure 6.61 shows the final condition of the west end of the specimen.

Table 6.7 is a summary of the displacement, load, displacement ductility, hysteretic energy and cumulative hysteretic energy per cycle data and the resulting normalized energy dissipation for the test. The cumulative energy dissipation per cycle for all eight tests can be seen in Figure 6.1(a). From Table 6.7 and Figure 6.1(a) it can be seen that a total of 42,200 kN-mm of energy was dissipated during the cycling of this specimen. This results in a normalized cumulative energy dissipation of 879. Almost 75% of the total energy that was dissipated during this test occurred between the 13th and 57th cycles. This range of cycles represented 54% of the total number of

cycles that were applied to the specimen during this test. Once the visible crack appeared, the following decreases in the hysteretic energy dissipation capabilities occurred until the failure point. From cycles 58 through to 73, the energy dissipated per cycle decreased by between 1.8 and 6% per cycle relative to the previous cycle. Following this point up to cycle 66 the loss of energy dissipation ability slowed to 1% per cycle. From cycle 74 to failure the dissipated energy per cycle decreased at a rate of approximately 10% per cycle and during the final loading cycle, only 78 kN-mm of energy was dissipated. This value represents an 88% decrease in the energy dissipation per cycle capabilities of the specimen.

6.9 Test 8 - Specimen 4 - Second Web-to-Flange Intersection Point

The results of the nondestructive evaluation for this test have been included as columns one to three in Table 5.4 and in Table 5.5. From Table 5.4 it can be calculated that the average thickness of the material for this test is 11.20 mm with a minimum value of 10.37 mm. The mean ten point height of irregularities roughness values obtained from the Testex replication procedure, were 166 and 150 μm for the south and north sides of the web respectively. From an initial inspection of the specimen a lamination was found on the east end located from 60 to 70 mm from the underside of the flange.

From the initial loading of the member, it was found that yield occurred at a displacement of 14.0 mm and at a loading of 6.00 kN. The hysteretic force displacement curve for this test is shown in Figure 6.62. From this figure it can be seen that the hysteretic behavior of the specimen is relatively stable up to the 52nd cycle. At this point a slight decrease in the applied loading was noticed and several hairline cracks were found on the south face of the web. Figure 6.63 shows the location of the hairline crack that was found during the inspection of the south face of the web after the 52nd cycle. This crack was located between 70 and 80 mm from the west side of the specimen along the line of measurements closest to the bottom flange of the specimen. The thickness measurements that correspond to the approximate location of the crack has been shown

in bold in column number one in Table 5.4 and the location of the initial crack can be seen in Figure 5.12. The mean of the thickness measurements for the area that the five cracks covered of 10.78 mm is 3.8% below the mean thickness value of 11.20 mm. Cracking on the north face of the web was found when the loading was reversed during the 53rd cycle. Several hairline cracks were found between 85 and 120 mm from the east side of the specimen as can be seen in Figure 6.64. During the cycling of the specimen during the 55th cycle a popping noise was heard. From the inspection that followed it was found that the north face crack had propagated and opened significantly, as can be seen in Figure 6.65. At this point in the testing the south face crack and the end lamination had not significantly increased in length or width. Over the next two cycles there was a decrease in applied load of 1.27 kN or 13.3%. A view of the north face crack after the 57th cycle can be seen in Figure 6.66. By the 60th cycle the south face crack had also propagated significantly, as can be seen in Figure 6.67, and by the 64th cycle the specimen was at the point of failure. A view of the final condition of the south face of the specimen at failure can be seen in Figure 6.68.

Table 6.8 is a summary of the displacement, load, displacement ductility, hysteretic energy and cumulative hysteretic energy per cycle data and the resulting normalized energy dissipation for the test. The cumulative energy dissipation per cycle for all eight tests can be seen in Figure 6.1(a). From Table 6.8 and Figure 6.1(a) it can be seen that a total of 59,376 kN-mm of energy was dissipated during the cycling of this specimen. This results in a normalized cumulative energy dissipation of 707. Almost 76% of the total energy that was dissipated during this test occurred between the 13th and 52nd cycles, before visible crack initiation. This range of cycles represented 63% of the total number of cycles that were applied to the specimen during this test. Once the visible crack appeared, the following decreases in the hysteretic energy dissipation capabilities occurred until the failure point. From cycles 52 through to 58, the energy dissipated per cycle decreased by approximately 4.2% per cycle. From cycle 59 to failure the dissipated energy per cycle decreased at a rate of approximately 14% per cycle and during the final loading cycle, only 182 kN-mm of energy was dissipated. This value represents an 84% decrease in the energy dissipation per cycle capabilities of the specimen.

CHAPTER 7
COMPARISON AND DISCUSSION OF RESULTS

7.1 Introduction

Table 7.1 has been included as a summary of results from the nondestructive and cyclic testing performed on the eight corroded web-to-flange intersection points. Included in this table is the following information: The test number, the assumed yield load and deflection, the mean thickness, the mean of the thickness readings from the area of initial cracking, visible crack location, the lowest thickness value for the test area, the mean ten point height of irregularities roughness for the north and south faces of the web, the total energy dissipated, the normalized dissipated energy, the number of cycles to initial cracking and the number of cycles to failure. This information was used to compare the performance of the eight web-to-flange intersection points.

When comparing the results from the eight tests, it should be noted that laminations were found through the thickness of the web material for Tests 5, 6, 7 and 8 during pretest inspections of the specimens. In several instances these flaws seemed to have had damaging effects upon the material's ability dissipate energy. Internal laminations propagated toward the surface of the web material and joined with surface cracks during Tests 5 and 7 and remained internal for Tests 6 and 8. These internal laminations may have contributed to the premature failures noticed during several tests. The most detrimental example of the negative effect of an internal lamination upon the energy dissipation abilities of a material occurred during Test 5. This test exhibited stable hysteretic behavior to only the 24th cycle at which point a loud "popping" noise was heard and a long tear was found on the web. Only 16,804 kN-mm of energy was dissipated during Test 5.

As a first step in comparing the data from the nondestructive and cyclic testing performed during Chapter 6, the mean thickness, mean ten point height of irregularities roughness values for the

entire test area, the number of cycles to initial cracking, the number of cycles to failure, and the total and normalized dissipated energy are ranked relative to the other seven tests, in Table 7.2, and then compared. The ranking is done from the worst condition (rank 1) to the best (rank 8), with the worst being defined as the thinnest test area, the roughest test area, the lowest energy dissipation for a test and the least number of cycles to cracking or failure. A discussion of the ranking results is included in Section 7.2 along with a general review of the information in Table 7.1. The information will be reviewed in terms of any qualitative trends that were noticed in the nondestructive and cyclic testing data.

Beyond this initial ranking comparison of the raw data, it was considered necessary that both parameters of interest, the surface roughness and the material thickness, should be analytically compared simultaneously to better understand their effects upon energy dissipation capabilities of a test material. This was done, to avoid diminishing the potential negative (or positive) effect of one of the two parameters, for example, the surface roughness, when comparing the material's thickness to its energy dissipation capabilities.

A thorough review of literature revealed no standard analytical methods of comparing the surface roughness and thickness of a material to its energy dissipation capabilities. To achieve these objectives, the following cumulative percentile estimation method was generated. Each test area would be separately compared to the test area with the greatest thickness. The comparison would be in terms of the decrease in mean thickness and difference in the mean ten point height of irregularities roughness. Since Tests 5 to 8 contained internal laminations, they were not used as a basis for comparison. Test 2, with a mean thickness of 11.56 mm, was compared to all other tests because it had the largest mean thickness and contained no internal laminations. To perform the comparison between two tests, the information from the thickness and roughness nondestructive evaluation of two tests would be used to provide an estimate of the total energy that would be dissipated during a test. This estimated value of total energy dissipation for the test would then be compared to the actual, experimentally obtained result to determine the accuracy of the cumulative percentile estimate.

It was decided that only the mean thickness and mean ten point height of irregularities roughness

would be used for the comparison because these parameters are the least affected by human judgement. For example, normalized energy dissipation was not used because it requires the an estimate of the point along the force displacement curve where yield had occurred, which is somewhat imprecise. Also, thickness values where the crack was first obtained were not used because this first occurrence of cracking is related to the level of inspection. Microscopic cracking may have occurred prior to the first visible crack at other locations on the web of the test area.

The comparison of results using the data from the nondestructive testing follows the assumptions that increased surface roughness and lower mean thicknesses both have equally detrimental effects upon a material's ability to dissipate energy. Table 7.3 is an example of the calculations that were performed while comparing Test 2 to Test 1. From this table it can be seen that the material for Tests 2 and 1 had mean thicknesses' of 11.56 and 10.51 mm and mean ten point height of irregularities roughness' of 131 and 140 μm respectively. Since the material for Test 1 is thinner and rougher than Test 2, it was speculated that it would dissipate less total energy than Test 2. The estimated decrease in the magnitude of energy dissipation capabilities between Test 1 and 2 was calculated by the following method.

The relative differences for the mean thickness and roughness of the two tests were first calculated as follows:

$$\Delta \bar{t} = \left[\frac{10.51 - 11.56}{11.56}\right][100\%] = -9.08\%$$

$$\Delta R_t = \left[\frac{140 - 131}{131}\right][100\%] = +6.87\%$$

In order to determine the estimated cumulative percentage decrease in energy dissipation between Test 2 and 1 the difference in the roughness values was subtracted from the difference of the mean thickness values. Note that the positive value for ΔR_t indicates increased roughness, or decrease in energy dissipation capabilities:

$$\Delta ED_{EST} = -9.08 - (+6.87) = -15.95\%$$

It was therefore estimated that 15.95% less energy would be dissipated during Test 1 than was

dissipated during Test 2. For Tests 1 and 2 the actual percentage decrease in dissipated energy can be calculated as follows:

$$\Delta ED_{EXP.} = \left(\frac{84312 - 98844}{98844}\right)(100\%) = -14.70\%$$

Comparing the relative difference in results from the cumulative percentile estimate and the experimentally obtained percent decrease in total energy dissipated between Tests 2 and 1 result in the following:

$$\Delta ED\% = -15.95 - (-14.70) = -1.25\%$$

Similar calculations have been performed to compare Test 2 to Test 1 and 3 to 8 and the results are included as Table 7.4. A discussion and comparison of results has been included in Section 7.3.

The next step in reviewing the results of the non-destructive testing and cyclic testing was to graph all thickness and roughness results included in Table 7.1 against the cyclic testing data to determine if any trends are noticeable. For this stage the mean thickness, thickness at the initial cracking location, low thickness and mean roughness were separately plotted against the total and normalized energy dissipation and the number of cycles to initial cracking and failure for all eight tests. These graphs have been included as Figures 7.1 to 7.4. Following this, the same procedure was performed including only tests which contained no laminations (ie: Tests 1 to 4). These results have been included as Figures 7.5 to 7.8. A discussion of Figures 7.1 to 7.8 is included in Section 7.4.

The final step in the comparison of results, the total energy dissipated during testing is normalized in terms of the mean thickness of the material and plotted against the mean ten point height of irregularities roughness values for Tests 1 to 4. Tests 5 to 8 were not considered at this point because of their internal laminations which biased the results in an uncontrolled manner. A graphical comparison is performed and is useful based on the observation that when the energy is normalized by the mean thickness, a constant value results, as can be seen from the following

algebraic manipulations. First, assuming bilinear elasto-plastic behavior, the elastic energy can be expressed as follows:

$$
\begin{aligned}
E_E &= P\Delta_Y \\
&= P\left(\frac{PL^3}{3EI}\right) \\
&= \frac{P^2L^3}{3EI} \\
&= \frac{(PL)(PL)L}{3EI} \\
&= \frac{M_P M_P L}{3EI} \\
&= \frac{M_P{}^2 L}{3EI} \\
&= \frac{\left(ZF_Y\right)^2 L}{3EI} \\
&= \frac{\left(\frac{Bt^2}{6}\right)^2 F_Y{}^2 L}{3EI} \\
&= \frac{\frac{B^2t^4F_Y{}^2L}{36}}{3E\left(\frac{Bt^3}{12}\right)} \\
&= \frac{B^2t^4F_Y{}^2L}{36} \times \frac{12}{3EBt^3} \\
&= \frac{BtF_Y{}^2L}{9E}
\end{aligned}
$$

where, P is the applied force, Δ_Y is the displacement, L is the distance from the applied force to the fixed end at the rigid base, E is the modulus of elasticity, I is the moment of inertia, M_P is the plastic moment, Z is the plastic modulus, B is the distance between the west and east ends of the structural section and t is the mean thickness of the material.

A similar algebraic manipulation can be performed for the nonlinear portion of the curve. The only difference between the elastic and plastic derivations is that the initial formula for the plastic derivation is as follows:

$$E_P = P\left(3\Delta_Y\right)$$

Adding the effects of the elastic and plastic portions of the curve results in the following:

$$E_{TOTAL} = E_E + E_P = \frac{BtF_Y^2 L}{9E} + \frac{BtF_Y^2 L}{3E} \tag{7.1}$$

where E_P is the plastic energy dissipation. When equation 7.1 is divided by t, the mean thickness of the material, the following result is obtained:

$$\frac{E_{TOTAL}}{t} = \frac{BF_Y^2 L}{9E} + \frac{30BF_Y^2 L}{9E} \tag{7.2}$$

From Equation 7.2 it can be seen that all remaining terms on the right side of the equation are constant values. The length of the Specimens for Tests 1 to 4 is a constant of 356 mm, the distance between the loading point and the underside of the flange remains constant at 343 mm, and the yield force, F_y, and, E, can be assumed to be constant. Equation 7.2 has been included as Figure 7.9 and a best fit curve to the data has been included as Figure 7.10. A review of Figures 7.9 and 7.10 has been included in Section 7.4.

7.2 Comparison of and Discussion Ranking Results

The results of the nondestructive and cyclic testing are compared in terms of their rankings for total and normalized energy dissipation, mean thickness and mean ten point height of irregularities roughness and the number of cycles to initial cracking and failure. The comparison proceeds from the test which dissipated the least total amount of energy during the cycling, to the one that dissipated the most total energy, with reference to Table 7.2. Although this comparison does not produce any numerical results to quantify the corrosion damage, it should lead to a general understanding of trends which may govern the performance of cyclically loaded corroded materials.

The least amount of energy dissipated during testing occurred during Test 5. A total of 16,804 kN-mm of energy was dissipated during 59 cycles with a normalized energy dissipation of 449. Note that Test 5 was one of the tests where an internal lamination propagated through the

thickness of the web and joined with (or caused) a surface crack. The following can be stated for this test:

- During the 24th cycle of this test a loud "popping" noise was heard and a long tear on the south face of the web was discovered.
- This test resulted in the lowest number of cycles to initial cracking (24) and failure (59).
- A much larger initial crack was found Test 5 than the hairline cracks that were initially found on all other specimens.
- Test 5 had the lowest normalized energy dissipation.
- Although the material for this was only the 3rd thinnest and 5th roughest it dissipated only 16,804 kN-mm of energy during the entire test. This result was approximately 50% of the 2nd lowest value.
- This low level of energy dissipation may have been a result of the internal lamination causing premature cracking and failure of the specimen.

The 2nd least amount of energy dissipated occurred during Test 4. A total of 33,227 kN-mm of energy was dissipated during this test over 82 cycles with a normalized energy dissipation of 954. The following points can be stated with respect to Test 4:

- This test possessed the roughest and 2nd thinnest material.
- Test 4 resulted in the 5th smallest normalized energy dissipation.

Following Test 4 the 3rd least amount of energy dissipation occurred during Test 3. A total of 36,701 kN-mm of energy was dissipated during this test over 139 cycles with a normalized energy dissipation of 1486. The following points can be stated for this test:

- The material for this test was the thinnest and 3rd third roughest.
- Although the material for Test 3 was thinner than for Test 4, it dissipated slightly more energy than Test 4.
- This may have been due to Test 4 having a larger magnitude of surface roughness (165 as compared to 153μm) than Test 3.
- Test 3 resulted in the largest normalized energy dissipation and the most cycles to failure (139).

Test 7 resulted in the 4th least amount of total energy dissipation. A total of 42,200 kN-mm of energy was dissipated during Test 7 over 83 cycles with a normalized energy dissipation of 879. Note that this test was performed on a web-to-flange intersection point that contained an internal lamination that propagated to the surface of the web. The following can be stated with respect to Test 7:

- The material for this test was the 4th thinnest and the 6th roughest.
- Test 7 resulted in the 4th smallest normalized energy dissipation.
- This test material was thinner and smoother than the material for Test 8 and test 7 dissipated less energy than Test 8.

The 5th least amount of total energy dissipation occurred during Test 8. A total of 59,376 kN-mm of energy was dissipated during this test over 64 cycles with a normalized energy dissipated of 707. This test area contained hairline internal laminations that did not propagate to the surface of the web or increase significantly in length or width during cycling. The following points can be stated with respect to Test 8:

- The material for Test 8 was the 2nd thickest and the 2nd roughest.
- Test 8 resulted in the 3rd smallest normalized energy dissipation and number of cycles to failure (64).
- Although the material for Test 8 was thicker than the material for Tests 1 and 2, Test 8 dissipated less total energy.
- The lower amount of total energy dissipated during Test 8 as compared to Test 1 and 2, may have been a result of the presence of an internal lamination.

Test 6 dissipated the 6th least amount of energy. A total of 74,342 kN-mm of energy was dissipated during this test over 61 cycles with a normalized energy dissipation of 879. Prior to the cycling of the material at this web-to-flange intersection point, an internal lamination was found in the web. The internal lamination did not significantly increase in length or width or propagate to the surface during this test. The following points can be stated with respect to Test 6:

- The material for this test was the thickest and 2nd smoothest material encountered during

testing.

- Test 6 resulted in the 2nd smallest normalized energy dissipation and the 2nd smallest number of cycles to initial cracking (42) and failure (61).
- The material for this test was smoother and thicker than the material for Test 8 and it dissipated more total energy.
- Although the material for Test 6 was thicker and smoother than the material for Test 1, it dissipated less energy.
- The lower amount of energy dissipation that occurred during this test as compared to Test 1 may have been caused by the internal lamination. Even though the lamination did not increase in size at the east and west ends of the test area, it may have contributed to premature cracking at other locations along the length of the specimen.

The second most energy dissipated occurred during Test 1. A total of 84,312 kN-mm of energy was dissipated during this test over 112 cycles with a normalized energy dissipation of 1151. The following points can be stated with respect to Test 1:

- The material for this test was the 5th thinnest and the 4th roughest.
- Test 1 resulted in the 6th smallest normalized energy dissipation.
- This test resulted in the most number of cycles to cracking (86) and the second most total number of cycles (112).
- Although the material for Test 6 was thicker and smoother than the material for this test, Test 1 dissipated more energy. This may be a result of the adverse effects of the internal laminations present during Test 6.
- The material for Test 1 was thinner and rougher than the material for Test 2 and Test 1 dissipated less total energy during cycling than Test 2.

The most total energy dissipated during the cyclic testing of the eight web-to-flange intersection points occurred during Test 2. A total of 98,844 kN-mm of energy was dissipated during this test over 112 cycles with a normalized energy dissipation of 1228. The following points can be stated with respect to Test 2:

- The material for Test 2 was the smoothest and the 3rd thickest of all tests and the thickest

material of the Tests that contained no laminations.

- Test 2 resulted in the 2nd highest normalized energy dissipation.
- This test resulted in the 2nd most number of cycles to initial cracking (82) and the second most number of cycles to failure (112).
- The material for Test 2 was thicker and smoother than for Test 1 and it dissipated more energy than Test 1.
- Test 8 had the lowest level of surface roughness and dissipated the largest amount of total energy.

Although no actual quantitative numerical data was obtained from the comparison of the relative ranking positions of the eight tests for various nondestructive and cyclic testing parameters, several qualitative trends were noticed. These trends were as follows:

- Thinner materials tend to dissipate less energy than thicker materials. This can be confirmed by the fact that the four thinnest specimens (3, 4, 5, and 7) have resulted in the four smallest amounts of total energy dissipation (5, 4, 3, and 7).
- Rougher materials tend to dissipate less energy than smoother materials.
- Internal laminations have a detrimental effect upon a materials ability to dissipate energy.

The most significant trend that was noticed while reviewing the information contained in Table 7.1 was the fact that in almost all cases, mean thickness in the area of initial cracking was lower than the mean thickness values for the entire area for a specific test. The only exception to this was Test 5, which failed abruptly at a low level of energy dissipation and low number of cycles. However, the poor performance during Test 5 was most likely caused by an internal lamination, and not by only the negative impacts of corrosion and fatigue. For all other tests the average mean thickness in the area of cracking was 9.09 mm as compared to 9.77 mm for the entire areas of nondestructive thickness evaluation. For tests 5 and 6, which contained internal laminations, the mean thickness in the areas of initial cracking was 8.02 mm as compared to 8.99 mm for the full test areas. This is a strong indication that low cycle fatigue, combined with the negative effects of corrosion induced surface roughness have a more detrimental effect upon thinner, lower strain areas of the cross section than they do upon the thicker, higher strained areas of the cross

section because the initial cracking locations were almost exclusively located in areas of lower mean thickness than the over all mean thickness of the full test area.

7.3 Comparison and Discussion of Cumulative Percentile Results

With reference to Table 7.4 it can be seen that the Tests with no internal laminations (1, 2, 3 and 4) compared relatively well to Test 2, while those Tests where laminations were noticed (5 to 8) did not. The mean value of percentile differences for Tests 1, 3 and 4 was 2.61% compared to 31.4% for Tests 5 to 8. Also, the Tests in which the internal laminations reached the surface (5 and 7) performed the poorest in terms of the percentile comparison. The following points can be made with reference to the eight Tests and Table 7.4.

- Experimentally, Test 1 dissipated 14.70% less energy than Test 2 whereas the cumulative percentage estimation method predicted that 15.95% less energy would be dissipated during testing. The resulting difference is 1.25%.
- Experimentally, Test 3 dissipated 62.87% less energy than Test 2 whereas the cumulative percentage estimation method predicted that 61.34% less energy would be dissipated during testing. The resulting difference is 1.53%.
- Experimentally, Test 4 dissipated 66.38% less energy than Test 2 whereas the cumulative percentage estimation method predicted that 61.34% less energy would be dissipated during testing. The resulting difference is 5.05%.
- Experimentally, Test 5 dissipated 83.00% less energy than Test 2 whereas the cumulative percentage estimation method predicted that 30.67% less energy would be dissipated during testing. The resulting difference is 52.33%. Note that during this test the most abrupt decrease in applied force occurred due to a long tearing failure on one face of the web.
- Experimentally, Test 6 dissipated 24.79% less energy than Test 2 whereas the cumulative percentage estimation method predicted that 2.16% less energy would be dissipated during testing. The resulting difference is 22.63%. Note that internal laminations were found on the ends of this test area but they did not propagate to the surface during

cycling.

- Experimentally, Test 7 dissipated 57.31% less energy than Test 2 whereas the cumulative percentage estimation method predicted that 22.92% less energy would be dissipated during testing. The resulting difference is 34.39%. Note that internal laminations propagated to the face of the web during this test.
- Experimentally, Test 8 dissipated 39.93% less energy than Test 2 whereas the cumulative percentage estimation method predicted that 23.73% less energy would be dissipated during testing. The resulting difference is 16.21%. Note that internal laminations found on this specimen did not propagate to the surface during cycling.

From Table 7.4 it can be stated that three levels of performance seem to exist within the eight tests; the tests where no internal laminations were found (1, 2, 3 and 4), the tests where internal lamination propagated to the surface (5 and 7) and the tests where internal laminations were present but did not propagate to the surface (6 and 8). The mean percentile differences for Test 1 to 4, Tests 5 and 7 and Tests 6 and 8 are 2.61, 43.35 and 19.4% respectively.

7.4 Comparison and Discussion of Figures Generated from Table 7.1 and Mean Thickness Normalized Energy Dissipation vs. Mean Ten Point Height of Irregularities Graph

Figures 7.1 to 7.4 have been included as summaries of the results of ranking the mean thickness, thickness at the location of initial cracking, low thickness and mean roughness in ascending order and separately plotting them against the total energy dissipated, the normalized energy dissipation and the number of cycles to cracking and failure for all eight tests. As can be seen in Figures 7.1 to 7.4 no obvious graphical trends exist. However, when reviewing Figures 7.5 to 7.8, several points of interest are noticeable. First, there is a general upward trend on the graph of mean thickness plotted against the total dissipated energy included in the top left hand corner of Figure 7.5. This graph indicates that as the mean thickness increases, so does the total energy dissipated during the testing. A similar trend is noticed for the mean thickness at cracking and low thickness plotted against the total energy dissipated graphs included in the top left corners of Figures 7.6

and 7.7 respectively. Finally, when reviewing the mean ten-point-height of irregularities roughness plotted against the total energy dissipated, shown in the top left hand corner of Figure 7.8 it can be seen that as the roughness increases, the total energy dissipated during a test decreases. It was for this reason that the mean thickness normalized energy dissipated vs. the mean ten-point-height of irregularity roughness was constructed in Figures 7.9 and 7.10.

Table 7.5 and Figures 7.9 and 7.10 have been included as a summary of the information that was obtained by normalizing the total energy dissipated during Tests 1 to 4 by the mean thickness of the test area to obtain a theoretically constant value. When these values were plotted against the mean ten point height of irregularity values for the specific tests it can be seen from Figure 7.9 that as the surface roughness values increase in magnitude, the material's ability to dissipate energy decreases. Although there are only four data points available it can be seen that there is a definite downward trend for the energy dissipation capabilities of a material (within this range of roughness values) as the magnitude of the mean ten point height of irregularities increases.

Figure 7.10 shows the original data curve and a line that was fitted to the data using a linear least square method of curve fitting. The equation of this best fit line was calculated to be:

$$Y = -128.2X + 25527 \qquad (7.3)$$

Where Y is the total energy dissipated normalized by the mean thickness of the material in units of kN-mm/mm and X is the measured value of the ten point height of irregulaties surface roughness in units of μm. From Equation 7.3 it can also be seen that the best fit line through the data points has a negative slope of -128.2 and a Y-axis intercept of 25,527 kN-mm/mm. Note that although Equation 7.3 indicates that negative energy dissipation values will result for ten point height of irregularity values greater than 200 μm, this equation is only valid within the limits of surface roughness that was encountered for Tests 1 to 4 (131 to 165 μm). Beyond the upper and lower limits of roughness for this testing it is not known what form the curve may take. However, although only a limited number of data points were used in the construction of Figure 7.10, it can be seen that a relatively constant negative slope exists through the four data points.

CHAPTER 8
CONCLUSIONS

8.1 Conclusions

The following conclusions can be drawn from the experimental results that were obtained from this investigation into the nondestructive evaluation and performance of cyclically loaded corroded bridge steel:

- The screw micrometer, with no anvil attachments, was best suited to thickness mapping of corroded bridge steel. This statement must be qualified by the fact that removal of corrosion products, beyond a vigorous brushing with a wire brush, to smooth steel was not performed, as this process would have destroyed the surface roughness that was also of interest in this research.
- The Testex replication procedure was the most successful method found for the numerical quantification of surface roughness of corroded bridge steel. The method was cost effective, simple to use and was well suited to in-situ testing at the bridge site. Also, once the Testex replication procedure had been performed, the sample could be tested on site to determine the ten point height of irregularity roughness or sent to a laboratory for inspection by an optical interference microscope.
- Grid spacing for thickness mapping, within the range considered in this study, did not have a significant effect upon the accuracy of the analytical finite element model's prediction of the experimentally obtained force-displacement curves.
- Uniform corrosion damage resulting in a decrease in cross sectional area has a negative effect upon a steel's ability to dissipate energy under cyclic loading.
- Pitting corrosion damage resulting in an increased magnitude of the ten point height of irregularities roughness has a negative effect upon a steel's ability to dissipate energy under cyclic loading.

- Internal laminations have a negative effect upon a corroded steel's ability to dissipate energy under cyclic loading.
- Thicker, larger strain areas of a corroded cross section perform better during low cycle corrosion fatigue testing of steel than thinner, low strain areas.
- A linear relationship was observed and quantified between the total dissipated energy, normalized by the mean thickness of a test area and the mean ten point height of irregularities of the same area. The relationship showed that as the mean ten point height of irregularity roughness increased in magnitude the total energy dissipated during a test, normalized by the mean thickness of the area, decreased.

8.2 Future Research Requirements

Although a limited amount of work has been performed on the nondestructive evaluation of cyclically loaded corroded bridge steel, additional information will be required before quantitative inspection programs can be developed. The following topics should be addressed:

- Further research should be performed to determine if advances have been made in ultrasonic and radiographic technologies that would make them more suited to the purpose of this work.
- Further investigations should be undertaken to fully understand the accuracy of the Testex replication procedure for the testing of corroded bridge steel. Much of the available data for this technology was related to roughness measurements of sand blasted surfaces, not corroded surfaces.
- Investigations should be undertaken to better understand the performance of steels with internal laminations present through their thickness. Ultrasonic flaw detectors can be used to map the size, depth from the surface and location of the laminations prior to testing. Once the nondestructive evaluation has been performed, the member should be subjected to cyclic loading designed to model the actual seismic forces that would be encountered during a major earthquake in order to better understand the effect of the laminations upon

a structural member's expected performance.

- Further research is required to better understand the graphical relationship between the energy (normalized by thickness) plotted against the ten point height of irregularity roughness. The four data points used in this work seems to indicate a decrease in energy dissipation capabilities as the magnitude of surface roughness increases. Cycling a large number of smaller corroded specimens to failure would be an efficient method of collecting this data. Subjecting a large number of new steel samples, all of a similar cross section, to laboratory controlled accelerated corrosion would result in test specimens with a similar thickness across their cross sections and various magnitudes of surface roughness. The surface roughness could be controlled by slightly extending or decreasing the length of exposure to the corrosive environment for various samples. Using a thinner width of the specimen (50 mm as compared to 356 mm) would allow the entire cross sectional surface to be mapped at the point of maximum moment.

More research must be under taken with respect to the nondestructive evaluation of the performance of cyclically loaded corroded bridge steel before any definitive inspection programs that result in numerical results, can be developed. However, if further research is conducted, the various forms of thickness and roughness mapping that are currently available could lead to cost effective, quantitative inspection programs that could be used to assist designers in developing cost effective seismic retrofit strategies for corroded steel bridges.

The research results presented here have identified the parameters that need to be considered, important trends in behavior, and some quantification of these trends, that set the direction for future research to validate and expand the range of applicability of those results.

References

American Institute of Steel Construction (1953). Iron and Steel Beams - 1873 to 1952 (AISC). New York, U.S.A..

Bruneau, M., and Zahrai, S. (1998). Some Observations on the Effect of Severe Corrosion on Cyclic Ductility of Steel. Ottawa-Carleton Earthquake Engineering Research Center. Ottawa, Canada.

Bill, R.C. (1982). A Review of Factors that Influence Fretting Wear, in Materials Evaluation Under Fretting Conditions. STP 780, ASTM 178-179.

Canadian General Standards Board (1981). Manual on Industrial Radiography. Ottawa, 37.

Fitgerald, R.W. (1967). Strength of Materials. Don Mills, Canada, 306-307.

Kaye, B.,H. (1988). A random Walk Through Fractal Dimensions. New York, U.S.A., 1-7.

Mandelbrot, B.B. (1977). Fractals: Form, Chance and Dimension. San Francisco, U.S.A.

Mitutoyo Corporation. Precision Dial Calipers. Toronto, Canada.

Mitutoyo Corporation. Screw Micrometers. Toronto, Canada.

Mitutoyo Corporation. Screw Micrometer Anvil Attachments. Toronto, Canada.

Mitutoyo Corporation. Surftest 211 Hand Held Stylus. Toronto, Canada.

Nondestructive Evaluation Institute of Canada (1995). Ultrasonic Level I Course Material. Hamilton, Canada. 3-8.

Panametrics Corporation. Epoch III Ultrasonic Flaw Detector. Toronto Canada.

Panametrics Corporation. Epoch III Ultrasonic Depth Meter. Toronto Canada.

Schindel, D.W., et al. (1995). The Design and Characterization of Micro Machined Air-Coupled Capacitance Transducers. IEEE Transaction on Ultrasonic, Ferro Electric and Frequency Control. Volume 42, Number 1, 42-43.

Testex Corporation (1999). Burnishing Tool and Replica Tape. Newark, U.S.A.

Zygo Corporation (1999). MetroPro Surface Texture Parameters. Middlefield, Connecticut, 1, 2, 9.

An Experimental Study on the Non-Destructive Evaluation of Corroded Bridge Steel

(Tables and Figures)

by

Stephen J. Burke

Thesis submitted to the School of Graduate Studies
in partial fulfilment of the requirements for the
Master of Applied Science Degree in Civil Engineering
under the auspices of the
Ottawa-Carleton Institute for Civil Engineering

September 2000

Department of Civil Engineering, University of Ottawa
Ottawa, Canada, 2000

GRADE	MEASUREMENT RANGE (μm)	APPROXIMATE COST PER SAMPLE ($)
FINE	0 - 10	1.00
MEDIUM	0 - 10	1.00
COARSE	20 - 50	1.00
X-COARSE	37.5 - 112.5	1.00
X-COARSE PLUS	100 - 162.5	1.50

Table 2.1 Testex Replication Tapre Grades (Testex 1999)

STATISTICAL PARAMETER	BALL TIP	SPLINE TIP	COMPARATOR TIP	D-METER
MEAN	0.9686	0.9811	0.9713	0.8588
MEDIAN	0.9690	0.9854	0.9756	0.9660
MODE	0.9646	0.9759	0.9451	0.9670
SKEWNESS	0.06998	-0.2112	-0.6354	-0.8378
KURTOSIS	1.4004	2.2422	1.1786	-0.5474
VARIANCE	0.0006775	0.0007281	0.0006042	0.04887
STANDARD DEVIATION	0.02603	0.02698	0.02458	0.2211
STANDARD ERROR	0.001879	0.001947	0.001774	0.01595
RANGE	0.1640	0.1865	0.1490	1.0530
MINIMUM	0.8921	0.8932	0.8930	0.3330
MAXIMUM	1.0561	1.0797	1.0420	1.3860

Table 3.1 Specimen 1 - Statistical Summary

STATISTICAL PARAMETER	BALL TIP	SPLINE TIP	COMPARATOR TIP	D-METER
MEAN	0.9721	0.9760	0.9695	0.9736
MEDIAN	0.9725	0.9777	0.9718	0.9880
MODE	0.9921	0.9436	0.9142	0.9770
SKEWNESS	0.9651	0.1461	0.01095	-2.9856
KURTOSIS	4.5073	6.6129	2.2050	10.4526
VARIANCE	0.0004292	0.0005281	0.0007173	0.01022
STANDARD DEVIATION	0.02071	0.02298	0.02678	0.1011
STANDARD ERROR	0.001495	0.001659	0.001933	0.007230
RANGE	0.1412	0.1989	0.1788	0.6480
MINIMUM	0.9170	0.8713	0.8803	0.5270
MAXIMUM	1.0582	1.0700	1.0591	1.1750

Table 3.2 Specimen 2 - Statistical Summary

STATISTICAL PARAMETER	BALL TIP	SPLINE TIP	COMPARATOR TIP	D-METER
MEAN	0.9592	0.9874	0.9712	0.9886
MEDIAN	0.9610	0.9918	0.9737	0.9960
MODE	0.9539	0.9974	0.9905	1.0050
SKEWNESS	0.06385	0.8734	-0.09931	0.1031
KURTOSIS	1.6743	6.8389	2.2659	0.2753
VARIANCE	0.0008498	0.0004441	0.001046	0.002730
STANDARD DEVIATION	0.02915	0.02107	0.03234	0.05225
STANDARD ERROR	0.002104	0.001521	0.002334	0.003771
RANGE	0.1835	0.1890	0.2219	0.3010
MINIMUM	0.8741	0.9171	0.8622	0..8450
MAXIMUM	1.0576	1.1061	1.0841	1.1460

Table 3.3 Specimen 3 - Statistical Summary

STATISTICAL PARAMETER	BALL TIP	SPLINE TIP	COMPARATOR TIP	D-METER
MEAN	0.9714	0.9816	0.9752	0.9900
MEDIAN	0.9728	0.9829	0.9778	0.9895
MODE	0.9515	0.9747	0.9433	0.9890
SKEWNESS	0.1971	1.2768	-0.1570	1.1112
KURTOSIS	4.7571	7.9954	3.7333	5.6871
VARIANCE	0.0005316	0.0003445	0.0003604	0.001428
STANDARD DEVIATION	0.02306	0.01856	0.01898	0.03780
STANDARD ERROR	0.001664	0.001340	0.001370	0.002728
RANGE	0.1781	0.1679	0.1525	0.3160
MINIMUM	0.8831	0.9105	0.8951	0.8890
MAXIMUM	1.0612	1.0784	1.0476	1.2050

Table 3.4 Specimen 4 - Statistical Summary

STATISTICAL PARAMETER	BALL TIP	SPLINE TIP	COMPARATOR TIP	D-METER
MEAN	0.9733	0.9839	0.9745	1.0047
MEDIAN	0.9745	0.9859	0.9760	1.0020
MODE	0.9707	0.9997	0.9670	0.9750
SKEWNESS	-0.3737	-0.2498	-0.01505	0.5261
KURTOSIS	6.3595	5.7833	5.9235	0.9959
VARIANCE	0.0002963	0.0003557	0.0003126	0.001249
STANDARD DEVIATION	0.01721	0.01886	0.01768	0.03535
STANDARD ERROR	0.001242	0.001361	0.001276	0.002551
RANGE	0.1679	0.1603	0.1682	0.2430
MINIMUM	0.8901	0.9085	0.8941	0.9000
MAXIMUM	1.0580	1.0688	1.0623	1.1430

Table 3.5 Specimen 5 - Statistical Summary

SAMPLE	AVERAGE MEAN	AVERAGE MEDIAN	AVERAGE MODE
1	0.9450	0.9740	0.9557
2	0.9728	0.9775	0.9567
3	0.9766	0.9806	0.9867
4	0.9796	0.9808	0.9646
5	0.9842	0.9846	0.9781

Table 3.6 Summary of Central Tendency Parameters

SAMPLE	% OF D-METER VARIANCE	% OF D-METER STANDARD DEVIATION	% OF D-METER STANDARD ERROR	% OF D-METER RANGE
1	1.4	1.2	1.2	1.6
2	5.5	23.5	23.5	26.7
3	28.6	52.7	52.7	65.8
4	28.9	53.4	53.4	52.6
5	25.7	50.7	50.7	68.0

Table 3.7 Comparison of Statistical Scatter Parameters for Average Micrometer Readings to Depth Meter Readings

OBJECTIVE	WIDTH (μm)	WIDTH (pixels)	SCALE FACTOR (μm/pixel)
5x	2000	520	3.8462
10x	1000	523	1.9120
20x	500	520	0.9615
40x	250	525	0.4762
60x	150	475	0.3158

Table 3.8 Bright Field Illumination Microscope Image Calibration Factors

TAPE GRADE	MAGNIFICATION	PV (μm)
COARSE	5	157.7
COARSE	10	97.5
COARSE	20	42.3
COARSE	40	11.9
COARSE	5	65.4
COARSE	10	45.9
COARSE	20	20.2
COARSE	40	11.0
EXTRA COARSE	5	238.5
EXTRA COARSE	10	152.0
EXTRA COARSE	20	85.6
EXTRA COARSE	40	42.4
EXTRA COARSE	5	61.5
EXTRA COARSE	10	42.1
EXTRA COARSE	20	52.9
EXTRA COARSE	40	40.0

Table 3.9 Peak-to-Valley Readings for Various Magnifications

STATISTICAL PARAMETER	SAMPLE	ZYGO RESULTS (μm)	VEECO RESULTS (μm)
PV	STEEL	240.597	542.08
	REPLICA#1	204.735	485.99
	REPLICA#2	218.189	607.03
Rtm	STEEL	179.745	454.98
	REPLICA#1	130.073	453.90
	REPLICA#2	157.686	478.87
RMS	STEEL	36.022	67.98
	REPLICA#1	24.820	77.06
	REPLICA#2	28.514	87.15
Ra	STEEL	29.255	55.04
	REPLICA#1	20.252	64.14
	REPLICA#2	23.659	73.27

Table 3.10 Summary of Zygo and Veeco Optical Interference Microscope Results

SPECIMEN	σ(yield) (ksi)	σ(ultimate) (ksi)	Py (kip)	Pu (kip)	tmean (mm)	% Loss	Py (KN)	Pu (KN)	Pu/Py (KN/KN)
1	25.3	34.7	14.23	19.52	7.264	-18.6	63.30	86.82	1.372
2	32.6	44.8	18.34	25.2	8.573	-3.9	81.57	112.10	1.374
3	22.6	31.9	12.71	17.94	7.216	-19.1	56.55	79.82	1.412
4	33.8	47.2	19.01	26.55	8.341	-6.5	84.57	118.10	1.397
5	33.8	48.6	19.01	27.34	8.923	0	84.57	121.60	1.438
CONTROL	45.7	65	25.71	36.56	9.5	+6.5	114.35	162.64	1.422

Table 4.1 Summary of Tensile Testing Results

GEOM. MODEL	YEILD STRESS (MPa)	MEASUREMENT METHOD	Py (KN)	Δy (mm)	Pu (KN)	Δu (mm)	Pf (KN)	Δf (mm)
COARSE	248.211	STANDARD	60.60	0.578	88.60	5.45	80.01	10.16
COARSE	248.211	BALL	60.60	0.576	88.60	5.45	80.01	10.16
COARSE	248.211	SPLINE	59.34	0.576	86.30	5.35	77.91	10.16
COARSE	248.211	COMPARATOR	58.45	0.576	85.40	5.25	76.29	10.16
COARSE	248.211	D-METER	50.75	0.576	74.70	5.59	68.6	10.16
COARSE	315.090	STANDARD	76.78	0.576	103.56	4.57	91.11	10.16
COARSE	315.090	BALL	76.78	0.576	103.56	4.57	91.11	10.16
COARSE	315.090	SPLINE	75.18	0.576	101.38	4.44	88.85	10.16
COARSE	315.090	COMPARATOR	74.00	0.576	99.79	4.23	86.66	10.16
COARSE	315.090	D-METER	64.31	0.576	87.13	4.27	77.49	10.16
FINE	248.211	STANDARD	58.74	0.5757	83.98	4.57	69.80	10.16
FINE	248.211	BALL	56.31	0.5757	80.22	4.20	64.94	10.16
FINE	248.211	SPLINE	57.20	0.5757	81.96	4.47	67.40	10.16
FINE	248.211	COMPARATOR	56.44	0.5842	80.20	3.89	67.69	9.271
FINE	248.211	D-METER	51.71	0.5842	74.78	5.61	70.40	7.62
FINE	315.090	STANDARD	73.11	0.5926	98.32	3.62	83.18	8.89
FINE	315.090	BALL	69.90	0.5842	94.09	3.45	78.15	8.89
FINE	315.090	SPLINE	71.13	0.5842	95.96	3.51	80.20	8.89
FINE	315.090	COMPARATOR	69.92	0.5842	94.18	3.43	77.75	8.89
FINE	315.090	D-METER	64.69	0.5842	87.42	4.29	73.63	8.89
ACTUAL	315.090	EXTENSOMETER	60.61	0.4129	86.43	7.75	17.01	10.38

Table 4.2 Summary of Finite Element Modeling Results for Specimen 1

GEOM. MODEL	YEILD STRESS (MPa)	MEASUREMENT METHOD	Py (KN)	Δy (mm)	Pu (KN)	Δu (mm)	Pf (KN)	Δf (mm)
COARSE	248.211	STANDARD	78.19	0.4572	115.54	7.24	115.07	7.62
COARSE	248.211	BALL	78.40	0.4572	112.57	7.47	112.42	7.62
COARSE	248.211	SPLINE	75.56	0.4572	111.52	7.19	111.01	7.62
COARSE	248.211	COMPARATOR	74.42	0.4572	109.92	7.09	109.14	7.62
COARSE	248.211	D-METER	76.30	0.4572	112.64	7.33	112.42	7.62
COARSE	315.090	STANDARD	99.29	0.4572	N/A	N/A	132.01	7.62
COARSE	315.090	BALL	95.46	0.4572	N/A	N/A	128.03	7.62
COARSE	315.090	SPLINE	95.94	0.4572	N/A	N/A	128.48	7.62
COARSE	315.090	COMPARATOR	94.47	0.4572	N/A	N/A	127.23	7.62
COARSE	315.090	D-METER	96.86	0.4572	N/A	N/A	128.04	7.62
FINE	248.211	STANDARD	77.00	0.4572	N/A	N/A	95.11	5.08
FINE	248.211	BALL	74.44	0.4572	N/A	N/A	92.59	5.08
FINE	248.211	SPLINE	74.74	0.4572	N/A	N/A	92.95	5.08
FINE	248.211	COMPARATOR	73.98	0.4572	N/A	N/A	92.31	5.08
FINE	248.211	D-METER	75.37	0.4572	N/A	N/A	92.71	5.08
FINE	315.090	STANDARD	97.86	0.4572	N/A	N/A	110.03	5.08
FINE	315.090	BALL	94.52	0.4572	N/A	N/A	107.05	5.08
FINE	315.090	SPLINE	94.94	0.4572	N/A	N/A	107.64	5.08
FINE	315.090	COMPARATOR	93.96	0.4572	N/A	N/A	106.77	5.08
FINE	315.090	D-METER	95.72	0.4572	N/A	N/A	108.17	5.08
ACTUAL	315.090	EXTENSOMETER	81.51	0.6352	N/A	N/A	89.06	26.71

Table 4.3 Summary of Finite Element Modeling Results for Specimen 2

GEOM. MODEL	YEILD STRESS (MPa)	MEASUREMENT METHOD	Py (KN)	Δy (mm)	Pu (KN)	Δu (mm)	Pf (KN)	Δf (mm)
COARSE	248.211	STANDARD	49.02	0.4572	71.98	4.91	68.53	7.62
COARSE	248.211	BALL	46.35	0.4572	67.98	4.86	64.71	7.62
COARSE	248.211	SPLINE	48.49	0.4572	71.36	4.85	68.10	7.62
COARSE	248.211	COMPARATOR	46.74	0.4572	68.86	4.77	65.53	7.62
COARSE	248.211	D-METER	48.69	0.4572	71.58	4.85	67.97	7.62
COARSE	315.090	STANDARD	62.13	0.5791	84.22	5.35	81.01	7.62
COARSE	315.090	BALL	58.75	0.5791	79.52	5.33	76.49	7.62
COARSE	315.090	SPLINE	61.46	0.5791	83.47	5.33	80.41	7.62
COARSE	315.090	COMPARATOR	59.24	0.5791	80.57	5.24	77.47	7.62
COARSE	315.090	D-METER	61.71	0.5791	83.73	5.37	80.39	7.62
FINE	248.211	STANDARD	53.49	0.4064	77.91	4.77	77.68	5.08
FINE	248.211	BALL	45.57	0.4064	66.68	4.61	66.42	5.08
FINE	248.211	SPLINE	47.91	0.4064	70.37	4.81	70.25	5.08
FINE	248.211	COMPARATOR	46.74	0.4064	68.71	4.78	68.53	5.08
FINE	248.211	D-METER	47.67	0.4064	70.08	4.81	69.86	5.08
FINE	315.090	STANDARD	61.34	0.4064	N/A	N/A	82.85	5.08
FINE	315.090	BALL	57.65	0.4064	N/A	N/A	77.91	5.08
FINE	315.090	SPLINE	60.76	0.4064	N/A	N/A	82.12	5.08
FINE	315.090	COMPARATOR	59.31	0.4064	N/A	N/A	80.15	5.08
FINE	315.090	D-METER	60.51	0.4064	N/A	N/A	81.54	5.08
ACTUAL	315.090	EXTENSOMETER	56.02	0.5525	N/A	N/A	60.122	2.05

Table 4.4 Summary of Finite Element Modeling Results for Sample 3

GEOM. MODEL	YEILD STRESS (MPa)	MEASUREMENT METHOD	Py (KN)	Δy (mm)	Pu (KN)	Δu (mm)	Pf (KN)	Δf (mm)
COARSE	248.211	STANDARD	79.45	0.3048	117.09	7.35	116.87	7.62
COARSE	248.211	BALL	77.58	0.3048	114.61	7.44	114.52	7.62
COARSE	248.211	SPLINE	78.13	0.3048	115.14	7.39	114.95	7.62
COARSE	248.211	COMPARATOR	77.66	0.3048	114.69	7.35	114.45	7.62
COARSE	248.211	D-METER	77.78	0.3048	114.90	7.19	114.45	7.62
COARSE	315.090	STANDARD	100.01	0.3048	N/A	N/A	132.64	7.62
COARSE	315.090	BALL	97.88	0.3048	N/A	N/A	129.39	7.62
COARSE	315.090	SPLINE	98.44	0.3048	N/A	N/A	130.54	7.62
COARSE	315.090	COMPARATOR	98.01	0.3048	N/A	N/A	129.84	7.62
COARSE	315.090	D-METER	99.36	0.3048	N/A	N/A	131.50	7.62
FINE	248.211	STANDARD	78.61	0.3048	N/A	N/A	95.88	5.08
FINE	248.211	BALL	75.87	0.3048	N/A	N/A	93.12	5.08
FINE	248.211	SPLINE	77.05	0.3048	N/A	N/A	94.19	5.08
FINE	248.211	COMPARATOR	76.88	0.3048	N/A	N/A	93.60	5.08
FINE	248.211	D-METER	78.23	0.3048	N/A	N/A	94.95	5.08
FINE	315.090	STANDARD	99.16	0.3048	N/A	N/A	110.74	5.08
FINE	315.090	BALL	95.61	0.3048	N/A	N/A	107.64	5.08
FINE	315.090	SPLINE	97.24	0.3048	N/A	N/A	108.98	5.08
FINE	315.090	COMPARATOR	97.01	0.3048	N/A	N/A	108.37	5.08
FINE	315.090	D-METER	98.80	0.3048	N/A	N/A	109.18	5.08
ACTUAL	315.090	EXTENSOMETER	86.32	0.3418	N/A	N/A	85.66	2.04

Table 4.5 Summary of Finite Element Modeling Results for Specimen 4

GEOM. MODEL	YEILD STRESS (MPa)	MEASUREMENT METHOD	Py (KN)	Δy (mm)	Pu (KN)	Δu (mm)	Pf (KN)	Δf (mm)
COARSE	248.211	STANDARD	77.78	0.3048	N/A	N/A	114.49	7.62
COARSE	248.211	BALL	75.12	0.3048	N/A	N/A	110.63	7.62
COARSE	248.211	SPLINE	75.87	0.3048	N/A	N/A	111.58	7.62
COARSE	248.211	COMPARATOR	75.05	0.3048	N/A	N/A	110.38	7.62
COARSE	248.211	D-METER	78.44	0.3048	N/A	N/A	115.76	7.62
COARSE	315.090	STANDARD	98.17	0.3048	N/A	N/A	111.10	5.08
COARSE	315.090	BALL	94.83	0.3048	N/A	N/A	108.49	5.08
COARSE	315.090	SPLINE	94.59	0.3048	N/A	N/A	108.84	5.08
COARSE	315.090	COMPARATOR	93.15	0.3048	N/A	N/A	108.04	5.08
COARSE	315.090	D-METER	98.91	0.3048	N/A	N/A	110.51	5.08
FINE	248.211	STANDARD	77.21	0.3048	N/A	N/A	94.47	5.08
FINE	248.211	BALL	74.82	0.3048	N/A	N/A	91.92	5.08
FINE	248.211	SPLINE	75.53	0.3048	N/A	N/A	93.05	5.08
FINE	248.211	COMPARATOR	74.69	0.3048	N/A	N/A	92.12	5.08
FINE	248.211	D-METER	78.08	0.3048	N/A	N/A	94.86	5.08
FINE	315.090	STANDARD	97.63	0.3048	N/A	N/A	111.25	5.08
FINE	315.090	BALL	94.58	0.3048	N/A	N/A	108.72	5.08
FINE	315.090	SPLINE	95.56	0.3048	N/A	N/A	109.87	5.08
FINE	315.090	COMPARATOR	94.39	0.3048	N/A	N/A	108.91	5.08
FINE	315.090	D-METER	98.43	0.3048	N/A	N/A	111.05	5.08
ACTUAL	N/A	STRAIN GUAGE	59.81	0.3052	N/A	N/A	86.97	2.05

Table 4.6 Summary of Finite Element Modeling Results for Specimen 5

	COARSE		FINE	
	ΔPy(KN)	ΔPu(KN)	ΔPy(KN)	ΔPu(KN)
STANDARD	16.18	14.96	14.27	14.34
BALL	16.18	14.96	13.59	13.83
SPLINE	15.84	15.08	13.92	14.00
COMPARATOR	15.55	14.39	13.48	13.98
D-METER	13.56	12.43	12.98	12.64
MEAN OF ΔP	15.46	14.37	13.65	13.76
% OF 248.211 MPa AVERAGE	26.7	16.9	24.3	17.2
% OF 315.090 MPa AVERAGE	21.0	14.5	19.6	14.6

Table 4.7 Comparison of Yield and Ultimate Strength Differences for Material Property Variations for Specimen 1

	COARSE		FINE	
	ΔPy(KN)	ΔPu(KN)	ΔPy(KN)	ΔPu(KN)
STANDARD	21.10	16.94	20.86	14.92
BALL	17.06	15.61	20.08	14.46
SPLINE	20.38	17.47	20.20	14.69
COMPARATOR	20.05	15.61	19.98	14.46
D-METER	20.56	16.94	20.35	15.46
MEAN OF ΔP	19.83	16.51	20.29	14.80
% OF 248.211 MPa AVERAGE	25.9	14.7	27.0	15.9
% OF 315.090 MPa AVERAGE	20.6	12.8	21.3	13.7

Table 4.8 Comparison of Yield and Ultimate Strength Differences for Material Property Variations for Specimen 2

	COARSE		FINE	
	ΔPy(KN)	ΔPu(KN)	ΔPy(KN)	ΔPu(KN)
STANDARD	13.11	12.24	7.85	5.17
BALL	12.40	11.52	12.08	11.49
SPLINE	12.97	12.11	12.85	11.87
COMPARATOR	12.50	11.71	12.57	11.62
D-METER	13.02	12.15	12.84	11.68
MEAN OF ΔP	12.80	11.95	11.64	10.37
% OF 248.211 MPa AVERAGE	26.8	19.7	24.1	14.7
% OF 315.090 MPa AVERAGE	26.5	14.5	19.4	12.8

Table 4.9 Comparison of Yield and Ultimate Strength Differences for Material Property Variations for Specimen 3

	COARSE		FINE	
	ΔPy(KN)	ΔPu(KN)	ΔPy(KN)	ΔPu(KN)
STANDARD	20.65	15.77	20.55	14.86
BALL	20.30	14.87	19.74	14.52
SPLINE	20.31	15.59	22.19	14.79
COMPARATOR	20.35	15.39	20.13	14.77
D-METER	21.58	17.05	20.57	14.23
MEAN OF ΔP	20.64	15.73	20.64	14.63
% OF 248.211 MPa AVERAGE	26.4	13.7	26.7	15.5
% OF 315.090 MPa AVERAGE	20.9	12.0	21.2	13.4

Table 4.10 Comparison of Yield and Ultimate Strength Differences for Material Property Variations for Specimen 4

	COARSE		FINE	
	ΔPy(KN)	ΔPu(KN)	ΔPy(KN)	ΔPu(KN)
STANDARD	20.39	**-3.39**	20.42	16.78
BALL	19.71	**-2.14**	19.76	16.80
SPLINE	18.72	**-2.74**	20.03	16.82
COMPARATOR	18.10	**-2.34**	19.70	16.79
D-METER	19.67	**-5.25**	20.35	16.19
MEAN OF ΔP	19.32	**3.17**	20.05	16.68
% OF 248.211 MPa AVERAGE	25.3	**2.8**	26.2	17.9
% OF 315.090 MPa AVERAGE	20.1	**2.9**	20.1	15.2

NOTE: Results shown in bold are a results of comparing models that converge at different final displacement values and should be considered void.

Table 4.11 Comparison of Yield and Ultimate Strength Differences for Material Property Variations for Specimen 5

	Fy=248.211 MPa		Fy=315.090 MPa	
	ΔPy(KN)	ΔPu(KN)	ΔPy(KN)	ΔPu(KN)
STANDARD	1.86	4.62	3.77	5.24
BALL	4.29	8.38	6.88	9.51
SPLINE	2.14	4.34	4.05	5.42
COMPARATOR	2.01	5.2	4.08	3.83
D-METER	0.96	-0.1	-0.4	-0.3
MEAN OF ΔP	2.25	4.53	3.84	4.46
% OF 248.211 MPa AVERAGE	3.9	5.3	5.2	4.9
% OF 315.090 MPa AVERAGE	4.0	5.6	5.5	5.2

Table 4.12 Comparison of Yield and Ultimate Strength Differences for Geometric Modeling Variations for Specimen 1

	Fy=248.211 MPa		Fy=315.090 MPa	
	ΔPy(KN)	ΔPu(KN)	ΔPy(KN)	ΔPu(KN)
STANDARD	1.19	**19.96**	1.43	**21.98**
BALL	3.96	**19.83**	0.94	**20.98**
SPLINE	0.82	**18.06**	1.00	**20.84**
COMPARATOR	0.44	**16.83**	0.51	**20.46**
D-METER	0.93	**19.71**	1.14	**19.87**
MEAN OF ΔP	1.47	**18.88**	1.00	**20.83**
% OF 248.211 MPa AVERAGE	1.9	**16.9**	1.0	**18.5**
% OF 315.090 MPa AVERAGE	2.0	**14.7**	1.1	**16.2**

NOTE: Results shown in bold are a result of comparing models that converge at different final displacement values and should be considered void.

Table 4.13 Comparison of Yield and Ultimate Strength Differences for Geometric Modeling Variations for Specimen 2

	Fy=248.211 MPa		Fy=315.090 MPa	
	ΔPy(KN)	ΔPu(KN)	ΔPy(KN)	ΔPu(KN)
STANDARD	-4.47	-5.93	0.79	-1.04
BALL	0.78	1.30	1.10	-1.42
SPLINE	0.58	0.99	0.70	-1.71
COMPARATOR	0	0.15	-0.07	-2.68
D-METER	1.02	1.50	1.20	-1.15
MEAN OF ΔP	1.37	1.97	0.77	1.6
% OF 248.211 MPa AVERAGE	2.9	2.8	1.6	1.6
% OF 315.090 MPa AVERAGE	2.2	2.4	1.3	1.4

Table 4.14 Comparison of Yield and Ultimate Strength Differences for Geometric Modeling Variations for Specimen 3

	Fy=248.211 MPa		Fy=315.090 MPa	
	ΔPy(KN)	ΔPu(KN)	ΔPy(KN)	ΔPu(KN)
STANDARD	0.84	**20.99**	0.85	**21.9**
BALL	1.71	**21.4**	2.27	**21.75**
SPLINE	1.08	**20.76**	1.20	**21.56**
COMPARATOR	0.78	**20.85**	1.00	**21.47**
D-METER	-0.45	**19.5**	0.56	**22.32**
MEAN OF ΔP	0.97	**20.70**	1.18	**21.80**
% OF 248.211 MPa AVERAGE	1.2	**18.0**	1.5	**16.7**
% OF 315.090 MPa AVERAGE	1.0	**21.9**	1.2	**20.0**

NOTE: Results shown in bold are a result of comparing models that converge at different final displacement values and should be considered void.

Table 4.15 Comparison of Yield and Ultimate Strength Differences for Geometric Modeling Variations for Specimen 4

	Fy=248.211 MPa		Fy=315.090 MPa	
	ΔPy(KN)	ΔPu(KN)	ΔPy(KN)	ΔPu(KN)
STANDARD	0.57	**20.20**	0.54	-0.15
BALL	0.30	**18.71**	0.25	-0.23
SPLINE	0.34	**18.53**	-0.97	-1.03
COMPARATOR	0.36	**18.26**	-1.24	-0.87
D-METER	0.36	**20.90**	0.48	-0.54
MEAN OF ΔP	0.39	**19.32**	0.70	0.56
% OF 248.211 MPa AVERAGE	0.5	**17.2**	0.7	0.5
% OF 315.090 MPa AVERAGE	0.4	**17.7**	0.9	0.5

NOTE: Results shown in bold are a results of comparing models that converge at different final displacement values and should be considered void.

Table 4.16 Comparison of Yield and Ultimate Strength Differences for Geometric Modeling Variations for Specimen 5

		TOP			BOTTOM	
	1	2	3	4	5	6
1	9.83	10.48	10.74	11.86	11.30	10.66
2	9.92	10.18	10.72	11.71	11.44	10.62
3	10.24	9.99	10.63	11.79	11.27	10.77
4	11.14	10.17	10.30	11.90	11.29	10.58
5	11.80	10.13	10.91	12.00	10.84	**10.35**
6	11.70	10.24	10.99	12.31	10.91	**10.03**
7	**10.01**	**9.53**	10.76	11.74	10.88	**10.02**
8	**9.89**	9.92	10.60	11.29	10.84	10.30
9	**10.15**	10.18	10.82	11.55	11.13	10.36
10	11.96	9.97	10.56	11.63	10.78	10.38
11	10.23	10.00	10.43	11.23	11.03	10.55
12	10.09	9.89	10.41	11.42	10.77	**10.03**
13	10.07	10.31	10.56	11.55	10.83	**10.28**
14	N/R	N/R	N/R	N/R	N/R	N/R
15	N/R	N/R	N/R	N/R	N/R	N/R
16	10.04	10.05	10.08	12.14	11.68	12.15
17	10.35	9.75	10.42	11.91	11.76	11.52
18	10.13	10.14	10.15	12.32	11.89	12.48
19	10.34	10.10	10.29	12.03	11.67	12.62
20	9.97	10.24	9.79	11.47	11.70	11.93
21	10.03	10.18	10.57	12.06	11.58	11.92
22	11.23	10.28	10.71	12.02	11.32	12.63
23	11.35	9.88	10.51	12.58	11.81	12.85
24	11.10	10.27	10.30	12.30	11.99	12.01
25	13.12	10.62	10.48	12.13	11.84	12.32
26	13.11	10.29	10.15	12.39	11.86	12.83
27	13.69	10.66	10.55	12.15	12.14	12.53
28	11.44	10.51	10.29	12.16	11.63	13.25

NOTE: Thickness measurements shown in bold indicate the location of initial cracking

Table 5.1 Thickness Measurements for Specimen 1

			TOP			BOTTOM		
	1	2	3	4	5	6	7	8
1	7.26	**6.86**	9.33	9.28	7.06	6.93	6.34	7.09
2	7.19	**6.53**	8.42	9.26	6.63	6.78	6.22	6.55
3	7.27	**6.48**	8.28	9.00	7.19	7.06	6.18	7.81
4	7.35	**6.26**	7.97	8.35	7.41	6.63	5.87	7.64
5	7.51	**6.25**	8.00	8.42	6.93	6.41	**6.26**	6.89
6	8.10	6.74	7.28	8.04	6.84	6.21	**4.59**	7.39
7	7.79	6.39	6.07	7.22	6.52	5.81	4.93	7.67
8	8.07	5.46	**4.65**	6.50	6.45	5.57	5.51	6.66
9	7.44	5.78	5.30	6.36	6.39	5.26	5.38	7.30
10	7.63	6.84	7.03	7.22	6.50	5.42	5.55	7.31
11	7.66	6.95	7.55	7.31	6.27	6.14	**5.44**	7.14
12	8.01	7.14	7.43	7.46	6.39	6.11	**5.25**	6.64
13	8.78	7.13	6.76	7.36	6.99	6.09	**5.58**	7.54
14	N/R	N/R	N/R	N/R	N/R	N/R	N/R	N/R
15	N/R	N/R	N/R	N/R	N/R	N/R	N/R	N/R
16	8.15	6.69	7.14	7.57	6.16	6.12	5.67	6.95
17	7.93	7.12	7.38	7.98	6.47	6.37	6.08	6.83
18	9.02	7.33	7.71	7.82	6.04	6.27	6.14	6.92
19	8.11	6.94	7.36	7.95	5.35	6.30	6.34	7.53
20	8.35	6.36	7.84	7.90	5.99	5.51	6.00	7.08
21	8.10	7.40	8.34	8.51	6.42	5.88	6.34	7.19
22	8.75	7.14	8.73	8.68	6.31	6.28	6.47	7.40
23	8.40	7.10	8.00	8.26	6.52	6.85	6.64	6.78
24	8.56	6.58	7.42	8.01	6.55	6.78	6.10	6.99
25	7.87	6.33	6.22	8.94	7.03	6.05	5.83	7.32
26	7.41	6.02	6.72	6.97	6.41	5.96	5.13	8.74
27	9.01	6.28	6.47	6.67	6.12	5.81	5.17	7.14
28	7.97	8.20	6.87	7.17	5.57	5.68	5.55	7.18

NOTE: Thickness measurements shown in bold indicate the location of initial cracking

Table 5.2 Thickness Measurements for Specimen 2

		TOP			BOTTOM		
	1	2	3	4	5	6	7
1	11.46	11.50	12.06	9.73	8.72	8.61	10.36
2	11.27	11.93	11.93	9.54	8.66	8.69	10.74
3	11.27	11.76	12.02	9.94	8.22	8.00	10.64
4	11.25	11.78	11.95	9.07	8.39	7.29	10.20
5	**11.17**	11.56	12.00	8.68	8.13	7.80	9.95
6	11.47	11.61	11.96	9.22	8.73	8.05	**10.41**
7	11.47	11.41	11.87	8.60	7.68	7.84	**10.25**
8	11.32	11.65	11.79	9.14	7.84	7.59	**16.00**
9	11.29	11.72	11.97	9.14	8.93	7.66	**10.08**
10	11.63	11.67	11.93	9.28	9.05	7.88	**10.20**
11	**11.18**	11.83	12.05	8.67	7.99	8.02	**9.98**
12	**11.33**	11.78	12.03	8.41	7.82	7.86	**10.30**
13	11.98	12.15	12.14	8.30	8.20	7.67	10.17
14	12.07	11.90	11.97	9.06	8.32	7.45	9.89
15	12.22	11.99	11.97	8.85	7.80	6.91	10.68
16	12.07	11.97	12.21	8.97	7.95	6.99	10.69
17	12.25	12.12	12.27	8.86	7.57	6.54	10.19
18	12.17	12.10	12.21	8.62	7.64	6.24	10.03
19	11.98	12.10	12.29	8.38	7.49	6.16	10.31
20	11.79	12.15	12.30	7.86	7.33	6.54	10.52
21	11.53	11.86	12.12	7.84	6.79	5.87	9.96

NOTE: Thickness measurements shown in bold indicate the location of initial cracking

Table 5.3 Thickness Measurements for Specimen 3

		TOP			BOTTOM	
	1	2	3	4	5	6
1	11.21	11.60	11.81	8.79	8.87	8.99
2	12.02	11.44	11.69	9.02	8.72	9.08
3	11.53	11.94	11.86	9.26	8.60	8.91
4	11.63	11.18	11.69	9.62	**8.50**	8.68
5	12.10	11.17	11.73	9.50	8.61	9.05
6	11.20	10.94	11.53	9.44	8.65	9.07
7	11.08	11.01	11.78	9.62	9.15	8.91
8	11.17	10.71	11.21	9.45	9.26	8.95
9	11.13	10.72	11.17	10.35	9.26	**9.01**
10	11.03	10.58	11.25	10.29	9.72	**9.20**
11	10.85	10.63	11.19	9.65	9.55	9.04
12	11.35	10.70	11.22	9.93	9.30	9.32
13	11.12	10.66	11.42	10.25	9.29	9.45
14	10.98	10.57	11.26	9.91	8.92	**9.32**
15	10.79	10.90	11.44	9.50	9.35	**8.92**
16	10.77	11.25	11.71	10.05	9.24	9.67
17	10.83	10.97	11.35	9.86	9.45	9.65
18	10.92	10.71	11.31	10.12	9.58	9.79
19	10.55	11.13	11.43	10.76	9.91	9.65
20	**10.37**	10.71	11.42	11.53	9.69	9.61
21	11.76	10.72	11.60	10.67	9.92	9.27

NOTE: Thickness measurements shown in bold indicate the location of initial cracking

Table 5.4 Thickness Measurement for Specimen 4

		AVERAGE MAX. PEAK-TO-VALLEY ROUGHNESS(μm)			
SPECIMEN	TEST - WEB FACE	1	2	3	MEAN
1	2 - SOUTH	117	117	99	111
1	2 - NORTH	157	132	160	150
1	1 - SOUTH	160	140	145	148
1	1 - NORTH	142	150	104	132
2	3 - SOUTH	168	152	165	162
2	3 - NORTH	152	130	147	143
2	4 - SOUTH	168	173	178	173
2	4 - NORTH	147	155	170	155
3	5 - SOUTH	152	163	137	151
3	5 - NORTH	130	132	117	126
3	6 - SOUTH	114	155	124	131
3	6 - NORTH	132	170	124	142
4	7 - SOUTH	150	140	155	148
4	7 - NORTH	109	145	124	126
4	8 - SOUTH	185	165	147	166
4	8 - NORTH	147	157	145	150

Table 5.5 Average Maximum Peak-to-Valley Roughness Readings

	DISPLACEMENT		LOAD	E_H	ΣE_H
CYCLE	δ_Y	(mm)	(KN)	(KN-mm)	(KN-mm)
1 to 3	0.5	5.75	2.95	0	0
4 to 6	1	11.5	6.37	48	144
7 to 9	2	23	8.19	261	927
10 to 12	3	34.5	9.46	572	2643
13 to 86	4	46	10.67	900	69243
87	4	46	10.53	890	70133
88	4	46	10.38	880	71013
89	4	46	10.24	870	71883
90	4	46	10.09	860	72743
91	4	46	9.95	850	73593
92	4	46	9.80	840	74433
93	4	46	9.59	826	75259
94	4	46	9.38	810	76069
95	4	46	9.17	790	76859
96	4	46	8.96	760	77619
97	4	46	8.75	719	78338
98	4	46	8.21	687	79025
99	4	46	7.68	641	79666
100	4	46	7.14	595	80261
101	4	46	6.61	549	80810
102	4	46	6.07	503	81313
103	4	46	5.54	460	81773
104	4	46	5.01	428	82201
105	4	46	4.48	396	82597
106	4	46	3.95	364	82961
107	4	46	3.42	332	83293
108	4	46	3.15	309	83602
109	4	46	2.88	273	83875
110	4	46	2.61	237	84112
111	4	46	2.34	200	84312

$$\Sigma E_H / P_Y \delta_Y = 1151$$

Table 6.1 Displacement Ductility and Hysteretic Energy Values for Test 1

	DISPLACEMENT		LOAD	E_H	ΣE_H
CYCLE	δ_Y	(mm)	(KN)	(KN-mm)	(KN-mm)
1 to 3	0.5	5.75	3.50	0	0
4 to 6	1	11.5	7.0	15	45
7 to 9	2	23	10.05	220	705
10 to 12	3	34.5	11.47	674	2727
13 to 42	4	46	13.29	1051	34257
43 to 62	4	46	13.05	1042	55097
63 to 82	4	46	12.94	1034	75777
83 to 87	4	46	12.72	1026	80907
88 to 92	4	46	12.51	1009	85952
93	4	46	12.06	997	86949
94	4	46	11.61	968	87917
95	4	46	11.16	939	88856
96	4	46	10.71	910	89766
97	4	46	10.26	881	90647
98	4	46	9.76	861	91508
99	4	46	9.26	814	92322
100	4	46	8.76	767	93089
101	4	46	8.26	720	93809
102	4	46	7.76	673	94482
103	4	46	7.36	638	95120
104	4	46	6.76	585	95705
105	4	46	6.16	540	96245
106	4	46	5.56	498	96743
107	4	46	4.96	456	97199
108	4	46	4.36	421	97620
109	4	46	3.76	375	97995
110	4	46	3.16	329	98324
111	4	46	2.36	283	98607
112	4	46	1.96	237	98844

$$\Sigma E_H / P_Y \delta_Y = 1228$$

Table 6.2 Displacement Ductility and Hysteretic Energy Values For Test 2

	DISPLACEMENT		LOAD	E_H	ΣE_H
CYCLE	δ_Y	(mm)	(KN)	(KN-mm)	(KN-mm)
1 to 3	0.5	6.75	0.80	0	0
4 to 6	1	13.5	1.83	6	18
7 to 9	2	27	2.43	78	252
10 to 12	3	40.5	2.70	194	834
13 to 72	4	54	2.95	332	20754
73 to 82	4	54	2.9	326	24014
83 to 92	4	54	2.85	311	27124
93	4	54	2.75	301	27425
94	4	54	2.73	298	27723
95	4	54	2.7	294	28017
96	4	54	2.68	291	28308
97	4	54	2.65	288	28596
98	4	54	2.63	284	28880
99	4	54	2.60	281	29161
100	4	54	2.58	278	29439
101	4	54	2.55	274	29713
102	4	54	2.53	271	29984
103	4	54	2.5	270	30254
104	4	54	2.45	264	30518
105	4	54	2.43	258	30776
106	4	54	2.41	252	31028
107	4	54	2.39	245	31273
108	4	54	2.37	243	31516
109	4	54	2.35	235	31751
110	4	54	2.30	234	31985
111	4	54	2.26	230	32215
112	4	54	2.22	225	32440
113	4	54	2.17	221	32661
114	4	54	2.13	216	32877
115	4	54	2.09	212	33089

	DISPLACEMENT		LOAD	E_H	ΣE_H
CYCLE	δ_Y	(mm)	(KN)	(KN-mm)	(KN-mm)
116	4	54	2.05	208	33297
117	4	54	2.01	203	33500
118	4	54	1.96	199	33699
119	4	54	1.92	195	33894
120	4	54	1.88	192	34086
121	4	54	1.78	188	34274
122	4	54	1.75	185	34459
123	4	54	1.72	181	34640
124	4	54	1.69	178	34818
125	4	54	1.66	174	34992
126	4	54	1.63	171	35163
127	4	54	1.59	167	35330
128	4	54	1.56	164	35494
129	4	54	1.53	157	35651
130	4	54	1.50	150	35801
131	4	54	1.47	142	35943
132	4	54	1.44	135	36078
133	4	54	1.39	115	36193
134	4	54	1.30	106	36299
135	4	54	1.20	98	36397
136	4	54	1.05	89	36486
137	4	54	0.90	80	36566
138	4	54	0.75	72	36638
139	4	54	0.60	63	36701

$$\Sigma E_H / P_Y \delta_Y = 1486$$

Table 6.3 Displacement Ductility and Hysteretic Energy Values for Test 3

	DISPLACEMENT		LOAD	E_H	ΣE_H
CYCLE	δ_y	(mm)	(KN)	(KN-mm)	(KN-mm)
1 to 3	0.5	6.75	1.14	0	0
4 to 6	1	13.5	2.58	15	45
7 to 9	2	27	3.77	124	417
10 to 12	3	40.5	4.00	304	1329
13 to 52	4	54	4.32	493	21049
53	4	54	4.18	465	21514
54	4	54	4.09	456	21970
55	4	54	4.00	448	22418
56	4	54	3.91	439	22857
57	4	54	3.82	430	23287
58	4	54	3.74	406	23693
59	4	54	3.70	401	24094
60	4	54	3.66	396	24490
61	4	54	3.62	391	24881
62	4	54	3.58	386	25267
63	4	54	3.54	381	26648
64	4	54	3.50	376	26042
65	4	54	3.46	371	26395
66	4	54	3.42	366	26761
67	4	54	3.35	361	27122
68	4	54	3.29	351	27473
69	4	54	3.22	343	27816
70	4	54	3.16	336	28152
71	4	54	3.09	328	28480
72	4	54	3.03	320	28800
73	4	54	2.94	308	29108
74	4	54	2.84	301	29409
75	4	54	2.75	293	29702
76	4	54	2.66	285	29987
77	4	54	2.57	278	30265

	DISPLACEMENT		LOAD	E_H	ΣE_H
CYCLE	δ_Y	(mm)	(KN)	(KN-mm)	(KN-mm)
78	4	54	2.47	270	30535
79	4	54	2.38	263	30798
80	4	54	2.29	255	31053
81	4	54	2.19	248	31301
82	4	54	2.10	240	31541
83	4	54	1.95	237	31778
84	4	54	1.80	223	32001
85	4	54	1.65	210	32211
86	4	54	1.50	198	32409
87	4	54	1.29	183	32592
88	4	54	1.17	165	32757
89	4	54	1.06	146	32903
90	4	54	0.94	127	33030
91	4	54	0.82	108	33138
92	4	54	0.70	89	33227

$$\Sigma E_H / P_Y \delta_Y = 954$$

Table 6.4 Displacement Ductility and Hysteretic Energy Values for Test 4

	DISPLACEMENT		LOAD	E_H	ΣE_H
CYCLE	δ_y	(mm)	(KN)	(KN-mm)	(KN-mm)
1 to 3	0.5	6.5	1.45	0	0
4 to 6	1	13	2.88	26	78
7 to 9	2	26	3.57	147	519
10 to 12	3	39	4.05	314	1461
13 to 24	4	52	4.50	535	7881
25	4	52	4.1	523	8404
26	4	52	4.01	494	8898
27	4	52	3.92	445	9343
28	4	52	3.82	404	9747
29	4	52	3.73	392	10139
30	4	52	3.70 (2.50)	353	10492
31	4	52	3.65 (2.45)	316	10808
32	4	52	3.60 (2.40)	310	11118
33	4	52	3.55 (2.30)	303	11421
34	4	52	3.50 (2.25)	295	11716
35	4	52	3.44 (2.20)	288	12004
36	4	52	3.38 (2.15)	280	12284
37	4	52	3.32 (2.10)	275	12559
38	4	52	3.25 (2.05)	270	12829
39	4	52	3.19 (1.95)	265	13094
40	4	52	3.14 (1.90)	260	13354
41	4	52	3.10 (1.85)	255	13609
42	4	52	3.05 (1.80)	251	13860
43	4	52	2.98 (1.75)	244	14104
44	4	52	2.90 (1.70)	237	14341
45	4	52	2.80 (1.65)	230	14571
46	4	52	2.64 (1.56)	223	14794
47	4	52	2.57 (1.47)	216	15010
48	4	52	2.45 (1.35)	205	15215
49	4	52	2.34 (1.26)	195	15410

	DISPLACEMENT		LOAD	E_H	ΣE_H
CYCLE	δ_Y	(mm)	(KN)	(KN-mm)	(KN-mm)
50	4	52	2.24 (1.20)	184	15594
51	4	52	1.70 (1.15)	173	15767
52	4	52	1.65 (1.06)	167	15934
53	4	52	1.57 (0.96)	156	16090
54	4	52	1.51 (0.87)	146	16236
55	4	52	1.45 (0.77)	135	16371
56	4	52	1.39 (0.68)	124	16495
57	4	52	1.33 (0.59)	114	16609
58	4	52	1.26 (0.49)	103	16712
59	4	52	1.20 (0.40)	92	16804

$$\Sigma E_H / P_Y \delta_Y = 449$$

Table 6.5 Displacement Ductility and Hysteretic Energy Values for Test 5

	DISPLACEMENT		LOAD	E_H	ΣE_H
CYCLE	δ_Y	(mm)	(KN)	(KN-mm)	(KN-mm)
1 to 3	0.5	7.5	3.10	0	0
4 to 6	1	15	7.38	56	168
7 to 9	2	30	9.21	430	1458
10 to 12	3	45	10.79	968	4362
13 to 42	4	60	11.84	1511	49692
43 to 52	4	60	11.75	1469	64382
53	4	60	11.58	1444	65826
54	4	60	10.97	1396	67222
55	4	60	9.24	1344	68566
56	4	60	8.37	1287	69853
57	4	60	7.50	1224	71077
58	4	60	5.67	987	72064
59	4	60	4.67	875	72939
60	4	60	3.67	657	73596
61	4	60	2.67	473	74069
62	4	60	1.67	273	74342

$$\Sigma E_H / P_Y \delta_Y = 672$$

Table 6.6 Displacement Ductility and Hysteretic Energy Values for Test 6

	DISPLACEMENT		LOAD	E_H	ΣE_H
CYCLE	δ_Y	(mm)	(KN)	(KN-mm)	(KN-mm)
1 to 3	0.5	6	1.61	0	0
4 to 6	1	12	4.00	26	78
7 to 9	2	24	5.26	171	591
10 to 12	3	36	6.05	367	1692
13 to 57	4	48	6.87	661	31437
58	4	48	6.80	650	32087
59	4	48	6.69	639	32726
60	4	48	6.58	628	33354
61	4	48	6.46	617	33971
62	4	48	6.35	603	34574
63	4	48	6.29	588	35162
64	4	48	6.09	574	35736
65	4	48	5.89	559	36295
66	4	48	5.69	544	36839
67	4	48	5.49	532	37371
68	4	48	5.16	510	37881
69	4	48	5.00	489	38370
70	4	48	4.85	467	38837
71	4	48	4.69	445	39282
72	4	48	4.53	434	39716
73	4	48	4.35	396	40112
74	4	48	3.97	359	40471
75	4	48	3.59	321	40792
76	4	48	3.20	283	41075
77	4	48	2.82	243	41318
78	4	48	2.16	216	41534
79	4	48	1.96	188	41722
80	4	48	1.76	161	41883
81	4	48	1.56	133	42016
82	4	48	1.36	106	42122
83	4	48	1.16	78	42200

$$\Sigma E_H/P_Y\delta_Y=879$$

Table 6.7 Displacement Ductility and Hysteretic Energy Values for Test 7

	DISPLACEMENT		LOAD	E_H	ΣE_H
CYCLE	δ_Y	(mm)	(KN)	(KN-mm)	(KN-mm)
1 to 3	0.5	7	2.80	0	0
4 to 6	1	14	6.00	39	117
7 to 9	2	28	8.02	317	1068
10 to 12	3	42	8.82	714	3210
13 to 42	4	56	9.90	1181	38640
43 to 52	4	56	9.80	1167	50310
53 to 55	4	56	9.52	1146	53740
56	4	56	9.02	1095	54843
57	4	56	8.25	1043	55888
58	4	56	7.60	993	56879
59	4	56	6.11	827	57706
60	4	56	4.62	662	58368
61	4	56	3.13	496	58664
62	4	56	1.64	330	59194
63	4	56	1.15	182	59376

$$\Sigma E_H / P_Y \delta_Y = 707$$

Table 6.8 Displacement Ductility and Hysteretic Energy Values for Test 8

1	2	3	4	5	6	7	8	9	10	11
Test Number	**P_Y (KN)**	**Δ_Y (mm)**	**t_{MEAN} (mm)**	**t_{CRACK} (mm)**	**$t_{MINIMUM}$ (mm)**	**Rough-ness (μm)**	**E_H (Total) (KNmm)**	**E_H (Norm.) (KNmm)**	**Cycles to Cracking (No.)**	**Cycles to Failure (No.)**
1	6.37	11.5	10.51	10.02	9.53	140	84312	1151	86	112
2	7.00	11.5	11.56	10.17	10.02	131	98844	1228	82	112
3	1.83	13.5	6.41	5.42	4.59	153	36701	1486	72	139
4	2.58	13.5	7.47	6.48	4.65	165	33227	954	52	82
5	2.88	13.5	8.72	10.6	5.87	139	16804	449	24	59
6	7.38	15.0	11.84	11.26	11.17	137	74342	672	42	61
7	4.00	12.0	9.44	9.11	8.5	137	42200	879	52	83
8	6.00	14.0	11.20	11.14	10.78	158	59376	707	52	64

Notes: Column 4 is the mean thickness of all thickness readings for the web-to-flange intersection being tested.
Column 5 is the mean thickness of the thickness readings located where the first crack was noticed.
Column 6 is the lowest thickness reading that was recorded for the web-to-flange intersection being tested.
Column 7 is the mean of the six ten point height of irregularity roughness measurements taken for each web-to-flange Intersection point.
Column 8 is the total energy that was dissipated during testing.
Column 9 is the normalized energy that was recorded during testing. The total energy dissipated was normalized by the yield displacement and yield force (Column 2 and 3).
Column 10 is the number of cycles between the beginning of testing to the point when cracking was first noticed.
Column 11 is the number of cycles from the beginning of testing to failure.

Table 7.1 Summary of Cyclic Testing Data

TEST NUMBER	MEAN THICK-NESS (mm)	MEAN ROUGH-NESS (μm)	E_H (TOT) (KN-mm)	E_H (NORM) (KN-mm)	CYCLES TO CRACK (NUM.)	CYCLES TO FAILURE (NUM.)
1	5	4	7	6	8	6,7
2	6	8	8	7	7	6,7
3	1	3	3	8	6	8
4	2	1	2	5	3,4,5	4
5	3	5	1	1	1	1
6	8	7	6	2	2	2
7	4	6	4	4	3,4,5	5
8	7	2	5	3	3,4,5	3

NOTE: A Rank of 1 is considered to be the thinnest, roughest, the least normalized or total energy dissipated during testing or the least number of cycles to cracking or failure.

Table 7.2 Summary of Ranking Information

1	2	3	4
TEST NUMBER	**MEAN THICKNESS (mm)**	**MEAN ROUGHNESS (μm)**	**TOTAL ENERGY DISSIPATED (KN-mm)**
2	11.56	131	98844
1	10.51	140	84312
% DIFFERENCE	-9.08	6.87	-14.72
		$\Delta ED_{EST.}$= COL 2 - COL 3	-15.95
		$\Delta ED_{EST.} - \Delta ED_{EXP.}$	-1.25

Table 7.3 Sample of Percentile Difference Calculation for the Comparison of Test 1 to Test 2

TEST	1	2	3	4	5	6	7	8
$\Delta ED_{EST.}$	-15.95	0	-61.34	-31.34	-30.67	-2.16	-22.92	-23.73
ΔED_{EXP}	-14.70	0	-62.87	-66.38	-83.00	-24.79	-57.31	-39.93
$\Delta ED_{EST.}$- ΔED_{EXP}	-1.25	0	1.53	5.05	52.33	22.63	34.39	16.21

Table 7.4 Summary of Cumulative Percentile Comparisons of all Tests to Test 2

1	2	3	4	5
TEST NUMBER	t_{MEAN} **(mm)**	E_H **(TOTAL) (KN-mm)**	**MEAN ROUGHNESS**	$\frac{E_H(TOTAL)}{t_{MEAN}(mm)}$ **(KN-mm/mm)**
1	10.51	84312	140	8022
2	11.56	98844	131	8551
3	6.41	36701	153	5726
4	7.47	33227	165	4448

Table 7.5 Summary of Data for the Construction of Thickness Normalized Total Energy vs. Mean Ten Point Height of Irregularity Roughness Graph (Figure 7.1)

Figure 2.1 Precision Dial Calipers (Mitutoyo)

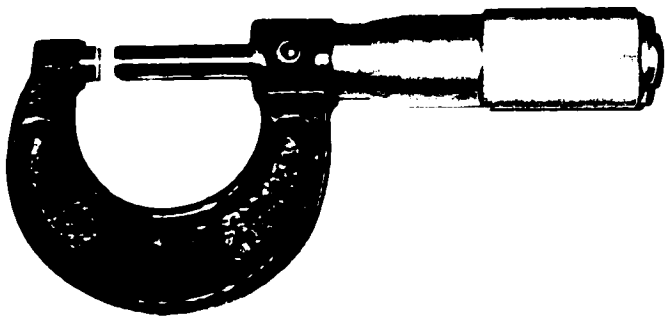

Figure 2.2 Screw Micrometer (Mitutoyo)

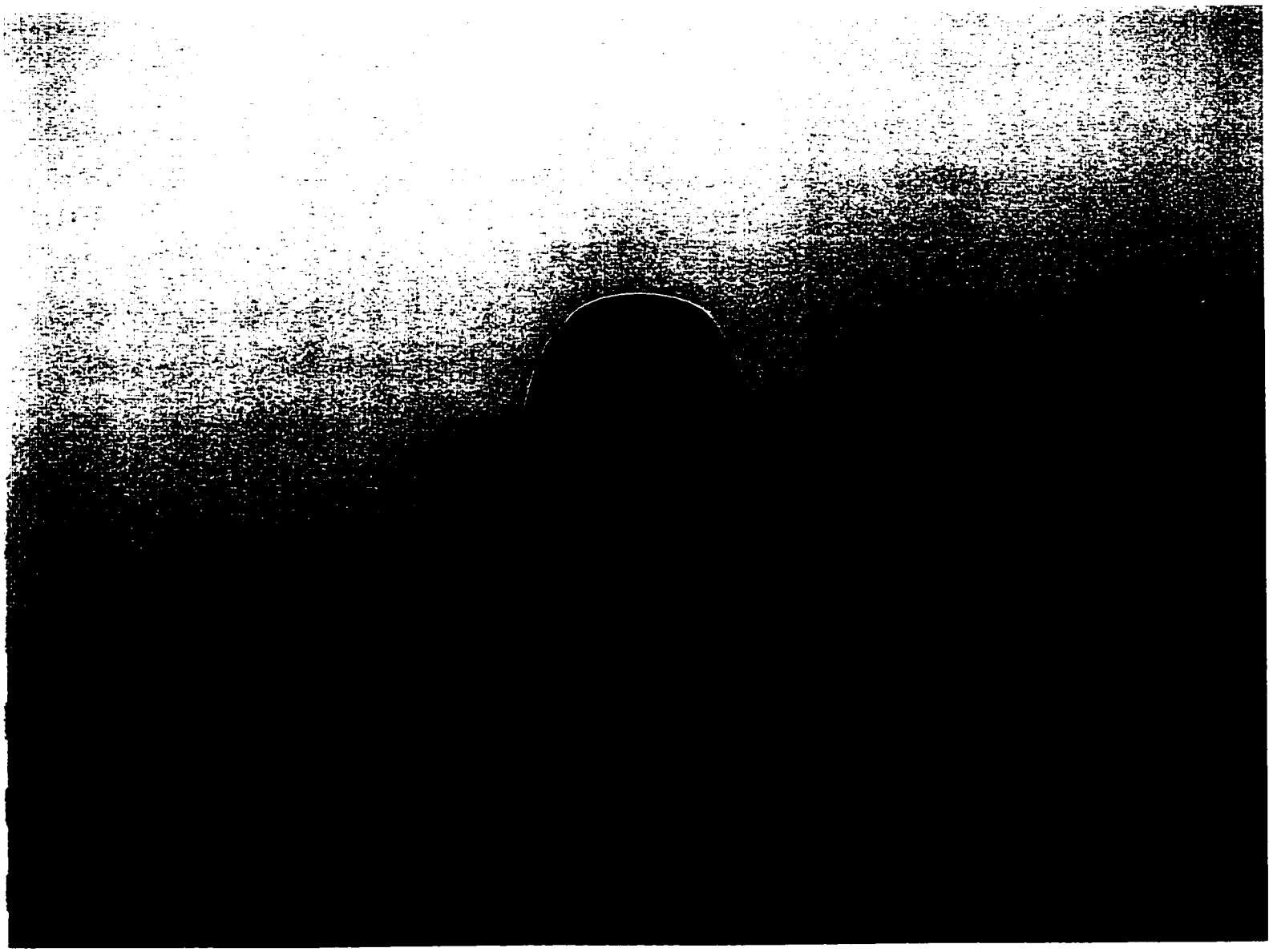

Figure 2.3 Ball Anvil Attachments for Screw Micrometers (Mitutoyo)

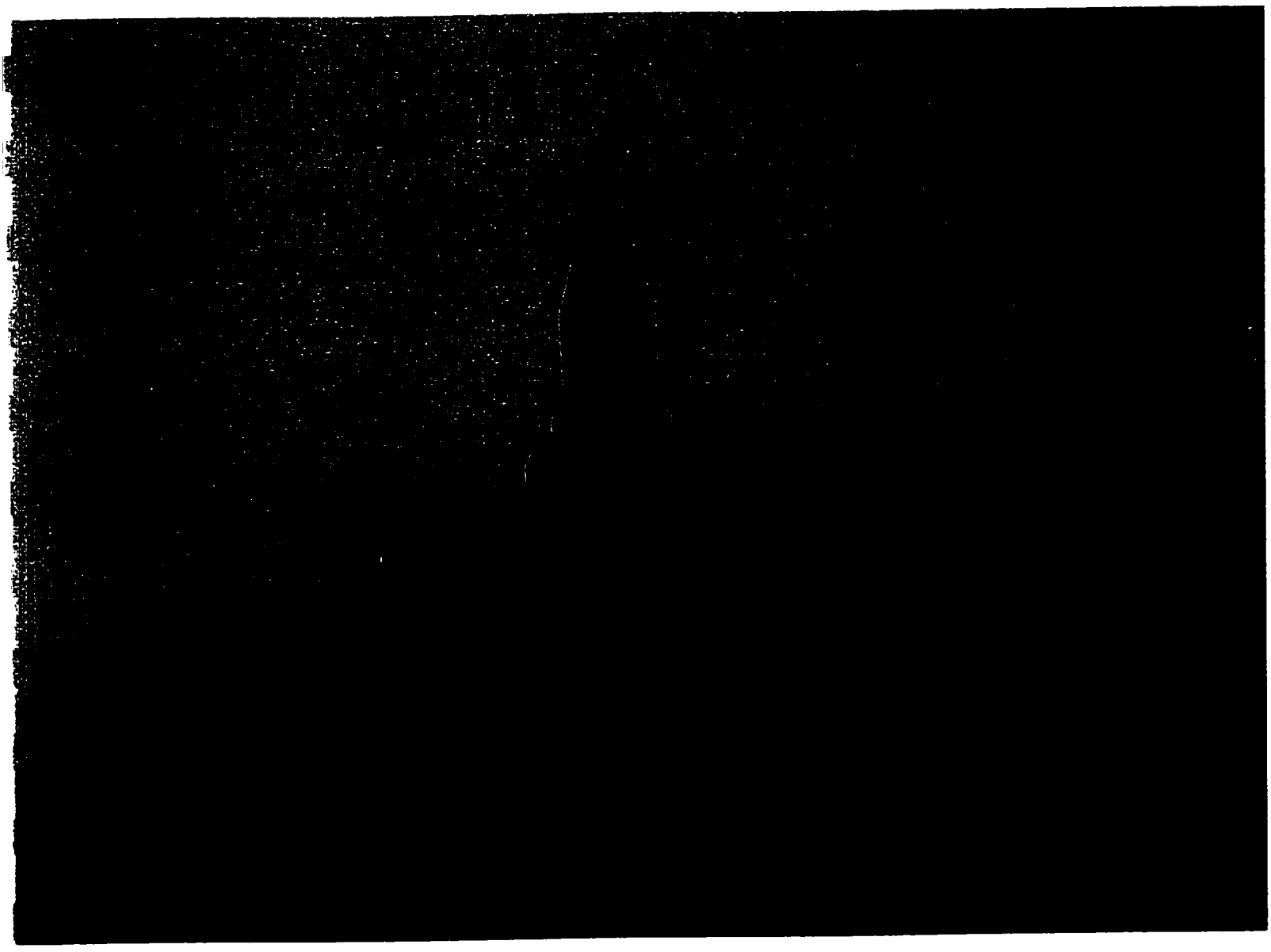

Figure 2.4 Comparator Anvil Attachments for Screw Micrometers (Mitutoyo)

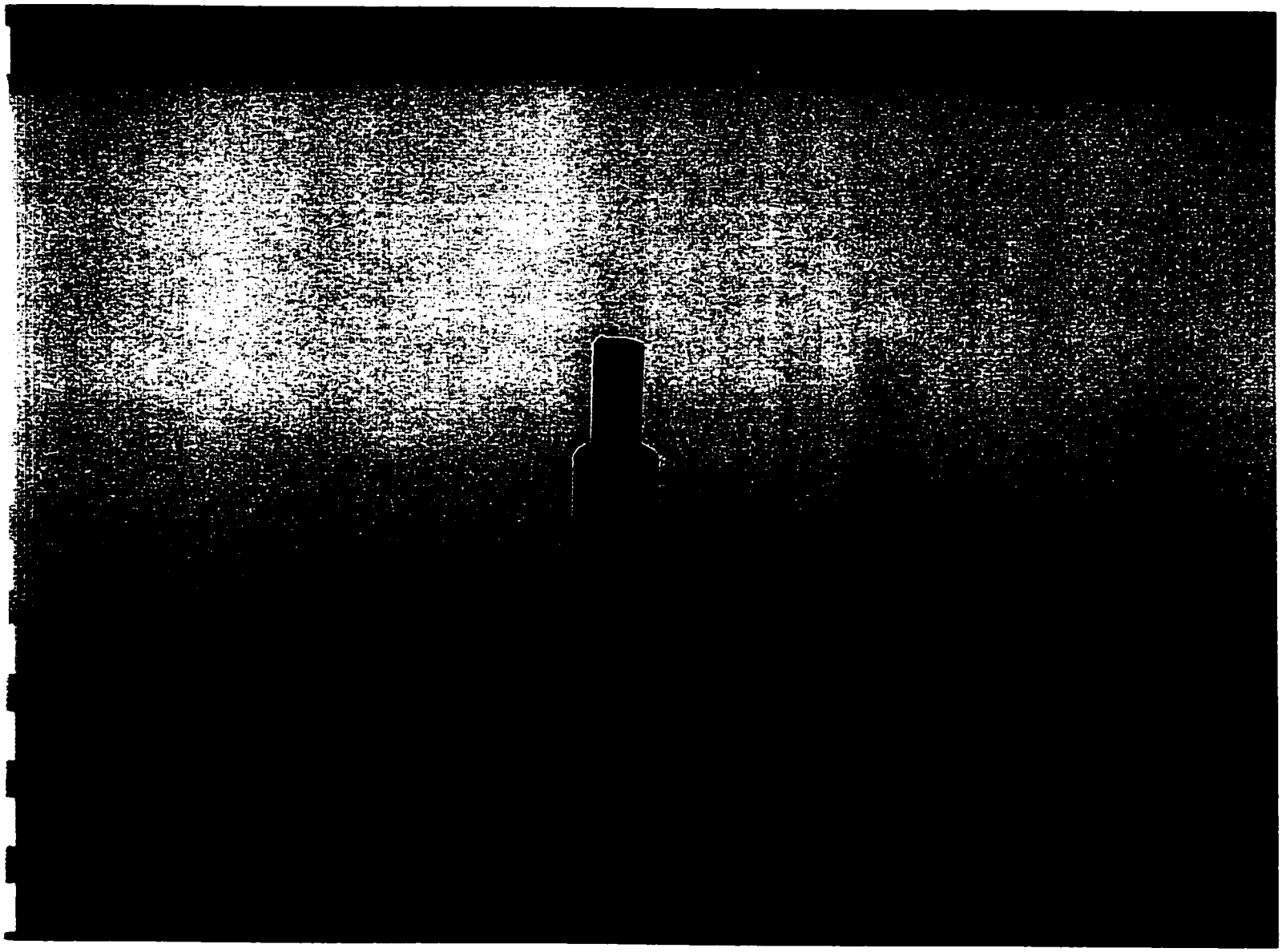

Figure 2.5 Spline Anvil Attachments for Screw Micrometers (Mitutoyo)

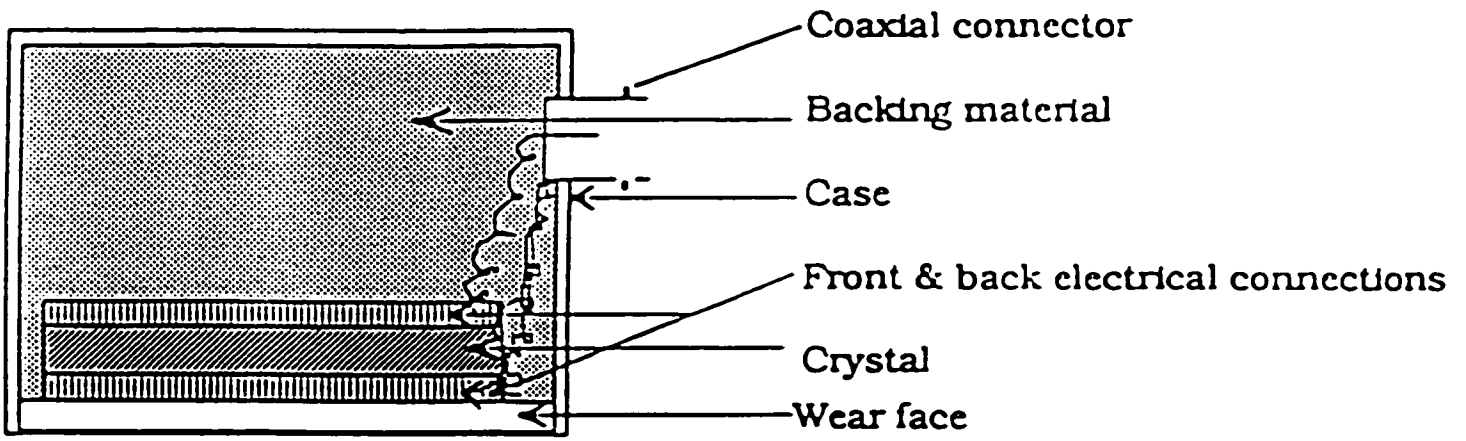

Figure 2.6 Ultrasonic Transducer Construction (Non-Destructive Evaluation Institute of Canada - Level I Course Material 1995)

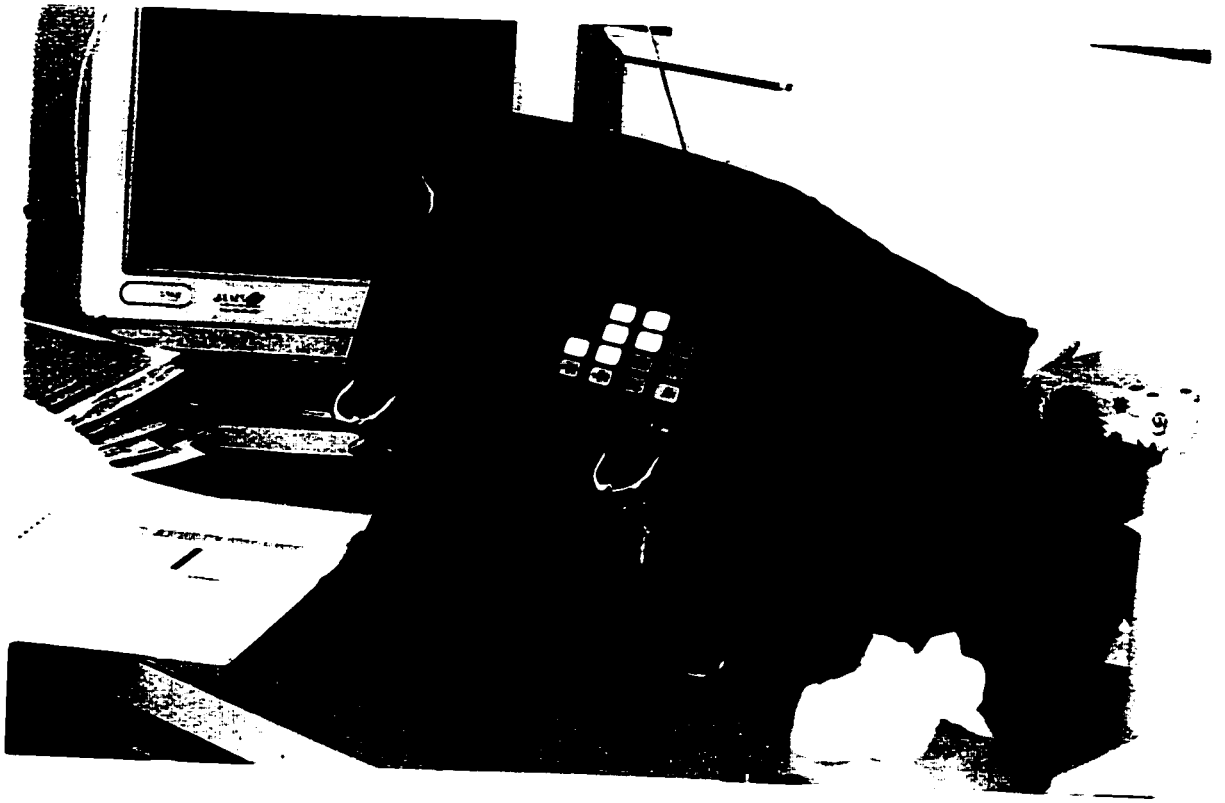

Figure 2.7 Ultrasonic Flaw Detector (Panameterics)

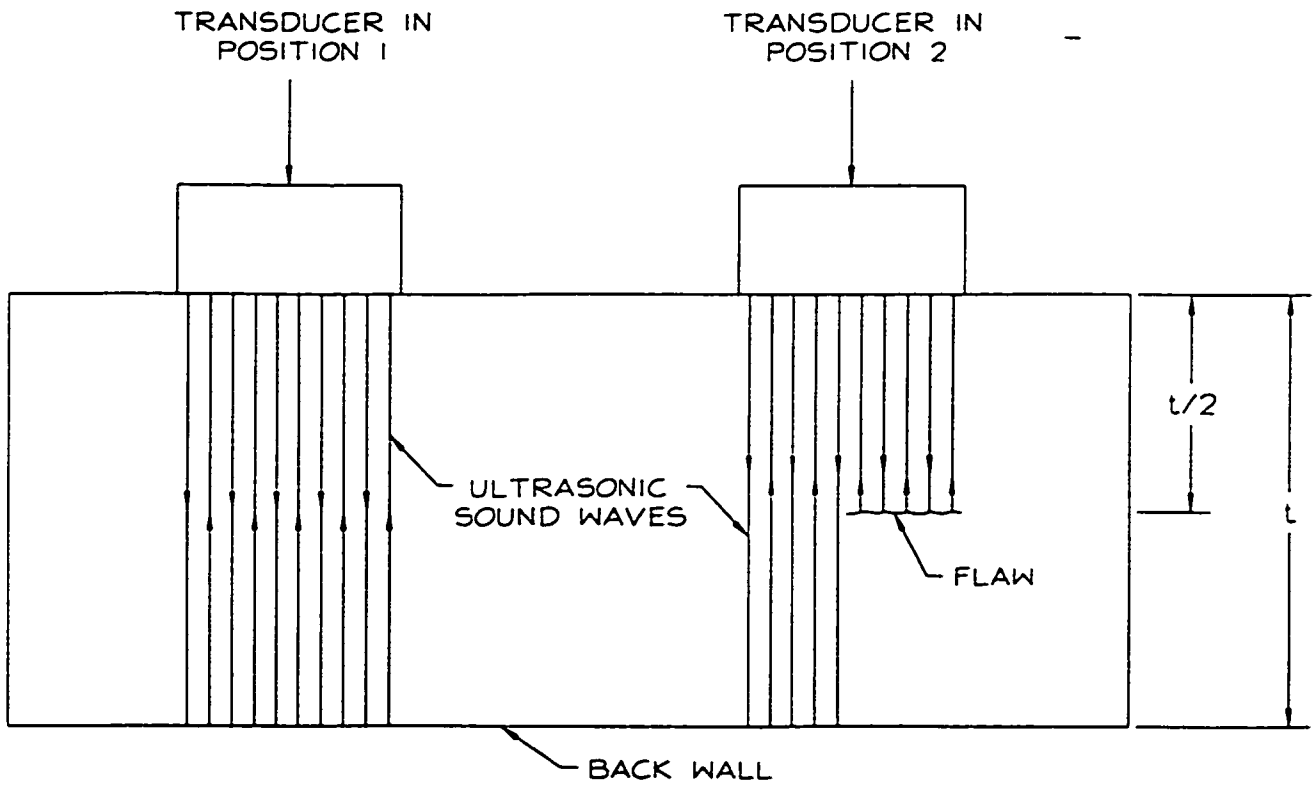

Figure 2.8 Test Coupon of Thickness "t" with a Flaw at Depth "t/2"

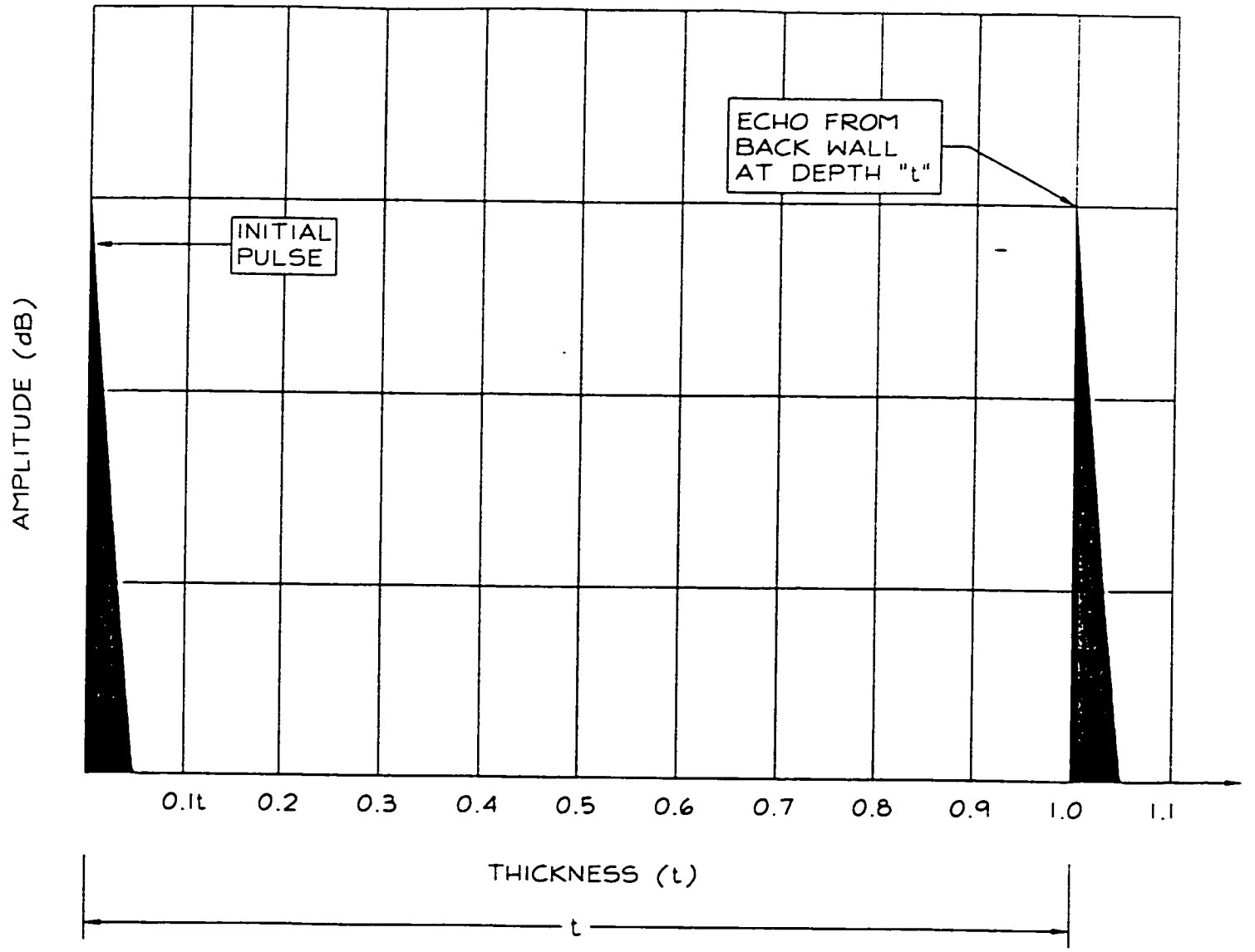

Figure 2.9 A-Scan Display with Transducer at Position 1 in Figure 2.8

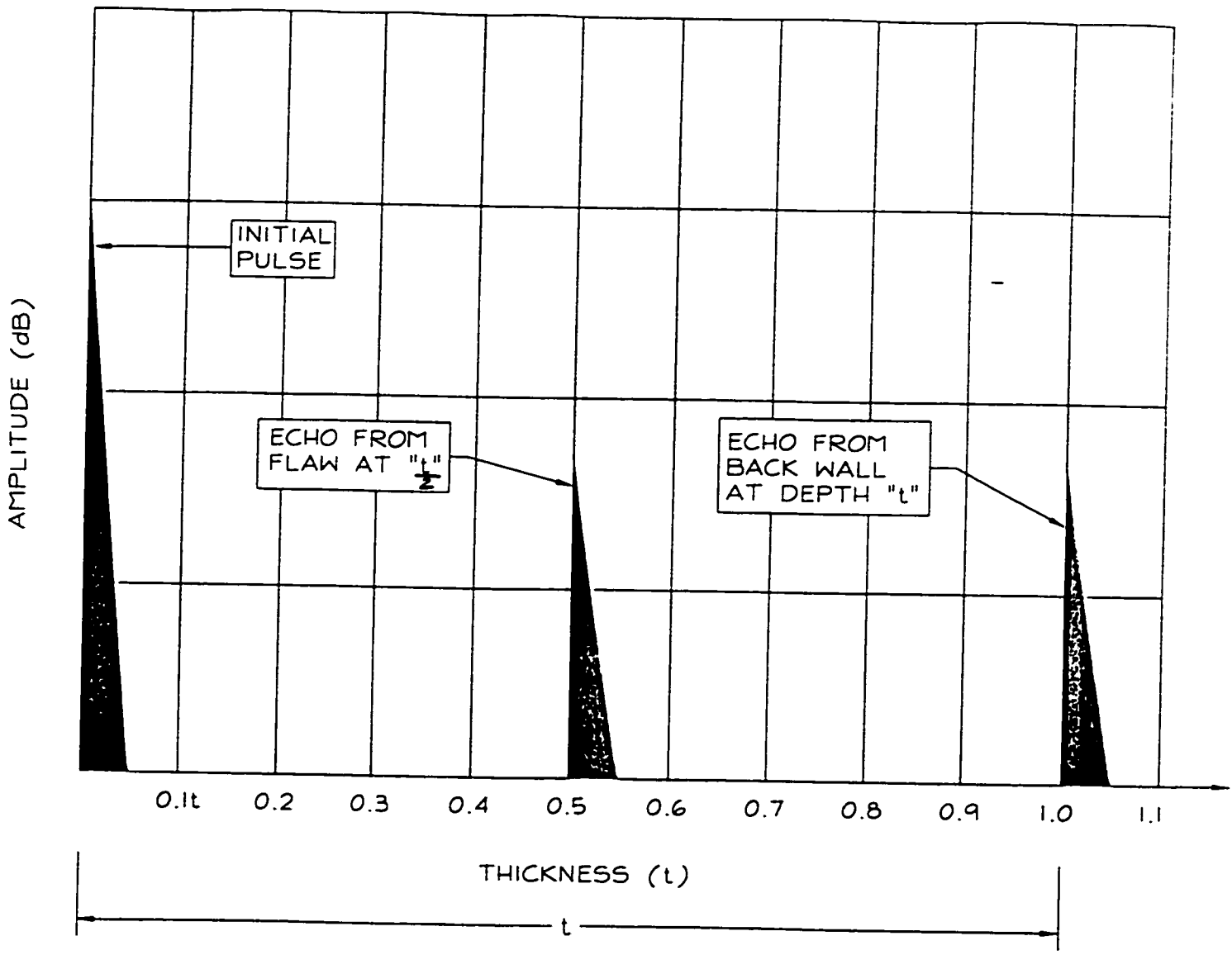

Figure 2.10 A-Scan Display with Transducer at Position 2 in Figure 2.6

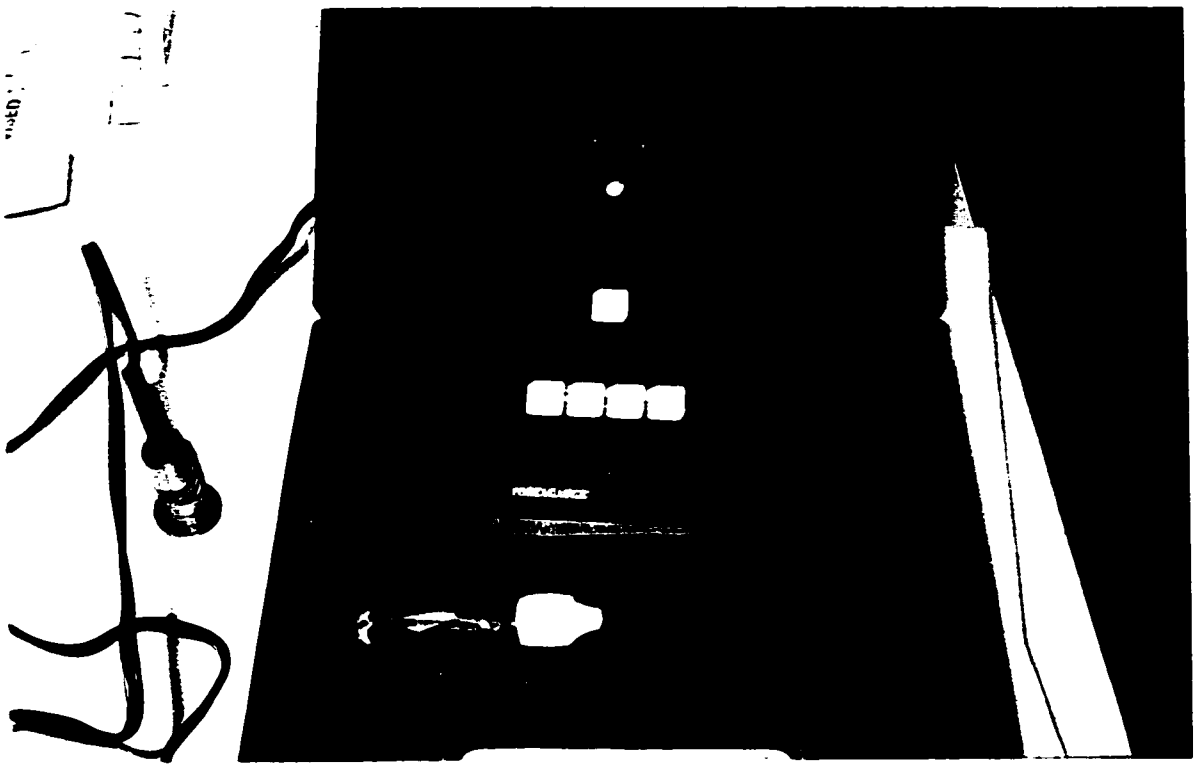

Figure 2.11 Ultrasonic Depth Meter coupled to a smooth test block (Panametrics)

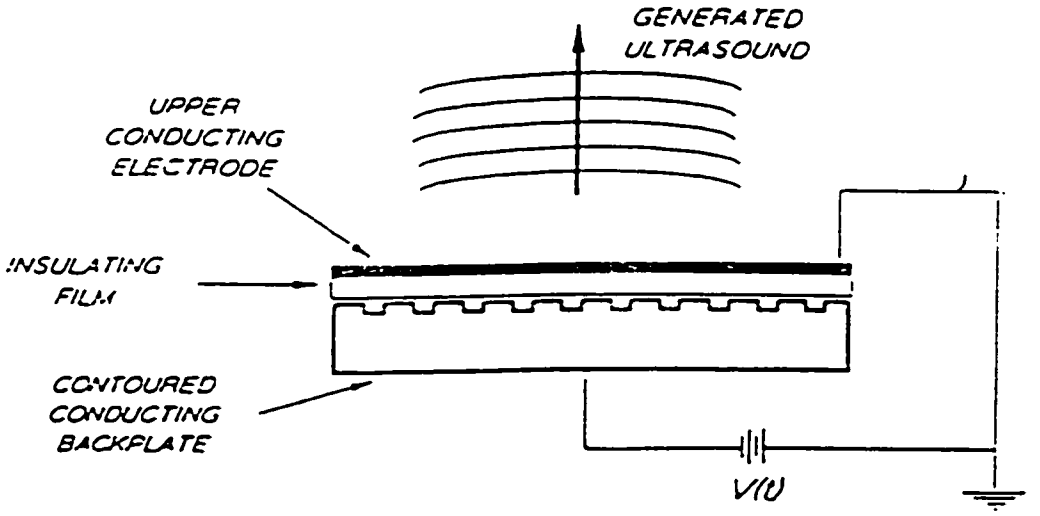

Figure 2.12 Air Coupled Transducer Construction
(Schindel et al. 1995)

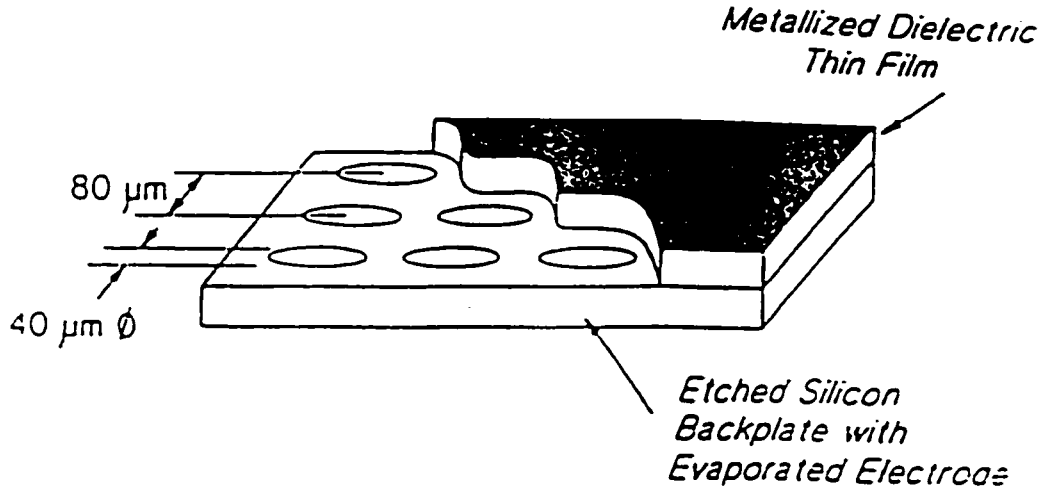

Figure 2.13 Air Coupled Transducer Construction (Schindel et al. 1995)

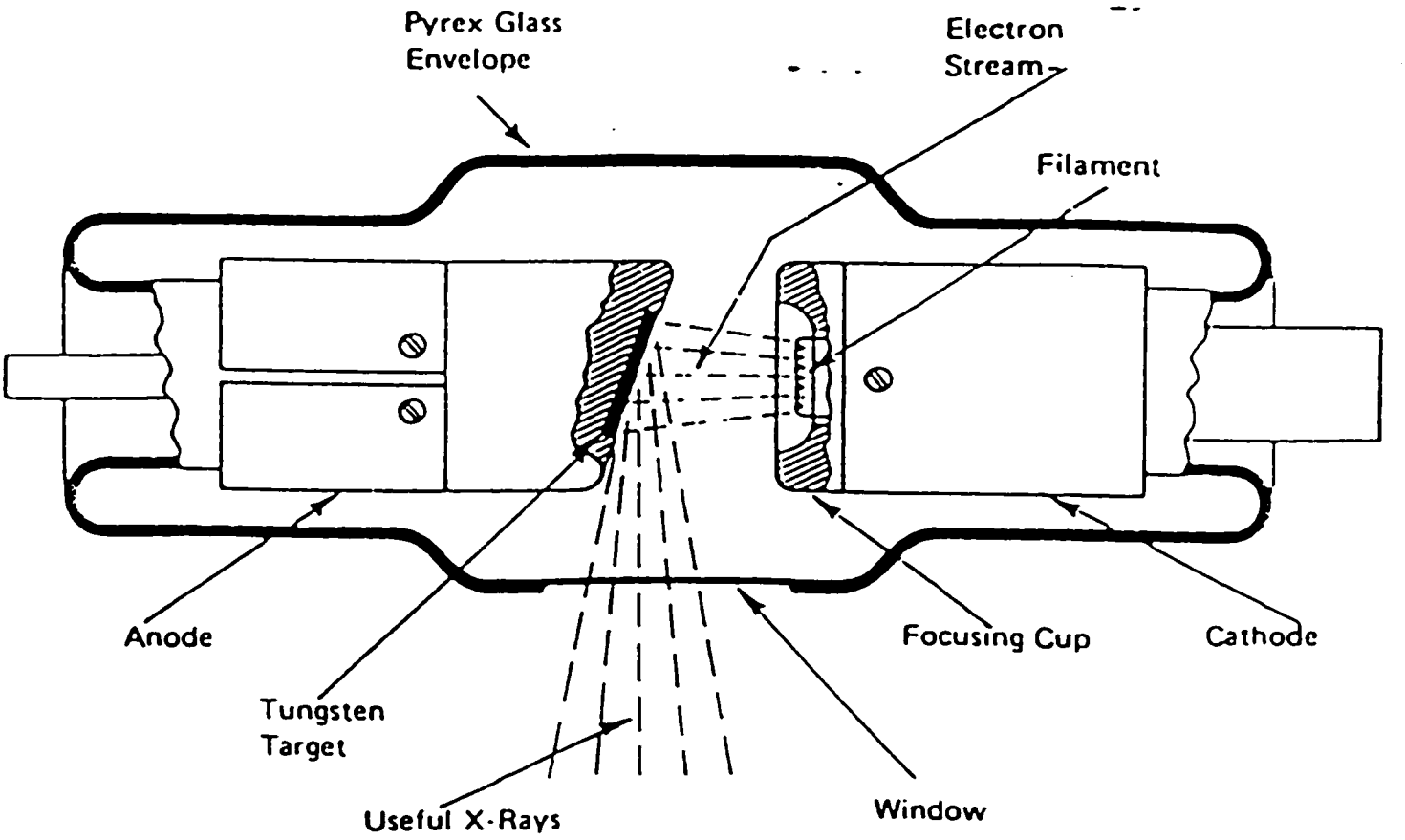

Figure 2.14 X-Ray Tube Construction (Canadian General Standards Board - Manual On Industrial Radiography)

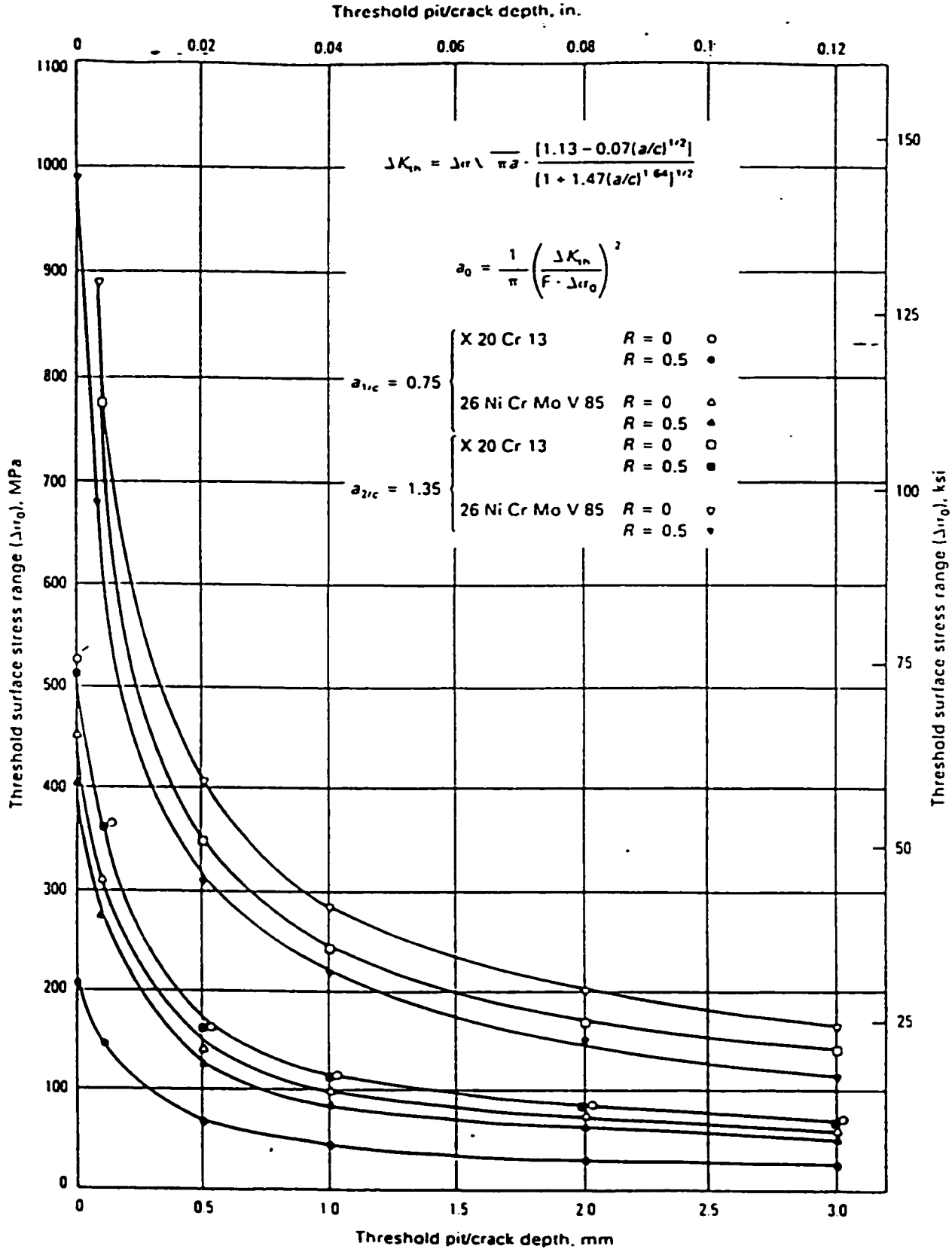

Figure 2.15 Threshold Surface Stress Range versus Threshold Pit/Crack Depth (Bill, 1982)

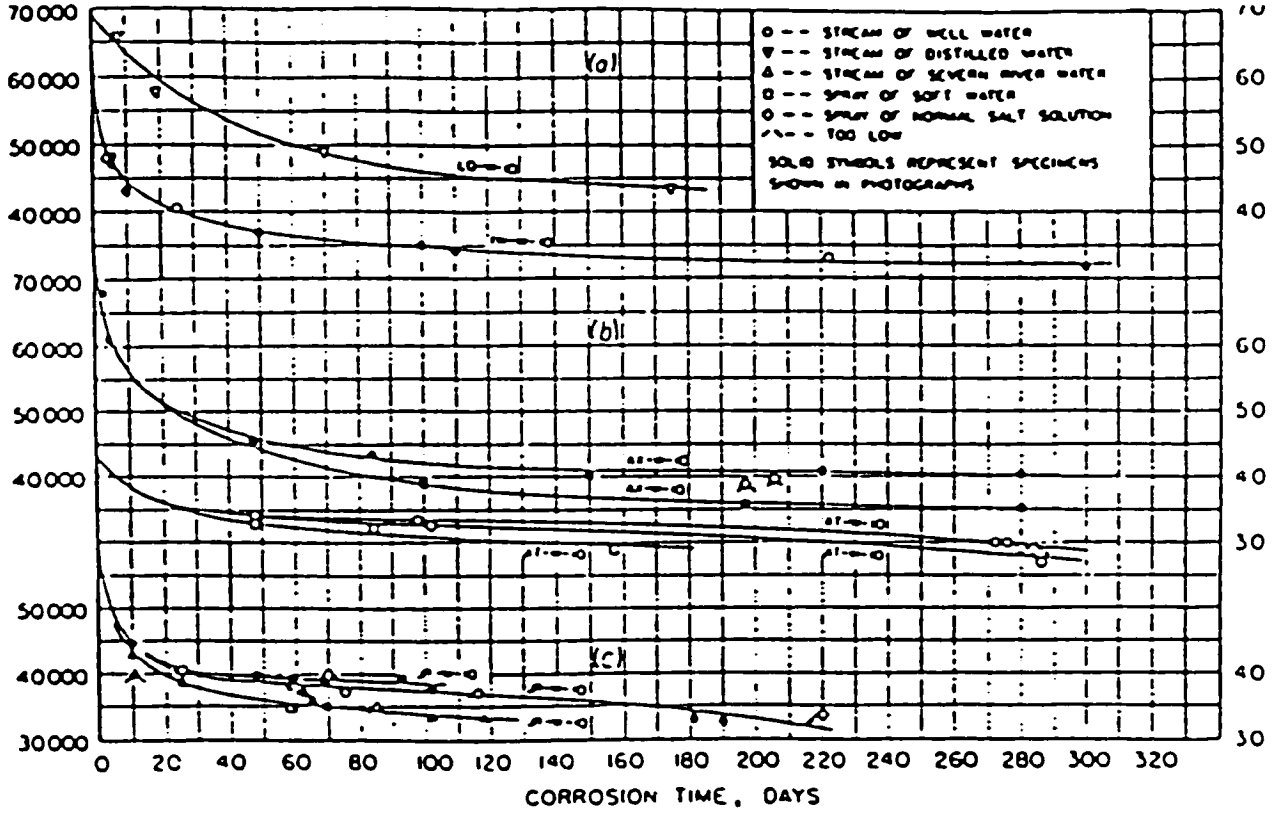

Figure 2.16 Exposure Time versus Cycles to Failure for Steel in Various Corrosive Environments (McAdam)

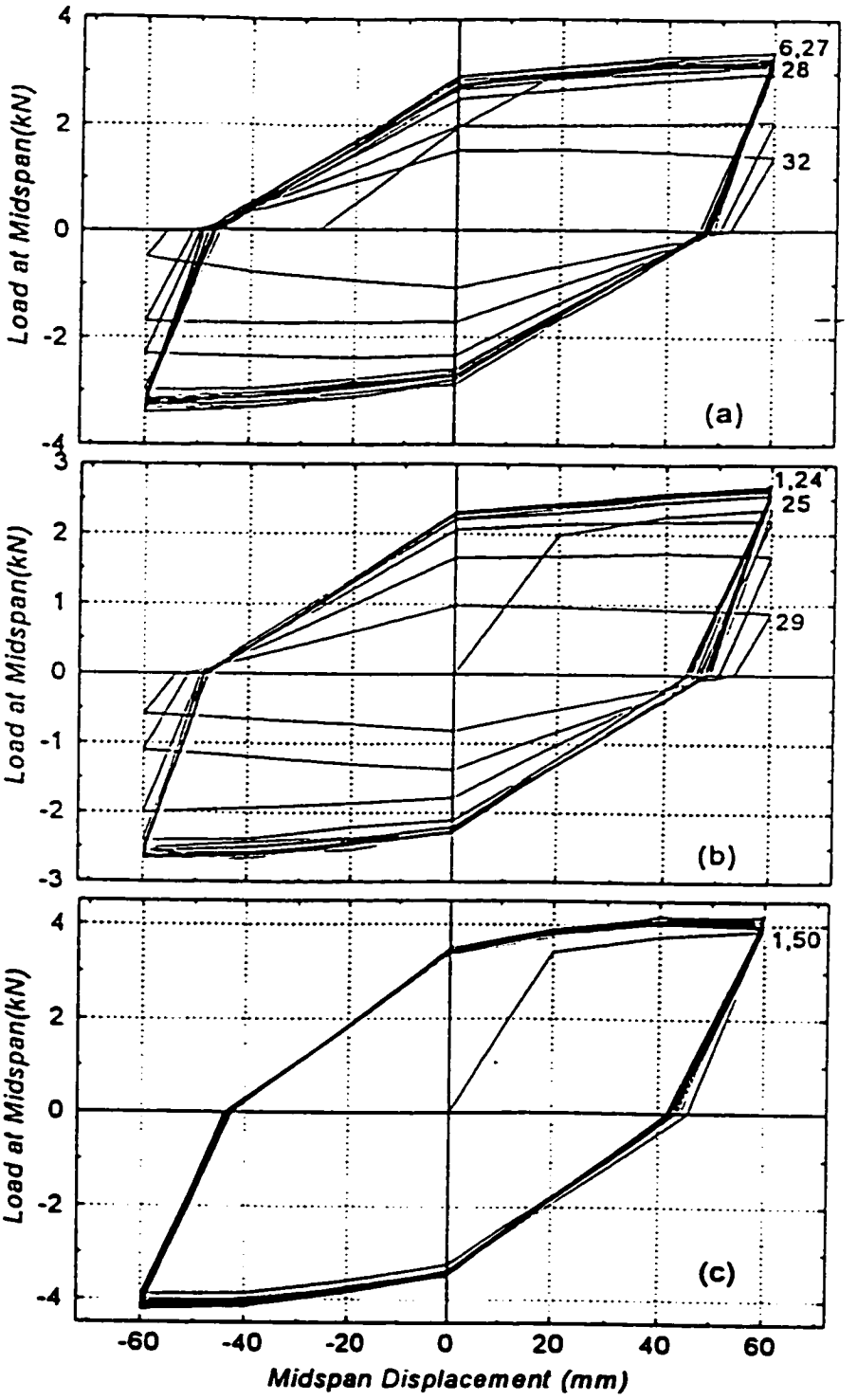

NOTE: The top two graphs are from testing corroded specimens and the bottom graph is a result of testing a smooth control specimen.

Figure 2.17 Simplified Hysteretic Behavior of Plate Specimens (Bruneau et. al., 1998)

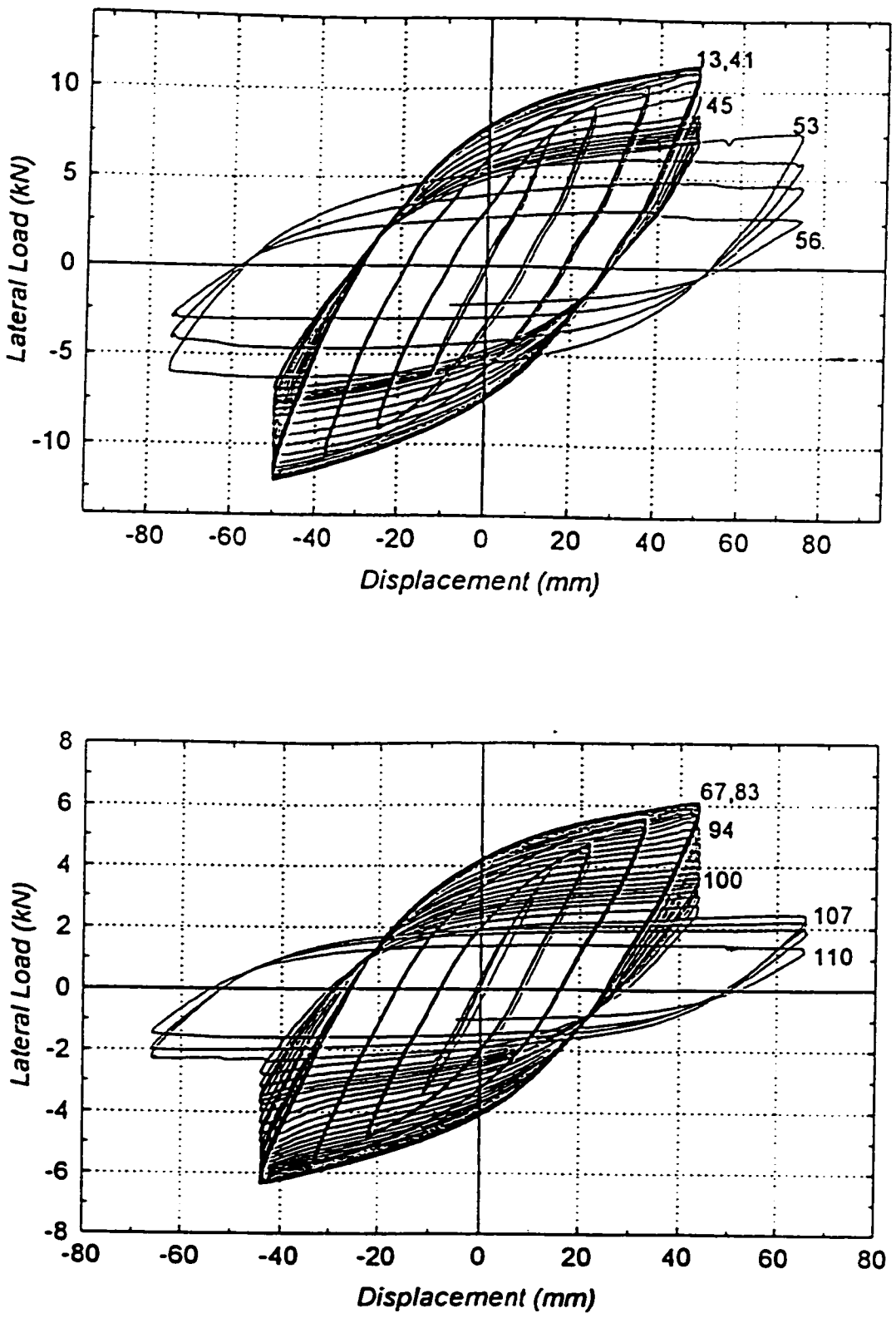

Figure 2.18 Hysteretic Behavior for Out of Plane Bending of Corroded I-Sections (Bruneau et. al., 1998)

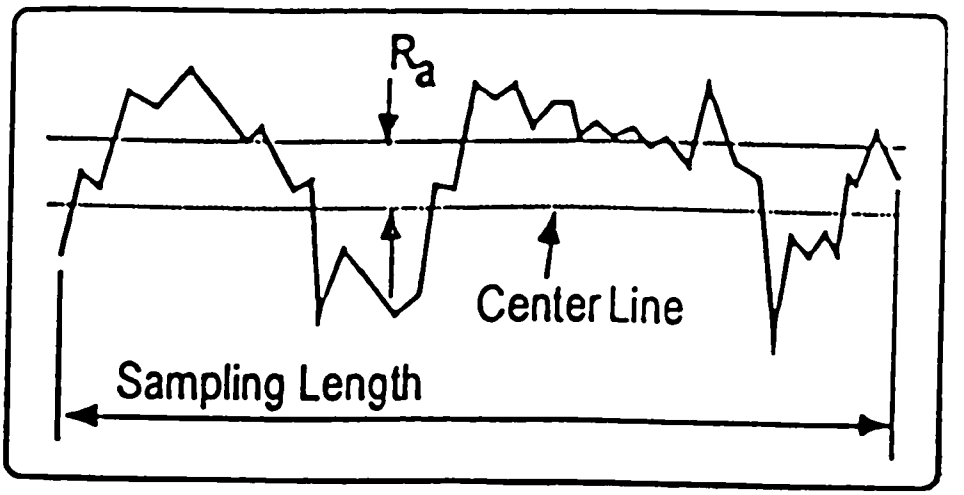

Figure 2.19 Arithmetic Mean Roughness (Ra) (Zygo Surface Roughness Parameters)

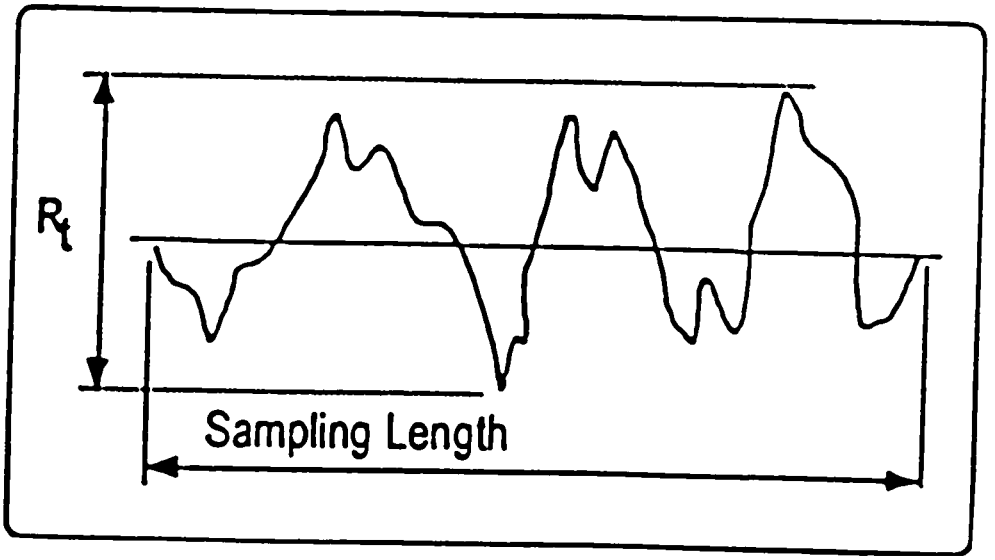

Figure 2.20 Maximum Peak to Valley Roughness (Rt) (Zygo Surface Roughness Parameters)

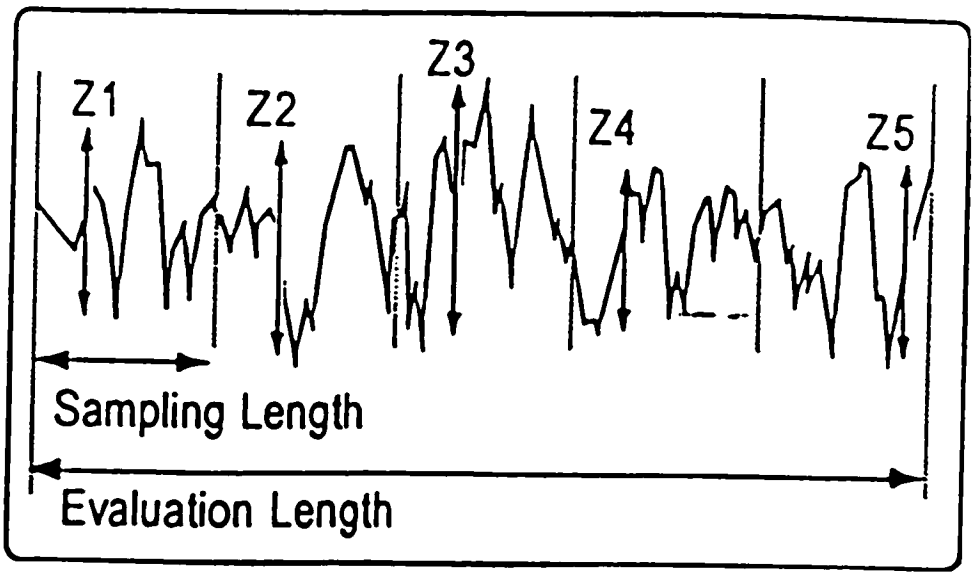

Figure 2.21 Mean Peak to Valley Roughness (Rtm) (Zygo Surface Roughness Parameters)

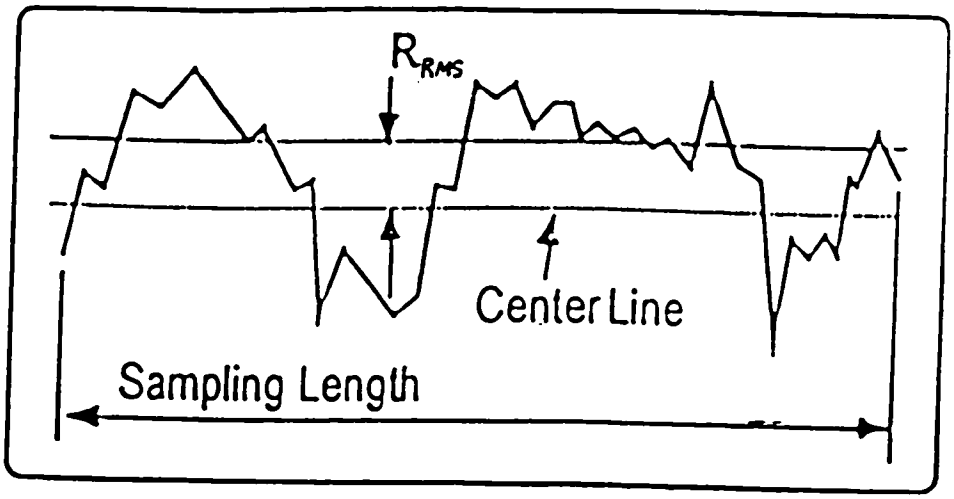

Figure 2.22 Root Mean Square Roughness (RMS) (Zygo Surface Roughness Parameters)

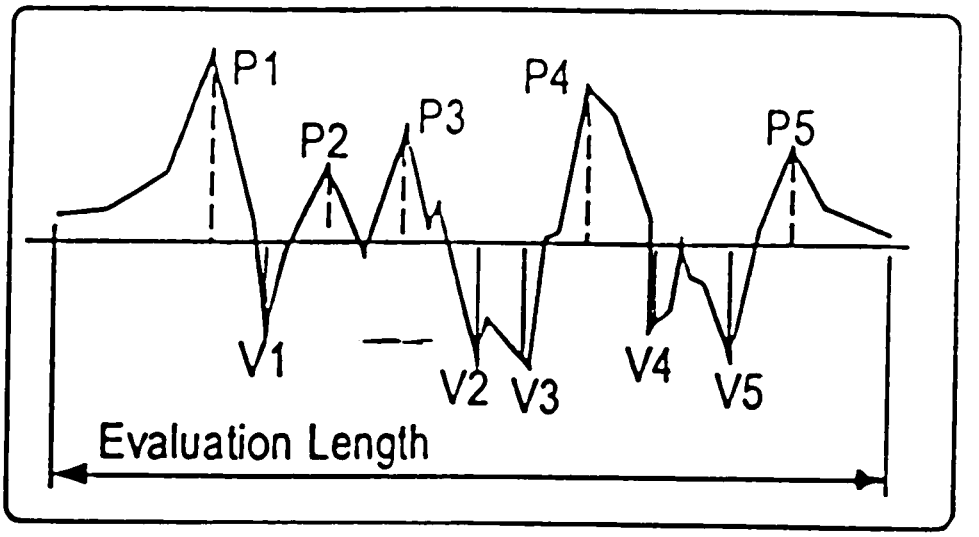

Figure 2.23 Ten-Point Height of Irregularities (Rz) (Zygo Surface Roughness Parameters)

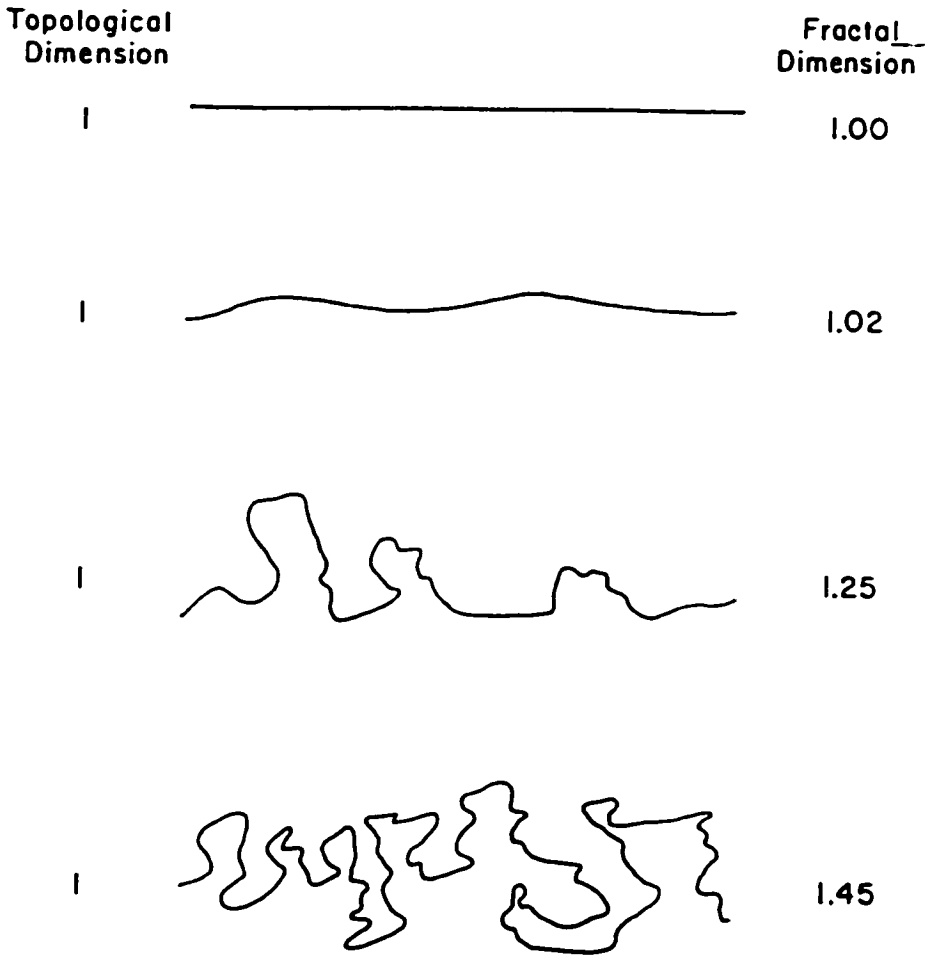

Figure 2.24 Comparison of the Topological and Fractional Dimensions for Various Lines (Kaye, 1989)

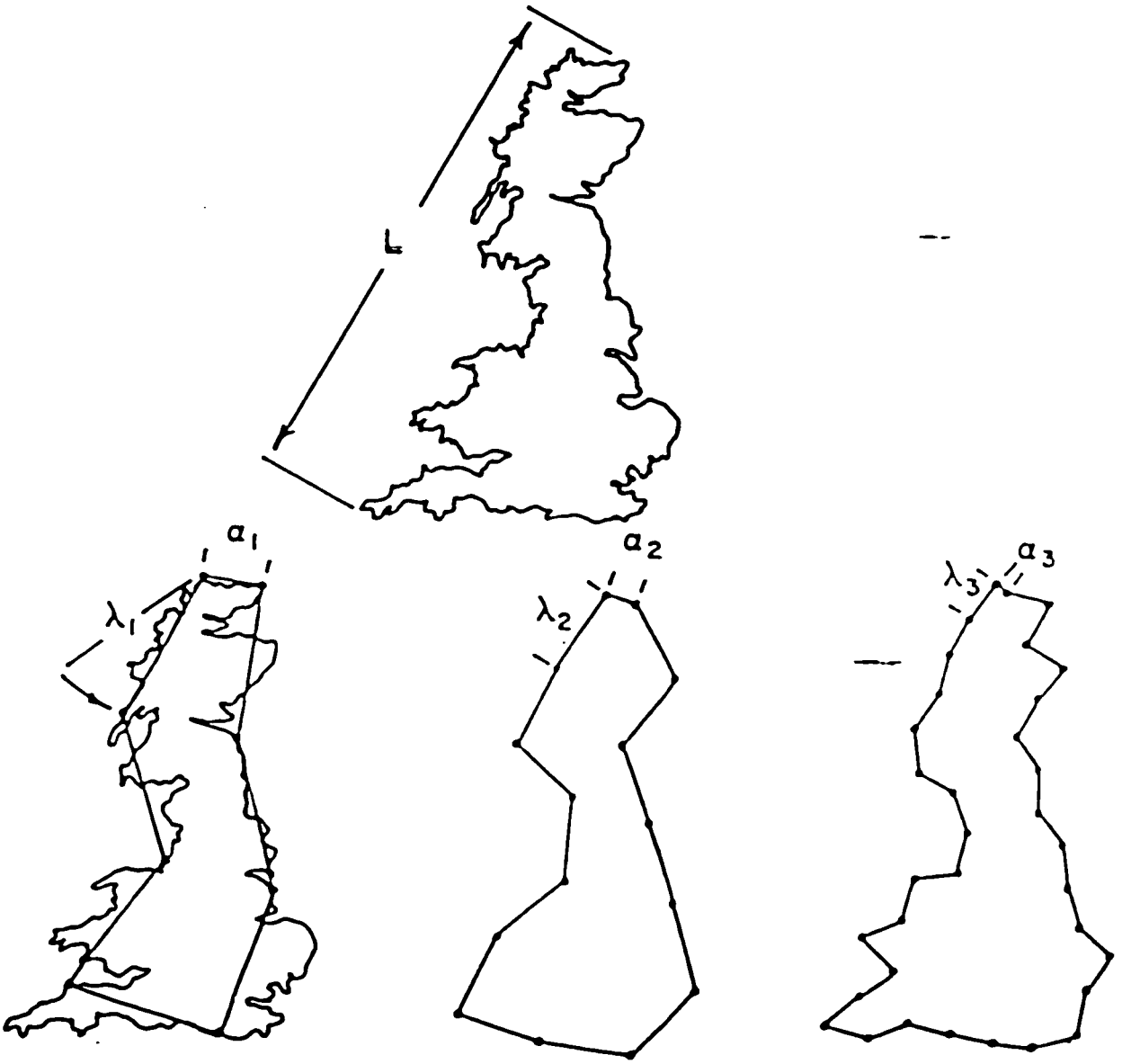

Figure 2.25 Coastline Perimeter Calculations at Various Step Sizes (Kaye, 1989)

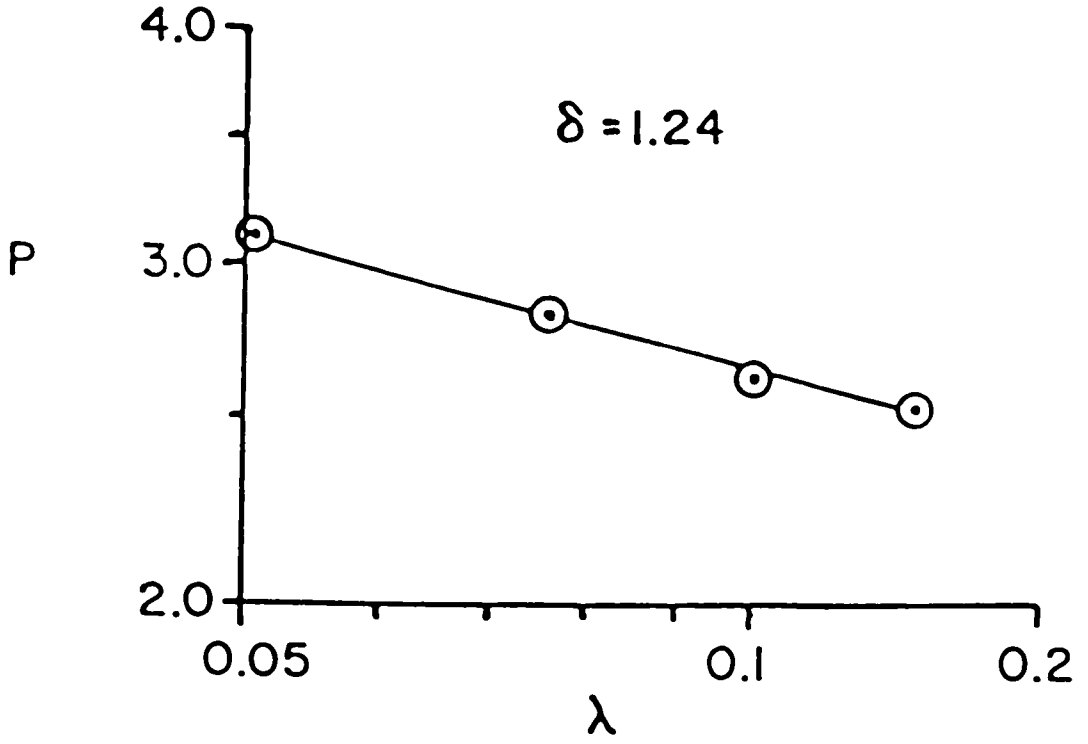

Figure 2.26 Fractal Plot of Coastline Perimeter Calculations for Various Step Sizes (Kaye, 1989)

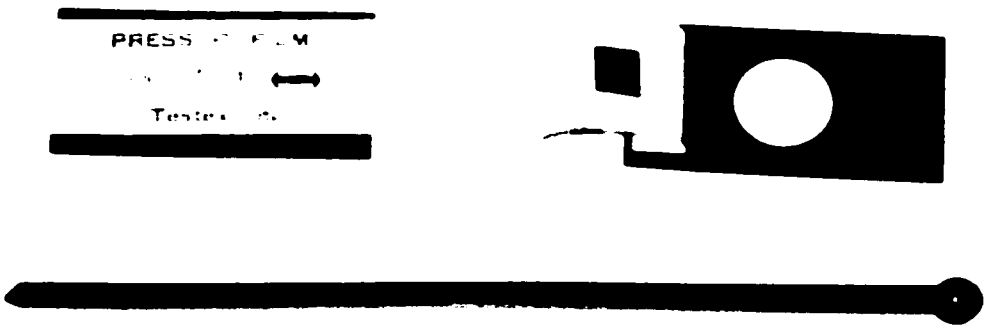

Figure 2.27 Testex Press-O-Film Replica Tape Sample and Burnishing Tool (Testex, 1999)

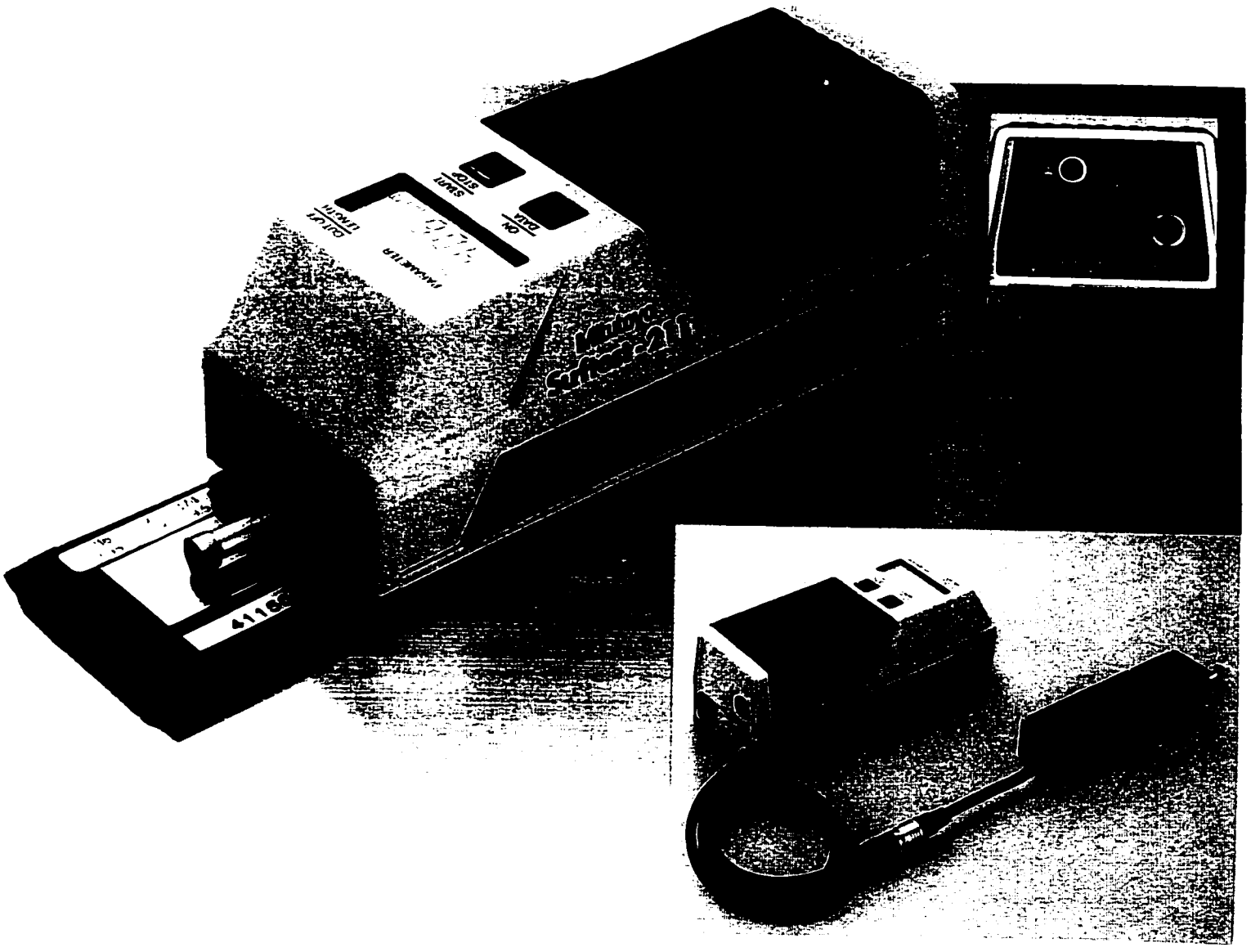

Figure 2.28 Hand Held Stylus (Mitutoyu)

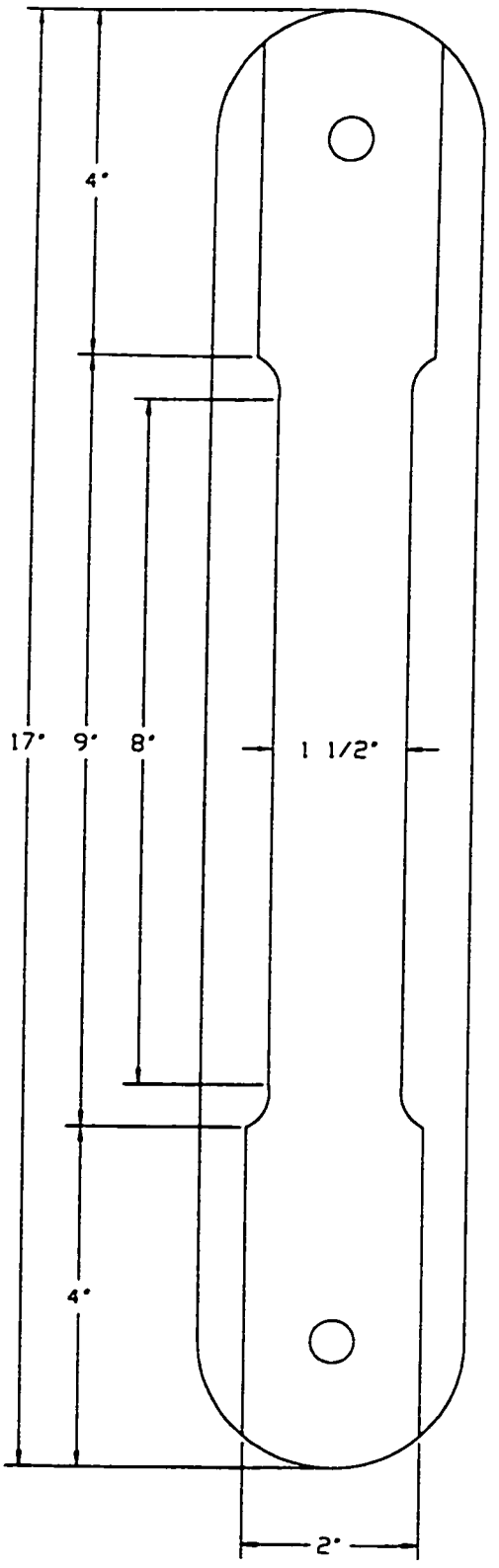

Figure 3.1 Dimensions of ASTM Long Tension Test Specimen

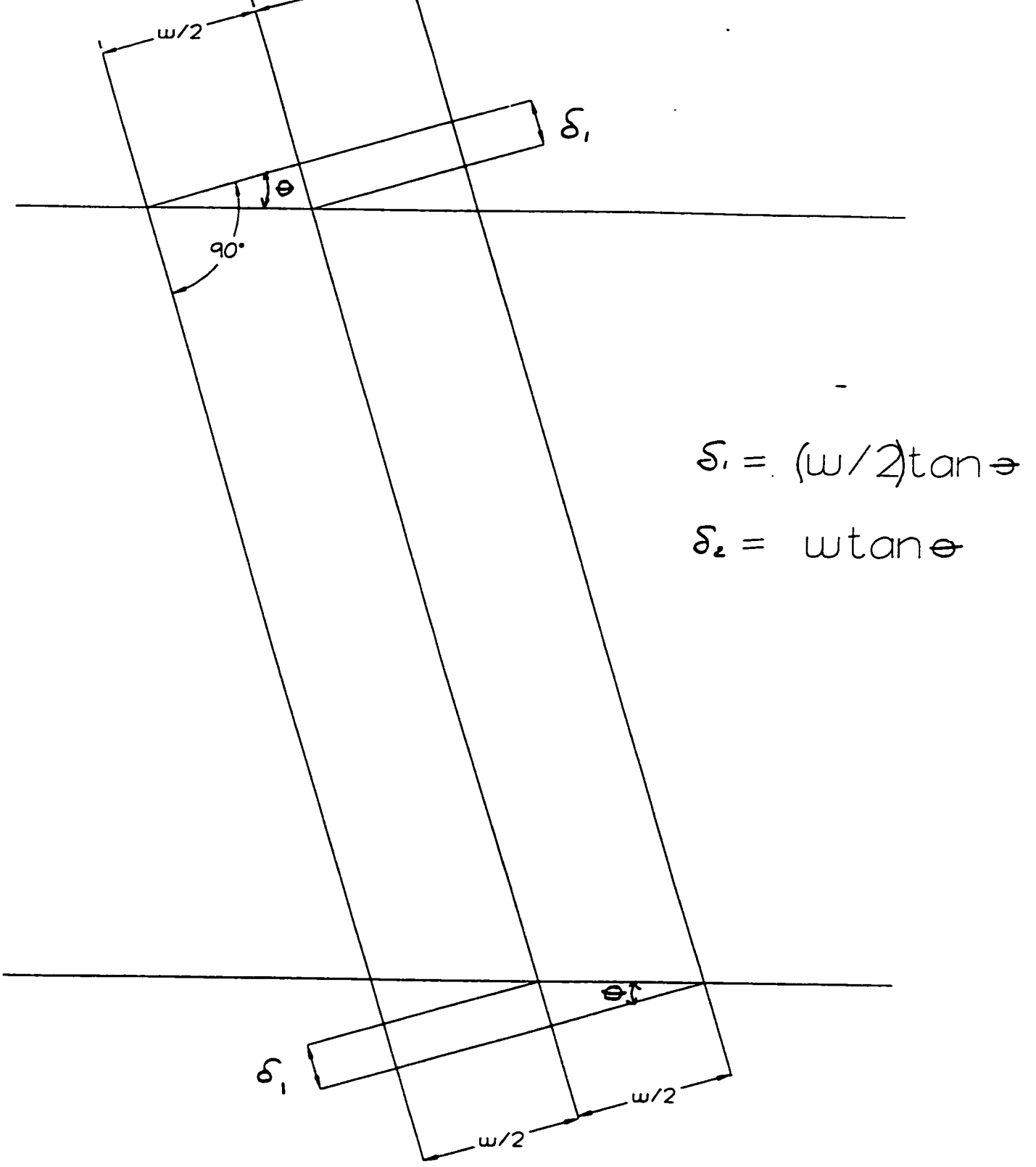

Figure 3.2 Tilt Error Sensitivity Derivation

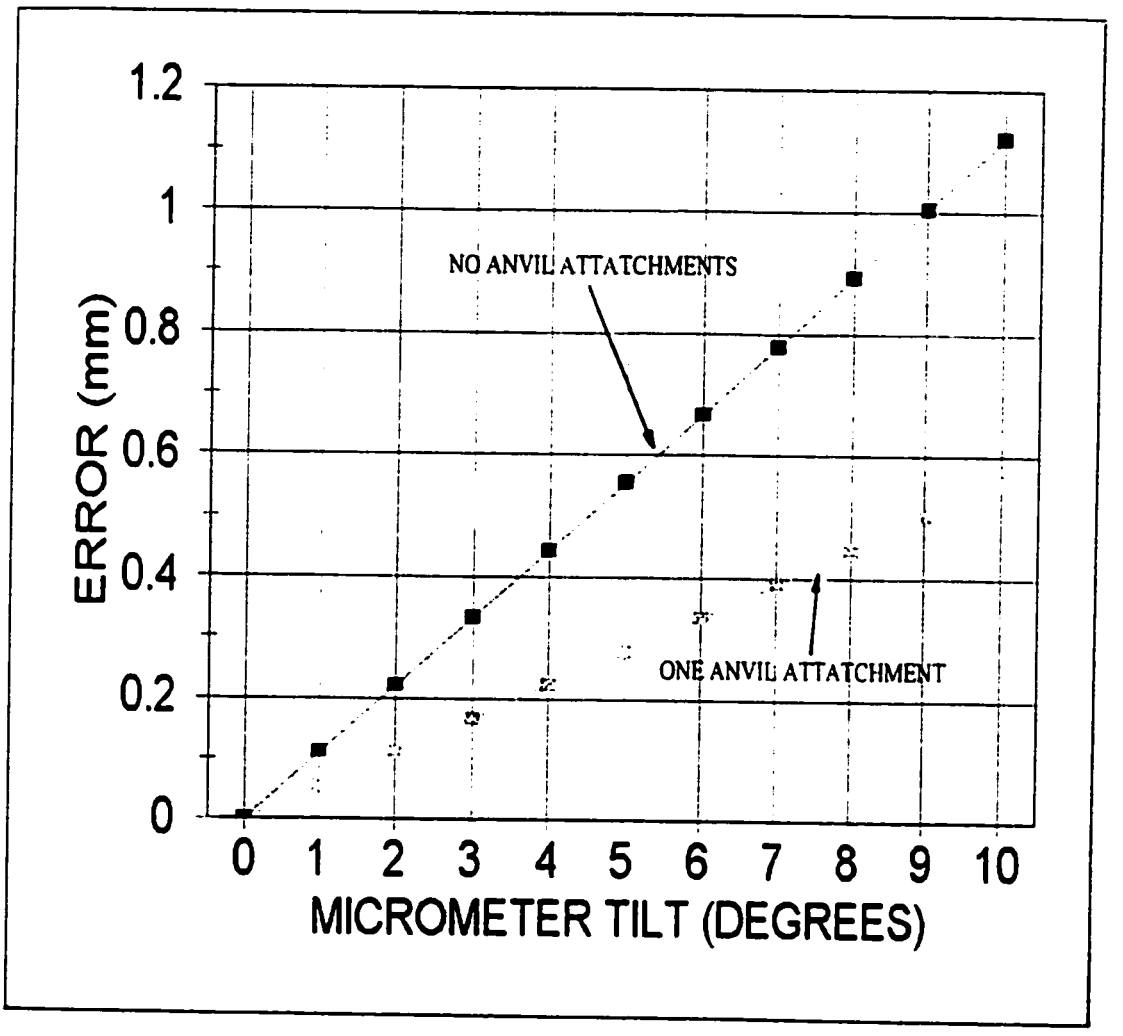

Figure 3.3 Tilt Error Sensitivity Curves

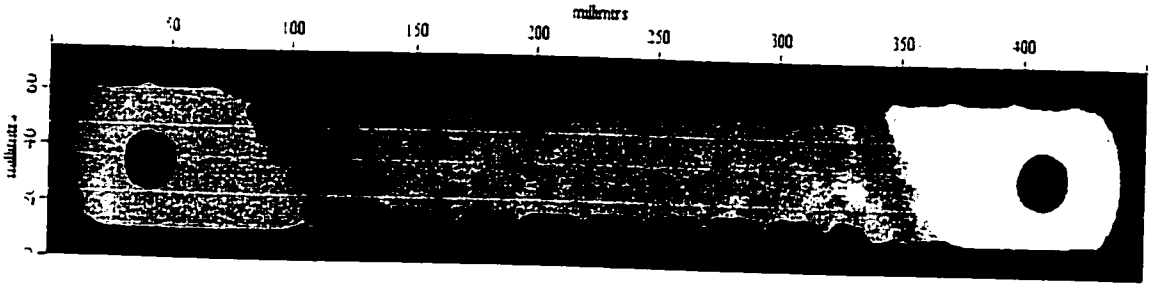

Figure 3.4 Air Coupled Transducer Image
(Schindel, 1998)

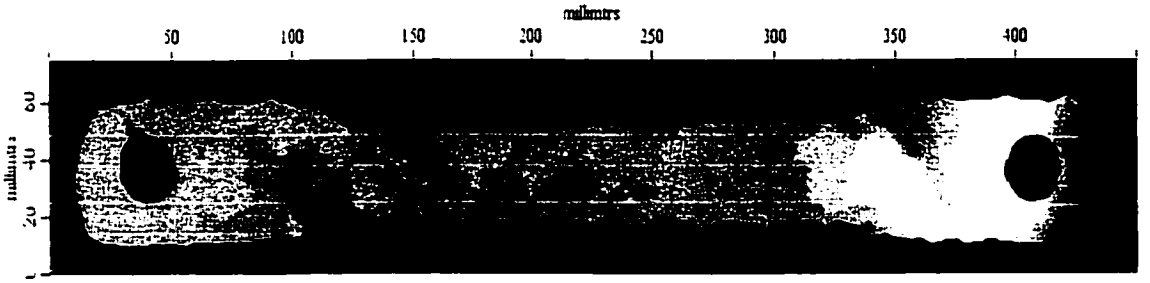

Figure 3.5 Air Coupled Transducer Image
(Schindel, 1998)

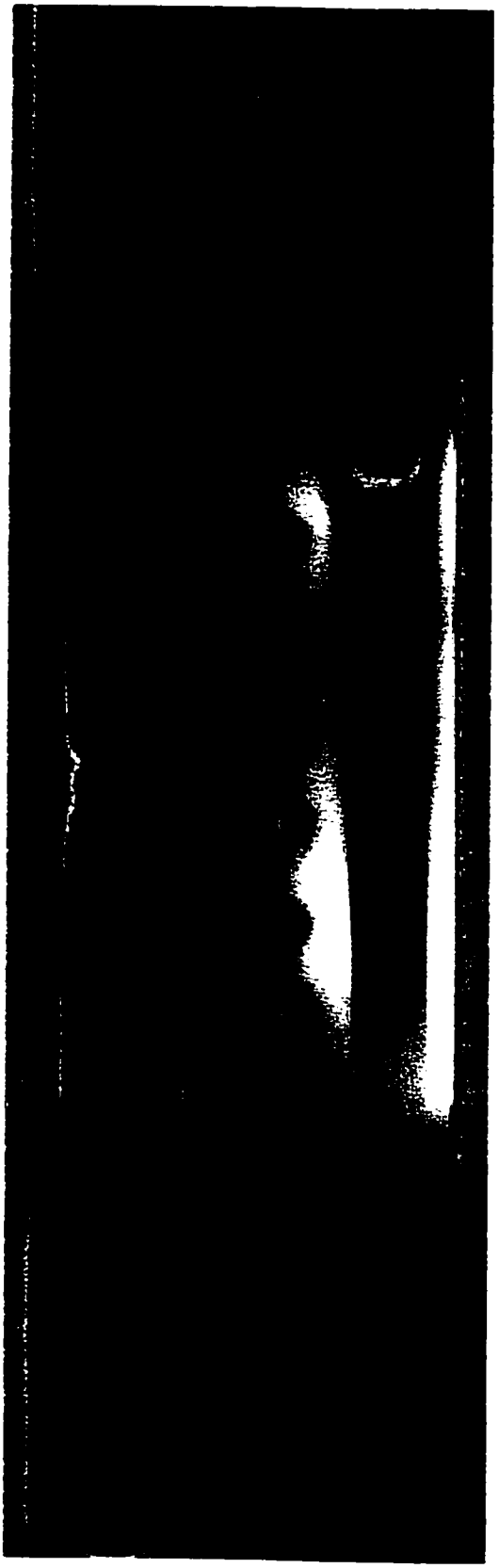

Figure 3.6 Digitized X-Ray of S1 from the National Research Council

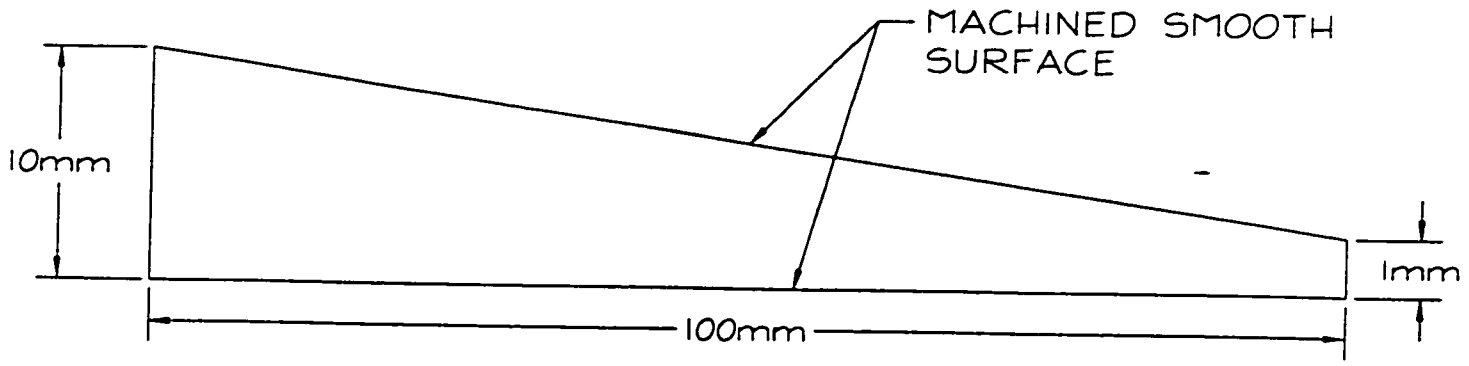

SECTION

Figure 3.7 Elevation View of Slope Wedge for X-Ray Inspection

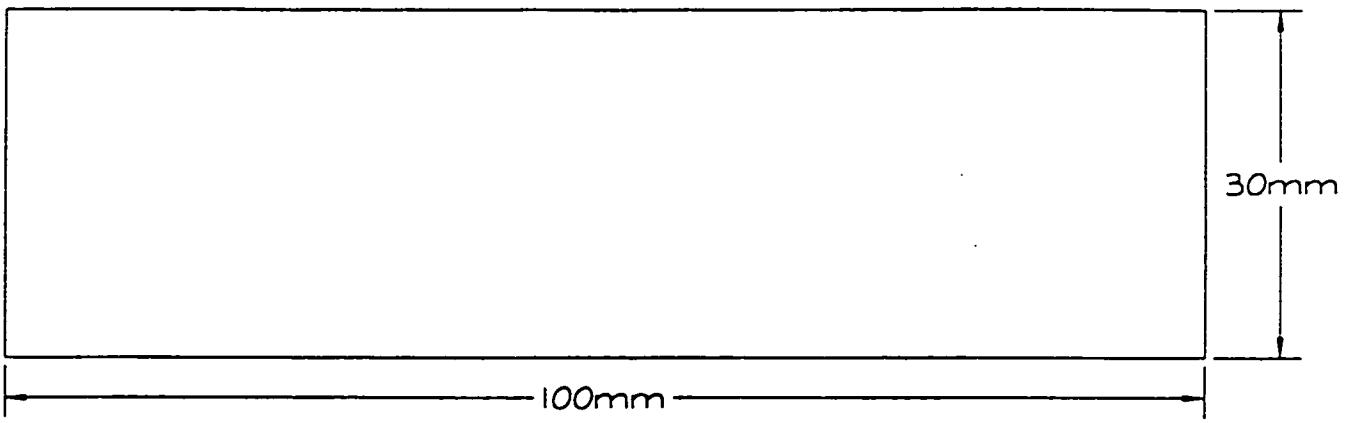

Figure 3.8 Plan View of Slope Wedge for X-Ray Inspection

Exposure Technique	Radiographic Viewing	Source-Weld-Film Arrangement: End View	Source-Weld-Film Arrangement: Side View	IQI Penetrameter: Selection	IQI Penetrameter: Placement	RADIOGRAPHIC TECHNIQUE SHEET
Single Wall T-271.1	Single Wall	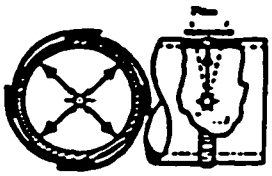 Exposure Arrangement - A		T-276 and Table T-276	Source Side T-277.1(a)	MATERIAL SECTION Type: Steel ☒ other ☐
						Thickness Range: 9.5mm
					Film Side T-277.1(b)	Reinforcement: NONE
						Surface Condition: IN-SERVICE CORROSION PITTING
Single Wall T-271.1	Single Wall	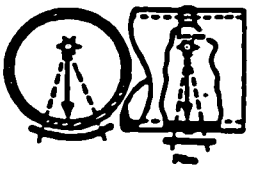 Exposure Arrangement - B		T-276 and Table T-276	Source Side T-277.1(a)	SOURCE SECTION Type: Ir 192 ☐ Co 60 ☐
						KV 160 MaMin 3mA/5min CuMin
					Film Side T-277.1(b)	MIN. SOD 750mm Max. source side of object to film dist. 9.5mm
						Geom. Unsharpness 0.063mm Focal spot size 5mm Source size 2x3mm
Single Wall T-271.1	Single Wall	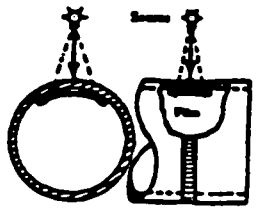 Exposure Arrangement - C		T-276 and Table T-276	Source Side T-277.1(a)	FILM SECTION Make: KODAK
						Type: AA Size: 4½ x 17
						Loading: Single ☒ Double ☐
					Film Side T-277.1(b)	Screens Used: REAR ONLY Thickness: 0.010 Pb
						Processing: Auto ☐ Manual ☒
Double Wall T-271.2(c) at least 3 Exposures 120 deg. to Each Other for Complete Coverage	Single Wall	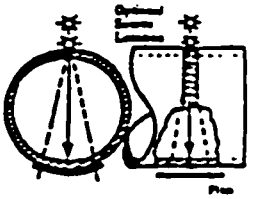 Exposure Arrangement - D		T-276 and Table T-276	Source Side T-277.1(a)	IQI SECTION Sensitivity Req'd: NONE REQUIRED INFORMATION ONLY
						IQI Type N/A Size(s) N/A
					Film Side T-277.1(b)	IQI Placement: Source Side ☐ Film Side ☐ N/A
						DENSITY SECTION VARYING DENSITIES FOR COMPARISON. Minimum Maximum
Double Wall T-271.2(c) at least 3 Exposures 120 deg. to Each Other for Complete Coverage	Single Wall	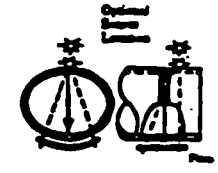 Exposure Arrangement - E		T-276 and Table T-276	Source Side T-277.1(a)	EXPOSURE ARRANGEMENT Indicate A-F or Make a Sketch
					Film Side T-277.1(b)	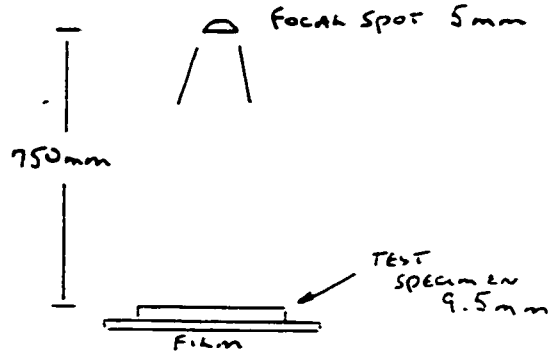
Double Wall T-271.2 (c)(1) at least 2 Exposures at 90 deg. to Each Other for Complete Coverage	Double Wall (Ellipse) Read Offset Source Side and Film Side Images	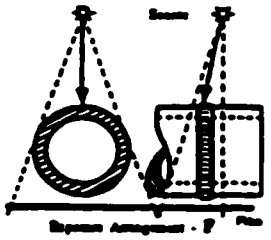 Exposure Arrangement - F		T-276 and Table T-276	Source Side T-277.1(b)	
						Personnel Certification CSGB II ASNT II Signature

Figure 3.9 Radiographic Technique Sheet from Steel Inspection Services

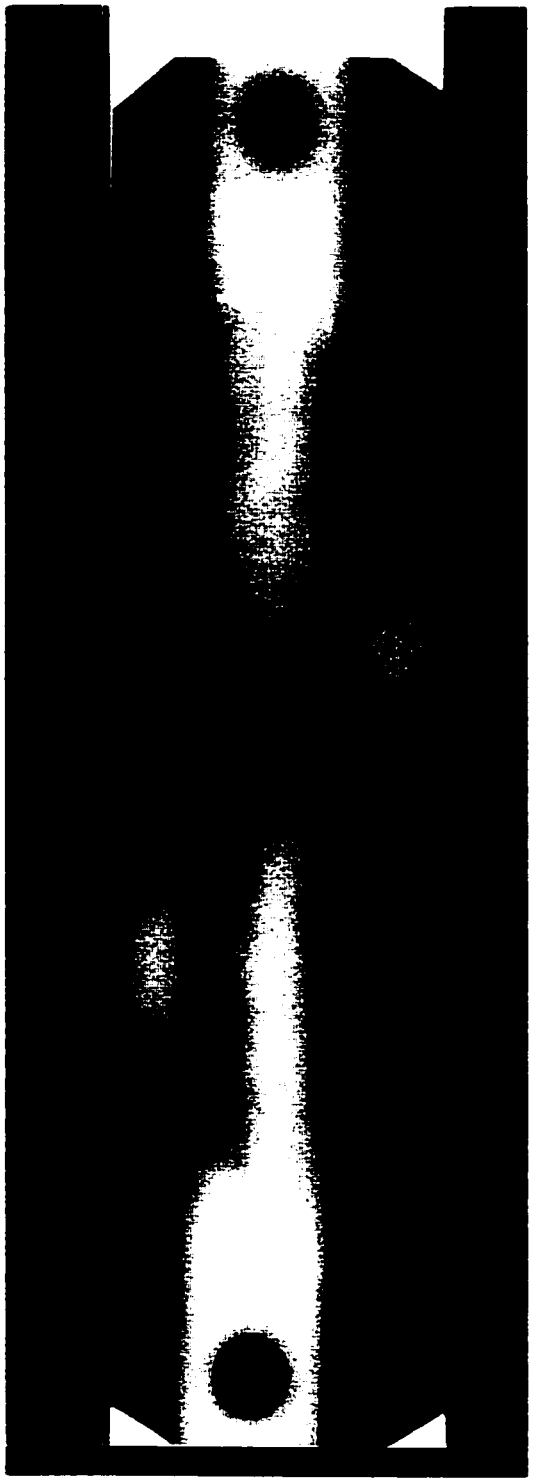

Figure 3.10 Specimen #1 - Digitized X-Ray Image

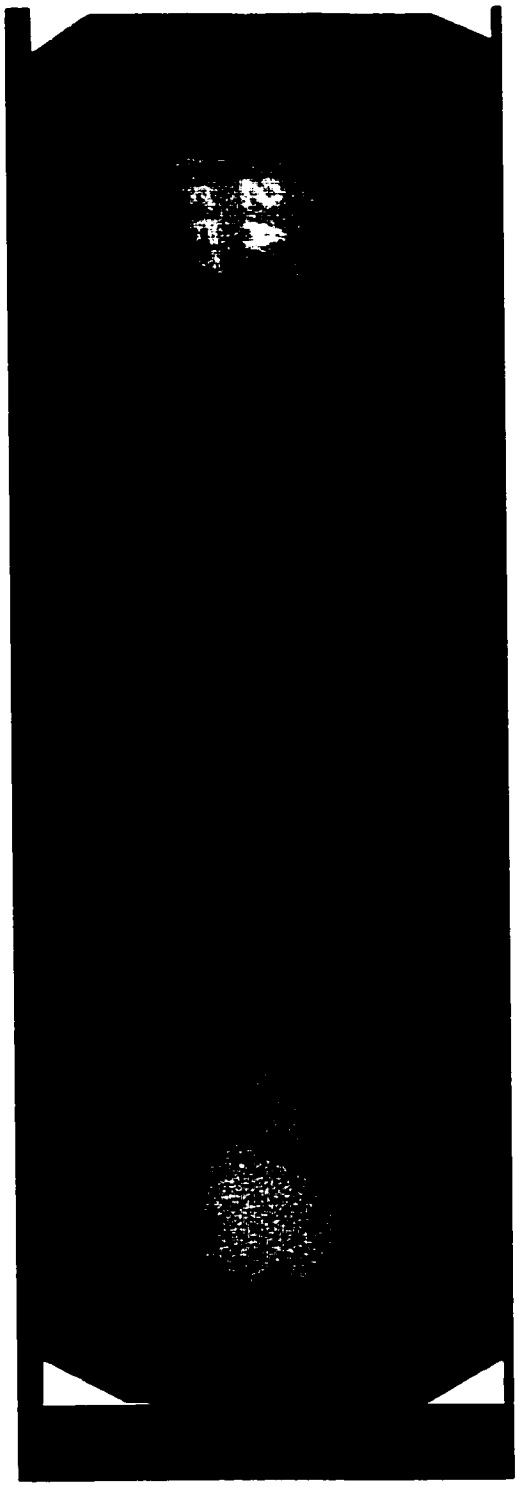

Figure 3.11 Specimen #2 - Digitized X-Ray Image

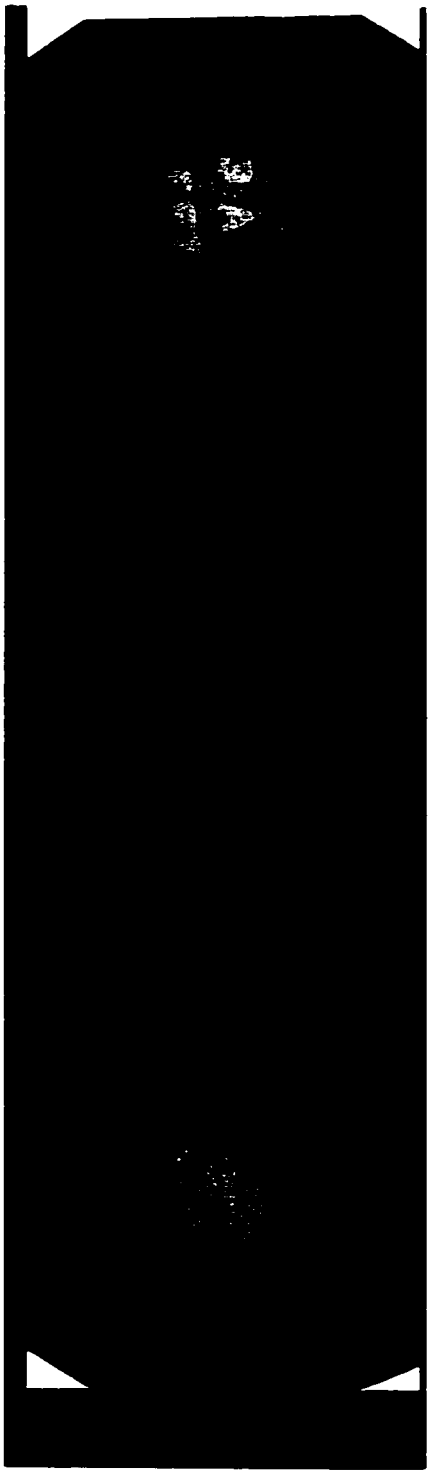

Figure 3.12 Specimen #3 - Digitized X-Ray Image

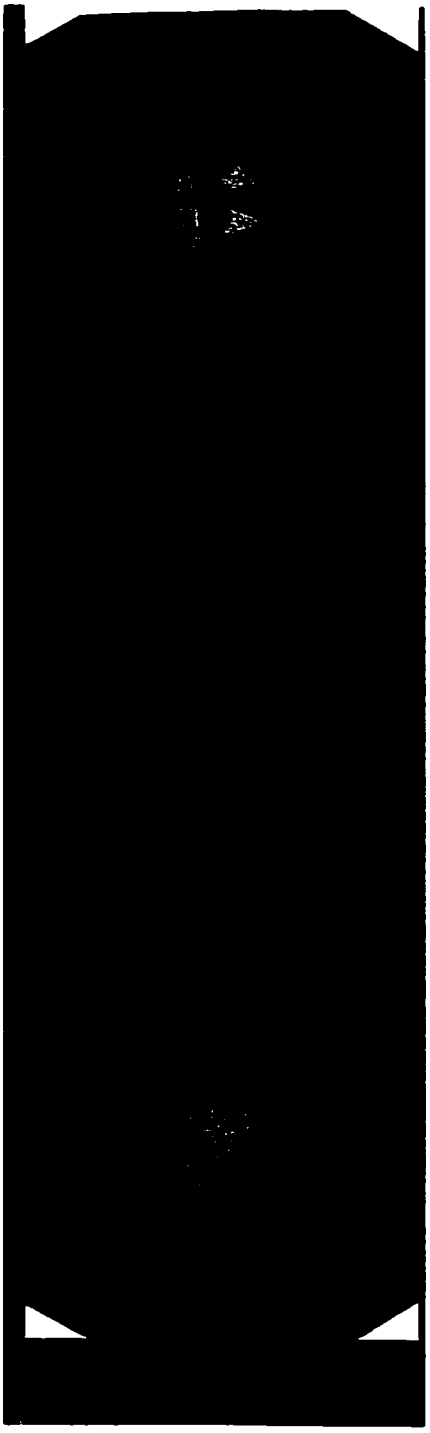

Figure 3.13 Specimen #4 -Digitized X-Ray Image

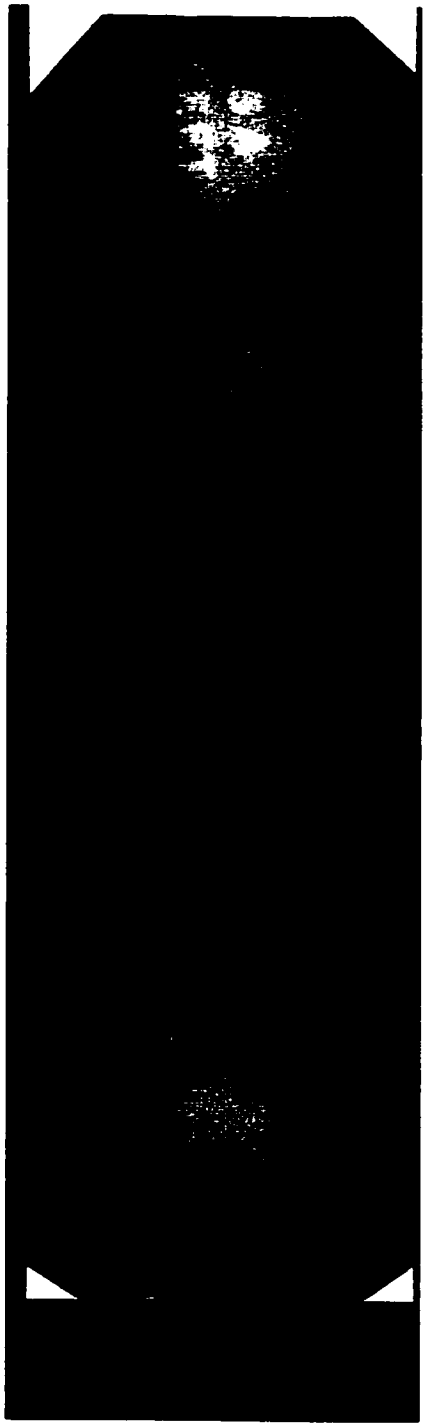

Figure 3.14 Specimen #5 - Digitized X-Ray Image

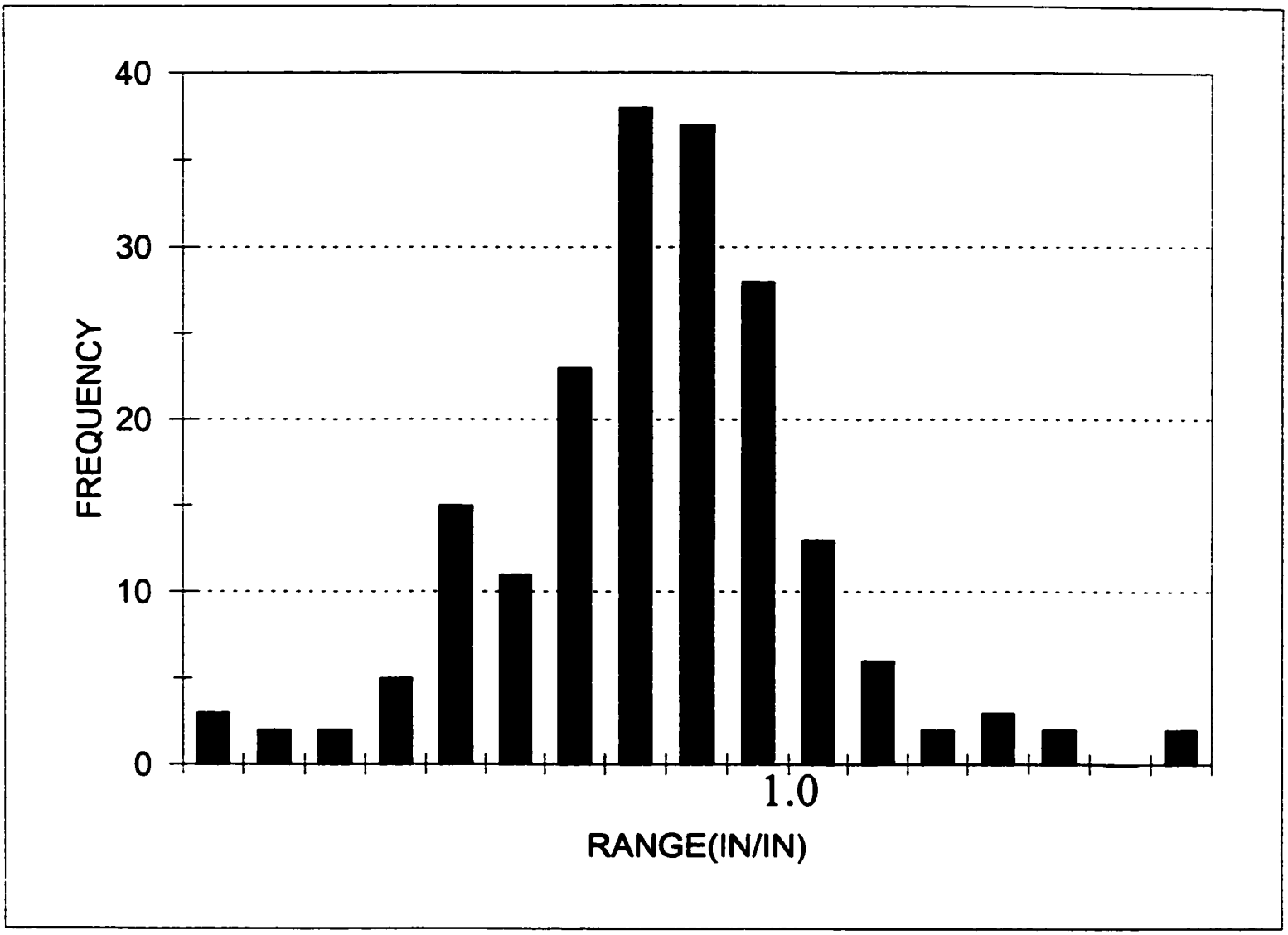

Figure 3.15 Specimen 1 - Ball Attachment Histogram

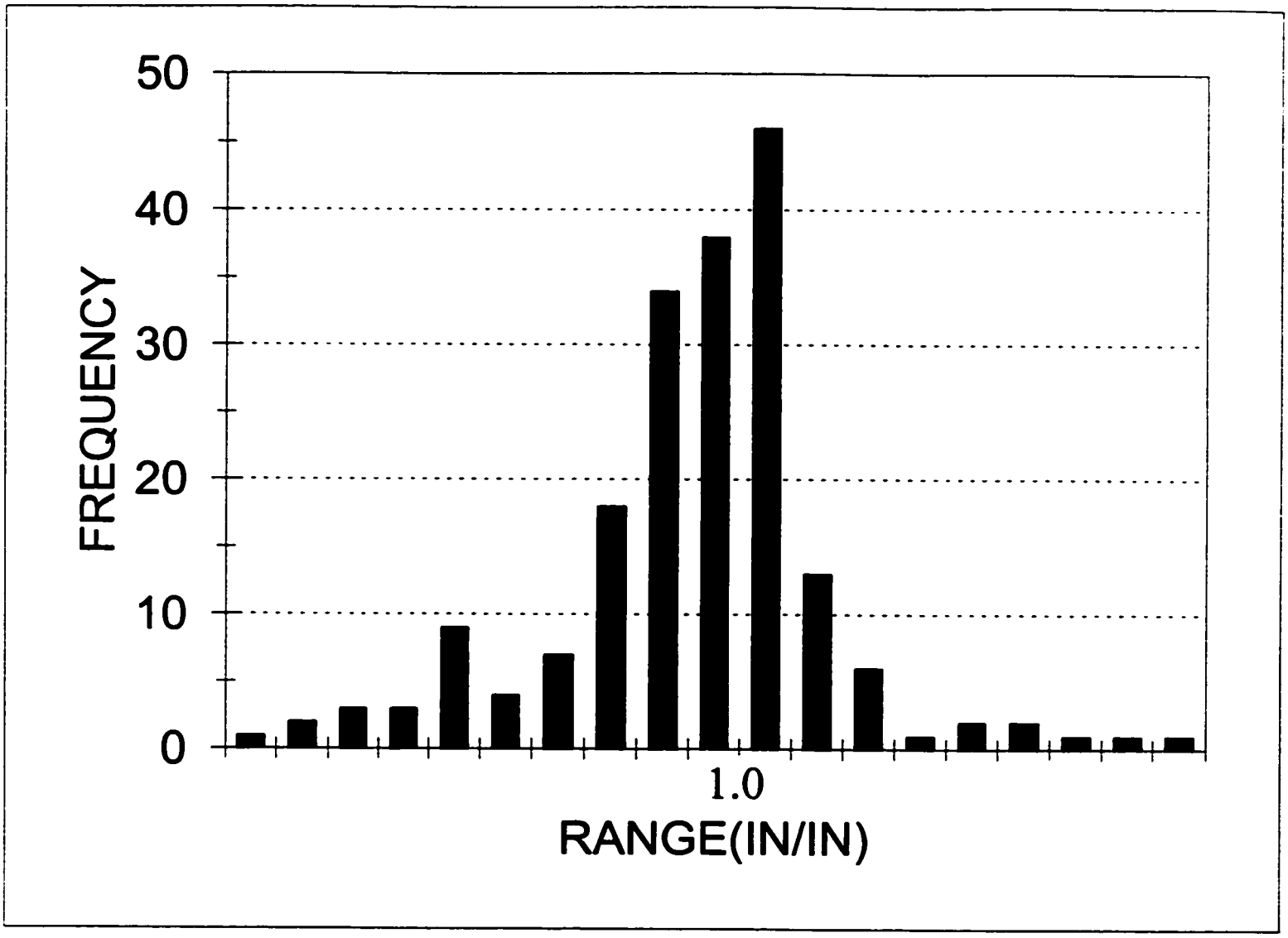

Figure 3.16 Specimen 1 - Spline Attachment Histogram

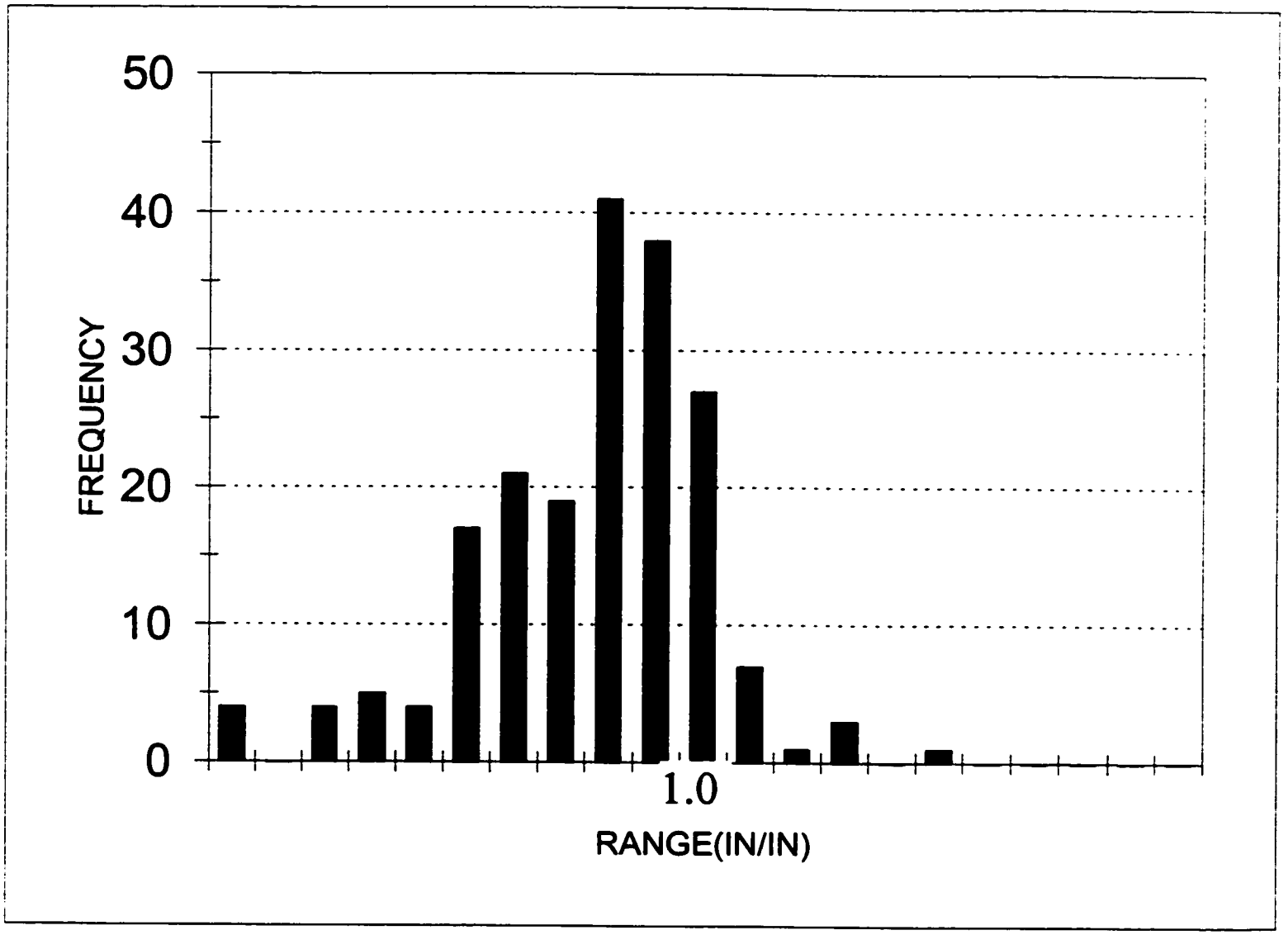

Figure 3.17 Specimen 1 - Comparator Attachment Histogram

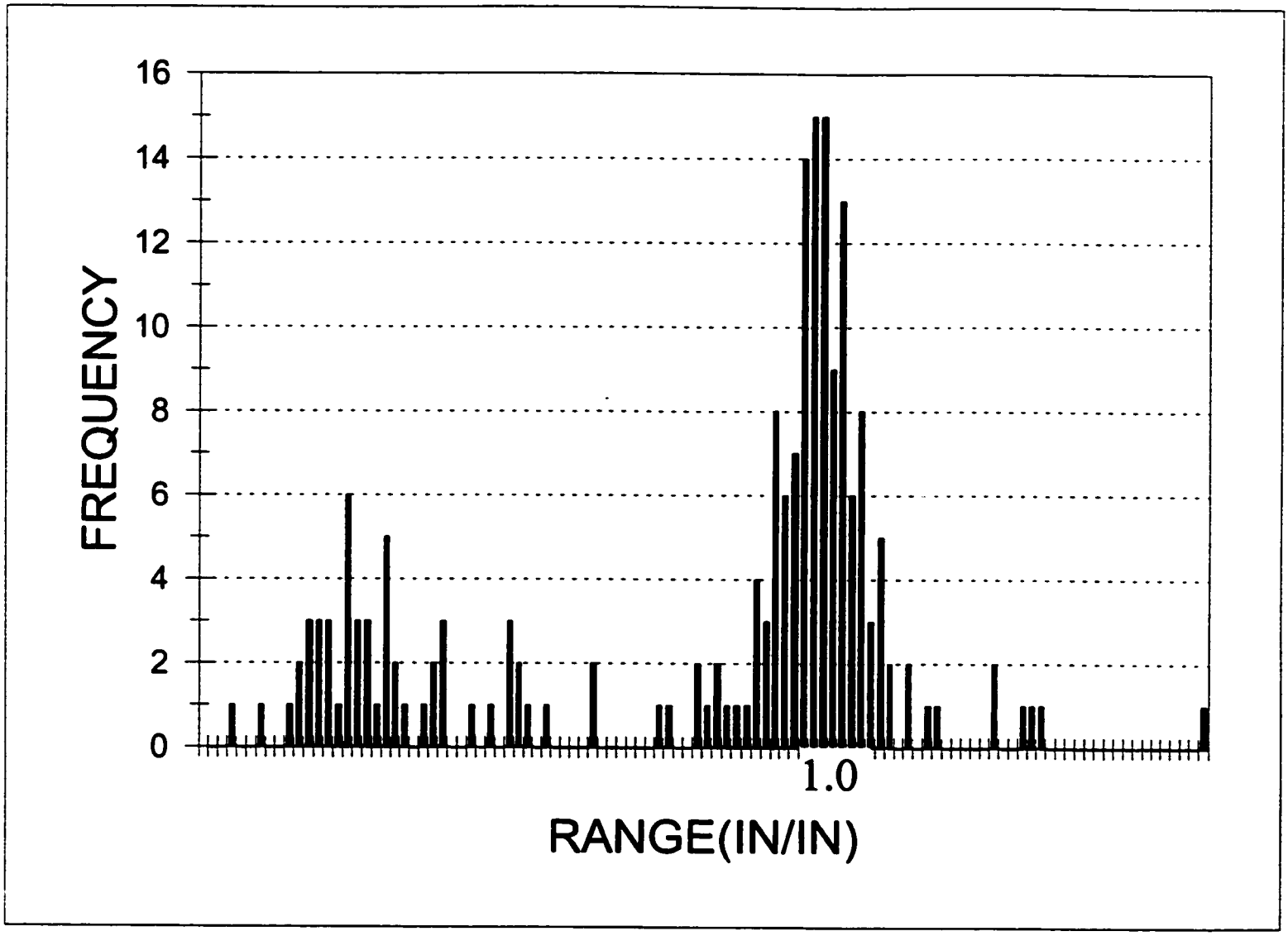

Figure 3.18 Specimen 1 - D-Meter Histogram

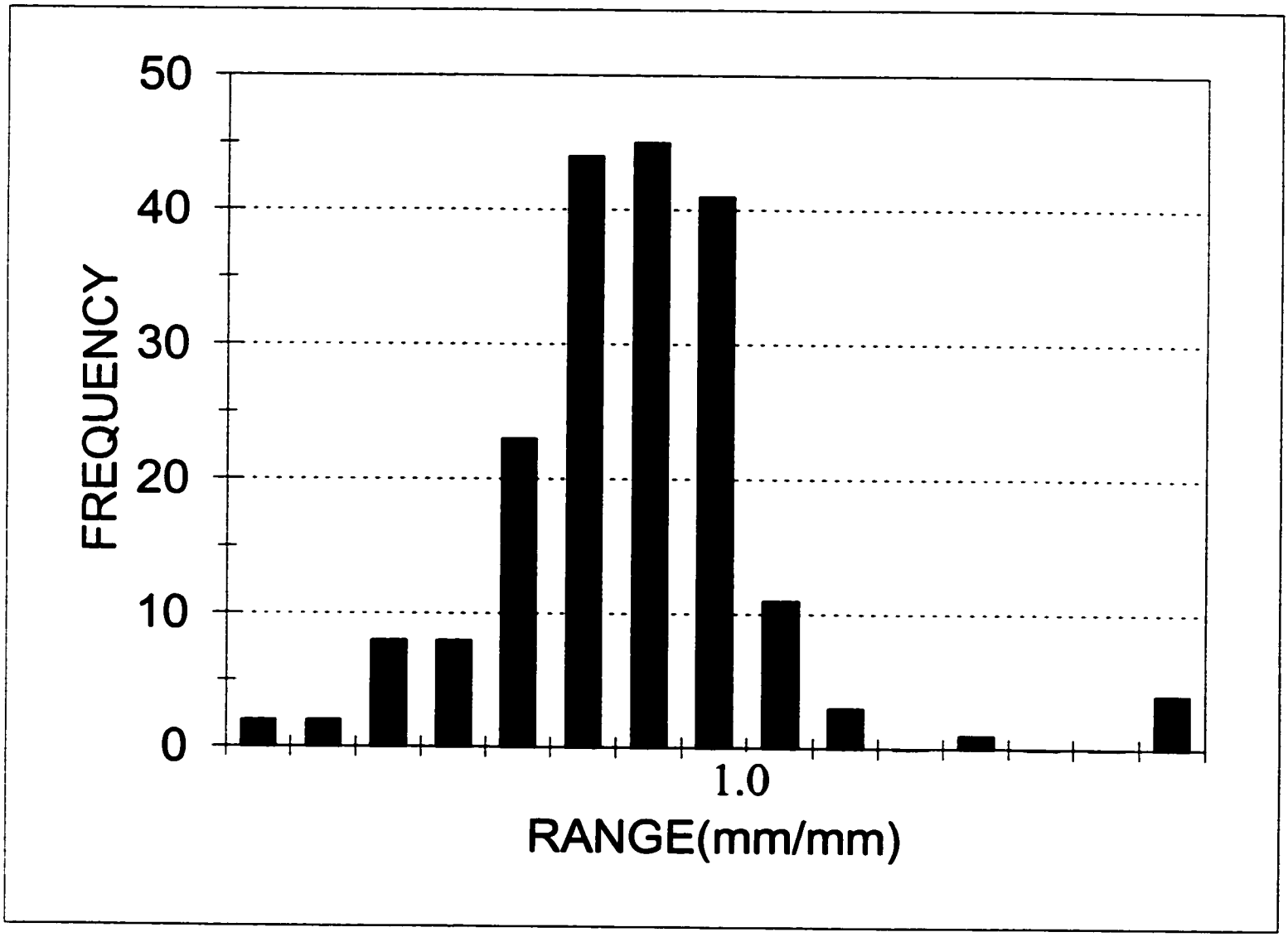

Figure 3.19 Specimen 2 - Ball Attachment Histogram

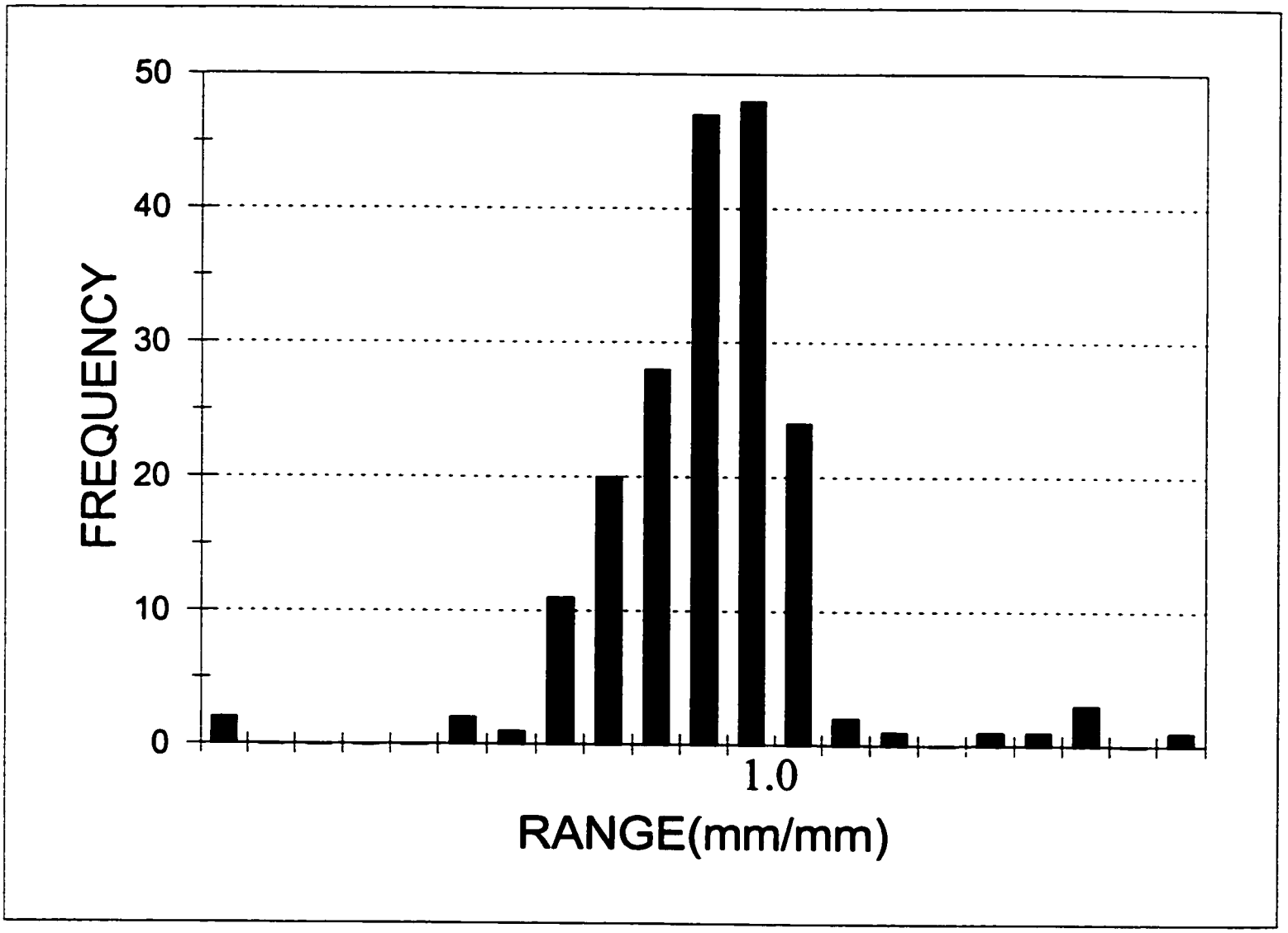

Figure 3.20 Specimen 2 - Spline Attachment Histogram

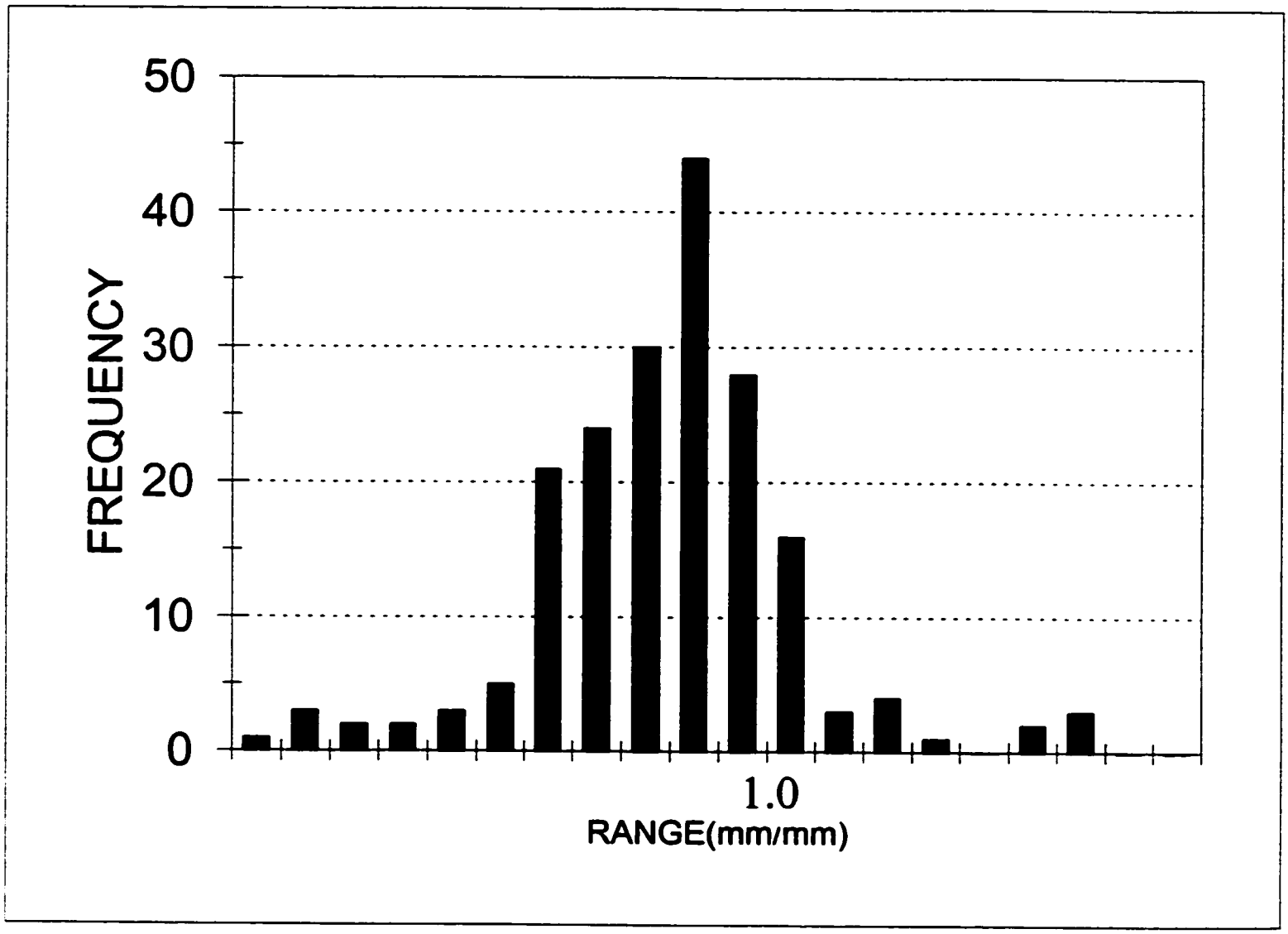

Figure 3.21 Specimen 2 - Comparator Attachment Histogram

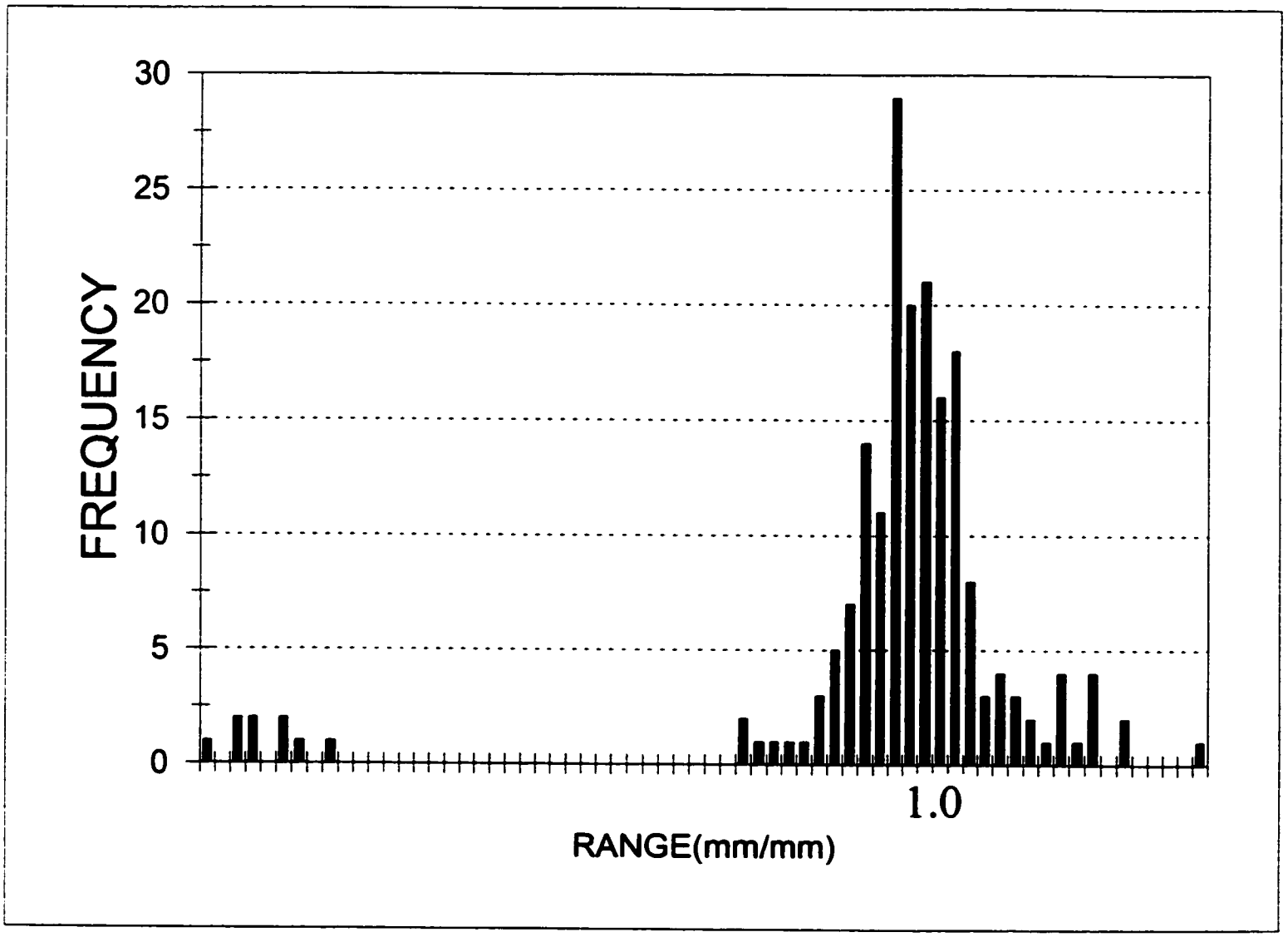

Figure 3.22 Specimen 2 - D-Meter Histogram

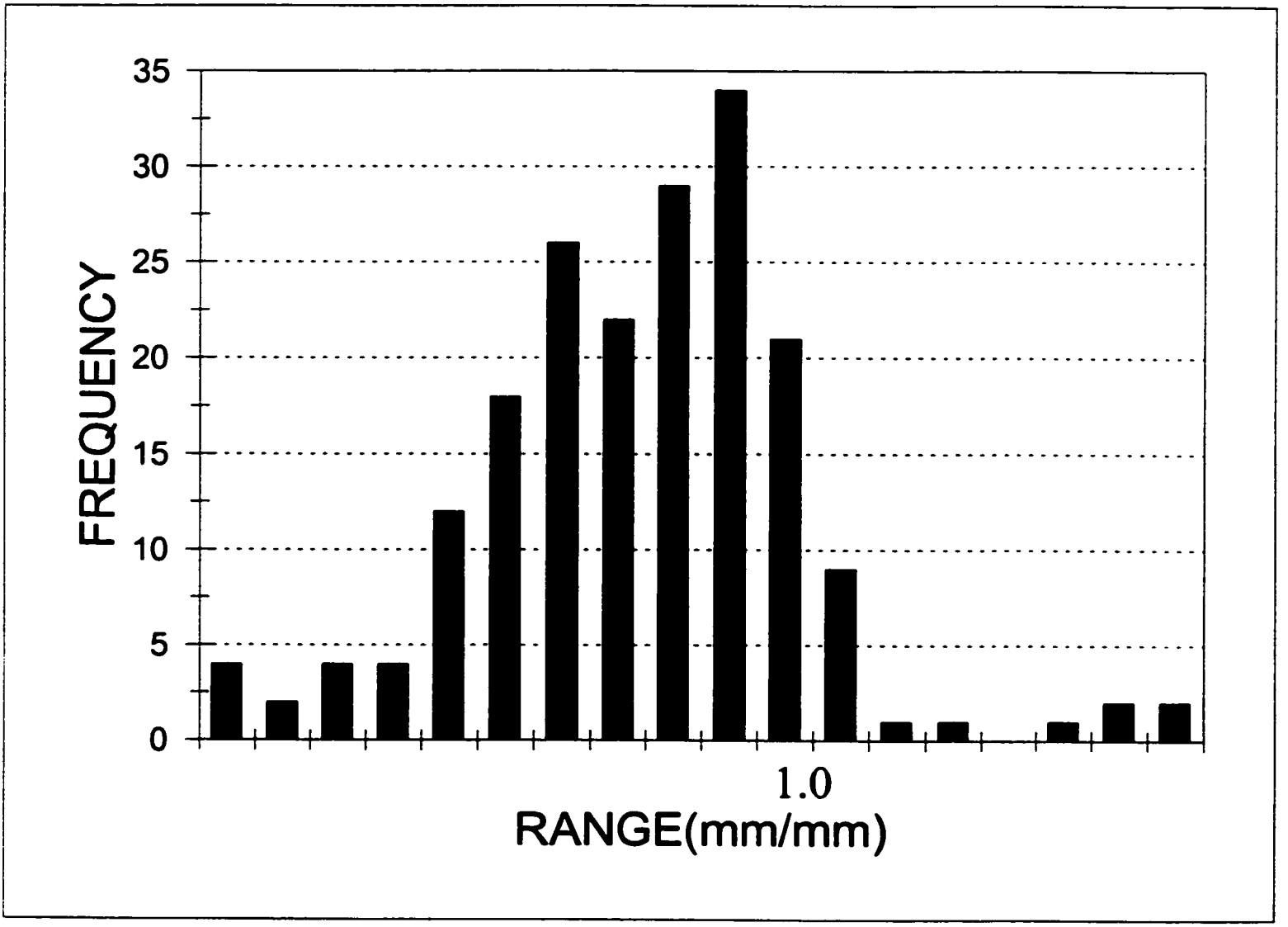

Figure 3.23 Specimen 3 - Ball Attachment Histogram

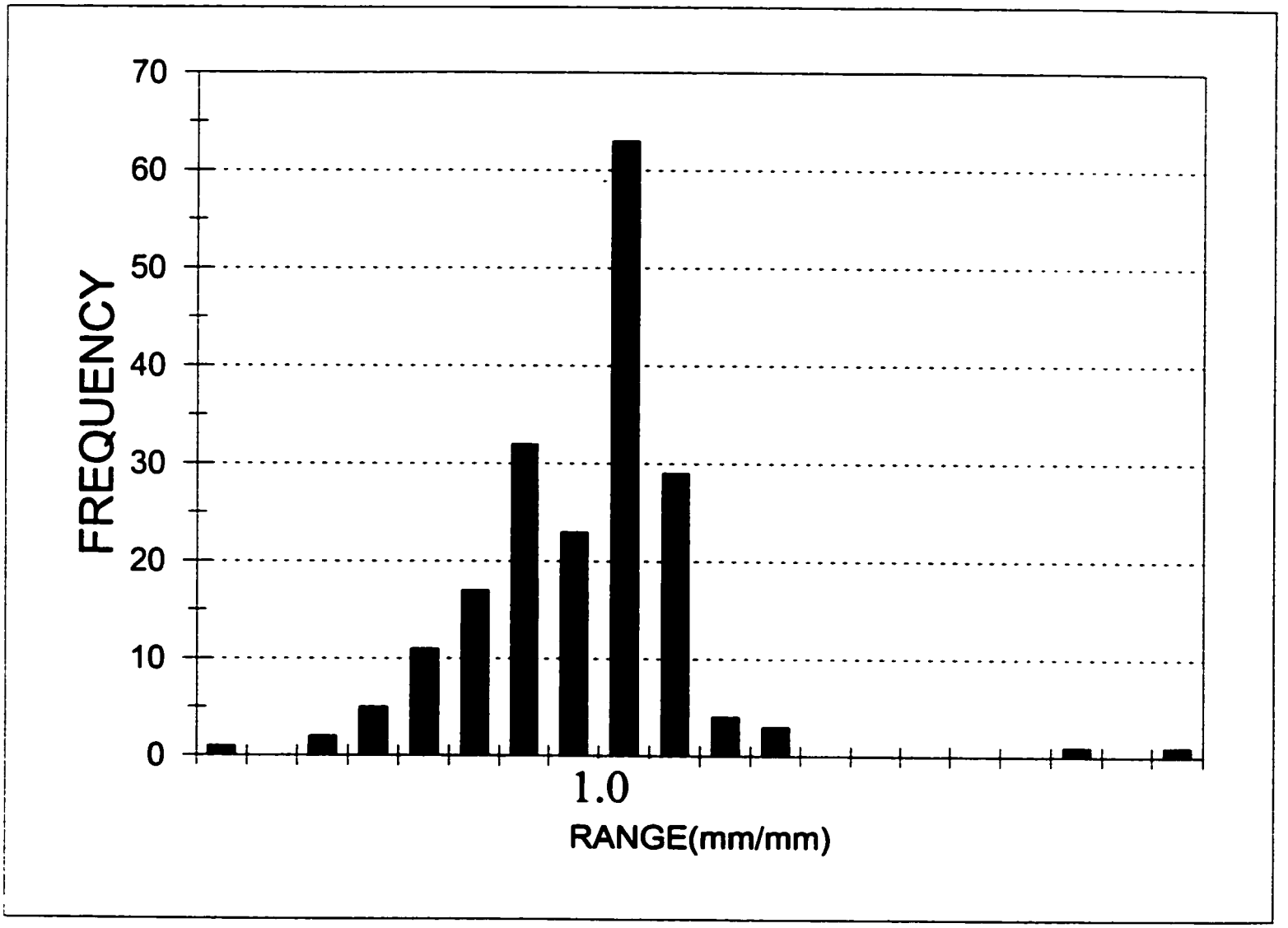

Figure 3.24 Specimen 3 - Spline Attachment Histogram

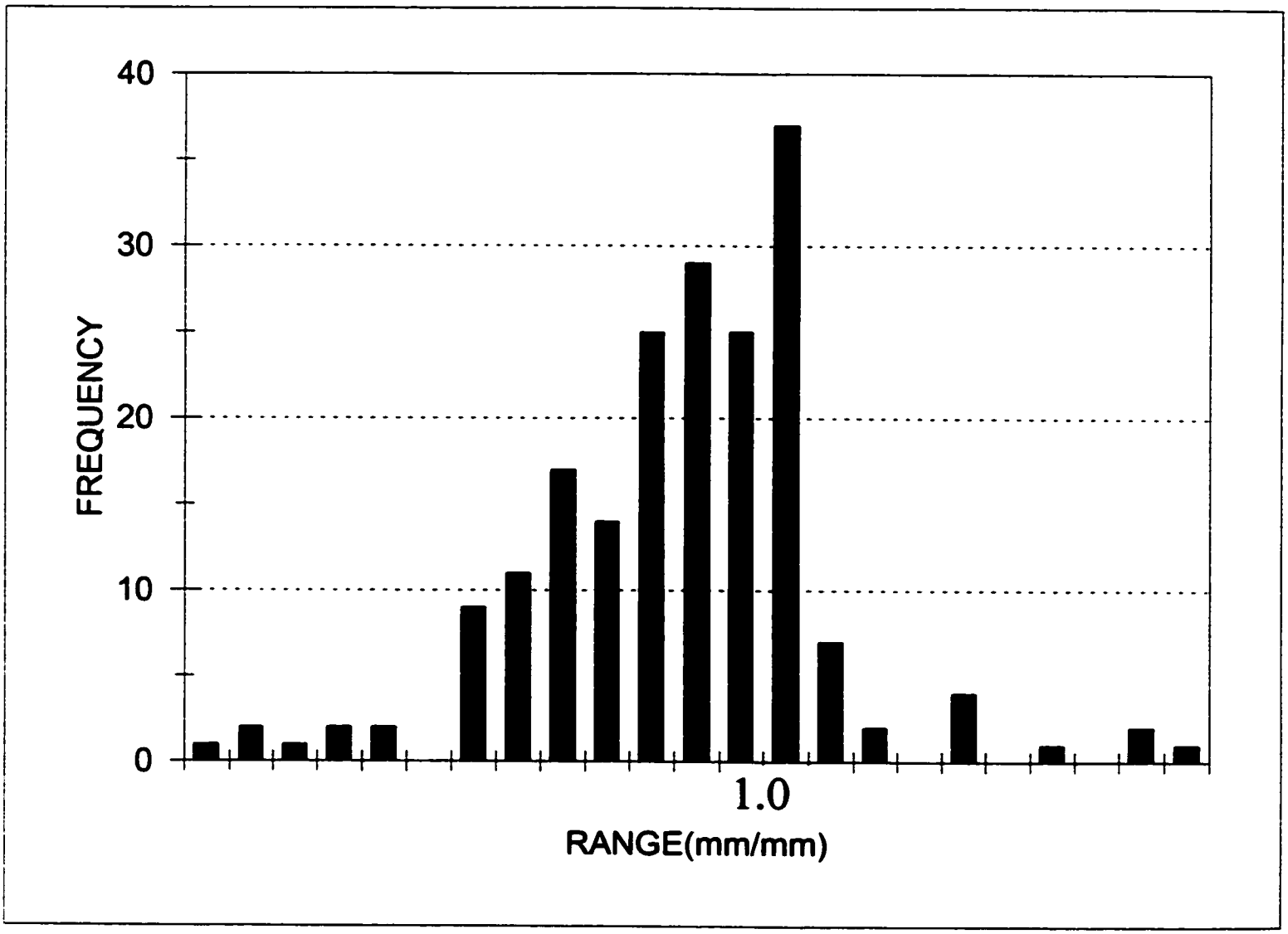

Figure 3.25 Specimen 3 - Comparator Attachment Histogram

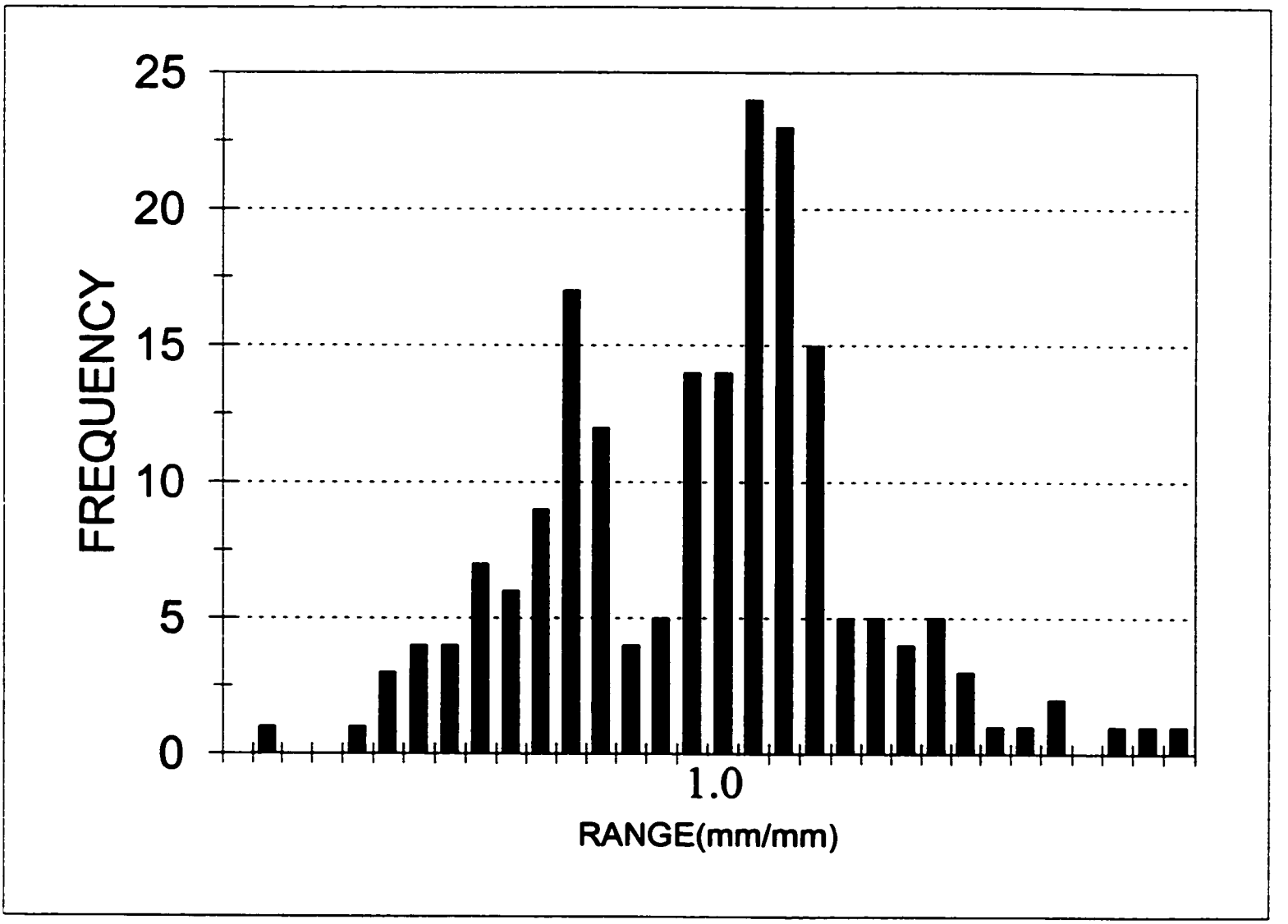

Figure 3.26 Specimen 3 - D-Meter Histogram

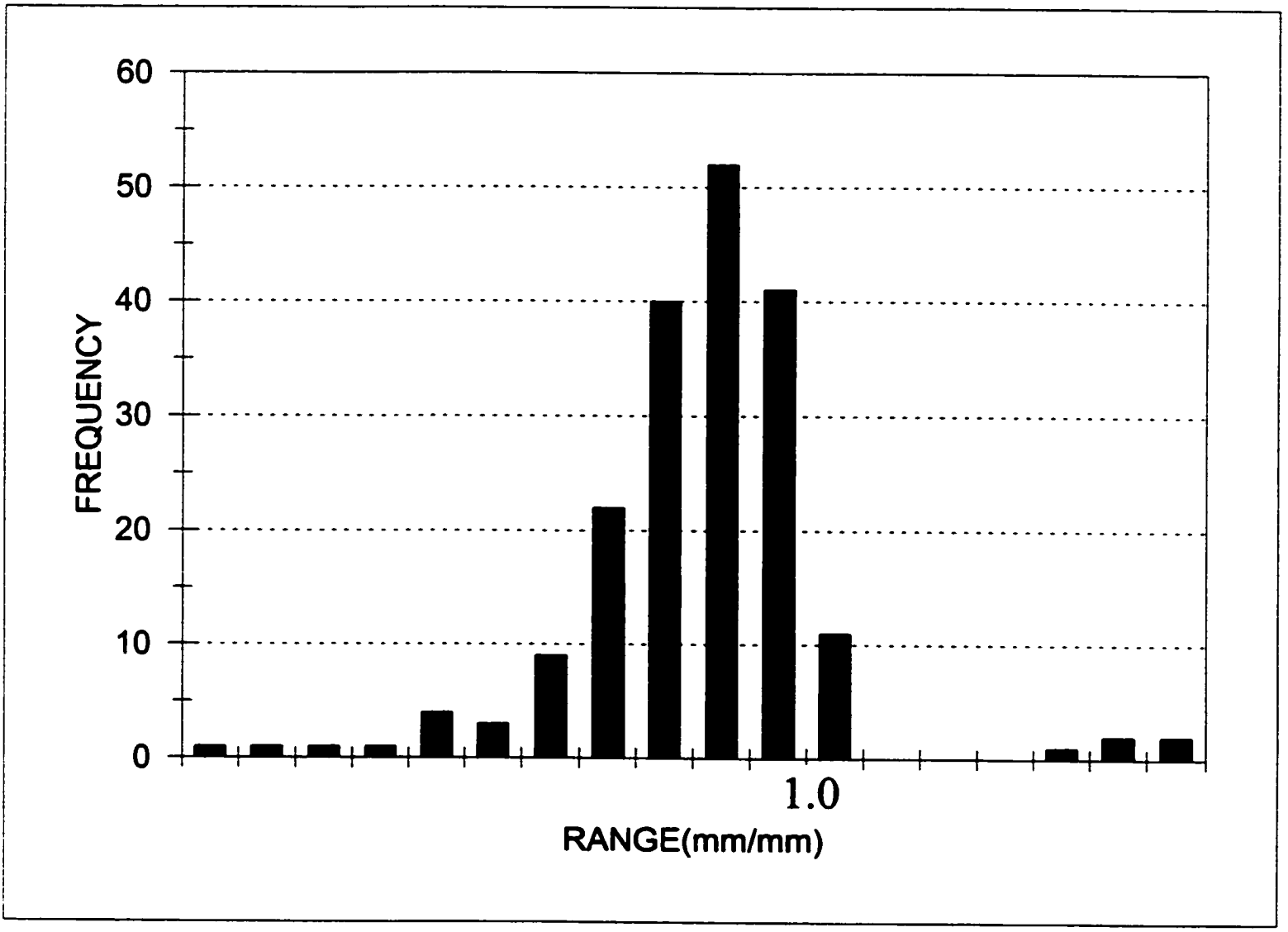

Figure 3.27 Specimen 4 - Ball Attachment Histogram

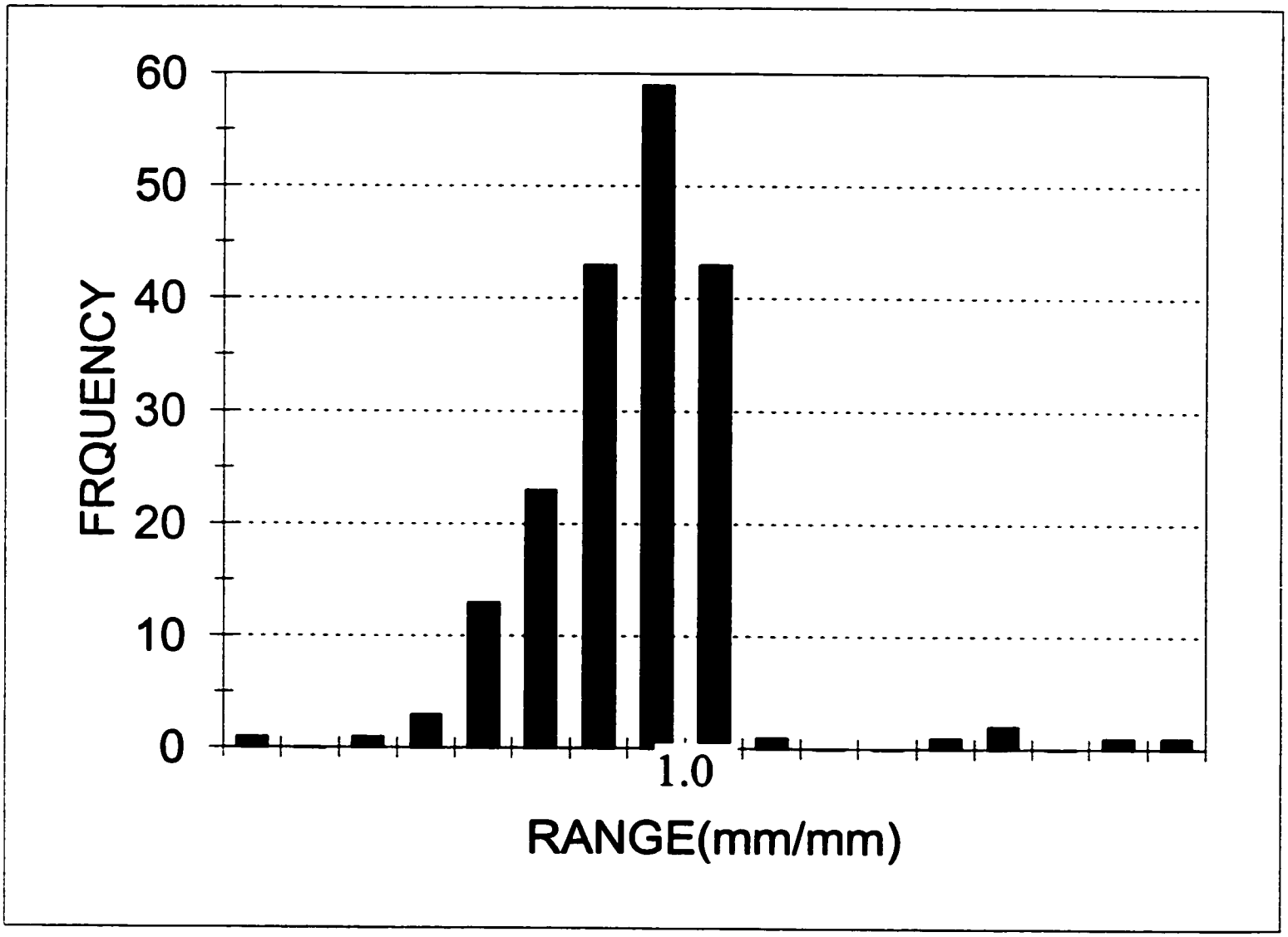

Figure 3.28 Specimen 4 - Spline Attachment Histogram

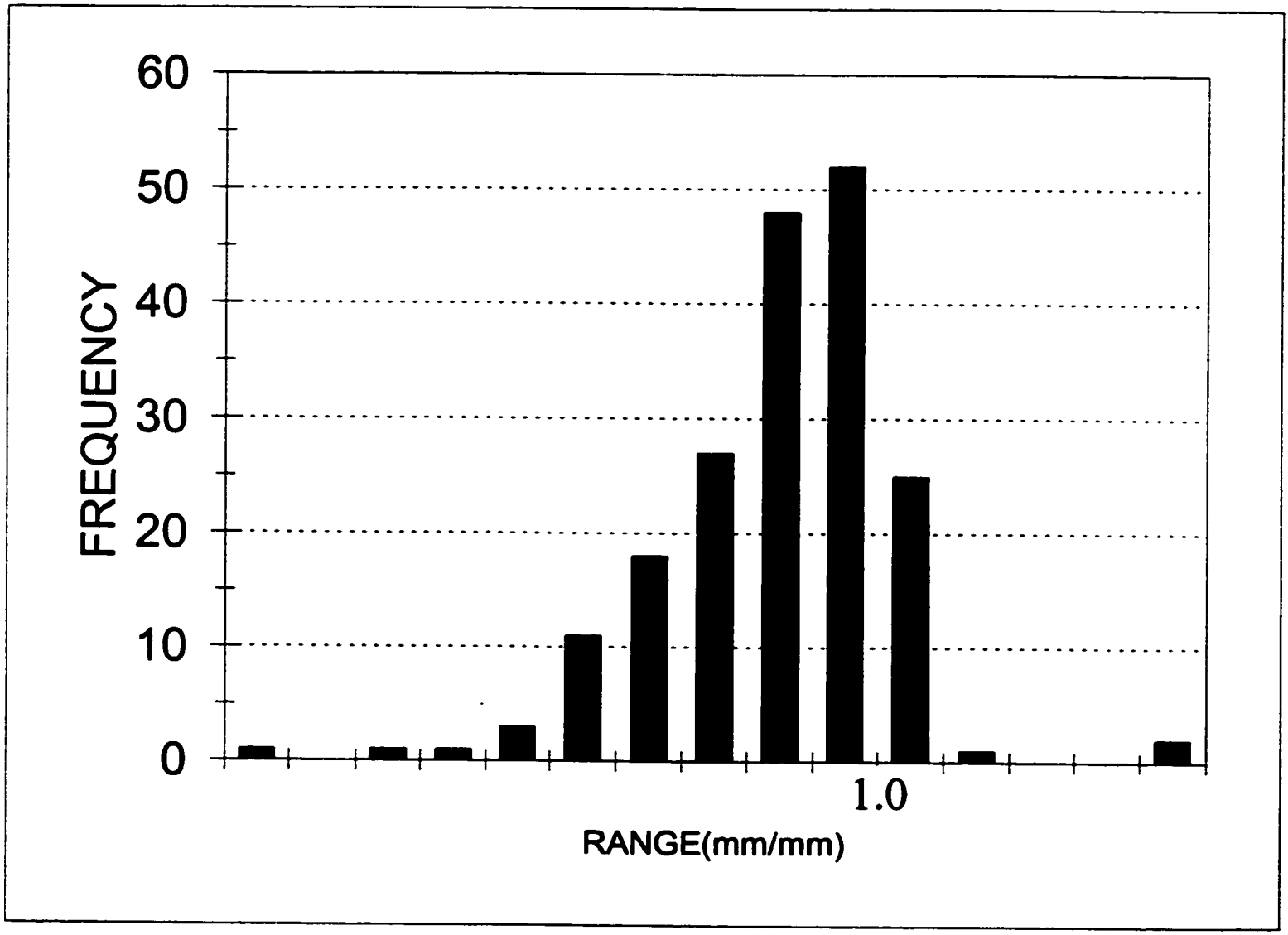

Figure 3.29 Specimen 4 - Comparator Attachment Histogram

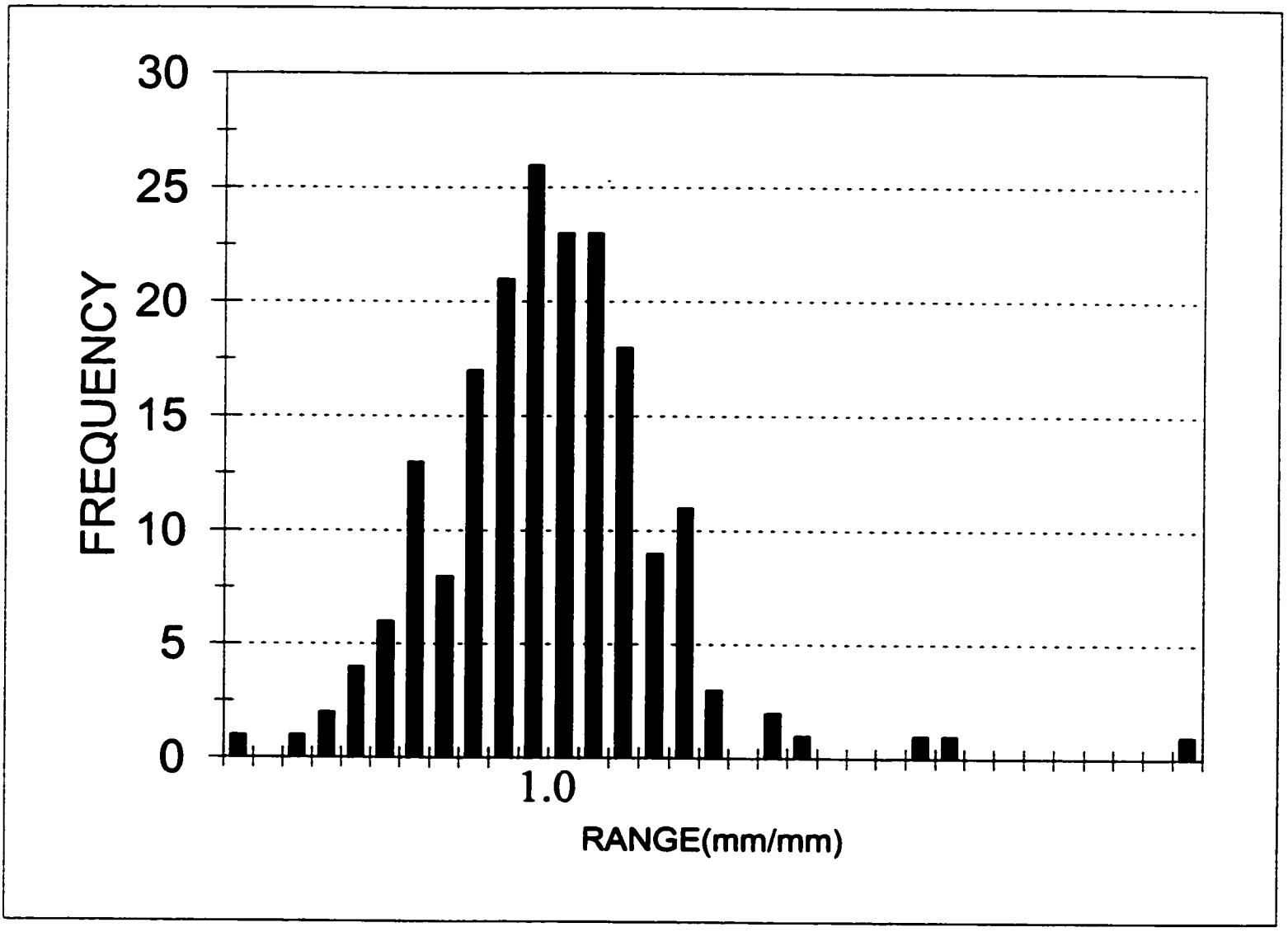

Figure 3.30 Specimen 4 - D-Meter Histogram

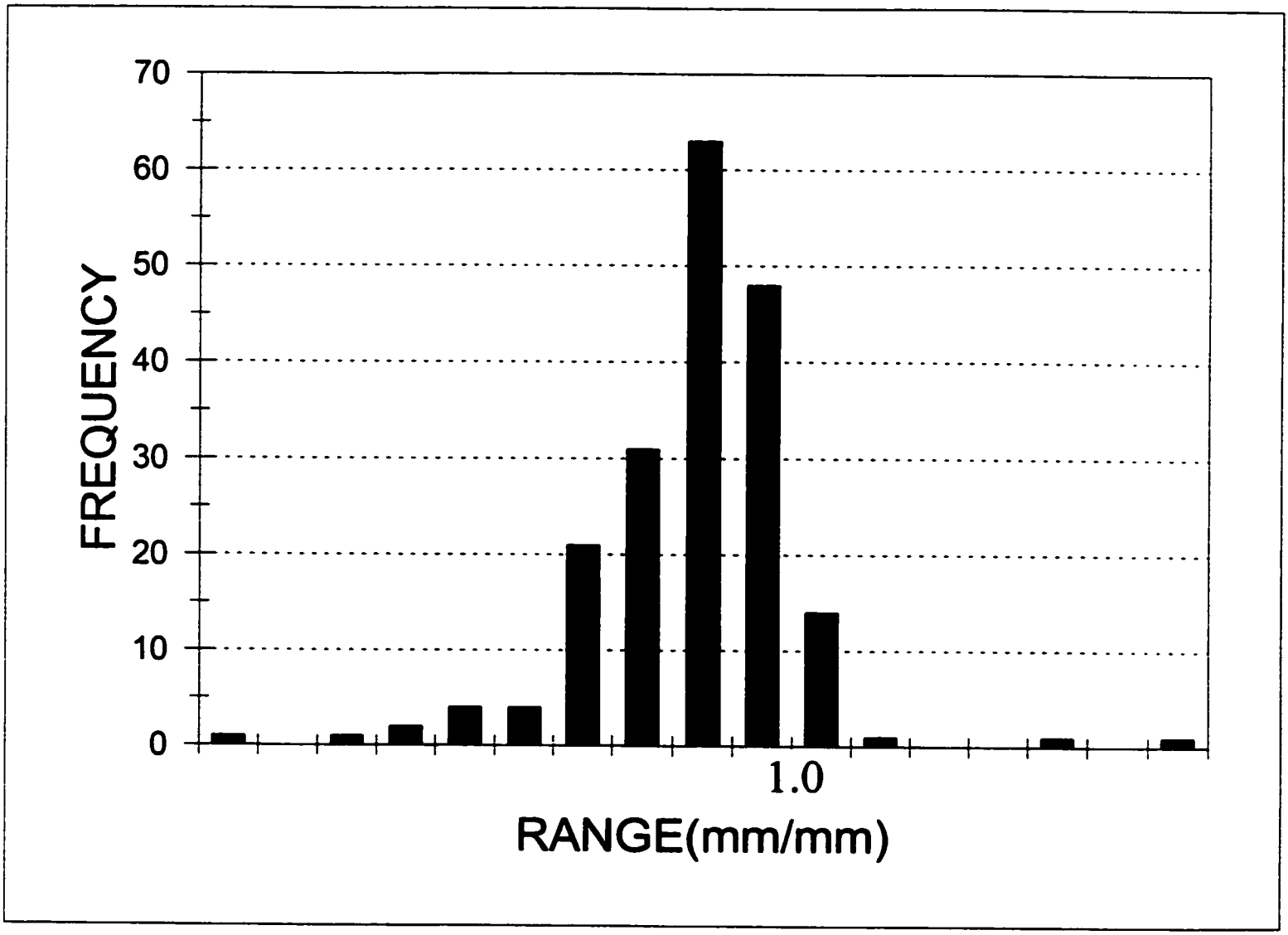

Figure 3.31 Specimen 5 - Ball Attachment Histogram

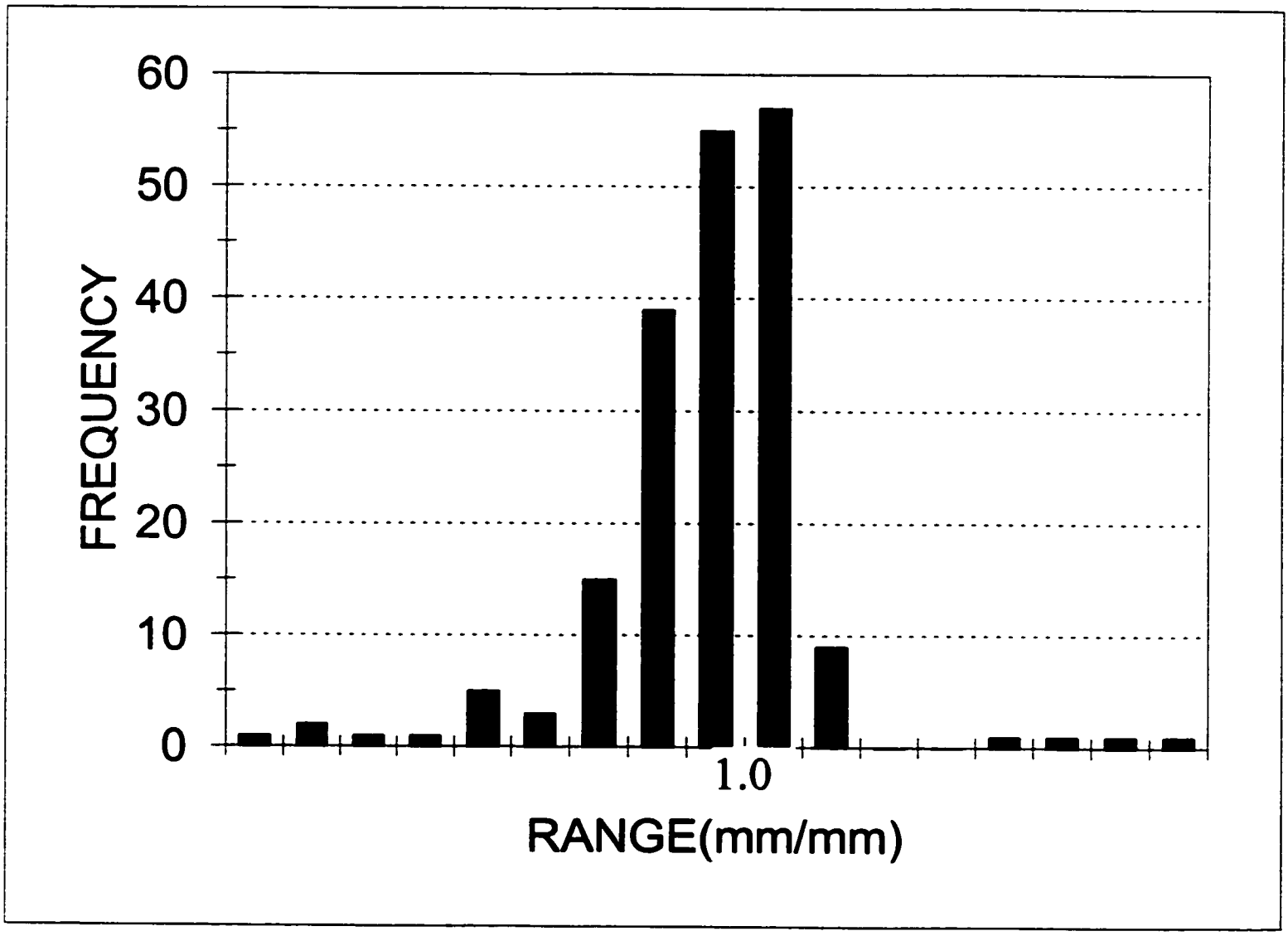

Figure 3.32 Specimen 5 - Spline Attachment Histogram

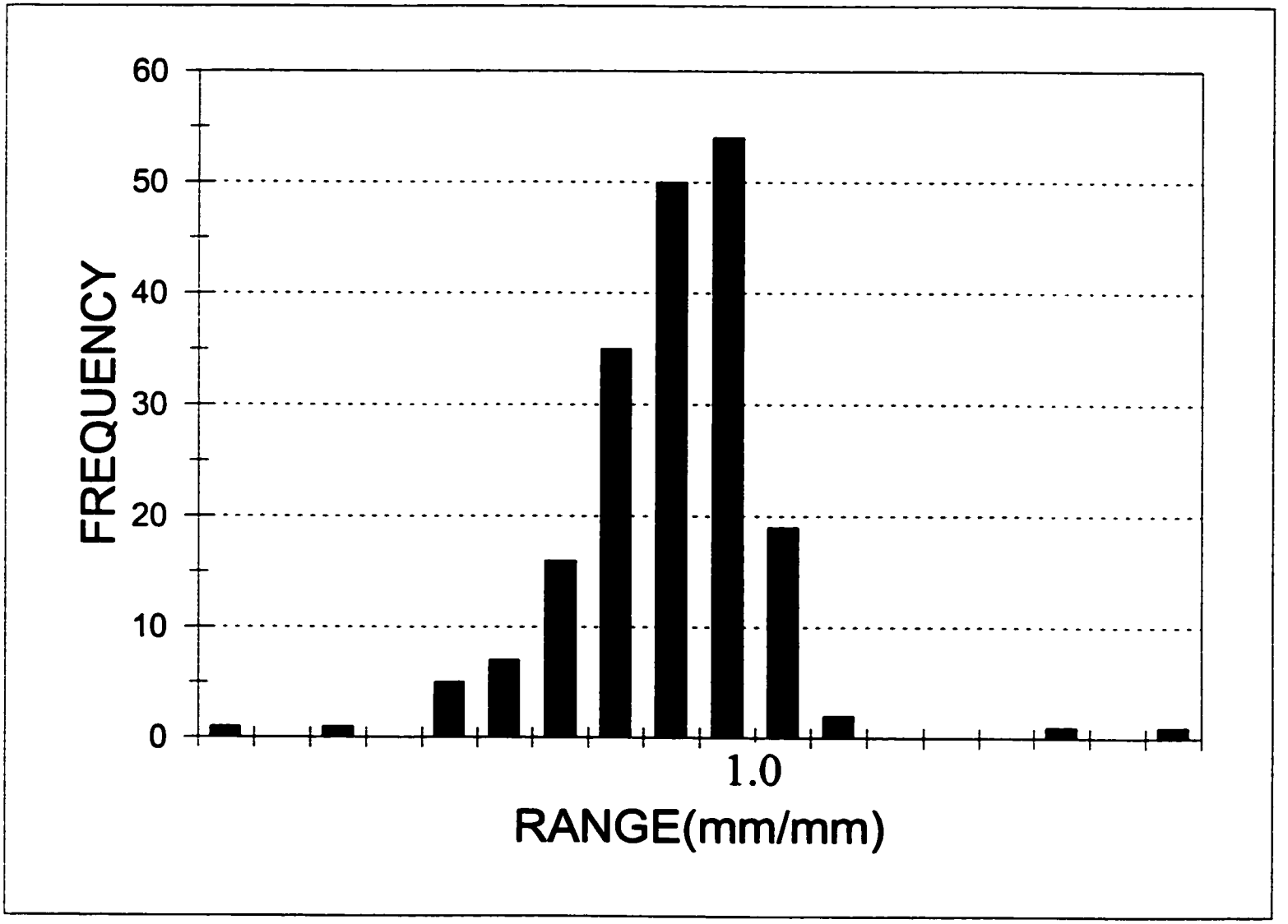

Figure 3.33 Specimen 5 - Comparator Attachment Histogram

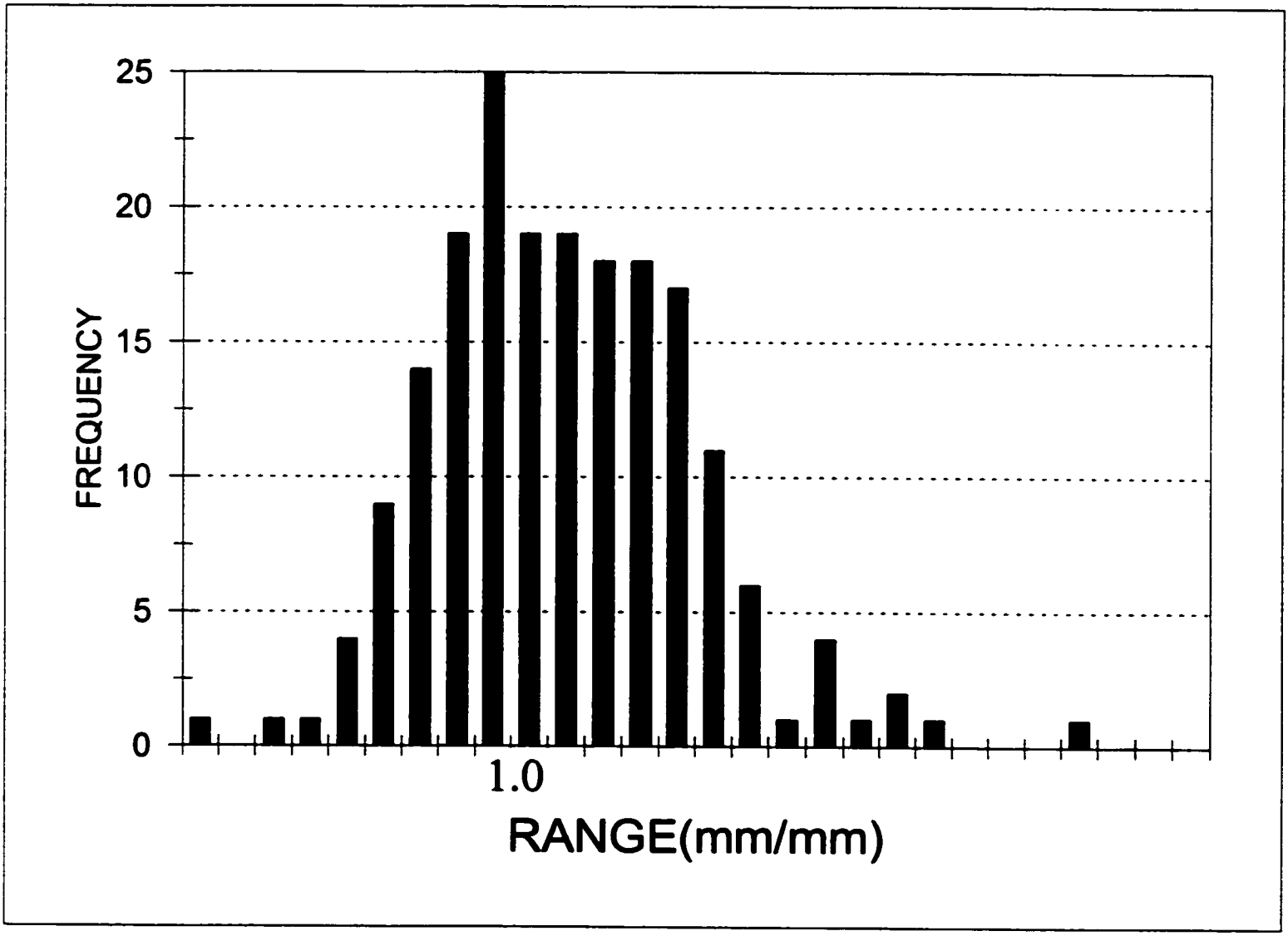

Figure 3.34 Specimen 5 - D-Meter Histogram

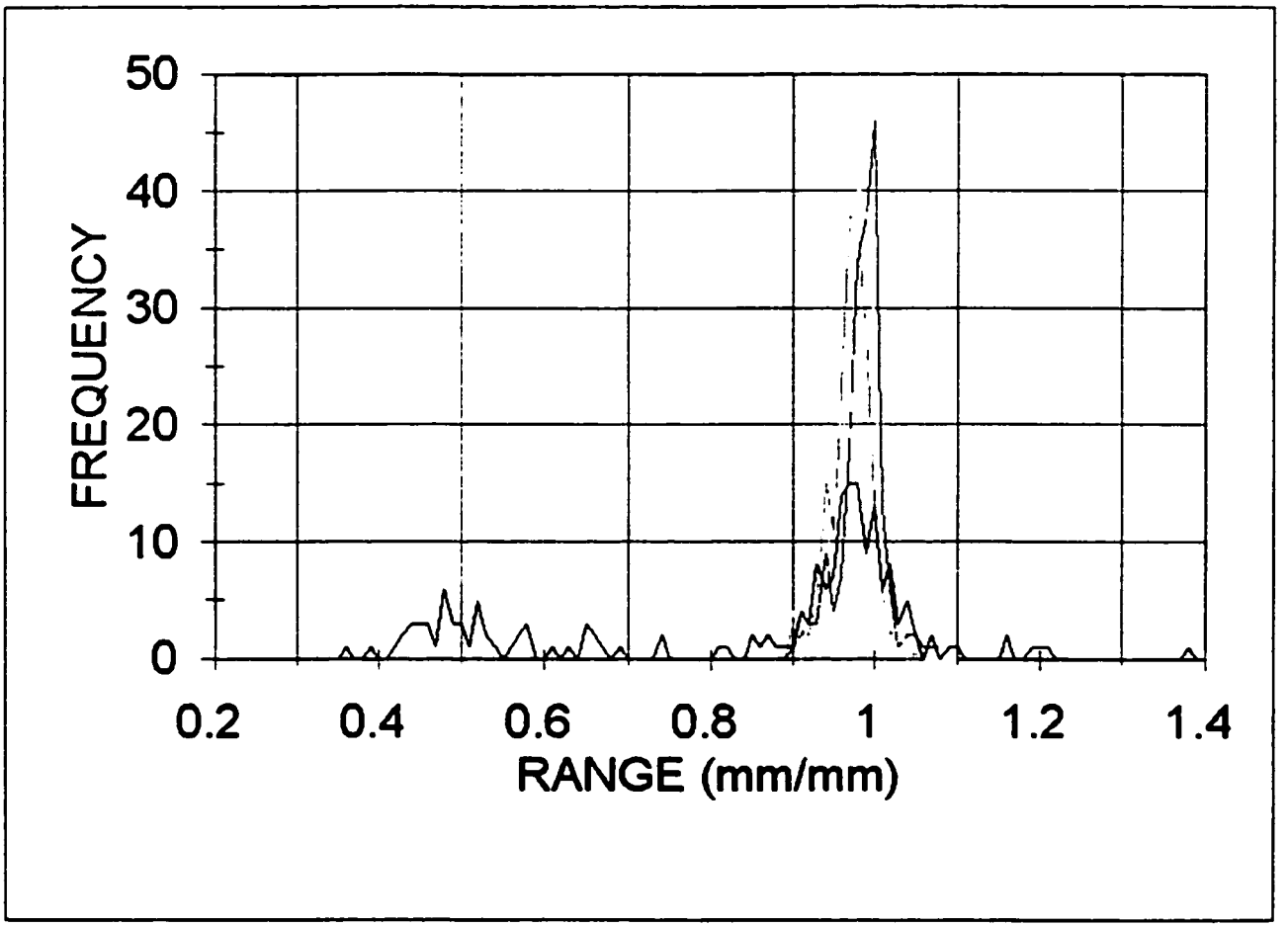

Figure 3.35 Specimen 1 - Summary of Normalized Results

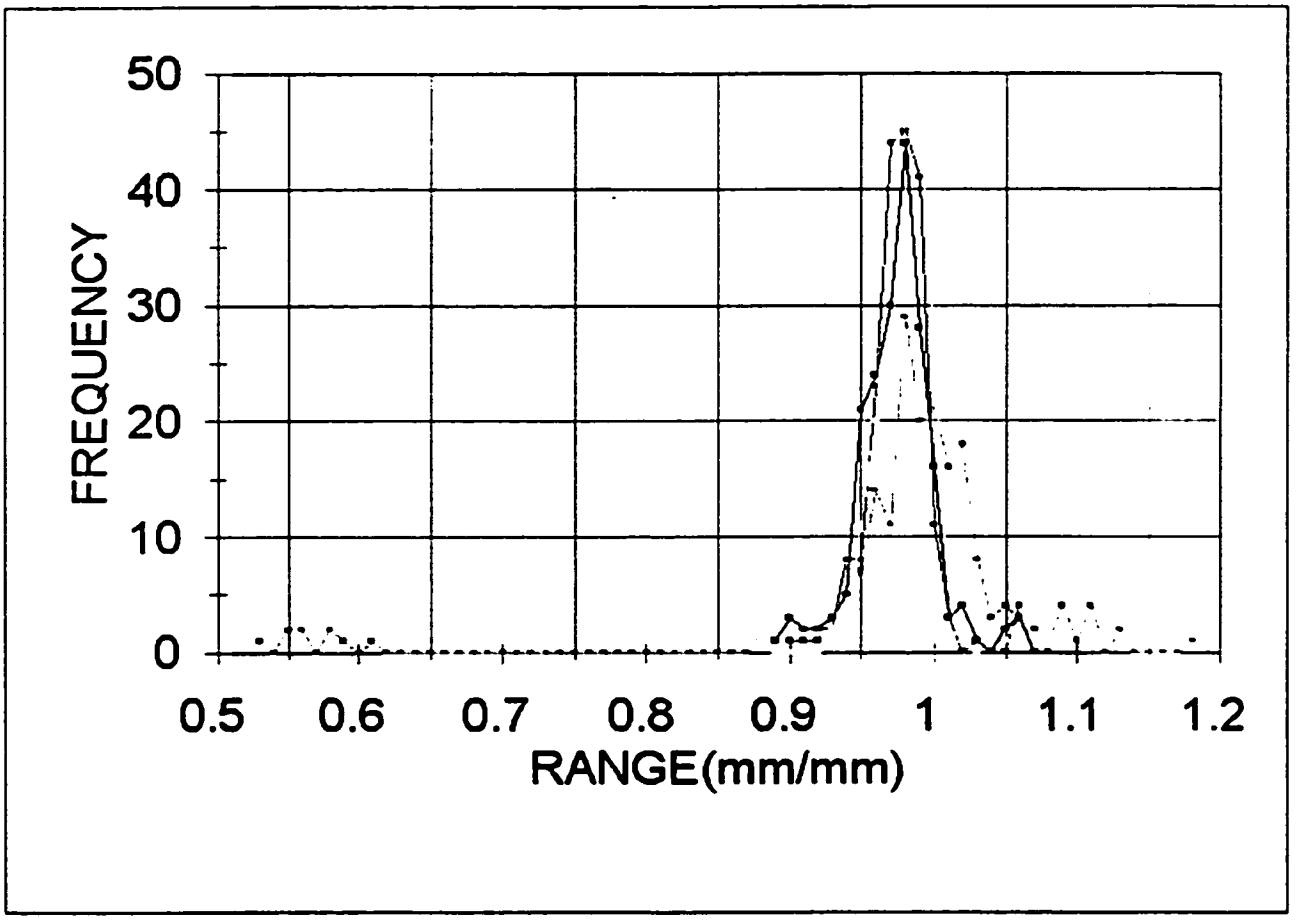

Figure 3.36 Specimen 2 - Summary of Normalized Results

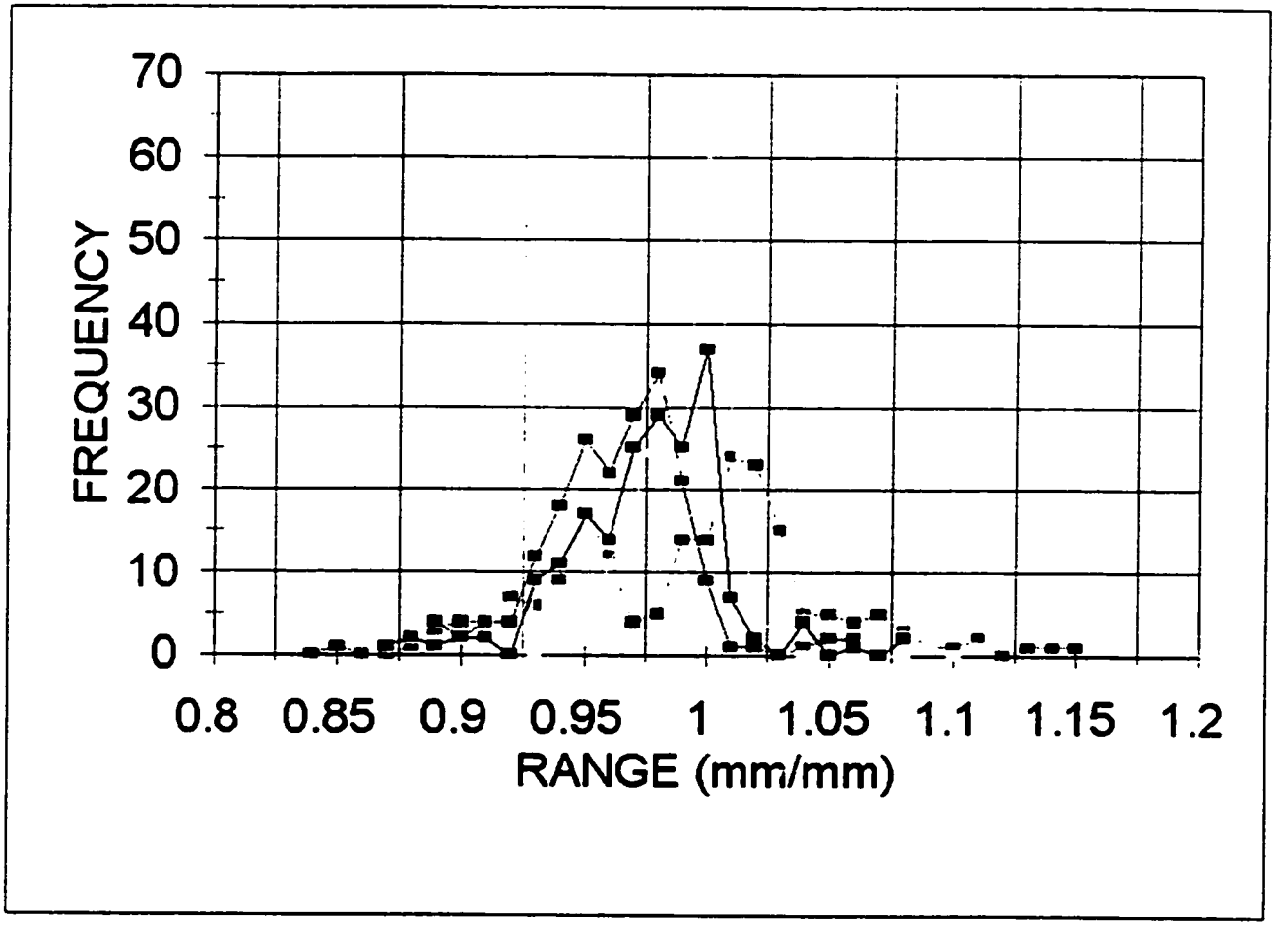

Figure 3.37 Specimen 3 - Summary of Normalized Results

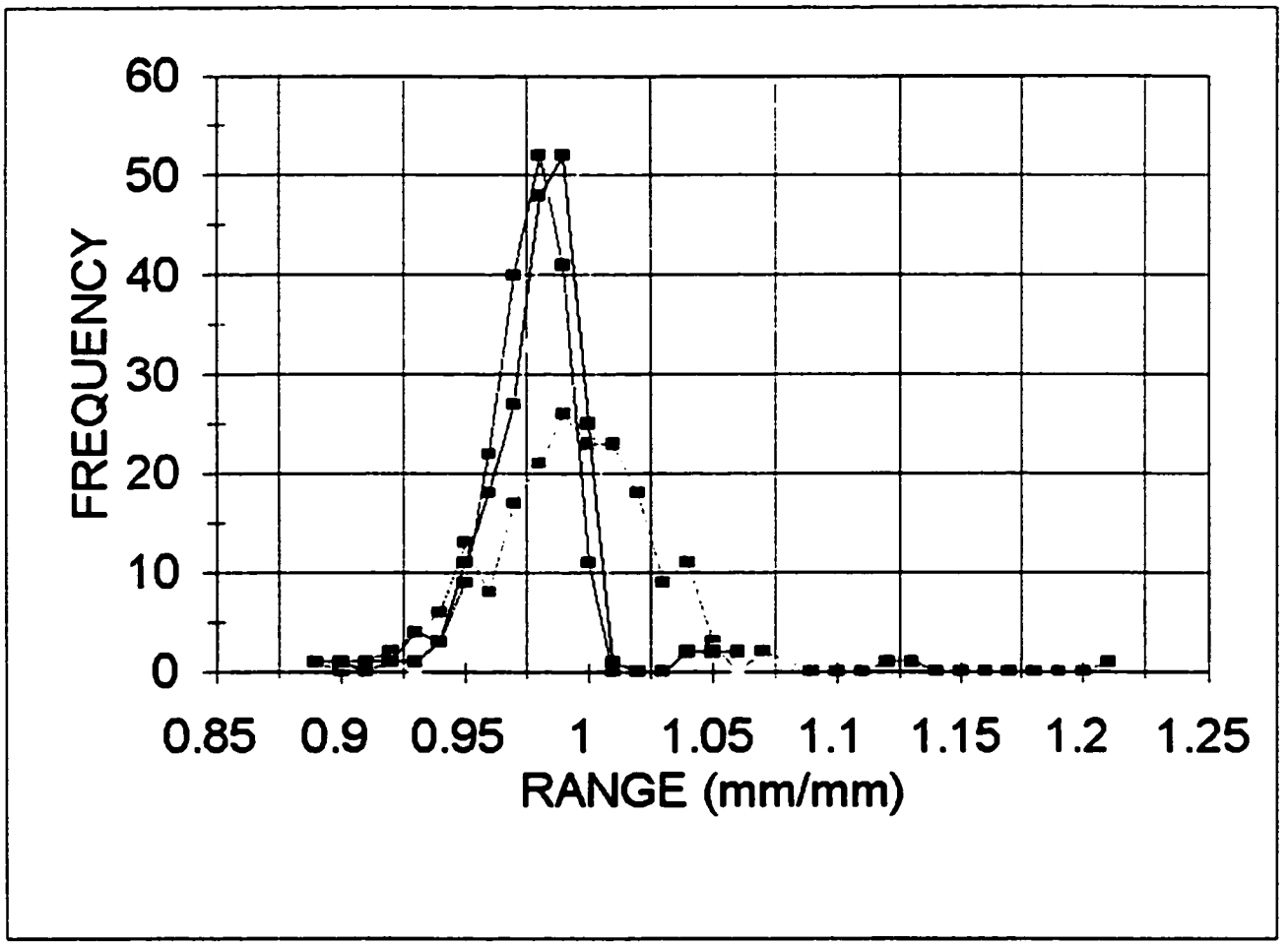

Figure 3.38 Specimen 4 - Summary of Normalized Results

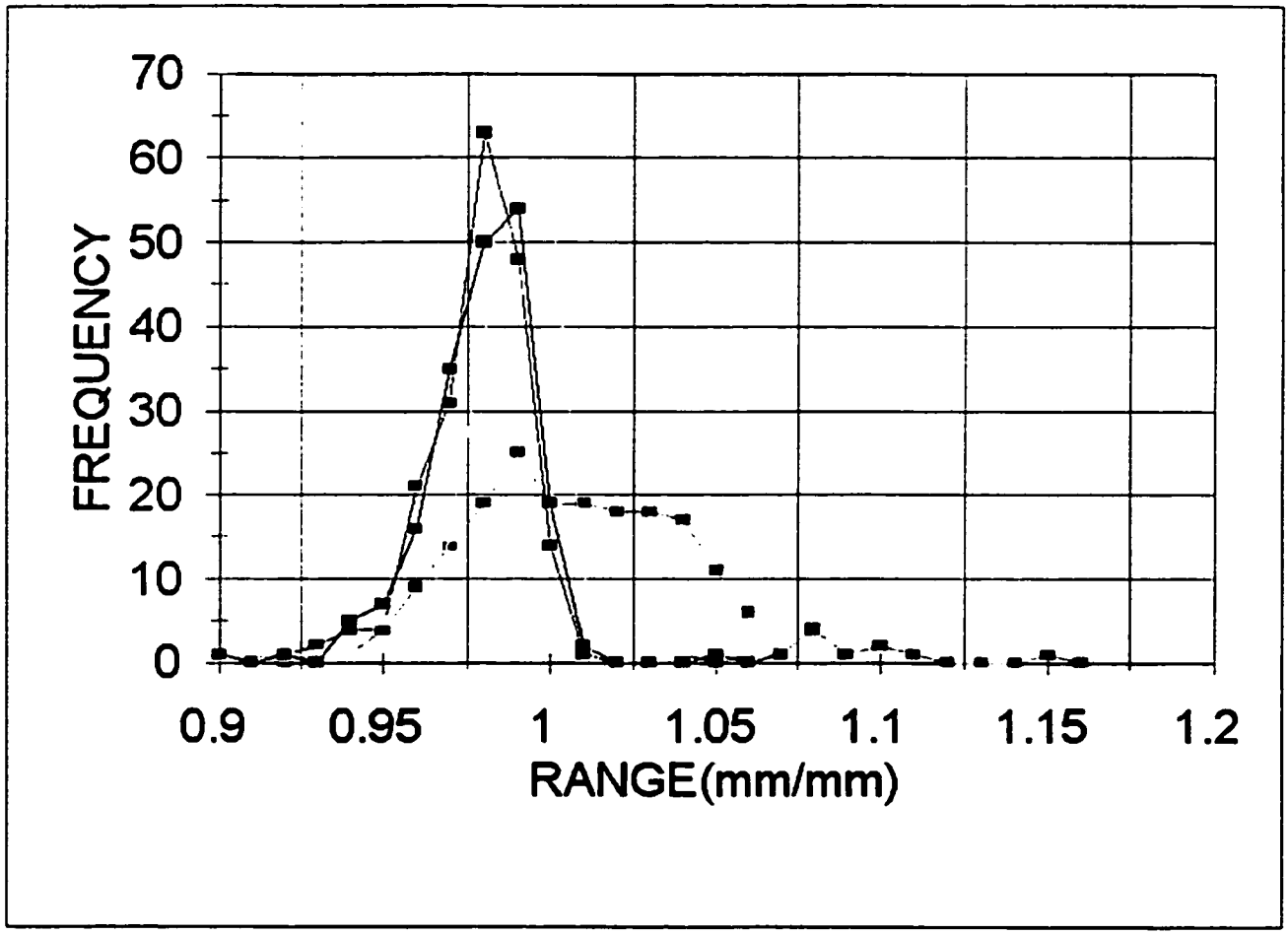

Figure 3.39 Specimen 5 - Summary of Normalized Results

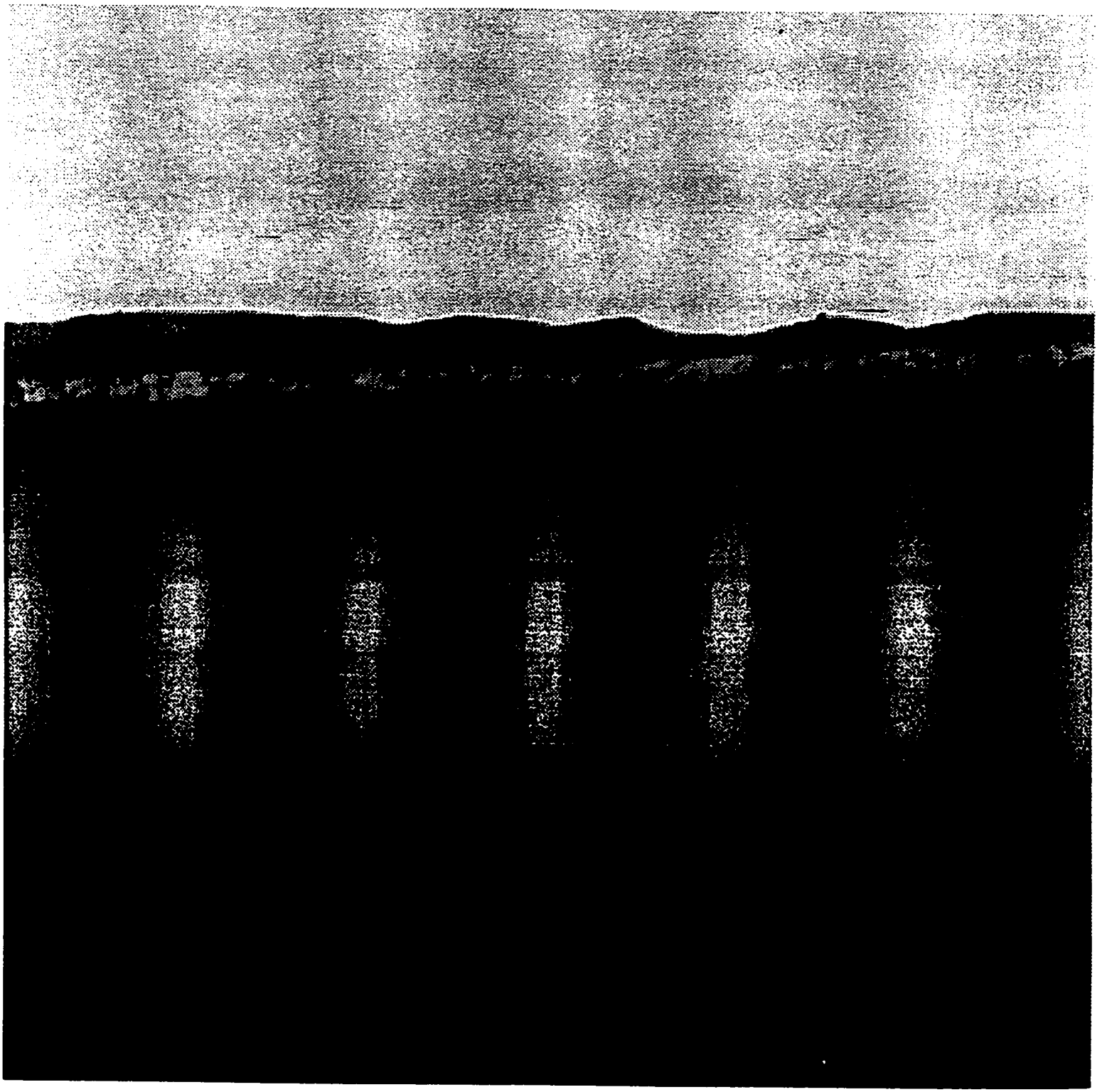

Figure 3.40 Bright Field Illumination Microscope Image Extra Coarse Tape 5x Magnification

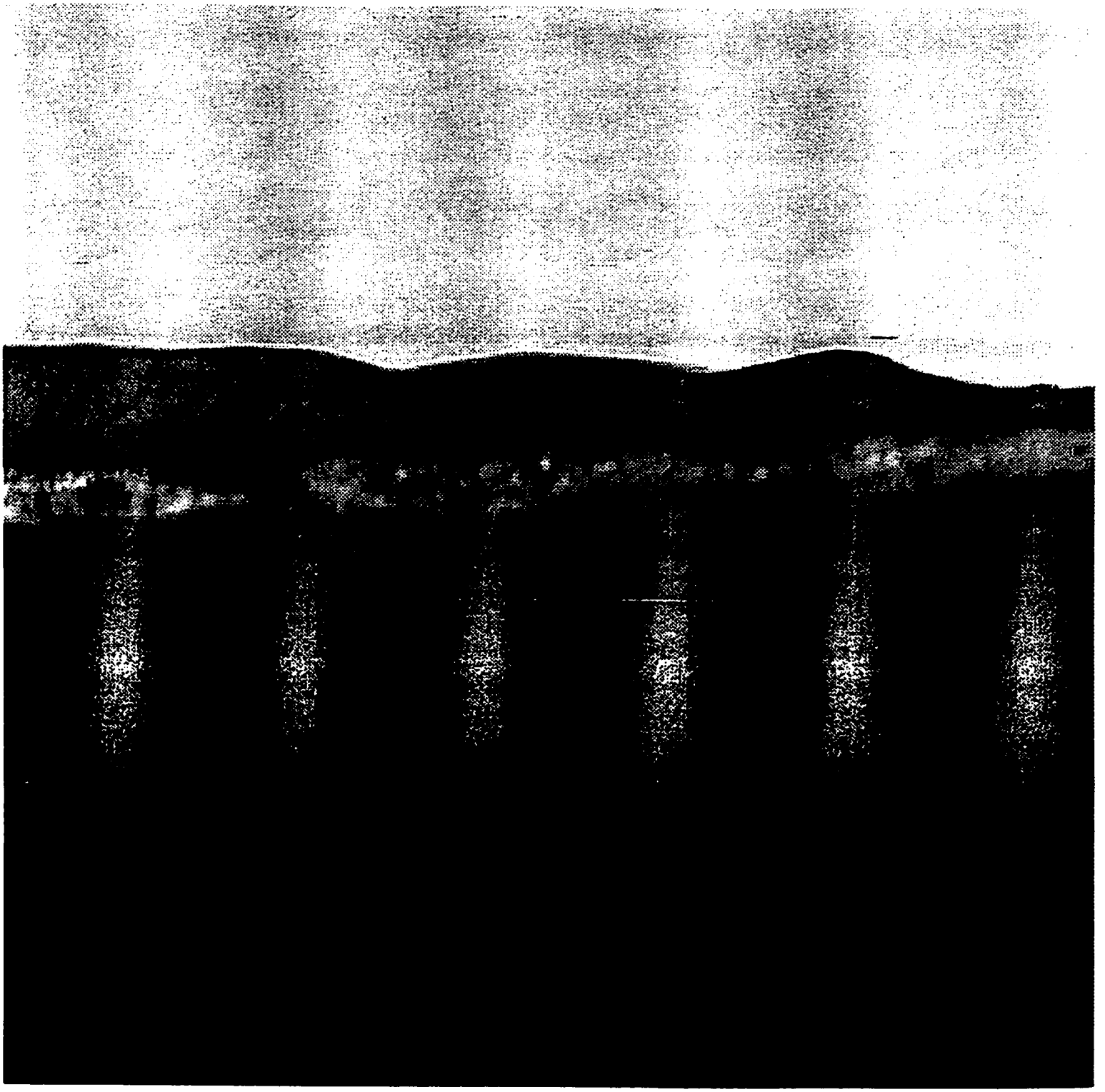

Figure 3.41 Bright Field Illumination Microscope Image Extra Coarse Tape 10x Magnification

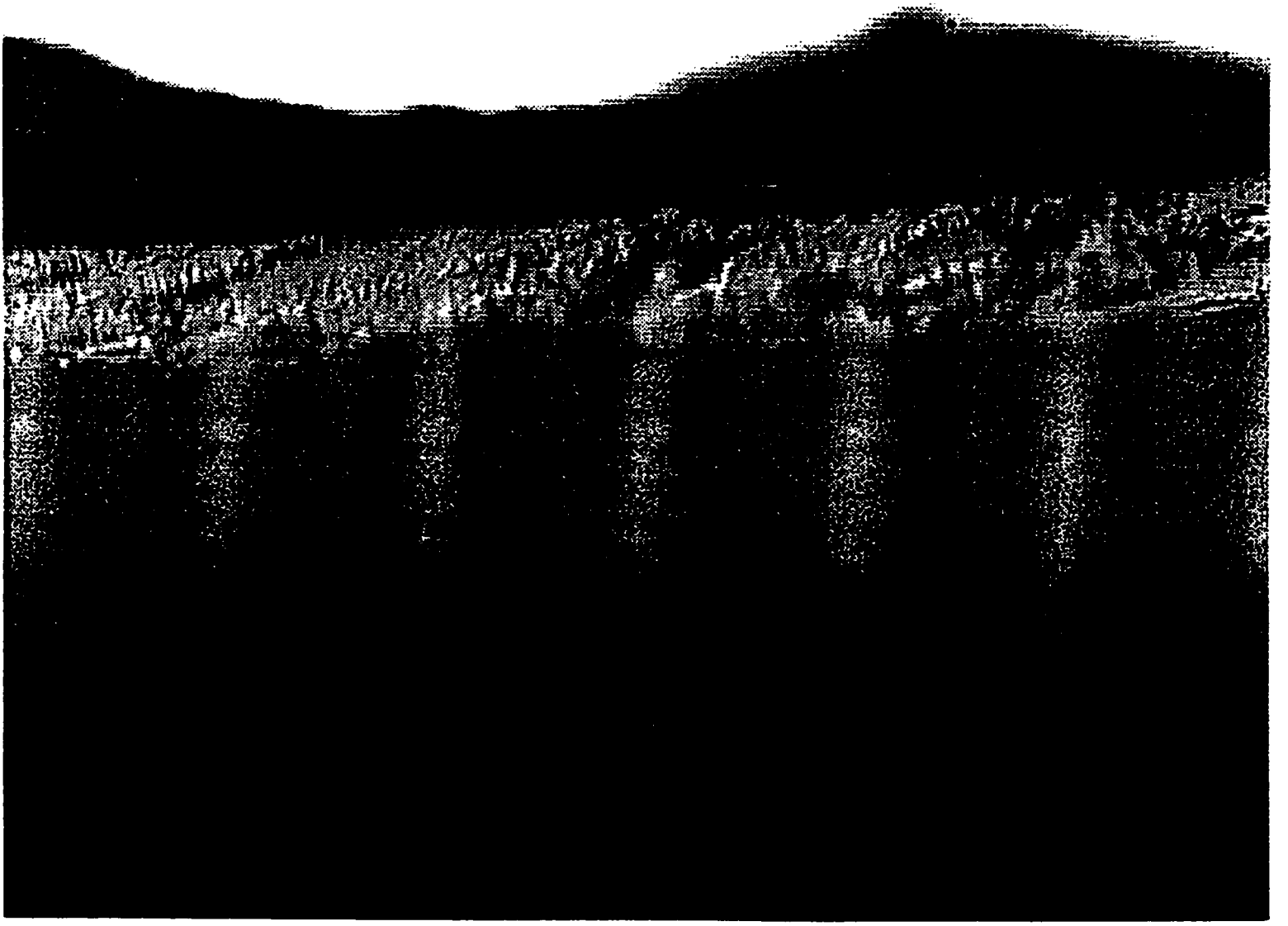

Figure 3.42 Bright Field Illumination Microscope Image Extra Coarse Tape 20x Magnification

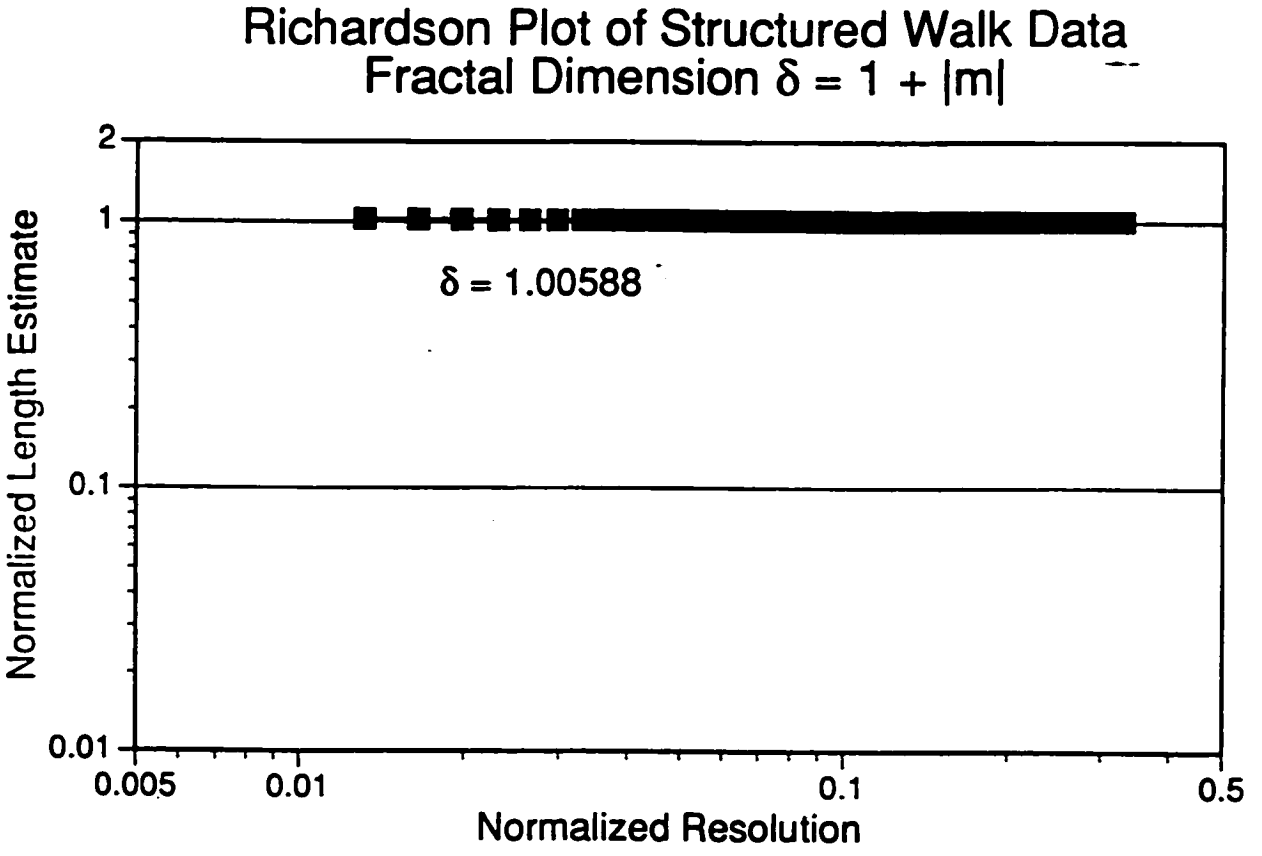

Figure 3.43 Fractal Plot of Bright Field Illumination Microscope Image Extra Coarse Tape 5x Magnification

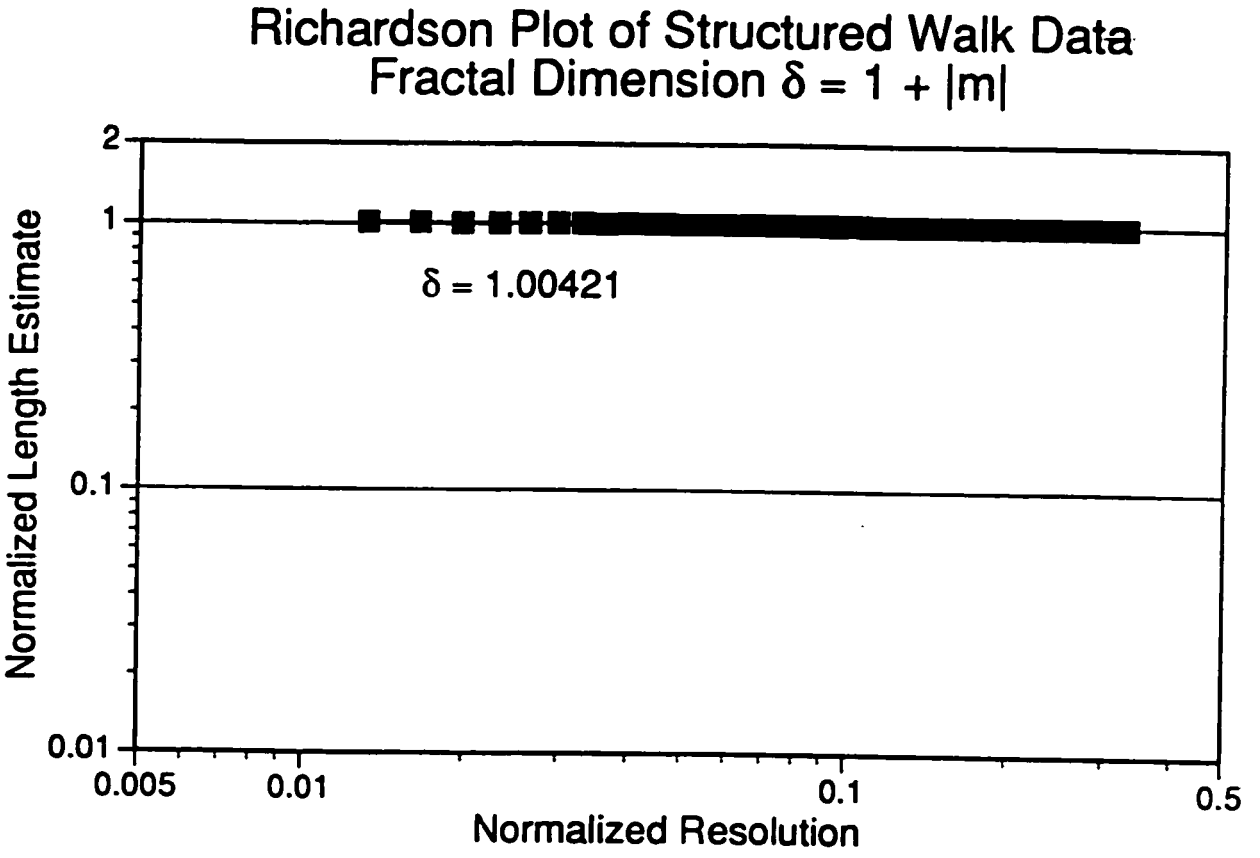

Figure 3.44 Fractal Plot of Bright Field Illumination Microscope Image Extra Coarse Tape 10x Magnification

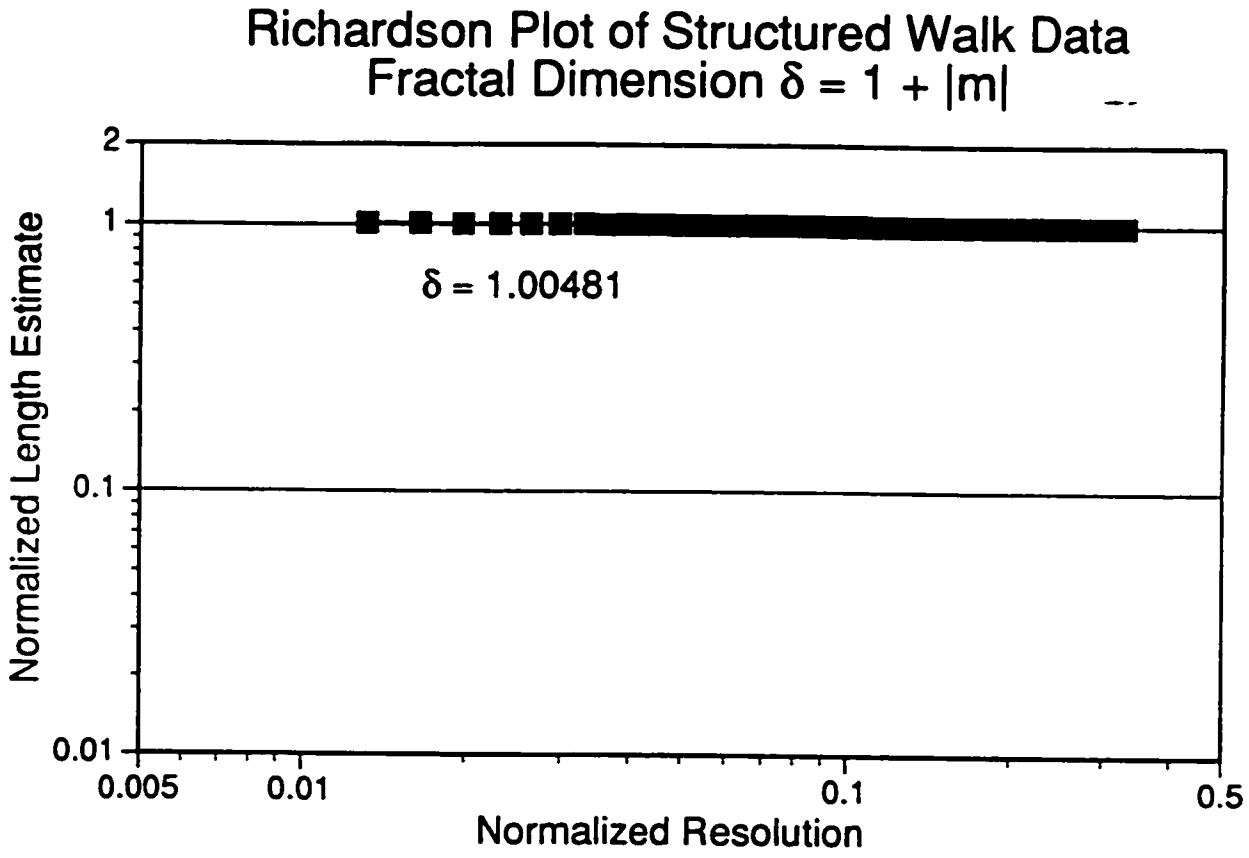

Figure 3.45 Fractal Plot of Bright Field Illumination Microscope Image Extra Coarse Tape 20x Magnification

Figure 3.46 Scanning Electron Microscope Image Medium Grade Gold Coated Replica Tape

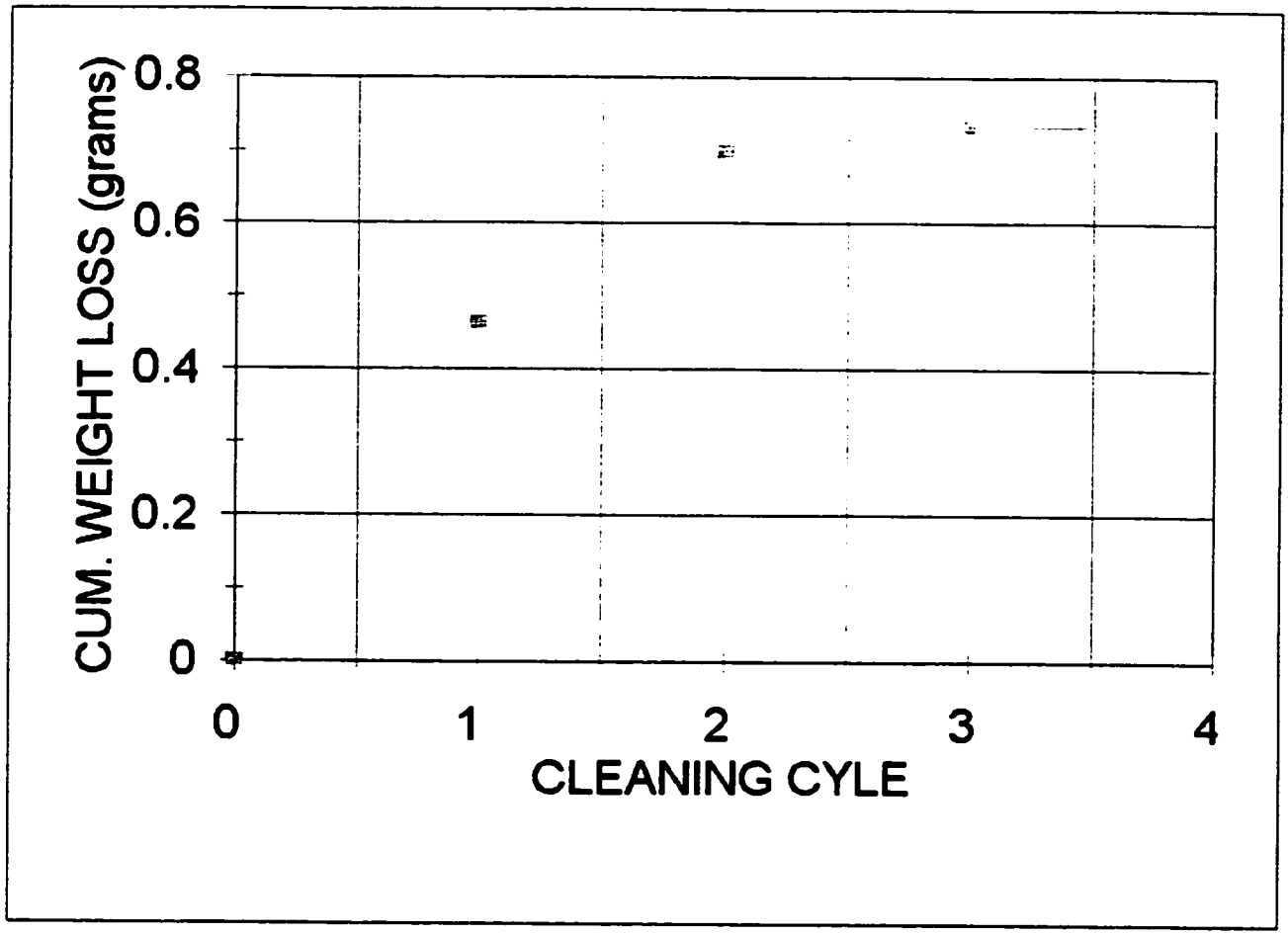

Figure 3.47 Corrosion Cleaning Procedure Cumulative Weight Loss Chart

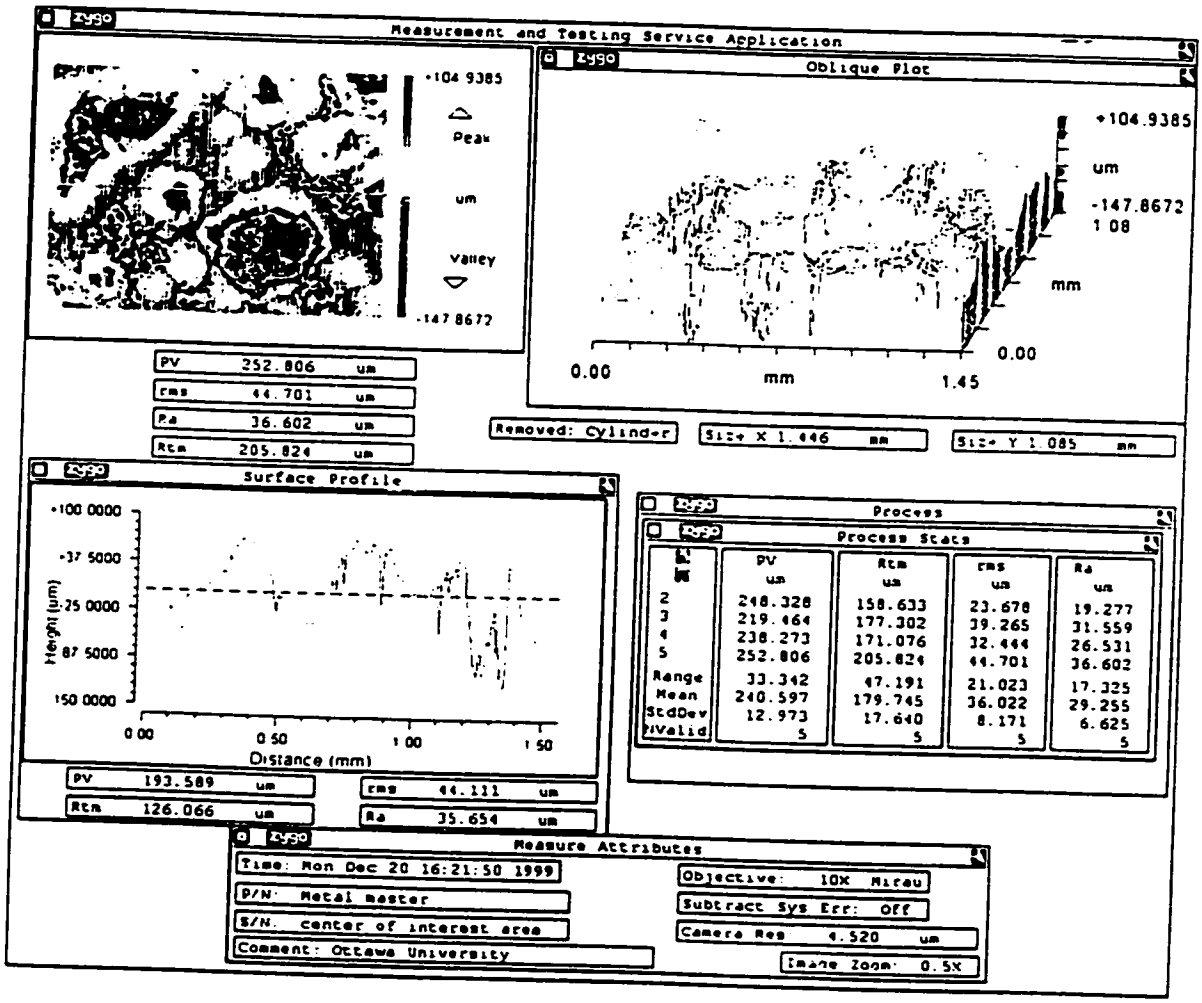

Figure 3.48 Optical Interference Microscope Zygo Process Output Window for 38.1 x 25.4 mm Steel Sample

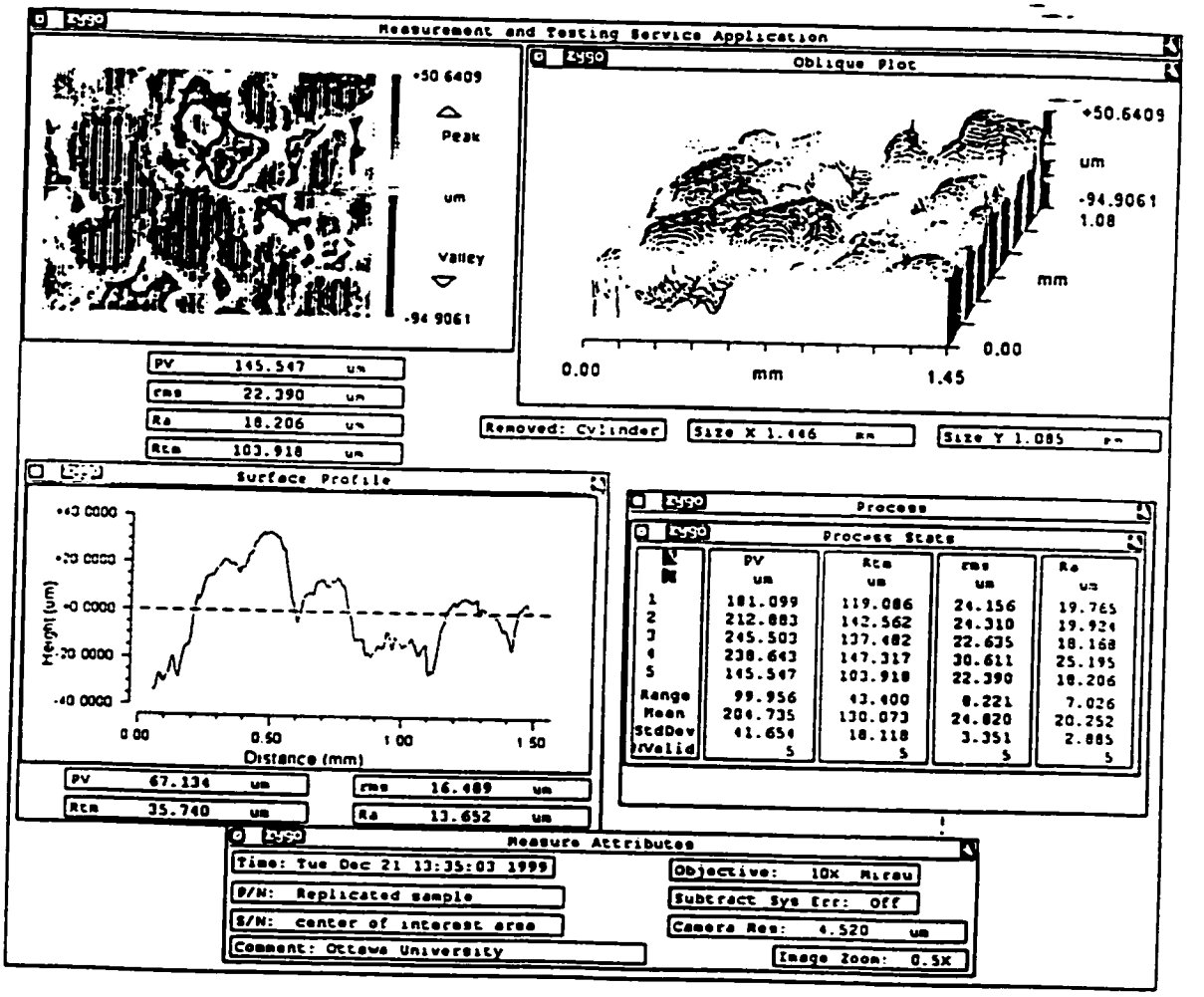

Figure 3.49 Optical Interference Microscope Zygo Process Output Window Replica Two

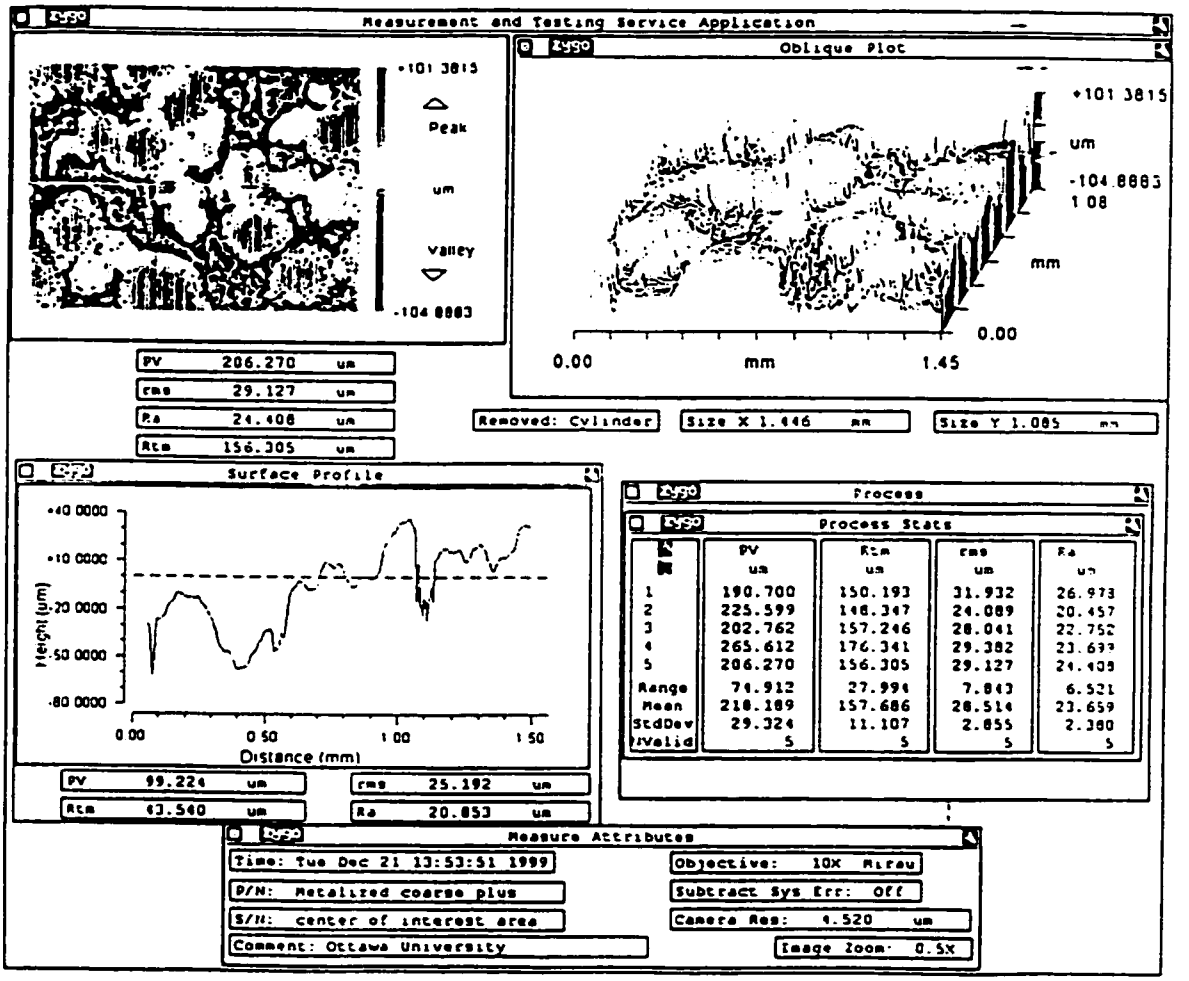

Figure 3.50 Optical Interference Microscope Zygo Process Output Window Replica One

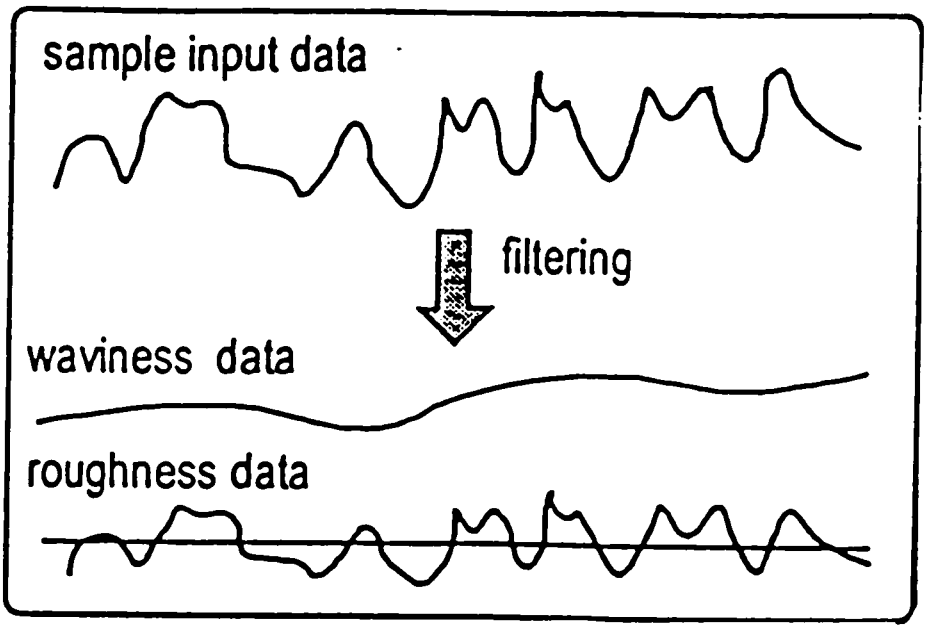

Figure 3.51 Waviness Filtration Methodology

Veeco

Mag: 2.6 X
Mode: VSI

Surface Data

Date: 01/05/2000
Time: 21:39:03

Surface Statistics:
Ra: 55.04 um
Rq: 67.98 um
Rz: 454.98 um
Rt: 542.08 um

Set-up Parameters:
Size: 1816 X 1446
Sampling: 6.54 um

Processed Options:
Terms Removed:
Tilt
Filtering:
Median

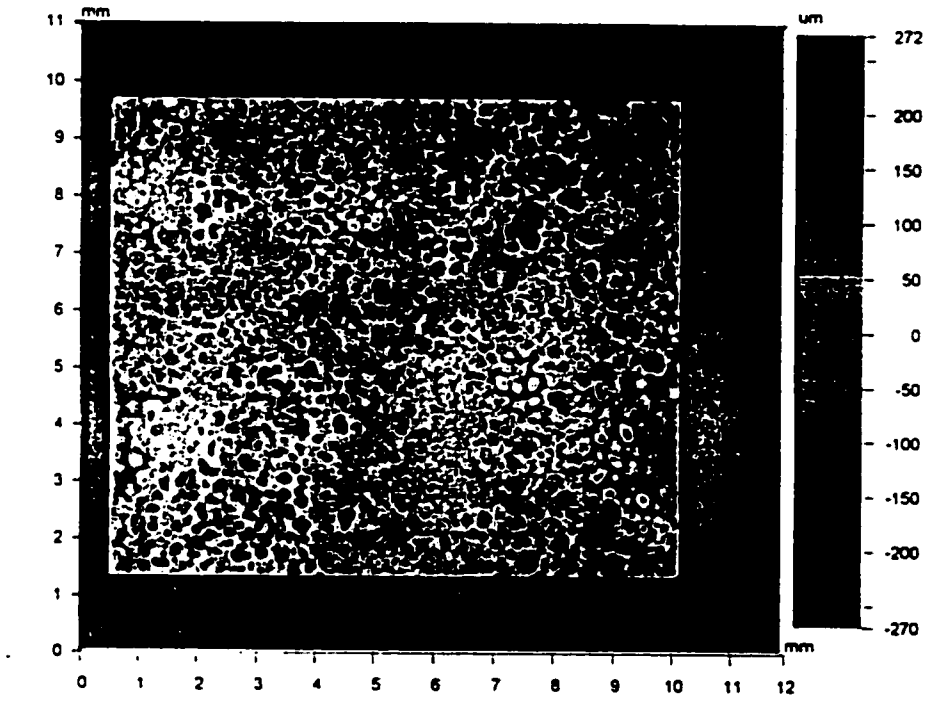

Title: Ottawa University
Note: Sample

Figure 3.52 Veeco Output - Metal Sample - Surface Data

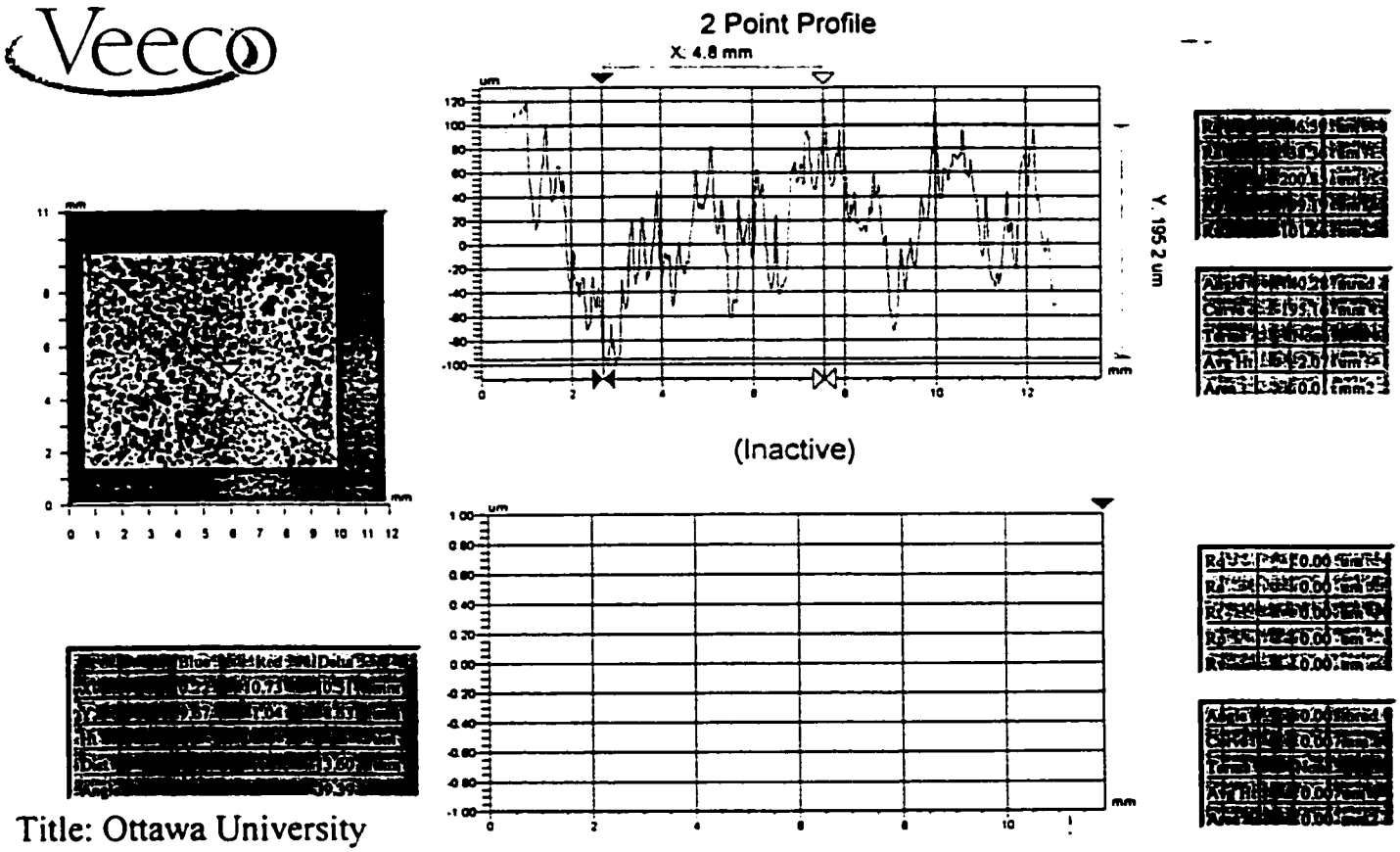

Figure 3.53 Veeco Output - Metal Sample - 2 Point Profile

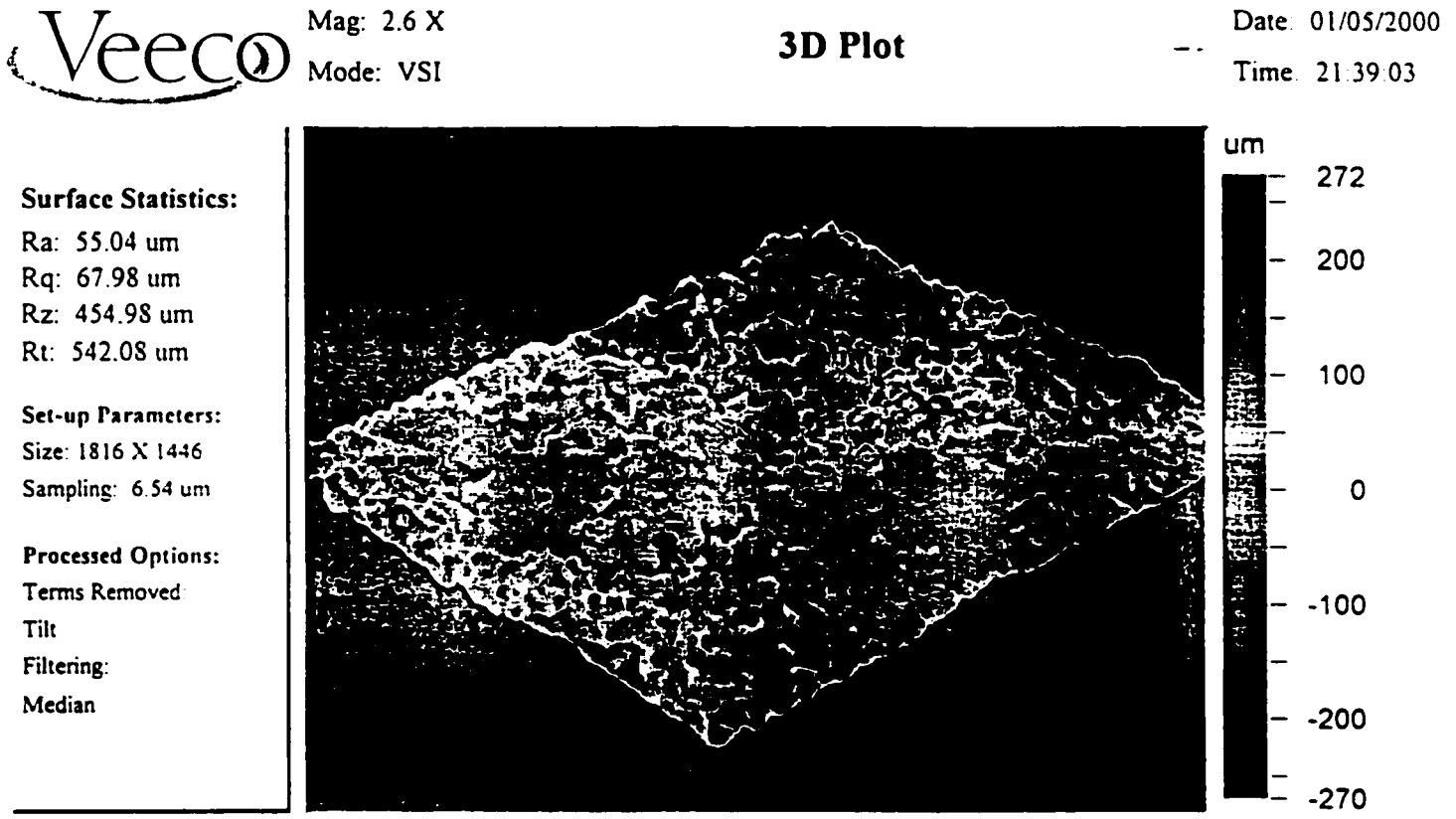

Figure 3.54 Veeco Output - Metal Sample - 3D Plot

3-Dimensional Interactive Display

Date: 01/05/2000
Time: 21:39:03

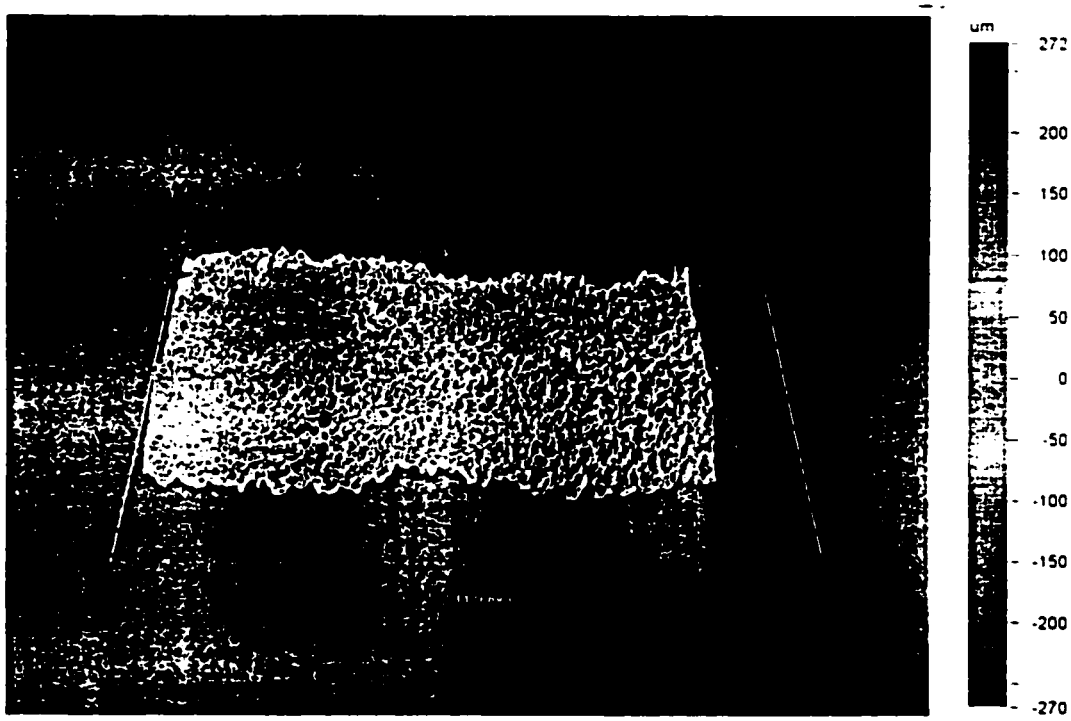

Surface Stats:

Ra: 55.04 um

Rq: 67.98 um

Rt: 542.08 um

Measurement Info:

Magnification: 2.57

Measurement Mode: VSI

Sampling: 6.54 um

Array Size: 1816 X 1446

Title: Ottawa University

Note: Sample

Figure 3.55 Veeco Output - Metal Sample - 3-Dimensional Interactive Display

Veeco

Mag: 2.5 X
Mode: VSI

Surface Data

Date: 01/19/2000
Time: 13:51:37

Surface Statistics:
Ra: 64.14 um
Rq: 77.06 um
Rz: 453.90 um
Rt: 485.99 um

Set-up Parameters:
Size: 1917 X 1758
Sampling: 6.74 um

Processed Options:
Terms Removed:
Tilt
Filtering:
Median

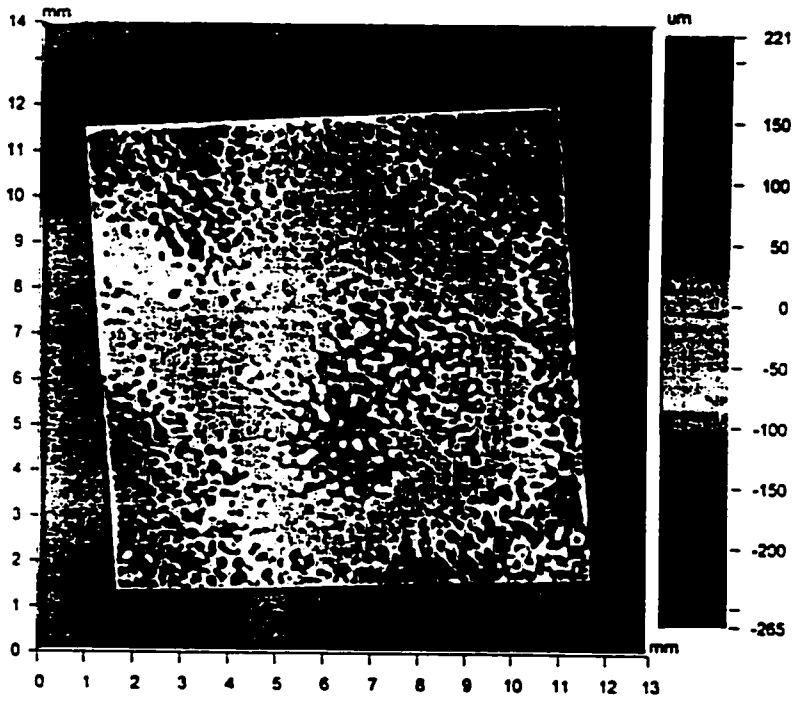

Title: Ottawa University
Note: Replica 1

Figure 3.56 Veeco Output - Replica 1 - Surface Data

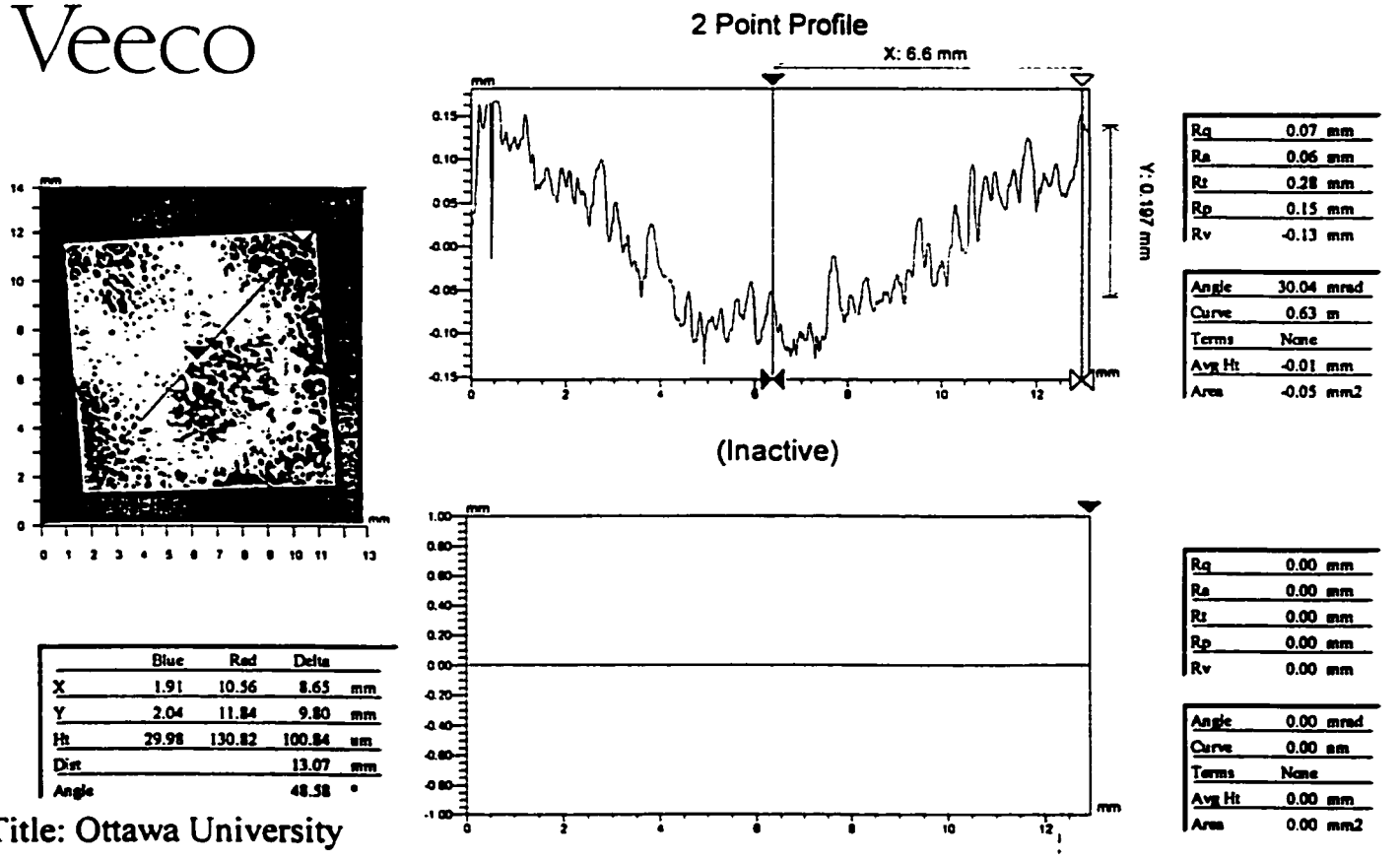

Figure 3.57 Veeco Output - Replica 1 - 2 Point Profile

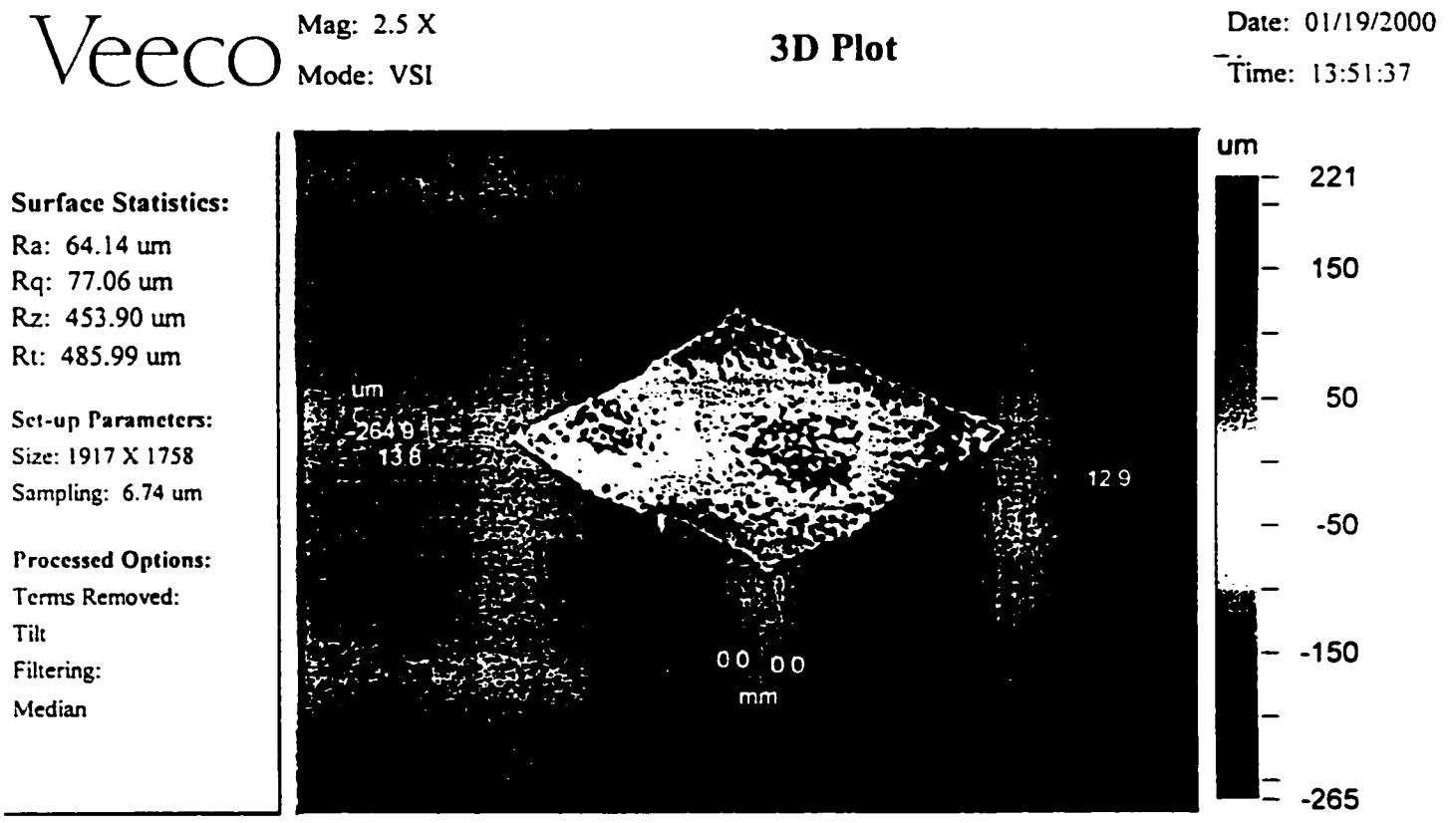

Figure 3.58 Veeco Output - Replica 1 - 3D Plot

3-Dimensional Interactive Display

Date: 01/19/2000
Time: 13:51:37

Surface Stats:

Ra: 64.14 um

Rq: 77.06 um

Rt: 485.99 um

Measurement Info:

Magnification: 2.49

Measurement Mode: VSI

Sampling: 6.74 um

Array Size: 1917 X 1758

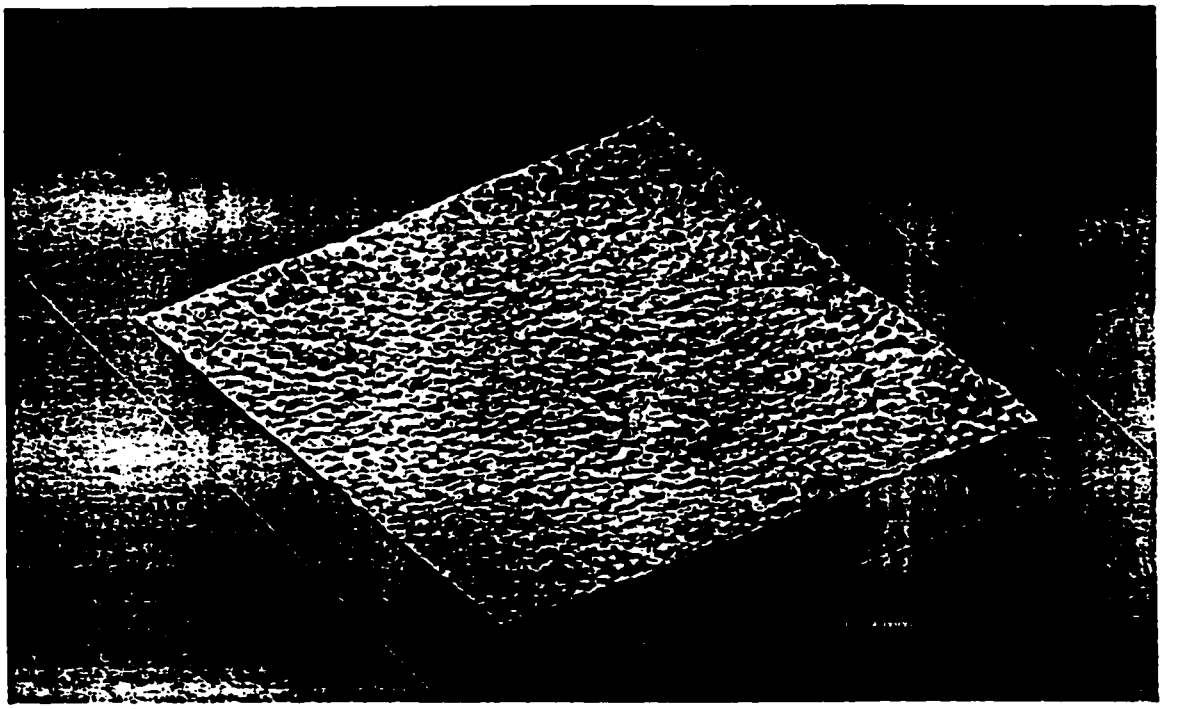

Title: Ottawa University

Note: Replica 1

Figure 3.59 Veeco Output - Replica 1 - 3-Dimensional Interactive Display

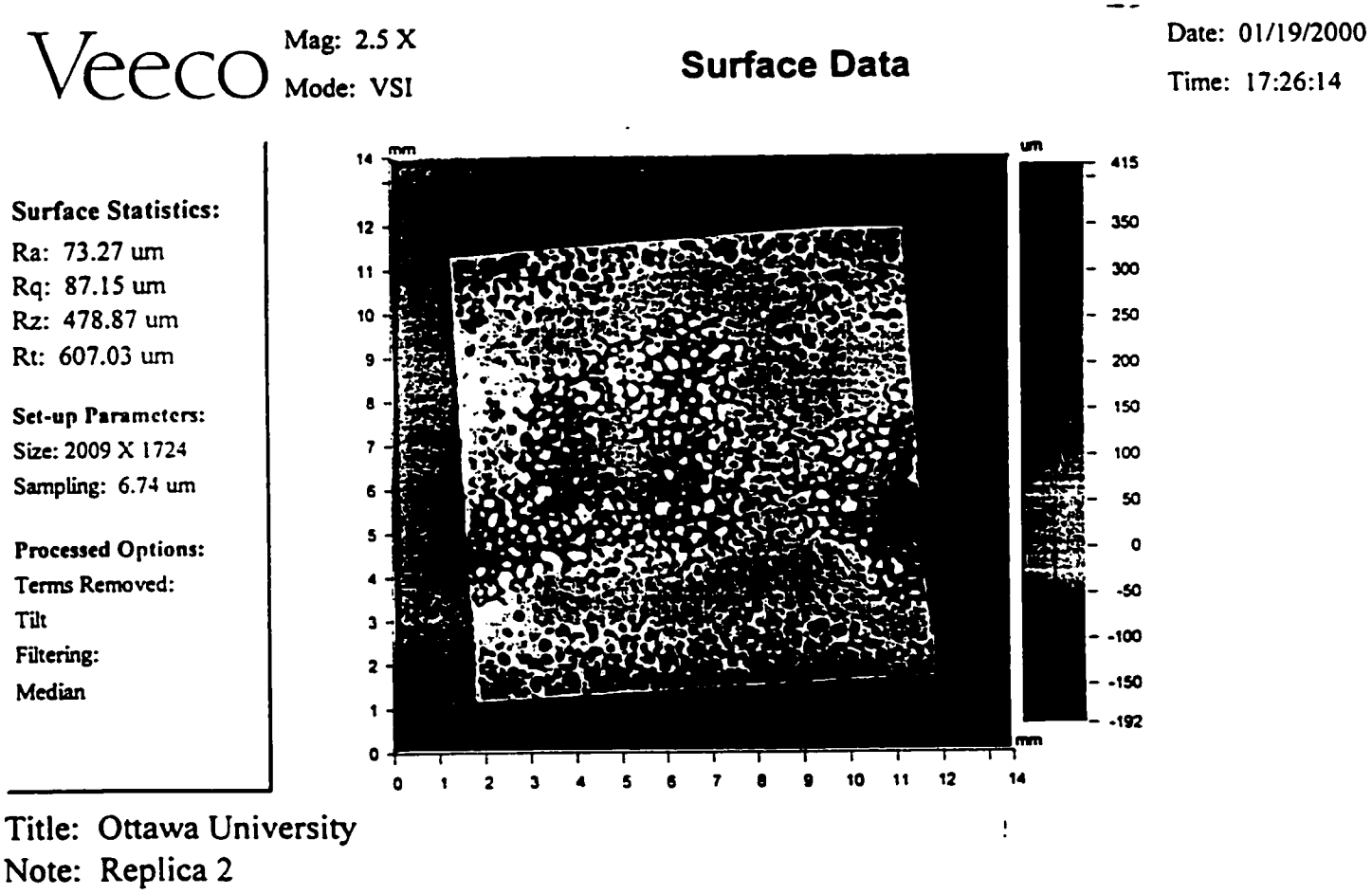

Figure 3.60 Veeco Output - Replica 2 - Surface Data

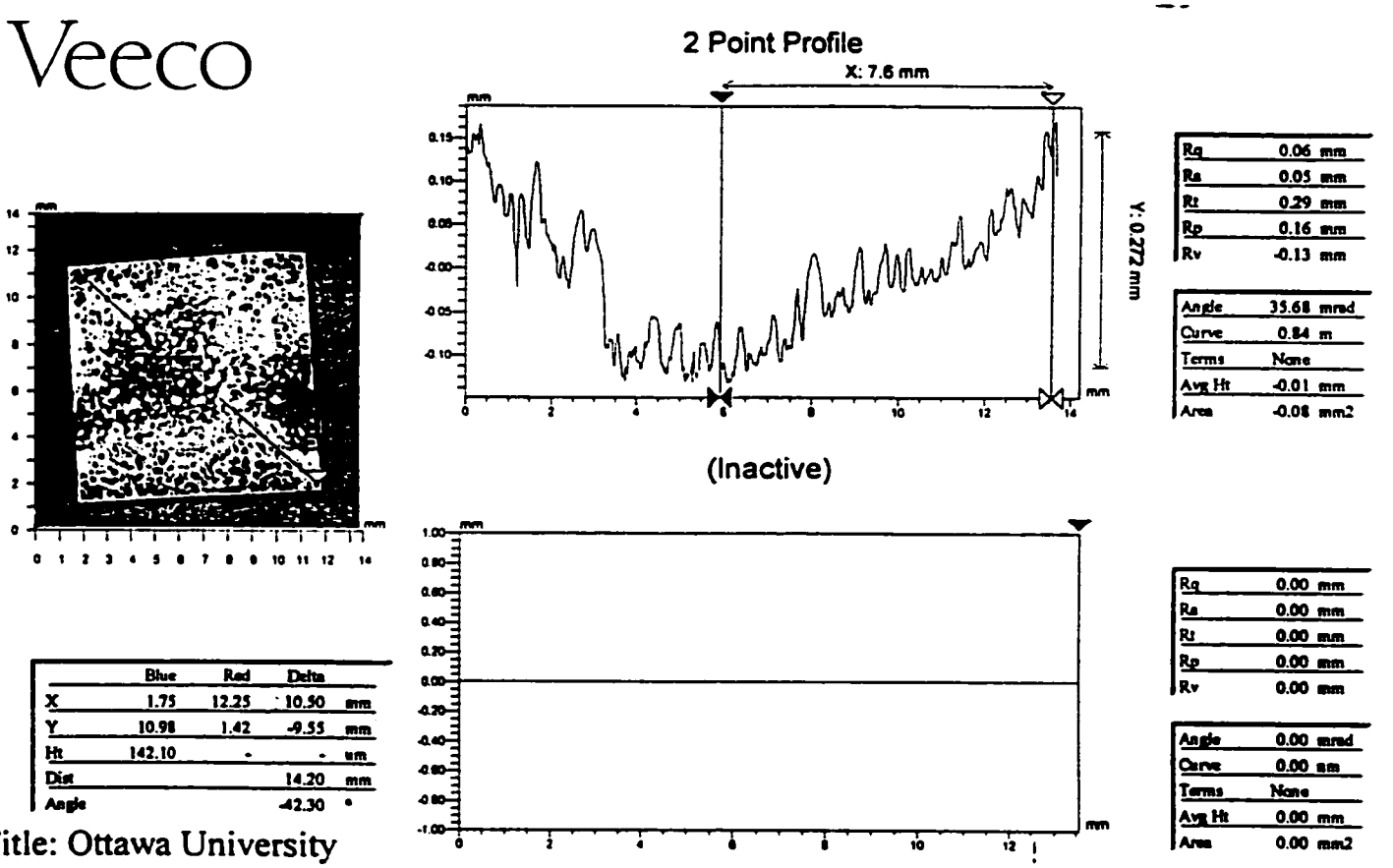

Figure 3.61 Veeco Output - Replica 2 - 2 Point Profile

3-Dimensional Interactive Display

Date: 01/19/2000
Time: 17:26:14

Surface Stats:

Ra: 73.27 um

Rq: 87.15 um

Rt: 607.03 um

Measurement Info:

Magnification: 2.49

Measurement Mode: VSI

Sampling: 6.74 um

Array Size: 2009 X 1724

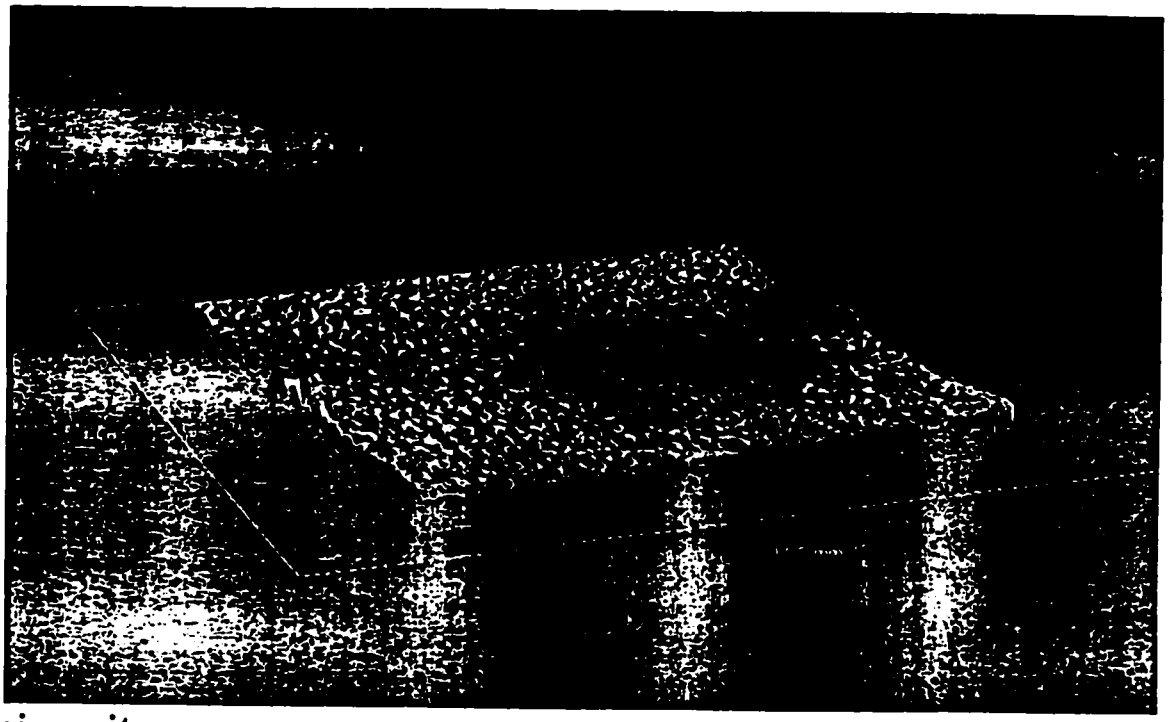

Title: Ottawa University

Note: Replica 2

Figure 3.62 Veeco Output - Replica 2 - 3-Dimensional Interactive Display

Cambridge
materials testing limited

1177 Franklin Boulevard,
Cambridge, Ontario N1R 7W4
Tel: (519) 621-6600 Fax: (519) 621-6082
www.cambridgematerials.com
ISO Accredited (1989)

Report for: Burke, Mr. Steve
C/O J.L. Richards & Associates Limited
469 Bouchard Street, Suite 217
SUDBURY, Ontario
P3E 2K8
Phone: 1-705-522-8174
Fax: 1-705-522-1512

Laboratory No. 233970-1999

Report Date: November 08, 1999
Received Date: September 21, 1999

Attention: Steve Burke

Specimen: #1, 3/8"Flat Steel Tensile Specimen

TENSILE TEST REPORT

Specimen Dimensions:	1.500 X 0.375 in.
Yield Strength (0.2% offset):	25,300 psi
Ultimate Tensile Strength:	34,700 psi
Elongation in 8 in.:	5.0 %

Testing performed according to ASTM A370-97a.

Cambridge Materials Testing Limited

Per _____ QUALITY ASSURANCE

Per _____ TECHNICIAN

NOTE: Specimen Dimensions, Yield and Ultimate Strength Values are Only Valid for the Smooth Control Specimen. See Table 4.1 for True Yield and Ultimate Values

Figure 4.1 Tensile Testing Report For Specimen One

Cambridge
materials testing limited

1177 Franklin Boulevard,
Cambridge, Ontario N1R 7W4
Tel: (519) 621-6600 Fax: (519) 621-6082
www.cambridgematerials.com
ISO Accredited (1989)

Report for: Burke, Mr. Steve
C/O J.L. Richards & Associates Limited
469 Bouchard Street, Suite 217
SUDBURY, Ontario
P3E 2K8
Phone: 1-705-522-8174
Fax: 1-705-522-1512

Laboratory No. 233971-1999

Report Date: November 08, 1999
Received Date: September 21, 1999

Attention: Steve Burke

Specimen: #2, 3/8" Flat Steel Tensile Specimen

TENSILE TEST REPORT

Specimen Dimensions:	1.500 X 0.375 in.
Yield Strength (0.2% offset):	32,600 psi
Ultimate Tensile Strength:	44,800 psi
Elongation in 8 in.:	16 %

Testing performed according to ASTM A370-97a.

Cambridge Materials Testing Limited

Per _____ QUALITY ASSURANCE

Per _____ TECHNICIAN

NOTE: **Specimen Dimensions, Yield and Ultimate Strength Values are Only Valid for the Smooth Control Specimen. See Table 4.1 for True Yield and Ultimate Values**

Figure 4.2 Tensile Testing Report For Specimen Two

Cambridge
materials testing limited

1177 Franklin Boulevard,
Cambridge, Ontario N1R 7W4
Tel: (519) 621-6600 Fax: (519) 621-6082
www.cambridgematerials.com
ISO Accredited (1989)

Report for: Burke, Mr. Steve
C/O J.L. Richards & Associates Limited
469 Bouchard Street, Suite 217
SUDBURY, Ontario
P3E 2K8
Phone: 1-705-522-8174
Fax: 1-705-522-1512

Laboratory No. 233972-1999

Report Date: November 08, 1999
Received Date: September 21, 1999

Attention: Steve Burke

Specimen: #3, 3/8" Flat Steel Tensile Specimen

TENSILE TEST REPORT

Specimen Dimensions:	1.500 X 0.375 in.
Yield Strength (0.2% offset):	22,600 psi
Ultimate Tensile Strength:	31,900 psi
Elongation in 8 in.:	10 %

Testing performed according to ASTM A370-97a.

Page 1 of 1

Cambridge Materials Testing Limited

Per _____ QUALITY ASSURANCE

Per _____ TECHNICIAN

NOTE: **Specimen Dimensions, Yield and Ultimate Strength Values are Only Valid for the Smooth Control Specimen. See Table 4.1 for True Yield and Ultimate Values**

Figure 4.3 **Tensile Testing Report For Specimen Three**

Cambridge
materials testing limited

1177 Franklin Boulevard,
Cambridge, Ontario N1R 7W4
Tel: (519) 621-6600 Fax: (519) 621-6082
www.cambridgematerials.com
ISO Accredited (1989)

Report for: Burke, Mr. Steve
C/O J.L. Richards & Associates Limited
469 Bouchard Street, Suite 217
SUDBURY, Ontario
P3E 2K8
Phone: 1-705-522-8174
Fax: 1-705-522-1512

Laboratory No. 233973-1999

Report Date: November 08, 1999
Received Date: September 21, 1999

Attention: Steve Burke

Specimen: #4, 3/8" Flat Steel Tensile Specimen

TENSILE TEST REPORT

Specimen Dimensions:	1.500 X 0.375 in.
Yield Strength (0.2% offset):	33,800 psi
Ultimate Tensile Strength:	47,200 psi
Elongation in 8 in.:	18 %

Testing performed according to ASTM A370-97a.

Cambridge Materials Testing Limited

Per _____ QUALITY ASSURANCE

Per _____ TECHNICIAN

NOTE: **Specimen Dimensions, Yield and Ultimate Strength Values are Only Valid for the Smooth Control Specimen. See Table 4.1 for True Yield and Ultimate Values**

Figure 4.4 Tensile Testing Report For Specimen Four

Cambridge
materials testing limited

1177 Franklin Boulevard,
Cambridge, Ontario N1R 7W4
Tel: (519) 621-6600 Fax: (519) 621-6082
www.cambridgematerials.com
ISO Accredited (1989)

Report for: Burke, Mr. Steve
C/O J.L. Richards & Associates Limited
469 Bouchard Street, Suite 217
SUDBURY, Ontario
P3E 2K8
Phone: 1-705-522-8174
Fax: 1-705-522-1512

Attention: Steve Burke

Specimen: #5, 3/8" Flat Steel Tensile Specimen

Laboratory No. 233974-1999

Report Date: November 08, 1999
Received Date: September 21, 1999

RECEIVED
NOV 15 1999
J.L. RICHARDS & ASSOCIATES LIMITED
SUDBURY, ONTARIO

TENSILE TEST REPORT

Specimen Dimensions:	1.500 X 0.375 in.
Yield Strength (0.2% offset):	33,800 psi
Ultimate Tensile Strength:	48,600 psi
Elongation in 8 in.:	15 %

Testing performed according to ASTM A370-97a.

Cambridge Materials Testing Limited

Per _____ QUALITY ASSURANCE

Per _____ TECHNICIAN

NOTE: **Specimen Dimensions, Yield and Ultimate Strength Values are Only Valid for the Smooth Control Specimen. See Table 4.1 for True Yield and Ultimate Values**

Figure 4.5 Tensile Testing Report For Specimen Five

Cambridge
materials testing limited

1177 Franklin Boulevard,
Cambridge, Ontario N1R 7W4
Tel: (519) 621-6600 Fax: (519) 621-6082
www.cambridgematerials.com
ISO Accredited (1989)

Report for: Burke, Mr. Steve
C/O J.L. Richards & Associates Limited
469 Bouchard Street, Suite 217
SUDBURY, Ontario
P3E 2K8
Phone: 1-705-522-8174
Fax: 1-705-522-1512

Laboratory No. 233975-1999

Report Date: November 08, 1999
Received Date: September 21, 1999

Attention: Steve Burke

Specimen: Control Specimen, 3/8" Flat Steel Tensile Specimen

TENSILE TEST REPORT

Specimen Dimensions:	1.498 X 0.318 in.
Yield Strength (0.2% offset):	45,700 psi
Ultimate Tensile Strength:	65,000 psi
Elongation in 8 in.:	27 %

Testing performed according to ASTM A370-97a.

Page 1 of 1

Cambridge Materials Testing Limited

Per _____ QUALITY ASSURANCE

Per _____ TECHNICIAN

NOTE: **Specimen Dimensions, Yield and Ultimate Strength Values are Only Valid for the Smooth Control Specimen. See Table 4.1 for True Yield and Ultimate Values**

Figure 4.6 Tensile Testing Report For Control Specimen

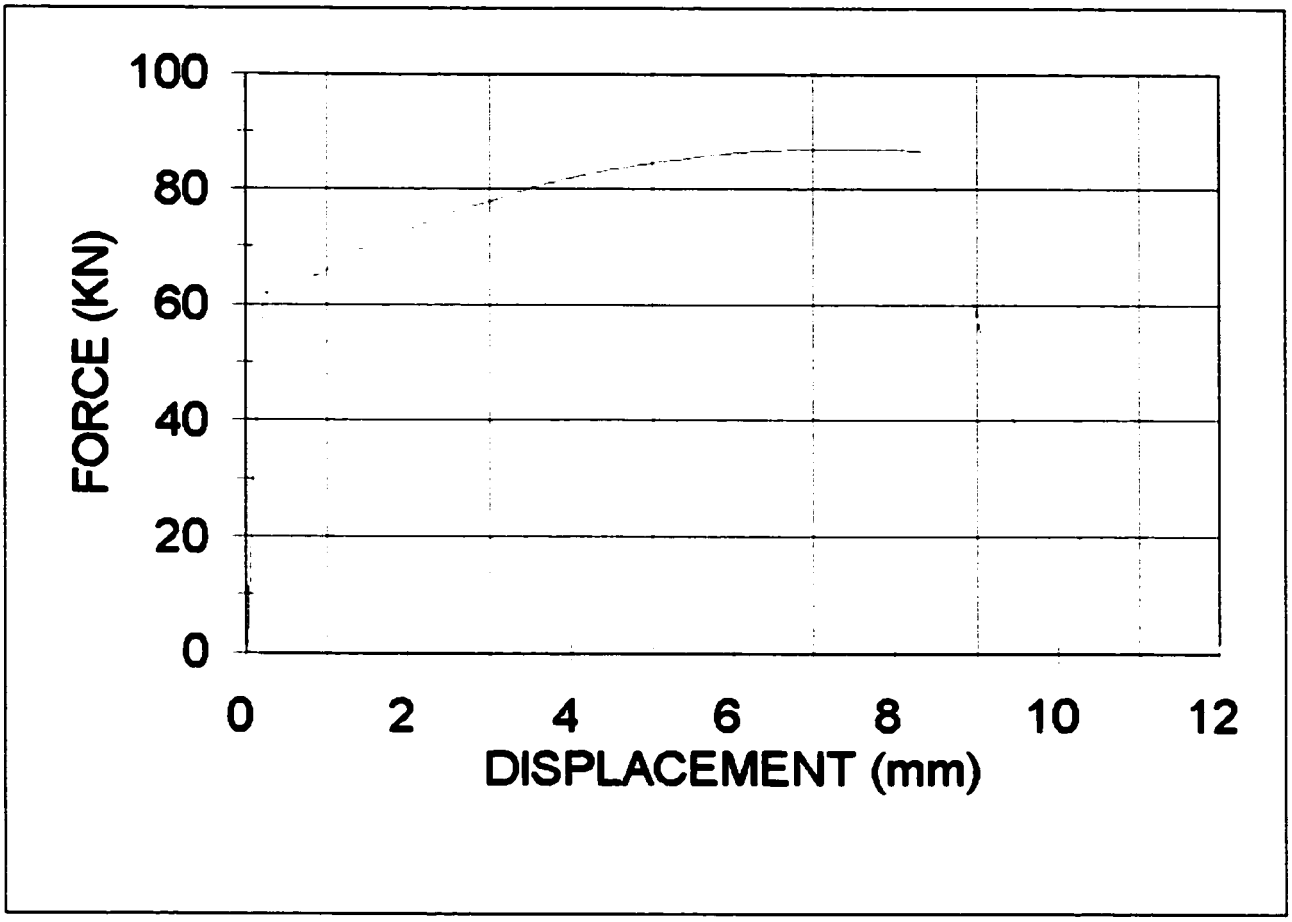

Figure 4.7 Force Displacement Curve for Specimen One

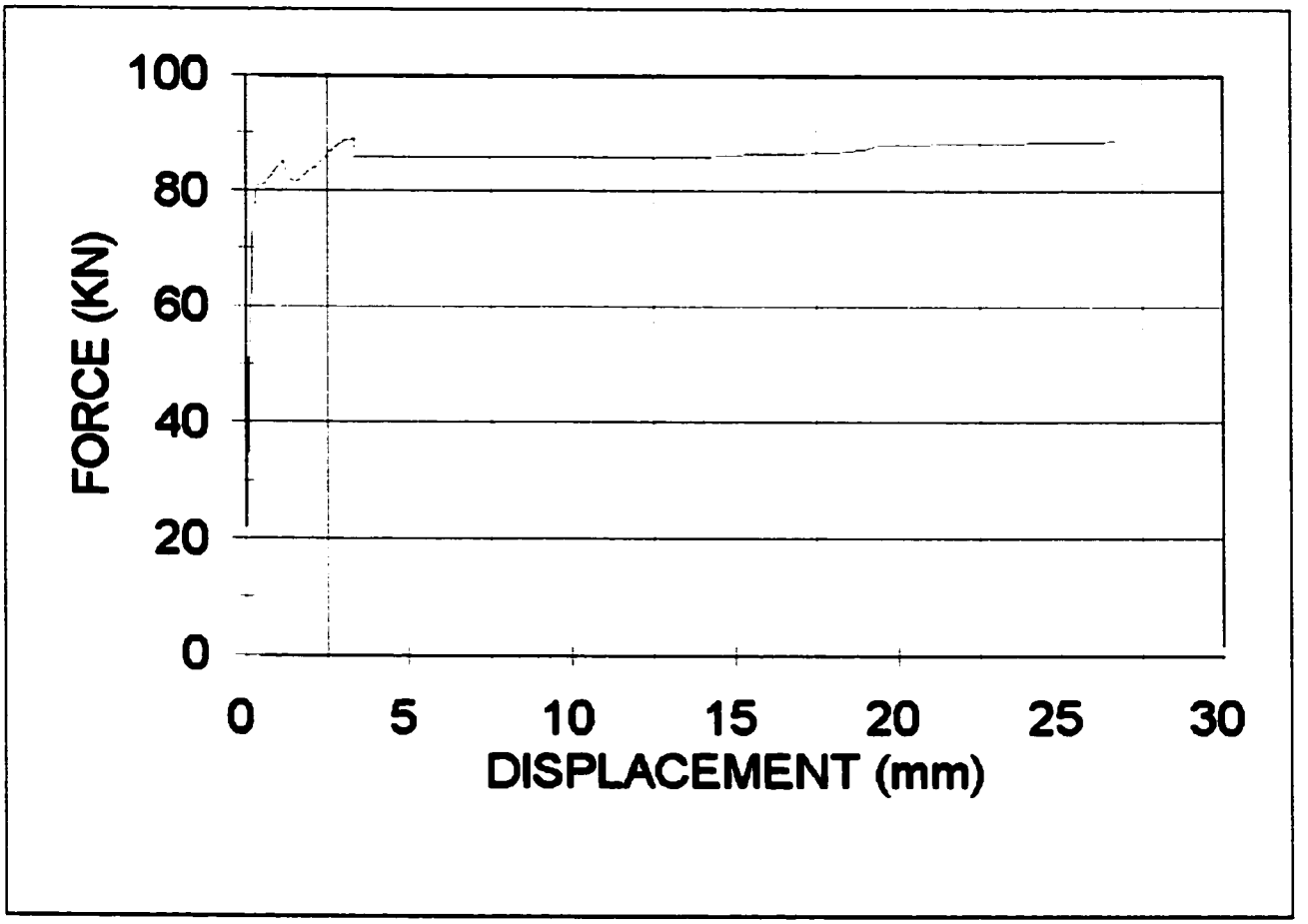

Figure 4.8 Force Displacement Curve for Specimen Two

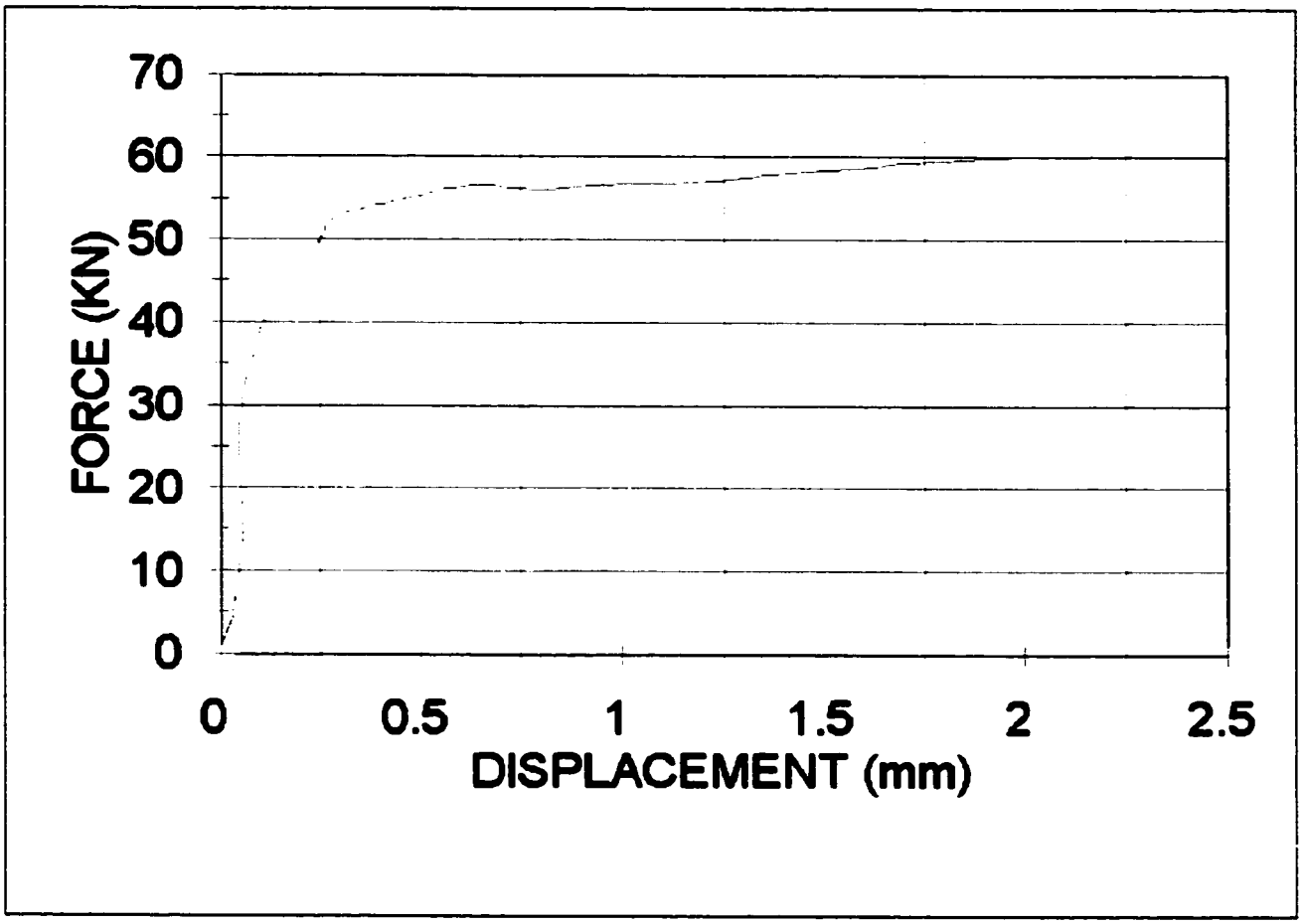

Figure 4.9 Force Displacement Curve for Specimen Three

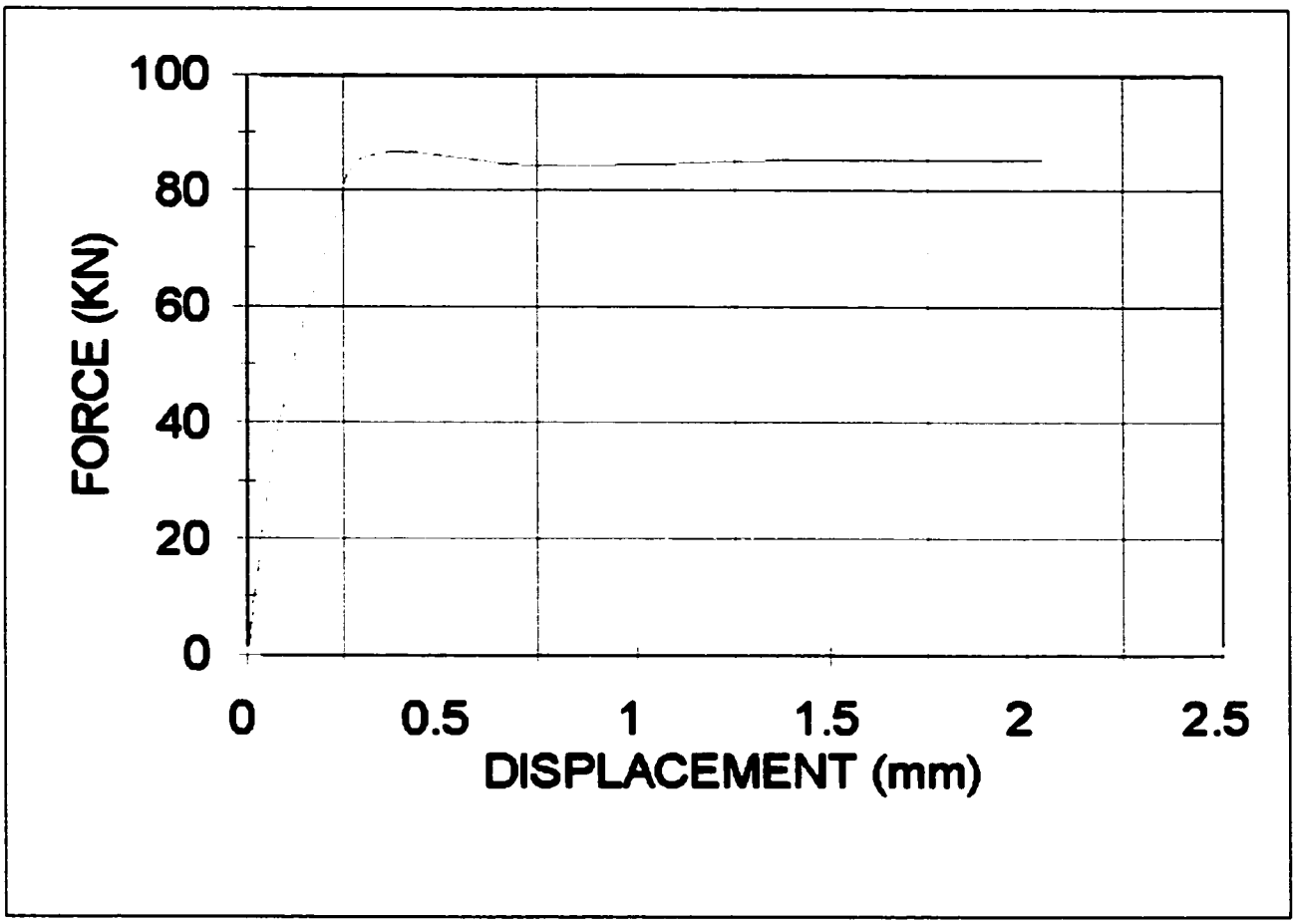

Figure 4.10 Force Displacement Curve for Specimen Four

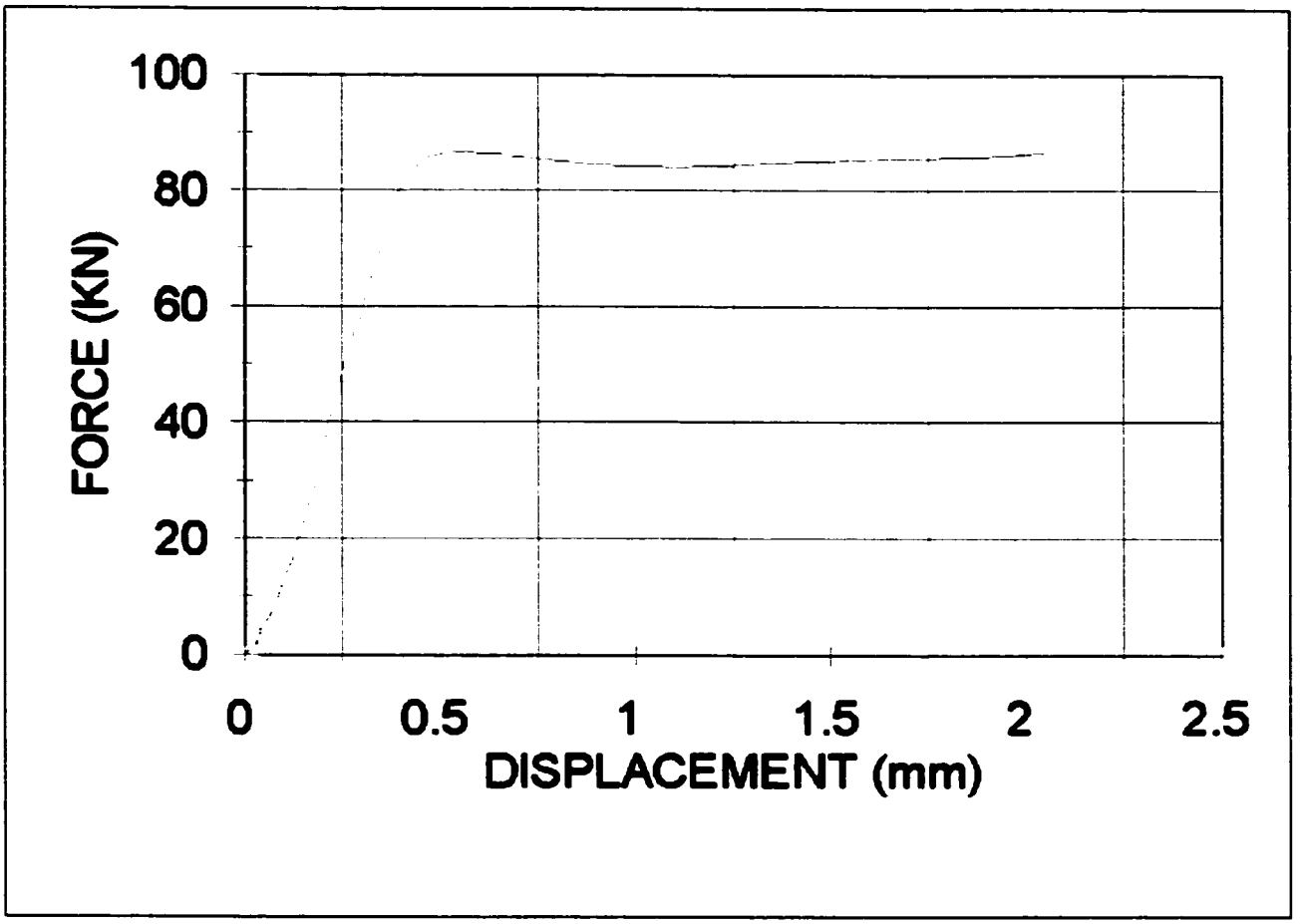

Figure 4.11 Force Displacement Curve for Specimen Five

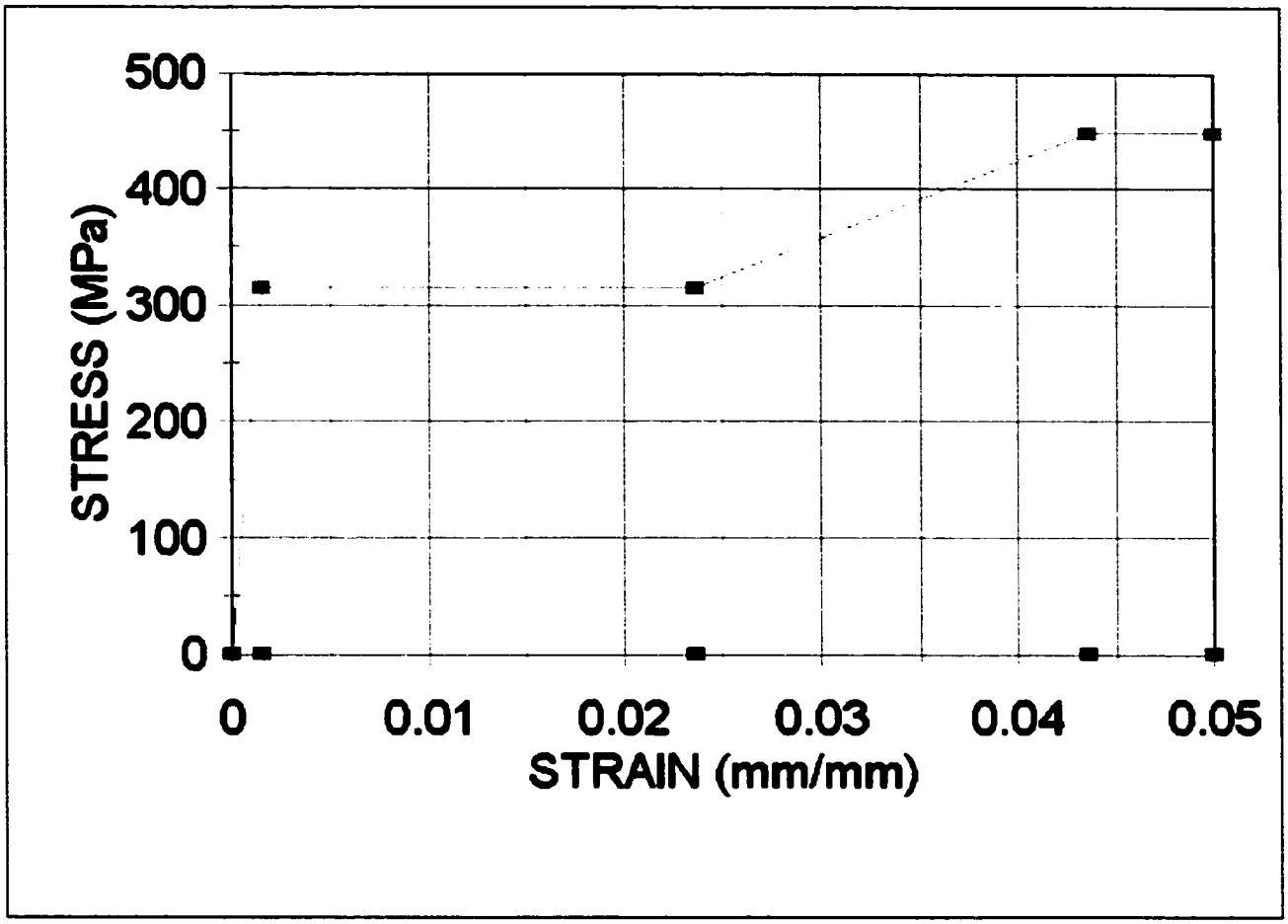

Figure 4.12 Stress Strain Relationship for Higher Yield Point

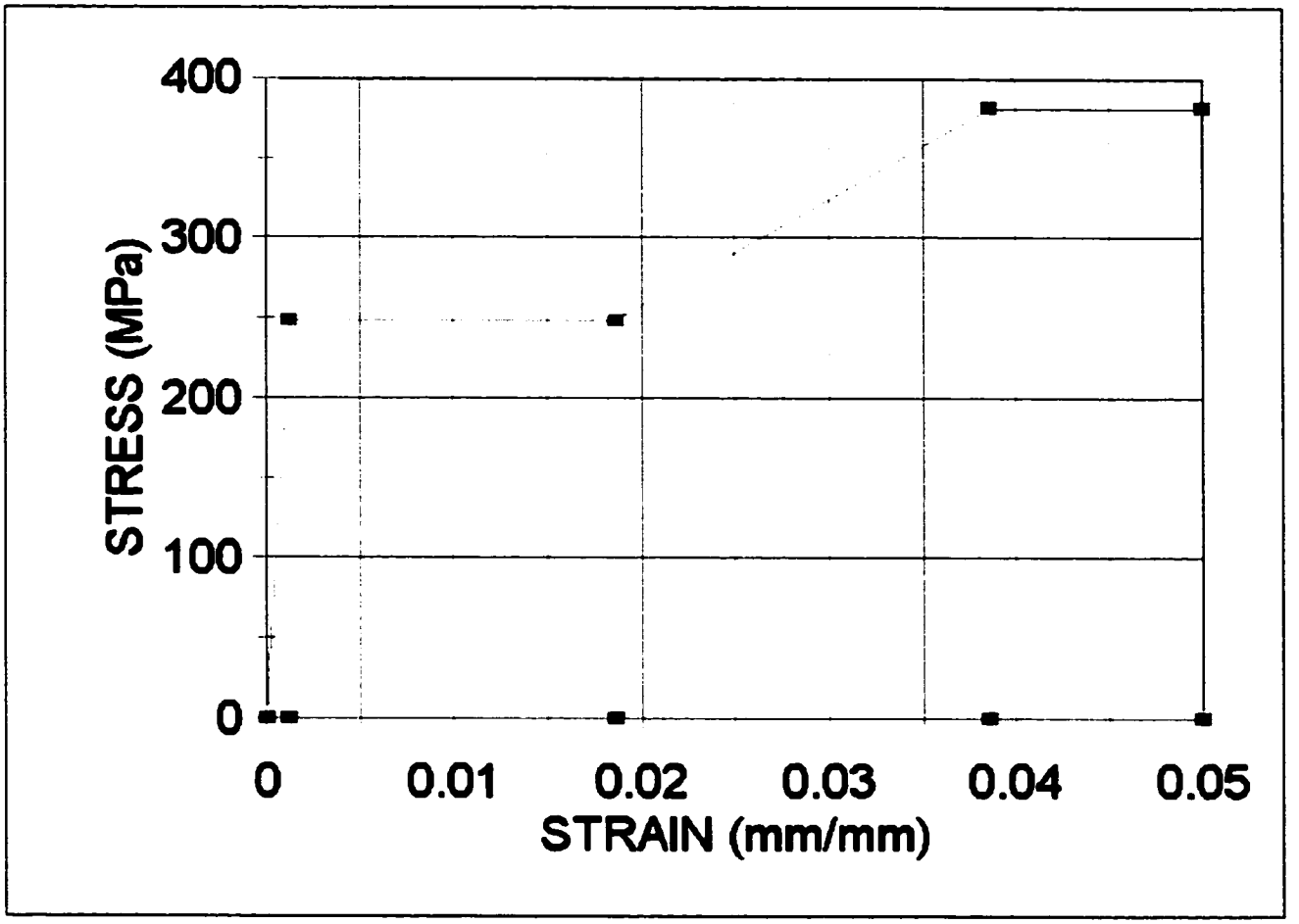

Figure 4.13 Stress Strain Relationship for Lower Yield Point

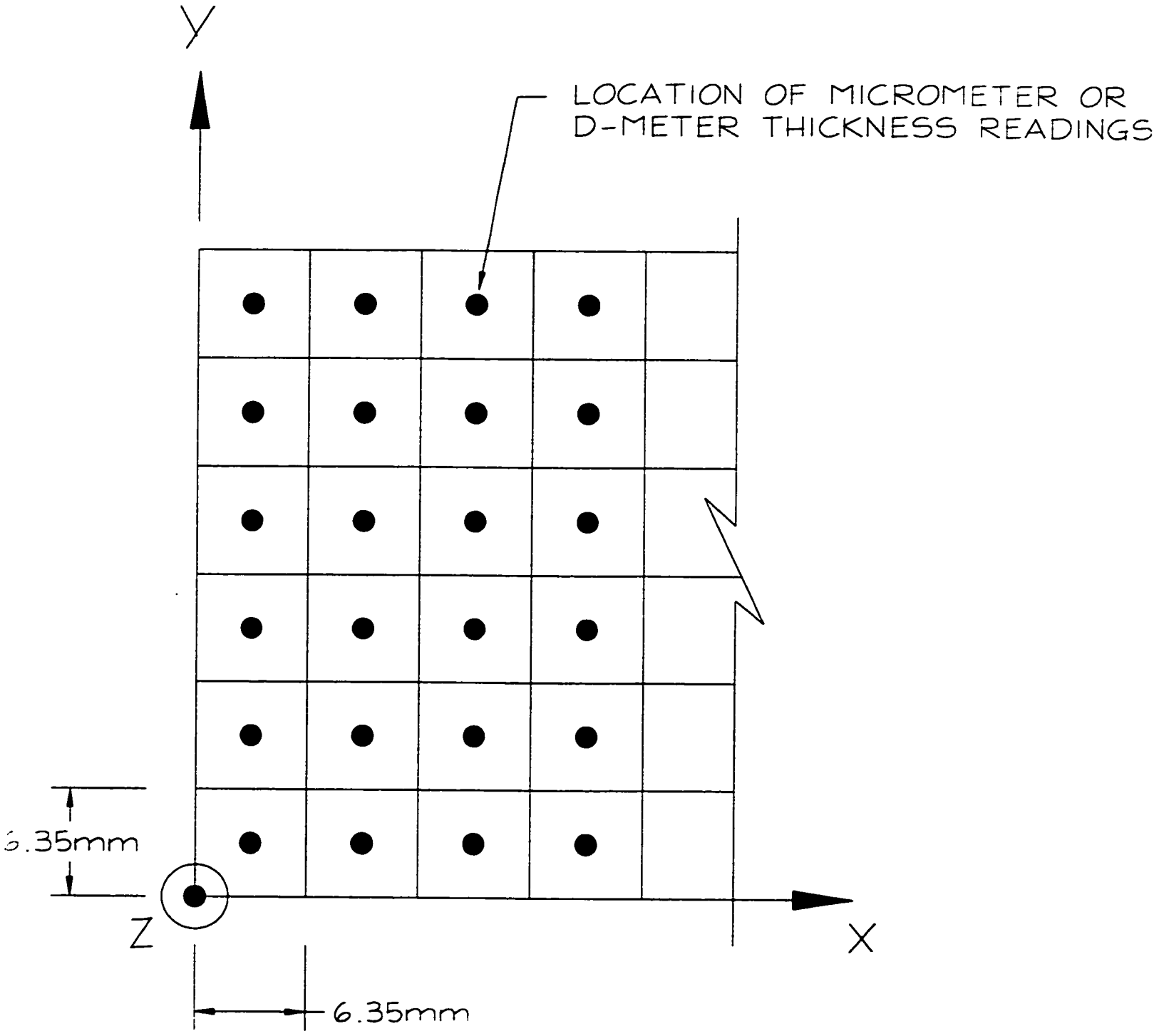

Figure 4.14 Location of Origin on the Specimen's Testing Surface

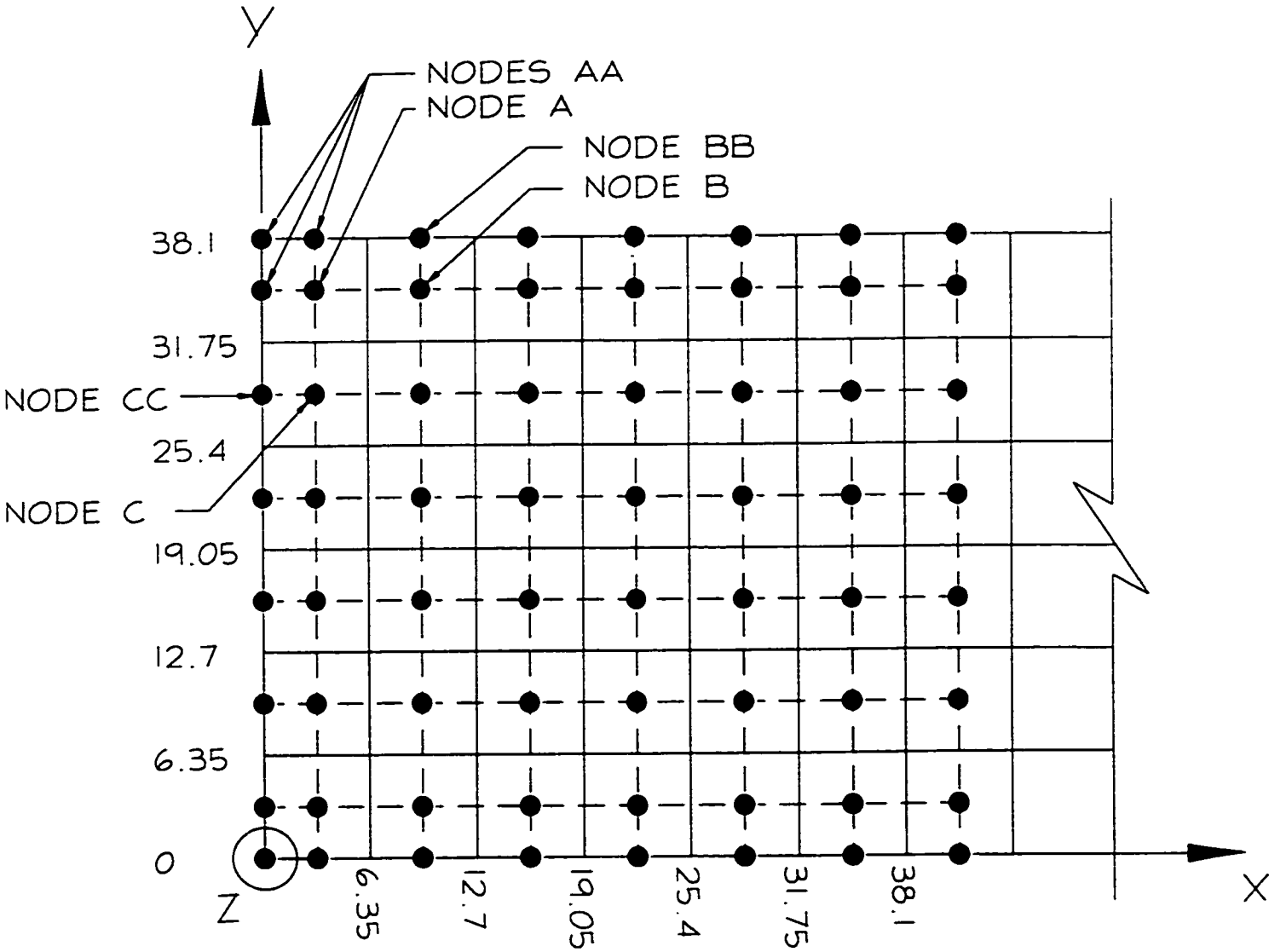

Figure 4.15 Construction Methodology for the Fine Mesh Geometric Model

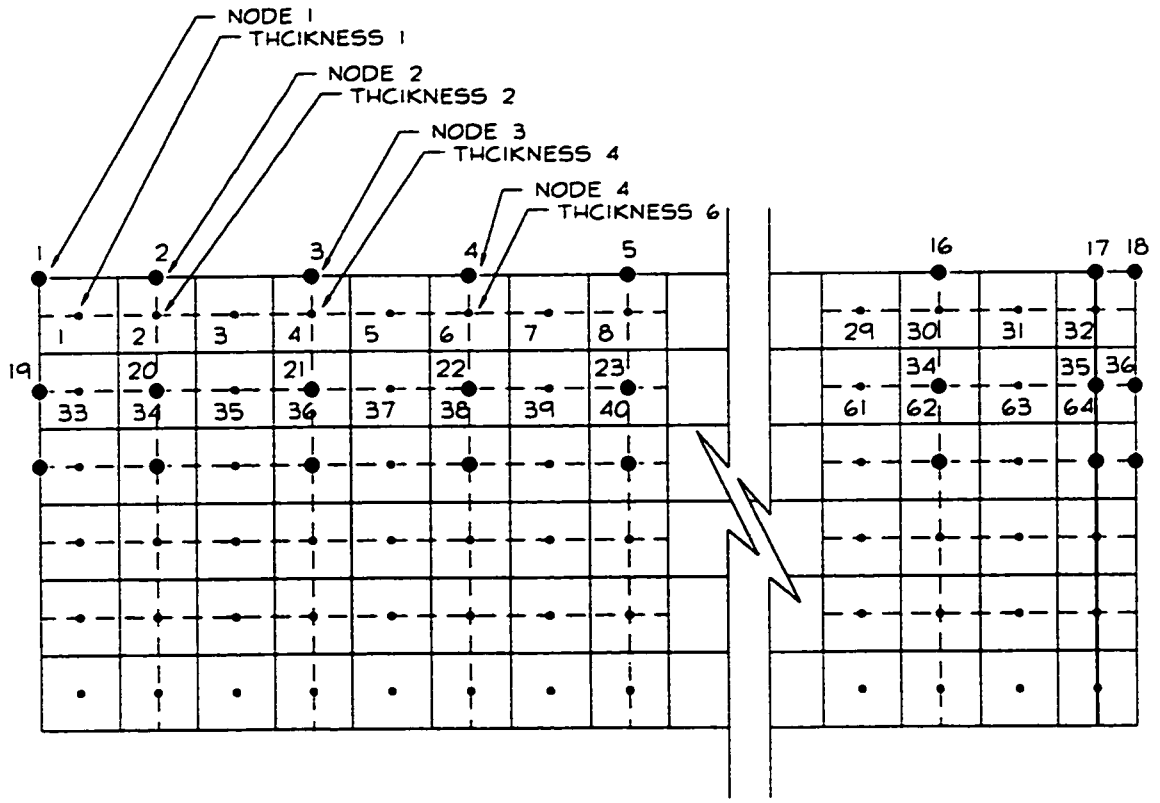

Figure 4.16 Construction Methodology for the Coarse Mesh Geometric Model

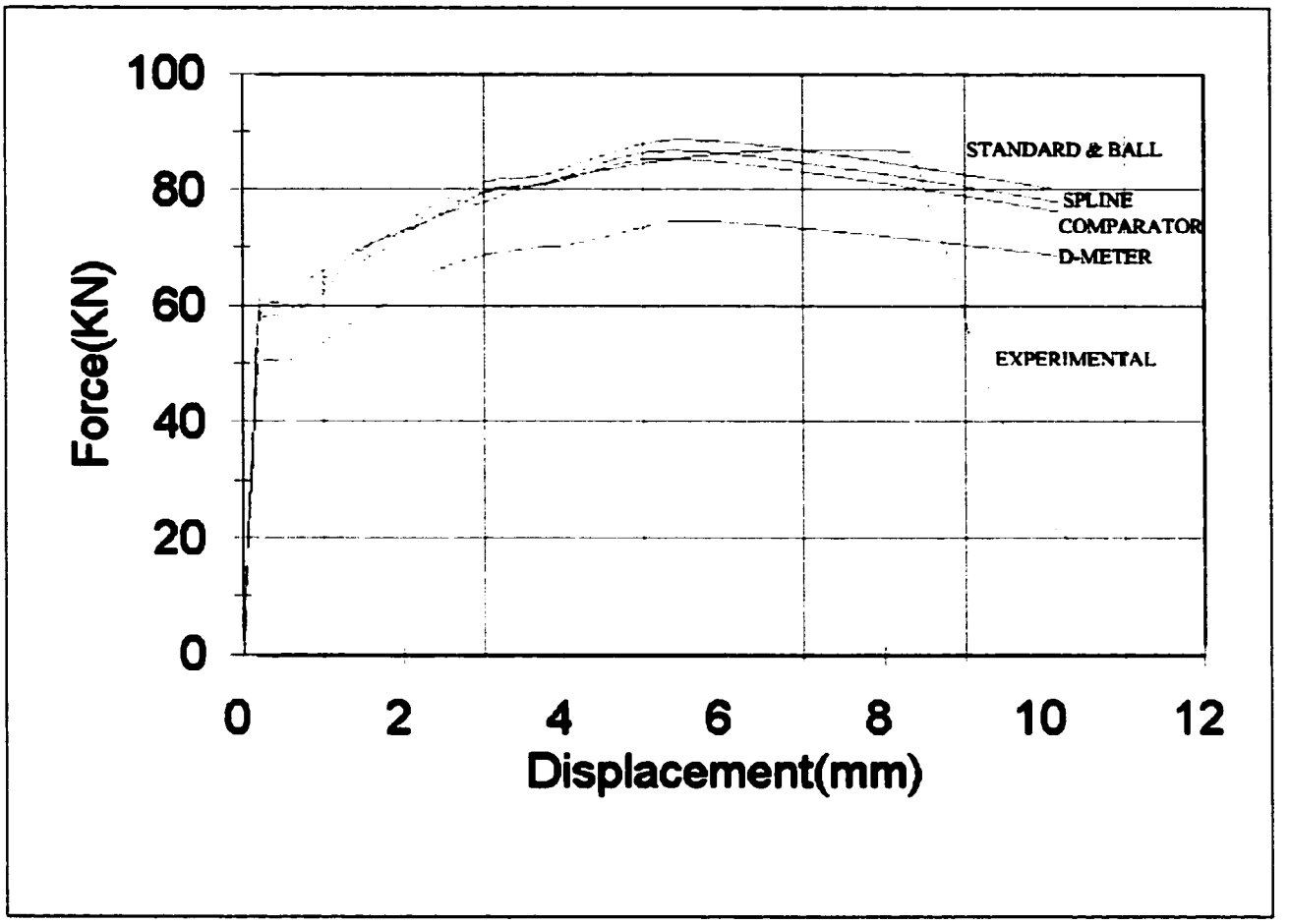

Figure 4.17 Force Displacement Curves for Sample#1 - Coarse Geometric Model - Yield Strength of 248.211 MPa

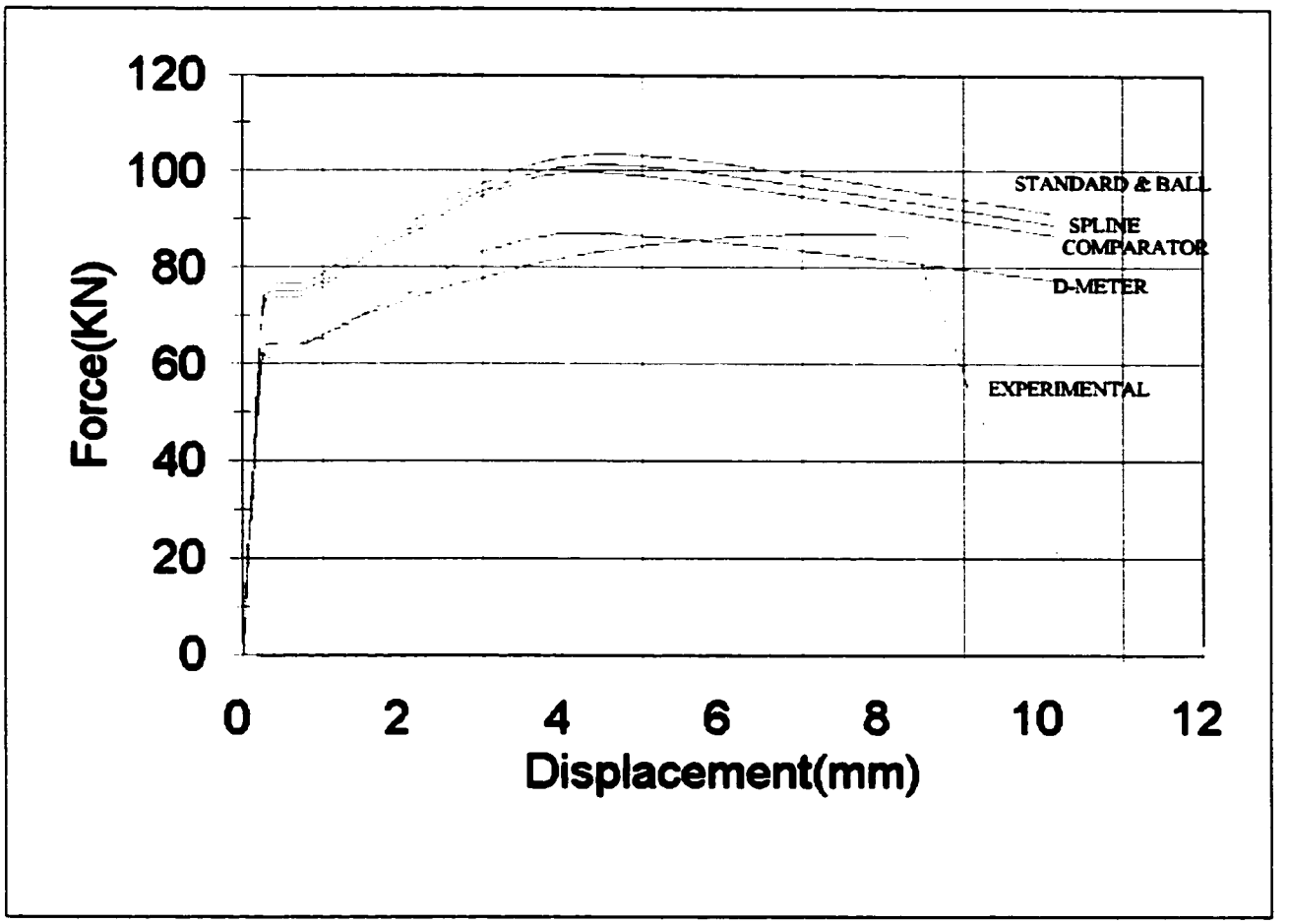

Figure 4.18 Force Displacement Curves for Sample#1 - Coarse Geometric Model - Yield Strength of 315.090 MPa

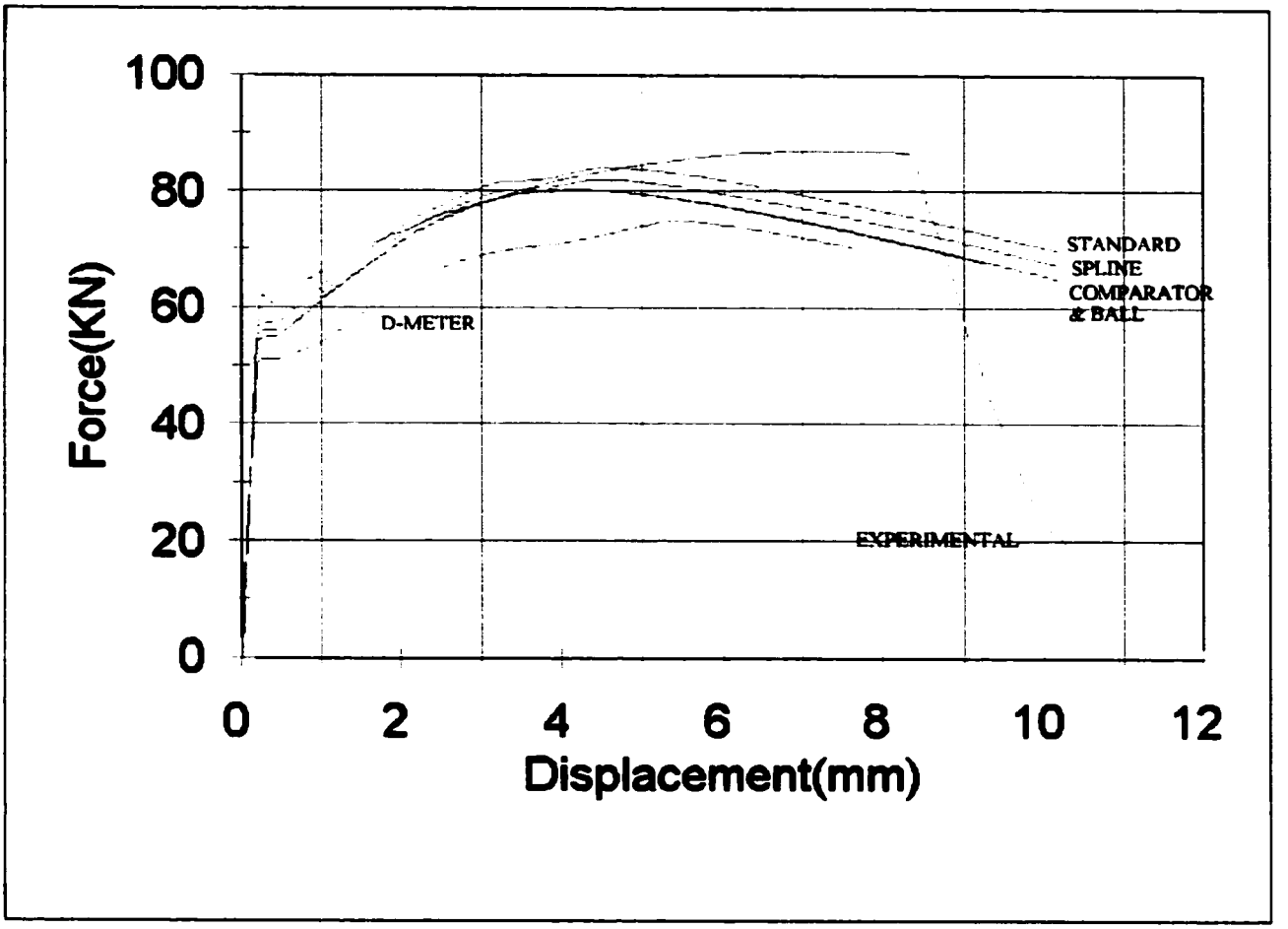

Figure 4.19 Force Displacement Curves for Sample#1 - Fine Geometric Model - Yield Strength of 248.211 MPa

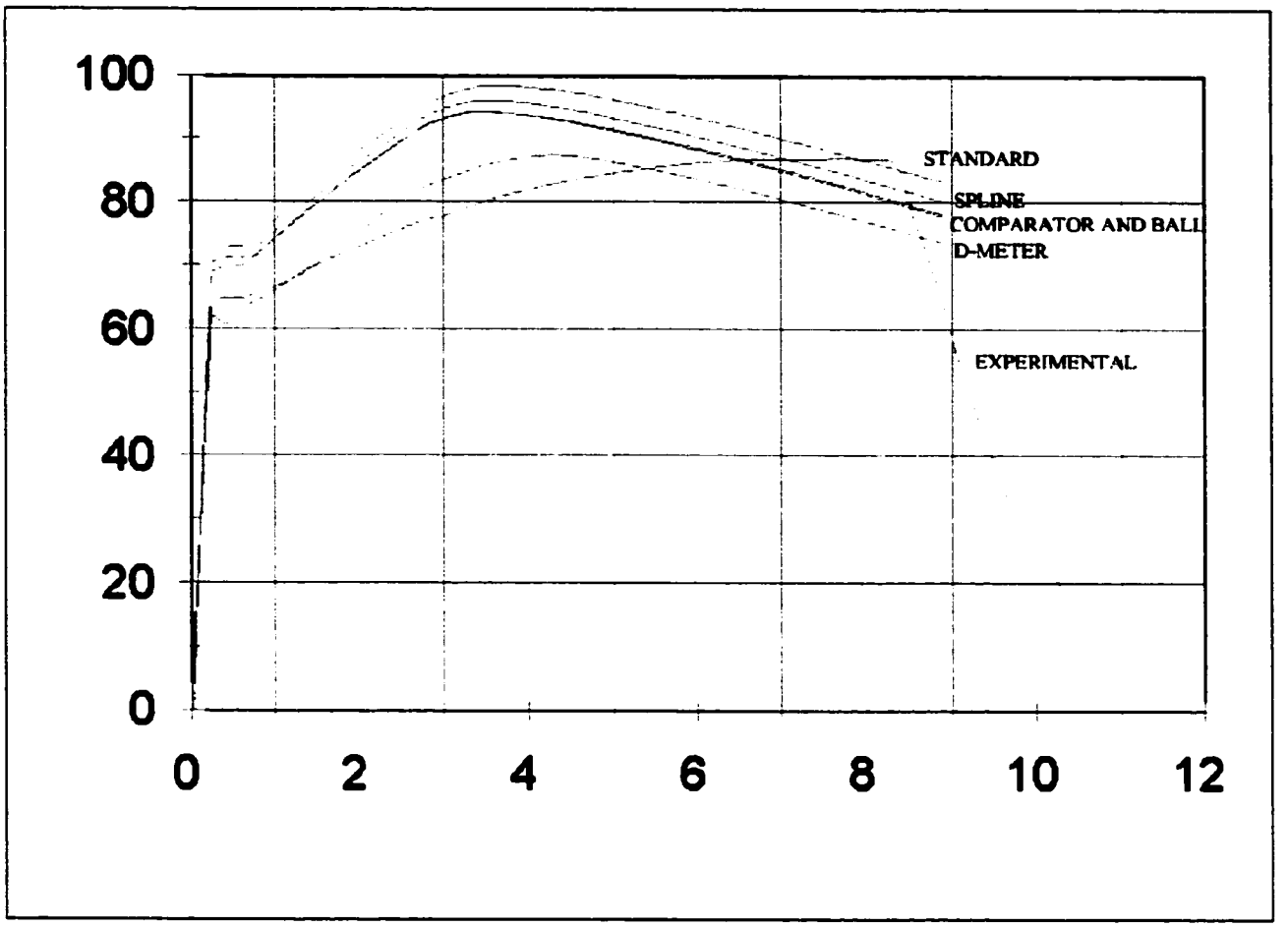

Figure 4.20 Force Displacement Curves for Sample#1 - Fine Geometric Model - Yield Strength of 315.090 MPa

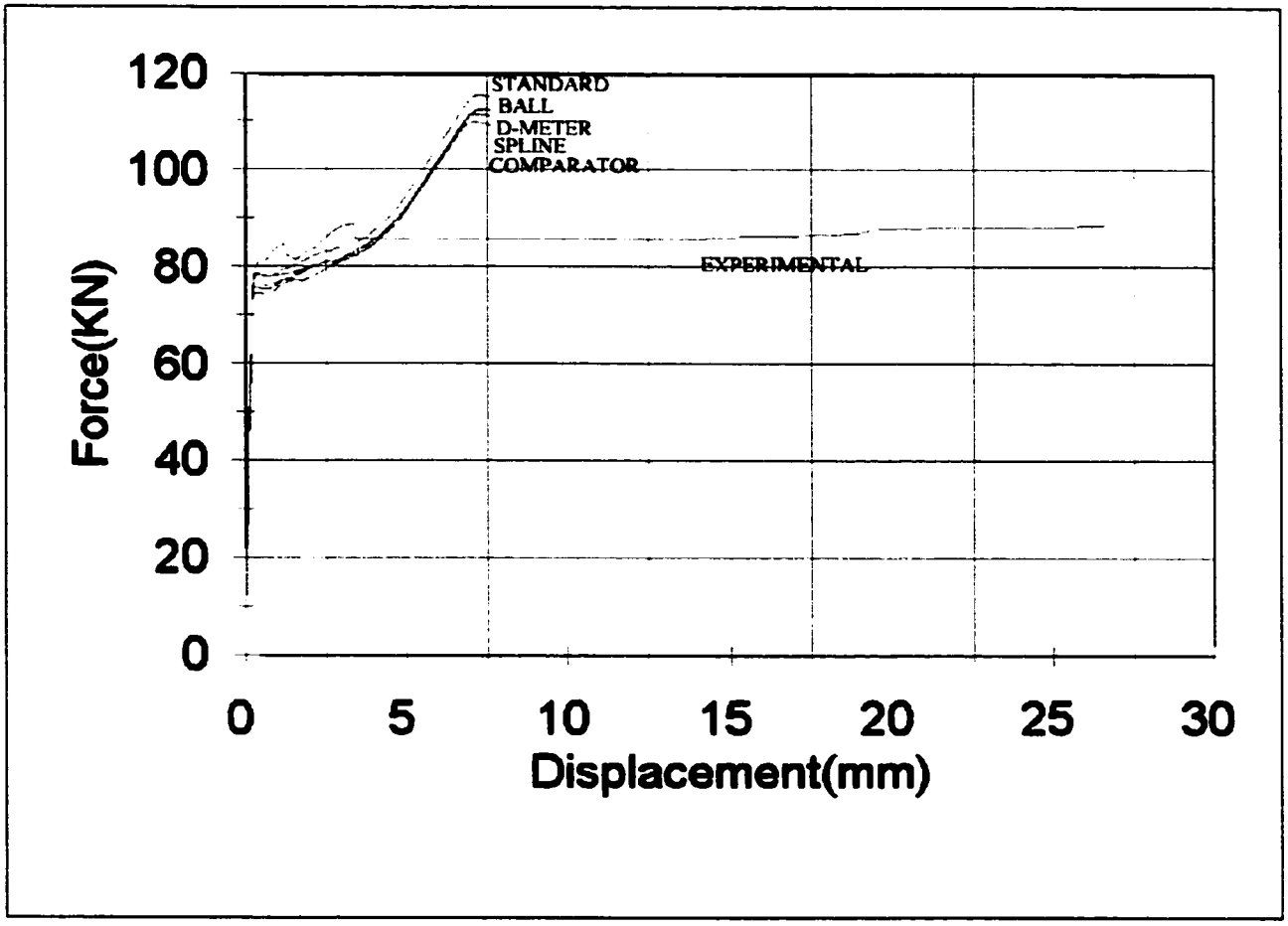

Figure 4.21 Force Displacement Curves for Specimen 2 - Coarse Geometric Model - Yield Strength of 248.2 MPa

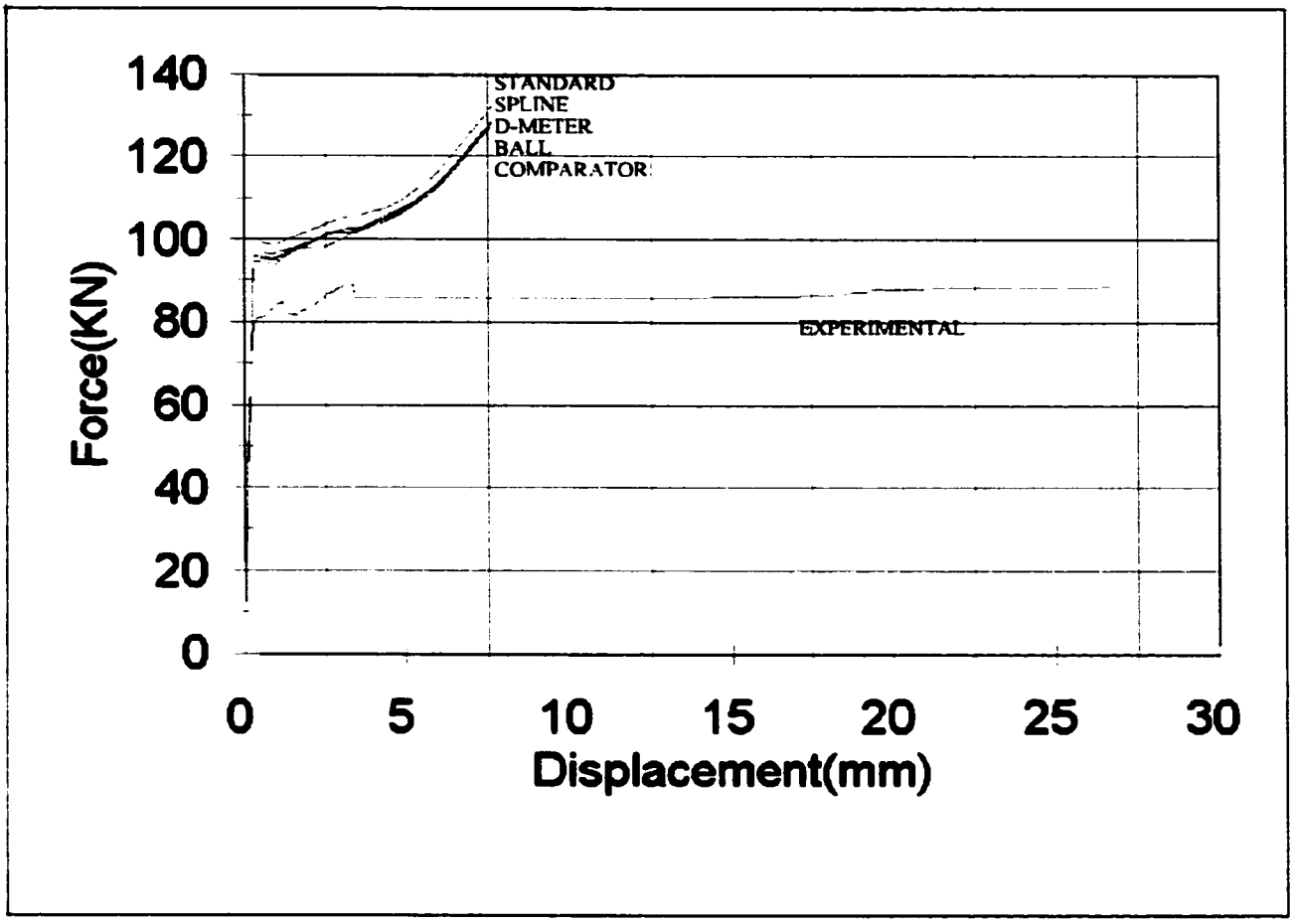

Figure 4.22 Force Displacement Curves for Specimen 2 - Coarse Geometric Model - Yield Strength of 315.1 MPa

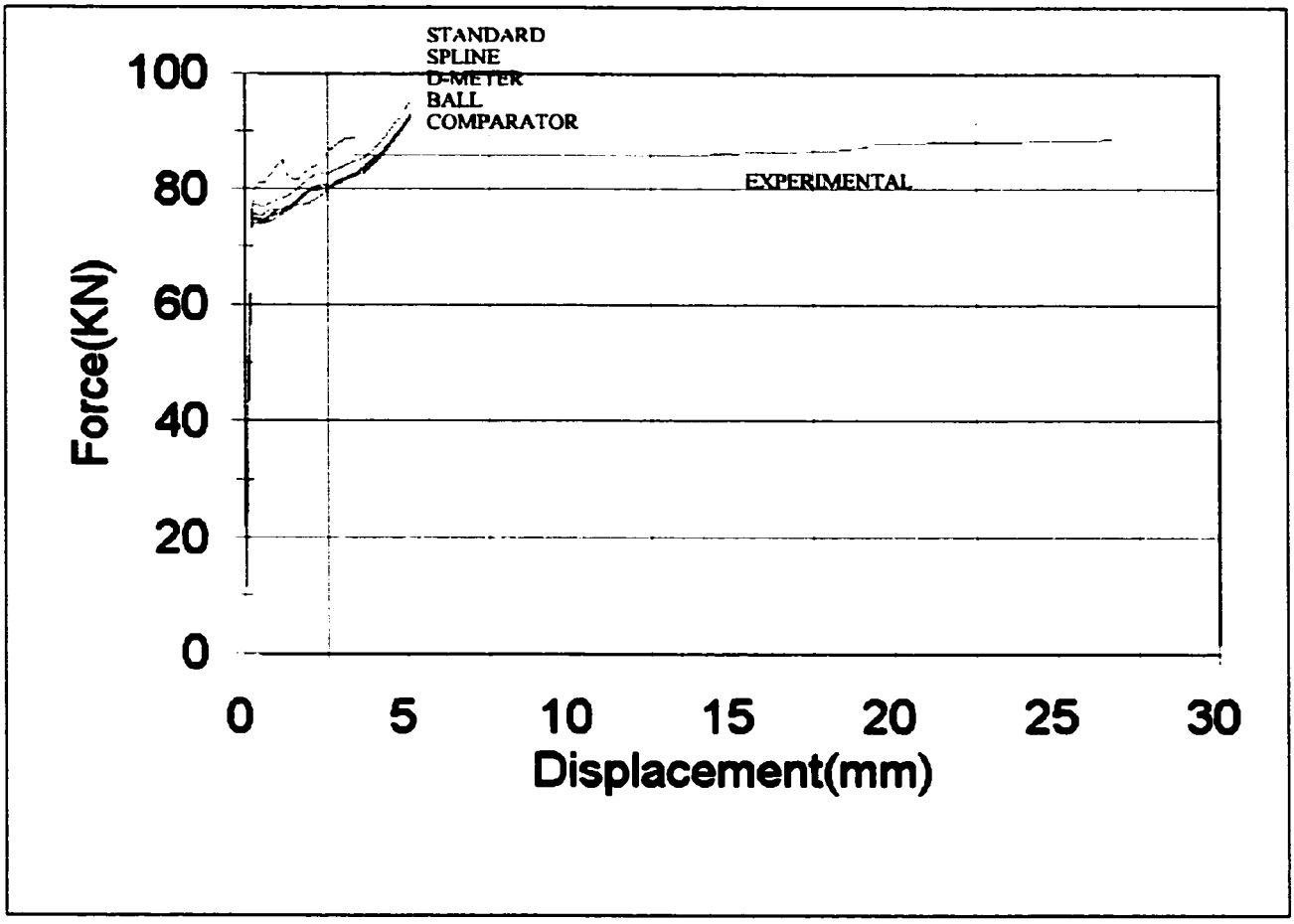

Figure 4.23 Force Displacement Curves for Specimen 2 - Fine Geometric Model - Yield Strength of 248.2 MPa

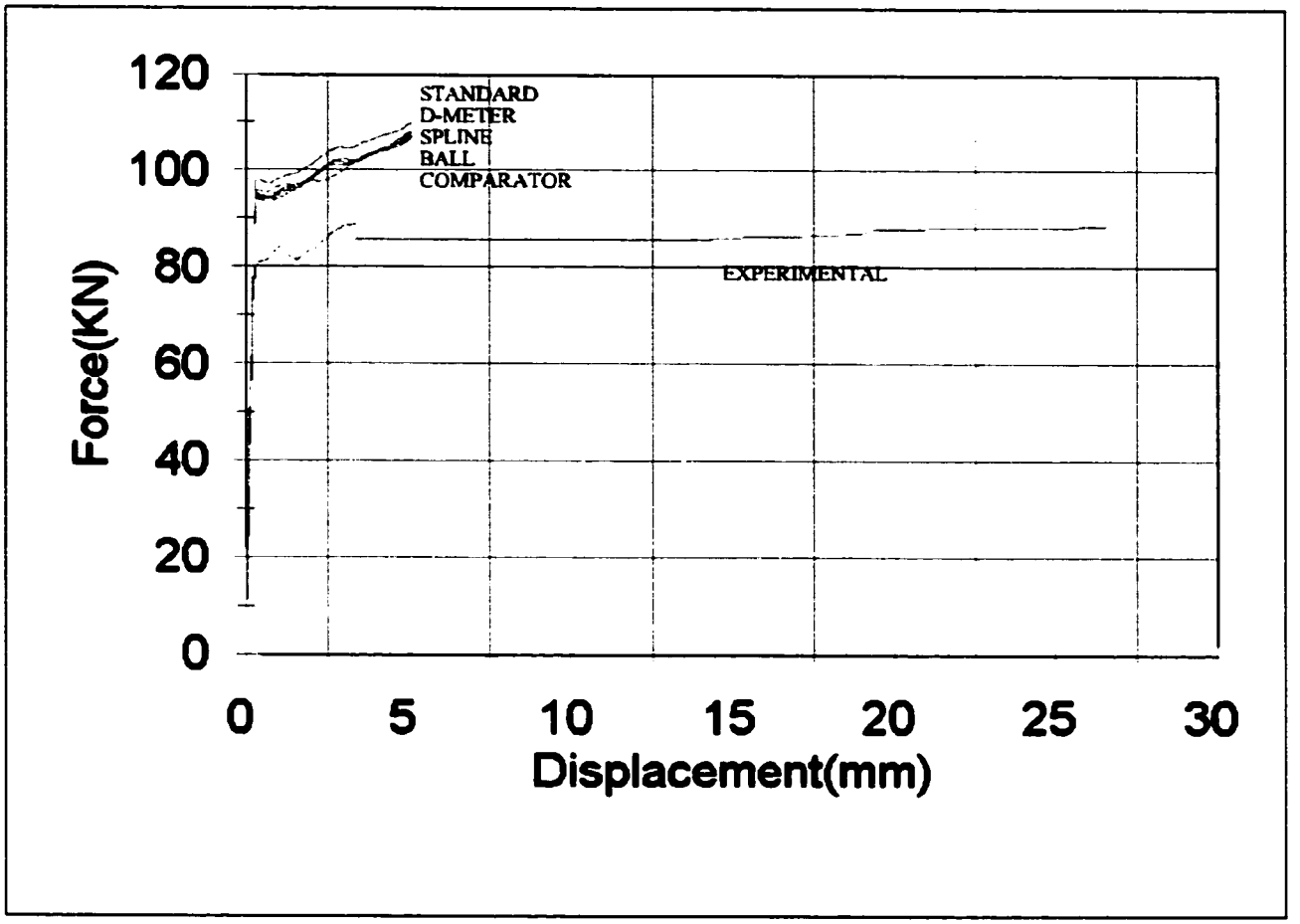

Figure 4.24 Force Displacement Curves for Specimen 2 - Fine Geometric Model - Yield Strength of 315.1 MPa

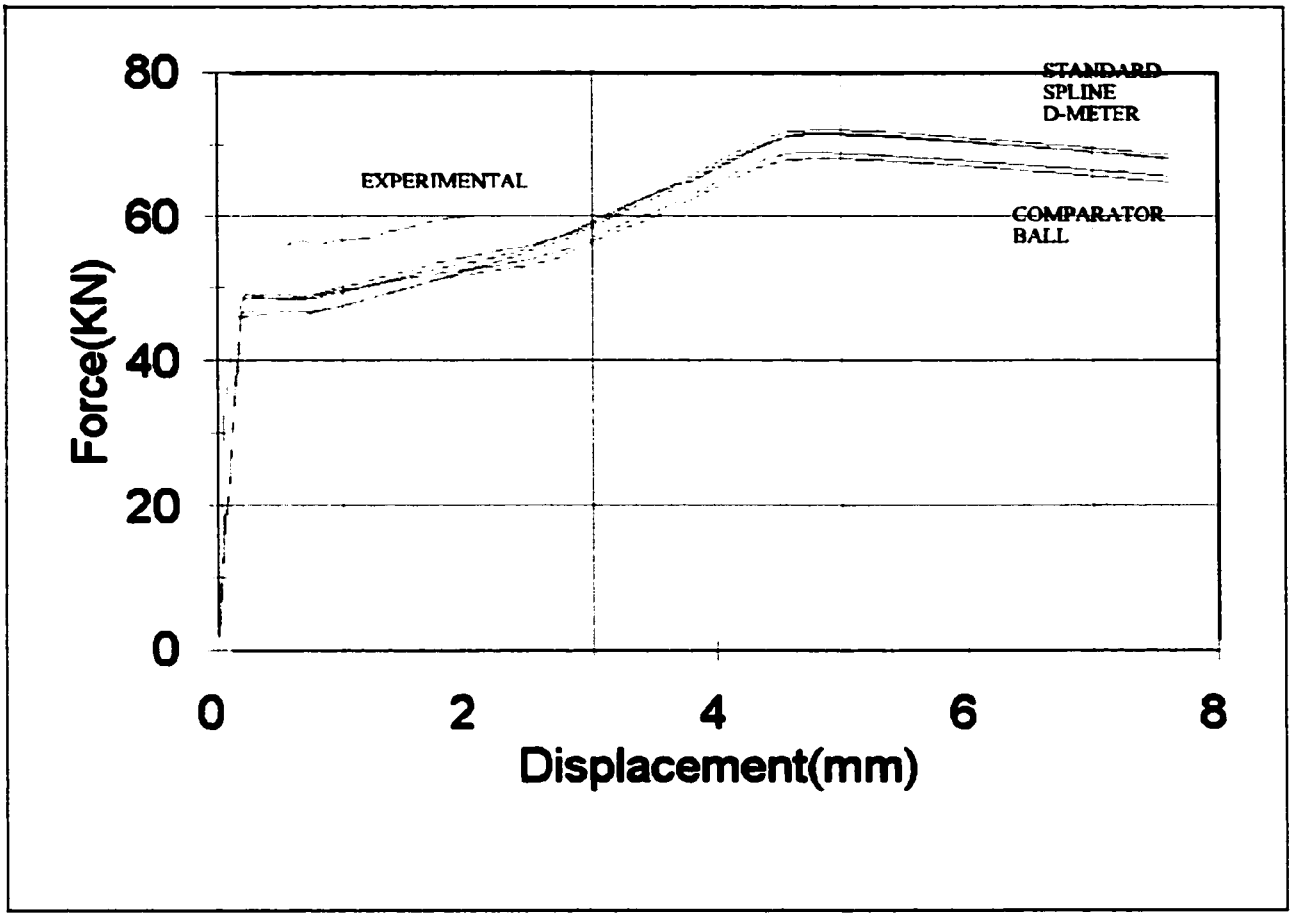

Figure 4.25 Force Displacement Curves for Specimen 3 - Coarse Geometric Model - Yield Strength of 248.2 MPa

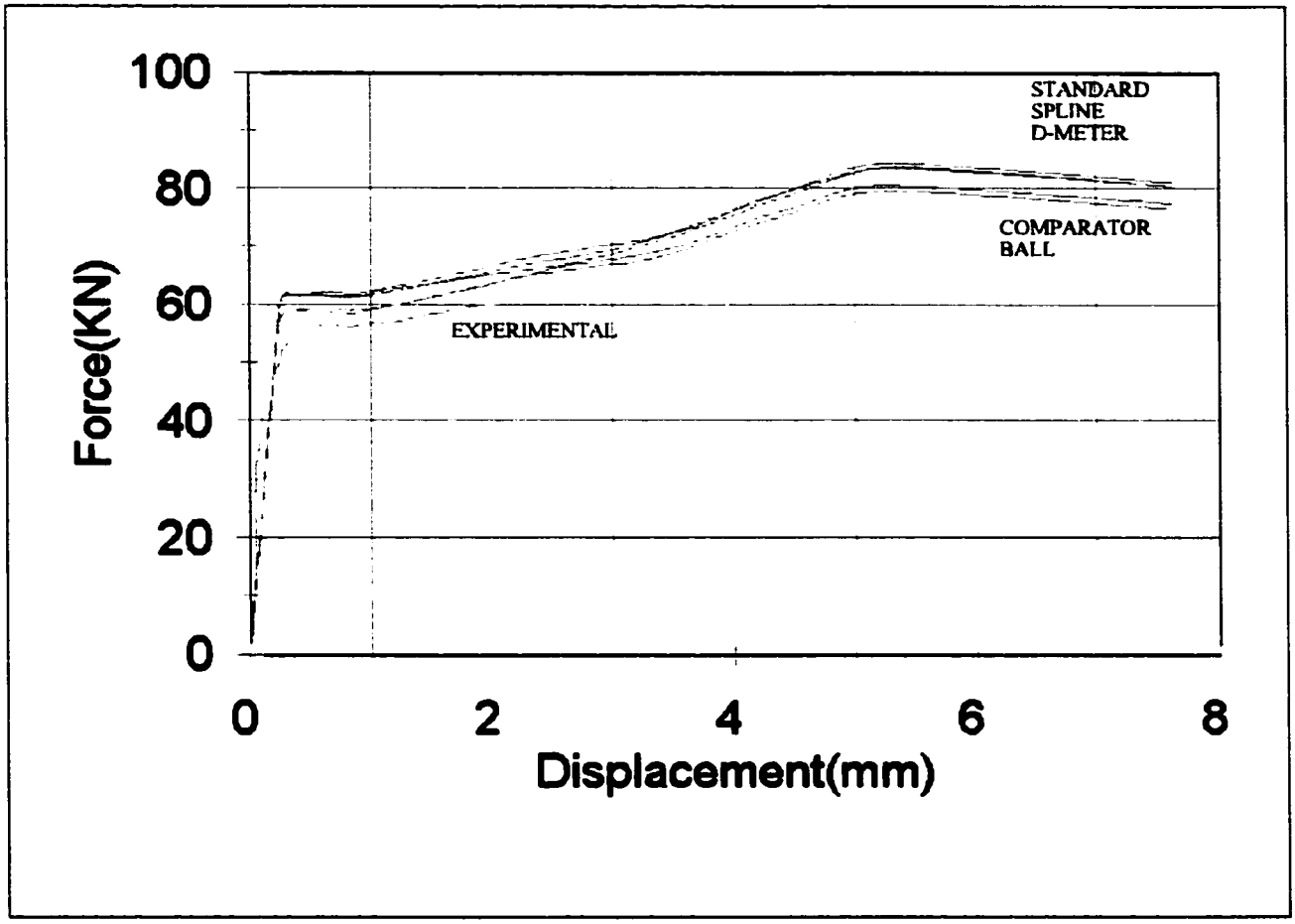

Figure 4.26 Force Displacement Curves for Specimen 3 - Coarse Geometric Model - Yield Strength of 315.1 MPa

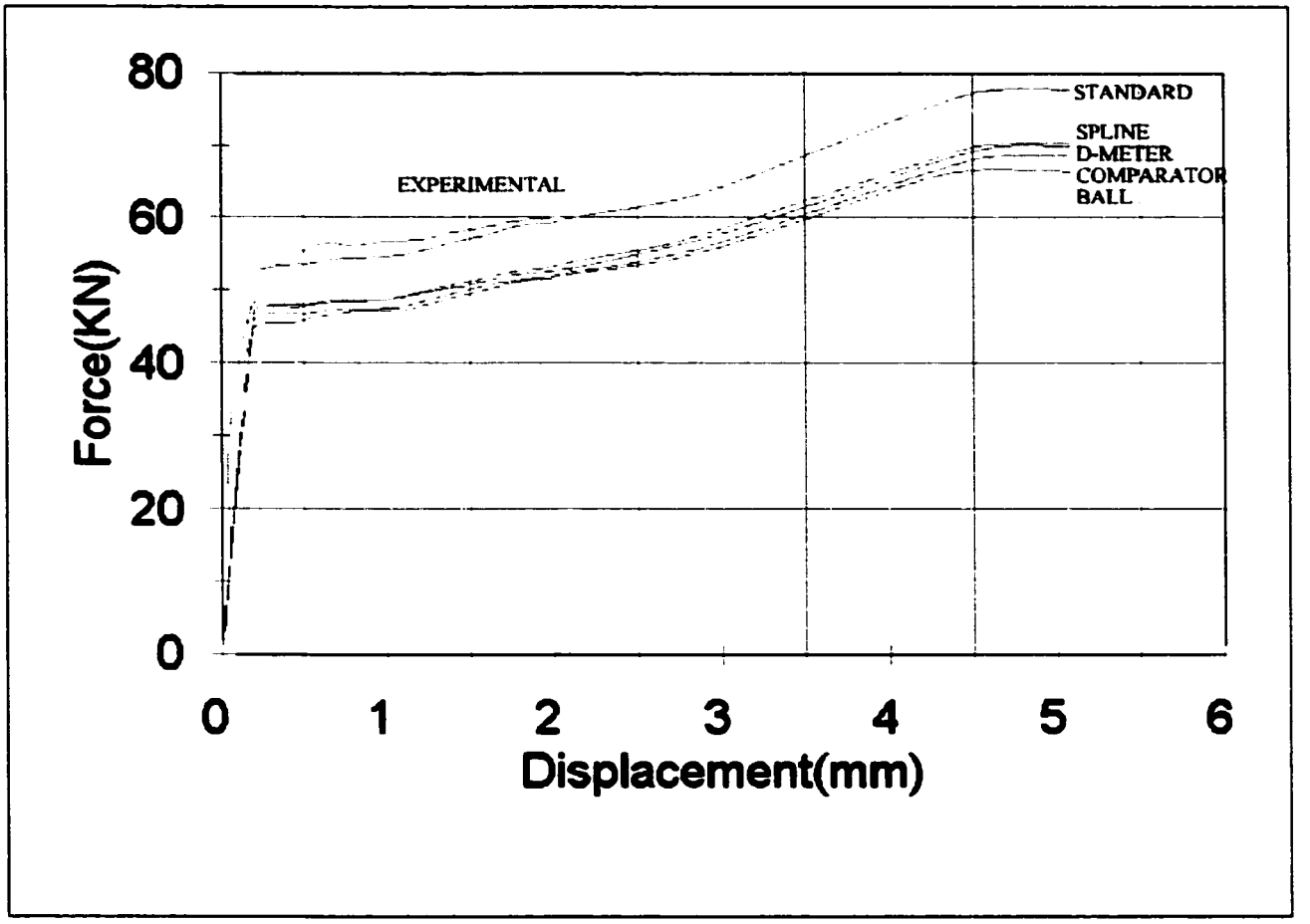

Figure 4.27 Force Displacement Curves for Specimen 3 - Fine Geometric Model - Yield Strength of 248.2 MPa

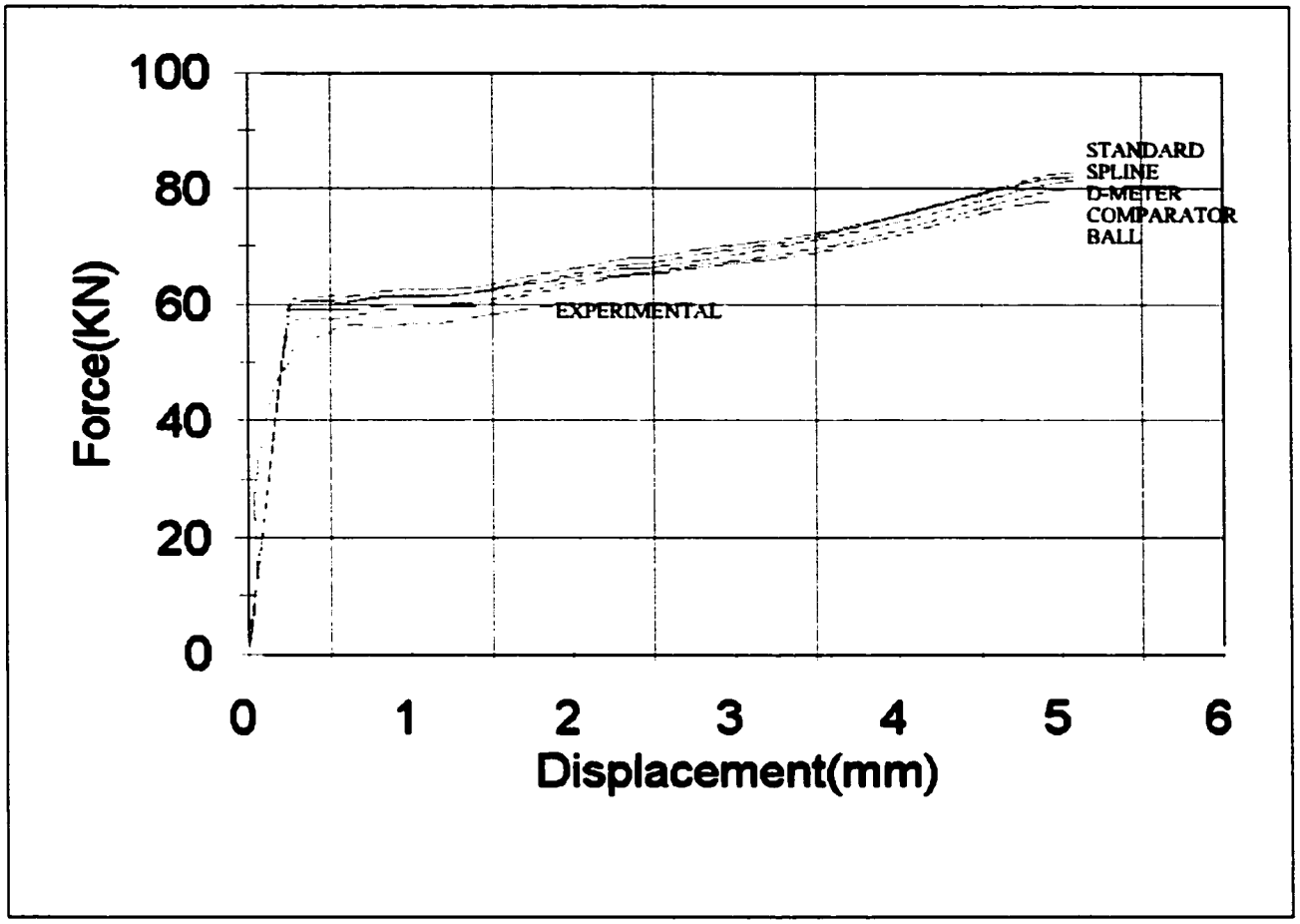

Figure 4.28 Force Displacement Curves for Specimen 3 - Fine Geometric Model - Yield Strength of 315.1 MPa

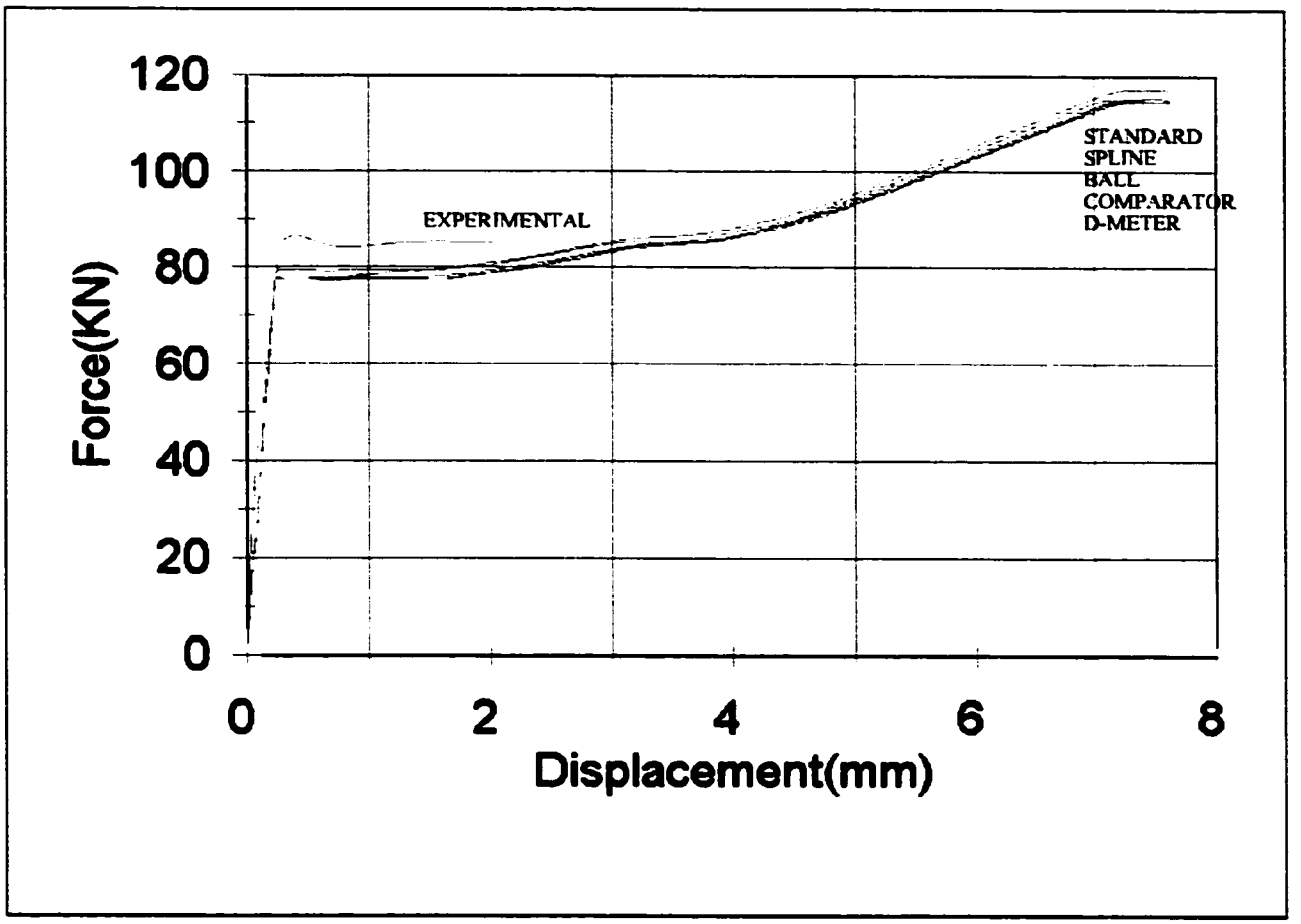

Figure 4.29 Force Displacement Curves for Specimen 4 - Coarse Geometric Model - Yield Strength of 248.2 MPa

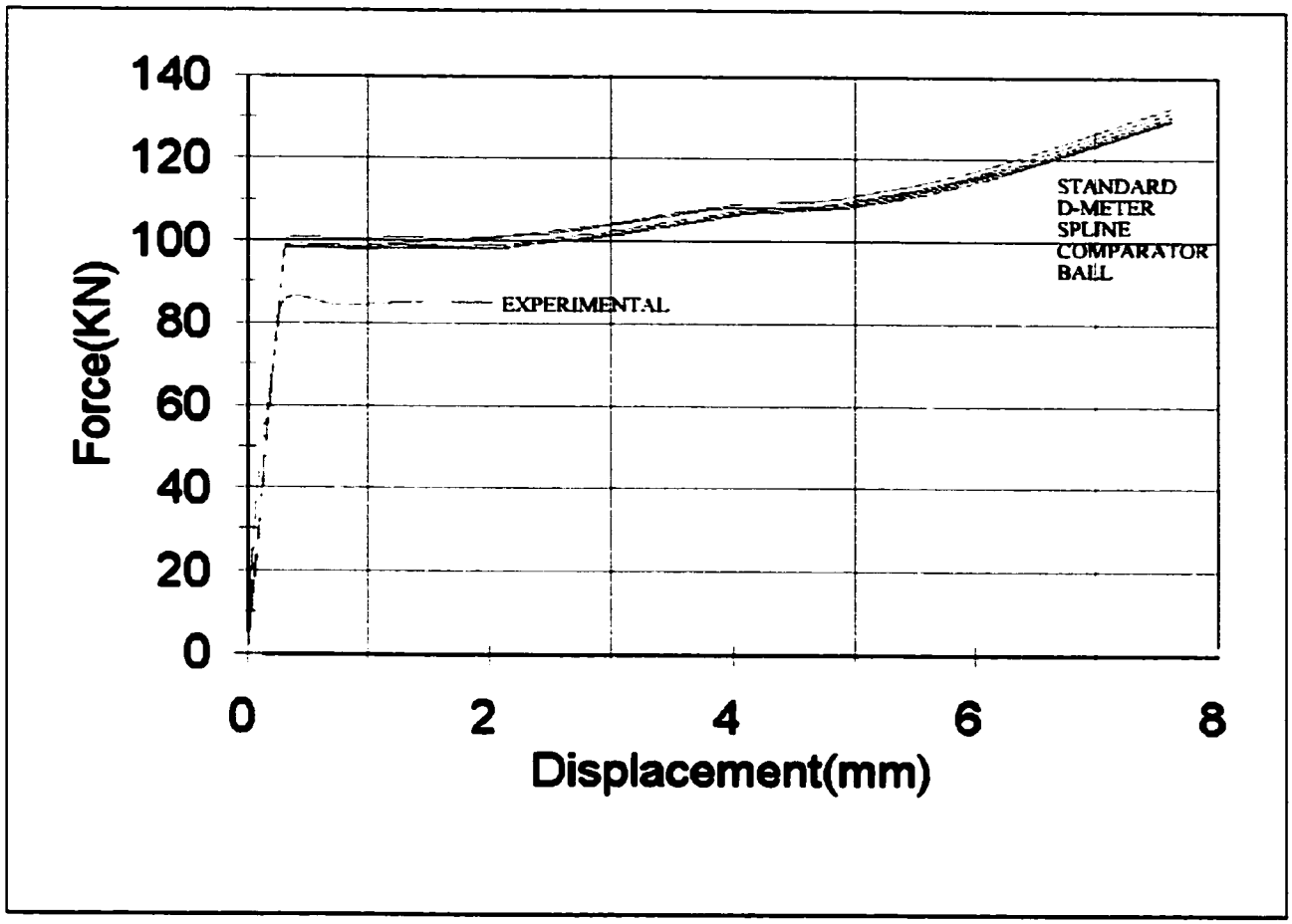

Figure 4.30 Force Displacement Curves for Specimen 4 - Coarse Geometric Model - Yield Strength of 315.1 MPa

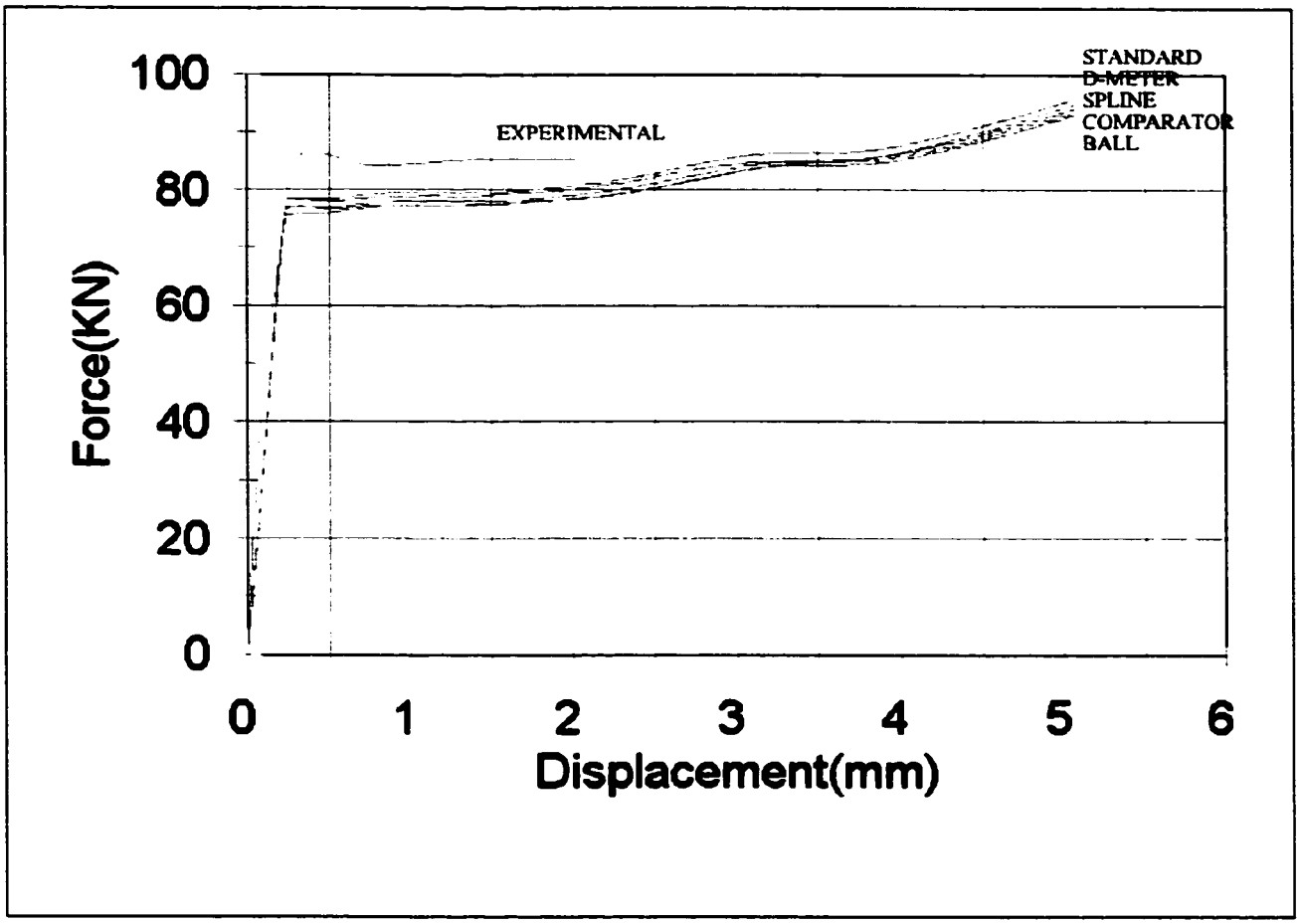

Figure 4.31 Force Displacement Curves for Specimen 4 - Fine Geometric Model - Yield Strength of 248.2 MPa

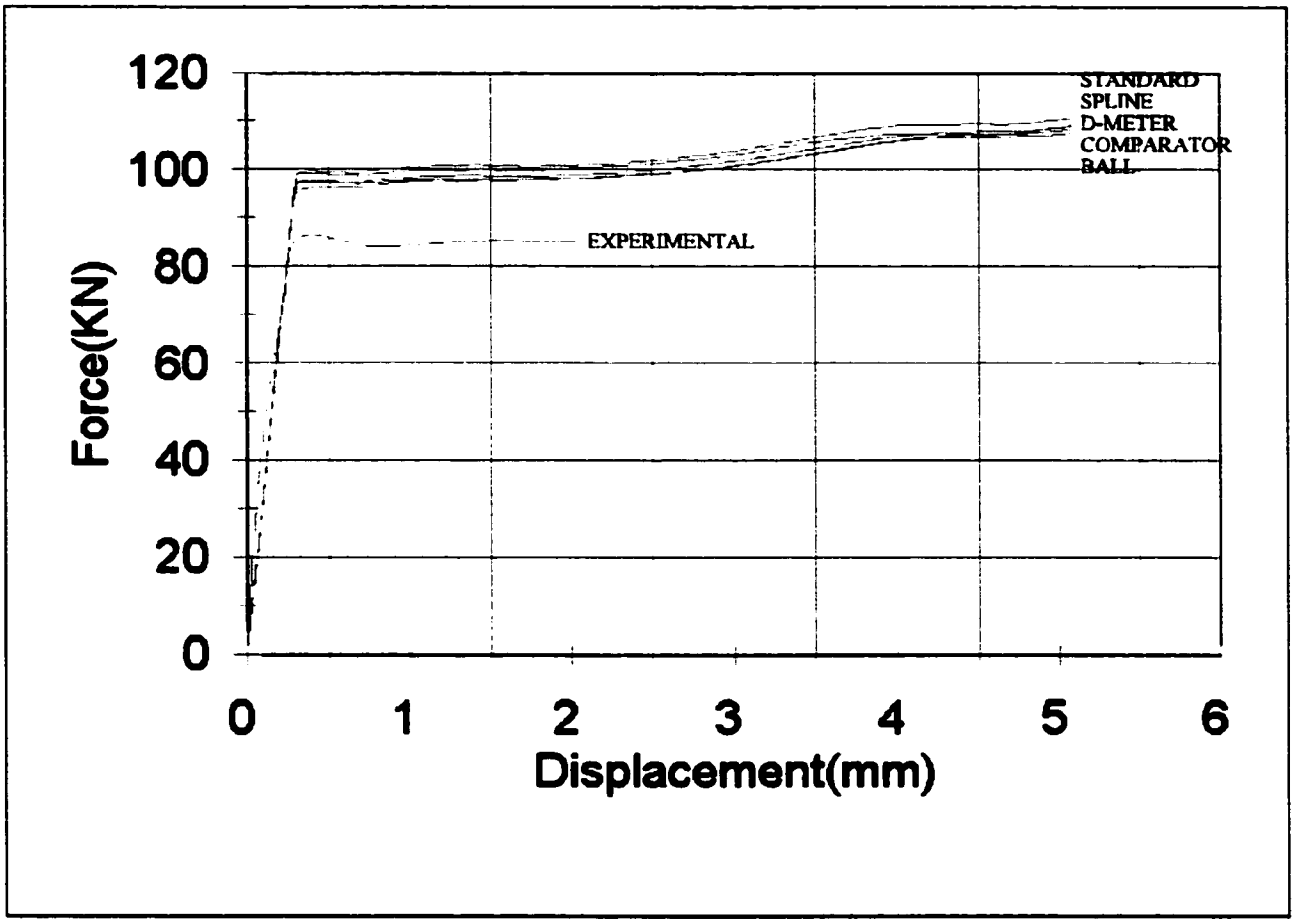

Figure 4.32 Force Displacement Curves for Specimen 4 - Fine Geometric Model - Yield Strength of 315.1 MPa

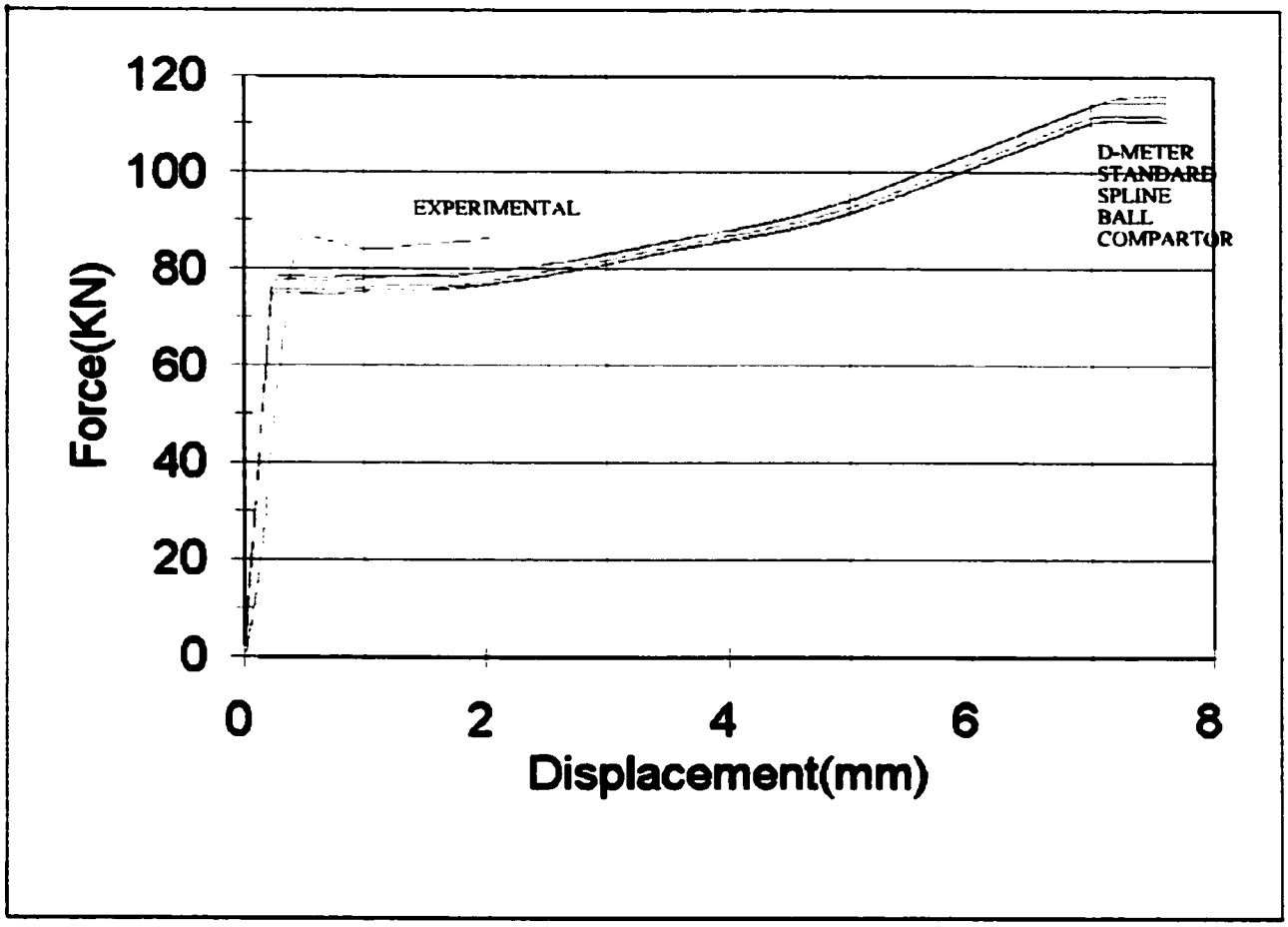

Figure 4.33 Force Displacement Curves for Specimen 5 - Coarse Geometric Model - Yield Strength of 248.2 MPa

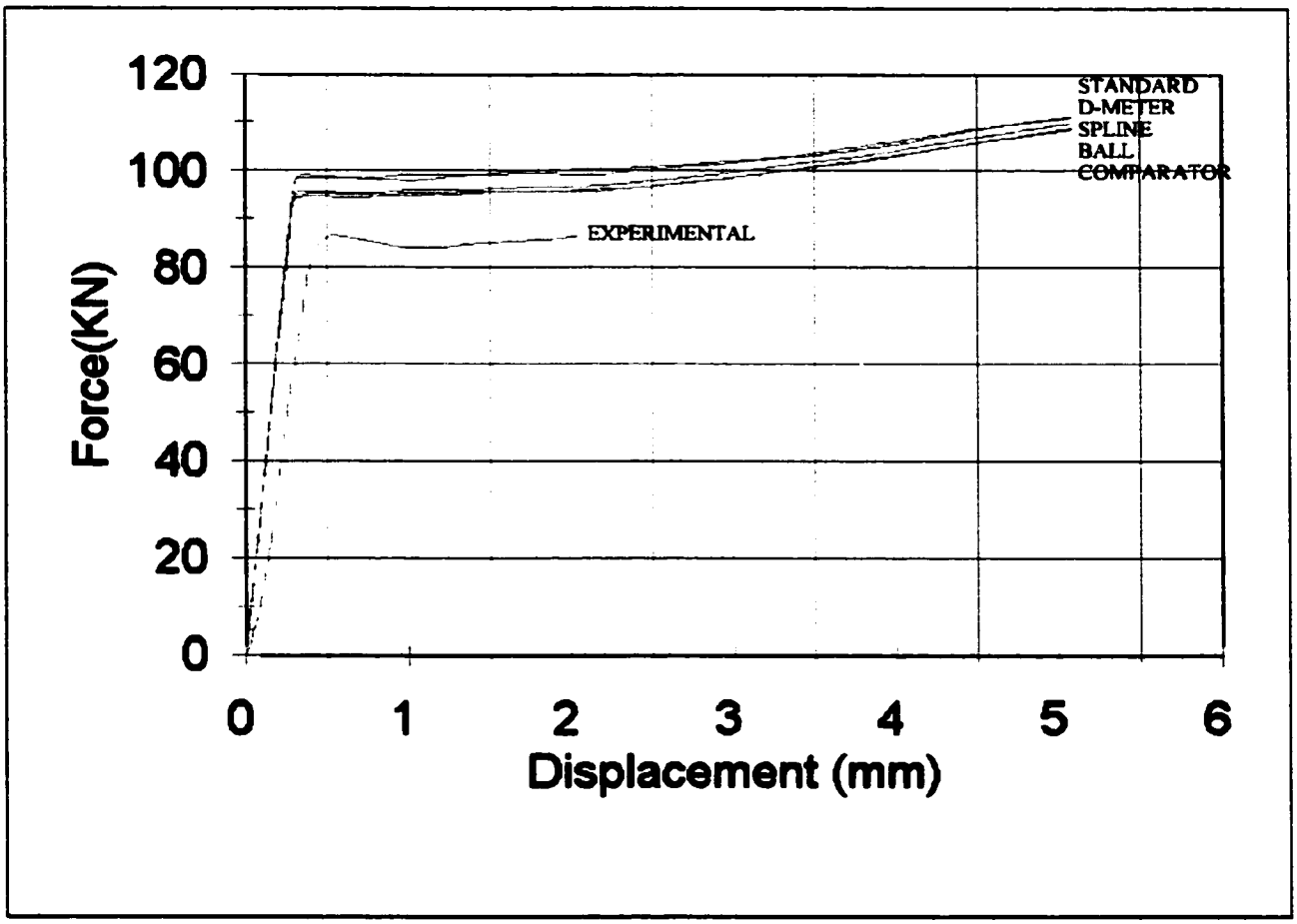

Figure 4.34 Force Displacement Curves for Specimen 5 - Coarse Geometric Model - Yield Strength of 315.1 MPa

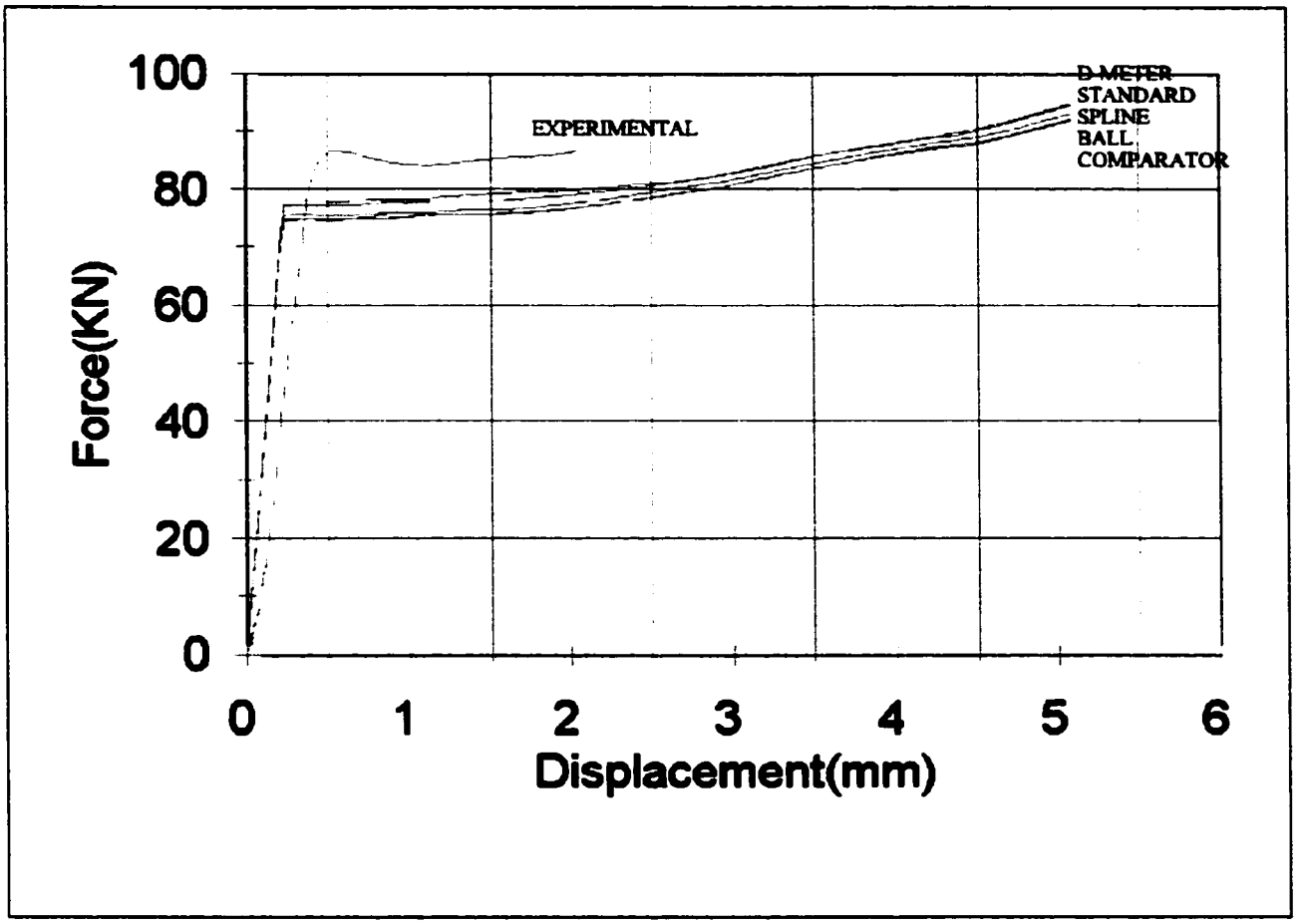

Figure 4.35 Force Displacement Curves for Specimen 5 - Fine Geometric Model - Yield Strength of 248.2 MPa

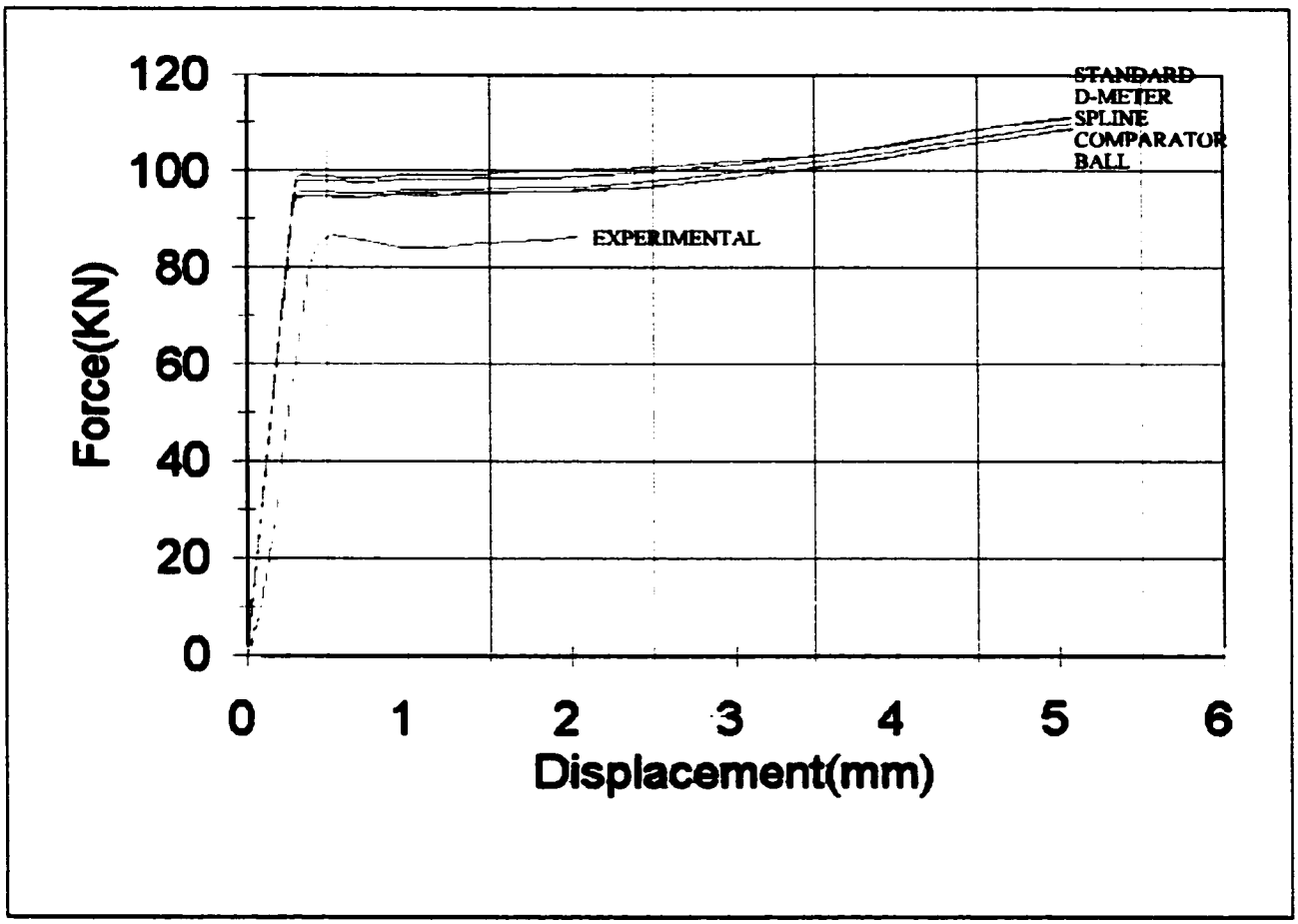

Figure 4.36 Force Displacement Curves for Specimen 5 - Fine Geometric Model - Yield Strength of 315.1 MPa

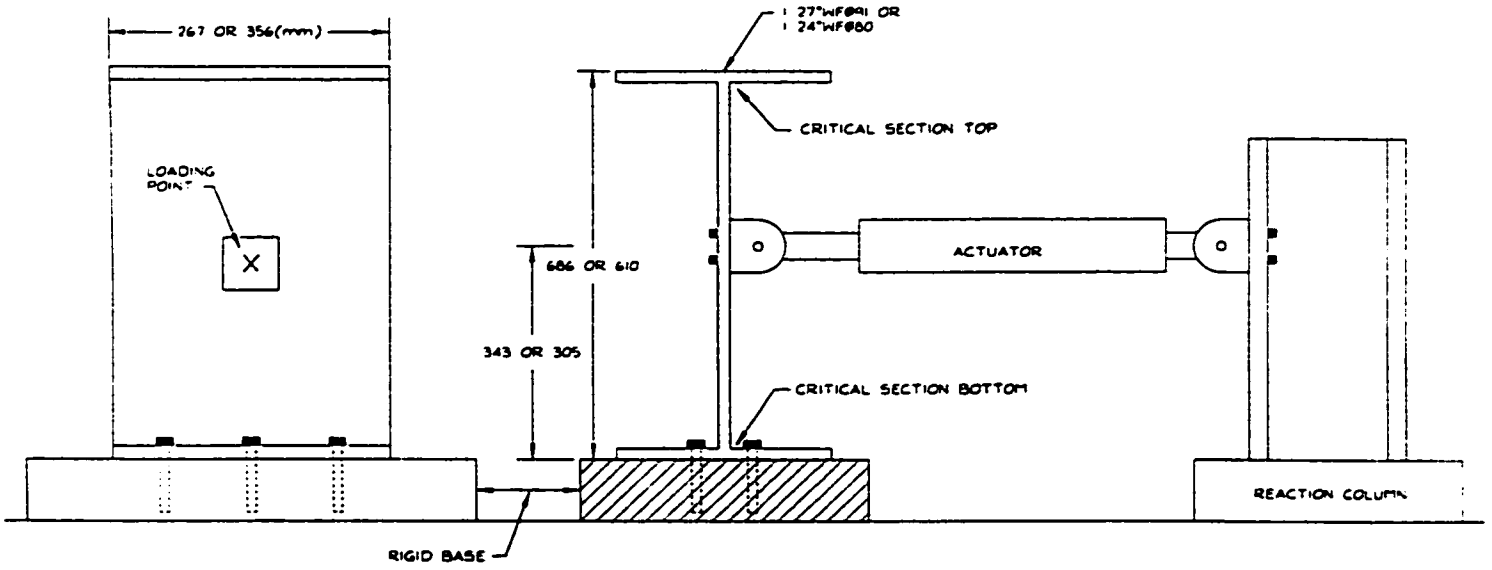

Figure 5.1 Experimental Set Up

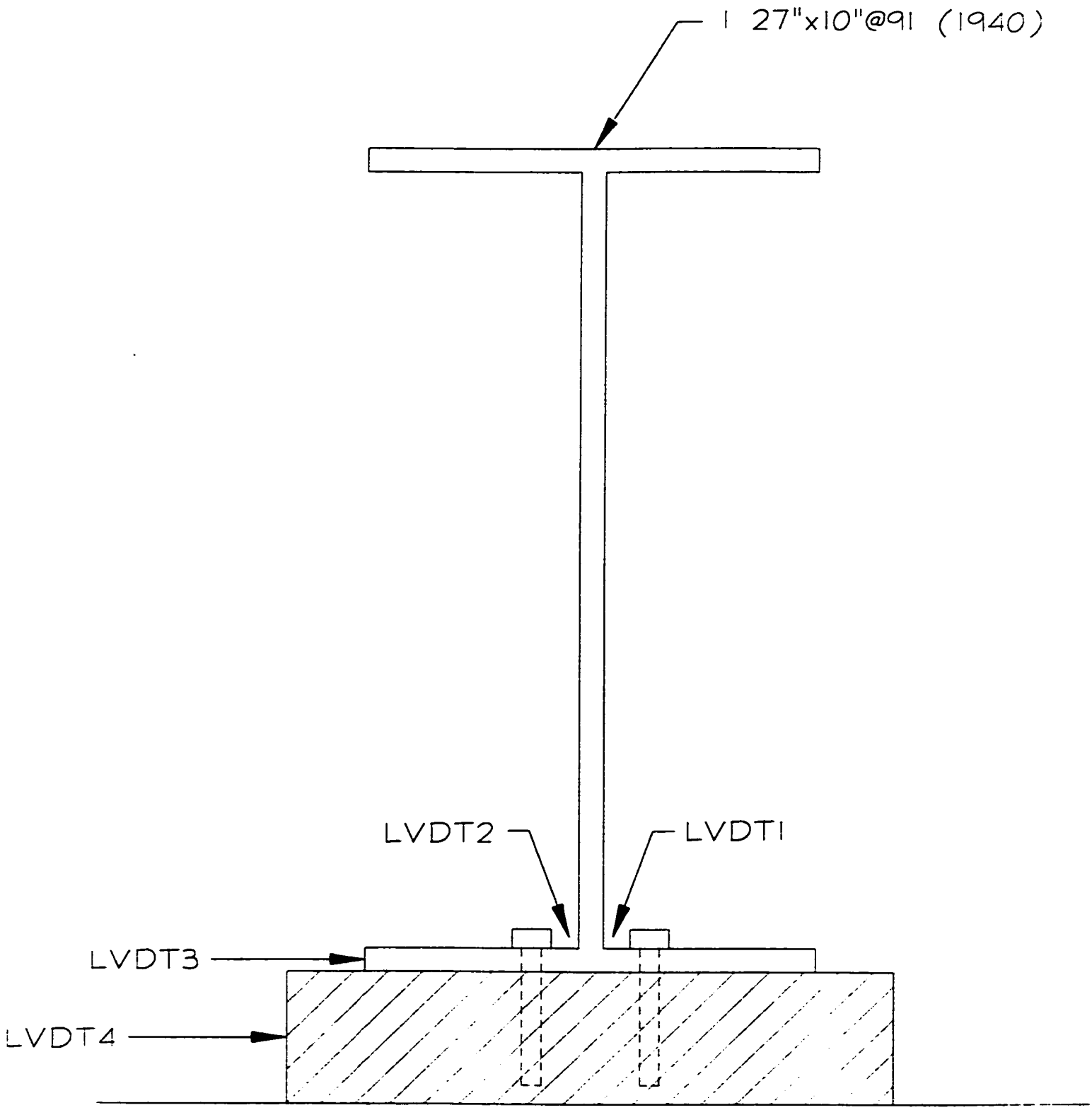

Figure 5.2 **Locations of External LVDTs**

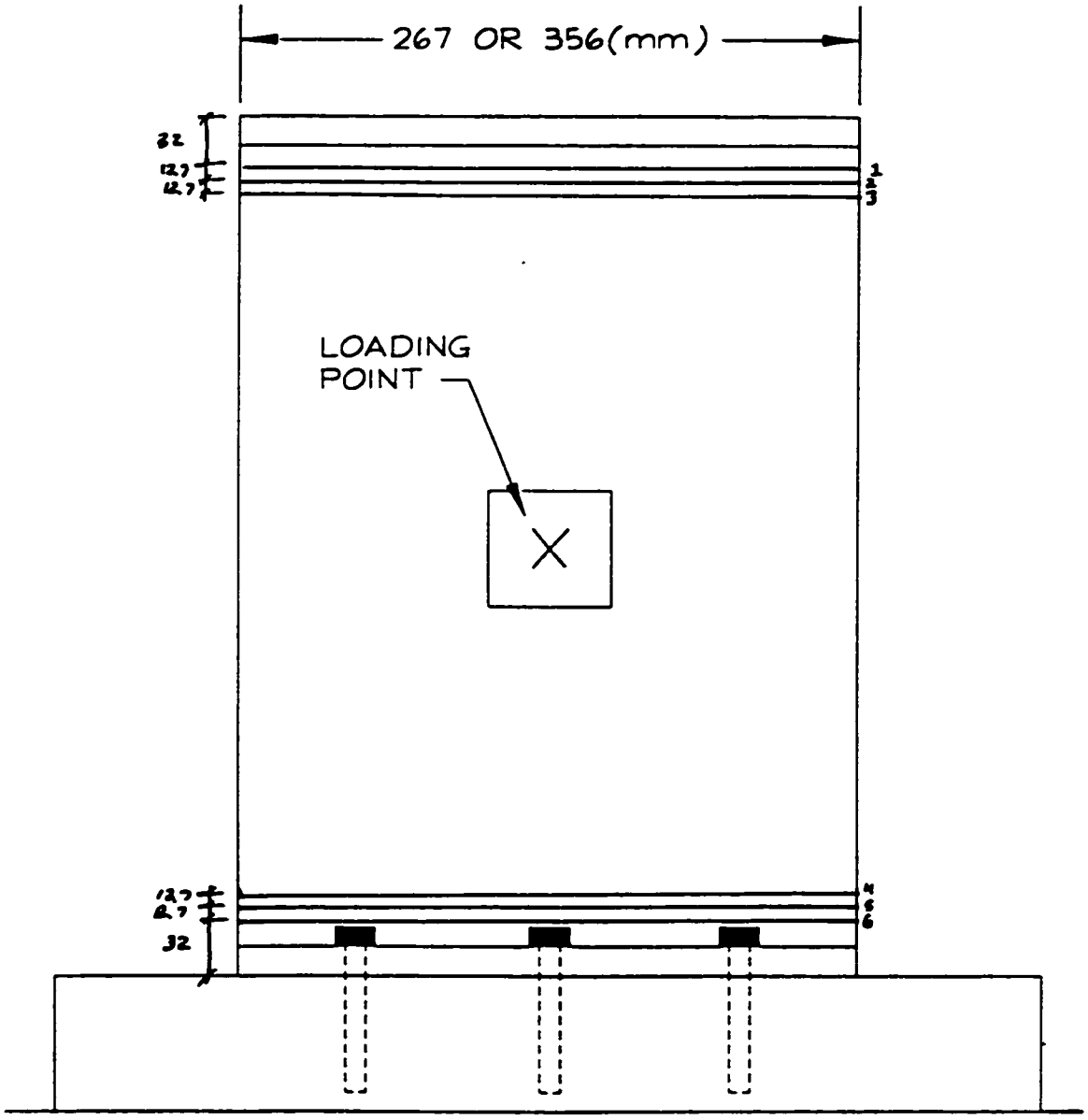

Figure 5.3 Typical Locations of Rows of Thickness Measurements

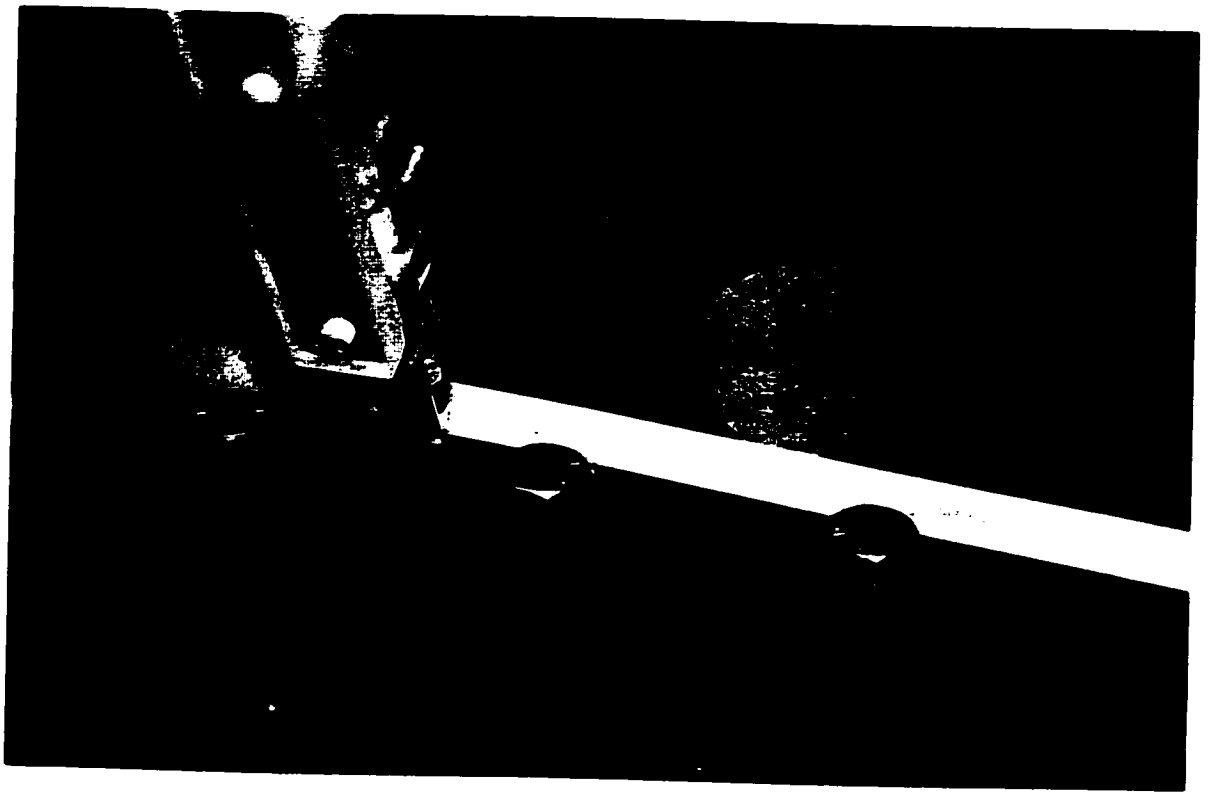

Figure 5.4 Typical 100 mm Diameter Area of Chemical Corrosion Product Removal

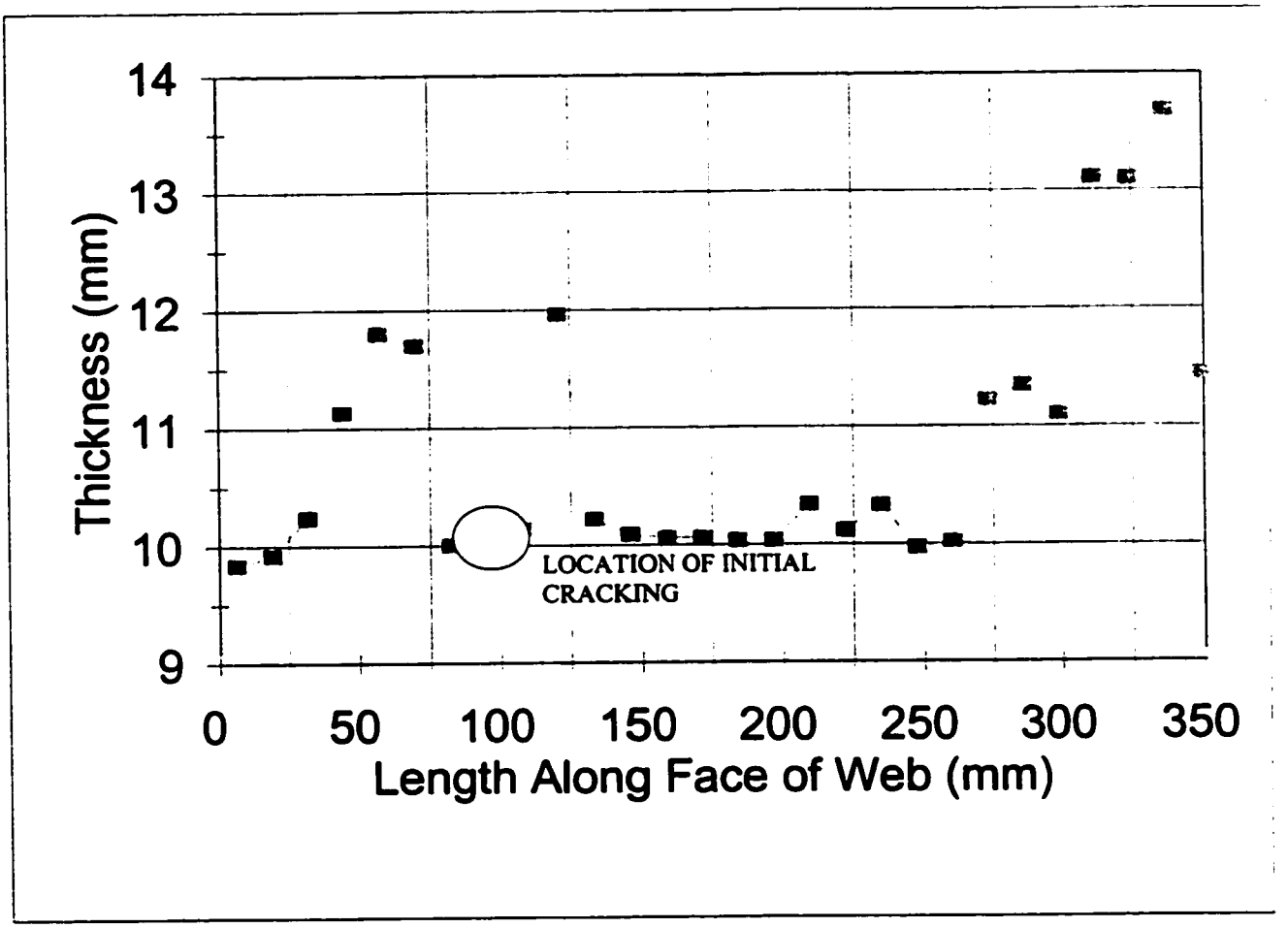

Figure 5.5 Initial Crack Location for Test 1

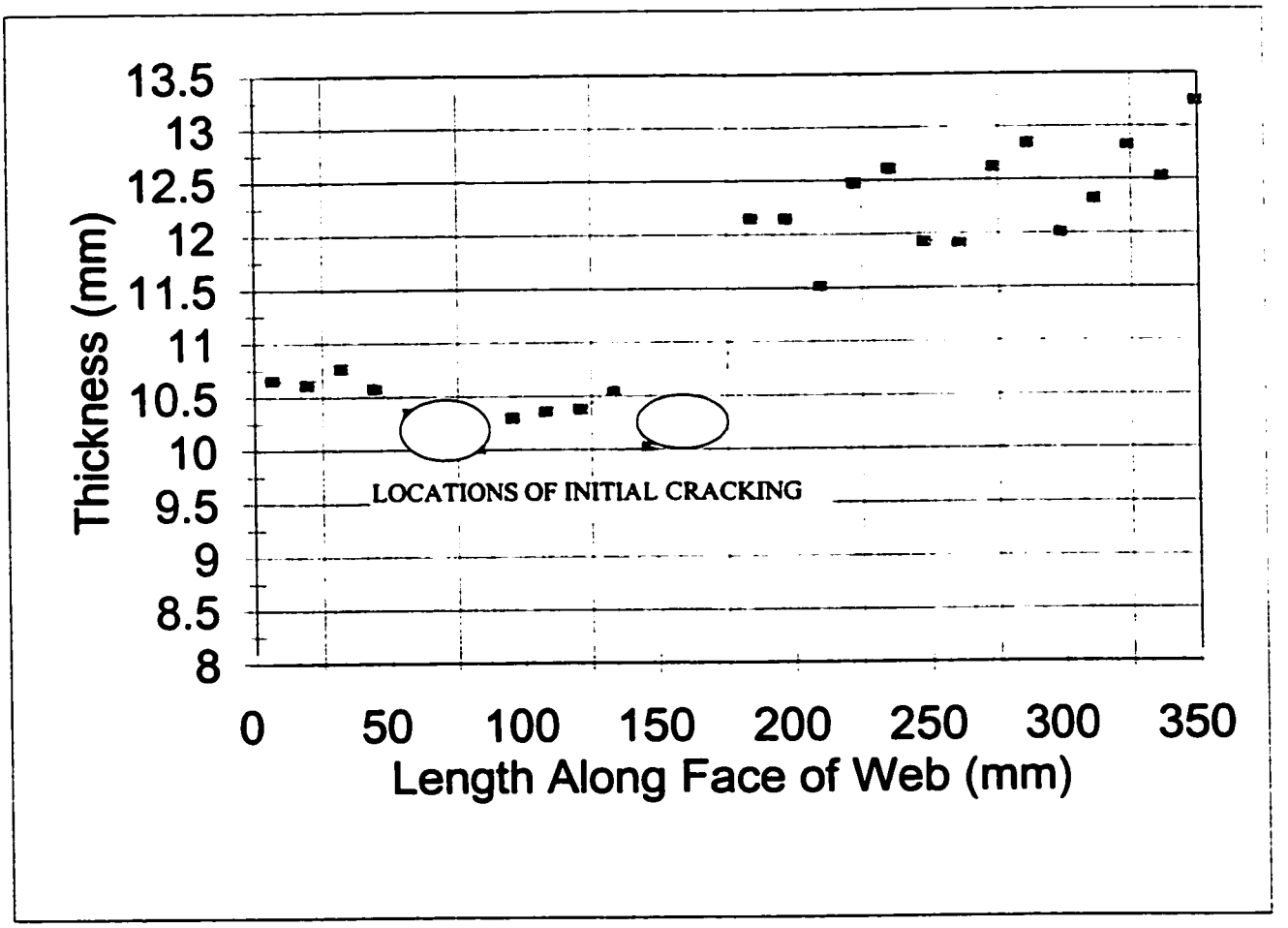

Figure 5.6 Initial Crack Location for Test 2

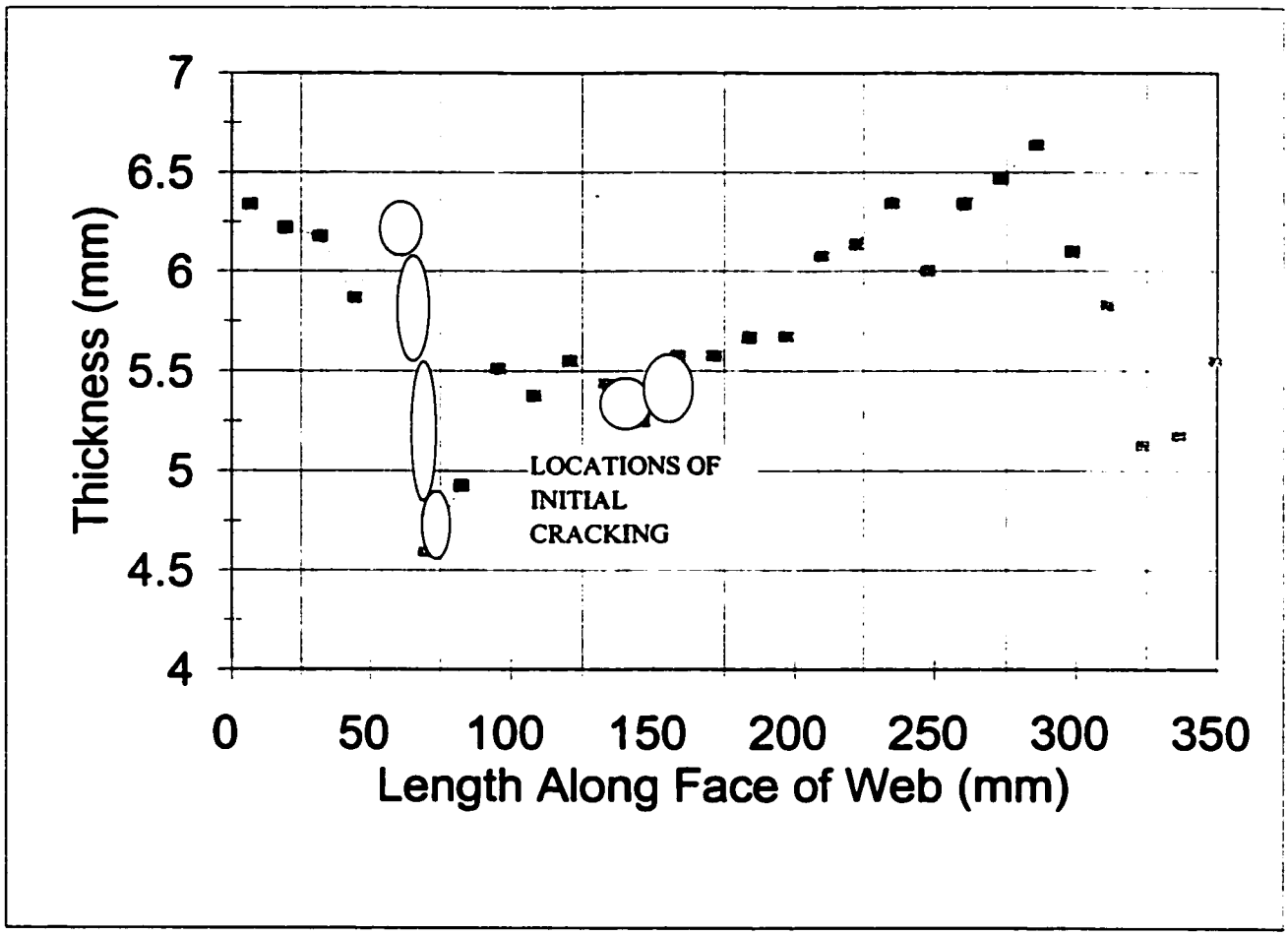

Figure 5.7 Initial Crack Location for Test 3

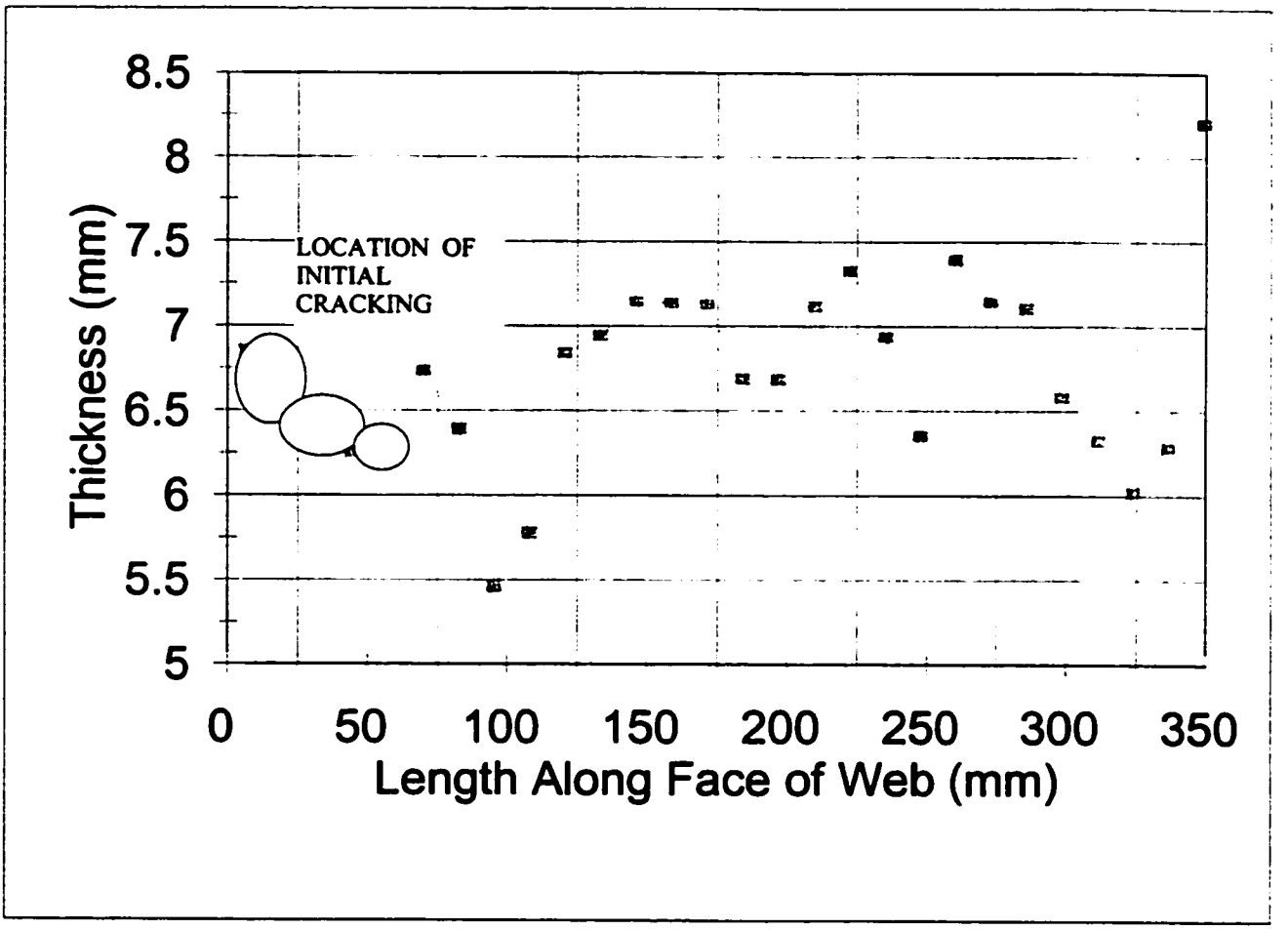

Figure 5.8 Initial Crack Location for Test 4

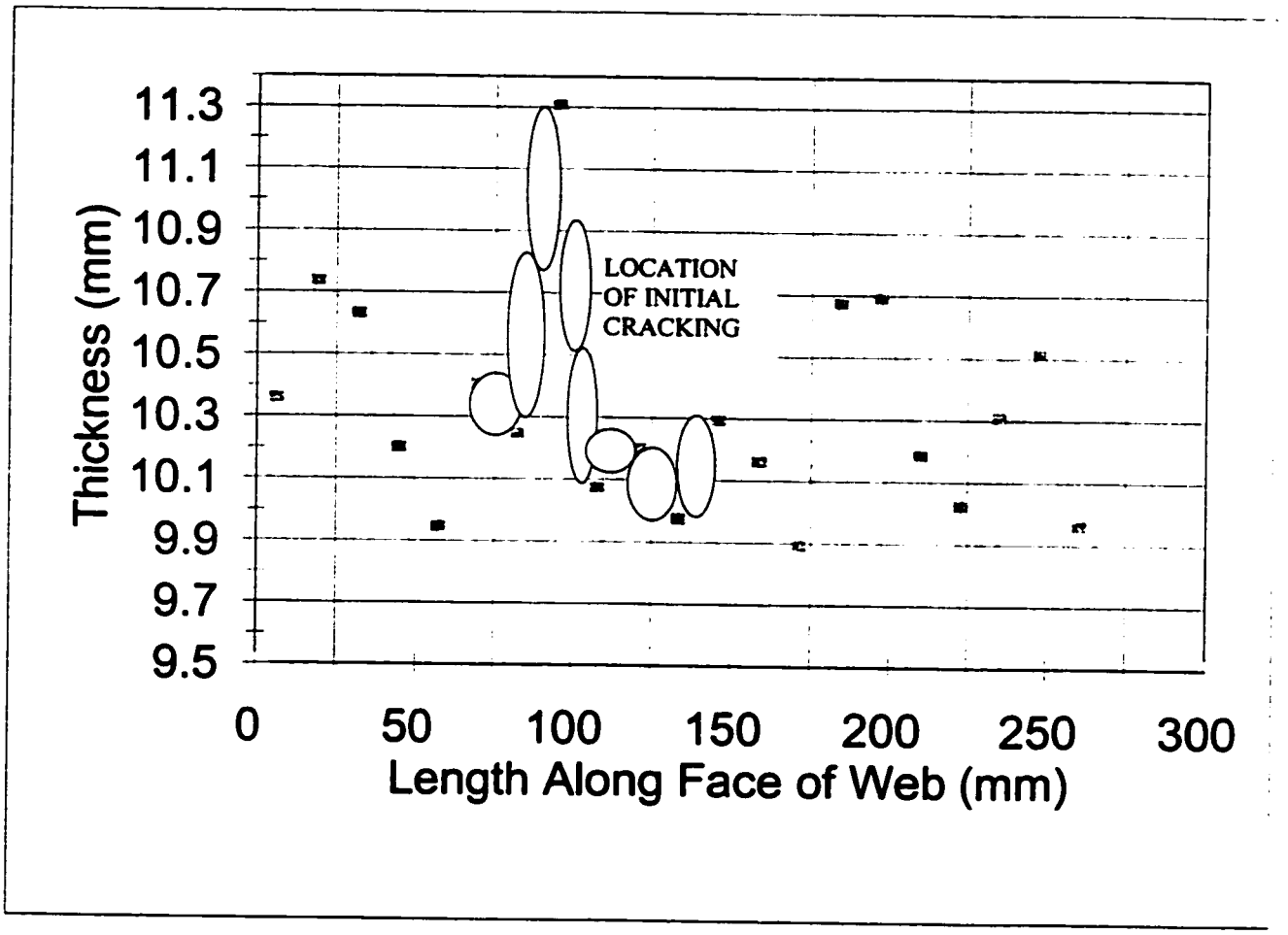

Figure 5.9 Initial Crack Location for Test 5

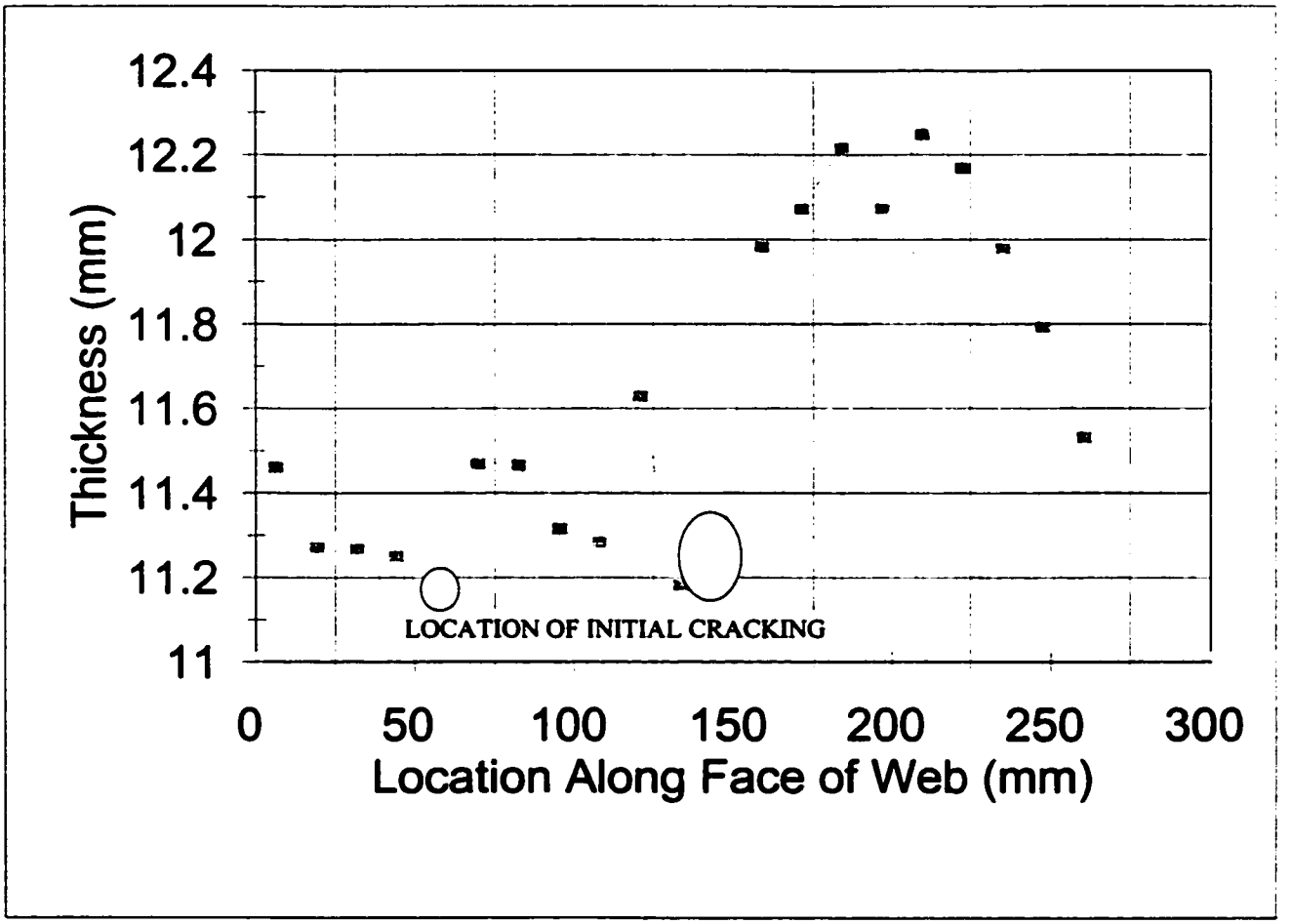

Figure 5.10 Initial Crack Location for Test 6

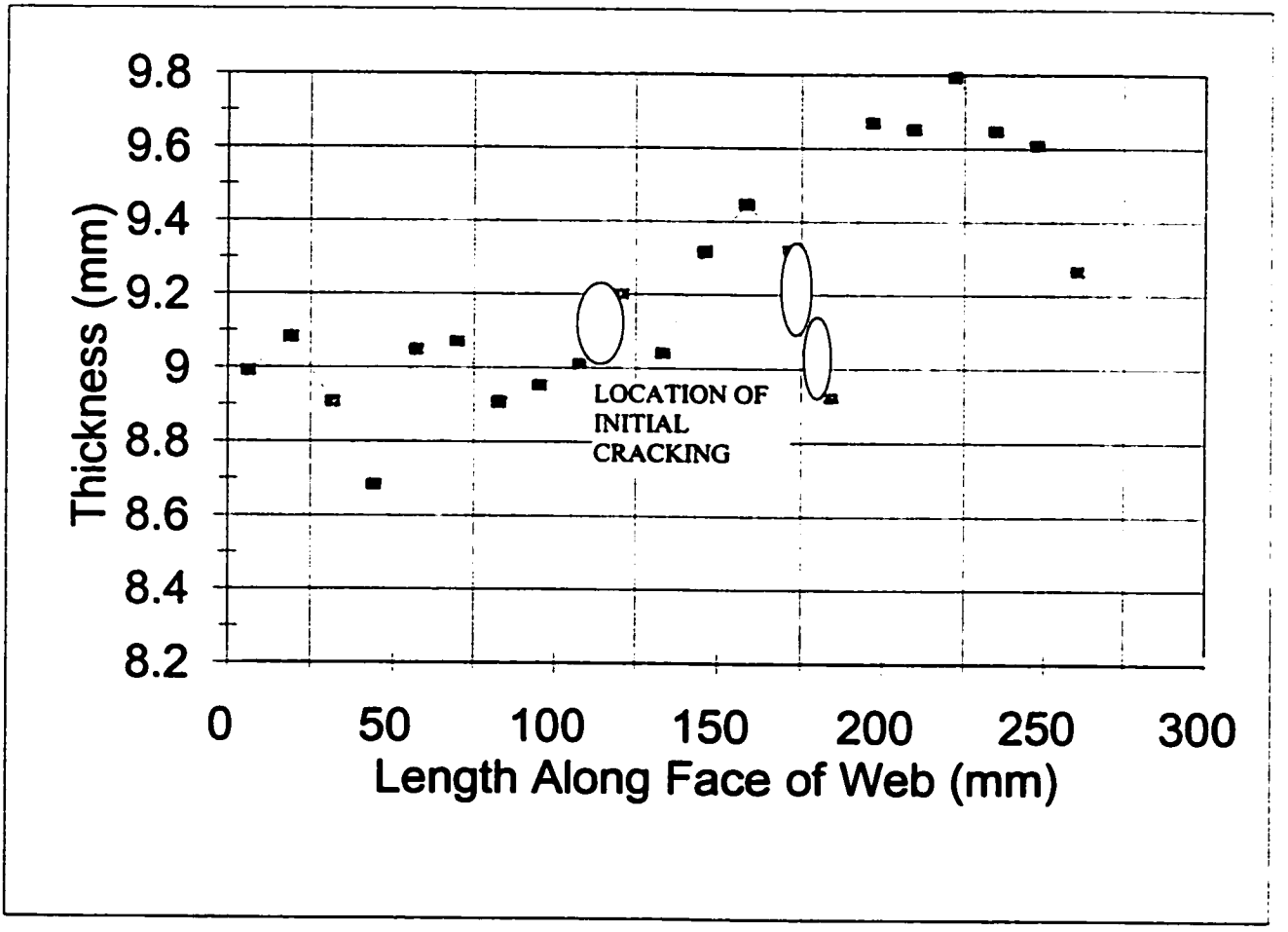

Figure 5.11 Initial Crack Location for Test 7

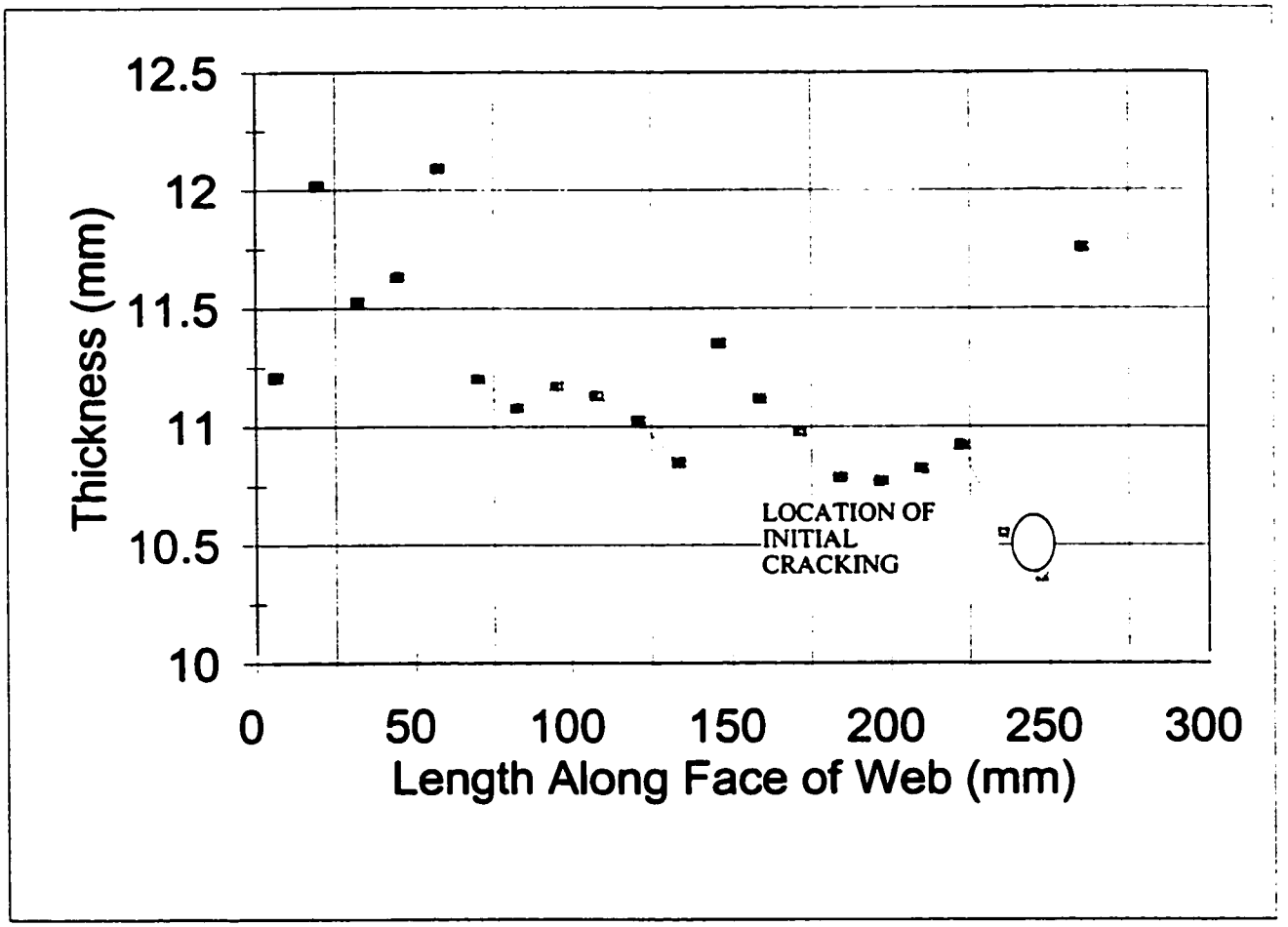

Figure 5.12 Initial Crack Location for Test 8

Figure 6.1 General View of Experimental Set-Up
Looking North West

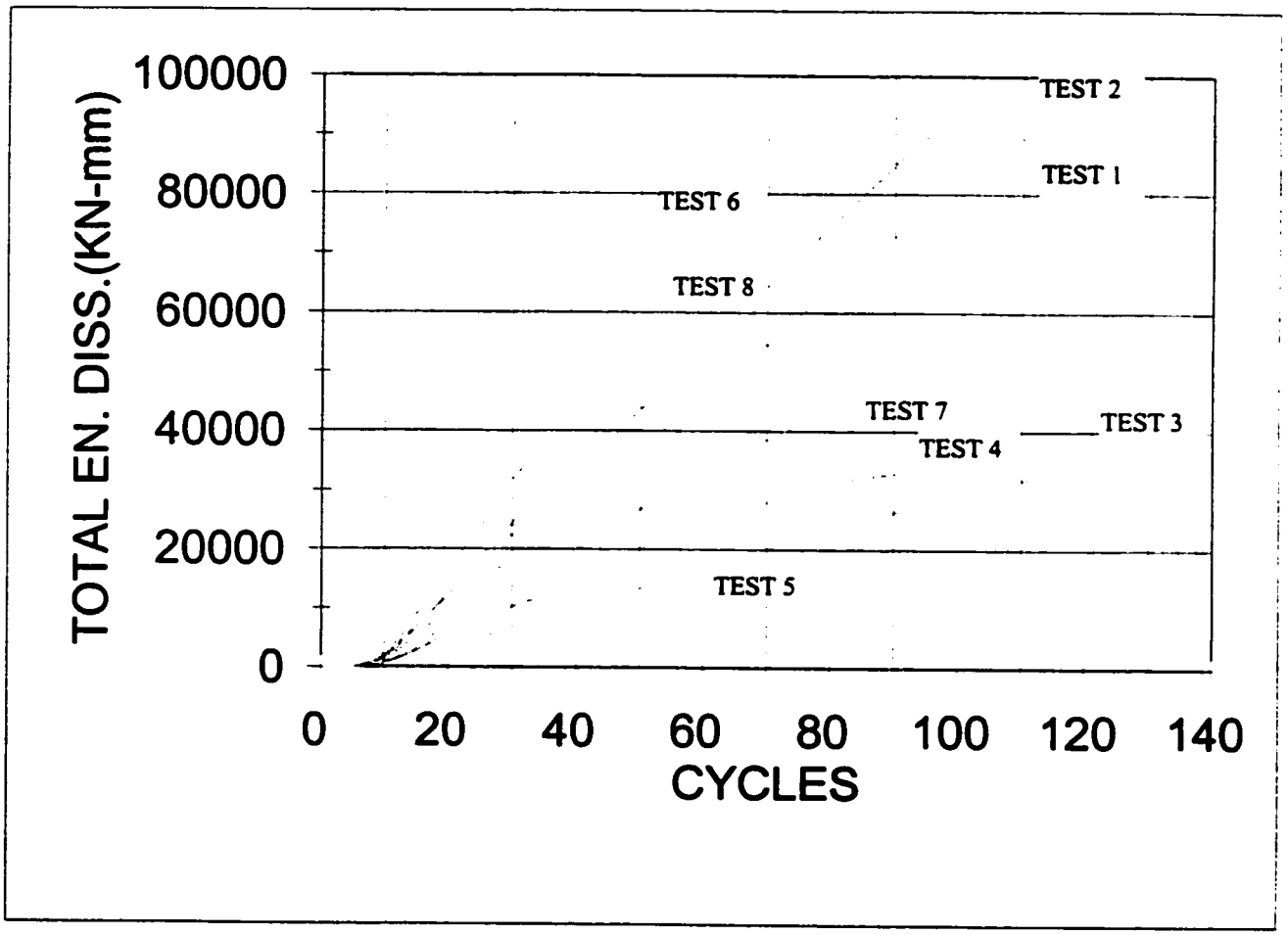

Figure 6.1(a) Cumulative Energy Dissipation During Cycling for Tests 1 to 8

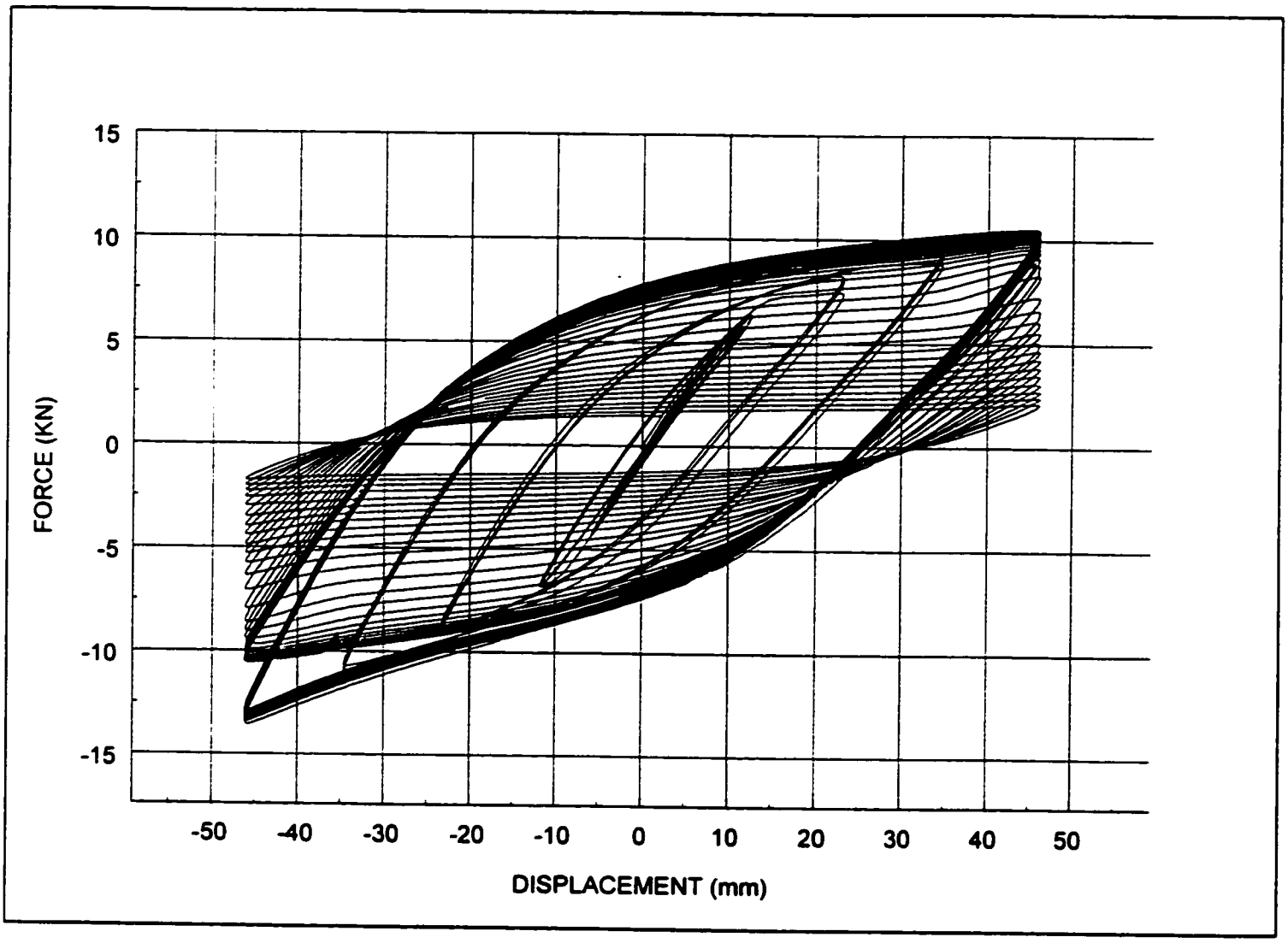

Figure 6.2 Hysteretic Curves for Test 1

Figure 6.3 Test #1 - Hairline Cracking on South Face after 87th Cycle

Figure 6.4 Test #1 - Propagation of South Face Crack after 97th Cycle

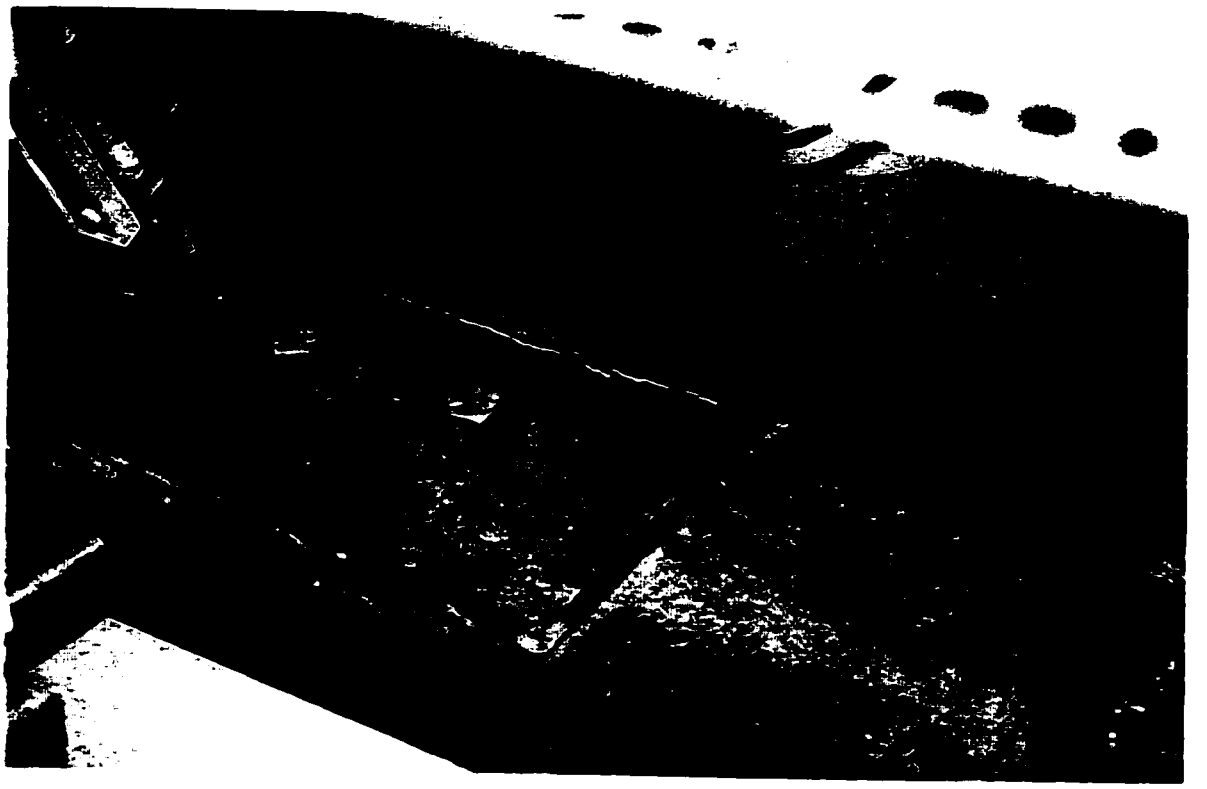

Figure 6.5 Test #1 - South Face at Failure

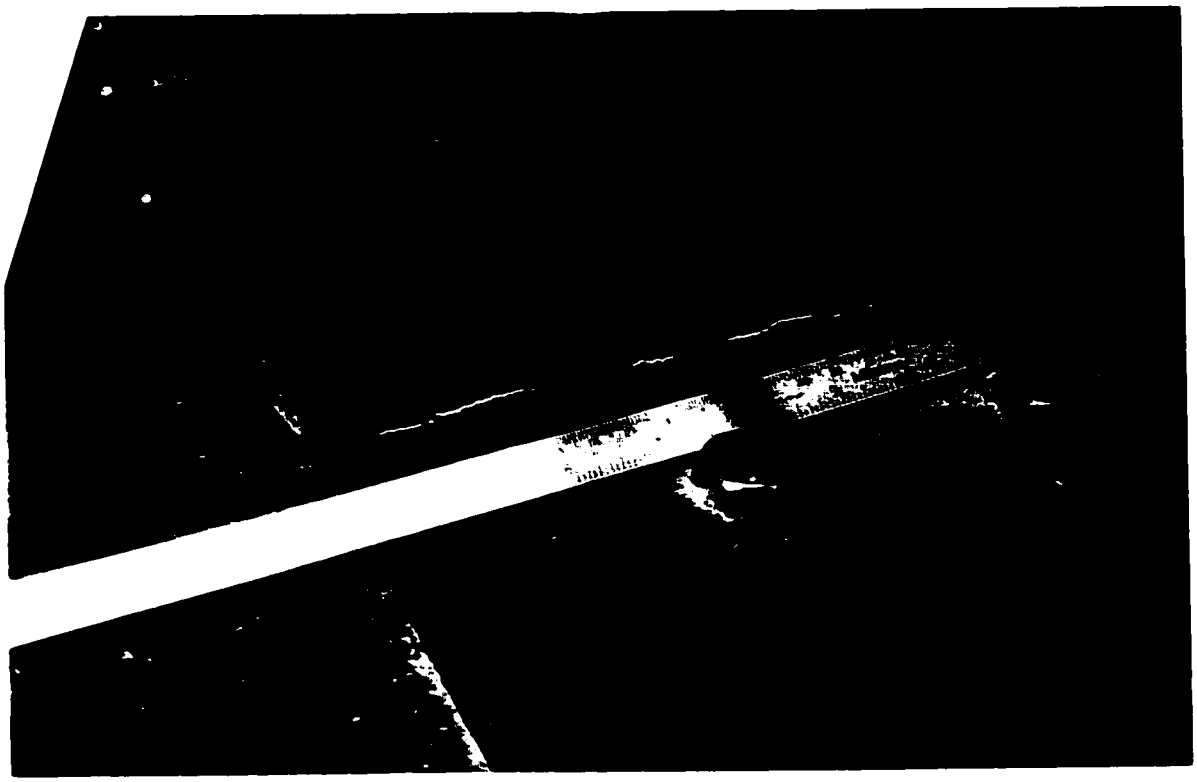

Figure 6.6 Test #1 - North Face at Failure

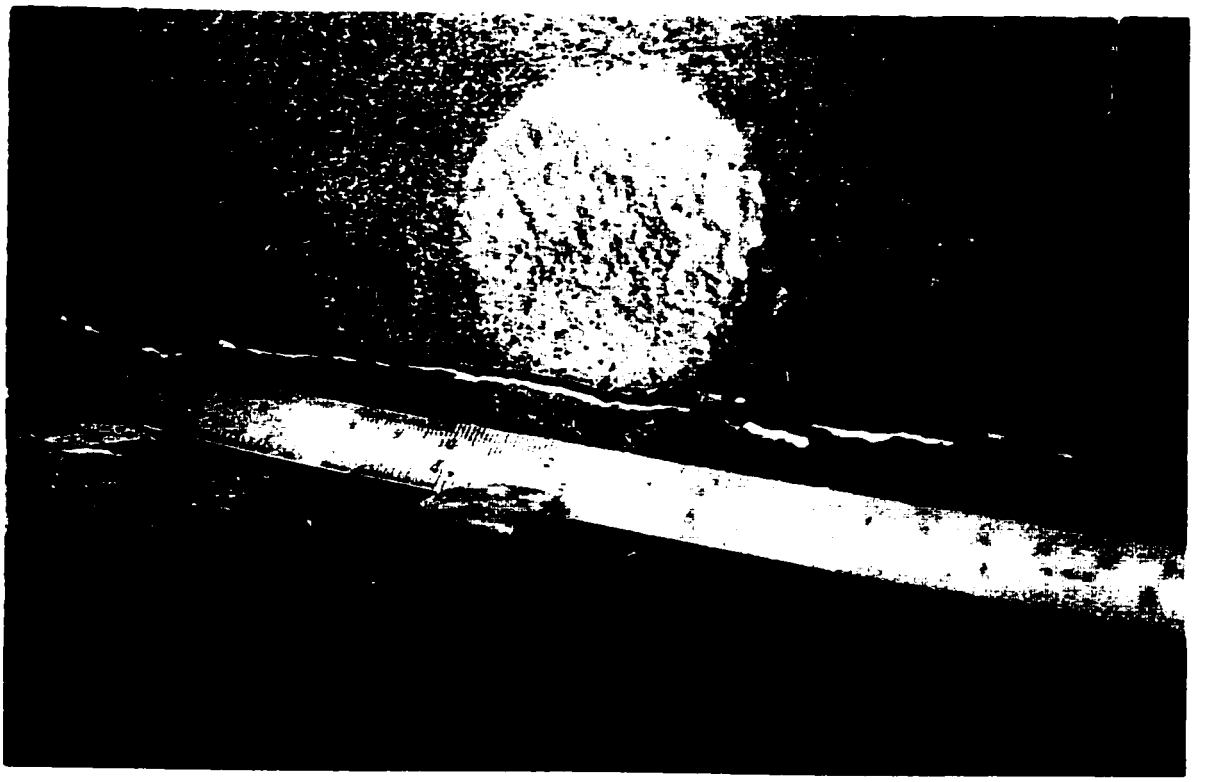

Figure 6.7 Test #1 - Close up View of South Face at Failure

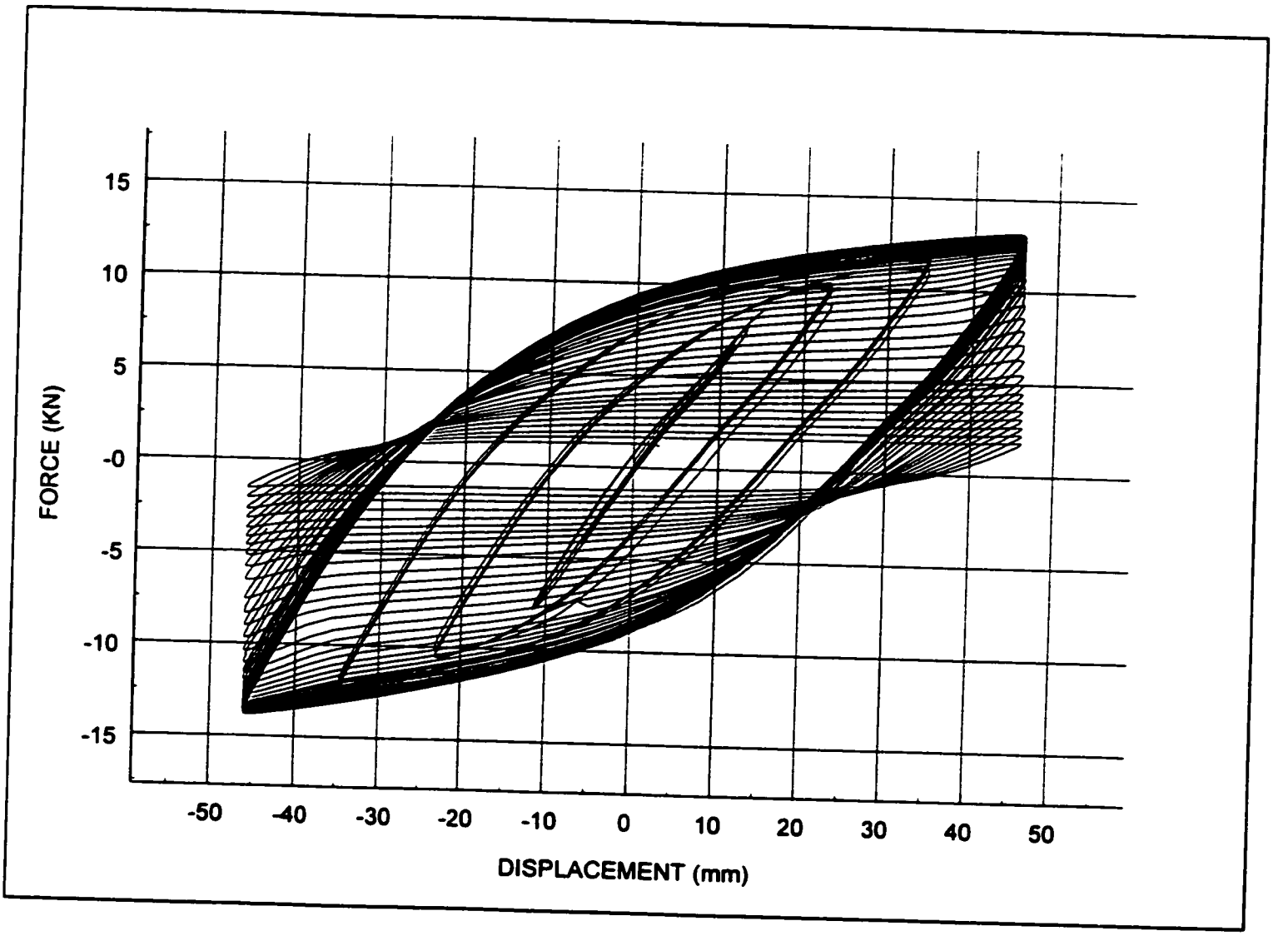

Figure 6.8 Hysteretic Curves for Test 2

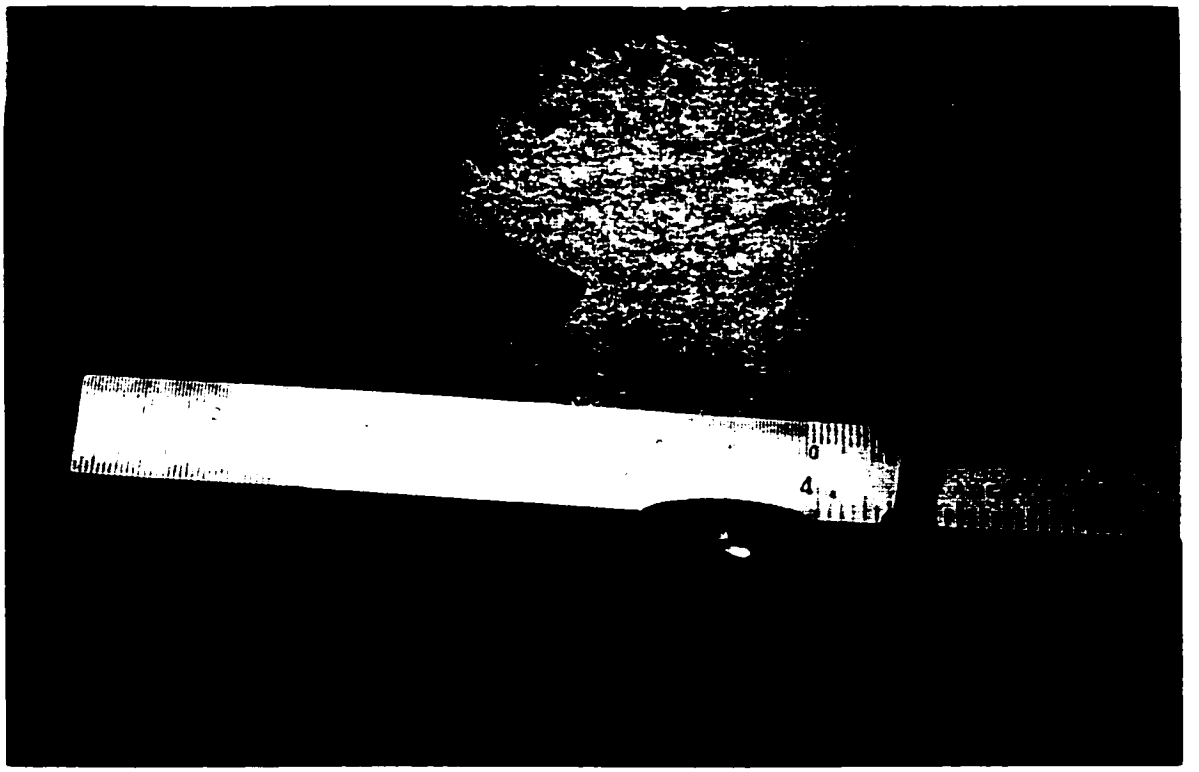

Figure 6.9 Test #2 - Hairline Cracking on South Face after 82nd Cycle

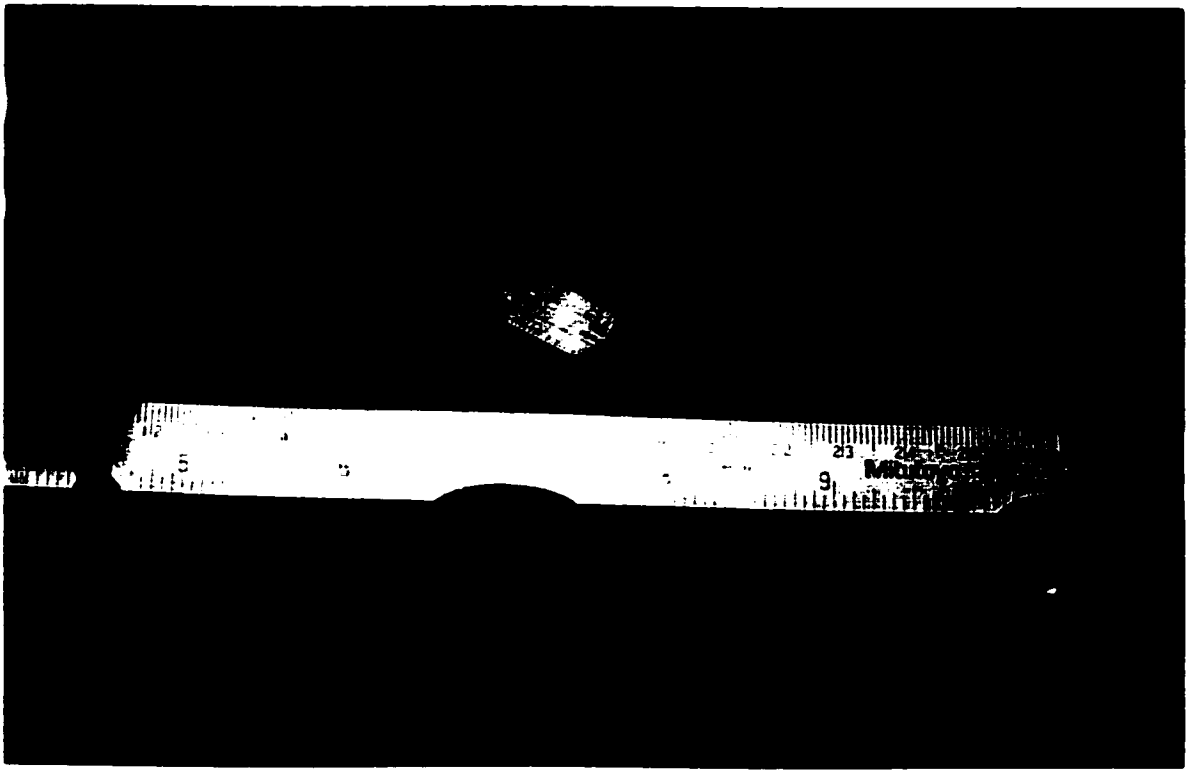

Figure 6.10 Test #2 - Hairline Cracking on South Face after 82nd Cycle

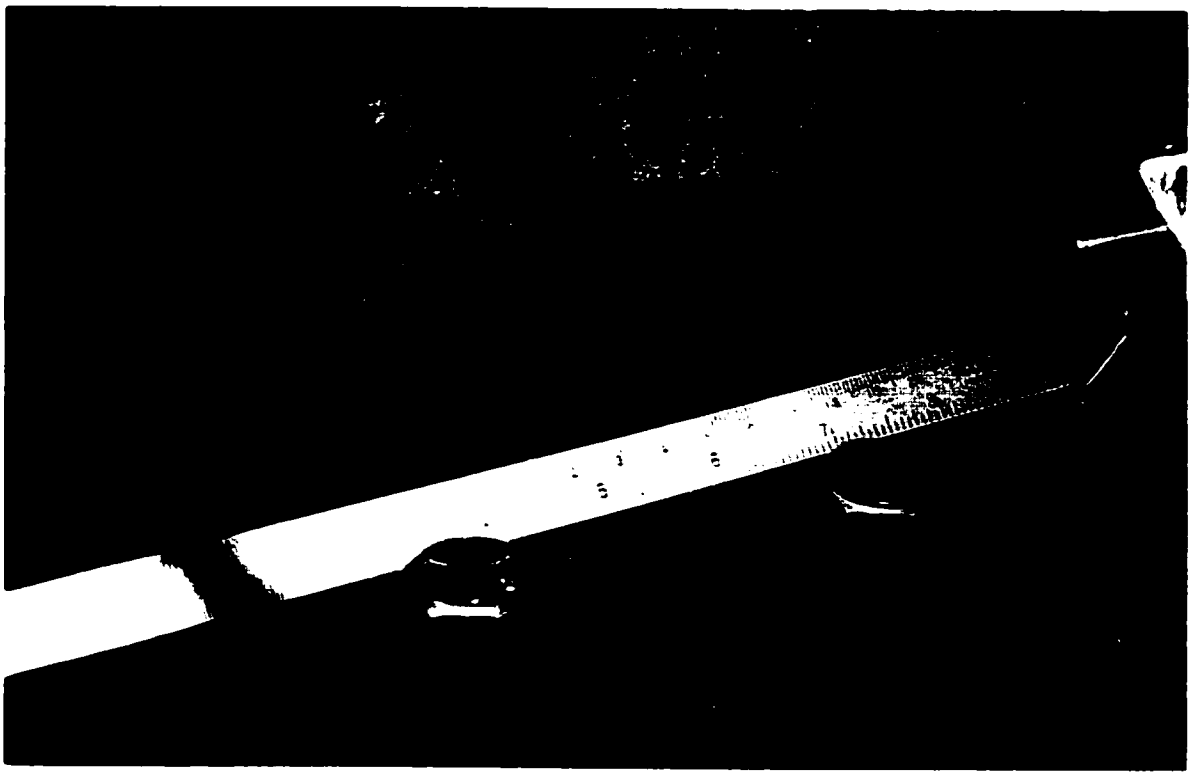

Figure 6.11 Test #2 - Cracking on the North Face after Cycle 87

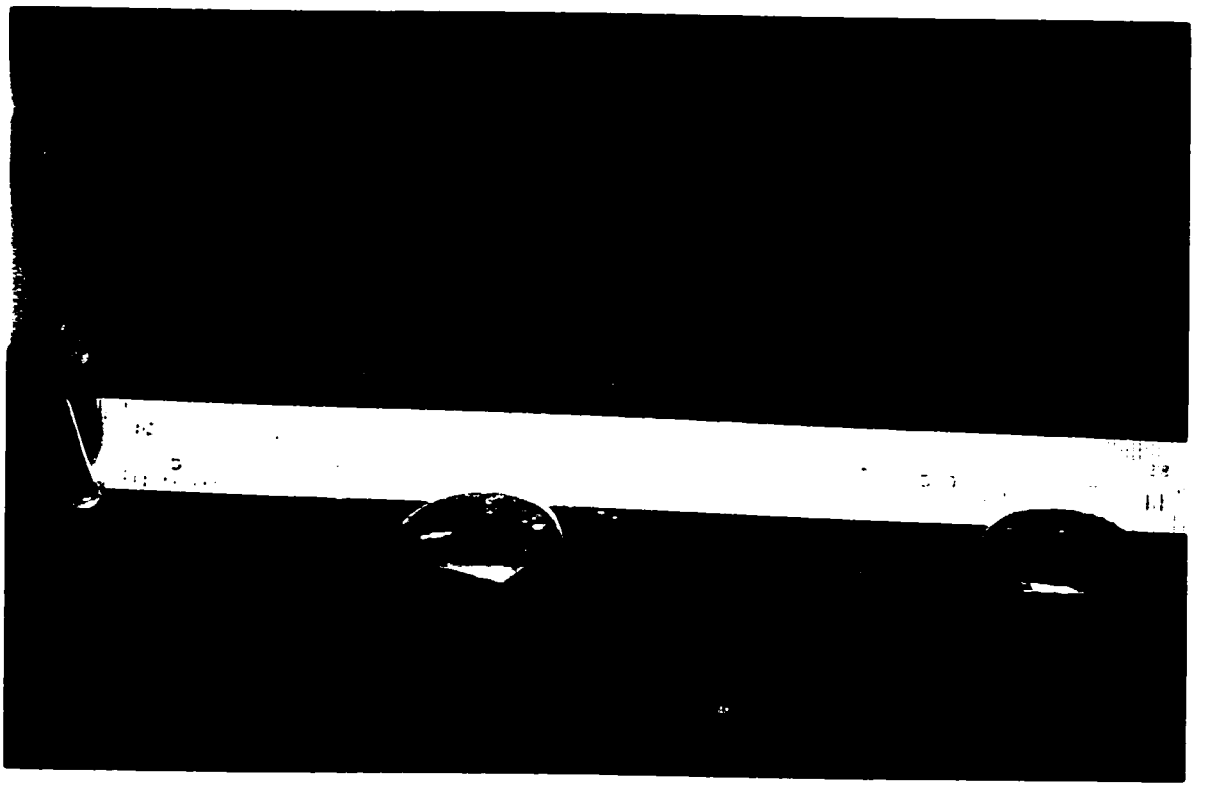

Figure 6.12 Test #2 - Propagation of South Face Cracking at Cycle 88

Figure 6.13 Test #2 - Propagation of North Face Cracking at Cycle 92

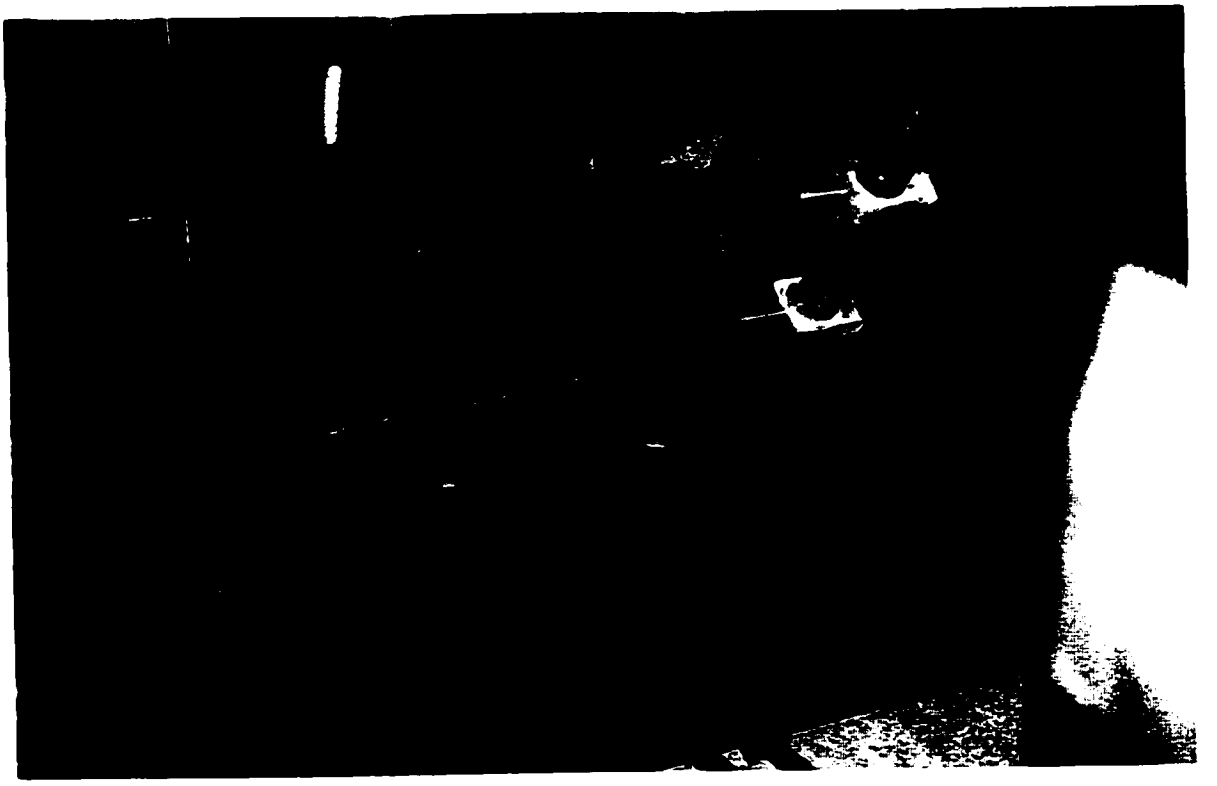

Figure 6.14 Test #2 - North Face at Failure

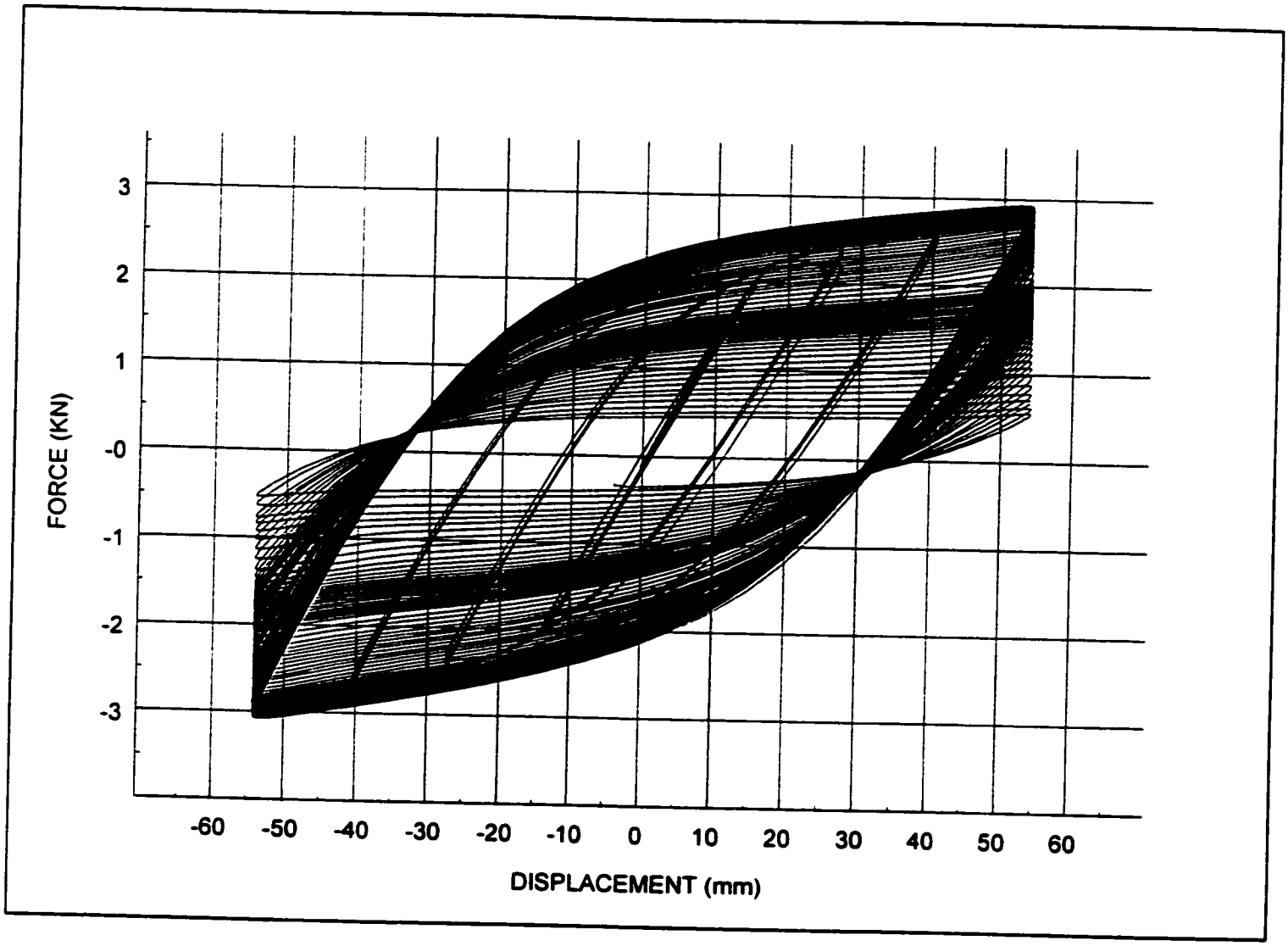

Figure 6.15 Hysteretic Curves for Test 3

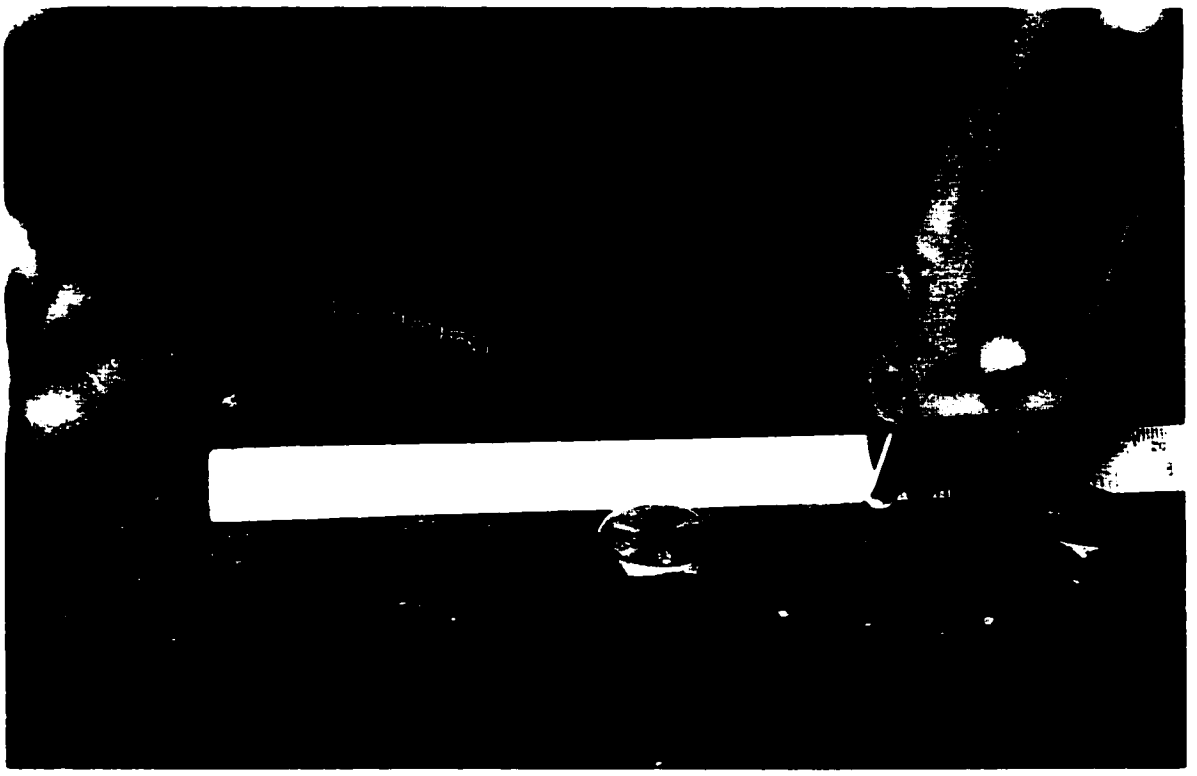

Figure 6.16 Test #3 - Hairline Cracking on South Face After 28th Cycle

Figure 6.17 Test #3 - Hairline Crack on North Face at 80th Cycle

Figure 6.18 Test #3 - Propagation of South Face Cracking After 83rd Cycle

Figure 6.19 Test #3 - Cracking on South Face at 92nd Cycle

Figure 6.20 Test #4 - Cracking on North Face at 92nd Cycle

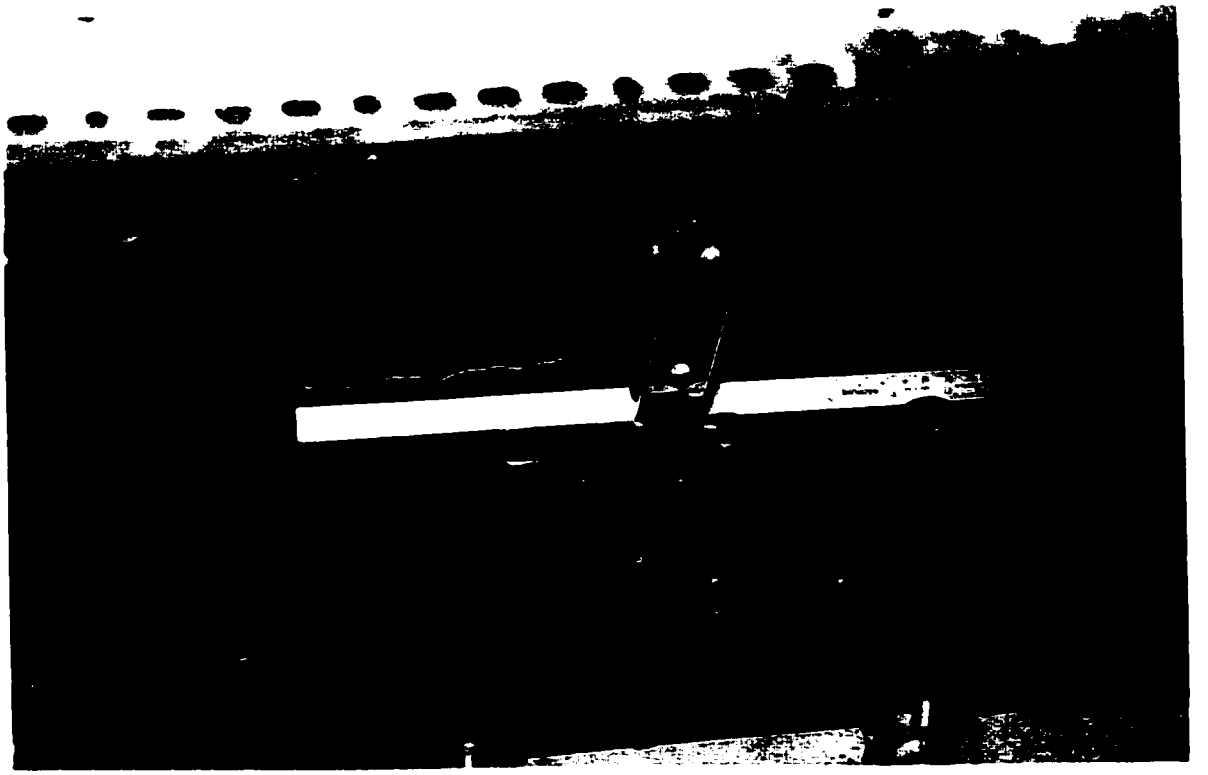

Figure 6.21 Test #4 - Final Condition of South Face at Failure

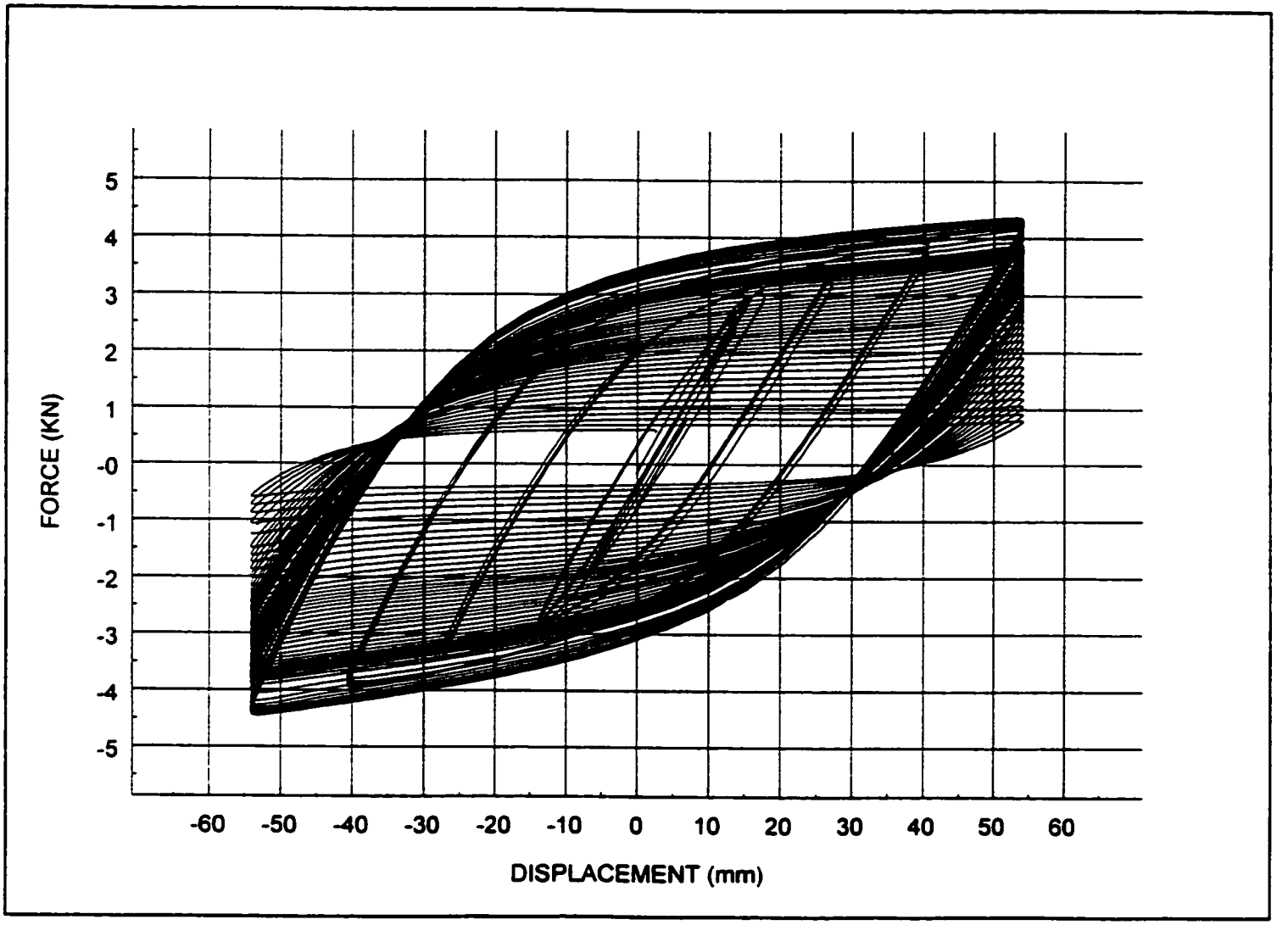

Figure 6.22 Hysteretic Curves for Test 4

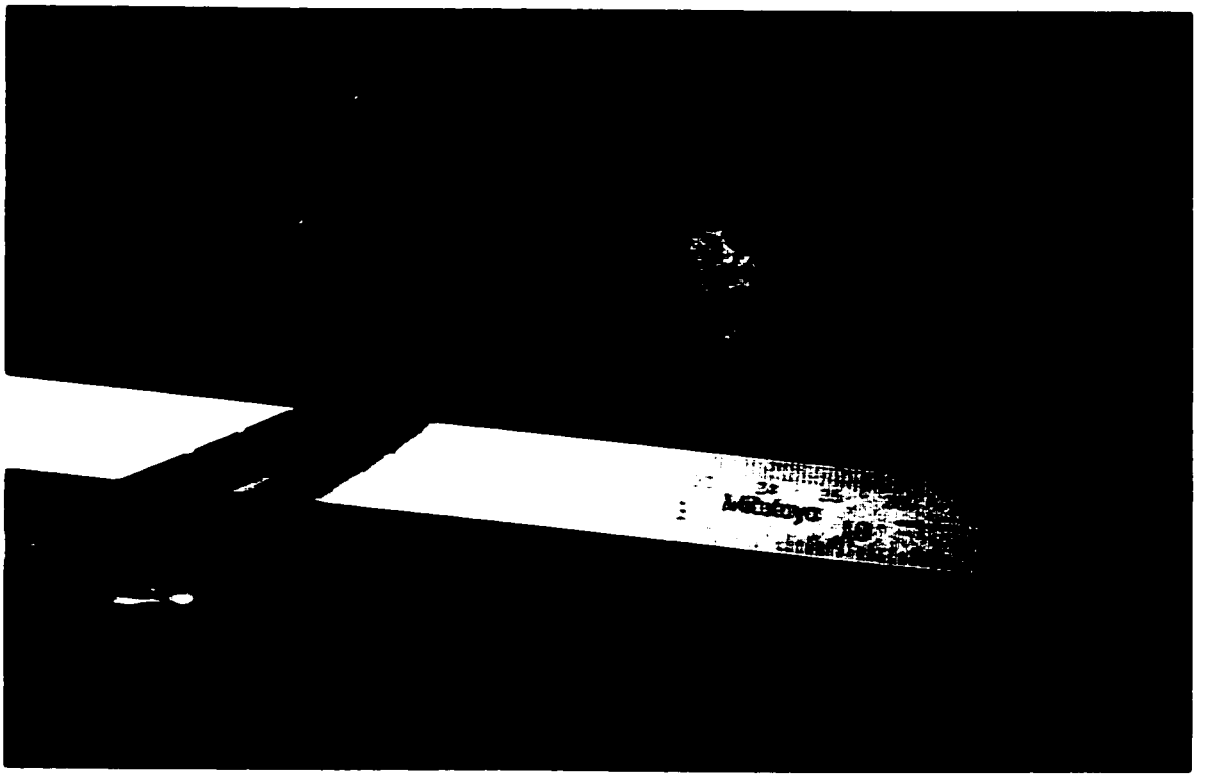

Figure 6.23 Test #4 - Five Hairline Cracks at South Face at 52nd Cycle

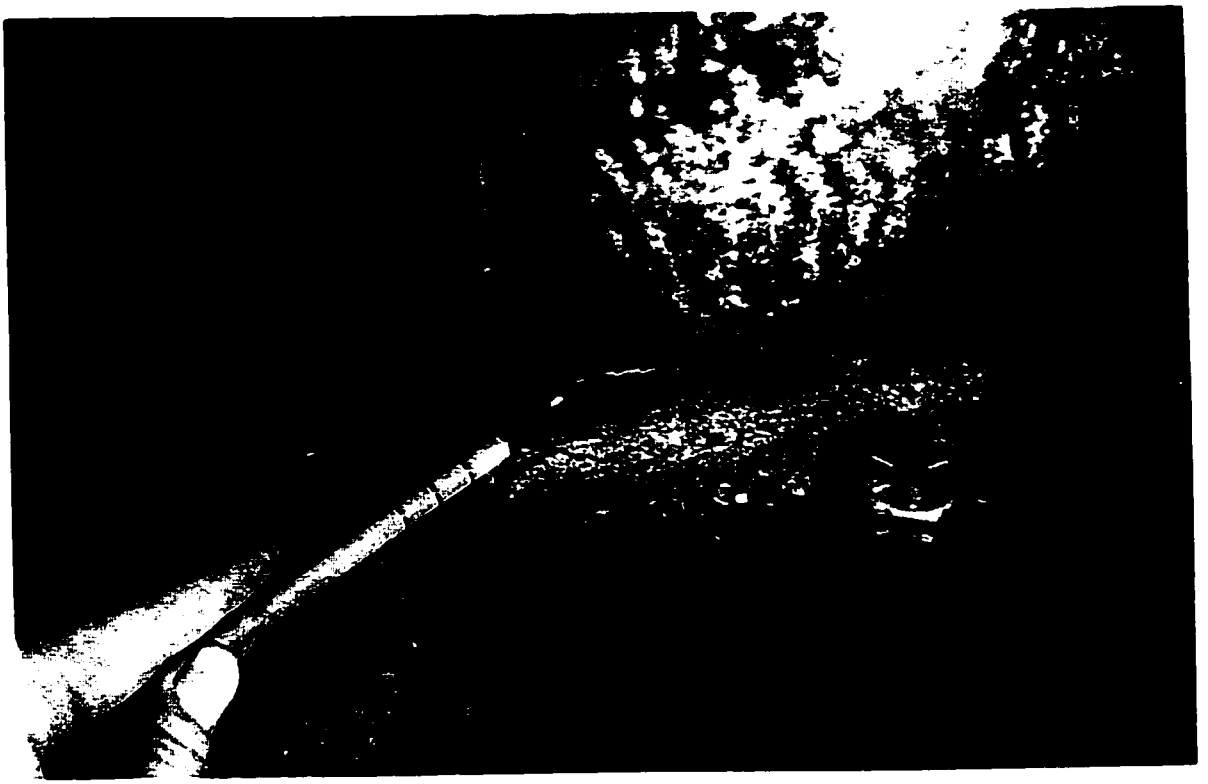

Figure 6.24 Test #4 - Hairline Cracking on North Face at 53rd Cycle

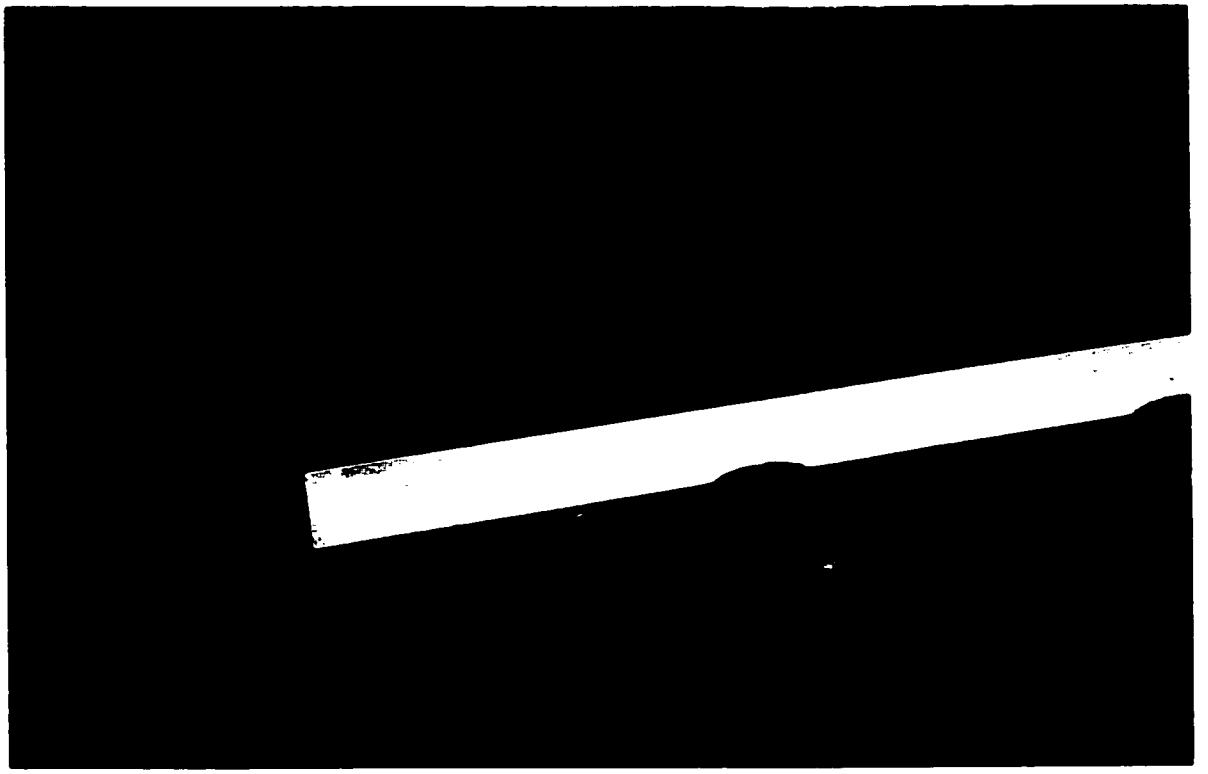

Figure 6.25 Test #4 - Propagation of North Face Cracking at 88th Cycle

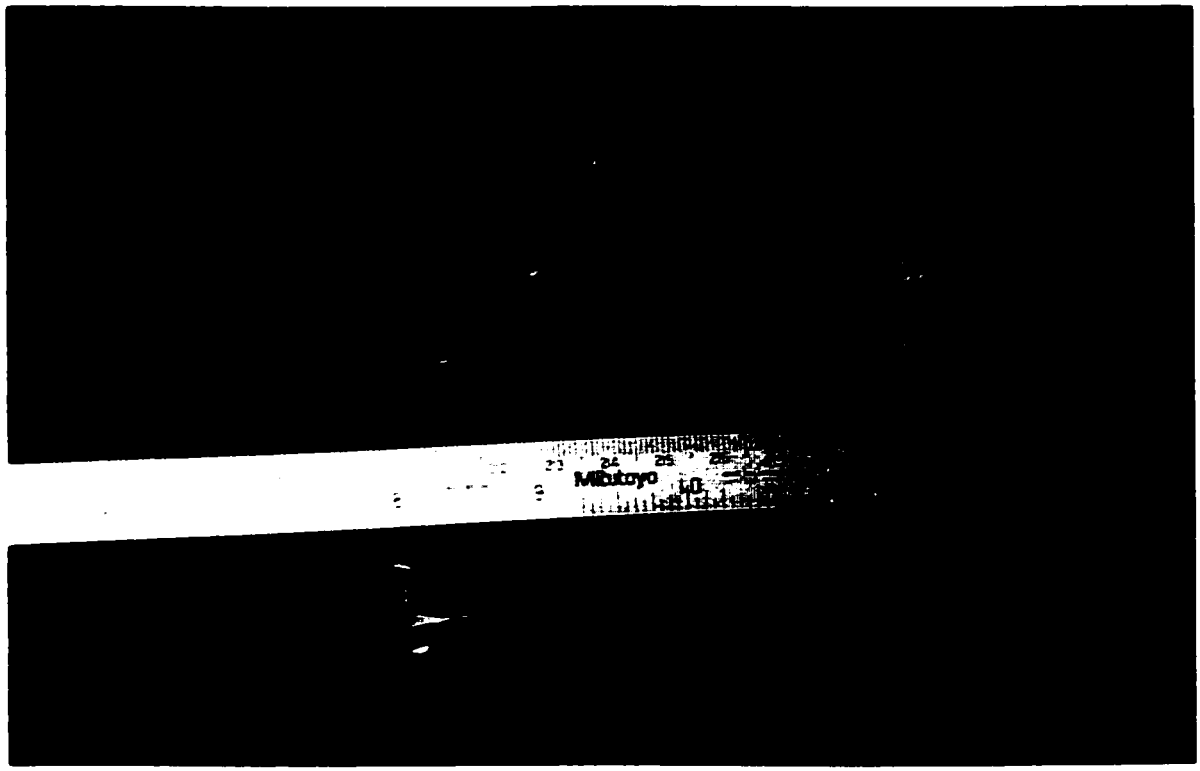

Figure 6.26 Test #4 - Propagation of South Face Cracking at 88th Cycle

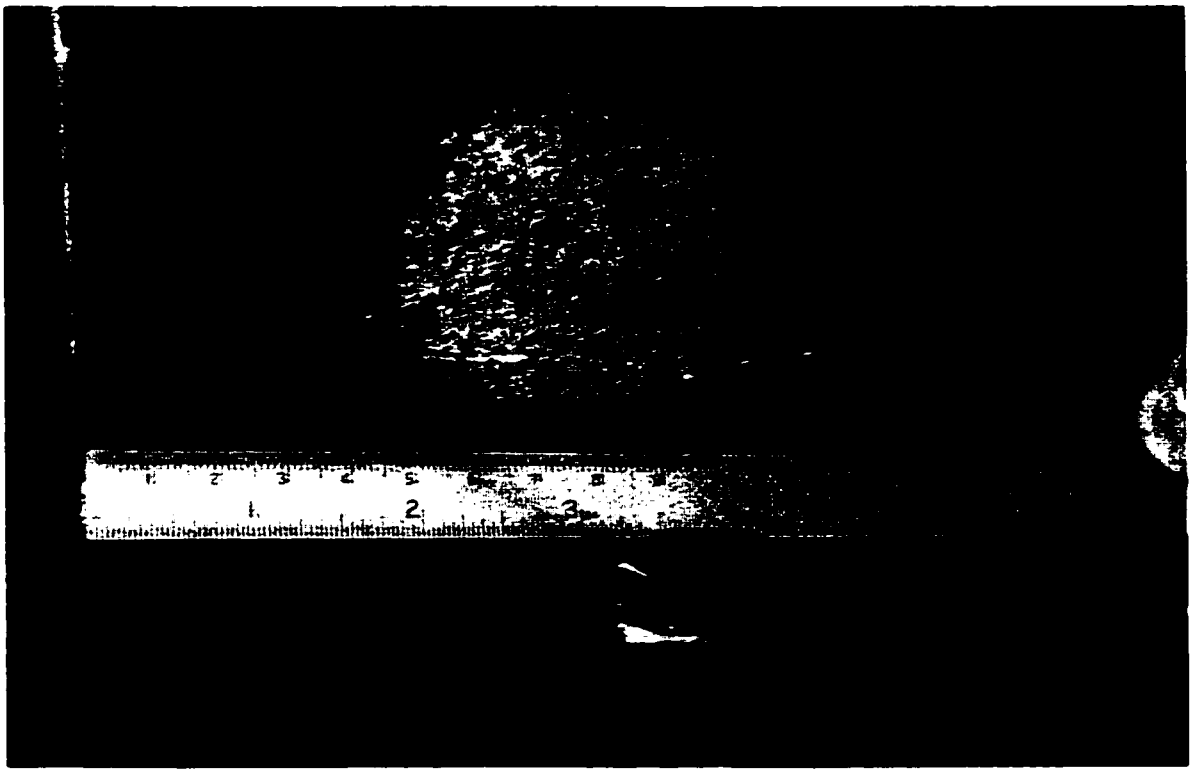

Figure 6.27 Test #4 - Propagation of South Face Cracking at 88th Cycle

Figure 6.28 Test #4 - Final Condition of North Face at Failure

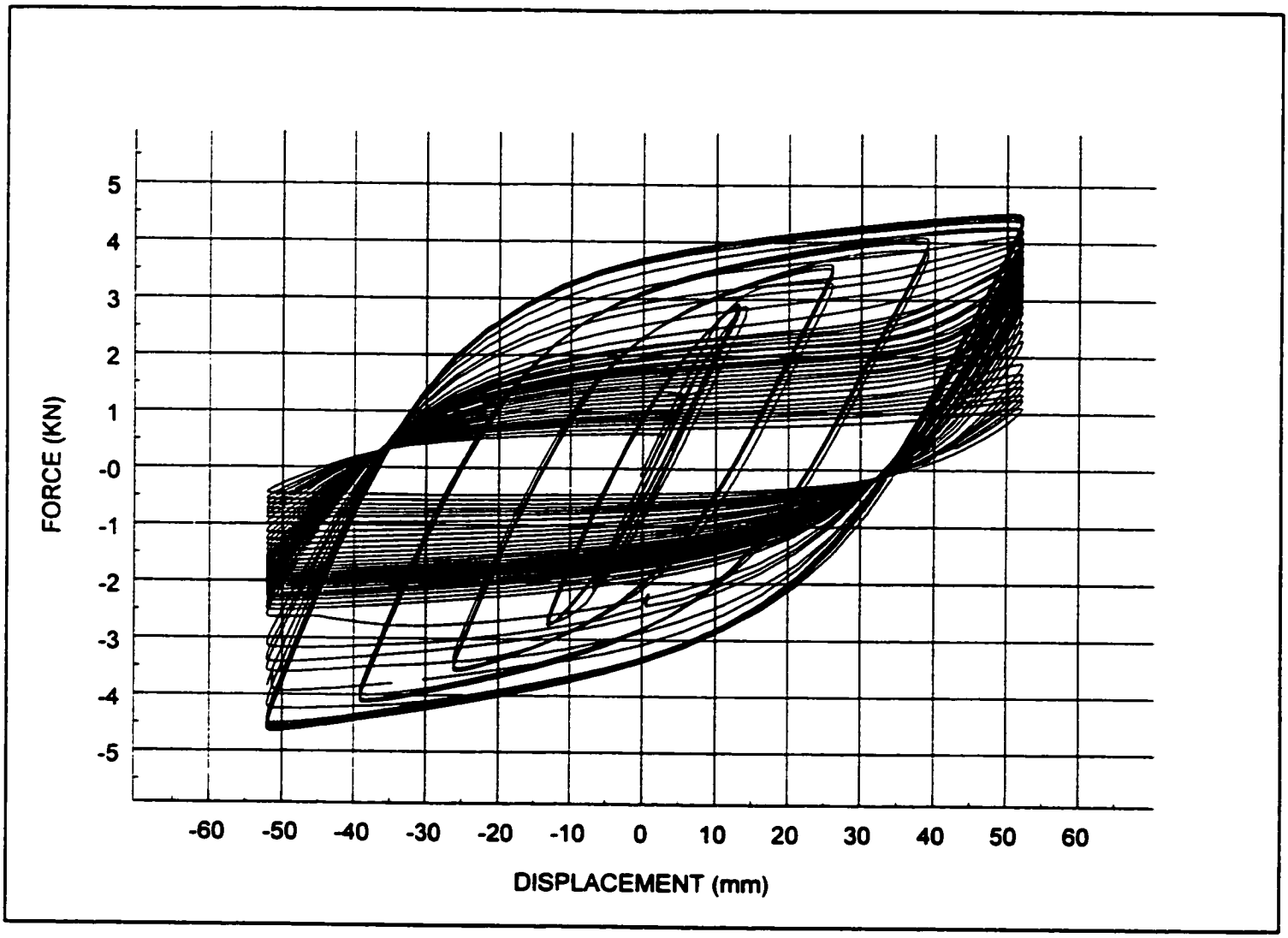

Figure 6.29 Hysteretic Curves for Test 5

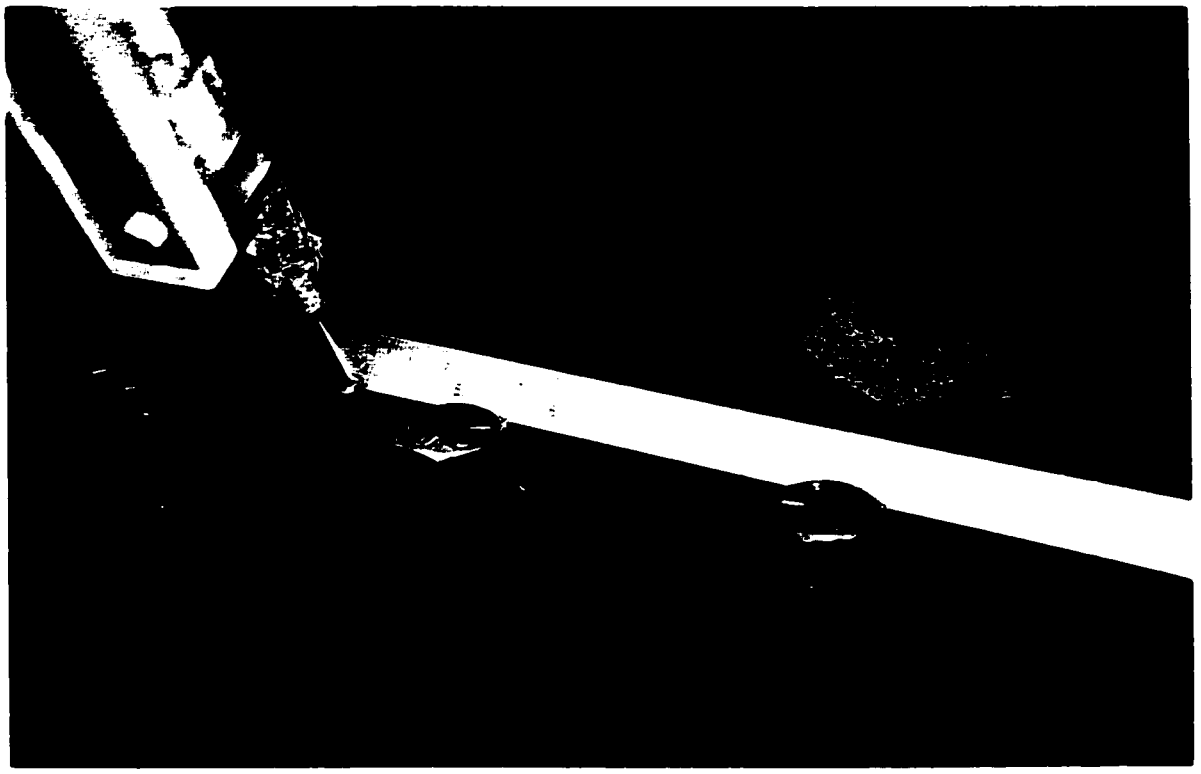

Figure 6.30 Test #5 - Tear in South Face at 24th Cycle

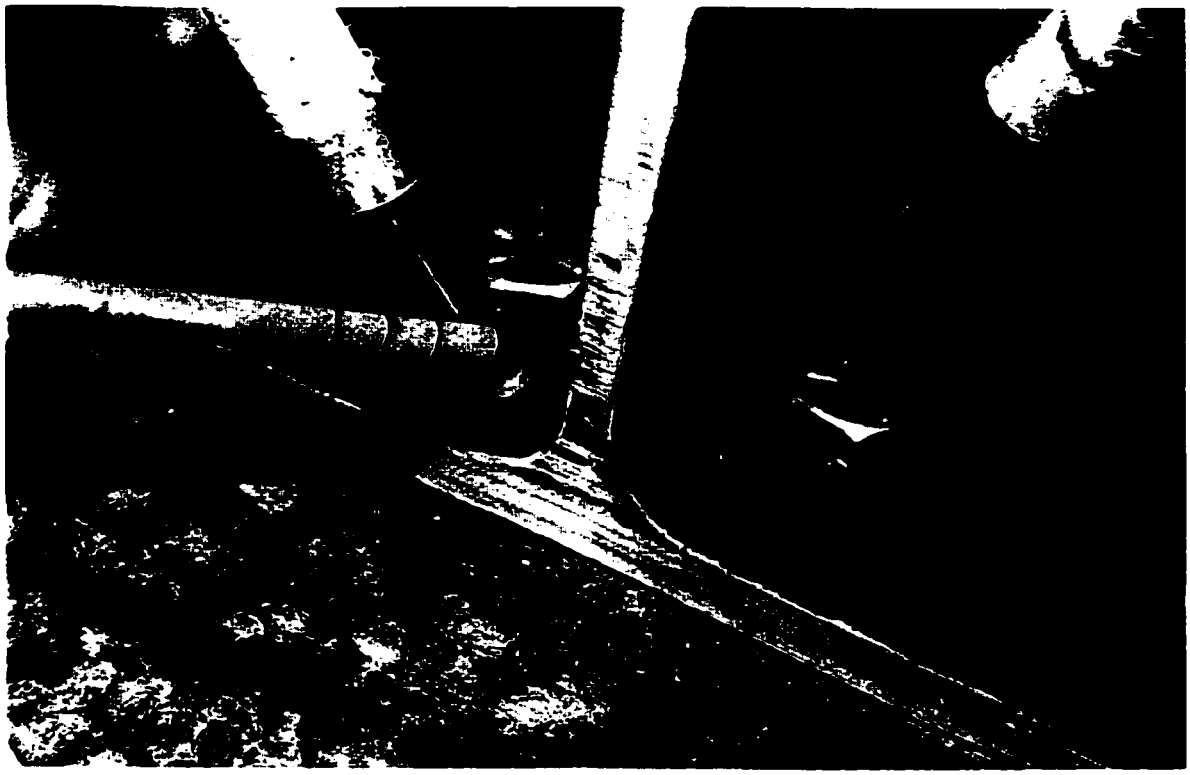

Figure 6.31 Test #5 - Lamination at West End of Specimen at 24th Cycle

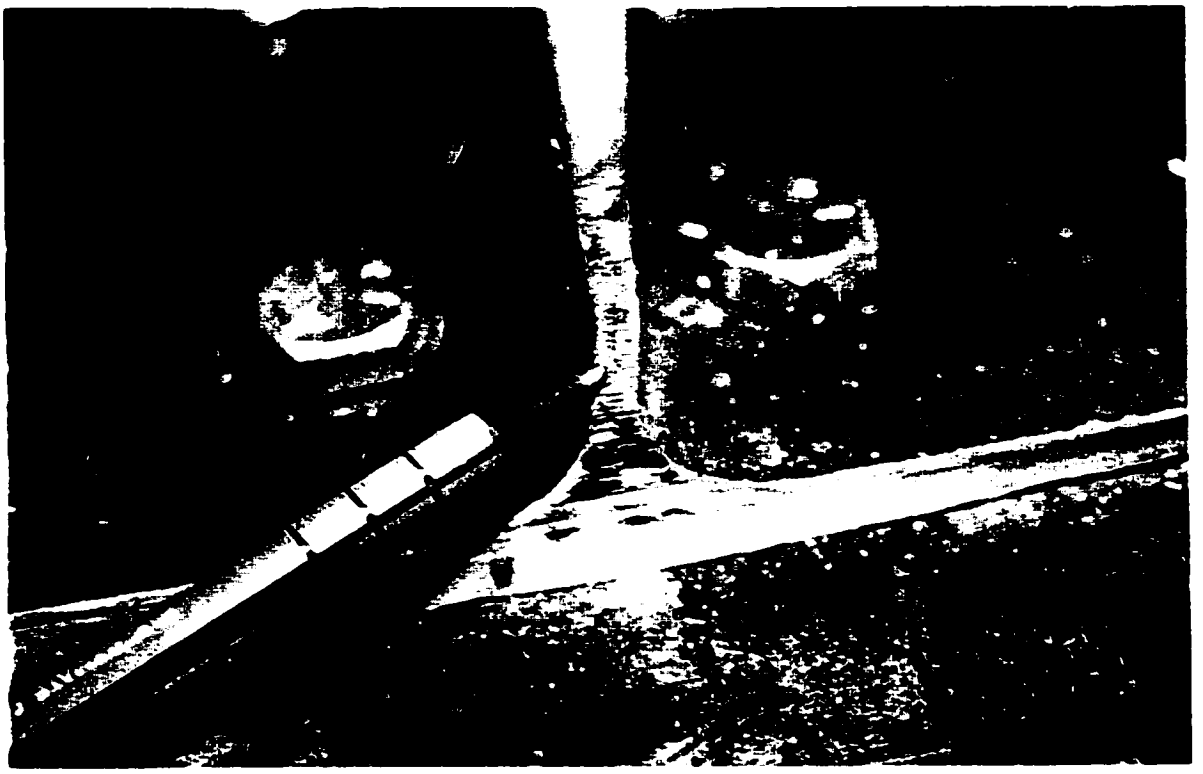

Figure 6.32 Test #5 - Lamination at West End of Specimen at 30th Cycle

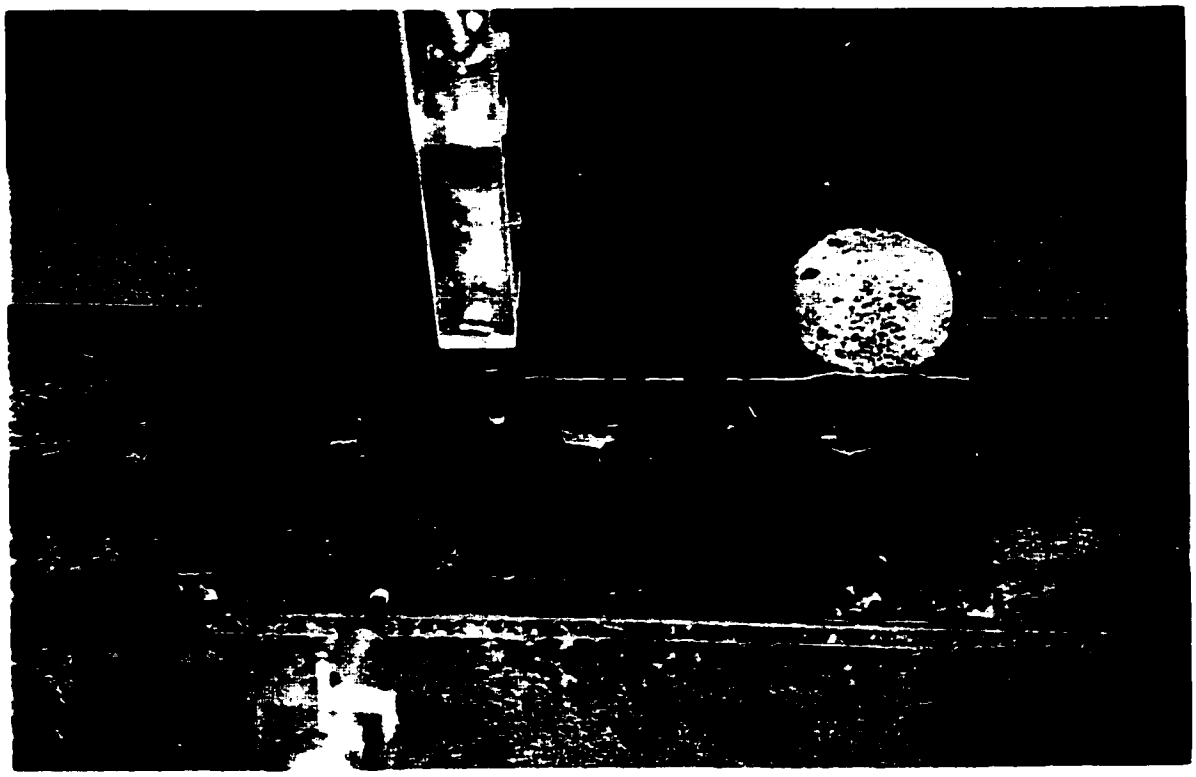

Figure 6.33 Test #5 - Propagation of South Face Teat at 30th Cycle

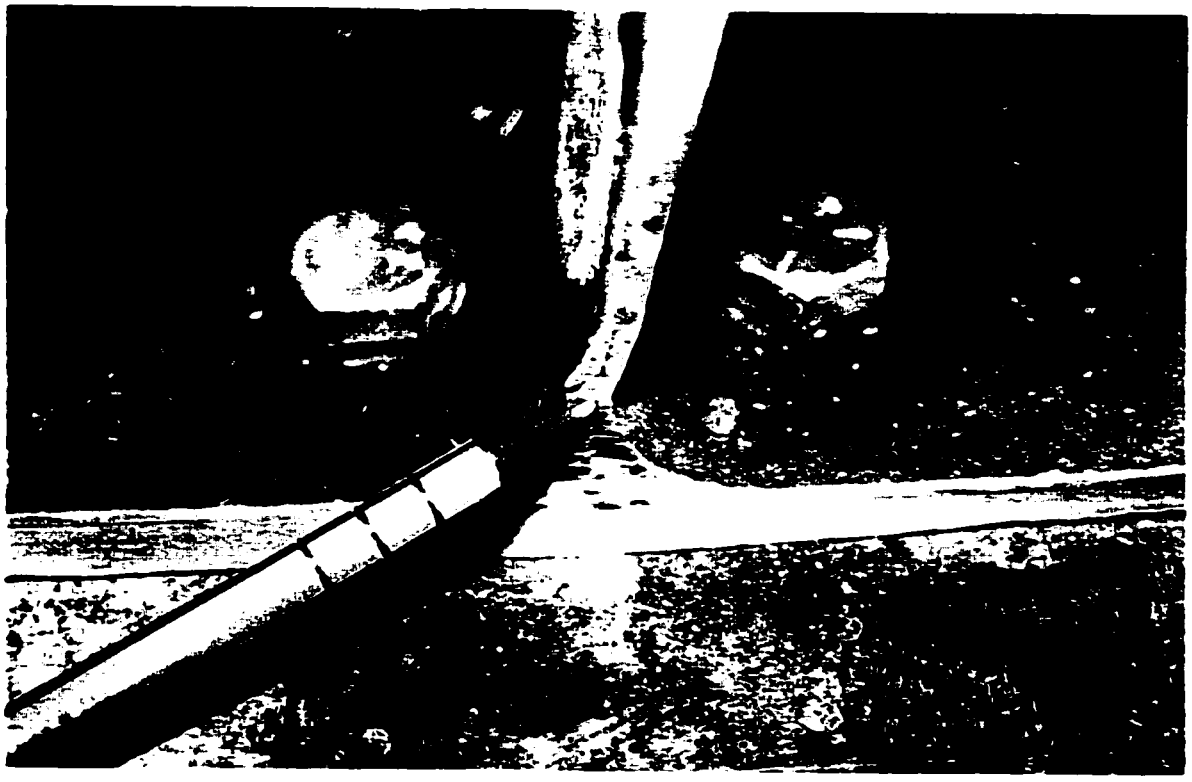

Figure 6.34 Test #5 - Lamination at East End of Specimen at 30th Cycle

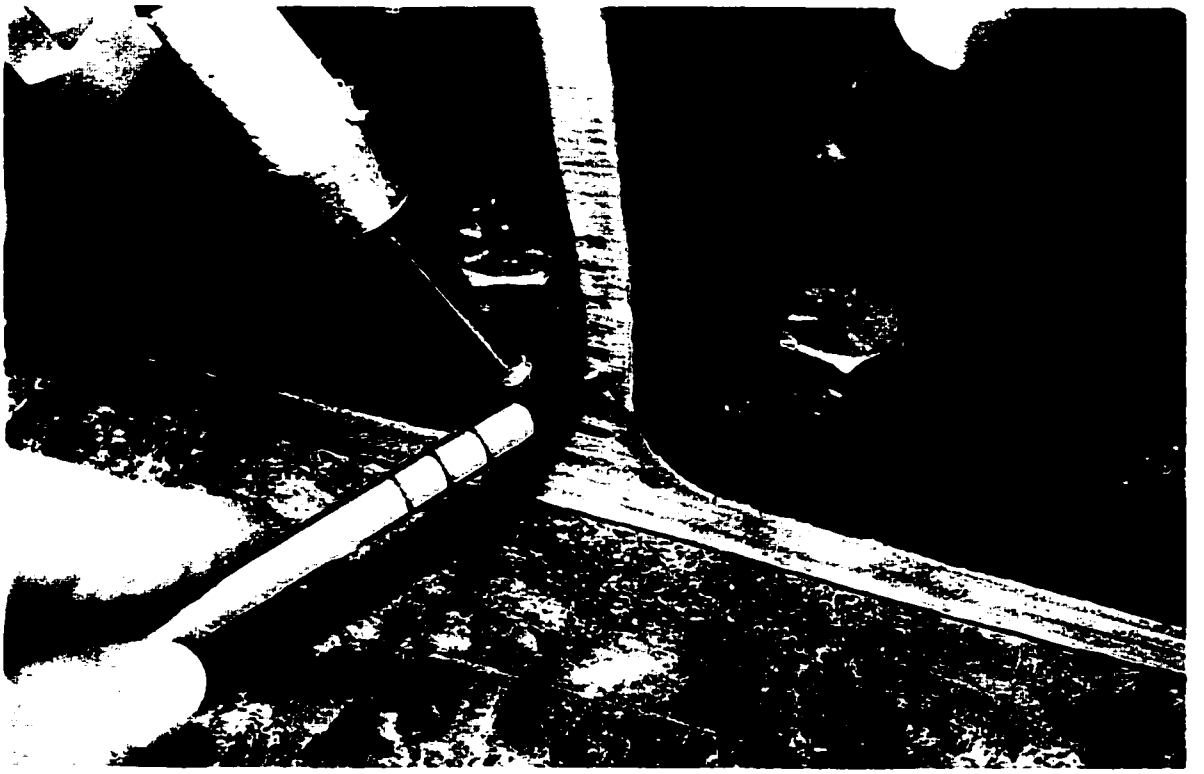

Figure 6.35 Test #5 - Solid West End of Specimen at 30th Cycle

Figure 6.36 Test #5 - Hairline Crack on North Face
After 45th Cycle

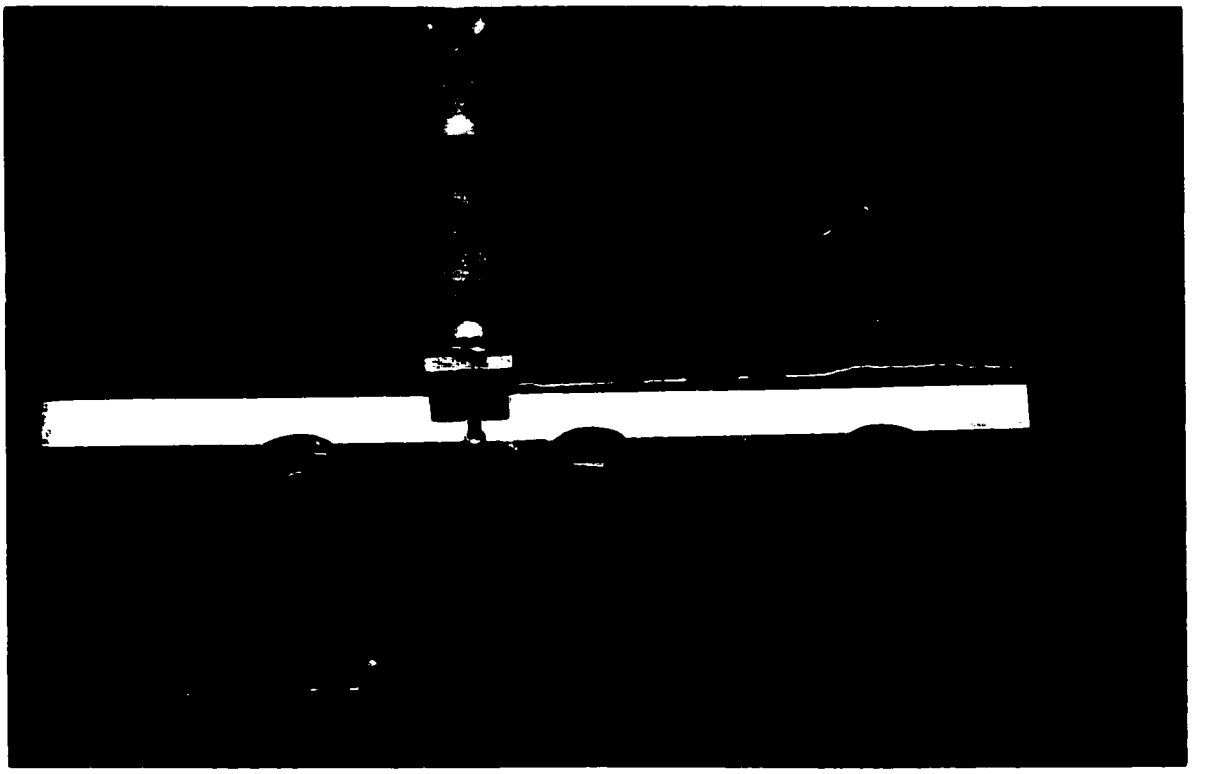

Figure 6.37 Test #5 - Extent of Cracking on South Face After 45th Cycle

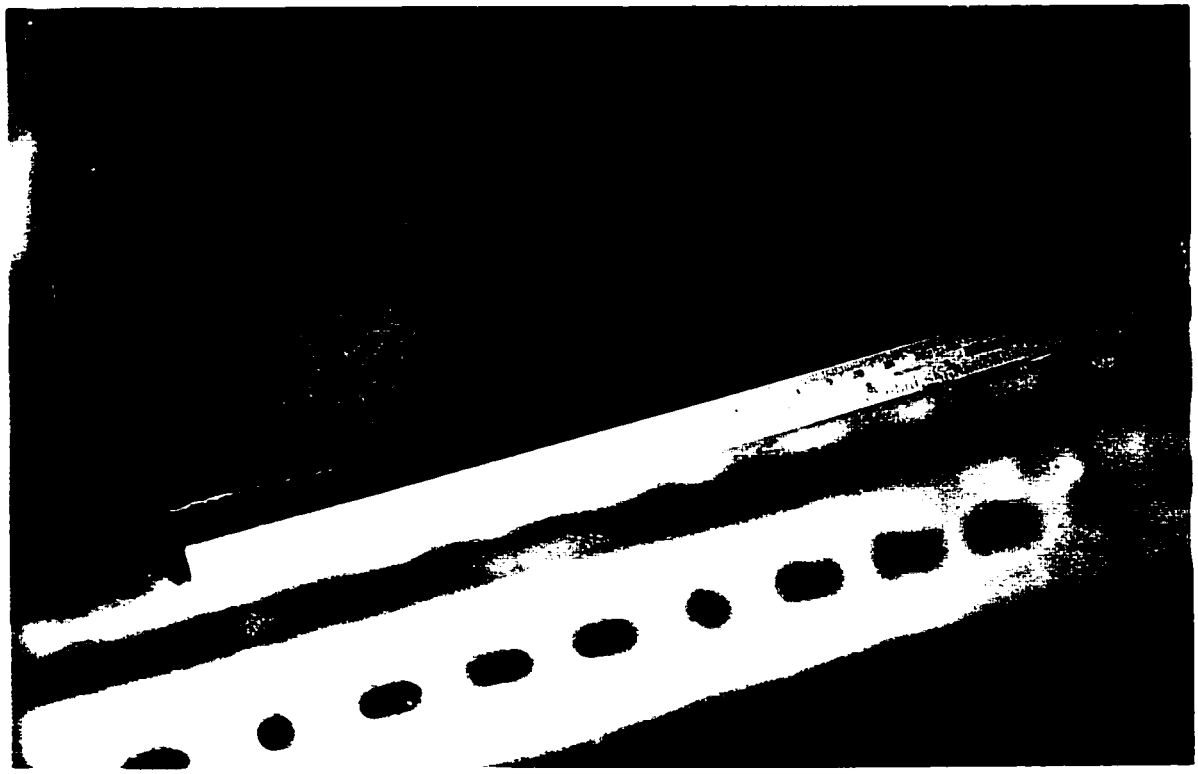

Figure 6.38 Test #5 - North Face Cracking at Failure

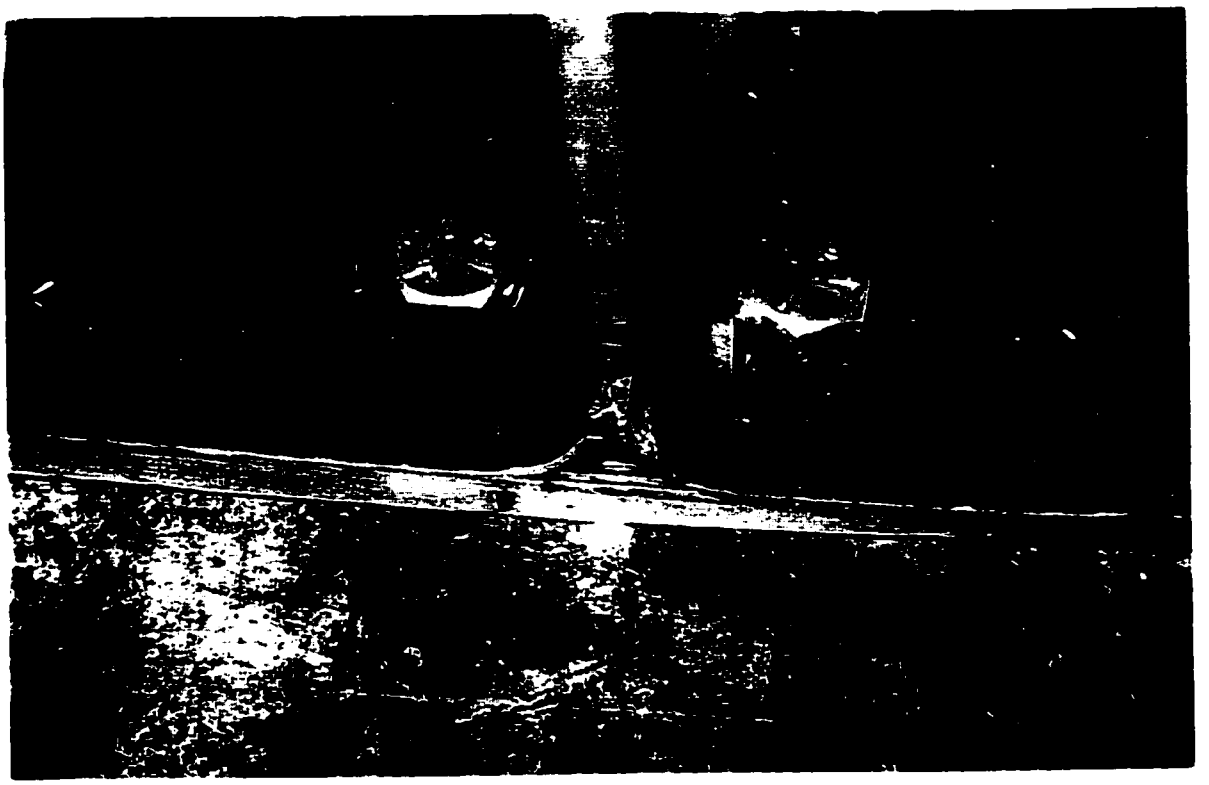

Figure 6.39 Test #5 -East End Lamination at Failure

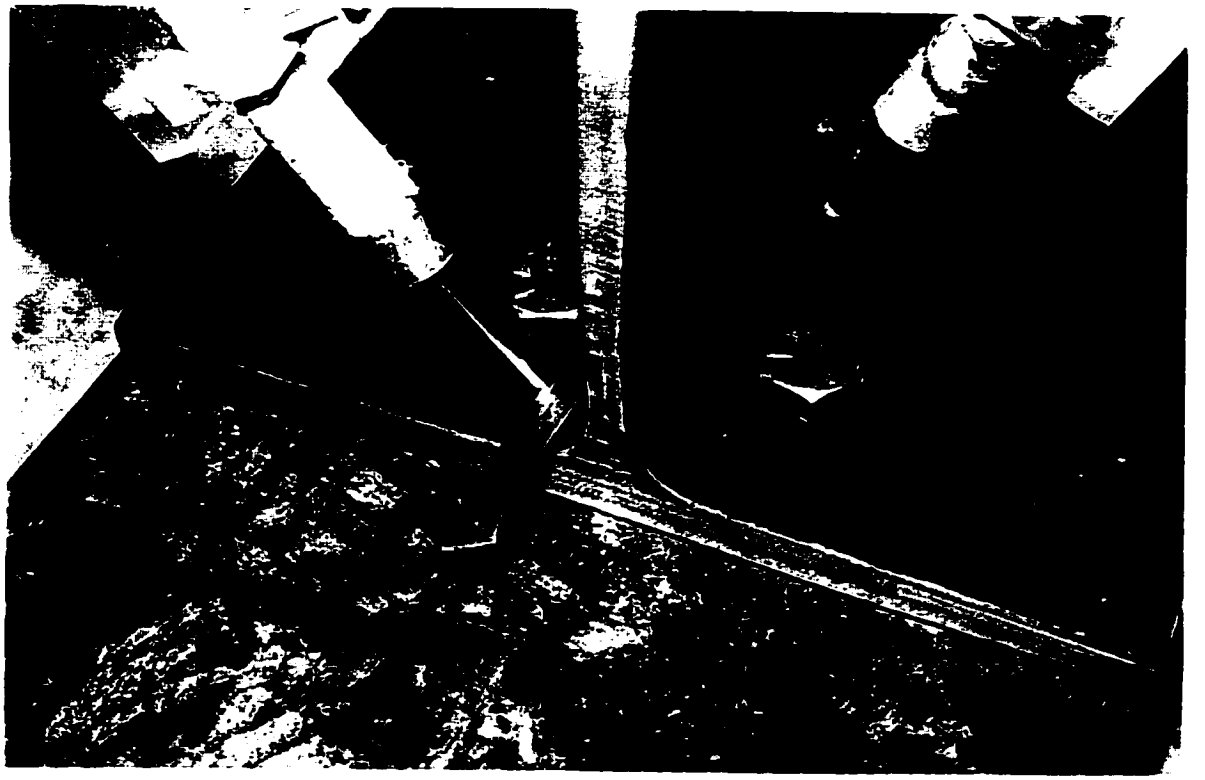

Figure 6.40 Test #5 - West End Lamination at Failure

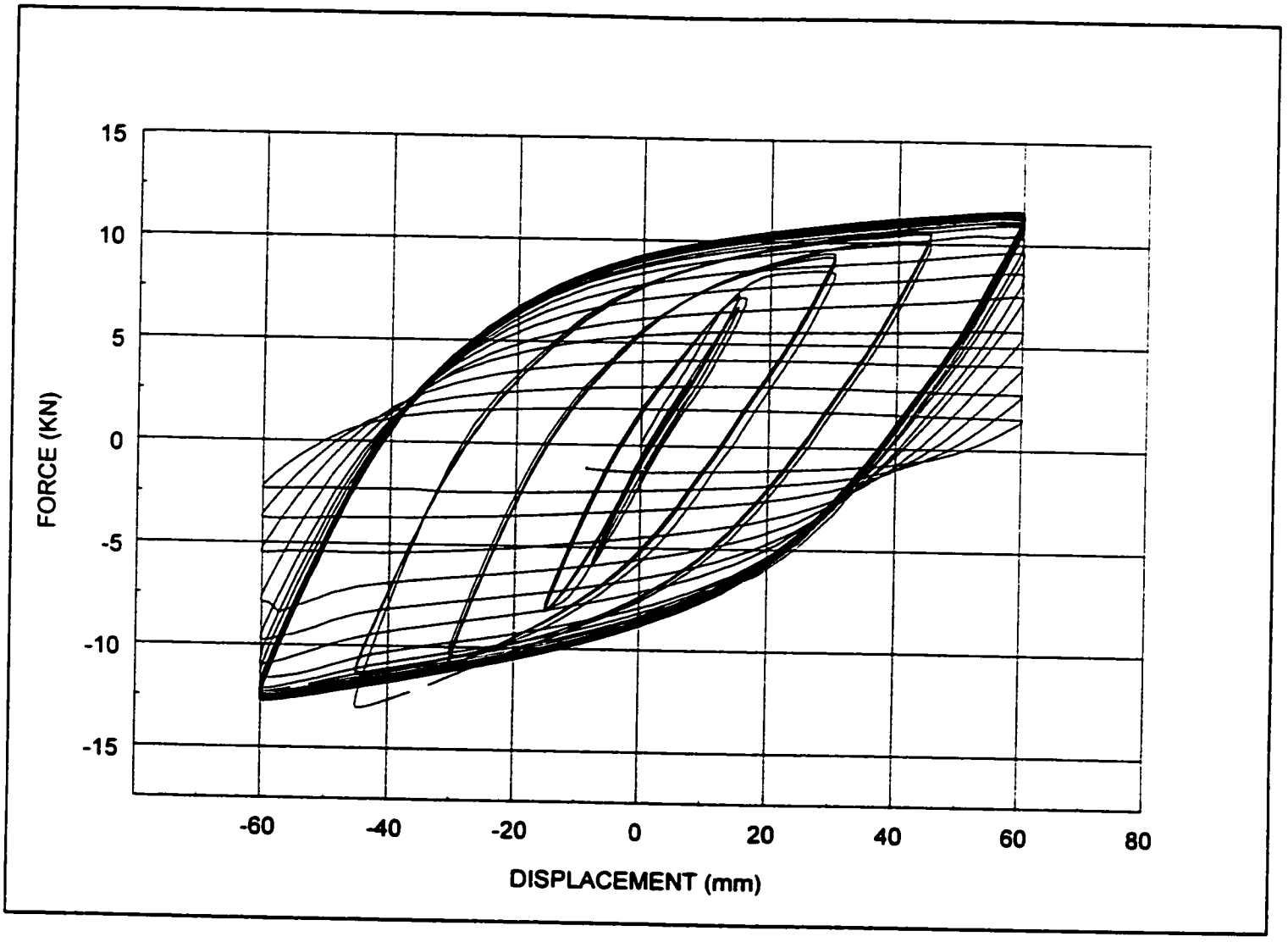

Figure 6.41 Hysteretic Curves for Test 6

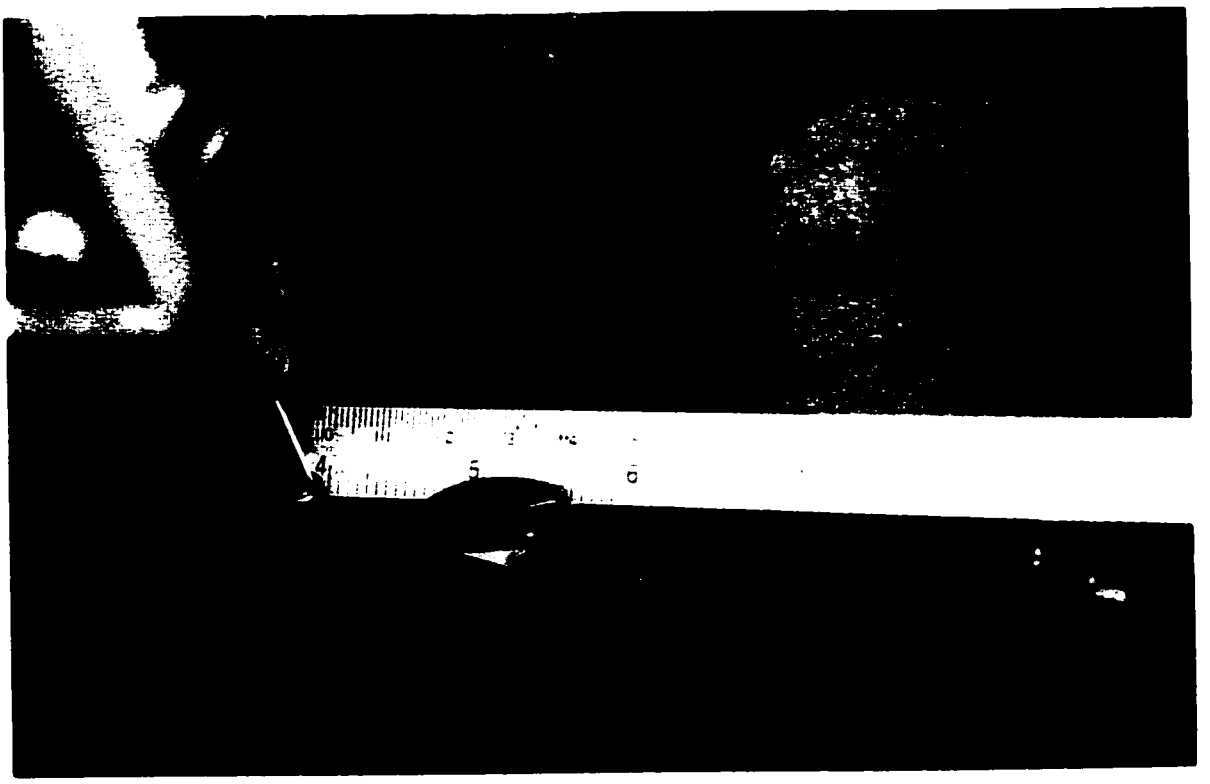

Figure 6.42 Test #6 - Hairline Cracking on South Face After 42nd Cycle

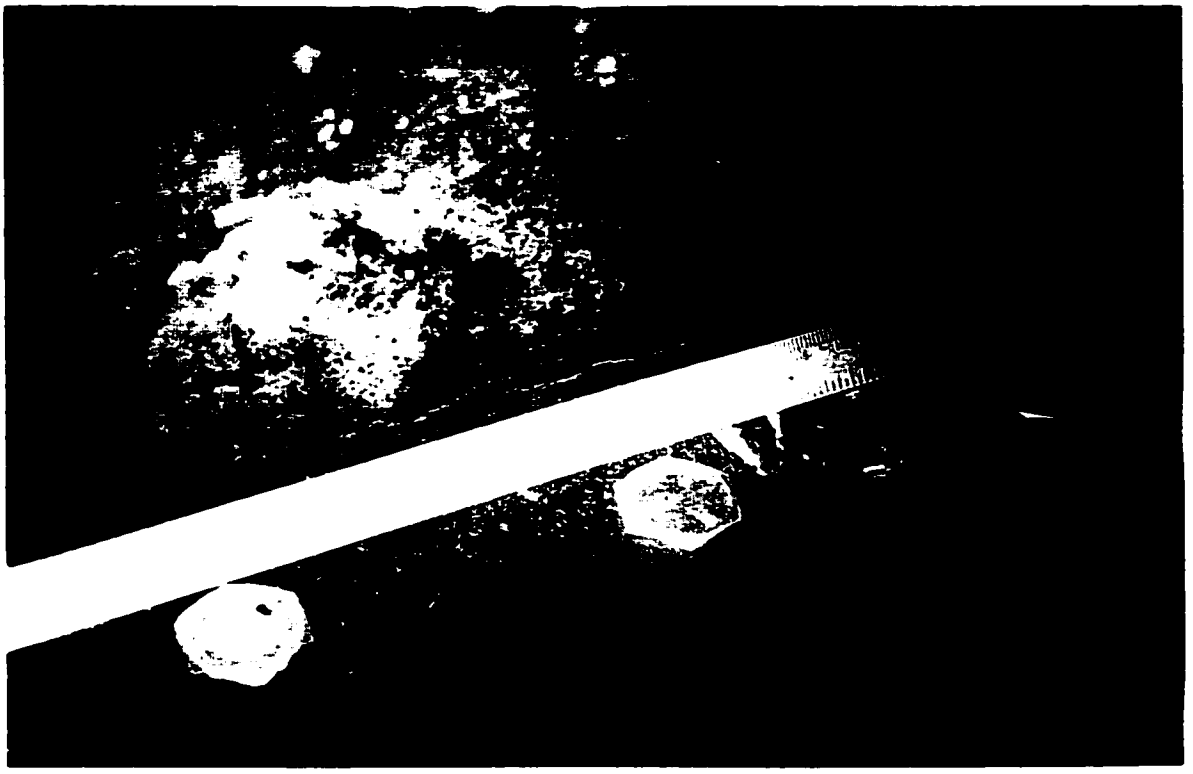

Figure 6.43 Test #6 - Hairline Cracking on North Face After 42nd Cycle

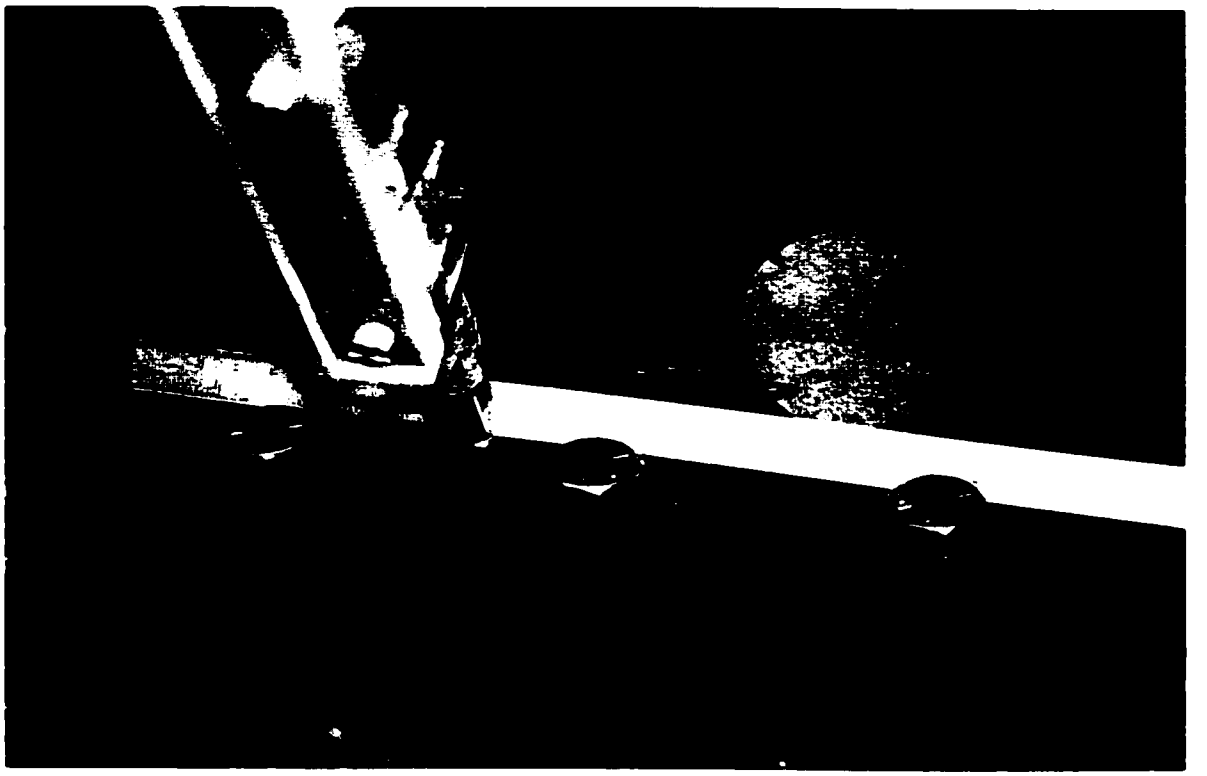

Figure 6.44 Test #6 - Propagation of South Face Crack After 49th Cycle

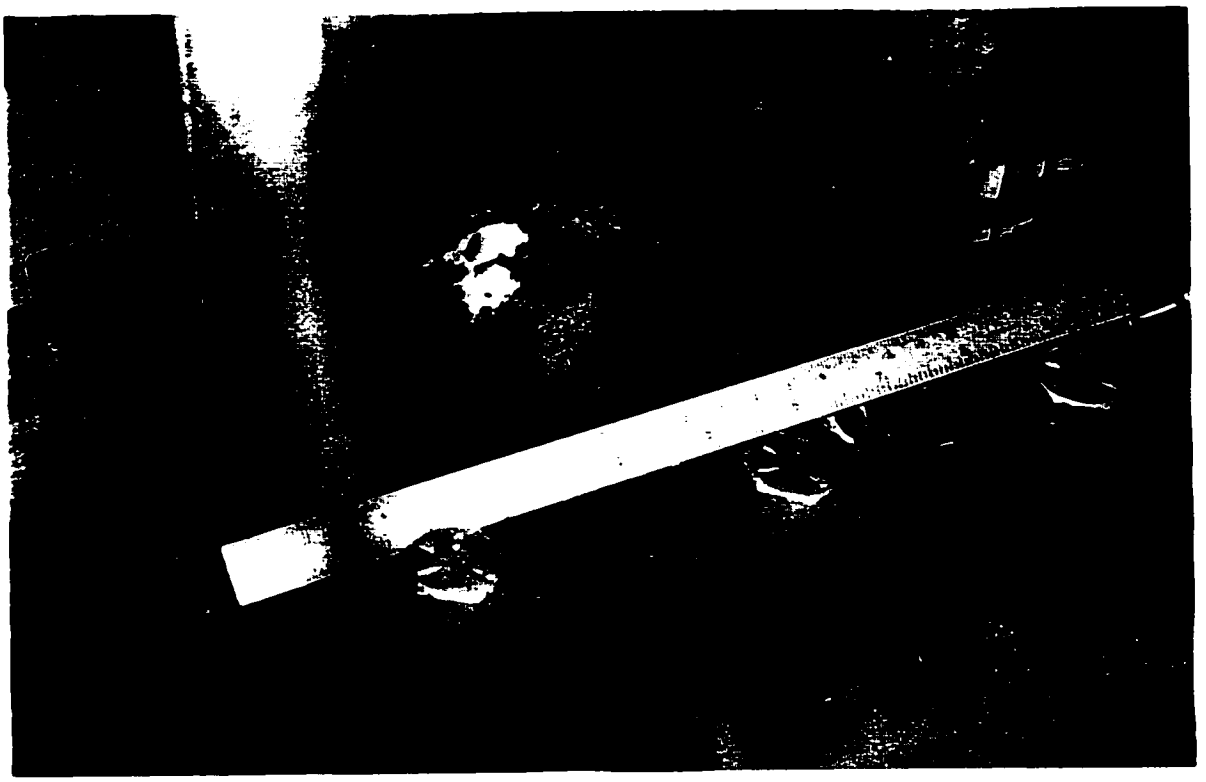

Figure 6.45 Test #6 - Propagation of North Face Crack After 49th Cycle

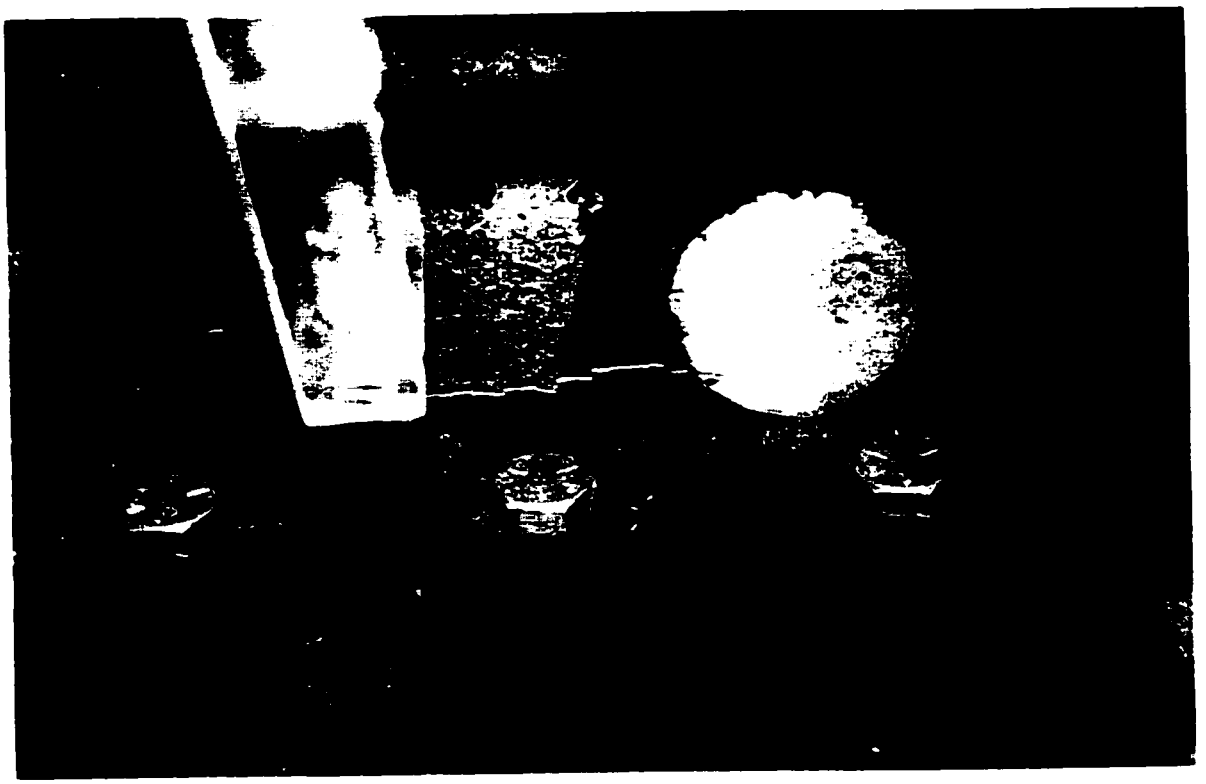

Figure 6.46 Test #6 - South Face Crack at Cycle 53

Figure 6.47 Test #6 - North Face Crack at Cycle 53

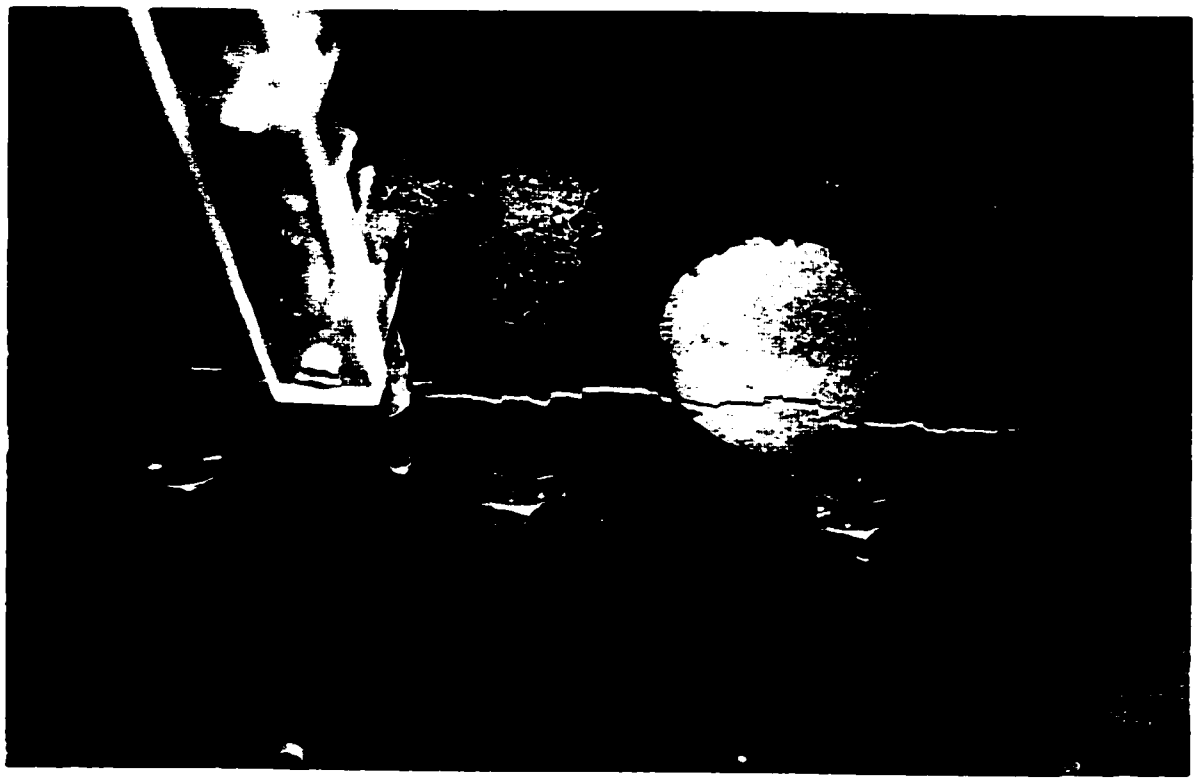

Figure 6.48 Test #6 - Extent of South Face Cracking After 58th Cycle

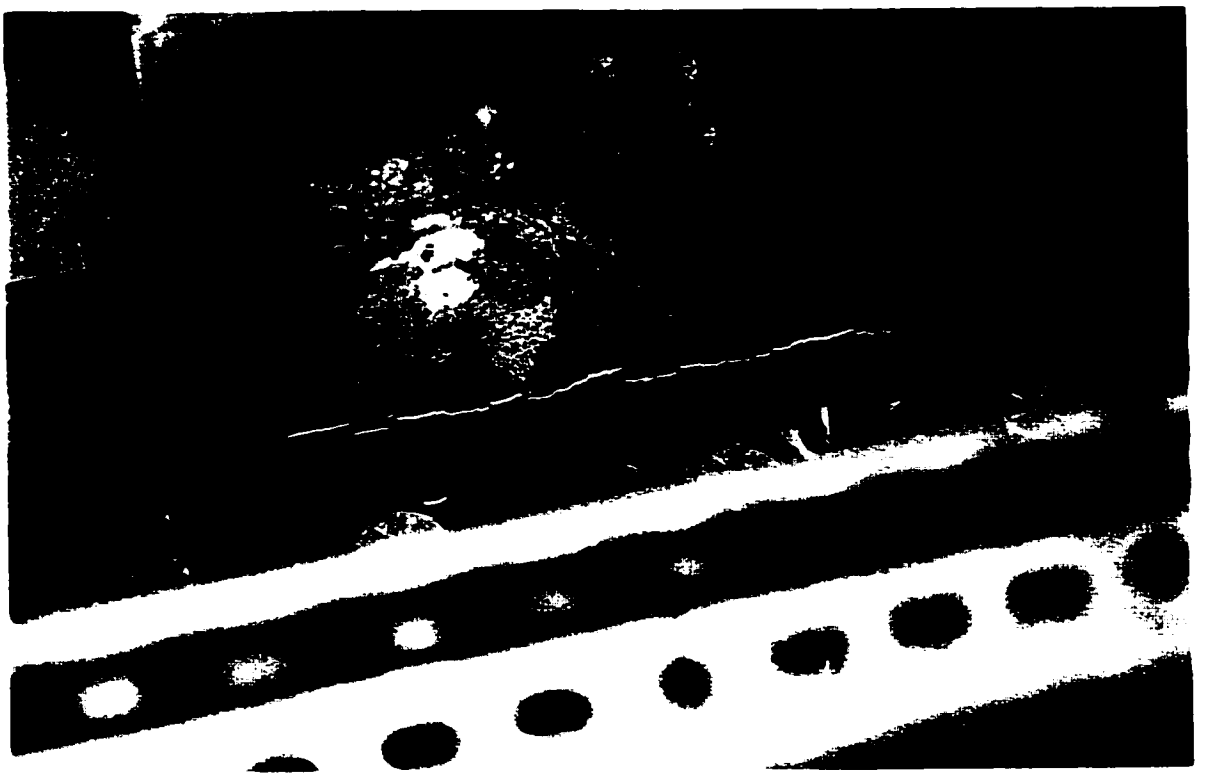

Figure 6.49 Test #6 - Extent of North Face Cracking After 58th Cycle

Figure 6.50 Test #6 - South Face at Failure

Figure 6.51 Test #6 - North Face at Failure

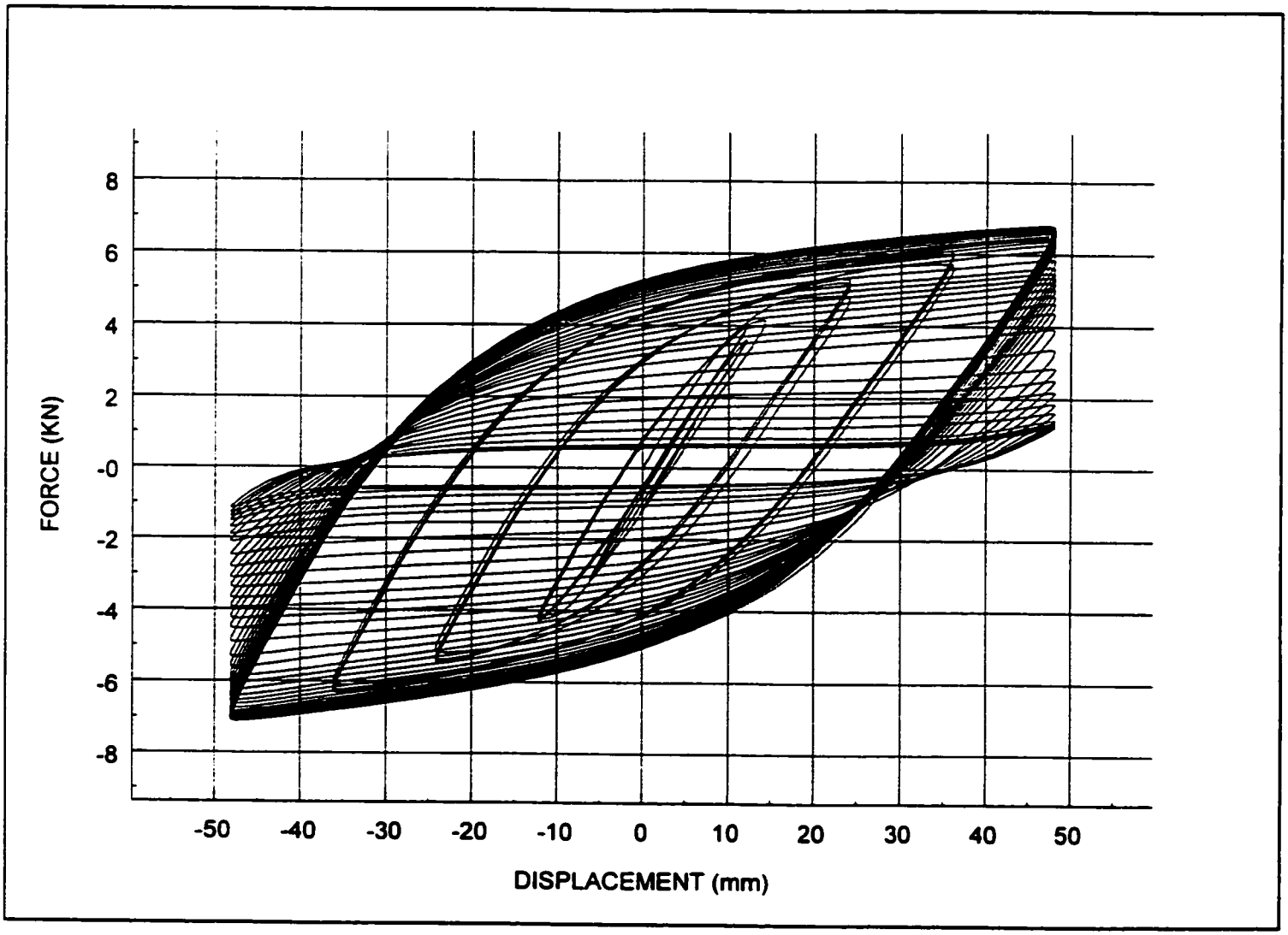

Figure 6.52 Hysteretic Curves for Test 7

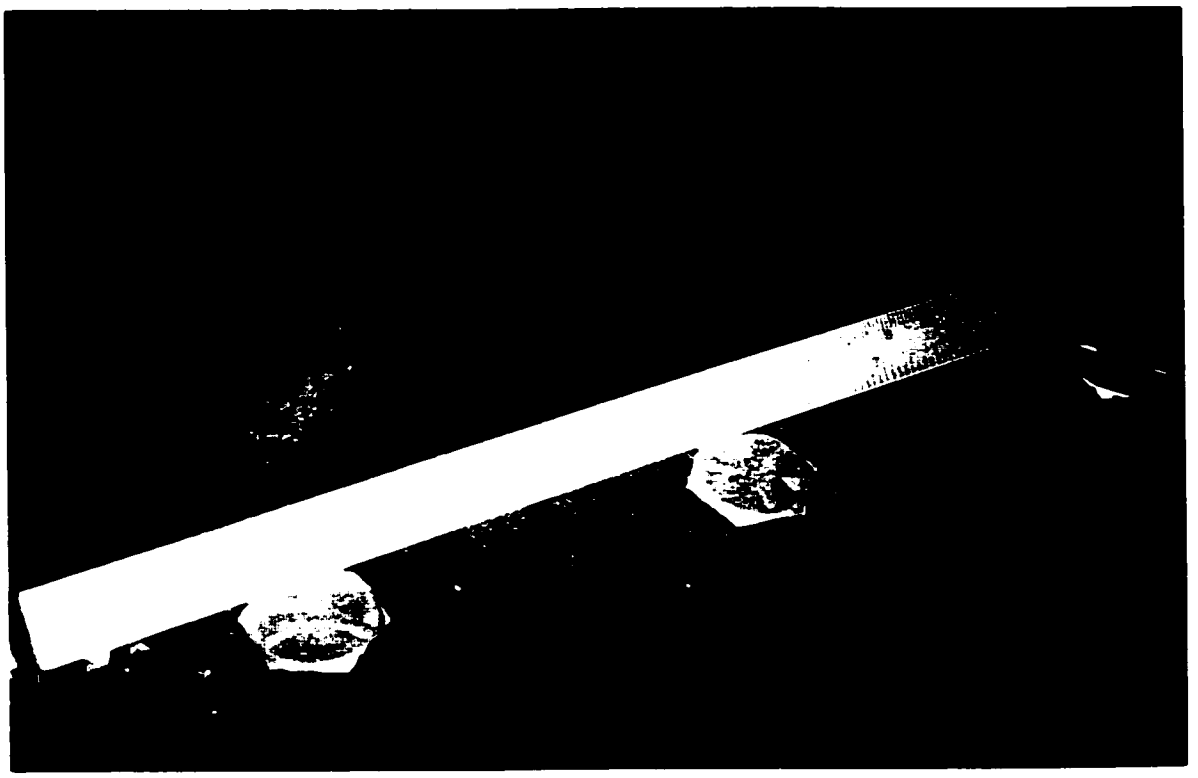

Figure 6.53 Test #7 - Hairline Cracking of North Fact at 54th Cycle

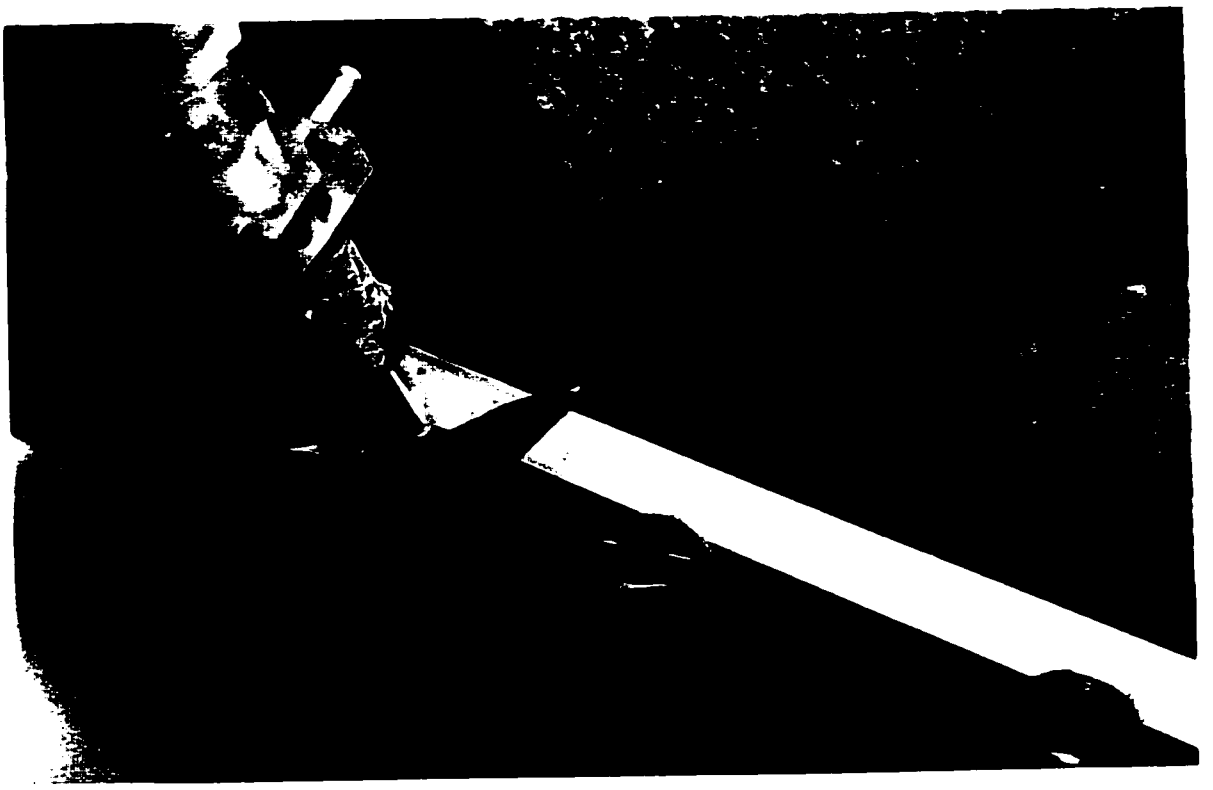

Figure 6.54 Test #7 - Hairline Cracking of South Face at 54th Cycle

Figure 6.55 Test #7 - Extent of Cracking of South Face at 58th Cycle

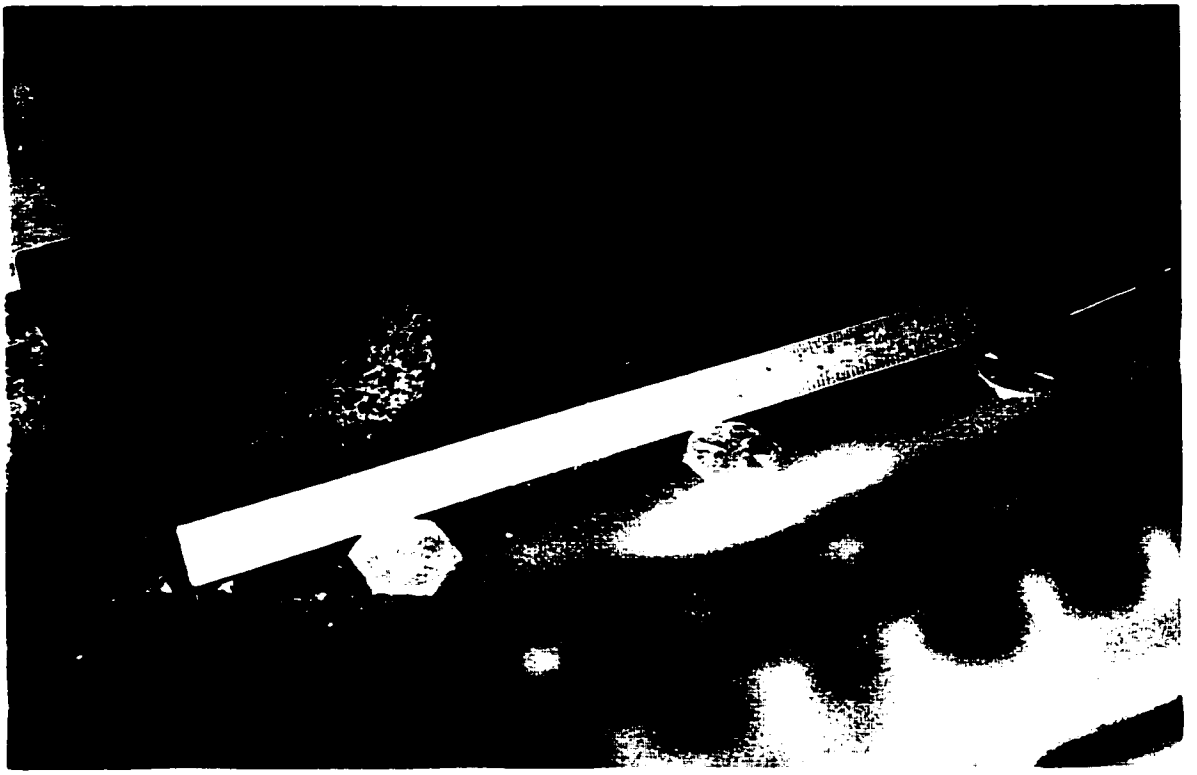

Figure 6.56 Test #7 - Extent of Cracking of North Face at 59th Cycle

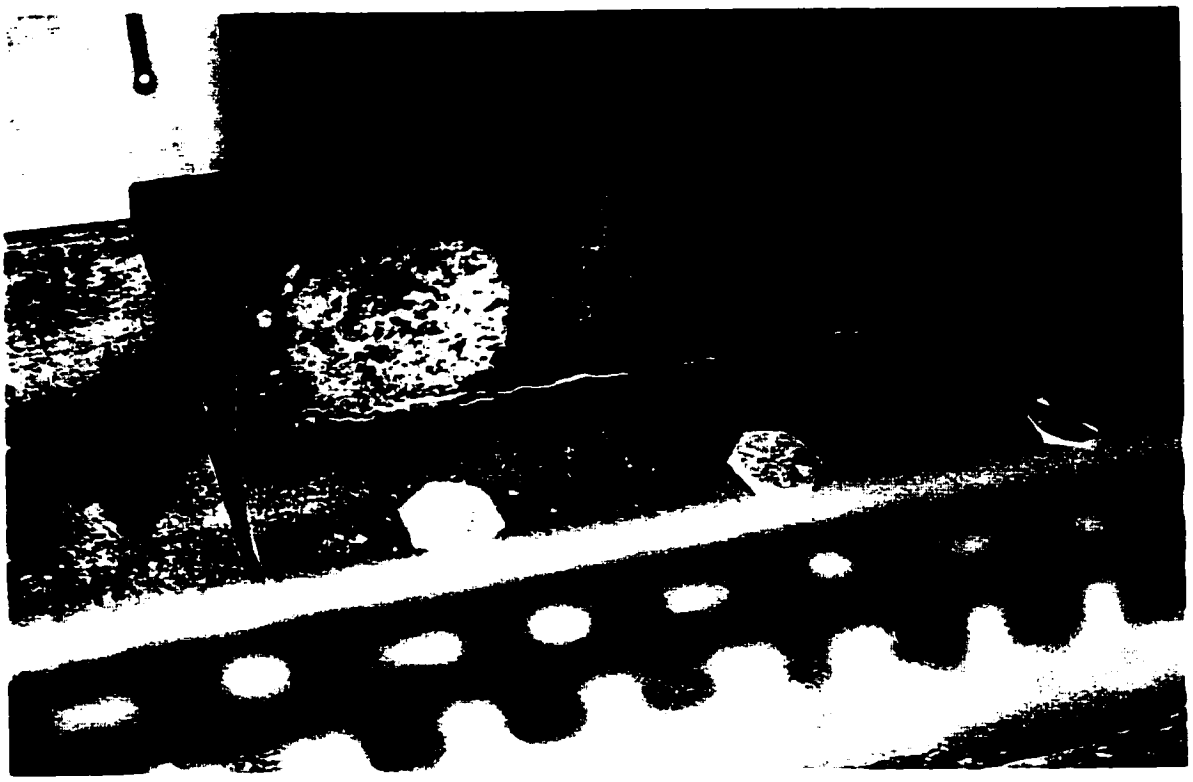

Figure 6.57 Test #7 - Extent of Cracking of South Face at 75th Cycle

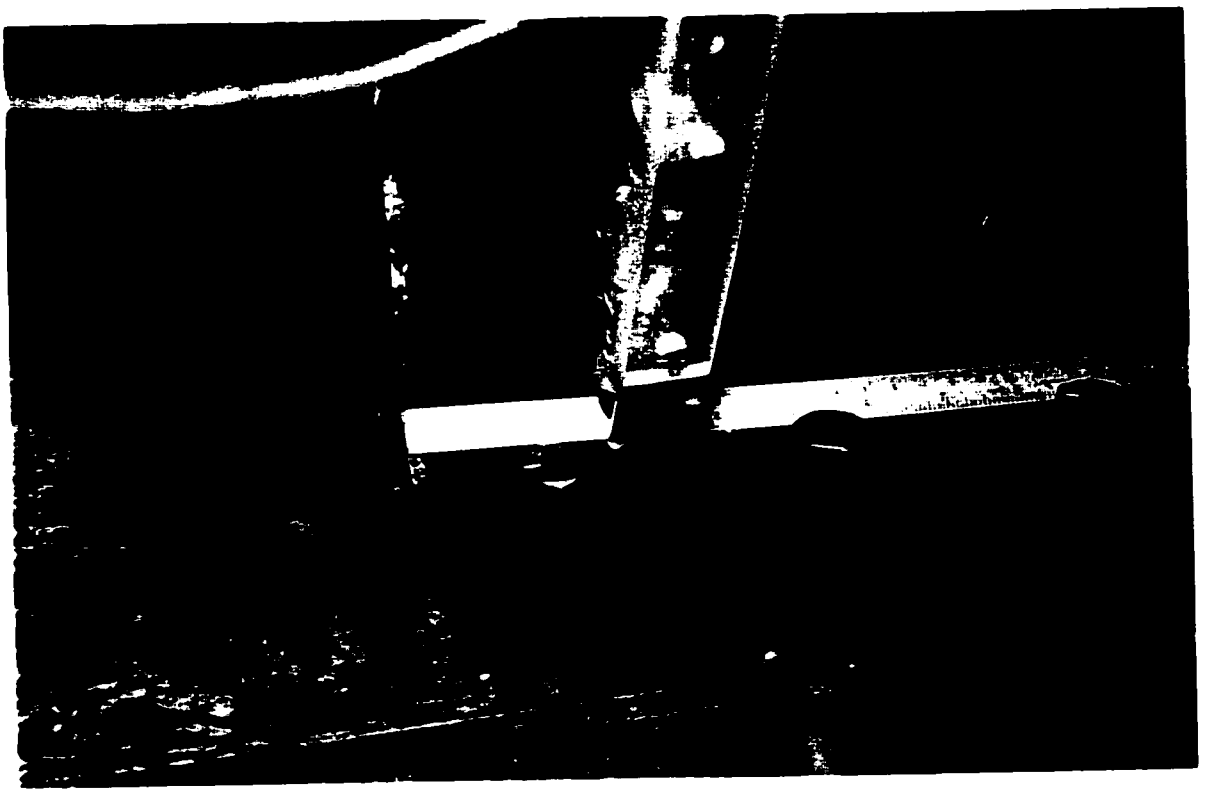

Figure 6.58 Test #7 - Extent of Cracking of North Face at 75th Cycle

Figure 6.59 Test #7 - West End Lamination at 80th Cycle

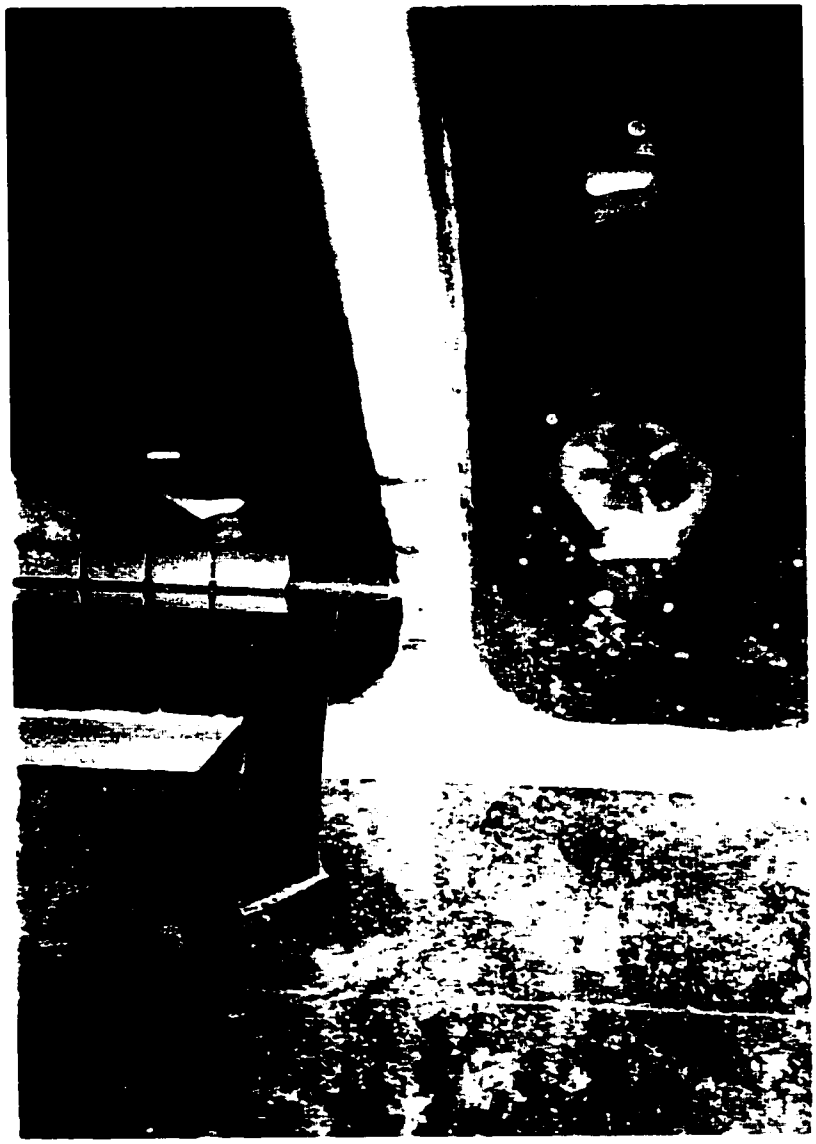

Figure 6.60 Test #7 - East End Lamination at 80th Cycle

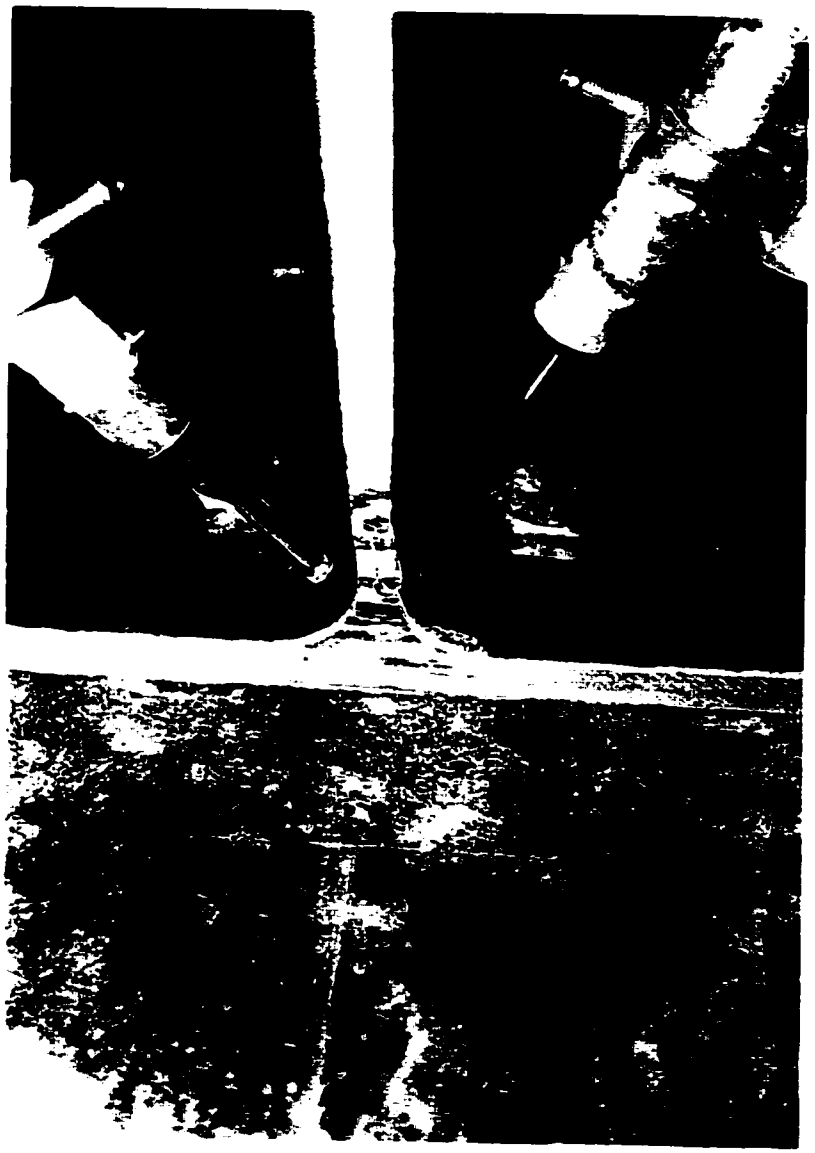

Figure 6.61 Test #7 - West End Lamination at 83rd Cycle

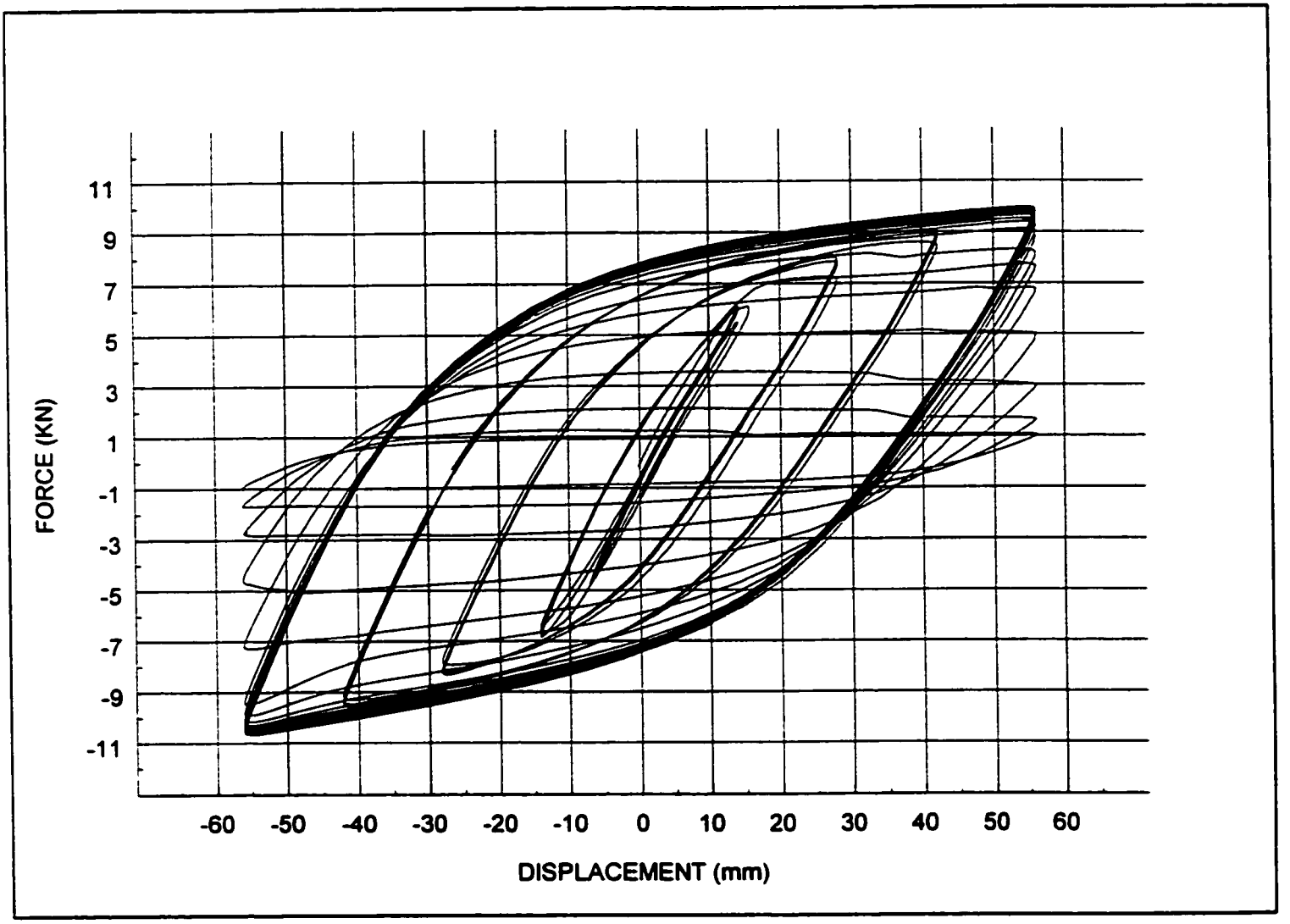

Figure 6.62 Hysteretic Curves for Test 8

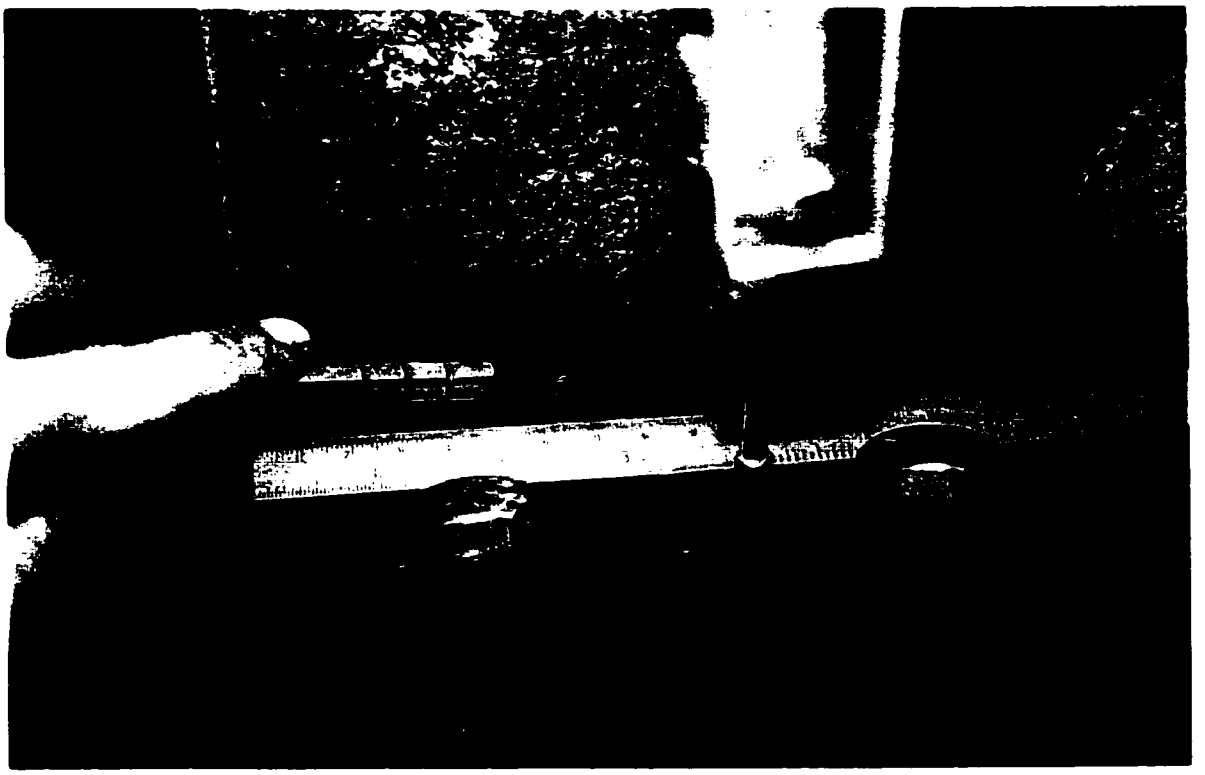

Figure 6.63 Test# 8 - South Face Cracking After 52nd Cycle

Figure 6.64 Test #8 - North Face Cracking After 52nd Cycle

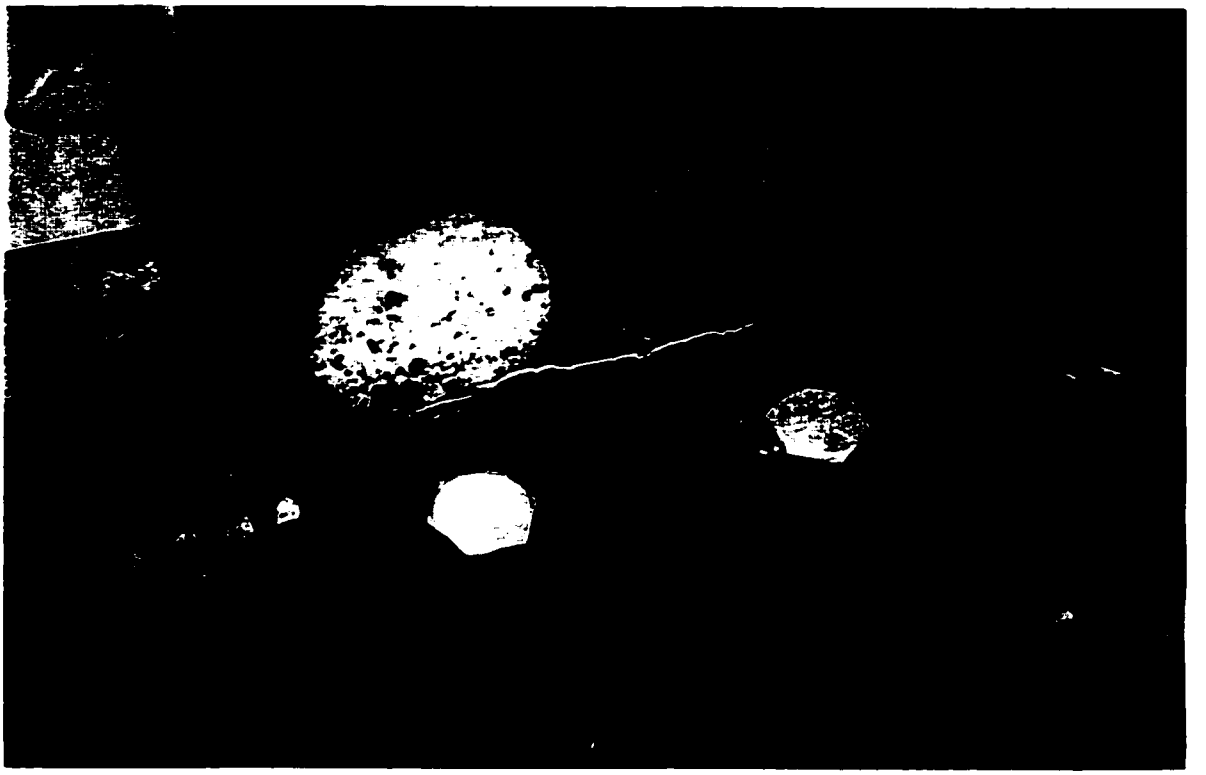

Figure 6.65 Test #8 - North Face Cracking After 55th Cycle

Figure 6.66 Test #8 - North Face Cracking After 57th Cycle

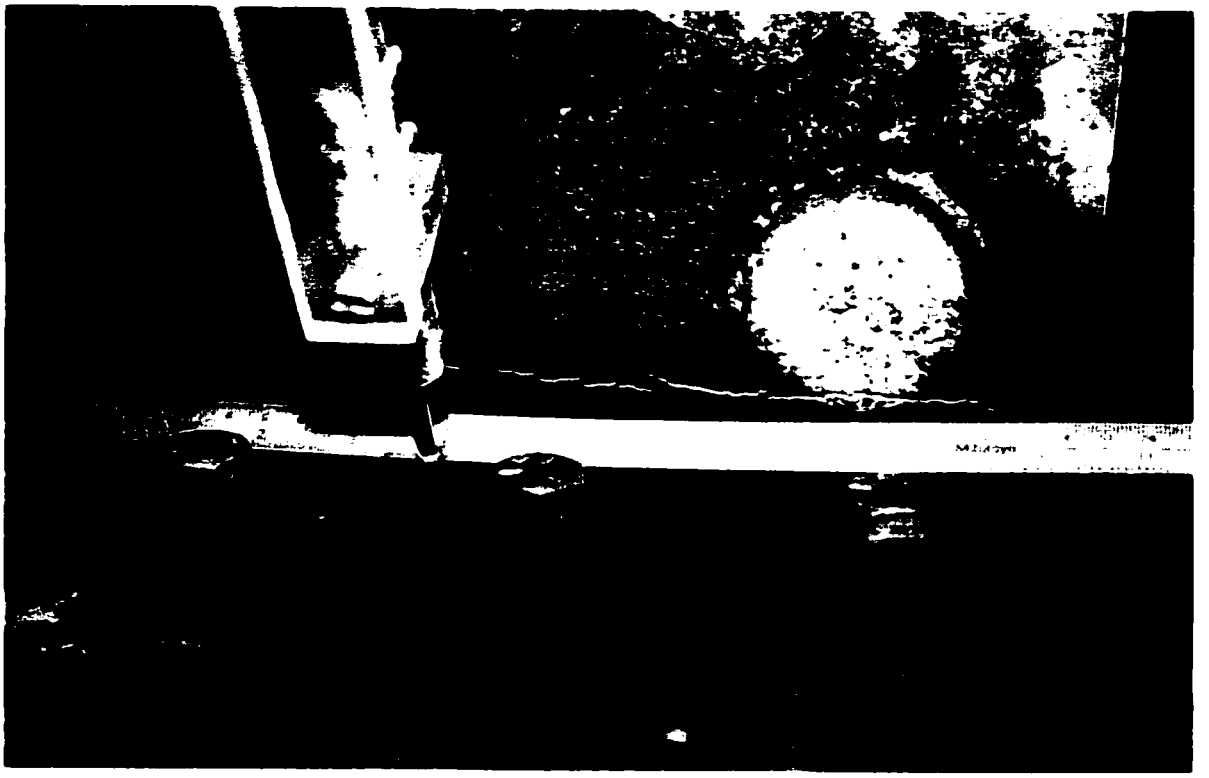

Figure 6.67 Test #8 - South Face Cracking After 60th Cycle

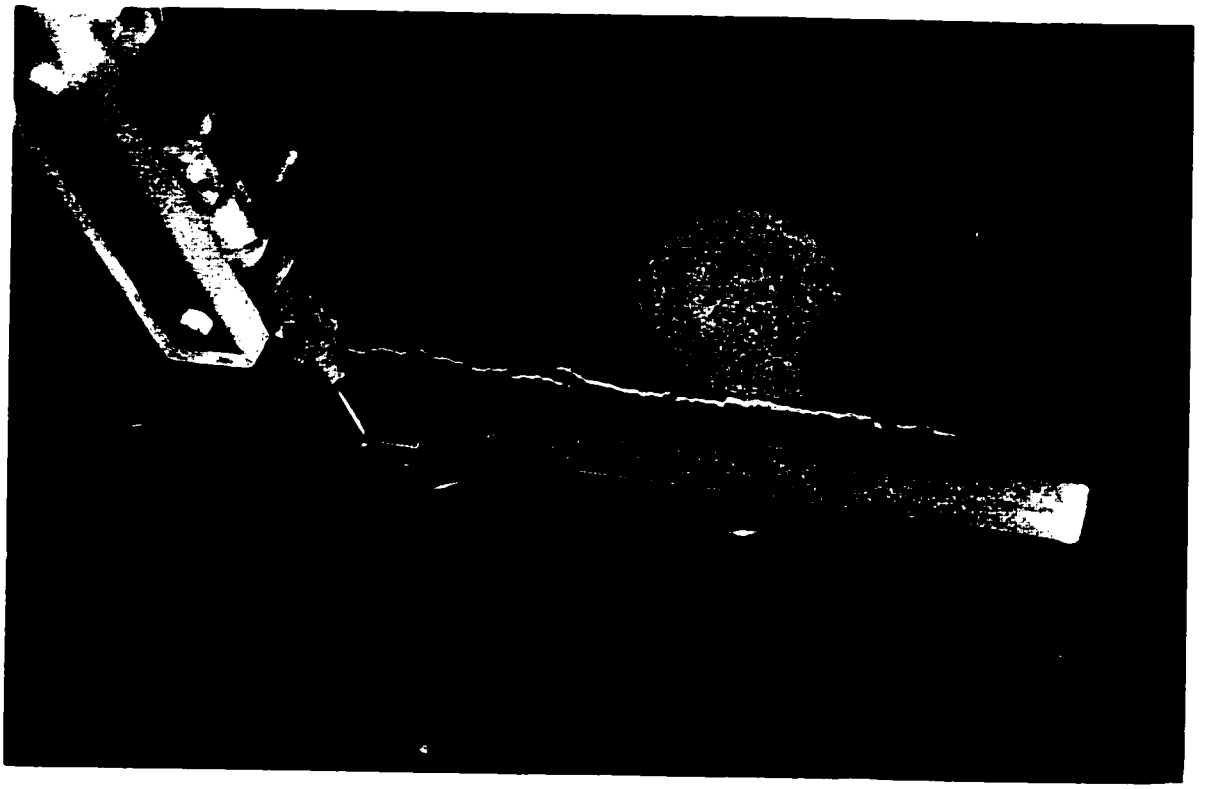

Figure 6.68 Test#8 - South Face at Failure

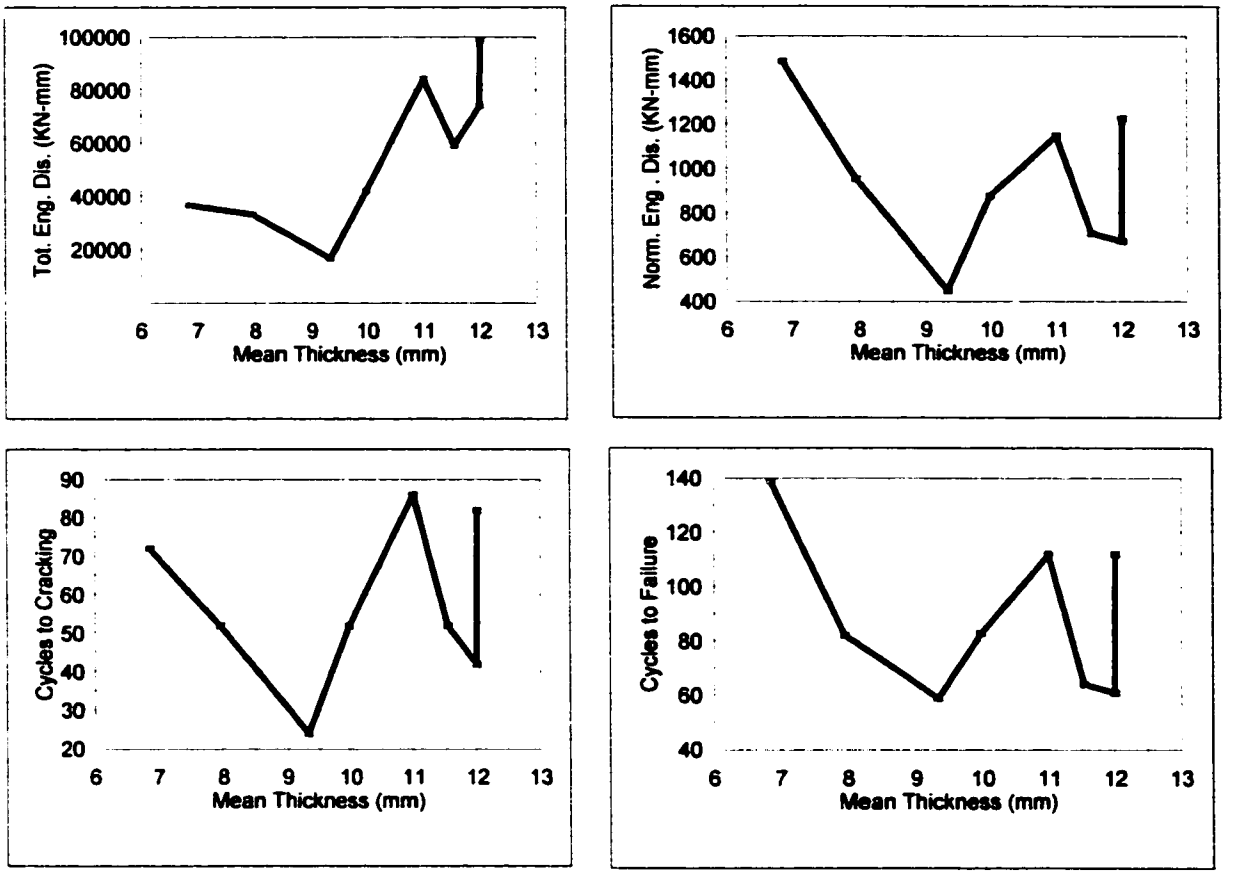

Figure 7.1 Mean Thickness vs. Total Energy Dissipated, Normalized Energy Dissipated, Cycles to Cracking and Cycles to Failure

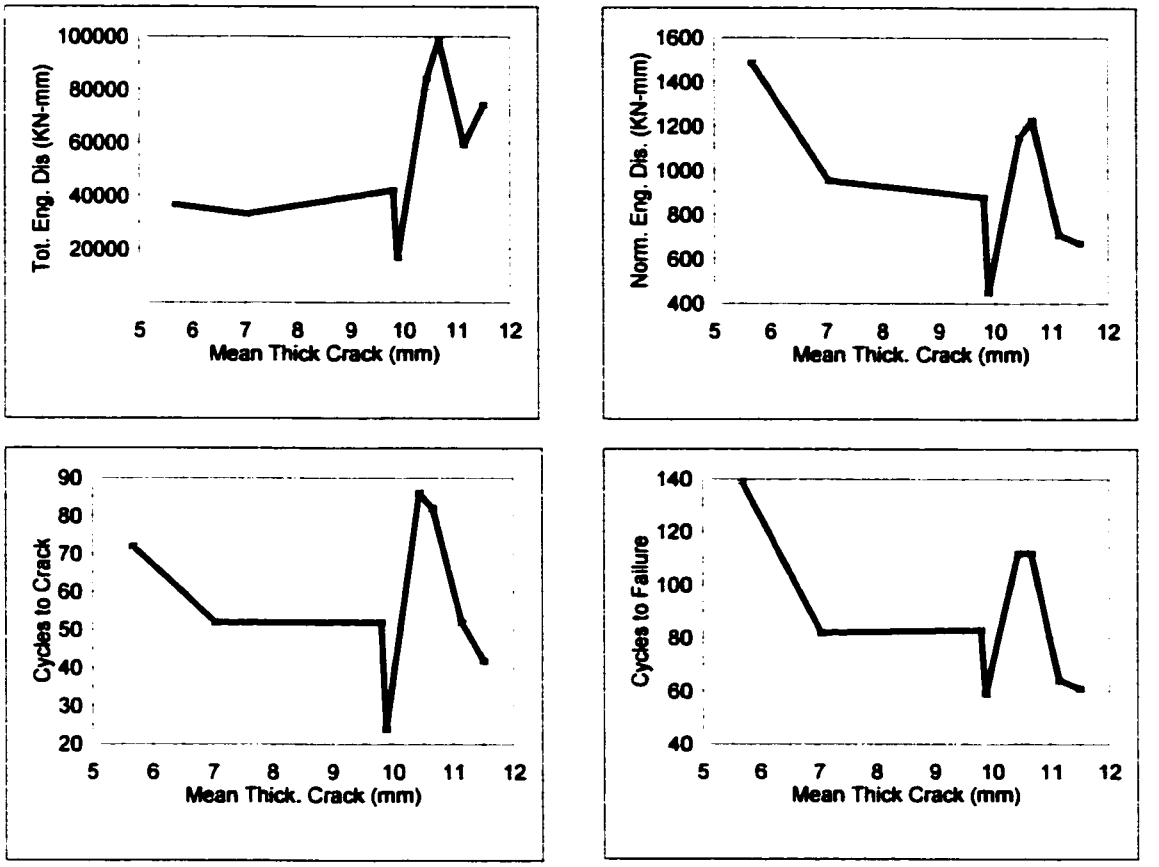

Figure 7.2 Mean Thickness at Cracking vs. Total Energy Dissipated, Normalized Energy Dissipated, Cycles to Cracking and Cycles to Failure

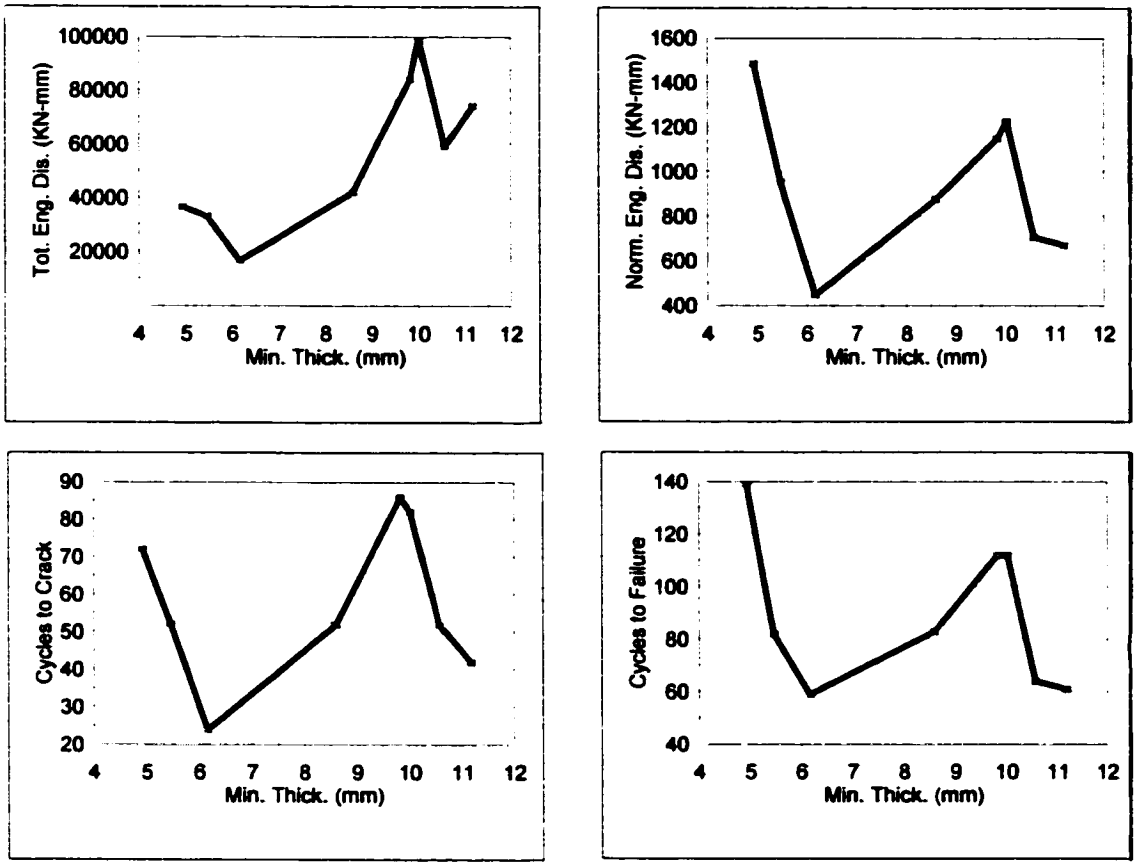

Figure 7.3 Minimum Thickness vs. Total Energy Dissipated, Normalized Energy Dissipated, Cycles to Cracking and Cycles to Failure

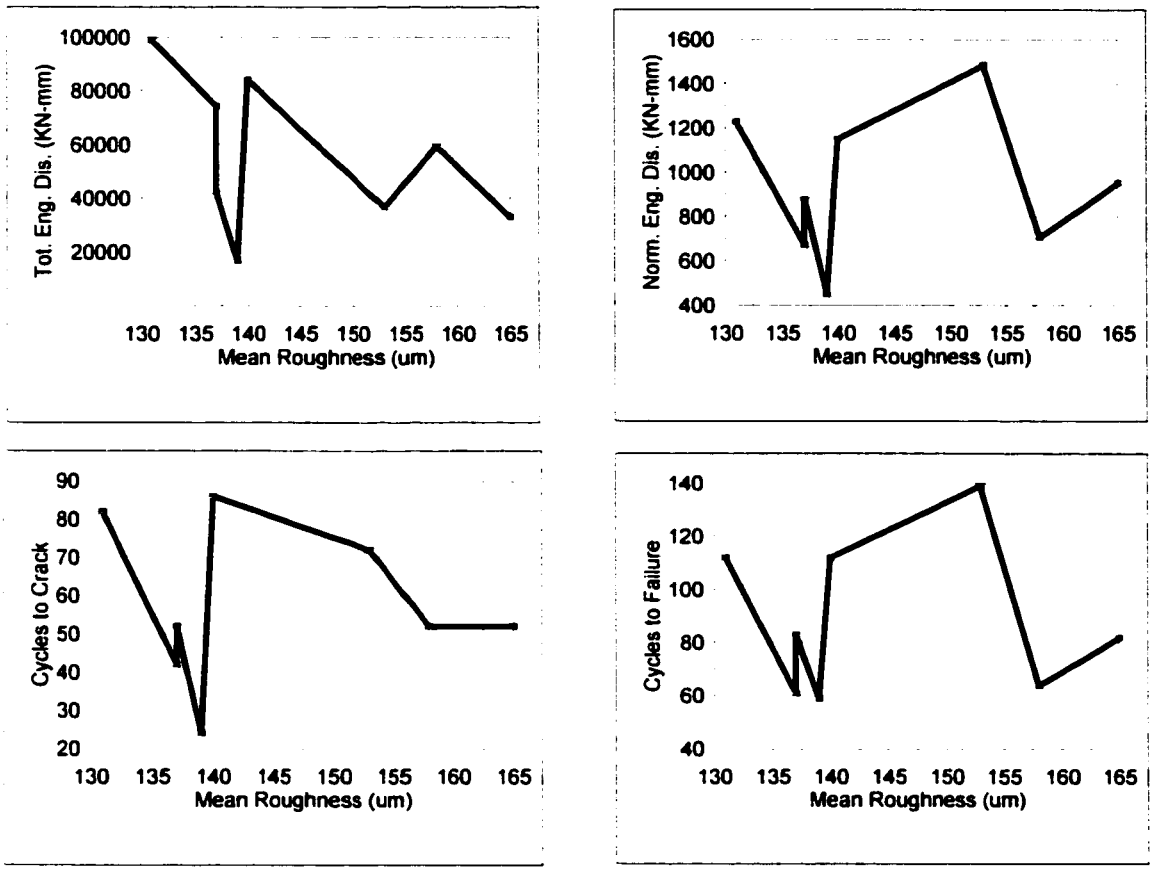

Figure 7.4 Mean Roughness vs. Total Energy Dissipated, Normalized Energy Dissipated, Cycles to Cracking and Cycles to Failure

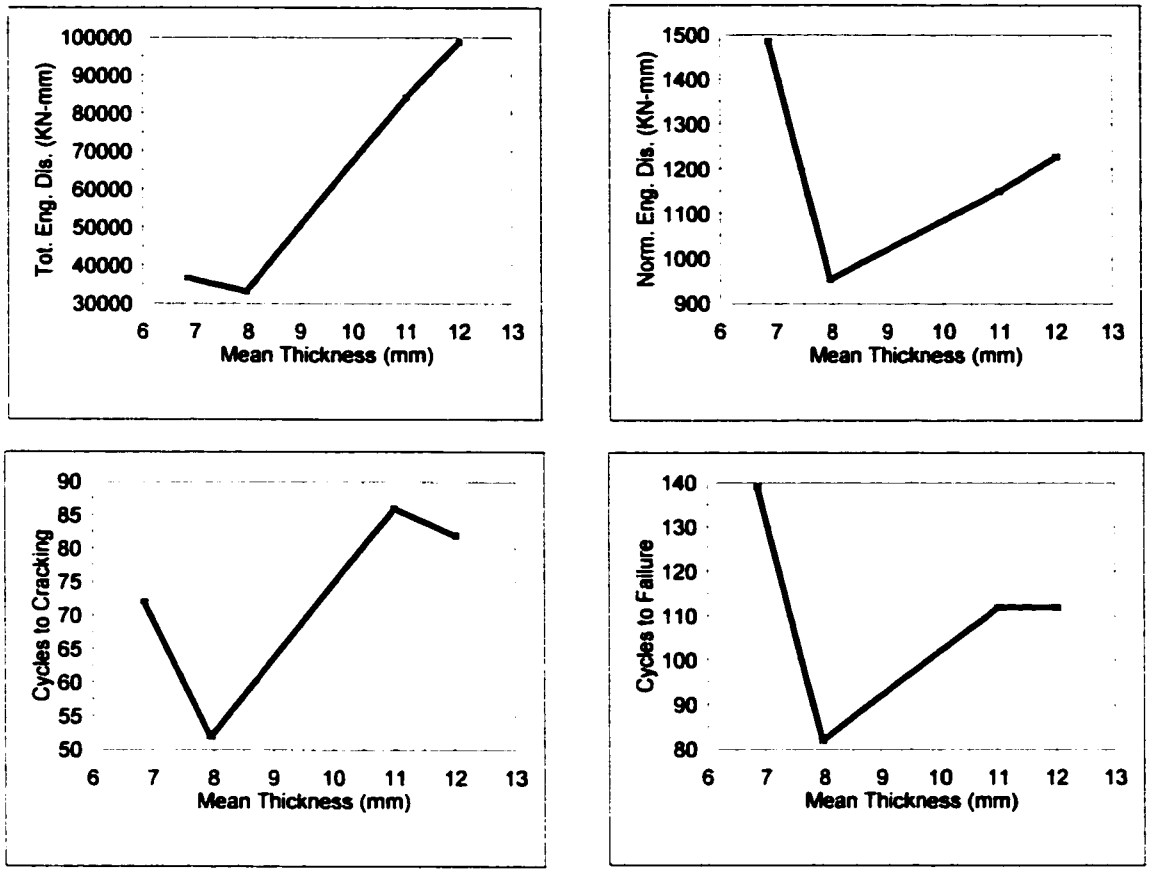

Figure 7.5 Mean Thickness vs. Total Energy Dissipated, Normalized Energy Dissipated, Cycles to Cracking and Cycles to Failure (Tests 1 to 4 Only)

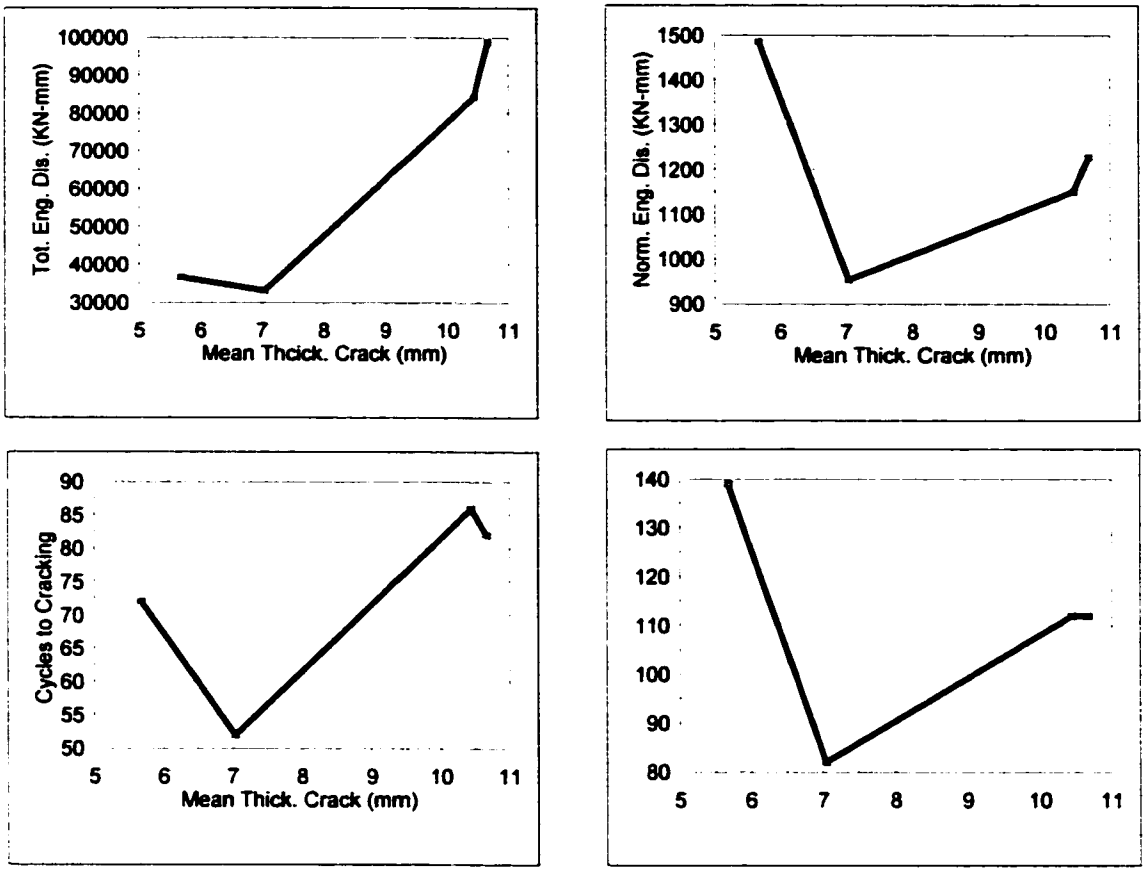

Figure 7.6 Mean Thickness at Cracking vs. Total Energy Dissipated, Normalized Energy Dissipated, Cycles to Cracking and Cycles to Failure (Tests 1 to 4 Only)

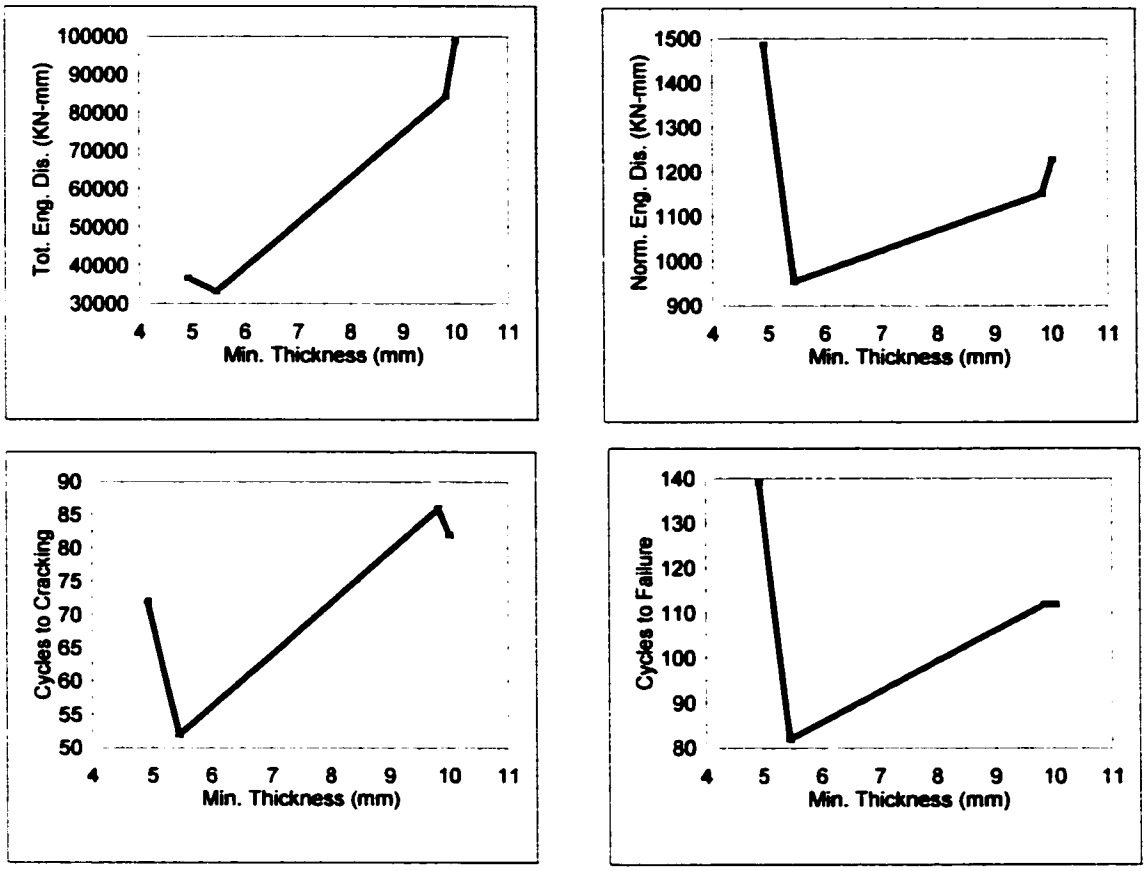

Figure 7.7 Minimum Thickness vs. Total Energy Dissipated, Normalized Energy Dissipated, Cycles to Cracking and Cycles to Failure (Tests 1 to 4 Only)

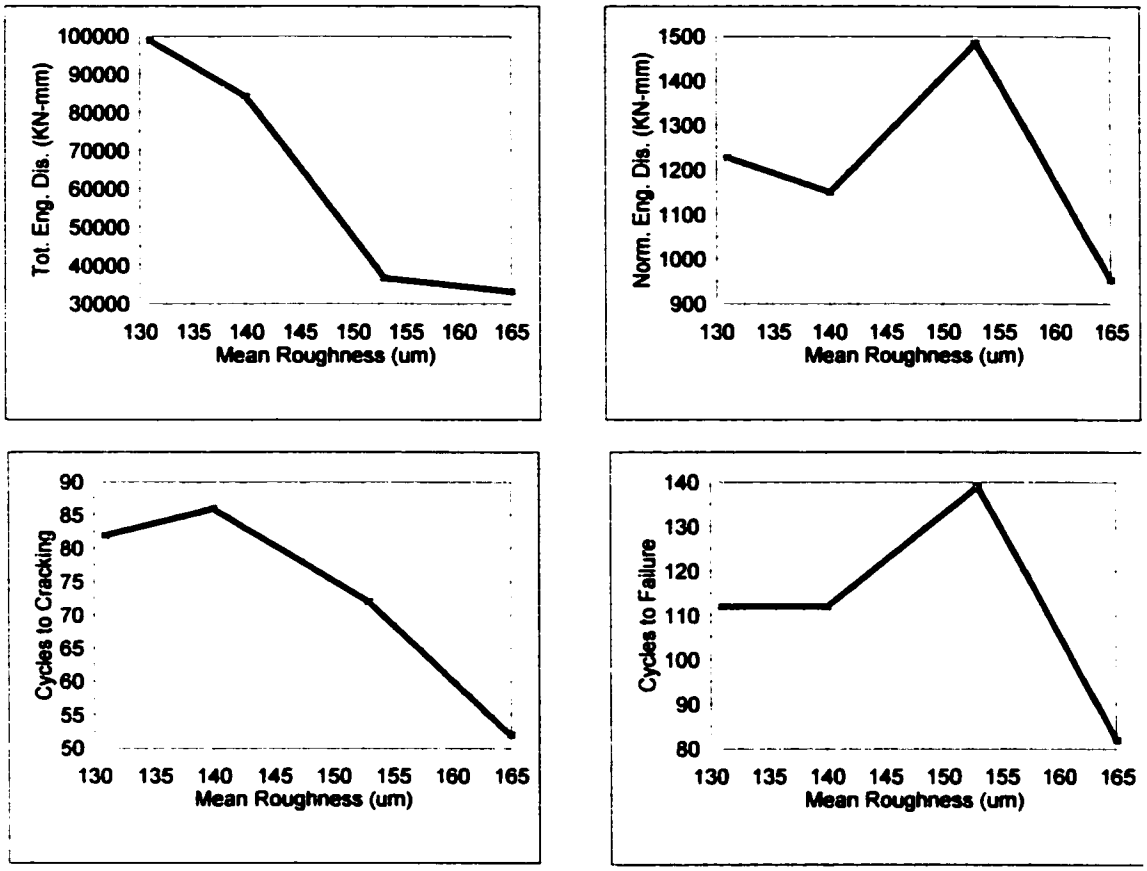

Figure 7.8 Mean Roughness vs. Total Energy Dissipated, Normalized Energy Dissipated, Cycles to Cracking and Cycles to Failure (Tests 1 to 4 Only)

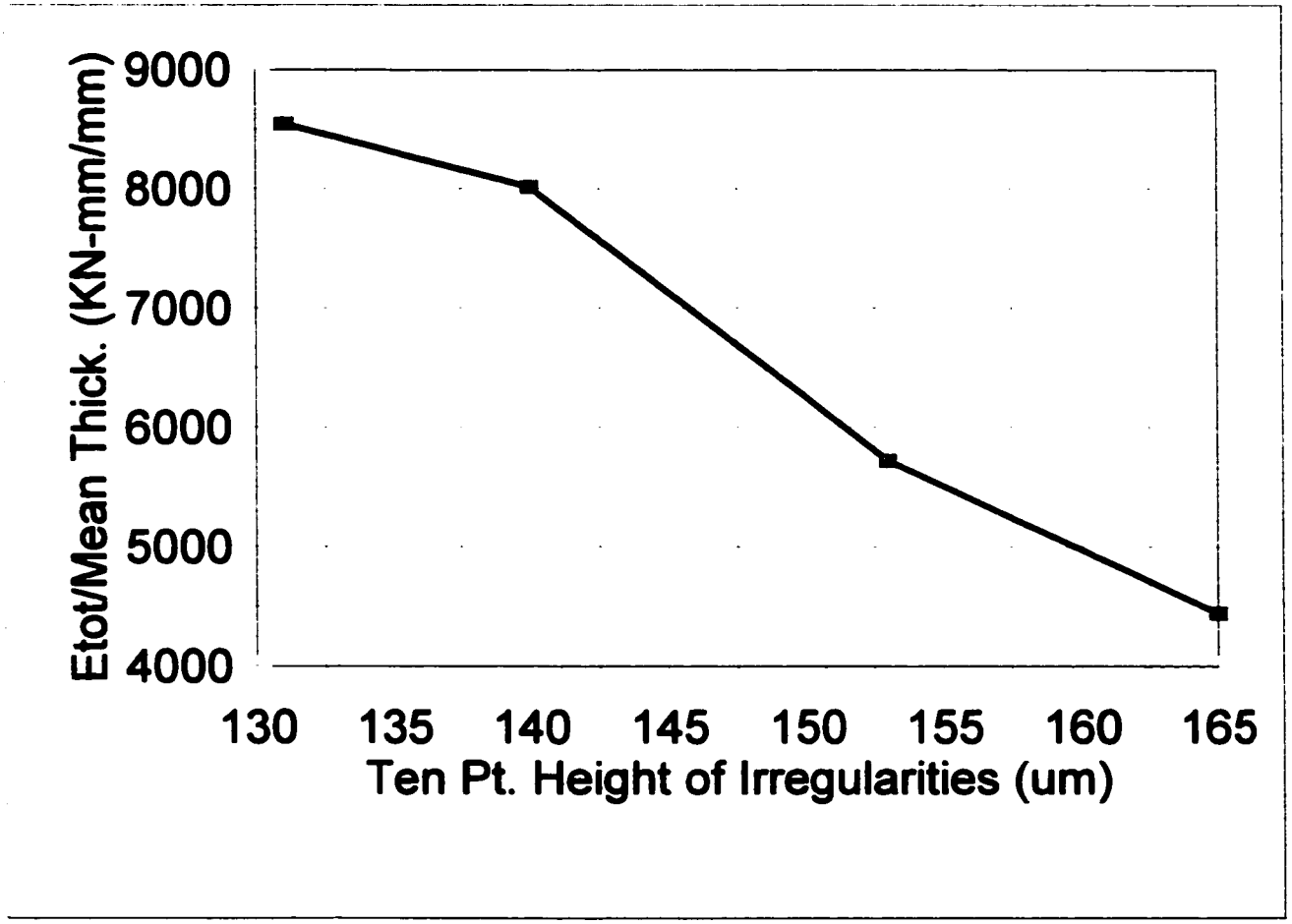

Figure 7.9 Total Energy Dissipated Normalized by Mean Thickness vs. Ten Point Height of Irregularities Roughness (Original Data)

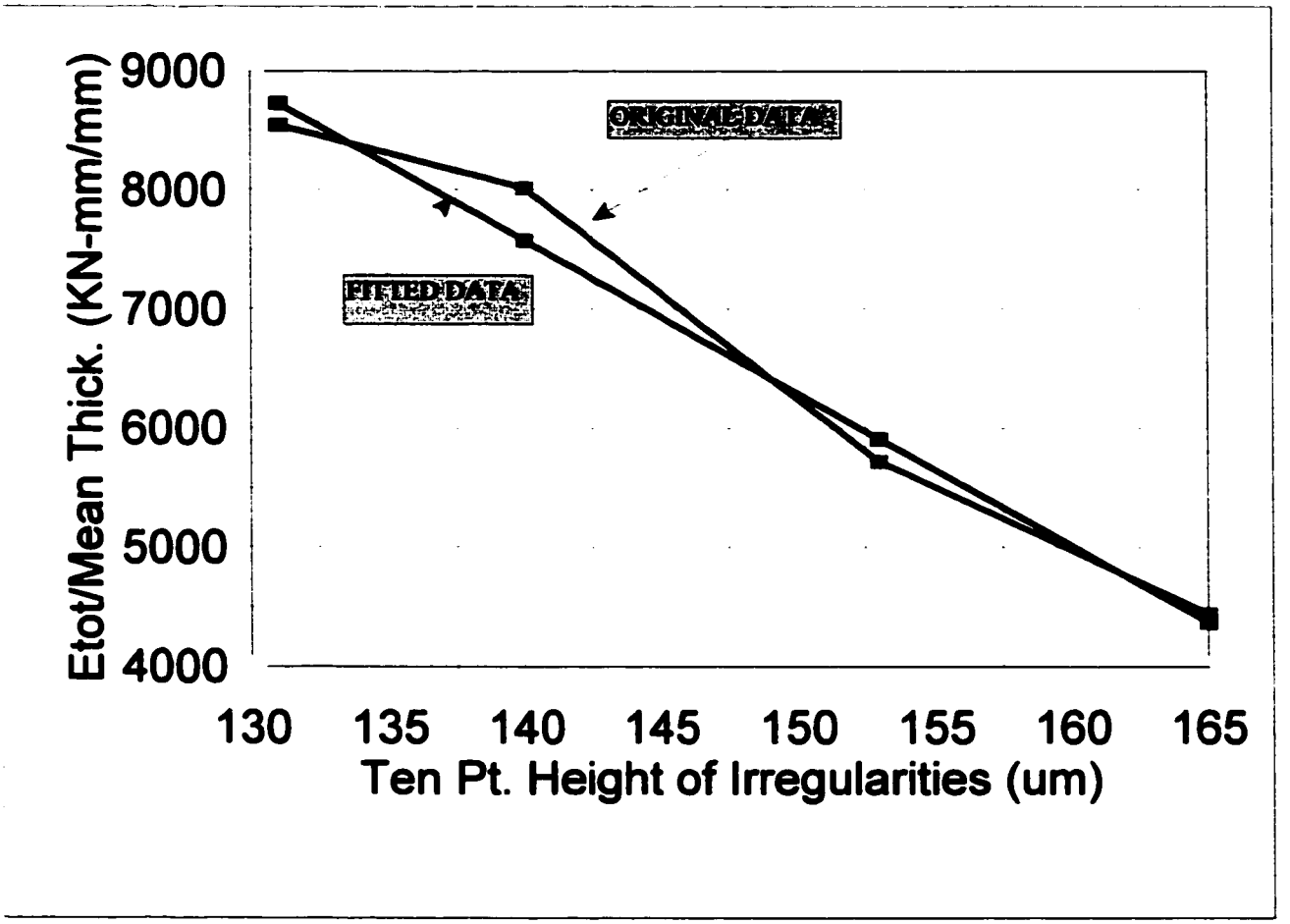

Figure 7.10 Total Energy Dissipated Normalized by Mean Thickness vs. Ten Point Height of Irregularities Roughness (Original Data and Best Fit Linear Curve)